Emergent phenomena in strongly correlated electron systems

Auxiliary particle approach to the many-body problem

Dissertation zur Erlangung des

naturwissenschaftlichen Doktorgrades

der Julius-Maximilians-Universität Würzburg

vorgelegt von

David Riegler

aus Engelskirchen

Würzburg 2022

Eingereicht am 04.03.2022
bei der Fakultät für Physik und Astronomie

1. Gutachter: Prof. Dr. Ronny Thomale
2. Gutachter: Prof. Dr. Titus Neupert
der Dissertation

Vorsitzender: Prof. Dr. Werner Porod

1. Prüfer: Prof. Dr. Ronny Thomale
2. Prüfer: Prof. Dr. Titus Neupert
3. Prüfer: Prof. Dr. Friedrich Reinert
im Promotionskolloquium

Tag des Promotionskolloquiums: 06.05.2022

Dedicated to my family.

We can now see that the whole becomes not merely more, but very different from the sum of its parts.

Philip W. Anderson

Abstract

Emergent phenomena in condensed matter physics like, e.g., magnetism, superconductivity, or non-trivial topology often come along with a surprise and exert great fascination to researchers up to this day. Within this thesis, we are concerned with the analysis of associated types of order that arise due to strong electronic interactions and focus on the high-T_c cuprates and Kondo systems as two prime candidates. The underlying many-body problem cannot be solved analytically and has given rise to the development of various approximation techniques to tackle the problem.

In concrete terms, we apply the auxiliary particle approach to investigate tight-binding Hamiltonians subject to a Hubbard interaction term to account for the screened Coulomb repulsion. Thereby, we adopt the so-called Kotliar-Ruckenstein slave-boson representation that reduces the problem to non-interacting quasiparticles within a mean-field approximation. Part I provides a pedagogical review of the theory and generalizes the established formalism to encompass Gaussian fluctuations around magnetic ground states as a crucial step to obtaining novel results.

Part II addresses the two-dimensional one-band Hubbard model, which is known to approximately describe the physics of the high-T_c cuprates that feature high-temperature superconductivity and various other exotic quantum phases that are not yet fully understood. First, we provide a comprehensive slave-boson analysis of the model, including the discussion of incommensurate magnetic phases, collective modes, and a comparison to other theoretical methods that shows that our results can be massively improved through the newly implemented fluctuation corrections. Afterward, we focus on the underdoped regime and find an intertwining of spin and charge order signaled by divergences of the static charge susceptibility within the antiferromagnetic domain. There is experimental evidence for such inhomogeneous phases in various cuprate materials, which has recently aroused interest because such correlations are believed to impact the formation of Cooper pairs. Our analysis identifies two distinct charge-ordering vectors, one of which can be attributed to a Fermi-surface nesting effect and quantitatively fits experimental data in $Nd_{2-x}Ce_xCuO_4$ (NCCO), an electron-doped cuprate compound. The other resembles the so-called Yamada relation implying the formation of periodic, double-occupied domain walls with a crossover to phase separation for small dopings.

Part III investigates Kondo systems by analyzing the periodic Anderson model and its generalizations. First, we consider Kondo metals and detect weakly magnetized ferromagnetic order in qualitative agreement with experimental observations, which hinders the formation of heavy fermions. Nevertheless, we suggest two different parameter regimes that could host a possible Kondo regime in the context of one or two conduction bands. The part is concluded with the study of topological order in Kondo insulators based on a three-dimensional model with centrosymmetric spin-orbit coupling. Thereby, we classify topologically distinct phases through appropriate $\mathbb{Z}_2$ invariants and consider paramagnetic and antiferromagnetic mean-

field ground states. Our model parameters are chosen to specifically describe samarium hexaboride (SmB_6), which is widely believed to be a topological Kondo insulator, and we identify topologically protected surface states in agreement with experimental evidence in that material. Moreover, our theory predicts the emergence of an antiferromagnetic topological insulator featuring one-dimensional hinge-states as the signature of higher-order topology in the strong coupling regime. While the nature of the true ground state is still under debate, corresponding long-range magnetic order has been observed in pressurized or alloyed SmB_6, and recent experimental findings point towards non-trivial topology under these circumstances. The ability to understand and control topological systems brings forth promising applications in the context of spintronics and quantum computing.

Zusammenfassung

Emergente Phänomene in der Physik der kondensierten Materie, wie z. B. Magnetismus, Supraleitung oder nicht-triviale Topologie gehen oft mit Überraschungen einher und faszinieren Wissenschaftler bis heute. Innerhalb dieser Arbeit befassen wir uns mit der Analyse damit assoziierter Art von Ordnung, die durch starke elektronische Wechselwirkungen entsteht und konzentrieren uns auf die Kuprat-Hochtemperatursupraleiter und Kondo-Systeme als zwei prominente Kandidaten. Das zugrunde liegende Vielteilchenproblem kann nicht analytisch gelöst werden und hat zur Entwicklung vielfältiger Näherungsverfahren geführt, um das Problem anzugehen.

Konkret wenden wir den Hilfsteilchenansatz an, um tight-binding Hamiltonoperatoren zu untersuchen, die einen Hubbard-Wechselwirkungsterm aufweisen, um die abgeschirmte Coulomb-Abstoßung zu berücksichtigen. Dabei benutzen wir die sogenannte Kotliar-Ruckenstein-Slave-Boson-Darstellung, die das Problem im Rahmen einer Molekularfeldnäherung auf nicht-wechselwirkende Quasiteilchen zurückführt. Teil I beinhaltet eine pädagogisch aufgearbeitete Zusammenfassung der Theorie und verallgemeinert durch die Berücksichtigung Gaußscher Fluktuationen um magnetische Grundzustände den etablierten Formalismus, was sich als entscheidender Schritt herausstellt, um neuartige Ergebnisse erzielen zu können.

Teil II befasst sich mit dem zweidimensionalen Einband-Hubbard-Modell, von dem bekannt ist, dass es näherungsweise die Physik der Kuprat-Hochtemperatursupraleiter beschreibt, welche Hochtemperatursupraleitung und verschiedene andere exotische Quantenphasen aufweisen, die noch nicht vollständig verstanden sind. Zunächst machen wir eine ausführliche Slave-Boson-Analyse des Modells, einschließlich der Diskussion inkommensurabler magnetischer Phasen, kollektiver Moden und eines Vergleichs mit anderen theoretischen Methoden, der zeigt, dass unsere Ergebnisse durch die neu implementierten Fluktuationskorrekturen massiv verbessert werden können. Danach konzentrieren wir uns auf den unterdotierten Bereich und finden eine Verflechtung von Spin- und Ladungsordnung, die durch Divergenzen der statischen Ladungssuszeptibilität innerhalb der antiferromagnetischen Domäne signalisiert wird. Es gibt experimentelle Hinweise auf derartige inhomogene Phasen in verschiedenen Kuprat-Materialien, was in letzter Zeit vermehrt Interesse geweckt hat, da angenommen wird, dass entsprechende Korrelationen die Bildung von Cooper-Paaren beeinflussen. Unsere Analyse identifiziert zwei unterschiedliche Ladungsordnungsvektoren, von denen einer einem Fermi-Flächeneffekt zugeschrieben werden kann und quantitativ zu experimentellen Daten von $Nd_{2-x}Ce_xCuO_4$ (NCCO), einer elektronendotierten Kupratverbindung, passt. Der andere erinnert an die sogenannte Yamada-Beziehung und impliziert die Bildung von periodischen, doppelt besetzten Domänenwänden und einem Übergang zu Phasenseperation für kleine Dotierungen.

Teil III untersucht Kondo-Systeme durch Analyse des periodischen Anderson-Modells und seiner Verallgemeinerungen. Zunächst betrachten wir Kondo-Metalle und finden schwach magnetisierte ferromagnetische Ordnung in qualitativer Übereinstimmung mit experimentellen Beobachtungen, welche die Bildung von

schweren Fermionen hemmt. Dennoch identifizieren wir zwei verschiedene Parameterbereiche, die ein mögliches Kondo-Regime im Kontext von einem oder zwei Leitungsbändern beherbergen könnten. Der Teil wird mit der Untersuchung topologischer Ordnung in Kondo-Isolatoren basierend auf einem dreidimensionalen Modell mit zentrosymmetrischer Spin-Bahn-Kopplung abgeschlossen. Dabei klassifizieren wir topologisch unterscheidbare Phasen durch geeignete $\mathbb{Z}_2$-Invarianten und betrachten paramagnetische und antiferromagnetische Molekularfeld-Grundzustände. Unsere Modellparameter wurden gewählt, um insbesondere Samariumhexaborid (SmB_6) zu beschreiben, von dem allgemein angenommen wird, dass es sich um einen topologischen Kondo-Isolator handelt, und wir identifizieren topologisch geschützte Oberflächenzustände in Übereinstimmung mit experimentellen Befunden in diesem Material. Darüber hinaus sagt unsere Theorie die Emergenz eines antiferromagnetischen topologischen Isolators mit eindimensionalen Randzuständen als Merkmal von Topologie höherer Ordnung im Parameterbereich starker Korrelationen voraus. Während das Wesen des korrekten Grundzustands noch umstritten ist, wurde eine entsprechende langreichweitige magnetische Ordnung in unter Druck stehendem oder legiertem SmB_6 beobachtet und kürzliche experimentelle Befunde weisen unter diesen Umständen auf nicht-triviale Topologie hin. Die Fähigkeit, topologische Systeme zu verstehen und zu kontrollieren, bringt vielversprechende Anwendungen im Kontext von Spintronik und Quantencomputing hervor.

Table of contents

CHAPTER 1

Introduction

When it comes to physics, the majority of the general public thinks of black holes or "god particles", whereas the field of condensed matter physics (CMP) rarely attracts broad media attention [1]. Nevertheless, a total of 37 Nobel prizes have been awarded in the context of CMP, and after a rapid growth that started in the second half of the 20th century, it is the largest branch of contemporary physics by now [2]. As we will further elaborate, innovations originating from basic research in CMP have had a tremendous impact on technological progress and society as a whole, shaping our modern way of living in a fundamental way. But what kind of problems does the field actually address? Originally referred to as *solid-state physics*, a major part is the study of insulators, semiconductors, and metals. The term CMP was adopted in the 70s when critical phenomena such as magnetism and superfluidity in the context of quantum mechanics (QM) and the *many-body problem* were brought to attention, making the conception of solid-state physics become insufficient to picture the variety of the field [3]. It features a broad overlap with other scientific subjects like, e.g., chemistry, material science, and nanotechnology and can generally be considered as the discipline of physics examining complex matter [4].

Impact of condensed matter physics

A device that has had a profound impact on technology and society like hardly any other is the transistor, which was invented by John Bardeen, Walter Brattain, and William Shockley at Bell Labs in 1947 within their studies of semiconductors [1]. This electronic building block provides the basis for all modern computers, and after decades of optimization in the industry, in order to create increasingly powerful chips, smartphones have turned into tiny supercomputers that typically contain over 15 billion transistors. Another prominent application of CMP is the digital storage of data on hard disk drives (HDDs) that record information by magnetizing a thin film of a ferromagnetic (FM) material. The emergence of magnetism in solids can be explained by a microscopic degree of freedom in quantum mechanics called *spin*, which can be interpreted like an intrinsic magnetic moment of electrons that aligns parallel for a large number of particles in ferromagnetic crystals in order to form a net magnetic moment. While HDDs are increasingly being replaced by solid-state drives (SSDs), there is also ongoing research on storage devices that use antiferromagnetic (AFM) materials, where spins align anti-parallel rather than parallel. These devices are envisioned to be more robust and much faster than regular HDDs [5], which has evoked the field of *antiferromagnetic spintronics* that aims to manipulate and control the origins of the magnetic order [6].

Another fascinating phenomenon within condensed matter physics is superconductivity (SC), a quantum state of matter discovered in 1911 [7] that can manifest at low temperatures and features a vanishing electrical resistivity with dissipation-less currents. At liquid helium cooling (-268.9°C), this technology is already

applied in medicine to produce strong magnetic fields that are required for magnetic resonance imaging. In 1986, another class of superconductivity with a differing microscopic origin, so-called high-temperature superconductivity (HTS), was discovered. Thereby, the critical temperature to uphold the quantum state was pushed beyond the boiling point of nitrogen (-195.8°C), which significantly simplifies the cooling process [8]. Nevertheless, superconducting materials have, as of now, not found broad applications within electrical grids due to the costly cooling and because the ceramic HTS compounds are not well suited to form electric wires. However, a company in Ismaning has developed a technique to overcome that obstacle and provides HTS material in order to build the longest superconducting cable in the world (12km) as a test project (SuperLink) in Munich [9]. It is expected to finish in 2023 and could, if successful, lead to an adaptation at a larger scale. Furthermore, high-temperature superconductors are also being applied in the context of magnetic levitation and are, e.g., used in the Maglev train that was unveiled in China in 2021 with a peak velocity of up to 620 km/h [10]. Considering the potential of these use cases, it is, of course, a major objective of CMP to achieve a superconducting state at ambient conditions, but such a material is yet to be discovered.

Despite usually being a long frame from theory to practical applications, these examples show that fundamental research can have a tremendous long-term impact, and it is hard to predict which discoveries will become important in the future. Apart from the previously discussed quantum phenomena, Kondo physics and topology have approached the center of attention in the last decade. We will further elaborate on the related properties later on and the exotic quantum states associated with these systems might pave the way towards possible quantum computers in the future [11, 12].

A brief history of condensed matter physics

In order to provide basic knowledge of CMP and present the most crucial achievements of the past century, we start off with a brief historical overview. Its origin traces back to the beginning of the 19th century, with Humphry Davy's studies of electrical and thermal conductivities of the forty chemical elements that were known at that time [13]. However, it was not before 1900 that a first classical theory of electrons in solids was proposed by Paul Drude that was able to explain some of the empirical observations but also came along with serious omissions [14]. The discovery of superconductivity in 1911 by Heike Kamerlingh Onnes [7] came as a surprise and raised even more questions that could ultimately only be explained with the advent of quantum mechanics.

The properties of QM states are determined by the solution of the so-called Schrödinger equation, a linear differential equation proposed by Erwin Schrödinger in 1925: $i\hbar\partial_t |\psi\rangle = \hat{H} |\psi\rangle$ [15]. Based on the Copenhagen interpretation, the absolute square of the wave-function $|\psi\rangle$ yields probabilities over the outcome of measurements of a system, and the Hamilton operator $\hat{H}$ describes its total energy. The corresponding problem for the simplest atom, i.e., hydrogen, which contains one proton and one electron, can be solved analytically. The Hamilton operator of the according *two-body-problem* is decomposed into the kinetic energy of the reduced mass and the Coulomb repulsion between both particles

$$\hat{H} = -\frac{\hbar^2}{2\mu}\nabla_r^2 - \frac{e^2}{4\pi\epsilon_0 r} \,,$$

and the respective solution explained the discrete energy levels of hydrogen that had already been measured via spectroscopy.

The Schrödinger equation for electrons is also bound to the Pauli exclusion principle [16] that dictates that each quantum state cannot be occupied by more than one electron. With the introduction of the *Fermi*

gas of free electrons in 1926 [17, 18], this principle was incorporated into the Drude model, which solved previous omissions like, e.g., the calculation of the electronic specific heat. However, the apparent success of the model was somewhat surprising because it completely neglected interactions between different electrons, and Hendrik Antoon Lorentz once allegedly said: "*In a theory which has given results like these, there must certainly be a great deal of truth*" [19].

Experimental breakthroughs that significantly helped to decipher the composition of solids were achieved by Friedrich *et al.* and Bragg *et al.* in the second decade of the 20th century by means of X-ray diffraction [20, 21]. Their work revealed that most solids are composed of a large number of identical unit cells that align in a regular way to form specific crystal structures. In 1929, Felix Bloch applied a periodic potential to the Schrödinger equation that modeled such a structure and pioneered the immensely successful *band theory* of solids [22]. He was able to show that those potentials initiate dense energy bands of quantum states that are filled successively in accordance with the Pauli principle. The specific band structure (BS) determines most of the key properties of a solid. For example, if there is a finite energy gap between the highest occupied and lowest unoccupied quantum state, we speak of an *insulator* or *semiconductor* because electrons cannot move freely in such a system due to the Pauli principle. In the opposite case, we have a metal, which employs different states at the same energy that form the so-called Fermi surface (FS). This band theory, however, still neglected the Coulomb repulsion between electrons. Lev Landau, with the introduction of Fermi liquid (FL)-theory in 1956 [23], was finally able to give a satisfactory explanation why this enormous simplification was justified in many cases. The essence of this theory is that electrons form quasiparticles (QPs) with well-defined momentum and spin in the presence of interactions that behave like a single electron with renormalized parameters like, e.g., an effective mass.

"More is different"

There are, however, also instances where the effective one-particle description of FL-theory breaks down, and something entirely new emerges as a result of a so-called FS-instability that occurs due to electronic interactions. Philip W. Anderson wrote in his famous essay "More is different" in 1972 on the topic: "*The behavior of large and complex aggregates of elementary particles, it turns out, is not to be understood in terms of a simple extrapolation of the properties of a few particles. Instead, at each level of complexity entirely new properties appear, and the understanding of the new behaviors requires research which I think is as fundamental in its nature as any other*" [24]. Such a system of interacting particles defines the quantum *many-body problem*, where we primarily focus on vast numbers of electrons that interact through the screened Coulomb repulsion.

The emergent behavior manifests in the form of sudden phase transitions that can depend on internal degrees of freedom like the energy scale of the interaction, or an external control parameter, e.g., the temperature. Those transitions have indeed been studied long before the advent of quantum mechanics, with water being an easy-to-grasp example that can be present as ice crystals, liquid, or steam depending on pressure and temperature. A very successful phenomenological theory for quantum phase transitions was introduced by Lev Landau in 1937 [25]. He classified different phases by a *local order parameter* that initiates an ordered phase by reducing symmetries of the original problem due to *spontaneous symmetry breaking*. A prominent illustration is the formation of ferromagnetism. The respective order parameter is the magnetization that can –with some simplification– be understood as the sum of electronic spins, envisioned as compass needles at fixed positions of a crystal lattice. Without interactions, these align randomly such that the net magnetization vanishes. For a ferromagnet, the spins align parallel in a specific direction such that there is a macroscopic magnetic moment in total. Both cases are illustrated in the top panel of Figure 1.1. At first sight, one might

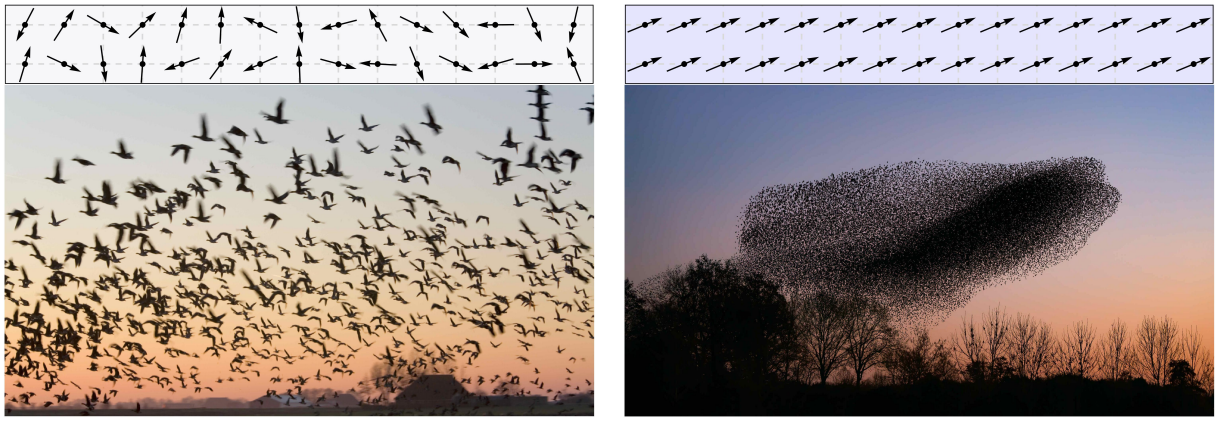

(a) Flying Barnacle geese. Source: Shutterstock.com.

(b) A flock of starlings. Source: Shutterstock.com.

Figure 1.1: A non-magnetic ground state can, at a simplified level, be visualized by randomly oriented spins with no net magnetization. We employ a chaotic movement of birds as a picturesque example for such an unordered state in the classical world. If the birds, however, strongly interact with their neighbors in order to form a flock that makes them more robust to predators, they move coherently as a whole in an ordered fashion. In the quantum world, we call the analog to the flock a collective mode of electrons. In our example of ferromagnetism, it comes along with an interaction-induced parallel alignment of spins, where the carrying electrons are correlated over a macroscopic distance.

claim that the ordered state appears to be more symmetric than the unordered one, but this is actually not true. The non-magnetic state is invariant under continuous spin rotations because the random alignment does not feature a preferential direction, whereas the ferromagnetic ordering spontaneously breaks that symmetry. But why do the spins order? The actual microscopic reasoning is not simple and will be addressed within this thesis, but let us consider a descriptive example from biology that can serve as some sort of analogy. Imagine a large number of flying birds, as illustrated in Figure 1.1. If those only interact weakly with each other, their movement seems unordered and unpredictable. If, however, a flock is formed, they create the impression of moving as a whole rather than individually. In such a state, single birds on opposite sides of the flock are highly correlated due to interactions between neighbored birds that can be extrapolated to large distances. In CMP, we call the analog to the flock a *collective mode* of electrons, or specifically a spin-wave, that correlates spins within a macroscopic distance as a consequence of microscopic, short-ranged interactions. Let us summarize the discussion of ordering phenomena as follows: A phase that emerges due to interaction-induced symmetry breaking brings forth something unprecedented; or to close the circle to Phil Anderson: "*In this case we can see how the whole becomes not only more than but very different from the sum of its parts*" [24].

In the history of interaction-enabled phenomena, first microscopic models to describe ferromagnetism and antiferromagnetism through the electron spin have been introduced by Ernst Ising and Louis E. F. Néel in the first half of the 20th century [26, 27]. A theoretical explanation of *conventional* superconductivity, which is also an interaction-driven quantum state, was provided by John Bardeen, Leon N. Cooper, and John Robert Schrieffer in 1957 with the formation of *Cooper pairs*, almost 50 years after its discovery [28]. However, a comprehensive understanding of the microscopic pairing mechanism of the *unconventional* high-temperature superconductors, discovered in 1986 [8], is still lacking. Another prominent example of strongly correlated electrons are Kondo systems in the context of magnetic impurities. The Kondo effect was first observed with a puzzling resistance minimum of metals at low temperatures in 1934 [29], and a theoretical explanation for a single impurity was given by Jun Kondo in 1964 [30]. For dense Kondo lattices with a periodic arrangement

of impurities, nonetheless, many open questions remain. These can give rise to so-called *heavy fermions*, i.e., quasiparticles that behave like electrons with an up to 1000 times higher effective mass than the bare particle, or Kondo insulators (KIs), i.e., semiconductors that become insulating at low temperatures due to interaction effects. With the discovery of the *quantum hall effect* in 1980 [31], topological systems that feature robust, *topologically protected surface states*, and recently especially topological Kondo insulators (TKIs) [32] have evolved as a major field of research in condensed matter physics. Topological insulators (TIs) are insulating in the interior but can conduct electrons on the boundaries due to their surface modes. Associated phase transitions between distinct topological or non-topological states are described by global properties rather than local order parameters, have initially been described for non-interacting systems, and do not necessarily break symmetries. These insights led to the paradigm shift that there are also types of order beyond Landau's interpretation. Therefore, regarding electronic interactions, one might say with a wink of the eye that "less is also different" sometimes. TKIs, however, are at the interface of strong correlations and topology, and associated phases may combine both: local order parameters and global properties.

Approximation techniques

To study those emergent phenomena, one ideally would like to solve the all-encompassing *many-body* Schrödinger equation that describes positively charged protons (label I, J) and negatively charged electrons (label i, j) with their respective Coulomb interactions and the Hamiltonian

$$\hat{H} = -\frac{\hbar^2}{2m_e}\sum_i^N \nabla_{\boldsymbol{r}_i}^2 - \frac{\hbar^2}{2M}\sum_I^N \nabla_{\boldsymbol{r}_I}^2 + \sum_{i,I}^N \frac{Z_I e^2}{4\pi\epsilon_0 |\boldsymbol{r}_i - \boldsymbol{r}_I|} - \frac{1}{2}\sum_{i,j}^N \frac{e^2}{4\pi\epsilon_0 \left|\boldsymbol{r}_i - \boldsymbol{r}_j\right|} - \frac{1}{2}\sum_{I,J}^N \frac{Z_I Z_J e^2}{4\pi\epsilon_0 \left|\boldsymbol{r}_I - \boldsymbol{r}_J\right|} \,.$$

The complexity of the problem, however, increases exponentially with the number of particles N, and a general analytic solution can only be achieved for the previously discussed *two-body* problem ($N = 2$), whereas a typical macroscopic solid contains electrons in the order of magnitude of $N \gtrsim 10^{23}$. We, therefore, need to rely on approximation techniques that usually aim for a description within statistical physics rather than to address the dynamics of individual particles.

A first simplification that is applied in most cases is the Born–Oppenheimer approximation, which neglects the motion of nuclei and replaces associated terms by a periodic potential that is generated by a static lattice of ions (in analogy to Bloch's approach), such that the problem is reduced to only encompass interactions between electrons. An immensely successful tool to tackle respective Hamiltonians is the density functional theory (DFT), whose development is mainly attributed to Walter Kohn and was awarded the Nobel prize [33]. A strength of DFT is that it requires relatively few assumptions, i.e., it can determine fundamental properties of molecules and solids *ab initio*, which also promoted its popularity in theoretical chemistry or even biology [34]. However, it comes with the downside that it is not suitable to accurately cover the strongly correlated regime and phase transitions in the sense of spontaneously symmetry breaking.

Thus it is required to employ further methods to investigate emergent phenomena in the context of the many-body problem. An approach that has proved to be quite successful is to constrain the spatial electronic degrees of freedom to a discrete set of lattice sites i rather than a continuous variable $\boldsymbol{r}_i$. A kinetic energy scale is then introduced by a matrix element t_{ij} that describes a hopping process from lattice site i to j, whose amplitude can be approximated by means of DFT calculations. Since the screened Coulomb repulsion is maximized when electrons are in close proximity, the simplest form of an effective interaction term is to apply an energy penalty $U > 0$ if two electrons with opposite spin occupy the same lattice site, which leads

up to the Hubbard model [35]

$$H^{\mathrm{Hub}} = -\sum_{<ij>,\sigma}^{N} t_{ij}\, \hat{f}^{\dagger}_{i,\sigma}\hat{f}_{j,\sigma} + U\sum_{i}^{N} \hat{f}^{\dagger}_{i,\uparrow}\hat{f}_{i,\uparrow}\hat{f}^{\dagger}_{i,\downarrow}\hat{f}_{i,\downarrow}\,.$$

In this second quantized notation, $\hat{f}^{\dagger}_{i,\sigma}$ creates an electron on lattice site i with spin $\sigma \in \{\uparrow,\downarrow\}$. The problem is still intriguingly hard to solve, and its inventor John Hubbard once allegedly replied – without even the faintest attempt of a serious explanation – when asked by his mother-in-law what the book he was reading (*The many-body problem*) was about: "*A murder mystery*" [36]. While some of the mysteries have been unraveled by now, others remain, and a plethora of methods have been developed to address Hubbard-type models that are highly relevant up to this day.

Different approximation techniques to investigate this problem of interacting electrons on a lattice have their strengths and weaknesses, respectively, and the nature of the true ground state should ideally be evaluated under the consideration of multiple methods. By so-called exact diagonalization (ED), one may determine properties of the system without additional simplifications, but the approach is limited to small system sizes ($N \lesssim 20$) since the computational expenditure grows exponentially with the number of lattice sites [37]. It is a powerful tool that can also serve as a benchmark for other techniques in certain limits but often suffers from finite-size effects. Quantum Monte Carlo (QMC) simulations are also statistically exact, and the numerical effort scales only polynomially with the system size [38]. There is, however, the so-called sign problem that often limits its applicability to specific parameter regimes. A popular approach that works in the thermodynamic limit and requires less numerical treatment is the mean-field (MF) method, where spatial- and time-dependent fields are approximated by their QM expectation values [39]. On the plus side, this procedure is practicable for arbitrarily strong interactions, allows to explicitly determine ground states of symmetry-broken phases, and often yields analytic expressions that are helpful to gain a physical intuition about the problem. On the other hand, it requires an *a priori* ansatz that limits the possible types of order, and it cannot be ruled out that the severe approximations that come along with this method eliminate essential physical properties of the problem. In order to partially overcome these downsides, the stability of the MF ground state should ideally be analyzed through a fluctuation calculation. Other sophisticated techniques that go beyond mean-field but are limited to finite system sizes or intermediate interaction strength are dynamical mean-field theory (DMFT) [40], density matrix embedding theory (DMET) [41], perturbation theory, and functional renormalization group (FRG) [42].

The auxiliary particle approach

Our method of choice is the *auxiliary particle* approach with a subsequent mean-field treatment plus fluctuation analysis. The basic concept is to rewrite second quantized operators that enter the Hamiltonian with the use of additional auxiliary operators in order to rephrase the problem in a way that is beneficial for consecutive approximations. A bosonic representation of the electronic spin operator proposed by Theodore Holstein and Henry Primakoff in 1940 [43] can be considered as pioneering work in that regard and was later refined by Julian Schwinger [44]. Alexei A. Abrikosov introduced an alternative way to express the spin operator through auxiliary fermionic operators known as pseudofermions in 1965 [45]. Based on these ideas, Stewart E. Barnes and Pierce Coleman formulated representations to investigate Kondo systems in the strongly interacting limit

[46, 47]. Auxiliary particles are better known as *slave-particles* in the scientific community, and we will adopt this term in the following[1].

This thesis will apply an auxiliary particle representation that combines fermionic and bosonic degrees of freedom based on Gabriel Kotilar's and Andrei E. Ruckenstein's approach introduced in 1986 [49], which is designed to address arbitrary interaction strength in contrast to the previous literature. To be specific, we adopt its generalization form known as spin-rotation invariant Kotliar–Ruckenstein (SRIKR) slave-bosons (SBs) [50] that provides a full representation of the spin operator as opposed to the original description, where the spin was projected onto the z-axis. Within a MF approximation of the occurring bosons, lattice models with Hubbard-type interactions become quadratic in fermionic operators, such that the MF Hamiltonian characterizes a renormalized theory of non-interacting quasiparticles. Due to the spin-rotation invariant form, the formalism allows for the implementation of a magnetic order parameter (magnetization) with an arbitrary ordering vector, which can describe ferromagnetism, antiferromagnetism, as well as magnetic order with large unit cells, including incommensurate magnetic order (ICM). Furthermore, we calculate Gaussian fluctuations around the MF ground state that provide a stability analysis through evaluation of the spin and charge susceptibility. The fluctuation formalism will also be applied to determine dynamic excitation spectra like, e.g., the spin-wave dispersion and to calculate leading order corrections to the MF magnetization.

The SRIKR approach is limited to models with one interacting orbital. In the late 2000s, other representations that can handle more than one have been introduced [51, 52], which, however, come along with an enormous increase of complexity and numerical cost.

Outline

Within this thesis, we investigate different microscopic lattice models that feature a Hubbard interaction and evaluate the resulting quantum states in the context of the many-body problem. In order to account for the associated repulsive electron-electron interaction, we apply the SRIKR slave-boson representation with consecutive MF approximation and fluctuation analysis.

Part I derives the SB method from scratch in a pedagogical fashion that is intended to address researchers or students who want to learn the technique or deepen their understanding of condensed matter field theories. We, moreover, extend the established fluctuation formalism to capture magnetic saddle points and models with additional non-interacting orbitals and therefore rely on our broad theoretical foundation to build in those features. If the reader is mainly interested in the applications, that part may be skipped and used as a work of reference. For convenience, the theoretical overhead is kept as short as possible in the subsequent parts of the thesis, where relevant details of the formalism are directly referred to the respective sections of Part I or the appendices in Part IV.

In Part II, we introduce the paradigmatic 2D Hubbard model in the context of the many-body problem as an effective minimal model for the high-T_c cuprates (HTCCs). We provide a comprehensive slave-boson analysis that includes the discussion of Mott physics, magnetically- and charge-ordered phases, phase separation, dynamic excitation spectra, and underlines the consistency between mean-field and fluctuation results. Our evaluation does not explicitly cover superconducting phases because the current SB formalism is not suitable to describe the *unconventional superconductivity* that is observed in these materials. We, however, identify a domain of intertwined spin and charge order that is in excellent agreement with experimental findings of the material $Nd_{2-x}Ce_xCuO_4$ (NCCO) and other electron-doped HTCCs. A deeper understanding of such phases is

[1] To be specific, the term "slave-boson" was proposed to Piers Coleman by Chandra Varma in a conversation at Bell Laboratories in 1983. It was included in a preprint and stuck to the scientific community, although it was removed in the final publication [48].

desirable because they are believed to have a subtle impact on the formation of Cooper pairs, and there has not been much success in increasing T_c since the late 90s.

In Part III, we consider Kondo systems based on the periodic Anderson model (PAM) and its generalizations that can be inferred from the Hubbard model with additional non-interacting orbitals and the possibility of spin-orbit coupling. First, we elaborate on the Kondo effect in the context of different material classes and emphasize its relevance in the present literature regarding experimental findings and theoretical modeling. Afterward, we discuss magnetic order and *heavy fermions* in the PAM and identify a domain of magnetic frustration induced by destructive interference of an effective RKKY-interaction that correlates localized spins mediated by the conduction electrons. Finally, we investigate topological phases in Kondo insulators utilizing a 3D minimal model. Thereby, we detect multiple topologically-distinct phases and study the interplay between topology and magnetism and the emergence of higher-order topology in the strongly correlated regime. Our theoretical predictions qualitatively coincide with experimental evidence in samarium hexaboride (SmB_6), which is widely believed to be a topological Kondo insulator.

The results that are presented within this thesis are partially included in joint publications [53–56] and also complemented by the Ph.D. thesis of Michael Klett [57].

I

Slave-boson theory of correlated electrons

Within this part, we present a pedagogical review of the spin-rotation invariant Kotliar–Ruckenstein (SRIKR) slave-boson (SB) formalism [49, 50] and comment on the historical development of the method and possible omissions. We moreover extend the established theory to encompass fluctuations about magnetic mean-field (MF) saddle points with additional non-interacting orbitals.

Chapter 2 derives the SB representation on operator level and introduces necessary constraints, which are implemented within the field-theoretical description of Chapter 3 to recover the physical subspace. Subsequently, Chapter 4 defines a magnetic MF ansatz that reduces models of interacting electrons with a quartic Hubbard-term to a renormalized, effectively non-interacting theory within the approximation. We then derive important quantities of statistical physics like, e.g., the free energy, magnetization, and electronic compressibility. Finally, Chapter 5 presents the (para-)magnetic fluctuation calculation that can, e.g., be applied to investigate the MF stability by an analysis of the spin and charge susceptibility. We moreover discuss the onset of possible phase separation (PS) that can consistently be determined from the MF and fluctuation results.

The content of this part has partially been published in References [53] and [55].

CHAPTER 2

Slave-boson formalism on operator level

Kotliar–Ruckenstein (KR) slave-bosons (SBs), originally introduced in 1986 [49], are designed to tackle interacting electrons on a lattice with a quartic Hubbard-type interaction [35, 58], whose ground state can in general not be determined exactly in the thermodynamic limit. The problem is thus treated approximately within a mean-field (MF) treatment, where the interaction becomes quadratic in auxiliary bosonic fields. The theory was refined in the 90s to consider Gaussian fluctuations around paramagnetic PM ground states for the Hubbard model [59–61] and recently generalized to consider magnetic saddle points with additional non-interacting orbitals [55, 56].

This theory is, therefore, well-suited to investigate the Hubbard model and variations of the periodic Anderson model (PAM) [62, 63] that yield from the implementation of additional conduction orbitals. Our according results in the context of the high-T_c cuprates and Kondo materials are presented in Parts II and III. To derive the theory in a consistent notation, we define the general Hamiltonian

$$\hat{H} = \hat{H}_{\text{Hub.}} + \hat{H}_{\text{cond.}} + \hat{H}_{\text{hyb.}} \tag{2.1}$$

with

$$\hat{H}_{\text{Hub.}} = \sum_{\sigma\sigma'} \sum_{i\neq j} \hat{f}^\dagger_{i,\sigma} t^f_{ij,\sigma\sigma'} \hat{f}_{j,\sigma'} + (\epsilon_f - \mu_0) \sum_{i,\sigma} \hat{f}^\dagger_{i,\sigma} \hat{f}_{i,\sigma} + U \sum_i \hat{f}^\dagger_{i,\uparrow} \hat{f}_{i,\uparrow} \hat{f}^\dagger_{i,\downarrow} \hat{f}_{i,\downarrow} \,, \tag{2.2a}$$

$$\hat{H}_{\text{cond.}} = \sum_{\sigma\sigma'} \left[\sum_{o=1}^{O} \sum_{i\neq j} \hat{c}^\dagger_{o,i,\sigma} t^o_{ij,\sigma\sigma'} \hat{c}_{o,j,\sigma'} + \sum_{o\neq o'}^{O} \sum_{ij} \left(\hat{c}^\dagger_{o,i,\sigma} \tilde{V}^{oo'}_{ij,\sigma\sigma'} \hat{c}_{j,\sigma'} + \text{h.c.} \right) \right] + \sum_{i,\sigma,o} (\epsilon_o - \mu_0)\, \hat{c}^\dagger_{o,i,\sigma} \hat{c}_{o,i,\sigma} \,, \tag{2.2b}$$

$$\hat{H}_{\text{hyb.}} = \sum_{\sigma\sigma'} \sum_{o=1}^{O} \sum_{ij} \left(\hat{c}^\dagger_{o,i,\sigma} V^{of}_{ij,\sigma\sigma'} \hat{f}_{j,\sigma'} + \text{h.c.} \right) \tag{2.2c}$$

in second quantization [64, 65]. In that notation, interacting electrons on lattice site i with spin $\sigma = \pm 1/2$ are created (annihilated) by the operator $\hat{f}^\dagger_{i,\sigma}$ ($\hat{f}_{i,\sigma}$) and non-interacting electrons at site i, spin σ and orbital o are created (annihilated) by $\hat{c}^\dagger_{o,i,\sigma}$ ($\hat{c}_{o,i,\sigma}$). Hopping amplitudes between different lattice sites $i \neq j$ are denoted by t^f, t^o, and the hybridization of conduction orbitals with the interacting orbital is given by V. Our theory also allows for spin-orbit coupling (SOC) and additional hybridizations between the conduction orbitals ($\tilde{V}$). Finally, U defines the strength of the Hubbard interaction, ϵ_f (ϵ^o) characterizes on-site potentials of the different orbitals that account for the crystal field of the lattice, and μ_0 represents the chemical potential that controls the total electron filling.

The usual anticommutation relations for fermionic operators that comply with the Pauli principle[1]

$$\begin{aligned}\left[\hat{c}_{o,i,\sigma}\ ,\ \hat{c}^{\dagger}_{o',j,\sigma'}\right]_{+} &= \delta_{oo'}\delta_{ij}\delta_{\sigma\sigma'}\ ,\\ \left[\hat{c}^{\dagger}_{o,i,\sigma}\ ,\ \hat{c}^{\dagger}_{o',j,\sigma'}\right]_{+} &= \left[\hat{c}_{o,i,\sigma}\ ,\ \hat{c}_{o',j,\sigma'}\right]_{+} = 0\ ,\end{aligned} \tag{2.3}$$

dictate a four-dimensional Hilbert space per lattice site and orbital, where an orbital-site can either be empty ($|\mathrm{vac}\rangle$), singly ($|\sigma\rangle$), or doubly occupied ($|2\rangle$). The respective states are created or annihilated by the fermionic ladder operators[2]

$$\begin{aligned}&|\mathrm{vac}\rangle\ , && \hat{c}_{\pm\sigma}\,|\mathrm{vac}\rangle = 0\ ,\\ &|\sigma\rangle = \hat{c}^{\dagger}_{\sigma}\,|\mathrm{vac}\rangle\ , && \hat{c}_{-\sigma}\,|-\sigma\rangle = |\mathrm{vac}\rangle\ ,\\ &|2\rangle = \hat{c}^{\dagger}_{\sigma}\hat{c}^{\dagger}_{-\sigma}\,|\mathrm{vac}\rangle\ , && \hat{c}_{\sigma}\,|2\rangle = |-\sigma\rangle\ .\end{aligned} \tag{2.4}$$

and the full Fock state is given by the tensor product over all sites and orbitals.

With the SB representation, we introduce auxiliary bosonic fields and construct the physical states by a combination of fermionic and bosonic ladder operators and the implementation of additional constraints. As we will show, the interaction term then becomes quadratic in bosonic operators at the cost of a more complicated hopping scheme that, however, also remains quadratic w.r.t. fermionic degrees of freedom. While the original Kotliar–Ruckenstein slave-boson representation [49] breaks spin-rotation symmetry [49], a generalization known as spin-rotation invariant Kotliar–Ruckenstein (SRIKR) slave-boson (SB) scheme was introduced shortly after [50, 66] to overcome that flaw. It provides a complete, bosonic representation of the spin operator, which allows for the treatment of SOC, incommensurate magnetic order (ICM) and a distinction between longitudinal and transversal spin excitation as main advantages over the simplified KR representation[3].

Adopting the SRIKR scheme, we introduce six bosonic operators $\hat{e}_i$, $\hat{p}_{0,i}$, $\hat{\boldsymbol{p}}_i = (\hat{p}_{x,i}, \hat{p}_{y,i}, \hat{p}_{z,i})$ and $\hat{d}_i$ per lattice site[4] i, which are associated with empty, singly and doubly occupied states, and two new auxiliary fermionic operators $\hat{f}_{i,\uparrow}$, $\hat{f}_{i,\downarrow}$, which are referred to as pseudofermions (PFs) in the following. Within this representation, we create the states of the Hilbert space by

$$|0\rangle = \hat{e}^{\dagger}\,|\mathrm{vac}\rangle\ , \tag{2.5a}$$

$$|\sigma\rangle = \sum_{\sigma'} \hat{p}^{\dagger}_{\sigma\sigma'}\hat{f}^{\dagger}_{\sigma'}\,|\mathrm{vac}\rangle\ , \tag{2.5b}$$

$$|2\rangle = \hat{d}^{\dagger}\hat{f}^{\dagger}_{\uparrow}\hat{f}^{\dagger}_{\downarrow}\,|\mathrm{vac}\rangle\ . \tag{2.5c}$$

Notice that opposed to the representation in Equation (2.4), we explicitly distinguish between the vacuum and empty state, since the latter contains an $\hat{e}$-boson. The occurring fermionic $\hat{f}_{i,\sigma}$ and bosonic $\hat{b}_{\alpha,i} \in \left\{\hat{e}_i, \hat{p}_{0,i}, \hat{\boldsymbol{p}}_i, \hat{d}_i\right\}$ operators fulfill the usual (anti-)commutation relations and consequently, any annihilation

[1] The (anti-)commutator is defined by $\left[\hat{A}\ ,\ \hat{B}\right]_{\pm} = \hat{A}\hat{B} \pm \hat{B}\hat{A}$.

[2] The same also holds for the interacting electrons $\hat{f}^{\dagger}_{\sigma}$.

[3] A further generalization is the spin- and charge-rotation invariant Kotliar–Ruckenstein (SCRIKR) SB representation [50], which makes it possible to address the particle-particle channel and has been applied in the context of conventional superconductivity [67, 68]. For the applications in this thesis, however, the SRIKR SB scheme is sufficient.

[4] The lattice site index will be dropped for better readability in the following and it is implied that all operators act on the same site, if it is not explicitly shown.

operator applied to the vacuum vanishes

$$\begin{aligned} \left[\hat{f}_{i,\sigma}\,,\,\hat{f}^{\dagger}_{j,\sigma'}\right]_{+} &= \delta_{\sigma\sigma'}\,\delta_{ij}\,, \quad \left[\hat{f}_{i,\sigma}\,,\,\hat{f}_{j,\sigma'}\right]_{+} = \left[\hat{f}^{\dagger}_{i,\sigma}\,,\,\hat{f}^{\dagger}_{j,\sigma'}\right]_{+} = 0\,, \\ \left[\hat{b}_{\alpha,i}\,,\,\hat{b}^{\dagger}_{\beta,j}\right]_{-} &= \delta_{\alpha\beta}\,\delta_{ij}\,, \quad \left[\hat{b}_{\alpha,i}\,,\,\hat{b}_{\beta,j}\right]_{-} = \left[\hat{b}^{\dagger}_{\alpha,i}\,,\,\hat{b}^{\dagger}_{\beta,j}\right]_{-} = 0\,, \\ \left[\hat{f}^{(\dagger)}_{i,\sigma}\,,\,\hat{b}^{(\dagger)}_{\alpha,i}\right]_{-} &= 0\,, \qquad \hat{b}_{\alpha,i}\,|\mathrm{vac}\rangle = 0\,, \quad \hat{f}_{\sigma,i}\,|\mathrm{vac}\rangle = 0\,. \end{aligned} \tag{2.5d}$$

In Section 2.1, we will derive the explicit form of the matrix $\hat{p}^{\dagger}_{\sigma\sigma'}$ and subsequently the fermionic ladder operator in SB representation. Afterward, we will learn in Section 2.2 that additional constraints are required to exclude unphysical states and that the SB representation is an exact mapping of the original problem on this constrained subspace. Moreover, we show how to enforce these constraints and their impact on gauge symmetries. Finally, in Section 2.3 we investigate how important fermionic operators are expressed utilizing the new SB and PF degrees of freedom.

2.1 Slave-boson representation

In order to transfer Hamiltonians into the SB picture, we need to derive the bosonic form of the $\hat{p}^{\dagger}_{\sigma\sigma'}$-matrix and find the SB representation of the fermionic ladder operator $\hat{f}^{(\dagger)}_{\sigma}$, which we do in the following based on References [50] and [53].

2.1.1 Construction of the p-matrix

Empty and doubly occupied sites transform like scalars under spin rotation, whereas the singly occupied state is required to transform like a spinor with a spin of $S = 1/2$ and can consequently $\hat{p}^{\dagger}_{\sigma\sigma'}$ be represented by a 2×2 matrix. The total spin per site yields from addition of the PF ($S_f = 1/2$) and bosonic spin, we thus introduce a spin zero ($S_{p_0} = 0$) scalar boson $\hat{p}_0$ and a spin one ($S_p = 1$) vector boson $\hat{\boldsymbol{p}} = (\hat{p}_x, \hat{p}_y, \hat{p}_z)$ and need to find a superposition such that the total spin is always $1/2$. The irreducible representation for the spin-one operator is given by [69, 70]

$$\hat{\underline{S}} = \begin{pmatrix} \underline{S}^x \\ \underline{S}^y \\ \underline{S}^z \end{pmatrix}, \quad \text{with} \quad \underline{S}^x = \frac{1}{\sqrt{2}}\begin{pmatrix} 0 & 1 & 0 \\ 1 & 0 & 1 \\ 0 & 1 & 0 \end{pmatrix}, \quad \underline{S}^y = \frac{1}{\sqrt{2}}\begin{pmatrix} 0 & -\mathrm{i} & 0 \\ \mathrm{i} & 0 & -\mathrm{i} \\ 0 & \mathrm{i} & 0 \end{pmatrix}, \quad \underline{S}^z = \begin{pmatrix} 1 & 0 & 0 \\ 0 & 0 & 0 \\ 0 & 0 & -1 \end{pmatrix}. \tag{2.6a}$$

We choose the $\boldsymbol{p}^{\dagger}$ operator to create a bosonic spin-one state, which is polarized towards the x, y and z direction in Cartesian coordinates with the magnetic quantum number $m = 0$ respectively, yielding the spinors

$$\chi_x = \frac{1}{\sqrt{2}}\begin{pmatrix} -1 \\ 0 \\ 1 \end{pmatrix}, \qquad \chi_y = \frac{1}{\sqrt{2}}\begin{pmatrix} \mathrm{i} \\ 0 \\ \mathrm{i} \end{pmatrix}, \qquad \chi_z = \begin{pmatrix} 0 \\ 1 \\ 0 \end{pmatrix}, \quad \text{with} \quad \underline{S}^{\alpha}\,|\chi_{\alpha}\rangle = 0\,. \tag{2.6b}$$

The relative phases of this orthonormal basis of the spin Hilbert space with $\langle\chi_{\alpha}|\chi_{\beta}\rangle = \delta_{\alpha\beta}$ are chosen such that the spinors are consistent under spin rotations by the angle ϕ, which are generated by the operator $\hat{\underline{U}}_{\phi} = \mathrm{e}^{-\mathrm{i}\phi\hat{\underline{S}}}$ [69, 70]

$$\chi_y = \mathrm{e}^{-\mathrm{i}\frac{\pi}{2}\underline{S}^z}\chi_x\,, \quad \chi_z = \mathrm{e}^{-\mathrm{i}\frac{\pi}{2}\underline{S}^x}\chi_y\,, \quad \chi_x = \mathrm{e}^{-\mathrm{i}\frac{\pi}{2}\underline{S}^y}\chi_z\,. \tag{2.6c}$$

In order to add spins, we conveniently apply the basis of eigenstates of the $\underline{S}^z$-operator $\hat{p}_{S=1,m}$, with $m \in \{-1, 0, 1\}$, which is given by the superposition

$$\hat{p}_{1,1} = -\frac{1}{\sqrt{2}}\left(\hat{p}_x + \mathrm{i}\hat{p}_y\right) , \quad \hat{p}_{1,0} = \hat{p}_z , \quad \hat{p}_{1,-1} = \frac{1}{\sqrt{2}}\left(\hat{p}_x - \mathrm{i}\hat{p}_y\right) . \tag{2.6d}$$

Consequently a state with total spin of $S = 1/2$, decomposed by the PF $\hat{f}_{\sigma'}$ ($S_f = 1/2$) and the vector boson $\hat{p}_{1,m}$ ($S_p = 1$) is given by [50]

$$|\sigma\rangle_{S=1/2} = \sum_{\sigma'=\pm\frac{1}{2}} C\left(S_p = 1, S_f = 1/2\,;\, m_p = \sigma - \sigma', m_f = \sigma' \,\middle|\, S = 1/2\,;\, \sigma\right) \hat{p}^\dagger_{1,m_p} \hat{f}^\dagger_{\sigma'} |\mathrm{vac}\rangle = \sum_{\sigma'=\pm 1/2} \left(\hat{p}^\dagger_{S=1}\right)_{\sigma\sigma'} \hat{f}^\dagger_{\sigma'} |\mathrm{vac}\rangle \ , \tag{2.6e}$$

with $\sigma = \pm 1/2$ and the Clebsch-Gordon coefficients [70]

$$C\left(1, 1/2\,;\, \sigma \mp 1/2, \pm 1/2 \,\middle|\, 1/2, \sigma\right) = \mp\sqrt{\frac{3 \mp 2\sigma}{6}} . \tag{2.6f}$$

In accordance with Equation (2.6e), we express the bosonic degrees of freedom in a convenient matrix notation

$$\underline{\hat{p}}^\dagger_{S=1} = \begin{pmatrix} -\sqrt{\frac{1}{3}}\hat{p}^\dagger_{1,0} & \sqrt{\frac{2}{3}}\hat{p}^\dagger_{1,1} \\ -\sqrt{\frac{2}{3}}\hat{p}^\dagger_{1,-1} & \sqrt{\frac{1}{3}}\hat{p}^\dagger_{1,0} \end{pmatrix}, \tag{2.6g}$$

and apply the PF basis

$$\hat{f}^\dagger = \begin{pmatrix} \hat{f}^\dagger_\uparrow , & \hat{f}^\dagger_\downarrow \end{pmatrix} . \tag{2.6h}$$

Finally, we need to consider the contribution of the $\hat{p}_0$-boson, which acts diagonally in spin space as a superposition, yielding

$$\underline{\hat{p}}^\dagger = \begin{pmatrix} \mathfrak{a}\hat{p}^\dagger_0 + \mathfrak{b}\hat{p}^\dagger_z & \mathfrak{b}(\hat{p}^\dagger_x - \mathrm{i}\hat{p}^\dagger_y) \\ \mathfrak{b}(\hat{p}^\dagger_x + \mathrm{i}\hat{p}^\dagger_y) & \mathfrak{a}\hat{p}^\dagger_0 - \mathfrak{b}\hat{p}^\dagger_z \end{pmatrix} . \tag{2.6i}$$

The coefficients $\mathfrak{a}$ and $\mathfrak{b}$ are constrained by the normalization condition[1]

$$\sum_{\sigma'\sigma''} \langle \mathrm{vac}| \hat{f}_{\sigma''} \hat{p}_{\sigma''\sigma} \hat{p}^\dagger_{\sigma\sigma'} \hat{f}^\dagger_{\sigma'} |\mathrm{vac}\rangle = 1 , \tag{2.6j}$$

with $\sigma = \pm 1/2$, i.e., we need to enforce $3\mathfrak{b}^2 + \mathfrak{a}^2 = 1$ and ratio $\mathfrak{a}/\mathfrak{b}$ is a free parameter. We choose $\mathfrak{a} = \mathfrak{b} = 1/2$ and finally find[2]

$$\underline{\hat{p}}^\dagger = \frac{1}{2}\sum_{\mu=0}^{3} \hat{p}^\dagger_\mu \underline{\tau}^\mu = \frac{1}{2}\begin{pmatrix} \hat{p}^\dagger_0 + \hat{p}^\dagger_z & \hat{p}^\dagger_x - \mathrm{i}\hat{p}^\dagger_y \\ \hat{p}^\dagger_x + \mathrm{i}\hat{p}^\dagger_y & \hat{p}^\dagger_0 - \hat{p}^\dagger_z \end{pmatrix} , \tag{2.7a}$$

$$\underline{\hat{p}} = \frac{1}{2}\sum_{\mu=0}^{3} \hat{p}_\mu \underline{\tau}^\mu = \frac{1}{2}\begin{pmatrix} \hat{p}_0 + \hat{p}_z & \hat{p}_x - \mathrm{i}\hat{p}_y \\ \hat{p}_x + \mathrm{i}\hat{p}_y & \hat{p}_0 - \hat{p}_z \end{pmatrix} , \tag{2.7b}$$

[1] In early works featuring SRIKR SB formalism, this normalization was not chosen correctly, leading to a prefactor of $1/\sqrt{2}$ instead of $1/2$ in Equation (2.7) [59, 66, 71, 72]. This was corrected in Reference [50].
[2] In the following notation, we identify the Cartesian coordinates x, y, z with the numbers $1, 2, 3$.

where $\underline{\tau}^\mu$ is the four-vector of Pauli matrices, including the identity matrix $\underline{\tau}^0 = \underline{\mathbb{1}}_2$. The commutator of these matrix operators is found to be

$$\left[\hat{p}_{\sigma_1\sigma_2}\,,\,\hat{p}^\dagger_{\sigma_3\sigma_4}\right]_- = \frac{1}{2}\delta_{\sigma_1\sigma_4}\delta_{\sigma_2\sigma_3}. \tag{2.7c}$$

2.1.2 Fermionic ladder operators

The fermionic ladder operator can formally be expressed as

$$\hat{f}^\dagger_\sigma = |\sigma\rangle\langle 0| + \mathrm{sgn}(\sigma)\,|2\rangle\langle -\sigma|\ . \tag{2.8}$$

With Equations (2.5b) and (2.7a), we have the tools to create an electron with spin σ in an empty side and thus a representation of the first term of Equation (2.8). For the second term, we need a matrix operator $\underline{\hat{p}}$, which removes a $\hat{\boldsymbol{p}}$-boson with opposite spin, which is given by[1]

$$\hat{\tilde{p}}_{\sigma\sigma'} = \mathrm{sgn}(\sigma)\,\mathrm{sgn}(\sigma')\hat{p}_{-\sigma'-\sigma} = \frac{1}{2}\left(\hat{p}_0\tau^0_{\sigma\sigma'} - \sum_{\mu=1}^{3}\hat{p}^\mu_{\sigma\sigma'}\right). \tag{2.9}$$

Consequently, we can express the ladder operators of the interacting electrons in SB representation by [50]

$$\hat{f}^\dagger_\sigma = \sum_{\sigma'}\hat{z}^\dagger_{\sigma\sigma'}\hat{f}^\dagger_{\sigma'}\,, \tag{2.10a}$$

$$\hat{f}_\sigma = \sum_{\sigma'}\hat{f}_{\sigma'}\hat{z}_{\sigma'\sigma}\,, \tag{2.10b}$$

with

$$\hat{z}^\dagger_{\sigma\sigma'} = \hat{p}^\dagger_{\sigma\sigma'}\hat{e} + \hat{d}^\dagger\hat{\tilde{p}}_{\sigma\sigma'}\,, \tag{2.11a}$$

$$\hat{z}_{\sigma\sigma'} = \hat{e}^\dagger\hat{p}_{\sigma\sigma'} + \hat{\tilde{p}}^\dagger_{\sigma\sigma'}\hat{d}\,. \tag{2.11b}$$

In Section 2.2, we will show that this representation of interacting electrons becomes exact with the addition of specific constraints to the Fock space. We identify $\hat{\tilde{p}}_{\sigma\sigma'}$ with the time reversed operator of $\hat{p}_{\sigma\sigma'}$. Fermionic operators transform under time-reversal (TR) as

$$\hat{\mathcal{T}}\hat{f}_\uparrow\hat{\mathcal{T}}^{-1} = \hat{f}_\downarrow\,,\quad \hat{\mathcal{T}}\hat{f}_\downarrow\hat{\mathcal{T}}^{-1} = -\hat{f}_\uparrow \tag{2.12a}$$

where $\hat{\mathcal{T}}$ denotes the anti-unitary TR-operator. The behavior of the PF and SB fields under TR can be inferred by expressing Equation (2.12a) with the SB representation of Equation (2.10) and comparing terms. We find [53]

$$\hat{\mathcal{T}}\hat{p}_0\hat{\mathcal{T}}^{-1} = \hat{p}_0\,,\quad \hat{\mathcal{T}}\hat{\boldsymbol{p}}\hat{\mathcal{T}}^{-1} = -\hat{\boldsymbol{p}}\,,\quad \hat{\mathcal{T}}\hat{e}\hat{\mathcal{T}}^{-1} = \hat{e}\,,\quad \hat{\mathcal{T}}\hat{d}\hat{\mathcal{T}}^{-1} = \hat{d}\,,\quad \hat{\mathcal{T}}\hat{f}_\uparrow\hat{\mathcal{T}}^{-1} = \hat{f}_\downarrow\,,\quad \hat{\mathcal{T}}\hat{f}_\downarrow\hat{\mathcal{T}}^{-1} = -\hat{f}_\uparrow\,, \tag{2.12b}$$

which is the expected result, considering that $\hat{p}_0$ represents a spin-singlet and $\hat{\boldsymbol{p}}$ a spin-triplet.

[1] In this notation $\sigma \to -\sigma$ corresponds to a spin flip i.e., an interchange of rows/columns of the according 2×2 matrix.

2.2 Constraints

In the following section, we will learn which constraints need to be enforced such that the SB representation that combines fermionic and bosonic degrees of freedom is an exact mapping of the original purely fermionic problem. Afterward, we show how to practically enforce these constraints and discuss their impact on gauge symmetries.

2.2.1 Exact recovery of the physical Hilbert space

Accounting for the fermionic anticommutators of the PFs and bosonic commutators of the SB operators, a general state is given by

$$|\mathrm{SB}\rangle = \prod_{s=\pm 1/2} \left(\hat{f}_s^\dagger\right)^{m_s} \prod_{\substack{b\in\{e,p_0,p_1,\\ p_2,p_3,d\}}} \frac{\left(\hat{b}^\dagger\right)^{n_b}}{\sqrt{n_b!}} |\mathrm{vac}\rangle \ , \tag{2.13}$$

with $m_s \in \{0,1\}$ and $n_b \in \mathbb{N}_0$. This general form contains unphysical states that are not designated by Equation (2.5) and need to be excluded by adequate constraints. To recover the physical subspace, we must first guarantee that every site is occupied by exactly one boson. Secondly, PF and SB degrees of freedom need to be coupled such that the remaining other forbidden states are eliminated. These two conditions can be fulfilled by enforcing [50, 66]

$$1 = \hat{e}^\dagger \hat{e} + \hat{d}^\dagger \hat{d} + \sum_{\mu=0}^{3} \hat{p}_\mu^\dagger \hat{p}_\mu \ , \tag{2.14a}$$

$$\hat{f}_{\sigma'}^\dagger \hat{f}_\sigma = 2 \sum_{\sigma_1} \hat{p}_{\sigma_1\sigma}^\dagger \hat{p}_{\sigma'\sigma_1} + \delta_{\sigma\sigma'} \hat{d}^\dagger \hat{d} \ , \tag{2.14b}$$

on each lattice site. Equation (2.14b) can be rewritten as four scalar equations by expanding in Pauli matrices (i.e., applying $\sum_{\sigma\sigma'} \tau^\mu_{\sigma\sigma'}$ on both sides of the equation) which also allows for a more intuitive interpretation[1]

$$\sum_\sigma \hat{f}_\sigma^\dagger \hat{f}_\sigma = \sum_{\mu=0}^{3} \hat{p}_\mu^\dagger \hat{p}_\mu + 2\hat{d}^\dagger \hat{d} \ , \tag{2.14c}$$

$$\sum_{\sigma\sigma'} \boldsymbol{\tau}_{\sigma\sigma'} \hat{f}_{\sigma'}^\dagger \hat{f}_\sigma = \hat{p}_0^\dagger \hat{\boldsymbol{p}} + \hat{\boldsymbol{p}}^\dagger \hat{p}_0 - \mathrm{i}\hat{\boldsymbol{p}}^\dagger \times \hat{\boldsymbol{p}} \ . \tag{2.14d}$$

The *first constraint* defined in Equation (2.14a) can be interpreted to uphold the Pauli principle because it excludes higher occupations. It comes along with important implications that greatly simplify many different calculations. Specifically, two bosonic annihilation (creation) operators to the very right (left) of an expression annihilate every state on the physical subspace, i.e., those terms are zero, which will be exploited in the following. The *second constraint* given by Equation (2.14c) matches the charge density of PFs and SBs in accordance with Equation (2.5). The *third constraint* in Equation (2.14d) relates the spin of PFs and SBs in agreement with Equation (2.6e). In Section 2.3, we will learn that it correlates the spin operator of PFs and SBs, i.e., a spin flip in PFs needs to be accompanied by a spin flip in SBs.

[1] In early works [59, 66, 71], the indices of the Paul matrix in Equation (2.14d) were mistakenly interchanged, i.e., regular Pauli matrices were displayed, whereas transposed Pauli matrices are correct. This was adjusted in Reference [50]. Moreover, some references claimed that additional constraints were necessary to recover the physical subspace [73, 74]. It was later on agreed that this assumption was incorrect [75, 76].

With that knowledge and Equations (2.7c) and (2.9), we now can verify that the fermionic ladder operators defined in Equation (2.10) indeed function as desired on the physical subspace[1]

$$\begin{aligned}
\hat{f}_\sigma^\dagger |0\rangle &= \sum_{\sigma'} \hat{z}_{\sigma\sigma'}^\dagger \hat{f}_{\sigma'}^\dagger \hat{e}^\dagger |\mathrm{vac}\rangle = \sum_{\sigma'} \hat{p}_{\sigma\sigma'}^\dagger \hat{f}_{\sigma'}^\dagger |\mathrm{vac}\rangle = |\sigma\rangle \ , \\
\hat{f}_\sigma^\dagger |\sigma'\rangle &= \sum_{\sigma_1\sigma_2} \hat{z}_{\sigma\sigma_1}^\dagger \hat{f}_{\sigma_1}^\dagger \hat{p}_{\sigma'\sigma_2}^\dagger \hat{f}_{\sigma_2}^\dagger |\mathrm{vac}\rangle = \mathrm{sgn}(\sigma)\delta_{-\sigma\sigma'} \hat{d}^\dagger f_\uparrow^\dagger f_\downarrow^\dagger |\mathrm{vac}\rangle = \mathrm{sgn}(\sigma)\delta_{-\sigma\sigma'} |2\rangle \ , \\
\hat{f}_\sigma^\dagger |2\rangle &= \sum_{\sigma'} \hat{z}_{\sigma\sigma'}^\dagger \hat{f}_{\sigma'}^\dagger \hat{d}^\dagger \hat{f}_\uparrow^\dagger \hat{f}_\downarrow^\dagger |\mathrm{vac}\rangle = 0 \ .
\end{aligned} \tag{2.15}$$

We are left to prove that the SB representation of the fermionic ladder operators fulfills the canonic anticommutation relations on the constrained subspace. We eliminate the PF degrees of freedom through Equation (2.14b) and apply Equations (2.7c) and (2.9) to achieve an ordering, where bosonic annihilation operators are on the right side. As discussed, all terms with two annihilation operators in that order vanish. Thus, we find

$$\begin{aligned}
\left[\hat{f}_\sigma \ , \ \hat{f}_{\sigma'}^\dagger\right]_+ &= \sum_{\sigma_1\sigma_2} \left(\hat{f}_{\sigma_1} \hat{z}_{\sigma_1\sigma} \hat{z}_{\sigma'\sigma_2}^\dagger \hat{f}_{\sigma_2}^\dagger + \hat{z}_{\sigma'\sigma_2}^\dagger \hat{f}_{\sigma_2}^\dagger \hat{f}_{\sigma_1} \hat{z}_{\sigma_1\sigma} \right) \\
&= \delta_{\sigma\sigma'} \left(\hat{e}^\dagger \hat{e} + \hat{d}^\dagger \hat{d} \right) + 2 \sum_{\sigma_1} \left(\mathrm{sgn}(\sigma)\,\mathrm{sgn}(\sigma') \hat{p}_{-\sigma\sigma_1}^\dagger \hat{p}_{\sigma_1-\sigma'} + \hat{p}_{\sigma'\sigma_1}^\dagger \hat{p}_{\sigma_1\sigma} \right) \ ,
\end{aligned} \tag{2.16a}$$

and the terms containing $\hat{p}$-bosons can be further decomposed

$$\sum_{\sigma_1} \hat{p}_{\sigma'\sigma_1}^\dagger \hat{p}_{\sigma_1\sigma} = \frac{1}{4} \sum_{\mu=0}^{3} \hat{p}_\mu^\dagger \hat{p}_\mu \delta_{\sigma\sigma'} + \frac{1}{4} \sum_{\mu=1}^{3} \tau_{\sigma'\sigma}^\mu \left(\hat{p}_\mu^\dagger \hat{p}_0 + \hat{p}_0^\dagger \hat{p}_\mu \right) + \frac{\mathrm{i}}{4} \sum_{\mu\mu'\nu=1}^{3} \epsilon_{\mu\mu'\nu} \tau_{\sigma\sigma'}^\nu \hat{p}_\mu^\dagger \hat{p}_{\mu'} \ . \tag{2.16b}$$

Making use of

$$\tau_{\sigma'\sigma}^\mu = -\,\mathrm{sgn}(\sigma)\,\mathrm{sgn}(\sigma')\tau_{-\sigma-\sigma'}^\mu \ , \tag{2.16c}$$

with $\mu \in \{1,2,3\}$ the terms containing Pauli matrices in Equation (2.16a) vanish and we find

$$\left[\hat{f}_\sigma \ , \ \hat{f}_{\sigma'}^\dagger\right]_+ = \delta_{\sigma\sigma'} \left(\hat{e}^\dagger \hat{e} + \hat{d}^\dagger \hat{d} + \sum_{\mu=0}^{3} \hat{p}_\mu^\dagger \hat{p}_\mu \right) = \delta_{\sigma\sigma'} \ . \tag{2.16d}$$

Consequently, the SB representation is an exact mapping of the original fermionic description on the constrained subspace.

Due to the constraints, there is considerable freedom of description, allowing for different but equivalent representations of the ladder operator. To be specific, it can be transformed by

$$\hat{z}_{\sigma\sigma'}^\dagger \to \tilde{\hat{z}}_{\sigma\sigma'}^\dagger = \hat{p}_{\sigma\sigma'}^\dagger \left(1 + \hat{O}_1\right) \hat{e} + \hat{d}^\dagger \left(1 + \hat{O}_2\right) \hat{\tilde{p}}_{\sigma\sigma'} \ , \tag{2.17}$$

and $\hat{O}_{1/2}$ need to be defined such that their contribution on the constrained subspace is zero. Since two bosonic annihilation operators to the very right vanish, these expressions may contain an arbitrary (infinite) series of SB operators under the condition that each summand ends with an annihilation operator. This ambiguity does not matter for the exact formulation but will be exploited to improve the quality of the approximative MF solution later on.

[1] The applicability of annihilation operators can be shown analogously.

2.2.2 Projectors and gauge symmetries

We define the constraint operators

$$\hat{\mathcal{A}} = \hat{e}^\dagger \hat{e} + \hat{d}^\dagger \hat{d} + \sum_{\mu=0}^{3} \hat{p}_\mu^\dagger \hat{p}_\mu - 1 \,, \tag{2.18a}$$

$$\hat{\mathcal{B}}_0 = \sum_\sigma \hat{f}_\sigma^\dagger \hat{f}_\sigma - \sum_{\mu=0}^{3} \hat{p}_\mu^\dagger \hat{p}_\mu - 2\hat{d}^\dagger \hat{d} \,, \tag{2.18b}$$

$$\hat{\boldsymbol{\mathcal{B}}} = \sum_{\sigma\sigma'} \boldsymbol{\tau}_{\sigma\sigma'} \hat{f}_{\sigma'}^\dagger \hat{f}_\sigma - \left(\hat{p}_0^\dagger \hat{\boldsymbol{p}} + \hat{\boldsymbol{p}}^\dagger \hat{p}_0 - \mathrm{i}\hat{\boldsymbol{p}}^\dagger \times \hat{\boldsymbol{p}} \right) \,, \tag{2.18c}$$

and need to enforce $\hat{\mathcal{A}} = \hat{\mathcal{B}}_0 = \hat{\boldsymbol{\mathcal{B}}} = 0$ to fulfill the constraints. In practice, this can be achieved by the projection operators[1] [53]

$$\hat{\mathcal{P}}_\alpha = \frac{1}{2\pi \mathrm{i} T} \int_{-\mathrm{i}\pi T}^{\mathrm{i}\pi T} \mathrm{e}^{\alpha \hat{\mathcal{A}}/T} d\alpha = \delta_{\hat{\mathcal{A}},0} \tag{2.18d}$$

$$\hat{\mathcal{P}}_{\beta_0} = \frac{1}{2\pi \mathrm{i} T} \int_{-\mathrm{i}\pi T}^{\mathrm{i}\pi T} \mathrm{e}^{\beta_0 \hat{\mathcal{B}}_0/T} d\beta_0 = \delta_{\hat{\mathcal{B}}_0,0} \tag{2.18e}$$

$$\hat{\mathcal{P}}_{\boldsymbol{\beta}} = \lim_{N\to\infty} \frac{1}{(2\pi \mathrm{i} N T)^3} \iiint_{-\mathrm{i}\pi NT}^{\mathrm{i}\pi NT} \prod_{\mu=1}^{3} \mathrm{e}^{\beta_\mu \hat{\mathcal{B}}_\mu/T} d\beta_\mu = \delta_{\hat{\boldsymbol{\mathcal{B}}},0} \tag{2.18f}$$

$$\hat{\mathcal{P}} = \hat{\mathcal{P}}_\alpha \hat{\mathcal{P}}_{\beta_0} \hat{\mathcal{P}}_{\boldsymbol{\beta}} . \tag{2.18g}$$

As of now, T is an arbitrary parameter, but we will identify it with the temperature to enforce the constraints within path integral formalism in Chapter 3. It is important to note that the constraint operators commute among themselves and with the Hamiltonian on the constrained subspace as shown in Appendix A.1

$$\left[\hat{H}\,,\,\hat{\mathcal{A}}\right]_- = 0\,, \quad \left[\hat{H}\,,\,\hat{\mathcal{B}}_0\right]_- = 0\,, \quad \left[\hat{H}\,,\,\hat{\boldsymbol{\mathcal{B}}}\right]_- = 0\,, \tag{2.19a}$$

$$\left[\hat{\mathcal{A}}\,,\,\hat{\mathcal{B}}_0\right]_- = 0\,, \quad \left[\hat{\mathcal{A}}\,,\,\hat{\mathcal{B}}_i\right]_- = 0\,, \quad \left[\hat{\mathcal{B}}_0\,,\,\hat{\mathcal{B}}_i\right]_- = 0 \quad \left[\hat{\mathcal{B}}_i\,,\,\hat{\mathcal{B}}_j\right]_- = 2\epsilon_{ijk}\hat{\mathcal{B}}_k \,. \tag{2.19b}$$

Consequently, the constraint operators and the Hamiltonian have common eigenstates, and all constraints can be fulfilled simultaneously as desired. According to the Heisenberg equation of motion [75]

$$\frac{\partial \hat{O}}{\partial t} = \left[\hat{H}\,,\,\hat{O}\right]_- \tag{2.20a}$$

this also implies that the constraint operators are conserved quantities, i.e., a physical state cannot propagate into an unphysical one. According to Noether's theorem [77], or to be specific its quantum analog, the Ward–Takahashi identities [78, 79], each conservation law underlies a continuous symmetry, in this case, local gauge transformations of the SB and PF operators, where the Lagrange multipliers α, β_0 and $\boldsymbol{\beta}$ act as gauge fields in the field theory. Since the constraint operators are hermitian, they can be utilized as generators of symmetry transformations [69, 80]

$$\hat{\mathcal{S}}_i = \mathrm{e}^{\mathrm{i}\phi_i \hat{O}_i} \,, \tag{2.20b}$$

[1] Since $\hat{\mathcal{A}}$ and $\hat{\mathcal{B}}_0$ only contain number operators, their spectrum is given by $\mathbb{N}_0$ and it is sufficient to integrate from $-\mathrm{i}\pi T$ to $-\mathrm{i}\pi T$, although the integration could also be extended to infinity. In the case of $\hat{\boldsymbol{\mathcal{B}}}$, one has to integrate to infinity because the spectrum may include non-integer values.

with $\phi_i \in \mathbb{R}$, under which the Hamiltonian remains invariant. The individual operators, however, are subject to change, and their transformation behavior is given by

$$\hat{b}' = \hat{\mathcal{S}}_i^\dagger \hat{b} \hat{\mathcal{S}}_i \,, \tag{2.21a}$$
$$\hat{f}'_\sigma = \hat{\mathcal{S}}_i^\dagger \hat{f}_\sigma \hat{\mathcal{S}}_i \,. \tag{2.21b}$$

By applying the identity

$$\mathrm{e}^{\hat{X}} \hat{Y} \mathrm{e}^{-\hat{X}} = \hat{Y} + \frac{1}{1!}\left[\hat{X}\,,\,\hat{Y}\right]_- + \frac{1}{2!}\left[\hat{X}\,,\,\left[\hat{X}\,,\,\hat{Y}\right]_-\right]_- + \ldots \,, \tag{2.22}$$

we find that Equations (2.18a) and (2.18b) yield a U(1) ⊗ U(1) gauge degree of freedom involving SB and PF operators

$$\hat{e}' = \hat{e}\ \mathrm{e}^{-\mathrm{i}\phi_\alpha} \,, \tag{2.23a}$$
$$\hat{d}' = \hat{d}\ \mathrm{e}^{-\mathrm{i}\phi_\alpha + 2\mathrm{i}\phi_{\beta_0}} \,, \tag{2.23b}$$
$$\boldsymbol{p}' = \boldsymbol{p}\ \mathrm{e}^{-\mathrm{i}\phi_\alpha + \mathrm{i}\phi_{\beta_0}} \,, \tag{2.23c}$$
$$\hat{\boldsymbol{f}}' = \hat{\boldsymbol{f}}\ e^{-\mathrm{i}\phi_{\beta_0}} \,, \tag{2.23d}$$

and we defined $\boldsymbol{p} = (p_0, p_1, p_2, p_3)^\top$. To obtain the transformation properties with respect to the non-diagonal $\boldsymbol{\beta}$-constraint, we may use the identity [81]

$$\mathrm{e}^{\mathrm{i}\phi\hat{X}}\ \hat{\xi}\ \mathrm{e}^{-\mathrm{i}\phi\hat{X}} = \hat{\xi}\ \mathrm{e}^{-\mathrm{i}\phi\underline{X}} \,, \tag{2.24}$$

where $\hat{X} = \sum_{ij} \hat{\xi}_i \boldsymbol{X}_{ij} \hat{\xi}_j$ is a single particle operator associated with a vector of hermitian matrices $\underline{\boldsymbol{X}}$ and $\hat{\boldsymbol{\xi}}$ represents a vector of fermions or bosons. With Equation (2.18c), we identify the single particle operator $\hat{\boldsymbol{X}}^f_{\boldsymbol{\beta}} = \hat{\boldsymbol{f}}^\dagger \underline{\tau}^\top \hat{\boldsymbol{f}}$ for the PFs. The bosonic part of the constraint can be rewritten by means of matrices

$$\left(\hat{p}_0^\dagger \hat{\boldsymbol{p}} + \hat{\boldsymbol{p}}^\dagger \hat{p}_0 - \mathrm{i}\hat{\boldsymbol{p}}^\dagger \times \hat{\boldsymbol{p}}\right) = \hat{\boldsymbol{p}}^\dagger \underline{\mathfrak{B}}\, \hat{\boldsymbol{p}} \,, \tag{2.25a}$$

with

$$\mathfrak{B}_1 = \begin{pmatrix} 0 & 1 & 0 & 0 \\ 1 & 0 & 0 & 0 \\ 0 & 0 & 0 & -\mathrm{i} \\ 0 & 0 & \mathrm{i} & 0 \end{pmatrix}, \quad \mathfrak{B}_2 = \begin{pmatrix} 0 & 0 & 1 & 0 \\ 0 & 0 & 0 & \mathrm{i} \\ 1 & 0 & 0 & 0 \\ 0 & -\mathrm{i} & 0 & 0 \end{pmatrix}, \quad \mathfrak{B}_3 = \begin{pmatrix} 0 & 0 & 0 & 1 \\ 0 & 0 & -\mathrm{i} & 0 \\ 0 & \mathrm{i} & 0 & 0 \\ 1 & 0 & 0 & 0 \end{pmatrix}, \tag{2.25b}$$

and we identify $\hat{\boldsymbol{X}}^p_{\boldsymbol{\beta}} = \hat{\boldsymbol{p}}^\dagger \underline{\mathfrak{B}}\, \hat{\boldsymbol{p}}$. We moreover observe that $\left[-\tau_i^\top/2\,,\,-\tau_j^\top/2\right]_- = \mathrm{i}\epsilon_{ijk}\left(-\tau_k^\top/2\right)$ and $\left[\mathfrak{B}_i^\top/2\,,\,\mathfrak{B}_j/2\right]_- = \mathrm{i}\epsilon_{ijk}\mathfrak{B}_k$. Consequently, we have a SU(2)-gauge symmetry associated to the $\boldsymbol{\beta}$-constraint and the transformation of the fields is given by

$$\hat{\boldsymbol{f}}' = \hat{\boldsymbol{f}}\ \mathrm{e}^{-\mathrm{i}\boldsymbol{\phi}_\beta \underline{\tau}^\top} \,, \tag{2.26a}$$
$$\hat{\boldsymbol{p}}' = \hat{\boldsymbol{p}}\ \mathrm{e}^{\mathrm{i}\boldsymbol{\phi}_\beta \underline{\mathfrak{B}}} \,. \tag{2.26b}$$

Operator representations	Creation operator	Double occupancy $\hat{D}$	Charge density operator $\hat{n}$	Spin density operator $\hat{\boldsymbol{S}}$
Original expression	$\hat{f}_\sigma^\dagger$	$\hat{f}_\uparrow^\dagger \hat{f}_\uparrow \hat{f}_\downarrow^\dagger \hat{f}_\downarrow$	$\sum_\sigma \hat{f}_\sigma^\dagger \hat{f}_\sigma$	$\frac{1}{2}\sum_{\sigma\sigma'} \hat{f}_\sigma^\dagger \boldsymbol{\tau}_{\sigma\sigma'} \hat{f}_{\sigma'}$
Pseudofermionic representation	*does not exist*	$\hat{f}_\uparrow^\dagger \hat{f}_\uparrow \hat{f}_\downarrow^\dagger \hat{f}_\downarrow$	$\sum_\sigma \hat{f}_\sigma^\dagger \hat{f}_\sigma$	*does not exist*
Bosonic representation	*does not exist*	$\hat{d}^\dagger \hat{d}$	$2\hat{d}^\dagger \hat{d} + \sum_{\mu=0}^{3} \hat{p}_\mu^\dagger \hat{p}_\mu$	$\frac{1}{2}\left(\hat{p}_0^\dagger \hat{\boldsymbol{\rho}} + \hat{\boldsymbol{\rho}}^\dagger \hat{p}_0 - \mathrm{i}\hat{\boldsymbol{\rho}}^\dagger \times \hat{\boldsymbol{\rho}}\right)$[1]
Mixed representation	$\sum_{\sigma'} \hat{z}_{\sigma\sigma'}^\dagger \hat{f}_{\sigma'}^\dagger$	*not suitable* [2]	*not suitable* [2]	$\frac{1}{2}\sum_{\sigma\sigma'} \hat{f}_\sigma^\dagger \boldsymbol{\tau}_{\sigma\sigma'} \hat{f}_{\sigma'} - \mathrm{i}\hat{\boldsymbol{\rho}}^\dagger \times \hat{\boldsymbol{\rho}}$ [1]

Table 2.1: Pseudofermionic (PF), bosonic and mixed representations of crucial fermionic operators within the SB scheme. Different descriptions are equivalent on the physical subspace enforced by the constraints and allow the interacting Hamiltonian defined in Equation (2.1) to become quadratic in PF operators. The bosonic $\underline{z}$-matrix is defined in Equation (2.10).

Combining Equations (2.23) and (2.26), there is a $\mathrm{U}(1) \otimes \mathrm{U}(1) \otimes \mathrm{SU}(2)$ gauge degree of freedom on each lattice site i, which is a direct consequence of the constraints. The five redundant phases are problematic within the field theory description and need to be gauged away or projected out as we will learn in Chapter 3.

2.3 Slave-boson operator representations

Finally, we discuss the SB representation of crucial physical quantities such as the double occupancy operator and the charge and spin density operator. As discussed earlier, the representations are not unique, and in many cases, there exists a purely bosonic and exclusively PF description, and it depends on the specific application, which one is to be preferred. The results are summarized in Table 2.1 and the respective proofs can be found in Appendix A.2.

Most importantly, the operator of double occupancy adapts a quadratic and purely bosonic form. On the other hand, the charge density operator is adventagously represented by the PF expression, which is form-invariant to the original fermions. Note that the bosonic representation of the spin operator fulfills the spin algebra $\left[\hat{S}^i\,,\,\hat{S}^j\right]_- = \mathrm{i}\epsilon_{ijk}\hat{S}^k$, which is proven in Appendix A.1. After all, the most complicated terms are given by the hopping and hybridization between different lattice sites because there is neither a purely PF nor an exclusively bosonic representation for the fermionic creation operator. Nevertheless, the resulting Hamiltonian is quadratic in PF operators, which was our initial goal. Consequently, the PF degrees of freedom can be integrated out in the field theory, while we still have direct access to the physical observables by means of the bosonic representations, which is the strength of the SB representation.

[1] We define $\hat{\boldsymbol{\rho}}^\dagger = (\hat{p}_1^\dagger, -\hat{p}_2^\dagger, \hat{p}_3^\dagger)^\top$. As we will learn in Chapter 3, $\hat{\boldsymbol{\rho}}^\dagger$ is a real field within the SB field theory after spurious degrees of freedom have been gauged away. At that point, the cross product vanishes and the fermionic and PF representations of the spin operators match, as one would expect.

[2] Because of the constraints, there is a remarkable freedom of description for the same operator and a mixed representation can always be found. However, pure bosonic or pseudofermionic representations are desired and exist for this operator, thus a mixed representation is of lesser use.

CHAPTER 3

Slave-boson field theory

In this chapter, we will learn about the field-theoretical description of the slave-boson (SB) formalism, where operators are replaced by eigenvalues of coherent states within a functional integral. Section 3.1 summarizes basic knowledge about the path integral formalism, whose initial idea goes back to P.A.M. Dirac in 1933 [82] and it was significantly further developed by R. Feynman [83]. The concept initially only allowed bosonic states but was extended to feature fermions with the introduction of anticommuting numbers that were proposed by J. Schwinger [84]. In order to study second quantized Hamiltonians in the thermodynamic limit, we adopt its application to statistical mechanics at finite temperature by means of imaginary time path integrals [85]. Subsequently, in Section 3.2, we apply the corresponding basis of coherent states to the SB representation in the radial gauge and calculate the atomic limit to demonstrate the evaluation of an analytically accessible limit. The final analytic form of the general SB Lagrangian is given by Equation (3.35) and builds the foundation for the mean-field and fluctuation analysis discussed in Chapters 4 and 5.

3.1 Imaginary time path integrals

In the following, we summarize important knowledge about imaginary time path integrals and quantum statistical mechanics based on References [86], [48], and [39]. Key results that will be applied throughout the thesis are the functional integral for the partition function [Equation (3.6)], the two-particle Green's function [Equation (5.51a)] and the expression for the Grand potential [Equation (3.19)].

3.1.1 Coherent states

Coherent states [87] are defined as eigenstates of the annihilation operator

$$\hat{\xi}_\alpha |\xi\rangle = \xi_\alpha |\xi\rangle \ , \tag{3.1a}$$

where the index α represents internal degrees of freedom like spin, orbital or lattice site. For bosons, the eigenvalues ξ_α are complex numbers and Grassmann variables in case of fermions[1]. The most important properties of coherent states are summarized by[2] [86]

[1] In order to incorporate the anticommutation relation of fermions, fermionic coherent state eigenvalues need to be anticommuting numbers that fulfill the Grassmann algebra. In particular they obey $\xi_a \xi_b + \xi_b \xi_a = 0$ and $\xi_a^2 = 0$, which also implicates special rules for differentiation and integration [88].

[2] The notation $: \hat{O}(\hat{a}_\alpha^\dagger, \hat{a}_\alpha) :$ means normal ordering of the operator $\hat{O}(\hat{a}_\alpha^\dagger, \hat{a}_\alpha)$, i.e., it is ordered such that all creation operators are on the left and all annihilation operators on the right side.

$$\left[\hat{\xi}_\alpha, \hat{\xi}_\beta^\dagger\right]_{-\zeta} = \delta_{\alpha\beta} \,, \tag{3.1b}$$

$$|\xi\rangle = \mathrm{e}^{\zeta \sum_\alpha \xi_\alpha \hat{\xi}_\alpha^\dagger} |0\rangle \,, \tag{3.1c}$$

$$\underline{\mathbb{1}} = \int \prod_\alpha \mathcal{D}\left[\xi_\alpha^*, \xi_\alpha\right] \mathrm{e}^{-\sum_\alpha \xi_\alpha^* \xi_\alpha} |\xi_\alpha\rangle \langle\xi_\alpha| \,, \tag{3.1d}$$

$$\langle\xi| : \hat{O}(\hat{\xi}_\alpha^\dagger, \hat{\xi}_\alpha) : |\xi'\rangle = \mathrm{e}^{\sum_\alpha \xi_\alpha^* \xi_\alpha'} \hat{O}(\xi_\alpha^* \xi_\alpha') \,, \tag{3.1e}$$

$$\mathrm{Tr}\,\hat{O} = \int \prod_\alpha \mathcal{D}\left[\xi_\alpha^*, \xi_\alpha\right] \mathrm{e}^{-\sum_\alpha \xi_\alpha^* \xi_\alpha} \langle\zeta\xi| \hat{O} |\xi\rangle \,, \tag{3.1f}$$

$$\int \prod_\alpha \mathcal{D}\left[\xi_\alpha^*, \xi_\alpha\right] \exp\left(-\sum_{\alpha\beta} \xi_\alpha^* \mathcal{M}_{\alpha\beta} \xi_\beta + \sum_\alpha \left(J_\alpha^* \xi_\alpha + \xi_\alpha^* J_\alpha\right)\right) = \left(\det \underline{\mathcal{M}}\right)^{-\zeta} \exp\left(\sum_{\alpha\beta} J_\alpha^* \mathcal{M}_{\alpha\beta}^{-1} J_\beta\right) \,, \tag{3.1g}$$

where we defined

$$\mathcal{D}\left[\xi_\alpha^*, \xi_\alpha\right] = \frac{d\xi_\alpha^* d\xi_\alpha}{\mathcal{N}} \,, \tag{3.1h}$$

$$\mathcal{N} = \begin{cases} 2\pi\mathrm{i} & \text{for } \hat{\xi}_\alpha \text{ bosonic} \\ 1 & \text{for } \hat{\xi}_\alpha \text{ fermionic} \end{cases} \tag{3.1i}$$

$$\zeta = \begin{cases} 1 & \text{for } \hat{\xi}_\alpha \text{ bosonic} \\ -1 & \text{for } \hat{\xi}_\alpha \text{ fermionic} \end{cases} . \tag{3.1j}$$

The integrals associated with the differential $\mathcal{D}$ are to be understood as multi-integrals over all fields with the limits $-\infty$ to $+\infty$, and ξ^* is defined as the complex conjugate of ξ.

3.1.2 Path integral for the partition function

We aim to calculate the partition function in the grand canonical ensemble[1]

$$Z = \mathrm{Tr}\,\mathrm{e}^{-\beta\hat{H}} = \int \prod_\alpha \mathcal{D}\left[\xi_\alpha^*, \xi_\alpha\right] \mathrm{e}^{-\sum_\alpha \xi_\alpha^* \xi_\alpha} \langle\zeta\xi| \mathrm{e}^{-\beta\hat{H}} |\xi\rangle \,, \tag{3.2}$$

with inverse temperature $\beta = 1/T$ by means of the coherent state basis, i.e., utilizing Equation (3.1f). In order to do so, we first consider the time evolution operator[2] in the coherent state basis, which is given by [86]

$$\hat{\mathcal{U}}\left(\xi_{t_f}^*, \xi_{t_i}\right) = \left\langle \xi_{t_f} \left| \mathrm{e}^{-\frac{\mathrm{i}}{\hbar}\hat{H}(t_f - t_i)} \right| \xi_{t_i} \right\rangle \tag{3.3a}$$

for non-explicitly time dependent Hamiltonians. Since $\mathrm{e}^{-\frac{\mathrm{i}}{\hbar}\hat{H}(t_f - t_i)}$ is not normal ordered, we cannot directly replace the creation and annihilation operators by their eigenvalues in the coherent state basis. To overcome that obstacle, we split the continuous time interval $\left[t_f, t_i\right]$ into infinitesimal time slices

$$\eta = \frac{t_f - t_i}{M} \,, \tag{3.3b}$$

[1] The chemical potential term has been absorbed into the definition of the Hamiltonian.
[2] In the Schrödinger picture, the time evolution operator generates translations in time, i.e., $|\psi(t)\rangle = \hat{\mathcal{U}}(t, 0) |\psi(0)\rangle$.

and find

$$\mathrm{e}^{-\frac{\mathrm{i}}{\hbar}\hat{H}\eta} =: \mathrm{e}^{-\frac{\mathrm{i}}{\hbar}\hat{H}\eta} : +\mathcal{O}(\eta^2) \,. \tag{3.3c}$$

Consequently, we can replace the regular exponential with the normal ordered one in the limit $M \to \infty$ and have marvelously eliminated the impact of the (anti-)commutator of the creation and annihilation operators. Now, we insert $M-1$ closure relations [Equation (3.1d)] between the M exponential factors and further apply Equation (3.1e) to find [86]

$$\begin{aligned}\hat{\mathcal{U}}\left(\xi_M^*, \xi_0\right) &= \lim_{M\to\infty} \left\langle \xi_M \middle| \left(: \mathrm{e}^{-\frac{\mathrm{i}}{\hbar}\hat{H}\eta} :\right)^M \middle| \xi_0 \right\rangle \\ &= \lim_{M\to\infty} \int \prod_\alpha \left(\prod_{m=1}^{M-1} \mathcal{D}\left[\xi_{\alpha,m}^* \xi_{\alpha,m}\right] \mathrm{e}^{-\xi_{\alpha,m}^* \xi_{\alpha,m}} \right) \prod_{m=1}^{M} \left\langle \xi_m \middle| : \mathrm{e}^{-\frac{\mathrm{i}\eta}{\hbar}\hat{H}\left(\hat{\xi}_\alpha^\dagger, \hat{\xi}_\alpha\right)} : + \mathcal{O}\left(\eta^2\right) \middle| \xi_{m-1} \right\rangle \\ &= \lim_{M\to\infty} \int \left(\prod_{m=1}^{M-1} \prod_\alpha \mathcal{D}\left[\xi_{\alpha,m}^* \xi_{\alpha,m}\right] \mathrm{e}^{-\xi_{\alpha,m}^* \xi_{\alpha,m}} \right) \left(e^{\sum_{m=1}^{M} \sum_\alpha \xi_{\alpha,m}^* \xi_{\alpha,m-1} - \frac{\mathrm{i}\eta}{\hbar} H\left(\xi_{\alpha,m}^*, \xi_{\alpha,m-1}\right)} \right) \,.\end{aligned} \tag{3.3d}$$

Now, we identify that the partition function can be written as trace of the time evolution operator under imaginary time propagation $\mathrm{i}t/\hbar \to \tau$ with the interval $\tau_f - \tau_i = \beta = M\eta$ and application of periodic boundary conditions (PBC) for bosons and anti-periodic boundary conditions (ABC) for fermions respectively

$$\xi_{\alpha,0} = \xi_\alpha \,, \tag{3.4a}$$

$$\xi_{\alpha,M}^* = \zeta \xi_\alpha^* \,. \tag{3.4b}$$

Utilizing Equations (3.2) and (3.3d), we finally find

$$Z = \lim_{M\to\infty} \prod_{m=1}^{M} \prod_\alpha \mathcal{D}\left[\xi_{\alpha,m}^* \xi_{\alpha,m}\right] \mathrm{e}^{-\mathcal{S}\left[\xi_{\alpha,m}^*, \xi_{\alpha,m}\right]} \,, \tag{3.5a}$$

with the action [86]

$$\mathcal{S}\left[\xi_{\alpha,m}^*, \xi_{\alpha,m}\right] = \eta \sum_{m=2}^{M} \left[\sum_\alpha \left(\xi_{\alpha,k}^* \frac{\xi_{\alpha,m} - \xi_{\alpha,m-1}}{\eta} + H\left(\xi_{\alpha,m}^*, \xi_{\alpha,m-1}\right) \right) \right] + \eta \left[\sum_\alpha \xi_{\alpha,1}^* \frac{\xi_{\alpha,1} - \zeta\xi_{\alpha,M}}{\eta} + H\left(\xi_{\alpha,1}^*, \zeta\xi_{\alpha,M}\right) \right] . \tag{3.5b}$$

This form of the partition function is often symbolically expressed in a continuous notation[1]

$$Z = \int \mathcal{D}\left[\boldsymbol{\xi}^*(\tau), \boldsymbol{\xi}(\tau)\right] \, \mathrm{e}^{-\mathcal{S}\left[\boldsymbol{\xi}^*, \boldsymbol{\xi}\right]} \,, \tag{3.6a}$$

with the action

$$\mathcal{S}\left[\boldsymbol{\xi}^*, \boldsymbol{\xi}\right] = \int_0^\beta d\tau \mathcal{L}\left[\boldsymbol{\xi}^*(\tau), \boldsymbol{\xi}(\tau)\right] \,, \tag{3.6b}$$

[1] The integral is to be performed over all internal degrees of freedom α and all imaginary times τ under the constraint $\boldsymbol{\xi}(\beta) = \zeta\boldsymbol{\xi}(0)$.

and the Lagrangian

$$\mathcal{L}[\boldsymbol{\xi}^*(\tau), \boldsymbol{\xi}(\tau)] = \sum_\alpha \xi^*_\alpha(\tau)\partial_\tau \xi_\alpha(\tau) + H\left(\xi^*_\alpha(\tau), \xi_\alpha(\tau)\right) . \tag{3.6c}$$

Such an expression is called *functional integral*, because it involves integrating over the histories of all fields. It is important to note that the discrete expression is formally correct since the continuum limit is not always well defined. We adopt the continuous notation in the following, and it is implied that the limit $M \to \infty$ is to be taken within the exact, discrete expression given by Equation (3.5).

3.1.3 Green's functions and correlations

Quantum mechanical expectation values are given by

$$\left\langle \hat{\xi}_\alpha(\tau) \right\rangle = \frac{\int \mathcal{D}[\boldsymbol{\xi}^*, \boldsymbol{\xi}] \;\; \xi_\alpha(\tau)\, \mathrm{e}^{-\mathcal{S}[\xi^*, \xi]}}{Z} \tag{3.7}$$

within path integral formalism, i.e., the quantum mechanics of many-body physics based on commutators is transformed to a statistical description with distribution function $\mathrm{e}^{-\mathcal{S}}$. Time-ordered correlations between two fields can be calculated analogously and are given by the two-point Green's function, which is defined by [48]

$$G_{\mu,\nu}(r - r') = -\left\langle \mathcal{T}_\tau \hat{\xi}_\mu(r) \hat{\xi}^\dagger_\nu(r') \right\rangle = -\frac{\int \mathcal{D}\left[\boldsymbol{\xi}^*, \boldsymbol{\xi}\right] \;\; \xi_\mu(r)\xi^*_\nu(r')\mathrm{e}^{-\mathcal{S}[\xi^*, \xi]}}{Z} , \tag{3.8}$$

where $r = (\boldsymbol{r}_i, \tau)$ is the space-time four index, μ, ν represent internal degrees of freedom, e.g., orbital and spin, and $\mathcal{T}_\tau$ is the time ordering operator, which is defined by

$$\mathcal{T}_\tau \hat{\xi}_\mu(\boldsymbol{r}, \tau)\hat{\xi}^\dagger_\nu(\boldsymbol{r}', \tau') = \begin{cases} \hat{\xi}_\mu(\boldsymbol{r}, \tau)\hat{\xi}^\dagger_\nu(\boldsymbol{r}', \tau') & \text{if } \tau > \tau' \\ \zeta\hat{\xi}^\dagger_\nu(\boldsymbol{r}', \tau')\hat{\xi}_\mu(\boldsymbol{r}, \tau) & \text{if } \tau < \tau' . \end{cases} \tag{3.9}$$

The Green's function depends only on the difference $\Delta r = r - r'$ due to translation symmetry, and consequently, the space-time degrees of freedom of the Lagrangian matrix can be diagonalized by means of Fourier transformation (FT)[1]. The FT w.r.t. imaginary time has to respect the (anti-)periodic boundary conditions of the path integral defined in Equation (3.4a), which can be achieved by the definition of Matsubara frequencies [89, 90]

$$\omega_n = \begin{cases} \frac{2n\pi}{\beta} & n \in \mathbb{Z}_0,\ \hat{\xi} \text{ bosonic} , \\ \frac{(2n+1)\pi}{\beta} & n \in \mathbb{Z}_0,\ \hat{\xi} \text{ fermionic} , \end{cases} \tag{3.10a}$$

[1](Anti-)symmetry w.r.t. to imaginary time occurs naturally in the path integral. Since we impose PBC for bulk Hamiltonians, we also have spatial translation symmetry. For open boundary calculations investigated in the context of topological edge modes in Chapter 12, translation symmetry is broken, i.e., $\boldsymbol{k}$ is not a good quantum number anymore, and the spatial degrees of freedom are absorbed into the indices μ, ν.

[2]With symmetric normalization, the FT is a unitary transformation, i.e., the integration measure of the path integral remains invariant. The FT of hermitian conjugated fields is found by $\xi \to \xi^*$ and $\mathrm{i} \to -\mathrm{i}$.

where $\beta = 1/T$ is the inverse temperature. For discrete imaginary times $\tau_m = m\eta$ with $M = \beta/\eta$, we define[1]

$$\begin{aligned} \xi_{\alpha,m} &= \frac{1}{\sqrt{M}} \sum_{n=-M/2}^{M/2} \mathrm{e}^{-\mathrm{i}\omega_n \tau_m} \xi_{\alpha,n} \,, \\ \xi_{\alpha,n} &= \frac{1}{\sqrt{M}} \sum_{m=-M/2}^{M/2} \mathrm{e}^{\mathrm{i}\omega_n \tau_m} \xi_{\alpha,m} \,, \end{aligned} \tag{3.10b}$$

and find the continuous description after the limit of infinite time slices $M \to \infty$

$$\begin{aligned} \xi_\alpha(\tau) &= \frac{1}{\sqrt{\beta}} \sum_{n=-\infty}^{\infty} \mathrm{e}^{-\mathrm{i}\omega_n \tau} \xi_{\alpha,n} \,, \\ \xi_{\alpha,n} &= \frac{1}{\sqrt{\beta}} \int_0^\beta d\tau \, \mathrm{e}^{\mathrm{i}\omega_n \tau} \xi_\alpha(\tau) \,. \end{aligned} \tag{3.10c}$$

Moreover, the FT from position to momentum space is defined by

$$\begin{aligned} \xi_\alpha(\boldsymbol{r}_i) &= \frac{1}{\sqrt{N}} \sum_{\boldsymbol{k}} \mathrm{e}^{\mathrm{i}\boldsymbol{k}\boldsymbol{r}_i} \xi_{\alpha,\boldsymbol{k}} \,, \\ \xi_{\alpha,\boldsymbol{k}} &= \frac{1}{\sqrt{N}} \sum_{\boldsymbol{k}} \mathrm{e}^{-\mathrm{i}\boldsymbol{k}\boldsymbol{r}_i} \xi_\alpha(\boldsymbol{r}_i) \,, \end{aligned} \tag{3.10d}$$

where N is the number of lattice sites and the sum is to be performed over the Brillouin zone (BZ) of the respective lattice. Within the limit of continuous imaginary time, we define the FT of the Green's function

$$[G_k]_{\mu,\nu} = \sum_{\Delta \boldsymbol{r}_i} \int_0^\beta d\tau \, G_{\mu,\nu}(\Delta r) \, \mathrm{e}^{-\mathrm{i}\boldsymbol{k}\Delta\boldsymbol{r}_i + \mathrm{i}\omega_n \Delta\tau} \,, \tag{3.11}$$

where $k = (\boldsymbol{k}, \mathrm{i}\omega_n)$ is the four-index in momentum-Matsubara frequency space.

3.1.4 Quantum statistics of non-interacting particles

In the following, we calculate the partition function and thermodynamic potentials for free particles with the Hamiltonian[2]

$$\hat{H}^{(0)} = \sum_\alpha \varepsilon_\alpha \hat{\xi}_\alpha^\dagger \hat{\xi}_\alpha \tag{3.12}$$

by applying the path integral formalism, which will be of great importance for the MF and fluctuation treatment of the SB fields in Chapter 4 and Chapter 5.

Discrete imaginary time

The partition function factorizes for the non-interacting particles, and we find with Equation (3.5) and the solution for the Gaussian integral given by Equation (3.1g) that we are left to determine the determinant of

[2]The calculation holds also for a non-diagonal Hamiltonian $\hat{H}^{(0)} = \sum_\alpha \xi^\dagger_{\alpha\beta} H_{\alpha\beta} \xi_\beta$, since it can be diagonalized by a unitary transformation $U_{\alpha\beta}$ and the resulting quasiparticles fulfill the same (anti-)commutation relations. Moreover, the Jacobi determinant $J = \det \underline{U} \det \underline{U^\dagger} = \det \underline{U}\,\underline{U^\dagger} = 1$ is equal to one, i.e., the integration measure of the path integral remains invariant.

the $M \times M$ matrix of the Lagrangian, where the number of time slices M goes to infinity

$$Z^{(0)} = \prod_{\alpha} \lim_{M\to\infty} \left(\det \underline{\mathcal{M}}\right)_{\alpha}^{-\zeta} . \tag{3.13}$$

The Lagrangian matrix is defined by the discrete expression in Equation (3.5b) and yields [86]

$$\underline{\mathcal{M}} = \begin{pmatrix} 1 & 0 & 0 & \cdots & 0 & -\zeta\gamma \\ -\gamma & 1 & 0 & & & 0 \\ 0 & -\gamma & 1 & \ddots & & \vdots \\ \vdots & 0 & -\gamma & \ddots & & \\ & & 0 & \ddots & & 0 \\ 0 & & & & -\gamma & 1 \end{pmatrix} , \tag{3.14a}$$

with

$$\gamma = 1 - \frac{\beta}{M}\varepsilon_{\alpha} . \tag{3.14b}$$

By Laplace expansion of the first row, the determinant is found to be

$$\det \underline{\mathcal{M}} = 1 + (-1)^{M-1}(-\gamma)^{M} . \tag{3.14c}$$

Evaluating the limit of infinite time slices, the partition function of free particles is given by

$$Z^{(0)} = \prod_{\alpha} \left(1 - \zeta \mathrm{e}^{-\beta\varepsilon_{\alpha}}\right)^{-\zeta} . \tag{3.14d}$$

Continuous imaginary time

The same result can be obtained in the limit of continuous imaginary time described by Equation (3.6). The Green's function corresponding to Equation (3.12) is then given by $\underline{G}^{(0)}(\tau) = \left(-\partial_{\tau} - \underline{H}^{0}\right)^{-1}$, which yields[1] [39, 48]

$$\left[G^{(0)}_{\mathrm{i}\omega_n}\right]_{\alpha,\beta} = \delta_{\alpha,\beta}\left(\mathrm{i}\omega_n - \varepsilon_{\alpha}\right)^{-1} \tag{3.15}$$

after FT to Matsubara space. In that basis, the action matrix becomes diagonal,

$$\mathcal{S}^{(2)}\left[\xi^{*}_{\mathrm{i}\omega_n,\alpha}, \xi_{\mathrm{i}\omega_n,\alpha}\right] = \sum_{\mathrm{i}\omega_n}\sum_{\alpha} \xi^{*}_{\mathrm{i}\omega_n,\alpha}\left(-\left[G^{(0)}_{\mathrm{i}\omega_n,\alpha}\right]^{-1}\right)\xi_{\mathrm{i}\omega_n,\alpha} \tag{3.16}$$

and the calculation of a determinant to obtain the partition function with Equation (3.1g) is simplified to the evaluation of an infinite product

$$Z^{(0)} = \left(\det\left(-\left[\underline{G}^{(0)}\right]^{-1}\right)\right)^{-\zeta} = \prod_{\alpha}\prod_{n}\left(-\mathrm{i}\omega_n + \varepsilon_{\alpha}\right)^{-\zeta} . \tag{3.17}$$

[1] For simplicity, we adapt the notation $\Delta\tau \to \tau$.

Now, we consider the grand potential (GP) of free particles

$$\Omega^{(0)} = -T \ln Z^{(0)} \,, \tag{3.18}$$

and after applying the identity $\ln\det \underline{\mathcal{A}} = \mathrm{Tr}\ln \underline{\mathcal{A}}$, we find

$$\Omega^{(0)} = T\zeta \ln\det\left(-\left[\underline{G}^{(0)}\right]^{-1}\right) = T\zeta\,\mathrm{Tr}\ln\left(-\left[\underline{G}^{(0)}\right]^{-1}\right) = T\zeta\sum_{\alpha,n}\ln(-\mathrm{i}\omega_n+\varepsilon_\alpha)\,. \tag{3.19a}$$

The occurring Matsubara sum can be evaluated analytically after multiplying with a convergence factor $\mathrm{e}^{\mathrm{i}\omega_n 0^+}$ and mapping on a complex contour integral[1] [48]

$$\begin{aligned}
\Omega^{(0)} &= T\zeta\sum_{\alpha,n}\ln(-\mathrm{i}\omega_n+\varepsilon_\alpha)\mathrm{e}^{\mathrm{i}\omega_n 0^+} = -\zeta\sum_\alpha\oint\frac{dz}{2\pi\mathrm{i}}n_\zeta(z)\ln\left(\varepsilon_\alpha - z\right)\mathrm{e}^{z0^+}\\
&= -\sum_\alpha\int_{-\infty}^{\infty}\frac{d\omega}{2\pi\mathrm{i}}n_\zeta(\omega)\left[\ln\left(\varepsilon_\alpha-\omega+\mathrm{i}0^+\right)-\ln\left(\varepsilon_\alpha-\omega-\mathrm{i}0^+\right)\right]\\
&= -\sum_\alpha\int_{-\infty}^{\infty}\frac{d\omega}{2\pi\mathrm{i}}n_\zeta(\omega)2\pi\mathrm{i}\,\Theta\left(\omega-\varepsilon_\alpha\right) = -\sum_\alpha\int_{\varepsilon_\alpha}^{\infty}d\omega n_\zeta(\omega)\\
&= \zeta T\sum_\alpha\ln\left(1-\zeta\mathrm{e}^{-\beta\varepsilon_\alpha}\right)\,,
\end{aligned} \tag{3.19b}$$

with

$$n_{+1}(\varepsilon_\alpha) = n_{\mathrm{B}}(\varepsilon_\alpha) = \frac{1}{\mathrm{e}^{\beta\varepsilon_\alpha}-1} \quad \text{Bose}-\text{Einstein distribution} \tag{3.20a}$$

$$n_{-1}(\varepsilon_\alpha) = n_{\mathrm{F}}(\varepsilon_\alpha) = \frac{1}{\mathrm{e}^{\beta\varepsilon_\alpha}+1} \quad \text{Fermi}-\text{Dirac distribution}\,. \tag{3.20b}$$

This result will be used later on to determine the MF grand potential and implicates the same partition function that we obtained for discrete imaginary times in Equation (3.14d) as desired. Finally, we want to establish a connection between the equal-time Green's function and quantum particle statistics.

$$G_\alpha^{(0)}(\Delta\tau = 0^-) = \frac{1}{\beta}\sum_{\mathrm{i}\omega_n}G^{(0)}_{\alpha,\mathrm{i}\omega_n}\mathrm{e}^{\mathrm{i}\omega_n 0^+} = \sum_\alpha\left(\mathrm{i}\omega_n-\varepsilon_\alpha\right)^{-1}\mathrm{e}^{\mathrm{i}\omega_n 0^+} = -\zeta n_\zeta(\varepsilon_\alpha)\,. \tag{3.21}$$

Details on the occurring Matsubara summations are provided in Appendix A.5.

3.2 Slave-boson Lagrangian

Applying the knowledge of Chapter 2, we map the general Hamiltonian in Equation (2.1) to the SB representation by utilizing the operator representations summarized in Table 2.1. We choose the PF description of the charge density operator because it can be integrated out exactly later on and adopt the bosonic representation of the Hubbard interaction that simplifies it to a quadratic form. The resulting theory is decomposed into a part containing both, PF and SB degrees of freedom and a purely bosonic part

$$\hat{H} = \hat{H}_F + \hat{H}_B \tag{3.22}$$

[1] The convergence factor needs to be added due to the ill-defined continuum limit. As can be seen in the discrete description, the fields entering the Hamiltonian differ by a single time slice, which is omitted in the continuous expression and leads to the necessity of the convergence factor.

with

$$\begin{aligned}\hat{H}_F = &\sum_{\sigma\sigma'\sigma_1\sigma_2}\sum_{i\neq j}\hat{f}^\dagger_{i,\sigma}\hat{z}^\dagger_{i,\sigma\sigma_1}t^f_{ij,\sigma_1\sigma_2}\hat{z}_{j,\sigma'\sigma_2}\hat{f}_{j,\sigma'} + (\epsilon_f-\mu_0)\sum_{i,\sigma}\hat{f}^\dagger_{i,\sigma}\hat{f}_{i,\sigma}\\ &+\sum_{\sigma\sigma'}\left[\sum_{o=1}^{O}\sum_{i\neq j}\hat{c}^\dagger_{o,i,\sigma}t^o_{ij,\sigma\sigma'}\hat{c}_{o,j,\sigma'} + \sum_{o\neq o'}^{O}\sum_{ij}\left(\hat{c}^\dagger_{o,i,\sigma}\tilde{V}^{oo'}_{ij,\sigma\sigma'}\hat{c}_{j,\sigma'} + \text{h.c.}\right)\right] + \sum_{i,\sigma,o}(\epsilon_o-\mu_0)\,\hat{c}^\dagger_{o,i,\sigma}\hat{c}_{o,i,\sigma}\,, \qquad (3.23a)\\ &+\sum_{\sigma\sigma'\sigma_2}\sum_{o=1}^{O}\sum_{ij}\left(\hat{c}^\dagger_{o,i,\sigma}V^{of}_{ij,\sigma\sigma_2}\hat{z}_{j,\sigma'\sigma_2}\hat{f}_{j,\sigma'} + \text{h.c.}\right)\\ \hat{H}_B = &\,U\sum_i \hat{d}^\dagger_i\hat{d}_i\,. \qquad (3.23b)\end{aligned}$$

To calculate the partition function on the physical subspace, we need to evaluate [53]

$$Z = \mathrm{Tr}\left(\mathrm{e}^{-\beta\hat{H}}\mathcal{P}\right)\,, \qquad (3.24)$$

where $\mathcal{P}$ is the projector defined in Equation (2.18). Within the coherent state path integral of SBs and PFs applied to all lattice sites i, the product of exponentials yielding from the projectors and $\mathrm{e}^{-\beta\hat{H}}$ can be written as a sum in one exponential. We, moreover, identify the arbitrary parameter T in the definition of the projectors with inverse temperature β. Consequently, we may divide the constraint operator terms into the same time slices as the Hamiltonian, and we need to add these to the Lagrangian. Applying Equation (3.6), we, therefore, find the effective Lagrangian [50, 53, 66]

$$\mathcal{L}\left[\psi^*,\psi,\phi^*,\phi\right] = \mathcal{L}_F\left[\psi^*,\psi,\phi^*,\phi\right] + \mathcal{L}_B\left[\psi^*,\psi\right] \qquad (3.25)$$

with

$$\mathcal{L}_F\left[\psi^*,\psi,\phi^*,\phi\right] = H_F\left[\boldsymbol{\Psi}^*,\boldsymbol{\Psi},\phi^*,\phi\right] + \sum_i\left[\phi^\dagger_i\partial_\tau\phi_i + \beta_{0,i}f^\dagger_i\underline{\tau}_0 f_i + \boldsymbol{\beta}_i\cdot\left(f^\dagger_i\underline{\tau}f_i\right)\right]\,, \qquad (3.26a)$$

$$\begin{aligned}\mathcal{L}_B\left[\psi^*,\psi\right] = \sum_i\Big[&\boldsymbol{\Psi}^\dagger_i\partial_\tau\boldsymbol{\Psi}_i + U\,d^*_i d_i + \alpha_i\left(e^*_i e_i + p^*_{0,i}p_{0,i} + \boldsymbol{p}^*_i\cdot\boldsymbol{p}_i + d^*_i d_i - 1\right)\\ &-\beta_{0,i}\left(p^*_{0,i}p_{0,i} + \boldsymbol{p}^*_i\cdot\boldsymbol{p}_i + 2d^*_i d_i\right) - \boldsymbol{\beta}_i\cdot\left(p^*_{0,i}\boldsymbol{p}_i + \boldsymbol{p}^*_i p_{0,i} - \mathrm{i}\boldsymbol{p}^*_i\times\boldsymbol{p}_i\right)\Big]\,.\end{aligned} \qquad (3.26b)$$

We, moreover, define

$$\boldsymbol{\Psi}_i = \left(e_i\,, d_i\,, p_{0,i}\,, p_{1,i}\,, p_{2,i}\,, p_{3,i}\right)^\top\,, \qquad (3.27a)$$

$$\phi_i = \left(c_{1,\uparrow,i}\,, c_{1,\downarrow,i}\,, \ldots\,, c_{O,\uparrow,i}\,, c_{O,\downarrow,i}\,, f_{\uparrow,i}, f_{\downarrow,i}\right)^\top \qquad (3.27b)$$

for the collection of SB and PF fields, and $\boldsymbol{\psi}$ represents the SBs including the Lagrange multipliers (LMs) $\alpha, \beta_0, \boldsymbol{\beta}$.

3.2.1 Radial gauge

In Section 2.2.2 it was shown that the constraints are conserved quantities, which according to the Noether theorem [77] implicate respective continuous symmetries, specifically a $\mathrm{SU}(2)\otimes\mathrm{U}(1)\otimes\mathrm{U}(1)$ gauge symmetry, where the LMs $\alpha, \beta_0, \beta_1, \beta_2, \beta_3$ act as gauge fields. The static MF approximation discussed in Chapter 4 does

not depend on the choice of gauge. The full functional integral, however, is only applicable if the gauge is fixed.

The gauge freedom does not correspond to a physical symmetry but is an artifact of the SB representation associated with the constraints, which is why those gauge fields are also referred to as *spurious* fields, or *Faddeev–Popov ghosts* [91]. In Section 3.2.3, we will explicitly calculate the exact atomic limit and show that an unfixed yields an incorrect partition function due to over-counting. In the case of Gaussian fluctuations discussed in Chapter 5, the spurious degrees of freedom cause unphysical divergences, which need to be projected out in order to evaluate correlation functions. These zero modes can be understood as Goldstone modes, originating in the spontaneously broken gauge symmetries of the MF approximation.

The correct gauge symmetry has been debated for quite some time, including wrong assumptions of a higher symmetry group [59, 60, 72, 92–95], until it was agreed to be $\mathrm{U}(1) \otimes \mathrm{U}(1) \otimes \mathrm{U}(1)$ for the original KR representation [96] and $\mathrm{SU}(2) \otimes \mathrm{U}(1) \otimes \mathrm{U}(1)$ for the SRIKR representation applied here [50]. Following References [53] and [50], the spurious degrees of freedom can be removed in the *radial gauge*, where the fields on each lattice site are expressed by their absolute value and phase[1]

$$\begin{aligned} e &= \mathrm{e}^{\mathrm{i}\theta}\,|e|\ , \\ d &= \mathrm{e}^{\mathrm{i}\Phi}|d|\ , \\ \underline{p} &= \mathrm{e}^{\mathrm{i}\chi_0}\mathrm{e}^{\mathrm{i}\boldsymbol{\chi}\underline{\boldsymbol{\tau}}}\underline{q}\ , \\ \underline{q} &= \frac{1}{2}\sum_{\mu=0}^{3} q_\mu \underline{\tau}^\mu\ , \end{aligned} \tag{3.28a}$$

with $q_\mu \in \mathbb{R}$. In order to do so, we need to simultaneously perform a local $\mathrm{SU}(2) \otimes \mathrm{U}(1)$ gauge transformation for the PFs and a U(1) gauge transformation for the d-and p-bosons respectively, where the gauge phases match their counterparts in the radial description

$$\begin{aligned} f &\to \mathrm{e}^{-\mathrm{i}\chi_0} f\, \mathrm{e}^{-\mathrm{i}\boldsymbol{\chi}\underline{\boldsymbol{\tau}}}\ , \\ d &\to \mathrm{e}^{\mathrm{i}(\theta+2\chi_0)} d\ , \\ \underline{p} &\to \mathrm{e}^{\mathrm{i}\theta}\underline{p}\ , \\ \underline{\tilde{p}} &\to \mathrm{e}^{\mathrm{i}\theta}\underline{\tilde{p}}\ . \end{aligned} \tag{3.28b}$$

Following these transformations, all terms associated with the five phases θ, χ_0, χ_1, χ_2 and χ_3 can be absorbed into the Lagrange multipliers by applying

$$\left(\alpha + \mathrm{i}\dot{\theta}\right) \to \alpha\ , \tag{3.29a}$$

$$\left(\beta_0 + \mathrm{i}\dot{\chi}_0\right) \to \beta_0\ , \tag{3.29b}$$

$$\left(\boldsymbol{\beta} - \mathrm{i}\left(\boldsymbol{n}\dot{\chi} + \dot{\boldsymbol{n}}\sin\chi\cos\chi - \dot{\boldsymbol{n}}\times\boldsymbol{n}\sin^2\chi\right)\right) \to \boldsymbol{\beta}\ , \tag{3.29c}$$

which is proven in Appendix A.3. Consequently, the phases of e, p_0, p_1, p_2 and p_3 are removed, i.e., they real fields and only the d-field remains complex. Without phases, the $\underline{p}$ and $\underline{q}$ matrices are equivalent, and we will go back to the previous notation involving $\underline{p}$, p_0 and e in the following and it implied that these fields are real-valued. This gauge reveals two major simplifications for the bosonic Lagrangian. First of all, the time derivatives of all real fields vanish due to PBCs of the path integral for which total derivatives vanish

[1]The gauge transformation is local, i.e., all fields employ the same space-time index r for the whole calculation. We will thus drop it for better readability, and the transformation is applied for each space-time independently.

($2e\partial_\tau e = \partial_\tau e^2 = 0$, etc.). Secondly, the cross product $\boldsymbol{p}^* \times \boldsymbol{p}$, which enters the $\boldsymbol{\beta}$-constraint vanishes and we find

$$\mathcal{L}_F\left[\psi_i, \phi_i^*, \phi_i\right] \to H_F\left(\boldsymbol{\Psi}_i, \phi_i^*, \phi_i\right) + \sum_i \left[\phi_i^\dagger \partial_\tau \phi_i + \beta_{0,i} f_i^\dagger \underline{\tau}_0 f_i + \boldsymbol{\beta}_i \cdot \left(f_i^\dagger \underline{\tau} f_i\right)\right] , \tag{3.30a}$$

$$\mathcal{L}_B[\psi_i] \to \sum_i \left[d_i^*(\partial_\tau + U)d_i + \alpha_i\left(e_i^2 + p_{0,i}^2 + \boldsymbol{p}_i^2 + d_i^* d_i - 1\right) - \beta_{0,i}\left(p_{0,i}^2 + \boldsymbol{p}_i^2 + 2d_i^* d_i\right) - \boldsymbol{\beta}_i \cdot 2p_{0,i}\boldsymbol{p}_i\right] . \tag{3.30b}$$

The PF part does not explicitly change except for the removed bosonic phases. This radial gauge will be denoted by the dependency ψ instead of ψ^*, ψ in the following. When calculating the partition function in this gauge, the integration measure also needs to be substituted [50]

$$\int_{-\infty}^{\infty} \frac{d\Psi^* d\Psi}{2\pi \mathrm{i}} \to \int_0^\infty d\Psi^2 . \tag{3.31}$$

Moreover, according to the Read-Newns path integral [97, 98], the Lagrange multipliers are promoted to dynamic potential fields, which need to be integrated along the entire imaginary axis [48].

3.2.2 Momentum-space representation

We impose PBCs to the Hamiltonian, and due to the resulting translation symmetry, the natural basis of $\mathcal{L}_F$ is in momentum space. We apply the FT defined in Equation (3.10d) to the collection of PFs ϕ_i as well as the bosonic $\underline{z}_i$-matrices and LM fields $\beta_{0,i}, \boldsymbol{\beta}_i$, where number of lattice sites is denoted by N. We then can rewrite the PF part of the Lagrangian through a SB-dependent hopping matrix $\underline{H}^{\psi}_{k_1,k_2}$ [53, 56, 99]

$$\mathcal{L}_F\left[\phi_{k_1}^*, \phi_{k_2}, \psi_{k_{1,2}}\right] = \sum_{k_1,k_2} \phi_{k_1}^\dagger \left(\partial_\tau \delta_{k_1,k_2} + \underline{H}^{\psi}_{k_1,k_2}\right)\phi_{k_2} , \tag{3.32}$$

with

$$\underline{H}^{\psi}_{k_1,k_2} = \delta_{k_1,k_2}\left(\underline{\epsilon} - \mu_0\right) + \frac{1}{\sqrt{N}}\left(\underline{B}\right)^\top_{k_1-k_2} + \frac{1}{N}\sum_{\boldsymbol{k}} \left(\underline{Z}^\dagger\right)^\top_{k-k_1} \underline{\mathcal{H}}_k \left(\underline{Z}\right)^\top_{k-k_2} . \tag{3.33a}$$

Moreover, we define the bare hopping matrix

$$\underline{\mathcal{H}}_k = \sum_{ij} \mathrm{e}^{\mathrm{i}k\boldsymbol{\Delta}_{ij}}\left(\underline{t}^o_{ij} + \underline{t}^f_{ij} + \underline{\tilde{V}}_{ij} + \underline{V}^{of}_{ij}\right) , \tag{3.33b}$$

that contains orbital and spin degrees of freedom and $\boldsymbol{\Delta}_{ij}$ connects lattice sites i and j. It describes the hopping matrix of the non-renormalized Hamiltonian, excluding on-site degrees of freedom. These need to be considered separately because they are not renormalized by the $\underline{z}$-matrices within the SB representation, and we define

$$\underline{\epsilon} = \mathrm{diag}(\epsilon_1, ..., \epsilon_O, \epsilon_f) . \tag{3.33c}$$

Also, we define a generalized $\underline{Z}$-matrix, where all non-interacting orbitals are represented by the identity matrix and a generalized Lagrange multiplier matrix, which of course vanishes for the non-interacting orbitals

$$\underline{Z}_k = (\underline{\mathbb{1}}_{2O\times 2O}\ \sqrt{N}\delta_{k,0}) \oplus \underline{z}_k , \tag{3.33d}$$

$$\underline{B}_k = \underline{0}_{2O\times 2O} \oplus \underline{\beta}_k \,, \tag{3.33e}$$

$$\underline{\beta}_k = \sum_{\mu=0}^{3} \beta_{\mu,k}\underline{\tau}^{\mu} \,. \tag{3.33f}$$

Finally, we define the PF Green's function

$$\underline{G}^{\psi}_{k_1,k_2} = -\left(\partial_\tau + \underline{H}^{\psi}_{k_1,k_2}\right)^{-1} \,. \tag{3.34}$$

After all, the SB Lagrangian is given by

$$\mathcal{L}\left[\phi^*,\phi,\psi\right] = \mathcal{L}_B\left[\psi_i\right] + \mathcal{L}_F\left[\phi^*_{k_1},\phi_{k_2},\psi_{k_{1,2}}\right] \,, \tag{3.35}$$

where $\mathcal{L}_B$ defined in Equation (3.30b) is kept in position-space and $\mathcal{L}_F$ given by Equation (3.32) is more conveniently handled in momentum-space.

3.2.3 Atomic limit

Our model of interacting electrons associated with the two-particle Hubbard term cannot be integrated out exactly within the path integral because the action contains terms of the order $\mathcal{O}\left(f^4\right)$ in the Lagrangian. This problem, of course, is not resolved by the SB representation because of the coupling of PF and SB fields in $\mathcal{L}_F$ produces terms of the order $\mathcal{O}\left(\Psi^4\phi^2\right)$, which is in general even more complicated. In the atomic limit where we consider only one lattice site, however, only quadratic terms remain and the fields can principally be integrated out analytically. The according Hamiltonian is given by

$$\hat{H}_{\text{Atom}} = -\mu_0 \sum_\sigma \hat{f}^\dagger_\sigma \hat{f}_\sigma + U\hat{f}^\dagger_\uparrow \hat{f}_\uparrow \hat{f}^\dagger_\downarrow \hat{f}_\downarrow \to -\mu_0 \sum_\sigma \hat{f}^\dagger_\sigma \hat{f}_\sigma + U\hat{d}^\dagger\hat{d} \,. \tag{3.36a}$$

The Hilbert space is only four dimensional $\{|0\rangle, |\uparrow\rangle, |\downarrow\rangle, |2\rangle\}$, and we find

$$Z_{\text{Atom}} = \text{Tr}\, e^{-\beta\hat{H}_{\text{Atom}}} = 1 + 2e^{\beta\mu_0} + e^{\beta(2\mu_0 - U)} \,. \tag{3.36b}$$

In the following, we will show that the SB path integral reproduces the correct atomic limit within the radial gauge under the assumption that the LM fields can be chosen to be time-independent, whereas the Cartesian gauge yields an incorrect result due to over-counting, which stresses the importance of the gauge fixing. Even though the LMs are formally time-dependent in the radial gauge, we assume them to be static in the atomic limit because the charge density $\hat{n} = \sum_\sigma \hat{f}^\dagger_\sigma \hat{f}_\sigma$ is a conserved quantity, which can be seen in the Heisenberg picture

$$\frac{\partial \hat{n}}{\partial \tau} = \frac{1}{\hbar}\left[\hat{H}_{\text{Atom}}\,,\,\hat{n}\right]_- = 0 \,. \tag{3.36c}$$

It would nevertheless be desirable to set up the formally correct calculation with time-dependent LMs, which has been established for the KR-SB representation at infinite interactions [100, 101], but is, as far as we know, still lacking for the general case.

We present the following atomic limit calculation based on Reference [53], which is a generalization from the KR representation shown in Reference [80] to the SRIKR case. According to Equation (3.30), the SB-atomic

limit Lagrangian in the radial gauge is given by

$$\mathcal{L}_{\text{Atom}} = -\alpha + \alpha e^2 + d^*(U + \partial_\tau + \alpha - 2\beta_0)d + \boldsymbol{p}^\top \underline{\mathcal{B}}\, \boldsymbol{p} + \boldsymbol{f}^\dagger \underline{\mathcal{F}} \boldsymbol{f} \tag{3.37a}$$

with

$$\begin{aligned} \boldsymbol{p} &= \begin{pmatrix} p_0 \\ p_1 \\ p_2 \\ p_3 \end{pmatrix}, \quad \underline{\mathcal{B}} = \begin{pmatrix} \alpha - \beta_0 & -\beta_1 & -\beta_2 & -\beta_3 \\ -\beta_1 & \alpha - \beta_0 & 0 & 0 \\ -\beta_2 & 0 & \alpha - \beta_0 & 0 \\ -\beta_3 & 0 & 0 & \alpha - \beta_0 \end{pmatrix}, \\ \boldsymbol{f} &= \begin{pmatrix} f_\uparrow \\ f_\downarrow \end{pmatrix}, \quad \underline{\mathcal{F}} = \begin{pmatrix} \partial_\tau - \mu_0 + \beta_0 + \beta_3 & \beta_1 + \mathrm{i}\beta_2 \\ \beta_1 - \mathrm{i}\beta_2 & \partial_\tau - \mu_0 + \beta_0 - \beta_3 \end{pmatrix}. \end{aligned} \tag{3.37b}$$

To integrate out the fields, one needs to diagonalize the matrices $\underline{\mathcal{B}}$ and $\underline{\mathcal{F}}$, whose eigenvalues are given by

$$\begin{aligned} \mathcal{B}_{1/2} &= \alpha - \beta_0 \,, \\ \mathcal{B}_{3/4} &= \alpha - \beta_0 \pm \beta \,, \\ \mathcal{F}_{1/2} &= \partial_\tau - \mu_0 + \beta_0 \pm \beta \end{aligned} \tag{3.37c}$$

where $\beta = \sqrt{\beta_1^2 + \beta_2^2 + \beta_3^2}$. In this quasiparticle (QP) basis, we have a diagonal Lagrangian of non interacting fermions and bosons and we apply Equation (3.14d) to integrate out the fields. Consequently, we find

$$\begin{aligned} Z_{\text{Atom}} = \lim_{N\to\infty} \frac{1}{(2\pi\mathrm{i}T)^2} \frac{1}{(2\pi\mathrm{i}NT)^3} \int_{-\mathrm{i}\pi T}^{\mathrm{i}\pi T} \mathrm{d}\alpha \int_{-\mathrm{i}\pi T}^{\mathrm{i}\pi T} \mathrm{d}\beta_0 \iiint_{-\mathrm{i}\pi NT}^{\mathrm{i}\pi NT} \mathrm{d}^3\beta \, \mathrm{e}^{\alpha/T} \left(1 - \mathrm{e}^{-\alpha/T}\right)^{-1} \left(1 - \mathrm{e}^{-(\alpha - 2\beta_0 + U)/T}\right)^{-1} \\ \times \left(1 - \mathrm{e}^{-(\alpha-\beta_0)/T}\right)^{-2} \left(1 - \mathrm{e}^{-(\alpha-\beta_0+\beta)/T}\right)^{-1} \left(1 - \mathrm{e}^{-(\alpha-\beta_0-\beta)/T}\right)^{-1} \left(1 + \mathrm{e}^{-(\beta_0+\beta-\mu_0)/T}\right) \left(1 + \mathrm{e}^{-(\beta_0-\beta-\mu_0)/T}\right) \end{aligned} \tag{3.38a}$$

and are left to determine the integrals over the LMs. We start with the integration of α, and observe that the partition function can be written as an integral over a function of $\mathrm{e}^{\alpha/T}$

$$Z_{\text{Atom}} = \frac{1}{2\pi\mathrm{i}T} \int_{-\mathrm{i}\pi T}^{\mathrm{i}\pi T} f\left(\mathrm{e}^{\alpha/T}\right) d\alpha \,, \tag{3.38b}$$

and after substituting $\alpha/T \to \mathrm{i}\alpha$, we find

$$\frac{1}{2\pi\mathrm{i}T} \int_{-\mathrm{i}\pi T}^{\mathrm{i}\pi T} f\left(\mathrm{e}^{\alpha/T}\right) d\alpha \to \frac{1}{2\pi} \int_{-\pi}^{\pi} f\left(\mathrm{e}^{\mathrm{i}\alpha}\right) d\alpha \,. \tag{3.38c}$$

Now, we may exploit that the projectors defined in Equation (2.18) are invariant under the addition of an arbitrary imaginary part to the Lagrange multipliers $\alpha \to \alpha + \mathrm{i}\tilde{\alpha}$, which by substitution $z = \mathrm{e}^{-\mathrm{i}\alpha}$ maps the integral onto a complex contour integral with radius $\mathrm{e}^{-\tilde{\alpha}}$ around the origin

$$\frac{1}{2\pi} \int_{-\pi}^{\pi} f\left(\mathrm{e}^{\mathrm{i}\alpha}\right) d\alpha \to -\frac{1}{2\pi\mathrm{i}} \oint \frac{1}{z} f\left(\frac{1}{z}\right) dz \,. \tag{3.38d}$$

Since $\tilde{\alpha}$ may be chosen arbitrary small, we may determine the integral by its residue at $z = 0$ and after applying the substitution given by Equation (3.38c) to all LMs, we find

$$Z_{\text{Atom}} = -\text{Res}\left[\frac{1}{z} f\left(\frac{1}{z}\right), z = 0\right] = \lim_{N\to\infty} \frac{1}{2\pi} \frac{1}{(2\pi N)^3} \int_{-\pi}^{\pi} \mathrm{d}\beta_0 \iiint_{-\pi N}^{\pi N} \mathrm{d}^3\beta \left(1 + \mathrm{e}^{-(2\mathrm{i}\beta_0 + U/T)} + 2\mathrm{e}^{-\mathrm{i}\beta_0 - \mathrm{i}\beta} + 2\mathrm{e}^{-\mathrm{i}\beta_0 + \mathrm{i}\beta}\right) \times \left(1 + \mathrm{e}^{\mathrm{i}\beta_0 + \mathrm{i}\beta + \mu_0/T}\right)\left(1 + \mathrm{e}^{\mathrm{i}\beta_0 - \mathrm{i}\beta + \mu_0/T}\right) . \tag{3.38e}$$

The β_0-integral may be carried out in the same way, yielding

$$Z_{\text{Atom}} = 1 + \mathrm{e}^{-(U-2\mu_0)/T} + 2\mathrm{e}^{\mu_0/T} + \mathrm{e}^{\mu_0/T} \lim_{N\to\infty} \frac{1}{(2\pi N)^3} \iiint_{-\pi N}^{\pi N} \mathrm{d}^3\beta \left(2\cos(2\beta) + 4\cos(\beta)\right) . \tag{3.38f}$$

The remaining integral vanishes in the limit $N \to \infty$ and thus we recover the correct result for the partition function of the atomic limit in the radial gauge[1]

$$Z_{\text{Atom}} = 1 + 2\mathrm{e}^{\mu_0/T} + \mathrm{e}^{(2\mu_0 - U)/T} . \tag{3.38g}$$

The calculation can be carried out in the same way with complex fields in the Cartesian gauge, with the only difference that there are additional contributions from the cross product $\boldsymbol{p}^* \times \boldsymbol{p}$. By explicit calculation one finds that this term causes an over-counting yielding the wrong partition function $1 + \mathrm{e}^{-(U-2\mu_0)/T} + 4\mathrm{e}^{\mu_0/T}$ [53]. It is, therefore, crucial to remove the spurious fields in order to have a well-defined path integral[2].

We will argue for the Gaussian fluctuations in Chapter 5 that the best way to approximatively fulfill the α-constraint is to replace an arbitrary SB field by direct application of $1 = e^2 + d^* d + \sum_{\mu=0}^{3} p_\mu^2$. This, however, is not correct for exact calculations like the atomic limit, where the replacement yields a wrong partition function and the result even depends on which field has been replaced[3].

[1] We use $\int x^2 \left(\cos(2x) + 2\cos(x)\right) dx = x^2 \left(2\sin(x) + \sin(x)\cos(x)\right) + x \left(4\cos(x) + \frac{1}{2}\cos(2x) - 4\sin(x) - \frac{1}{2}\cos(x)\sin(x)\right)$ and apply spherical coordinates. Since the trigonometric functions are bounded, we find the integral to be of the order $\mathcal{O}\left(N^2\right)$ and considering the normalization, we find $\lim_{N\to\infty} \frac{\mathcal{O}(N^2)}{\mathcal{O}(N^3)} = 0$.

[2] It was understood early in the literature that the cross product of the $\boldsymbol{p}$-fields is problematic. So it was at some point suggested in the literature to add an additional constraint $\gamma\left(\hat{\boldsymbol{p}}^\dagger \times \hat{\boldsymbol{p}}\right) = 0$ to force the cross product to be zero [73, 74]. This, however, was agreed to be incorrect in the following literature [75, 76]. And an explicit analogous calculation of the partition function would also yield the wrong result, to be specific $1 + \mathrm{e}^{(2\mu_0 - U)/T}$.

[3] Replacing e^2, e.g., yields $Z_{\text{Atom}} = 1 + 2\mathrm{e}^{\mu_0/T} + \mathrm{e}^{(2\mu_0 - U)/T} + 4\mathrm{e}^{2\mu_0/T}$, i.e., we explicitly find that not integrating the α-constraints causes states, which are occupied by more than one boson.

CHAPTER 4

Static mean-field approximation

As we pointed out in Chapter 3, the slave-boson (SB)-Lagrangian is of the order $\mathcal{L} = \mathcal{O}\left(\phi^2\Psi^4\right)$ in pseudofermion (PF) and SB fields, and those in total cannot be integrated out exactly. We, therefore, solve the problem approximately by imposing a static, uniform mean-field (MF) ansatz to the SB and Lagrange multiplier (LM) fields, i.e., replacing respective space-time dependent fields by their quantum mechanical (QM) expectation values[1]

$$\psi^{(*)}_{\mu,i}(\tau) \to \left\langle \psi^{(*)}_{\mu,i}(\tau) \right\rangle = \psi_\mu \,. \tag{4.1a}$$

Following Equation (3.7), the QM expectation value is given by

$$\left\langle \psi^{(*)}_{\mu,i}(\tau) \right\rangle = \frac{\int \mathcal{D}\left[\boldsymbol{\psi}, \boldsymbol{\phi}^*, \boldsymbol{\phi}\right] \; \psi^{(*)}_{\mu,i}(\tau)\, \mathrm{e}^{-\mathcal{S}^{(0)}[\phi^*,\phi]}}{Z^{(0)}} \,, \tag{4.1b}$$

where $\mathcal{S}^{(0)}$ denotes the MF action and $Z^{(0)}$ the MF partition function, which are of 0th order in bosonic fields. Because of translation symmetry of the Lagrangian w.r.t. space-time $\mathcal{L}(r) = \mathcal{L}(r + \Delta r)$, the expectation value ψ_μ does not depend on $r = (\boldsymbol{r}_i, \tau)$ and is thus simply given by a real number. Within this ansatz, the action becomes quadratic in PF degrees of freedom and can be integrated out exactly. Since $\mathcal{S}^{(0)}$ does not depend on bosonic fields, our MF ansatz does not implicate a direct self consistency equation like e.g., in BCS theory[2] [28, 102]. We will rather minimize the MF free energy (FE) $F^{(0)}$, while enforcing the MF constraints, to determine the ground state. Within this uniform MF ansatz, the SB-dependent hopping matrix introduced in Equation (3.32) becomes diagonal, because the $\underline{z}$-matrices do not carry space-time degrees of freedom any more, i.e., $\underline{H}^{\psi}_{k_1,k_2} \to \underline{H}^{\langle\psi\rangle}_{k}$.

4.1 Spiral magnetic mean-field ansatz

Although the internal spatial degrees of freedom are removed by the uniform MF ansatz, we may impose non-uniform, symmetry-breaking order by means of an external ordering vector $\boldsymbol{Q}$. The SB method is well-

[1] Since the MF Lagrangian is hermitian, its eigenvalues only depend on $\left\langle \psi_\mu \right\rangle \left\langle \psi^*_\mu \right\rangle$, consequently the MF variables ψ_μ can be chosen to be real.

[2] In BCS theory and most other fermionic MF theories, the two-particle vertex of the order $\mathcal{O}\left(f^4\right)$ is replaced by a quadratic expression times the MF expectation value, yielding the order $\mathcal{O}\left(f^2 \langle f \rangle^2\right)$, which makes the action quadratic. However, in opposite to the SB case, the BCS MF action still depends on the same fields that also appear in the expectation value, which implicates a self-consistency condition. It can be shown that solving the resulting gap-equation is equivalent to minimizing the MF free energy (FE) [39]. Since the SB mean-field variables are coupled to the PFs (which still enter the action as fields) by the constraints, one can, however, argue that the saddle point equations, which determine the ground state, are also self-consistency equations.

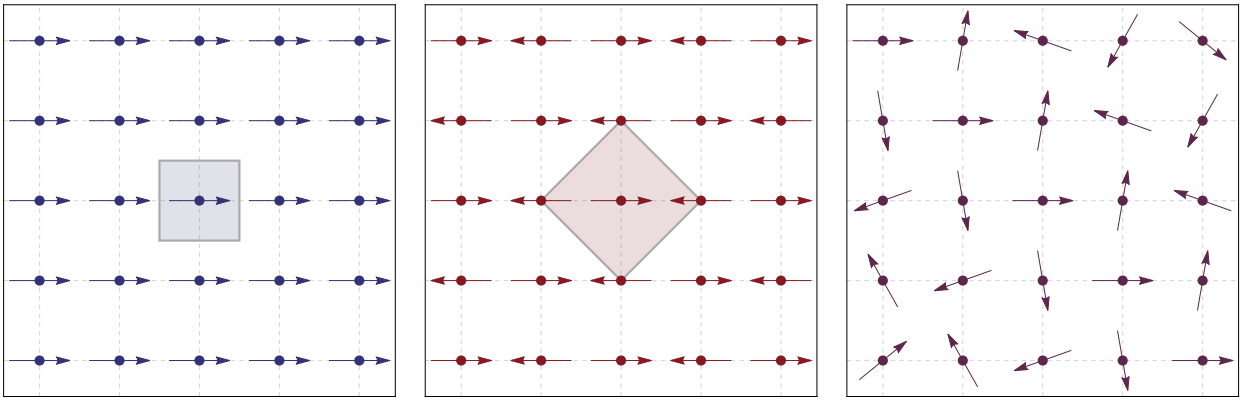

(a) FM, i.e., $\boldsymbol{Q} = 0$. The magnetic unit cell encompasses one lattice site and is identical to the PM unit cell.

(b) AFM order, i.e., $\boldsymbol{Q} = (\pi, \pi)^\top$. The magnetic unit cell encompasses two lattice sites and is doubled in size compared to the PM unit cell.

(c) ICM order with $\boldsymbol{Q} = (1.4, 1.4)$. There is no spatial translation invariance, i.e., the unit cell is given by the whole lattice.

Figure 4.1: Visualization of the average spin structure in accordance with the spiral magnetic MF for three different ordering vectors in two spatial dimensions. The dots represent lattice sites and arrows depict the orientation of the respective MF spin. The translation invariant magnetic unit cell is displayed by the gray squares.

suited for the investigation of magnetic order because of the simple form of the SB spin operator $\hat{\boldsymbol{S}}_i = \hat{\boldsymbol{\rho}}_i \hat{p}_{0,i}$. Accordingly, we define the MF ansatz [53, 55, 71, 74, 103–105]

$$\boldsymbol{p}_i(\tau) \to p \begin{pmatrix} \cos(\boldsymbol{Q}\boldsymbol{R}_i) \\ \sin(\boldsymbol{Q}\boldsymbol{R}_i) \\ 0 \end{pmatrix} , \tag{4.2a}$$

$$p_{0,i}(\tau) \to p_0 , \tag{4.2b}$$

$$e_i(\tau) \to e , \tag{4.2c}$$

$$d_i(\tau) \to d , \tag{4.2d}$$

which incorporates a spin spiral in the x-y plane[1] , where the absolute value of the spin expectation value, i.e., the (staggered) magnetization is given by

$$m = \left| \left\langle \hat{\boldsymbol{S}} \right\rangle \right| = p p_0 , \tag{4.3}$$

and the spatial periodicity, and thus also the size of the magnetic unit cell [19] is controlled by the external ordering vector $\boldsymbol{Q}$. For simplicity of notation, we have dropped the brackets $\langle \cdot \rangle$, but the MF variables are to be understood as expectation values, which are positive semidefinite $\{p, p_0, e, d\} \in \mathbb{R}_0^+$ and we recognize that $p = |\boldsymbol{p}|$. Moreover, we define the spin-spiral periodicity P as the minimal integer that satisfies

$$P\boldsymbol{Q} \bmod 2\pi = 0 \tag{4.4}$$

For a more intuitive understanding, P is also identified with the number of atoms per magnetic unit, i.e., its size is proportional to P, and the size of the magnetic BZ is reduced by a factor $1/P$ in comparison to the PM

[1] For SRI models, the spin-plane is arbitrary, and we can make this choice w.l.o.g. If spin-orbit coupling (SOC) is present, the orientation may play a role and can be rotated as discussed in Appendix B.4.

case. The two most important types of magnetic order covered by the MF ansatz are ferromagnetism (FM) ($\boldsymbol{Q} = (0,0,0)^\top$, $P = 1$) and antiferromagnetism (AFM) ($\boldsymbol{Q} = (\pi,\pi,\pi)^\top$, $P = 2$). If components of $\boldsymbol{Q}/2\pi$ are not a rational number, we find $P \to \infty$ and the BZ shrinks to a single point, implying that the momentum $\boldsymbol{k}$ is no longer a good quantum number. This type of order is called incommensurate magnet (ICM). The three discussed examples of magnetic ground states are illustrated in Figure 4.1.

Since the constraints defined in Equation (2.14) can also not be integrated out exactly within the field theory, we need to consider them in the static MF ansatz as well. In order to do so, the constraint fields act as Lagrange multipliers (LMs) to enforce the constraints on average by fixing the occupation of bosons and matching the expectation values of the SB and PF representations of the spin and charge density

$$1 = e^2 + d^2 + p_0^2 + p^2 \,, \tag{4.5a}$$

$$\langle \hat{n}_F \rangle = \langle \hat{n}_B \rangle = 2d^2 + p_0^2 + p^2 \,, \tag{4.5b}$$

$$\left| \left\langle \hat{\boldsymbol{S}}_F \right\rangle \right| = \left| \left\langle \hat{\boldsymbol{S}}_B \right\rangle \right| = p p_0 \,. \tag{4.5c}$$

Moreover, the PFs need to be constrained to the same spin-spiral as the SBs, which leads to the ansatz [53, 55, 71, 74, 103–105]

$$\alpha_i \to \alpha \,, \tag{4.6a}$$

$$\beta_{0,i} \to \beta_0 \,, \tag{4.6b}$$

$$\boldsymbol{\beta}_i \to \beta \begin{pmatrix} \cos(\boldsymbol{Q}\boldsymbol{R}_i) \\ \sin(\boldsymbol{Q}\boldsymbol{R}_i) \\ 0 \end{pmatrix} , \tag{4.6c}$$

with $\alpha, \beta_0, \beta \in \mathbb{R}$. Notice that the constraint given by Equation (4.5a) fixes the normalization of the magnetization to the expected continuous interval $m \in \left[0, \frac{1}{2}\right]$. PM states, defined by a vanishing magnetization, are recovered by $p = 0$, and the corresponding ground state does not depend on the ordering vector $\boldsymbol{Q}$. This limit also implicates $\beta = 0$ because the PF expectation value of the spin does not vanish otherwise.

4.2 Non-interacting limit

The discussed lattice Hamiltonians are exactly solvable in the limit of zero interaction $U \to 0$ in the original fermionic description. It is desirable that our MF approach correctly reproduces that limit, which requires $\underline{z} = \underline{\mathbb{1}}_2$ for $U = 0$, since the $\underline{z}$-matrix renormalizes the hopping and hybridization amplitudes of the PFs. In order to achieve that goal, we exploit the freedom of description of the exact theory on the constrained subspace according to Equation (2.17). We may thus renormalize the $\underline{\hat{z}}$-matrix operator[1] [73]

$$\underline{\hat{z}} = \hat{e}^\dagger \underline{\hat{p}} + \underline{\hat{\bar{p}}}^\dagger \hat{d} \to \left(\hat{e}^\dagger \, \underline{\hat{L}} \, \hat{M} \, \underline{\hat{R}} \, \underline{\hat{p}} + \underline{\hat{\bar{p}}}^\dagger \, \underline{\hat{L}} \, \hat{M} \, \underline{\hat{R}} \hat{d} \right) , \tag{4.7a}$$

[1] In early works, the renormalization was not correct in the non-interacting limit, which in some cases came along with a wrong normalization of the $\underline{p}$-matrix [50, 59, 61, 66, 71], this was corrected in Reference [73]. It was also recognized that the normalization factors break the normal order of the path integral [75], which we will further discuss in Section 5.1.

with

$$\hat{\underline{L}} = \left((1-\hat{d}^\dagger\hat{d})\underline{\tau}_0 - 2\,\hat{\underline{p}}^\dagger\hat{\underline{p}}\right)^{-1/2}, \tag{4.7b}$$

$$\hat{M} = \left(1+\hat{d}^\dagger\hat{d}+\hat{e}^\dagger\hat{e}+\sum_\mu \hat{p}_\mu^\dagger\hat{p}_\mu\right)^{1/2}, \tag{4.7c}$$

$$\hat{\underline{R}} = \left((1-\hat{e}^\dagger\hat{e})\underline{\tau}_0 - 2\,\hat{\underline{p}}^\dagger\hat{\underline{p}}\right)^{-1/2}, \tag{4.7d}$$

without impacting the exact theory, whereas the MF approximation is subject to change. As shown in Appendix A.4, the renormalized $\underline{z}$-matrix can be expressed in a more convenient way, where the renormalization factors $\hat{L}$ and $\hat{R}$ become diagonal by expansion in the basis of Pauli matrices. Within the spiral MF ansatz defined in Equation (4.2), it is found to be [53, 99]

$$\underline{z}_i = \frac{z_+ + z_-}{2}\underline{\tau}^0 + \frac{z_+ - z_-}{2}\sum_{\mu=1}^{3}\frac{p_{\mu,i}}{p}\underline{\tau}^\mu = \begin{pmatrix} \mathcal{Z}_+ & \mathcal{Z}_-\,\mathrm{e}^{-\mathrm{i}\boldsymbol{Q}\boldsymbol{R}_i} \\ \mathcal{Z}_-\,\mathrm{e}^{\mathrm{i}\boldsymbol{Q}\boldsymbol{R}_i} & \mathcal{Z}_+ \end{pmatrix}, \tag{4.8a}$$

with

$$\mathcal{Z}_\pm = \frac{z_+ \pm z_-}{2}, \tag{4.8b}$$

$$z_\pm = \frac{p_0(e+d) \pm p(e-d)}{\sqrt{2\left[1-d^2-(p_0\pm p)^2/2\right]\left[1-e^2-(p_0\mp p)^2/2\right]}}. \tag{4.8c}$$

In the PM limit, the matrix reduces to

$$\underline{z}_0 = \frac{p_0(e+d)}{\sqrt{2(1-d^2-p_0^2/2)(1-e^2-p_0^2/2)}}\underline{\tau}^0 = z_0\underline{\tau}^0. \tag{4.8d}$$

Returning to the question of the non-interacting limit, we may assume Equation (4.8d) to be present because there is no magnetic order without interaction and need to show that $z_0 = 1$ for $U = 0$. For free particles, the two possible electronic states $|\uparrow\rangle, |\downarrow\rangle$ are under consideration of the Pauli principle randomly occupied with the same probability on each site. For an average filling of $0 \leq n \leq 2$ per site, the mean occupation of $|\uparrow\rangle$ or $|\downarrow\rangle$ is given by $n/2$. Consequently, the average number of doubly occupied sites is given by $d^2 = (n/2)^2$, the mean value of singly occupied sites yields $p_0^2 = 2(n/2)(1-n/2)$ by accounting for the spin degeneracy. Finally, it is $e^2 = 1 - d^2 - p_0^2 = (1-n/2)^2$. Inserting these expressions into Equation (4.8d), one finds $z_0 = 1$ independent of n as demanded, which correctly fixes the non-interacting limit[1] [53, 99].

[1] There are still multiple different choices of renormalization factors that fulfill the correct non-interacting limit. The MF renormalization, e.g., remains unchanged if creation operators are substituted by annihilation operators. However, the established choice employing particle operators is reasonable because the renormalized Hamiltonian remains hermitian in the exact theory. Moreover, the MF solution in the non-interacting limit is invariant under the substitution $\hat{\underline{p}}^\dagger \to \hat{\underline{p}}^\dagger$, because it features $p = 0$. However, the particular chosen form is necessary to recover the exact original KR-SB representation [49] in the limit $p_1 = p_2 = 0$. Moreover, the chosen form recovers the symmetry of simultaneously interchanging $e \leftrightarrow d$ and $\hat{\underline{p}}^\dagger \leftrightarrow \hat{\underline{p}}^\dagger$, which is present in the exact representation within the MF ansatz. We confirmed by numerical analysis that breaking this symmetry causes inconsistent and unphysical results for the MF solution. After all, there remains some ambiguity about the choice of the renormalization factors, but the presented form has been commonly agreed on in the SB community, and we provided strong arguments why it is reasonable. Finally, another point is that the numerical results calculated with this renormalization compare well to other theoretical methods.

4.3 Mean-field Lagrangian

Under application of the MF ansatz defined in Equations (4.2) and (4.6), the SB Lagrangian given by Equation (3.35) is simplified to [53, 54]

$$\mathcal{L}^{(0)}\left[\phi^*,\phi\right] = \mathcal{L}_B^{(0)} + \mathcal{L}_F^{(0)}\left[\phi^*,\phi\right] \ , \tag{4.9a}$$

with

$$\mathcal{L}_B^{(0)} = N\left[Ud^2 + \alpha(e^2+d^2+p_0^2+p^2-1) - \beta_0(2d^2+p_0^2+p^2) - 2\beta p_0 p\right] \ , \tag{4.9b}$$

$$\mathcal{L}_F^{(0)}\left[\phi^*,\phi\right] = H_F\left[\phi^*,\phi\right] + \sum_i \left[\phi_i^\dagger \partial_\tau \phi_i + \beta_0 f_i^\dagger \underline{\tau}^0 f_i + \beta\left(f_i^\dagger\left[\cos\left(\boldsymbol{Q}\boldsymbol{R}_i\right)\underline{\tau}^x + \sin\left(\boldsymbol{Q}\boldsymbol{R}_i\right)\underline{\tau}^y\right] f_i\right)\right] \ , \tag{4.9c}$$

where N denotes the total number of lattice sites. The corresponding MF action is given by

$$\mathcal{S}^{(0)} = \int_0^\beta d\tau\, \mathcal{L}^{(0)}\left[\phi^*,\phi\right] = \mathcal{S}_B^{(0)} + \mathcal{S}_F^{(0)} \tag{4.10}$$

and since $\mathcal{L}_B^{(0)}$ is constant w.r.t. the field theory, the bosonic part is simply given by

$$\mathcal{S}_B^{(0)} = \beta\, \mathcal{L}_B^{(0)} \ . \tag{4.11}$$

Since $\mathcal{S}_F^{(0)}$ is quadratic in PF fields, it describes a renormalized effectively non-interacting field theory that can be treated in analogy to the discussion in Section 3.1.4. To integrate out the PFs later on, we exploit the translation invariance by adapting a diagonal basis in momentum-space and need calculate the SB-dependent hopping matrix $\underline{H}_{\boldsymbol{k}}^{\psi,Q}$ as MF analog to Equation (3.33a). Despite having only one internal momentum index, the external ordering vector $\boldsymbol{Q}$ correlates two fields with a momentum overlap of $\pm\boldsymbol{Q}$, which generally increases the dimension of $\underline{H}_{\boldsymbol{k}}^{\psi,Q}$ as a consequence of an enlarged magnetic unit cell for $\boldsymbol{Q} \neq 0$. Since we require $\phi_{k+2\pi} = \phi_k$ to hold, a suitable basis that captures all possible correlations and exploits translation invariance w.r.t. the magnetic unit cell, is found by[1]

$$\begin{aligned} \phi_{\boldsymbol{k}}^Q &= \left(\phi_{\boldsymbol{k}}\ ,\ \phi_{\boldsymbol{k}+\boldsymbol{Q}}\ ,\ \phi_{\boldsymbol{k}+2\boldsymbol{Q}}\ ,\ \dots\ ,\ \phi_{\boldsymbol{k}+(P-1)\boldsymbol{Q}}\right)^\top \ , \\ \phi_{\boldsymbol{k}} &= \left(c_{1,\boldsymbol{k},\uparrow}\ ,\ c_{1,\boldsymbol{k},\downarrow}\ ,\ \dots\ ,\ c_{O,\boldsymbol{k},\uparrow}\ ,\ c_{O,\boldsymbol{k},\downarrow}\ ,\ f_{\boldsymbol{k},\uparrow}\ ,\ f_{\boldsymbol{k},\downarrow}\right)^\top \ . \end{aligned} \tag{4.12}$$

With the definition of the spin-spiral periodicity in Equation (4.4), it enables a ladder of possible momentum overlaps with PBCs. In analogy to Equation (3.16), the action can then in Matsubara-space be expressed by

$$\mathcal{S}_F^{(0)} = \sum_k \left(\phi_k^Q\right)^\dagger \left(-\mathrm{i}\omega_n + \underline{H}_{\boldsymbol{k}}^{\psi,Q}\right)\phi_k^Q = -\sum_k \left(\phi_k^Q\right)^\dagger \left[\underline{G}_k^\psi\right]^{-1}\phi_k^Q \ , \tag{4.13}$$

with the PF mean-field Green's function

$$\underline{G}_k^\psi = \left(\mathrm{i}\omega_n - \underline{H}_{\boldsymbol{k}}^{\psi,Q}\right)^{-1} \ . \tag{4.14}$$

The specific forms of $\underline{H}^{\psi,Q}$ for the three models that we discuss within this thesis, i.e., the Hubbard model, periodic Anderson model (PAM) and topological Kondo insulator (TKI) model, are derived in Appendix B. In

[1] As shown in [55], this basis is connected to a real space sublattice basis by a unitary transformation. However, the chosen basis is more convenient, especially with its simplificaton for spin degenerate models.

general, the dimension of the SB-dependent hopping matrix is given by $\dim \underline{H}^{\psi,\boldsymbol{Q}} = 2\times(O+1)\times P$, proportional to the spin-spiral periodicity P, which makes the evaluation of large magnetic unit cells numerically costly. For models without spin-orbit coupling (SOC) (i.e., the Hubbard model and PAM in our case), however, there is a block-diagonality such that only equal spins with the same momenta and opposite spins with a momentum transfer of $\boldsymbol{Q}$ couple. In this case, we can express $\underline{H}^{\psi,\boldsymbol{Q}}$ in the reduced basis

$$\phi_{\boldsymbol{k}}^{\boldsymbol{Q}} \to \left(c_{1,\boldsymbol{k},\uparrow}, c_{1,\boldsymbol{k}-\boldsymbol{Q},\downarrow}, \dots, c_{O,\boldsymbol{k},\uparrow}, c_{O,\boldsymbol{k}-\boldsymbol{Q},\downarrow}, f_{\boldsymbol{k},\uparrow}, f_{\boldsymbol{k}-\boldsymbol{Q},\downarrow}\right)^{\top} , \tag{4.15}$$

whose dimension is independent of $\boldsymbol{Q}$ and P. This property comes with the convenience that $\boldsymbol{Q}$ can be considered as a continuous MF parameter without adapting the respective matrix $\underline{H}^{\psi,\boldsymbol{Q}}$. We can, therefore, easily determine MF ground-states with arbitrary $\boldsymbol{Q}$, including the possibility of incommensurate magnetic (ICM) order. For models with SOC, this cannot be easily achieved, and it is preferred to determine the leading magnetic ordering vector by means of a PM fluctuation calculation (compare Section 5.3.3) and then determine the magnetic MF ground state for the corresponding fixed value of $\boldsymbol{Q}$.

4.4 Saddle point equations

In order to determine the MF ground state, we need to minimize the desired thermodynamic potential, i.e., grand potential (GP) or free energy (FE) w.r.t. the SB mean-field variables while simultaneously enforcing the constraints. The GP per lattice site is given by

$$\Omega^{(0)} = -\frac{T}{N} \ln Z^{(0)} , \tag{4.16a}$$

with the MF partition function

$$Z^{(0)} = \int \mathcal{D}\left[\phi^*, \phi\right] \, \mathrm{e}^{-\mathcal{S}^{(0)}[\phi^*,\phi]} . \tag{4.16b}$$

For the MF action defined in Equation (4.10), it factorizes into a purely bosonic and a PF part $Z^{(0)} = Z_B^{(0)} Z_F^{(0)}$ which yields

$$\Omega^{(0)} = \Omega_B^{(0)} + \Omega_F^{(0)} \tag{4.17a}$$

The bosonic part is constant w.r.t. the field theory and thus simply given by

$$\Omega_B^{(0)} = -\frac{T}{N} \ln Z_B^{(0)} = -\frac{T}{N} \ln \mathrm{e}^{-\mathcal{S}_B^{(0)}} = \frac{1}{N} \mathcal{L}_B^{(0)} . \tag{4.17b}$$

The PF contribution is determined by the action in Equation (4.13) and integration over all fields within a diagonal basis in analogy to Equation (3.19b), yielding

$$\Omega_F^{(0)} = -\frac{T}{N} \sum_{\boldsymbol{k}\in \mathrm{BZ}_{\boldsymbol{Q}}} \sum_{o,s,p,\boldsymbol{k}} \ln\left(1 + \mathrm{e}^{-\varepsilon_{\boldsymbol{k}}^{o,s,p}/T}\right) . \tag{4.17c}$$

The SB-dependent eigenvalues of $\underline{H}^{\psi,\boldsymbol{Q}}$ are denoted by $\varepsilon_{\boldsymbol{k}}^{o,s,p}$, where the indices o, s, p represent the orbital, spin and periodicity degrees of freedom for a total number of $(O+1)\times 2\times P$ bands. The remaining sum is to be performed over the magnetic BZ, which is defined by back-folding w.r.t. the reciprocal lattice vector $\boldsymbol{Q}$. For models without SOC, it holds $\varepsilon_{\boldsymbol{k}}^{p+1} = \varepsilon_{\boldsymbol{k}+\boldsymbol{Q}}^{p}$ [56]. Therefore, the reduced basis with $(O+1)\times 2$ bands defined

in Equation (4.15) already considers the back-folding by the reduced number of bands and the momentum sum has to be performed over the non back-folded, paramagnetic BZ that satisfies $\sum_{\boldsymbol{k}\in\mathrm{BZ}_0} = P \sum_{\boldsymbol{k}\in\mathrm{BZ}_Q}$.

4.4.1 Enforcement of mean-field constraints

Since the Lagrange multipliers (LMs) appear linear in the MF action, they behave like chemical potentials, and we may enforce the constraints by demanding the derivative of the GP w.r.t. the respective LM to vanish. This can most clearly be seen in the real-space representation

$$\frac{\partial\Omega^{(0)}}{\partial\alpha} = -\frac{T}{N}\frac{1}{Z^{(0)}}\int \mathcal{D}\left[\phi^*,\phi\right]\ \beta\left(e^2+d^2+p_0^2+p^2-1\right)\mathrm{e}^{-S^{(0)}[\phi^*,\phi]} = 0\,, \tag{4.18a}$$

$$\frac{\partial\Omega^{(0)}}{\partial\beta_0} = -\frac{T}{N}\frac{1}{Z^{(0)}}\int \mathcal{D}\left[\phi^*,\phi\right]\left(\beta\left(2d^2+p_0^2+p^2\right)-\frac{1}{N}\sum_i\int_0^\beta f_i^\dagger \underline{\tau}^0 f_i\right)\mathrm{e}^{-S^{(0)}[\phi^*,\phi]} = 0\,, \tag{4.18b}$$

$$\frac{\partial\Omega^{(0)}}{\partial\beta} = -\frac{T}{N}\frac{1}{Z^{(0)}}\int \mathcal{D}\left[\phi^*,\phi\right]\left(2\beta p p_0-\frac{1}{N}\sum_i\int_0^\beta f_i^\dagger \underline{\tau}^\top f_i\begin{pmatrix}\cos(\boldsymbol{Q}\boldsymbol{R}_i)\\ \sin(\boldsymbol{Q}\boldsymbol{R}_i)\\ 0\end{pmatrix}\right)\mathrm{e}^{-S^{(0)}[\phi^*,\phi]} = 0\,, \tag{4.18c}$$

where we identify that the QM expectation values of bosonic and PF representations of the spin and charge density are matched as claimed in Equation (4.5). An explicit evaluation of PF expectation values for the Hubbard model through the equal space-time Green's function is provided in Appendix B.1 to illustrate the validity of the constraint implementation.

In practice, the purely bosonic α-constraint can be enforced by directly replacing an arbitrary bosonic MF parameter with Equation (4.5a). The remaining two constraints must be enforced numerically, and since the second derivatives

$$\frac{\partial^2\Omega^{(0)}}{\partial\beta_0^2} = -\frac{1}{T}\left\langle\left(n_f-\hat{n}_{f,\mathrm{PF}}\right)^2\right\rangle = -\frac{1}{T}\mathrm{Var}\,\hat{n}_{f,\mathrm{PF}} \tag{4.19a}$$

$$\frac{\partial^2\Omega^{(0)}}{\partial\beta^2} = -\frac{4}{T}\left\langle\left(S_f-\hat{S}_{f,\mathrm{PF}}\right)^2\right\rangle = -\frac{4}{T}\mathrm{Var}\,\hat{S}_{f,\mathrm{PF}} \tag{4.19b}$$

are negative definite quantities related to the variance of the charge and spin density, it is guaranteed that the MF values of β_0 and β are always uniquely determined. The constraints can thus be enforced by maximizing the GP w.r.t. β_0 and β, i.e., the system pays an extremized energy penalty if it deviates from the constraints.

4.4.2 Grand potential

According to Equation (4.17), the GP is given by

$$\Omega^{(0)} = -\frac{T}{N}\sum_{\boldsymbol{k}\in\mathrm{BZ}_Q}\sum_{o,s,p}\ln\left(1+\mathrm{e}^{-\varepsilon_{\boldsymbol{k}}^{o,s,p}/T}\right)+Ud^2+\alpha(e^2+d^2+p_0^2+p^2-1)-\beta_0(2d^2+p_0^2+p^2)-2\beta p_0 p\,. \tag{4.20}$$

The MF ground state is determined by minimizing the GP w.r.t. the SB variables, while simultaneously enforcing the constraints, i.e., maximizing w.r.t. the LMs. The corresponding saddle point equations are given by[1]

$$\frac{\partial\Omega^{(0)}}{\partial e} = \frac{1}{N}\sum_{k\in \mathrm{BZ}_Q}\sum_{o,s,p} n_{\mathrm{F}}\left(\varepsilon_k^{s,o,p}\right)\frac{\partial\varepsilon_k^{s,o,p}}{\partial e} + 2\alpha e = 0, \tag{4.21a}$$

$$\frac{\partial\Omega^{(0)}}{\partial p_0} = \frac{1}{N}\sum_{k\in \mathrm{BZ}_Q}\sum_{o,s,p} n_{\mathrm{F}}\left(\varepsilon_k^{s,o,p}\right)\frac{\partial\varepsilon_k^{s,o,p}}{\partial p_0} + 2p_0(\alpha-\beta_0) - 2\beta p = 0\,, \tag{4.21b}$$

$$\frac{\partial\Omega^{(0)}}{\partial p} = \frac{1}{N}\sum_{k\in \mathrm{BZ}_Q}\sum_{o,s,p} n_{\mathrm{F}}\left(\varepsilon_k^{s,o,p}\right)\frac{\partial\varepsilon_k^{s,o,p}}{\partial p} + 2p(\alpha-\beta_0) - 2\beta p_0 = 0, \tag{4.21c}$$

$$\frac{\partial\Omega^{(0)}}{\partial d} = \frac{1}{N}\sum_{k\in \mathrm{BZ}_Q}\sum_{o,s,p} n_{\mathrm{F}}\left(\varepsilon_k^{s,o,p}\right)\frac{\partial\varepsilon_k^{s,o,p}}{\partial d} + 2d(U+\alpha-2\beta_0) = 0\,, \tag{4.21d}$$

$$\frac{\partial\Omega^{(0)}}{\partial \alpha} = e^2 + p_0^2 + p^2 + d^2 - 1 = 0\,, \tag{4.21e}$$

$$\frac{\partial\Omega^{(0)}}{\partial \beta_0} = \frac{1}{N}\sum_{k\in \mathrm{BZ}_Q}\sum_{o,s,p} n_{\mathrm{F}}\left(\varepsilon_k^{s,o,p}\right)\frac{\partial\varepsilon_k^{s,o,p}}{\partial \beta_0} - 2d^2 - p_0^2 - p^2 = 0,\,, \tag{4.21f}$$

$$\frac{\partial\Omega^{(0)}}{\partial \beta} = \frac{1}{N}\sum_{k\in \mathrm{BZ}_Q}\sum_{o,s,p} n_{\mathrm{F}}\left(\varepsilon_k^{s,o,p}\right)\frac{\partial\varepsilon_k^{s,o,p}}{\partial \beta} - 2p_0 p = 0\,, \tag{4.21g}$$

$$\frac{\partial\Omega^{(0)}}{\partial \boldsymbol{Q}} = \frac{1}{N}\sum_{k\in \mathrm{BZ}_Q}\sum_{o,s,p} n_{\mathrm{F}}\left(\varepsilon_k^{s,o,p}\right)\frac{\partial\varepsilon_k^{s,o,p}}{\partial \boldsymbol{Q}} = 0\,, \tag{4.21h}$$

where n_F denotes the Fermi-Dirac distribution defined in Equation (3.20). These saddle point equations smoothly include the PM limit and are applicable to general Hamiltonians that may feature SOC and an arbitrary number of conduction bands, but also include the well-known cases of the Hubbard model [50, 71] and the PAM [74].

As stated earlier, Equation (4.21e) should be enforced by directly replacing an arbitrary SB parameter using Equation (4.5a), which reduces the number of saddle point equations by two. The MF value of α for the ground state may formally be determined by

$$\overline{\alpha} = -\frac{1}{2\overline{e}}\frac{1}{N}\sum_{k}\sum_{o,s,p} n_{\mathrm{F}}\left(\varepsilon_k^{s,o,p}\right)\frac{\partial\varepsilon_k^{s,o,p}}{\partial e}\bigg|_{\overline{\psi}}\,, \tag{4.22}$$

where $\overline{\psi}$ denotes a set of MF parameters that satisfies all saddle point equations and the derivative is to be taken without enforcing the α-constraint for the eigenvalues ε. However, $\overline{\alpha}$ does not impact the quasiparticle (QP) band structure and doesn't have an important physical interpretation.

If we solely want to study PM solutions and explicitly exclude the possibility of magnetic order, we need to additionally enforce $p = \beta = 0$. The resulting GP is independent of $\boldsymbol{Q}$, only three saddle point equations remain, and the original KR-SB representation [49] is reproduced for the Hubbard model. Moreover, it has

[1] We once more remind that $\varepsilon^{o,s,p}$ label the eigenvalues of the SB-dependent hopping matrix $\underline{H}_k^{\psi}$ that is derived in Appendix B for the specific models that we study within this thesis. The indices o, s, p represent orbital, spin and spin-spiral periodicity degrees of freedom respectively. The index $p \in \{0, 1, \ldots, P-1\}$ reflects an enlarged magnetic unit cell that occurs for $\boldsymbol{Q} \neq 0$, which implies the summation over the back-folded magnetic BZ that satisfies $P\sum_{\mathrm{BZ}_Q} = \sum_{\mathrm{BZ}_0}$. For spin-rotation-invariant models, we employ the reduced basis defined in Equation (4.15) that does not feature the index p and requires a summation over the paramagnetic BZ for arbitrary $\boldsymbol{Q}$.

been shown that this PM saddle point solution is equivalent to the Gutzwiller approximation [49, 106–109]. PM ground states, however, may feature magnetic instabilities within the study of Gaussian fluctuations (compare Section 5.3.3). In our analysis of different models [53–56] within the framework of a combined (para-) magnetic MF and fluctuation analysis, we found that magnetic instabilities of PM ground states ($p = 0$, enforced) always coincide with a non vanishing magnetization of a magnetic MF analysis ($p > 0$), where the ordering vector $\boldsymbol{Q}$ of the MF magnetization matches the leading divergence of the PM spin susceptibility $1/\chi_s^{\mathrm{PM}}(\boldsymbol{q} = \boldsymbol{Q}) = 0$. We thus find the two approaches to be perfectly consistent. First-order transitions on the other side cannot be directly seen in the PM fluctuation calculation because the respective GP features a local minimum at $p = 0$ that indicates a meta-stable ground state. In that case, a magnetic phase transition comes along with a discontinuous jump of the order parameter p that can be seen found within the magnetic MF analysis by globally minimizing the GP. Correspondingly, there are multiple different saddle points, and it needs to be taken care that the numerical minimization algorithm does not get stuck in a local minimum.

For models without SOC, where tune $\boldsymbol{Q}$ can be tuned as a continuous MF parameter that is included in the minimization process, one should always consider the magnetic point equations because the corresponding ground states automatically resolve magnetic instabilities that would otherwise arise in a PM fluctuation analysis. We, nevertheless, suggest simultaneously solving the simpler PM saddle point equations as a benchmark, which can be especially helpful to distinguish between global and local minima in the context of first-order transitions. On the other hand, for models that feature SOC, Equation (4.21h) cannot be directly applied because the dimension of $\underline{H}^{\psi}$ depends on the ordering vector $\boldsymbol{Q}$. In that case, we recommend determining the leading ordering vector through a PM fluctuation calculation and afterward solving the magnetic saddle point equations for the corresponding fixed $\boldsymbol{Q}$.

4.4.3 Free energy

If it is desired to fix the total electron filling per site n instead of the chemical potential μ_0, we may solve the saddle point equations of the free energy (FE) per lattice site. It is related to the GP by the Legendre transformation

$$F^{(0)}(T, n) = \Omega^{(0)}(T, \mu_0) - \mu_0 \left(\frac{\partial \Omega^{(0)}}{\partial \mu_0}\right)_T , \tag{4.23a}$$

with

$$\left(\frac{\partial \Omega^{(0)}}{\partial \mu_0}\right)_T = -\frac{1}{N} \sum_{\boldsymbol{k} \in \mathrm{BZ}_Q} \sum_{o,s,p} n_{\mathrm{F}}\left(\varepsilon_{\boldsymbol{k}}^{s,o,p}\right) = -n . \tag{4.23b}$$

The total filling is fixed by an additional constraint in the field theory, where μ_0 acts as LM. In the exact path integral, we would have to integrate over μ_0 in the same way as the other LMs, but to determine the MF saddle point that constraints the filling on average, we need to maximize the FE

$$F^{(0)} = -\frac{T}{N} \sum_{\boldsymbol{k} \in \mathrm{BZ}_Q} \sum_{o,s,p} \ln\left(1 + \mathrm{e}^{-\varepsilon_{\boldsymbol{k}}^{o,s,p}/T}\right) + Ud^2 + \alpha(e^2 + d^2 + p_0^2 + p^2 - 1) - \beta_0(2d^2 + p_0^2 + p^2) - 2\beta p_0 p + \mu_0 n \tag{4.24}$$

w.r.t. μ_0. The role of the chemical potential looks very similar to β_0 within the theory. However, both quantities are different on a physical level of understanding. While μ_0 controls the number of electrons in the system by coupling to an external particle bath, β_0 renormalizes the energy level of the interacting electrons as a response to the energy cost due to interaction. We may, however, reduce the number of saddle point equations if the filling n_f of interacting electrons is fixed by an external bath.

Hubbard model

For the one-band Hubbard model, it is $n = n_f = 2d^2 + p_0^2 + p^2$, and we may fix the total filling by directly constraining the SB variables. In that case, however, the maximizations w.r.t. μ_0 and β_0 are not well defined anymore, since both LMs appear identically the theory. We thus have to substitute $\mu_{\text{eff}} = \mu_0 - \beta_0$. In these variables, μ_0 appears only in the bosonic Lagrangian, while μ_{eff} plays the role of an effective chemical potential, which fixes the filling of the PF band structure and β_0 drops out of the equations

$$F^{(0)} \to -\frac{T}{N}\sum_{\boldsymbol{k}\in\mathrm{BZ}_0,s} \ln\left(1+\mathrm{e}^{-\varepsilon^s_{\boldsymbol{k},\mu_{\text{eff}}}/T}\right) + Ud^2 + \alpha(e^2+d^2+p_0^2+p^2-1) + \mu_{\text{eff}}(2d^2+p_0^2+p^2) - 2\beta p_0 p - \mu_0(2d^2+p_0^2+p^2-n). \tag{4.25}$$

The two purely bosonic constraints connected to α and μ_0 can be satisfied by directly enforcing

$$1 = e^2 + d^2 + p_0^2 + p^2\,, \tag{4.26a}$$

$$n = 2d^2 + p_0^2 + p^2\,, \tag{4.26b}$$

$$\mu_{\text{eff}} = \mu_0 - \beta_0\,. \tag{4.26c}$$

and maximizing the FE w.r.t. μ_{eff} rather than μ_0 and β_0. We choose w.l.o.g. to replace e and d by means of Equation (4.26) and need to solve the saddle pointe equations [53]

$$\left.\frac{\partial F^{(0)}_{\text{eff}}}{\partial p}\right|_{(4.26)} = \left.\frac{\partial F^{(0)}_{\text{eff}}}{\partial p_0}\right|_{(4.26)} = \left.\frac{\partial F^{(0)}_{\text{eff}}}{\partial \beta}\right|_{(4.26)} = \left.\frac{\partial F^{(0)}_{\text{eff}}}{\partial \mu_{\text{eff}}}\right|_{(4.26)} = 0\,, \tag{4.27a}$$

of the constrained FE

$$\left.F^{(0)}_{\text{eff}}\right|_{(4.26)} = -\frac{T}{N}\sum_{\boldsymbol{k}\in\mathrm{BZ}_0}\sum_s \ln\left(1+\mathrm{e}^{-\varepsilon^s_{\boldsymbol{k},\mu_{\text{eff}}}/T}\right)\Big|_{(4.26)} + \frac{U}{2}\left(n - p_0^2 - p^2\right) - 2\beta p_0 p + \mu_{\text{eff}} n\,. \tag{4.27b}$$

For PM solutions (additionally enforcing $p = \beta = 0$), only two independent saddle point equations remain that reduce to a single equation in certain limits where the solution can be determined analytically [49, 50, 53]. We may recover β_0 and μ_0 by resubstitution of Equations (4.26b) and (4.26c) and evaluating the derivative

$$\overline{\beta}_0 = \frac{1}{4\overline{d}}\frac{1}{N}\sum_{\boldsymbol{k}\in\mathrm{BZ}_0}\sum_s n_{\mathrm{F}}\left(\varepsilon^{o,s,p}_{\boldsymbol{k},\mu_{\text{eff}}}\right)\left.\frac{\partial \varepsilon^{o,s,p}_{\boldsymbol{k},\mu_{\text{eff}}}}{\partial d}\right|_{(4.26a),\overline{\psi}} + \frac{U}{2}\,. \tag{4.27c}$$

at the saddle point solution $\overline{\psi}$. While the MF band structure only depends on μ_{eff}, it is essential to recover the original variables μ_0 and β_0 in order to compare the saddle point of the FE with ground states of the GP, to calculate the electronic compressibility (compare Section 4.6) and to evaluate Gaussian fluctuations (compare Chapter 5).

Multi-band models

In models with at least one additional non-interacting orbital, the maximization w.r.t. μ_0 and β_0 is well defined, and the saddle point is determined by

$$\frac{\partial F^{(0)}}{\partial e} = \frac{\partial F^{(0)}}{\partial p_0} = \frac{\partial F^{(0)}}{\partial p} = \frac{\partial F^{(0)}}{\partial d} = \frac{\partial F^{(0)}}{\partial \alpha} = \frac{\partial F^{(0)}}{\partial \beta_0} = \frac{\partial F^{(0)}}{\partial \beta} = \frac{\partial F^{(0)}}{\partial \boldsymbol{Q}} = \frac{\partial F^{(0)}}{\partial \mu_0} = 0\,. \tag{4.28}$$

In some cases, especially in the context of Kondo physics, we are interested in directly tuning the filling n_f of the interacting orbital instead of the on-site potential ϵ_f. This can be achieved by coupling the f-orbital to an additional independent particle bath and performing a substitution in analogy to the previously discussed Hubbard model

$$1 = e^2 + d^2 + p_0^2 + p^2 \,, \tag{4.29a}$$

$$n_f = 2d^2 + p_0^2 + p^2 \,, \tag{4.29b}$$

$$\epsilon_{\text{eff}} = -\epsilon_f - \beta_0 \,. \tag{4.29c}$$

The according constrained FE is given by[1] [56]

$$F^{(0)}_{\text{eff}}\Big|_{(4.29)} = -\frac{T}{N}\sum_{\boldsymbol{k}\in \text{BZ}_Q}\sum_{o,s,p} \ln\left(1+\mathrm{e}^{-\varepsilon^{o,s,p}_{\boldsymbol{k},\epsilon_{\text{eff}}}/T}\right)\Big|_{(4.29)} + \frac{U}{2}\left(n_f - p_0^2 - p^2\right) - 2\beta p_0 p + \epsilon_{\text{eff}} n_f + \mu_0 n + \epsilon_f n_f \,, \tag{4.30a}$$

and we need to solve the saddle point equations

$$\frac{\partial F^{(0)}_{\text{eff}}}{\partial p}\Big|_{(4.29)} = \frac{\partial F^{(0)}_{\text{eff}}}{\partial p_0}\Big|_{(4.29)} = \frac{\partial F^{(0)}_{\text{eff}}}{\partial \beta}\Big|_{(4.29)} = \frac{\partial F^{(0)}_{\text{eff}}}{\partial \epsilon_{\text{eff}}}\Big|_{(4.29)} = \frac{\partial F^{(0)}_{\text{eff}}}{\partial \mu_0}\Big|_{(4.29)} = \frac{\partial F^{(0)}_{\text{eff}}}{\partial \boldsymbol{Q}}\Big|_{(4.29)} = 0 \,. \tag{4.30b}$$

We may recover β_0 by

$$\overline{\beta}_0 = \frac{1}{4\overline{d}}\frac{1}{N}\sum_{\boldsymbol{k}\in \text{BZ}_Q}\sum_{o,s,p} n_{\text{F}}\left(\varepsilon^{o,s,p}_{\boldsymbol{k},\epsilon_{\text{eff}}}\right)\frac{\partial \varepsilon^{o,s,p}_{\boldsymbol{k},\epsilon_{\text{eff}}}}{\partial d}\Big|_{(4.29a),\overline{\psi}} + \frac{U}{2} \,. \tag{4.30c}$$

While the MF band structure only depends on ϵ_{eff}, it is important to recover the original variables ϵ_f and β_0 in order to evaluate Gaussian fluctuations (compare Chapter 5). Guidelines on how to efficiently implement and numerically solve the previously discussed saddle point equations are provided in Appendix D.

4.5 Interpretation of the mean-field ground state

The interaction-renormalized MF band structure described by the hopping matrix $\underline{H}^{\psi,Q}$ is characterized by five renormalization parameters, involving the so-called z-factors $\mathcal{Z}_+, \mathcal{Z}_-$ which are defined in Equation (4.8a) as functions of the SB parameters e, d_1, p_0, p, the Lagrange multipliers (LMs) β_0, β and the magnetic ordering vector $\boldsymbol{Q}$. As discussed earlier, only $\mathcal{Z}_+$ and β_0 are non-zero in the PM limit. The parameter $\mathcal{Z}_+$ decreases the hopping amplitude of the interacting electrons ($t^f \to \mathcal{Z}_+^2 t^f$), which reduces the overall bandwidth and can be interpreted to be a consequence of the reduced mobility of the electrons in order to avoid the interaction cost U of doubly occupied sites. The LM β_0 increases the on-site potential of the interacting electrons ($\epsilon_f \to \epsilon_f + \beta_0$), because the occupation cost is higher on average for growing U. It has been shown, that the PM saddle point approximation reproduces results of the Gutzwiller approximation [49, 106–109]. If the magnetic ordering parameter p is non-zero, the SU(2) spin-rotation-symmetry is spontaneously broken, and the ground state is magnetic. If $\boldsymbol{Q} \neq 0$, translation symmetry is additionally broken but can be recovered with an enlarged magnetic unit cell, yielding a smaller BZ where $\boldsymbol{Q}$ becomes a reciprocal lattice vector. The energy gap between different spin species is given by β, and $\mathcal{Z}_-$ induces a hopping amplitude between opposite spins,

[1] The term $\epsilon_f n_f$ in the bosonic Lagrangian is just a constant and does not impact the saddle point solution. In order to compare different ground states and fix the absolute energy scale, however, it is essential to add this contribution after the saddle point has been determined and ϵ_f can be recovered using Equations (4.29c) and (4.30c).

MF renormalization parameters	Equal-spin SB hopping amplitude $0 \leq \mathcal{Z}_+ \leq 1$	Opposite-spin SB hopping amplitude $-1 \leq \mathcal{Z}_- \leq 1$	LM on-site energy $\beta_0 \geq 0$	LM spin gap $\beta \leq 0$
Generic	$\mathcal{Z}_+ = \frac{z_+ + z_-}{2}$	$\mathcal{Z}_- = \frac{z_+ - z_-}{2}$	β_0	β
Half-filled f-orbital ($n_f = 1$)	$\mathcal{Z}_+ \to z_+$	$\mathcal{Z}_- \to 0$	β_0	β
PM limit ($p = 0$)	$\mathcal{Z}_+ \to z_0$	$\mathcal{Z}_- \to 0$	β_0	$\beta \to 0$
Non-interacting limit ($U = 0$)	$\mathcal{Z}_+ \to 1$	$\mathcal{Z}_- \to 0$	$\beta_0 \to 0$	$\beta \to 0$

Table 4.1: The MF renormalization of the PF quasiparticle band structure is determined by the five parameters: $\mathcal{Z}_+, \mathcal{Z}_-, \beta_0, \beta$ and $\boldsymbol{Q}$. The table summarizes their behavior under certain limits and shows their respective interval of possible values on the constrained subspace. In the non-interacting limit, all parameters arrange such that the exact non-renormalized band structure is recovered. The SB-weights z_+, z_- and z_0 have been defined in Equation (4.8a).

which additionally modulates the magnetic gap function. Table 4.1 summarizes the properties of the MF renormalization parameters in prominent limits.

Finally, we want to briefly discuss the MF ground state in the context of Fermi liquid (FL) theory [23, 110]. Interaction effects in FLs are commonly addressed by means of the self-energy $\Sigma(\boldsymbol{k}, \omega)$, which is defined by the Dyson equation [39, 48]

$$G_k^{\text{int}} = G_k^0 + G_k^0 \Sigma(\boldsymbol{k}, \mathrm{i}\omega_n) G_k^{\text{int}} \quad \Leftrightarrow \quad G_k^{\text{int}} = \frac{1}{\left(G_k^0\right)^{-1} - \Sigma\left(\boldsymbol{k}, \mathrm{i}\omega_n\right)} \,. \tag{4.31}$$

Real and imaginary part of the self-energy are connected to the QP weight $Z_{\boldsymbol{k}}$ and lifetime τ_k [39]

$$Z_{\boldsymbol{k}}^{-1} = 1 - \frac{\partial}{\partial \omega} \operatorname{Re} \Sigma(k_F^{\text{int}}, \omega)\Big|_{\omega=0} \,, \tag{4.32a}$$

$$\tau_{\boldsymbol{k}}^{-1} = -2 Z_{\boldsymbol{k}} \operatorname{Im} \Sigma\left(\boldsymbol{k}, \omega\right) \,, \tag{4.32b}$$

which are measurable by means of the spectral function

$$A(\boldsymbol{k}, \omega) = -\frac{1}{\pi} \operatorname{Im} G(\boldsymbol{k}, \omega + \mathrm{i}\eta) \,. \tag{4.33}$$

The SB-MF Green's function defined in Equation (4.14) corresponds to a real valued self-energy $\Sigma^{\psi}(\boldsymbol{k})$ that is frequency independent in its diagonalzing basis[1] , which implies a unity QP weight $Z_{\boldsymbol{k}}^{\psi} = 1$ and infinite lifetime $\tau_k \to \infty$, i.e., the MF ground state corresponds to an effectively non-interacting FL with a renormalized band structure. Magnetically ordered states are, nevertheless, not adiabatically connected to the non-interacting limit [39].

[1] To be specific, the imaginary part is given by the infinitesimal convergence factor that yields from analytic continuation to the real axis $\mathrm{i}\omega_n = \omega + \mathrm{i}\eta \to \operatorname{Im} \Sigma^{\psi} = -\eta$.

4.6 Breakdown of the mean-field ground state

An effective way to assess the stability of the MF ground state is the analysis of static susceptibilities within the Gaussian fluctuation formalism (compare Section 5.3.3). We may, however, already identify instabilities in the context of phase separation (PS) and negative electronic compressibility [53, 55, 103, 105, 111] from a mere MF perspective. In the following, we elaborate on the associated theoretical concepts that will be applied in Section 8.5 and Chapter 9 to describe inhomogeneous MF ground states of the Hubbard model in the vicinity to half-filling.

The saddle points of the GP and FE are equivalent if the Legendre transformation [112, 113]

$$F^{(0)}(T,n) = \Omega^{(0)}(T,\mu_0) - \mu_0 \left(\frac{\partial \Omega^{(0)}}{\partial \mu_0}\right)_T = \Omega^{(0)}(T,\mu_0) + \mu_0 n \ , \tag{4.34a}$$

$$\Omega^{(0)}(T,\mu_0) = F^{(0)}(T,n) - \left(\frac{\partial F^{(0)}}{\partial n}\right)_T n = F^{(0)}(T,n) - \mu_0 n \ , \tag{4.34b}$$

between them invertible, i.e., uniquely defined[1]. This holds, if derivatives

$$\left(\frac{\partial \Omega^{(0)}}{\partial \mu_0}\right)_T = -n(\mu_0) \ , \tag{4.35a}$$

$$\left(\frac{\partial F^{(0)}}{\partial n}\right)_T = \mu_0(n) \ , \tag{4.35b}$$

of the potentials are monotonous functions, or in other words, if the isothermal electronic compressibility

$$\kappa_T = \frac{1}{n^2}\left(\frac{\partial n}{\partial \mu_0}\right) \tag{4.36}$$

is continuous and positive for all μ_0. While this is guaranteed for non-interacting systems, interaction effects which are embedded in the SB-renormalized MF potentials may cause anomalies that revoke the applicability of the Legendre transformation in a specific parameter range as a signature of possible FS instabilities that go beyond magnetic ordering. For a deeper insight, we may investigate the implied non-equivalent ground states suggested by the GP or FE, and discern that the unusual be occurs if at least one of the potentials undergoes a first-order phase transition such that its derivative w.r.t. the corresponding base variable μ_0 or n is discontinuous.

4.6.1 Phase separation

Let us consider the ground state of the GP, where we can tune μ_0 as a continuous parameter and assume that there is a first-order phase transition at $\mu_0 = \mu_0^c$. While the differential $d\Omega^{(0)}$ is well defined for a second-order transition, a first-order transition is characterized such that the derivative of the potential w.r.t. the parameter that induced the phase transition is discontinuous. As a consequence, the filling n jumps at $\mu_0 = \mu_0^c$ according to

$$-\lim_{\delta\mu_0 \to 0} \left.\frac{\partial \Omega^{(0)}}{\partial \mu_0}\right|_{\mu_0^c - \delta\mu_0} = -\left.\frac{\partial \Omega_1^{(0)}}{\partial \mu_0}\right|_{\mu_0^c, \overline{\psi}_1} = n_1 \ , \tag{4.37a}$$

[1] In that case, switching between those potentials is just a trick to save calculation time. One could also determine the saddle point of a particular filling n by extremizing $\Omega^{(0)}$ and adapting μ_0 by a divide and conquer algorithm until the desired filling is reached.

$$-\lim_{\delta\mu_0\to 0}\left.\frac{\partial\Omega^{(0)}}{\partial\mu_0}\right|_{\mu_0^c+\delta\mu_0} = -\left.\frac{\partial\Omega_2^{(0)}}{\partial\mu_0}\right|_{\mu_0^c,\overline{\psi}_2} = n_2 \tag{4.37b}$$

with $n_1 < n_2$. In the context of the spiral magnetic MF, this can happen if the GP features multiple local minima at different saddle points[1] characterized by two sets of MF parameters $\overline{\psi}_1 \neq \overline{\psi}_2$ and the first order transition occurs, if two minima become energy degenerate $\Omega_1^{(0)} = \Omega_2^{(0)}$. The discontinuity implicates that there exists a range of fillings $n_1 < n < n_2$ without a corresponding uniform ground state of the GP. Assuming that the two different energy degenerate phases mix in the sense of phase separation (PS) with a fraction of x [53],

$$\Omega_{\mathrm{PS}}^{(0)} = x\Omega_1^{(0)} + (1-x)\Omega_2^{(0)} \,, \tag{4.38a}$$

we may, however, recover the full range of fillings

$$n = -\frac{\partial\Omega_{\mathrm{PS}}^{(0)}}{\partial\mu_0} = xn_1 + (1-x)n_2 \,. \tag{4.38b}$$

This PS can equivalently be identified utilizing of the FE, which gives us access to the function $\mu_0(n)$ rather than $n(\mu_0)$. To recover the MF saddle points $\overline{\psi}_1$ and $\overline{\psi}_2$ in the phase mix, we need to perform a Maxwell construction, i.e., determine two fillings such that

$$0 = \int_{n_1}^{n_2} \left(\mu_0(n) - \mu_0^c\right) dn = F_2^{(0)}(n_2) - F_1^{(0)}(n_1) - \mu_0^c\,(n_2 - n_1) = \Omega_2^{(0)}(n_2) - \Omega_1^{(0)}(n_1) \,. \tag{4.39}$$

We can thus recover the energy-degenerate saddle points of the GP, and the two potentials are equivalent outside of the PS region as expected. The phase-separated FE is given by

$$F_{\mathrm{PS}}^{(0)}(n) = \Omega_{1/2}^{(0)}\left(\mu_0^c\right) + n\mu_0^c \,, \tag{4.40}$$

with $n_1 < n < n_2$ and a constant chemical potential in the PS domain. It reduces the energy compared to the homogeneous case[2]

$$\begin{aligned} F^{(0)}(n) - F_{\mathrm{PS}}^{(0)}(n) &= F^{(0)}(n) - \Omega^{(0)}(\mu_0^c) - \mu_0^c n + F^{(0)}(n1) - \mu_0^c n_1 - F^{(0)}(n1) + \mu_0^c n_1 \\ &= \int_{n_1}^{n} \left(\mu_0(n) - \mu_0^c\right) dn \geq 0 \,, \end{aligned} \tag{4.41}$$

i.e., PS is identified as the globally minimizing MF ground state.

The phenomenon of PS is most commonly known in the context of an isothermal compression of a gas, where the liquid and gas phase coexist in a specific range of volumes while the pressure remains constant. This breakdown of homogeneity is also interaction-induced since the ideal gas law cannot describe phase transitions. We can see the analogy to our quantum case if we identify the filling n with the volume, the chemical potential μ_0 with the pressure, and the electronic compressibility defined in Equation (4.36) with the compressibility of the gas.

[1] These various sets of MF parameters that each satisfy all saddle point equations typically involve different magnetic ordering vectors $\boldsymbol{Q}$ and deviating magnetizations m.

[2] The occurring integral is only zero for $n = n_2$ as shown in Equation (4.39) (except for the trivial case $n = n_1$). Moreover at the lower end of the PS domain where the Legendre transformation is still well defined, we have $\partial\mu_0(n)/\partial n|_{n_1} > 0$ and $\mu_0(n_1) = \mu_0^c$, and consequently the inequality holds.

4.6.2 Negative electronic compressibility

The type of phase separation described Section 4.6.1, unfortunately, completely neglects boundary effects between the two coexisting phases. Since those surfaces are usually associated with considerable energy cost, the possibility of a charge-ordered (CO) phase that minimizes this contribution by periodic domains walls rather than a completely disordered phase should be taken into account. As alternative to the PS ground state, we may thus consider the homogeneous saddle point of the FE, which represents some kind of average of the PS system, and investigate possible emerging FS instabilities through Gaussian fluctuations [55]. This approach is particulary interesting if the FE does not feature a first-order transition in an interval $n_1 < n < n_2$ that is phase-separated according to the GP. Then, the Maxwell construction described in Equation (4.39) does not originate in a discontinuity of $n(\mu_0)$, but rather yields from a continuous regime of negative compressibility

$$\kappa_T(n) = \frac{1}{n^2}\left[\left(\frac{\partial \mu_0}{\partial n}\right)_T\right]^{-1} = \frac{1}{n^2}\left[\left(\frac{\partial^2 F^{(0)}}{\partial n^2}\right)_T\right]^{-1} , \tag{4.42}$$

which is encompassed by two diverging points. Since it is $\kappa_T \propto \partial^2\Omega^{(0)}/\partial^2\mu_0^2$, we can infer in analogy to Equation (4.19) that the compressibility is proportional to the variance of the electron filling n. We will moreover learn in Section 5.3.2, that it is also proportional to the static charge susceptibility at the Γ-point

$$\kappa_T \propto \mathrm{Var}\,\hat{n}_f \propto \chi_c(\boldsymbol{q} = 0, \omega = 0) , \tag{4.43}$$

which associates a diverging compressibility with a FS instability in the charge channel. Overall, states that feature $\kappa_T < 0$ can, therefore, be classified as unstable whereas saddle points of the FE with positive compressibility within the PS domain are meta-stable.

4.6.3 Specific heat

Theoretically, we could also see PS, of two states with different entropy S, if the Legendre transformation between the internal energy and FE breaks down

$$E^{(0)}(S,n) = F^{(0)}(T,n) - T\left(\frac{\partial F^{(0)}}{\partial T}\right)_n = F^{(0)}(T,n) + TS \tag{4.44a}$$

$$F^{(0)}(T,n) = E^{(0)}(S,n) - S\left(\frac{\partial E^{(0)}}{\partial S}\right)_n = E^{(0)}(S,n) - TS . \tag{4.44b}$$

In that case, the specific heat

$$C_n = -T\left(\frac{\partial^2 F^{(0)}}{\partial T^2}\right)_n \tag{4.45}$$

would feature discontinuities or negative regimes in analogy to the previous section. We do, however, not find evidence for such a kind of PS within the analysis of this thesis.

CHAPTER 5

Gaussian fluctuations around the mean-field saddle point

Gaussian fluctuations around the paramagnetic saddle point solutions have initially been considered for the Hubbard model to provide a stability analysis of the MF solution and to analyze dynamic excitation spectra by means of the charge and spin susceptibility[1] [59–61, 96]. We extend the fluctuation formalism to be applicable to models with additional non-interacting orbitals [53, 54, 56, 99], magnetic saddle points [55] and also suggest a fluctuation basis whose dimension is reduced by two compared to previous studies, but correctly reproduces established results [53]. As we will learn, this theoretical framework enables us to study the interplay between emerging spin and charge order, magnon dispersion relations in the symmetry broken phase, fluctuation corrections to the magnetization, and to evaluate the stability of magnetic saddle points. Respective results for the Hubbard model and Kondo systems will be discussed in Parts II and III.

From a field theory perspective, the pseudofermions (PFs) have been integrated out exactly within the static MF approximation introduced in Chapter 4, while only zeroth-order contributions of slave-bosons (SBs) were considered. The essence of the fluctuation calculation is to refine the approximation of the action

$$\mathcal{S} = \int_0^\beta d\tau \mathcal{L}\left[\boldsymbol{\psi}(\tau)\right] \ , \tag{5.1a}$$

by including the next leading order in bosonic fields. Since first-order variations vanish per definition at the MF saddle point, we will investigate the second-order variation of the action w.r.t. bosonic fields

$$\mathcal{S} = \mathcal{S}^{(0)} + \mathcal{S}^{(2)} + \mathcal{O}\left(\boldsymbol{\psi}^3\right) = \mathcal{S}^{(0)}\Big|_{\overline{\psi}} + \frac{1}{\sqrt{N\beta}} \iint_0^\beta d\tau \, d\Delta\tau \sum_{\boldsymbol{r}_i, \Delta\boldsymbol{r}_i} \sum_{\mu\nu} \delta\psi^*_{\mu,\boldsymbol{r}_i,\tau} \left[\mathcal{M}(\Delta\boldsymbol{r}_i, \Delta\tau)\right]_{\mu,\nu} \delta\psi_{\nu,\boldsymbol{r}_i+\Delta\boldsymbol{r}_i,\tau+\Delta\tau} + \mathcal{O}\left(\boldsymbol{\psi}^3\right) \tag{5.1b}$$

around the MF saddle point. We define the fluctuation fields $\delta\psi_{\mu,r} = \psi_{\mu,r} - \overline{\psi}_\mu$ with $r = (\boldsymbol{r}_i, \tau)$ as deviation from the MF solution and the fluctuation matrix

$$\left[\mathcal{M}(\Delta r)\right]_{\mu,\nu} = \frac{1}{2}\sqrt{N\beta} \frac{\partial^2 \mathcal{S}}{\partial\psi^*_{\mu,r}\partial\psi_{\nu,r+\Delta r}}\bigg|_{\overline{\psi}} \ . \tag{5.1c}$$

Due to translation invariance w.r.t. the magnetic unit cell, the fluctuation matrix only depends on the relative difference $\Delta\boldsymbol{r}_i$ between lattice sites and not on the absolute value. This will be exploited in Section 5.1 to find a diagonalizing basis through Fourier transformation (FT) to momentum and Matsubara-frequency space in

[1] In most of the early literature, the radial gauge was applied incorrectly, and dynamic contributions of the complex d-field, which are crutial for $\omega \neq 0$ have been overlooked. This omission was corrected later on [114].

analogy to the MF basis introduced in Section 4.3. In section Section 5.2, we will derive the explicit form of the fluctuation matrix and show that all PF degrees of freedom can be integrated out exactly. The fluctuation matrix is connected to the bosonic fluctuation field Green's function by

$$\underline{\mathcal{G}} = -\underline{\mathcal{M}}^{-1} , \tag{5.1d}$$

which will be applied in Section 5.3 to calculate dynamic correlation functions in the context of linear response theory. Corresponding results may be applied to investigate collective modes, evaluate the stability of MF saddle points, and determine experimentally accessible quantities. Finally, in Section 5.4 we elaborate on why the effective theory does not represent free bosons despite being quadratic and explain how to compute fluctuation corrections to the magnetization by means of the bosonic equal space-time Green's function $\mathcal{G}(\Delta r = 0^-)$.

5.1 Fluctuation basis

Firstly, it must be considered which bosonic fields should be subject to fluctuations for a consistent theory. To acquire information beyond the MF saddle point, we have to allow deviations from the MF constraints, which adds β_0 and $\boldsymbol{\beta}$ to the fluctuation basis. As a consequence, the charge and spin expectation values of the fluctuation fields $\delta\boldsymbol{\psi}$ go beyond the bosonic and PF mean-field expectation values, which are matched through the Lagrange multipliers (LMs) β_0 and $\boldsymbol{\beta}$ at the saddle point, and provide a leading order fluctuation correction. However, the LM α does not couple to a direct physical degree of freedom but rather constraints the number of auxiliary bosons per lattice site. Its fluctuations could be interpreted as a violation of the Pauli principle and are to be avoided [53], which can be achieved by eliminating an arbitrary SB field by direct application of the constraint equation

$$1 = e^2 + d^* d + p_0^2 + \boldsymbol{p}^2 , \tag{5.2}$$

in analogy to the MF approach. We have confirmed by thorough numeric analysis that the bosonic propagator $\underline{\mathcal{G}}$, and thus all physical observables are invariant under the choice of which field is eliminated from the effective theory[1]. This is a strong confirmation of the consistency of our fluctuation basis and we will w.l.o.g. choose to the eliminate the e-field in the following. We found that the same result for $\underline{\mathcal{G}}$ may be obtained without eliminating any field from the theory if the $\hat{M}$-operator that appears in the renormalized $\underline{z}$-matrix [compare Equation (A.19)] is replaced by $\sqrt{2}$ like in previous studies [60, 61, 114].

Secondly, as pointed out in Section 2.2.2, the field theory includes spurious degrees of freedom in the Cartesian gauge, which are associated with gauge symmetries that are a consequence of the constraints as conserved quantities. Since the MF solution breaks those continuous symmetries, the field theory of the fluctuation fields contains unphysical Goldstone modes [115], which manifest as zero-eigenvalues of the fluctuation matrix that make the bosonic Green's function ill-defined. As shown in Section 3.2.1, this can be avoided in the radial gauge, where all spurious phases are removed, and only the d-field remains to be complex field. For convenience, we define $d = d_1 + \mathrm{i}d_2$, with $d_1, d_2 \in \mathbb{R}$ and thus have the basis

$$\boldsymbol{\psi}_r = (d_{1,r}\ , d_{2,r}\ , p_{0,r}\ , \beta_{0,r}\ , p_{1,r}\ , \beta_{1,r}\ , p_{2,r}\ , \beta_{2,r}\ , p_{3,r}\ , \beta_{3,r})^\top \tag{5.3}$$

of real valued fields within the space-time domain $r = (\boldsymbol{r}, \tau)$.

[1] In opposite to $\underline{\mathcal{G}}$, the fluctuation matrix $\underline{\mathcal{M}}$ does depend on which field is eliminated from the theory. The correlations of the eliminated field are determined by direct application of Equation (5.2), e.g., $\left\langle e_{-q} e_q \right\rangle = \left\langle 1 - d_{1,-q} d_{1,q} - d_{2,-q} d_{2,q} - \sum_{\mu=0}^{3} p_{\mu,-q} p_{\mu,q} \right\rangle$.

Thirdly, we want to point out, that the MF renormalized $\underline{z}$-matrix defined in Equation (A.19) is not normal ordered and consequently the coherent state path integral around the saddle point is not applicable in general [75]. The normal order is broken by the $\hat{\underline{L}}$ and $\hat{\underline{R}}$ matrices since $\left[\hat{\underline{p}}\ ,\ \hat{\underline{p}}^\dagger\right]_- \neq 0$ and by the $\hat{M}$ factor. In the radial gauge, however, where p-fields are phaseless it is $\hat{\underline{p}} = \hat{\underline{p}}^\dagger$ and consequently all contributions that violate the normal ordering are gauged away. As discussed earlier, we exclude fluctuations of the α-constraint and thus it is $\hat{M} \to \sqrt{2}$ and the normal order is recovered. This fact affirms the basis choice of Equation (5.3) and once more underlines the importance of the radial gauge.

Finally, we need to adapt the basis such that the PF degrees of freedom can be integrated out exactly. This can be achieved by matching the PF mean-field basis defined by Equation (4.12) in momentum and Matsubara frequency space $q = (\boldsymbol{q}, \mathrm{i}\omega_n)$ through FT of $\boldsymbol{\psi}_r$ according to Equation (3.10). The momenta $\boldsymbol{q}$ of the individual fields are then defined in the magnetic Brillouin zone (BZ), while gaining an additional external index that corresponds to the spin-spiral periodicity degree of freedom defined in Equation (4.4)

$$\boldsymbol{\psi}_q = \left(d_{1,q}\ , d_{2,q}\ , p_{0,q}\ , \beta_{0,q}\ , p_{1,q}\ , \beta_{1,q}\ , p_{2,q}\ , \beta_{2,q}\ , p_{3,q}\ , \beta_{3,q}\right)^\top\ , \tag{5.4a}$$

$$\boldsymbol{\psi}^a_q = \boldsymbol{\psi}_{\boldsymbol{q}+a\boldsymbol{Q},\mathrm{i}\omega_n}\ , \tag{5.4b}$$

with $a \in \{0, 1, \ldots, P-1\}$, where P is the number of lattice sites in the magnetic unit cell, and $\boldsymbol{Q}$ denotes the corresponding MF ordering vector. It has been shown in Reference [55] that this basis is connected to a basis of magnetic sublattices in position space by a unitary transformation. Since all fields are real-valued in position space, it holds

$$\left(\boldsymbol{\psi}^a_q\right)^* = \boldsymbol{\psi}^{-a}_{-q} = \boldsymbol{\psi}_{-\boldsymbol{q}-a\boldsymbol{Q},-\mathrm{i}\omega_n}\ . \tag{5.4c}$$

By FT of Equations (5.1b) and (5.1c) and exploiting the translation invariance, we may express the action in the convenient block-diagonal form [55]

$$\mathcal{S}^{(2)} = \sum_{\mathrm{i}\omega_n} \sum_{\boldsymbol{q}\in \mathrm{BZ}_{\boldsymbol{Q}}} \sum_{\mu\nu} \sum_{ab} \delta\psi^{-a}_{\mu,-q} \mathcal{M}^{a,b}_{\mu,\nu}(q) \delta\psi^b_{\nu,q}\ , \tag{5.5a}$$

with

$$\mathcal{M}^{a,b}_{\mu,\nu}(q) = \frac{1}{2} \frac{\partial^2 \mathcal{S}}{\partial\psi^{-a}_{\mu,-q} \partial\psi^b_{\nu,q}}\bigg|_{\overline{\psi}}\ . \tag{5.5b}$$

In opposite to the MF case, the fluctuation matrix does not become block diagonal w.r.t. the periodicity index a for models without spin-orbit coupling (SOC). Consequently, the dimension of the fluctuation matrix $\dim \underline{\mathcal{M}} = 10P$ increases linearly with the periodicity P, and the numerical evaluation becomes very costly for large magnetic unit cells. In the chosen basis, we may calculate correlations between fluctuation fields with the application of Equation (3.1g) and the addition of source terms, yielding [53]

$$\left\langle \delta\psi^{-a}_{\mu,-q} \delta\psi^b_{\nu,q} \right\rangle = \left[\mathcal{M}^{-1}(q)\right]^{a,b}_{\mu,\nu} = -\mathcal{G}^{a,b}_{\mu,\nu}(q)\ . \tag{5.6}$$

5.2 Derivation of the fluctuation matrix

In order to calculate the fluctuation matrix, we need to determine the second derivatives of the action w.r.t. the bosonic basis given by Equations (5.3) and (5.4) and evaluate them at the MF saddle point. Moreover, we shall

integrate the PFs and trace out the respective momentum, Matsubara frequency, orbital, spin, and periodicity degrees of freedom. According to Equation (3.35), the Lagrangian splits into a purely bosonic and a mixed PF and SB part. After eliminating the e field through direct application of the α-constraint as discussed in the previous section, we have

$$\mathcal{L}\left[\phi^*, \phi, \psi\right] = \mathcal{L}_B\left[\psi_r\right] + \mathcal{L}_F\left[\phi^*_{k_1}, \phi_{k_2}, \psi_{k_{1,2}}\right] \tag{5.7a}$$

with

$$\mathcal{L}_B[\psi_r] = \sum_{r_i}\left[U\left(d_{1,r}^2 + d_{2,r}^2\right) + \mathrm{i}d_{1,r}\partial_\tau d_{2,r} - \mathrm{i}d_{2,r}\partial_\tau d_{1,r} - \beta_{0,r}\left(p_{0,r}^2 + \boldsymbol{p}_r^2 + 2d_{1,r}^2 + 2d_{2,r}^2\right) - \boldsymbol{\beta}_r \cdot 2p_{0,r}\boldsymbol{p}_r\right], \tag{5.7b}$$

$$\mathcal{L}_F\left[\phi^*_{k_1}, \phi_{k_2}, \psi_{k_{1,2}}\right] = \sum_{k_1,k_2}\phi^\dagger_{k_1}\left(\partial_\tau\delta_{k_1,k_2} + \underline{H}^{\psi}_{k_1,k_2}\right)\phi_{k_2}\Big|_{e=\sqrt{1-d_1^2-d_2^2-p_0^2-\boldsymbol{p}^2}}, \tag{5.7c}$$

and the fluctuation matrix, therefore, also splits into two parts

$$\mathcal{M}^{a,b}_{\mu,\nu}(q) = \left[\mathcal{M}^B(\mathrm{i}\omega_n)\right]^{a,b}_{\mu,\nu} + \left[\mathcal{M}^F(q)\right]^{a,b}_{\mu,\nu}. \tag{5.7d}$$

Notice that by the construction of the path integral, all SB and PF degrees of freedom in Equation (5.7c) are discretized with the same underlying time slices. Consequently, the frequency mesh after FT to Matsubara space also matches and the summation over a function depending on both, bosonic [$\omega_n = 2n\pi/\beta$] and fermionic [$\omega_n = (2n+1)\pi/\beta$] frequencies yields

$$\sum_{\mathrm{i}\omega_n}\mathcal{L}_F\left[\omega_n, \omega_n\right] = \sum_{n=-\infty}^{\infty}\mathcal{L}_F\left[\frac{2n\pi}{\beta}, \frac{(2n+1)\pi}{\beta}\right]. \tag{5.8}$$

Hence, the PF action can be expressed as

$$\mathcal{S}_F = \sum_{k_1,k_2}\phi^\dagger_{k_1}\left(-\mathrm{i}\omega_{n_1}\delta_{k_1,k_2} + \underline{H}^{\psi}_{k_1,k_2}\right)\phi_{k_2}, \tag{5.9a}$$

where

$$\underline{H}^{\psi}_{k_1,k_2} = \delta_{k_1,k_2}\left(\underline{\epsilon} - \mu_0\right) + \frac{1}{\sqrt{N\beta}}\left(\underline{\beta}\right)^\top_{k_1-k_2} + \frac{1}{N\beta}\sum_k\left(\underline{Z}^\dagger\right)^\top_{k-k_1}\underline{\mathcal{H}}_k\left(\underline{Z}\right)^\top_{k-k_2}, \tag{5.9b}$$

is the SB-dependent Hamiltonian defined in Section 3.2.2 after FT to Matsubara space and the corresponding Green's function is given by

$$\underline{G}^{\psi}_{k_1,k_2} = \left(\mathrm{i}\omega_{n_1}\delta_{k_1,k_2} - \underline{H}^{\psi}_{k_1,k_2}\right)^{-1}. \tag{5.9c}$$

The PF degrees of freedom can be integrated out using Equation (3.17), which yields

$$Z_F = \det\left(-\left[\underline{G}^{\psi}_{k_1,k_2}\right]^{-1}\right). \tag{5.10a}$$

Applying the identity $\ln\det\underline{\mathcal{A}} = \mathrm{Tr}\ln\underline{\mathcal{A}}$, we find the effective SB-dependent action, which results from the integration of the PFs

$$\mathcal{S}_F = -\,\mathrm{Tr}\ln\left[\left(-\mathrm{i}\omega_{n_1}\delta_{k_1,k_2} + \underline{H}^{\psi}_{k_1,k_2}\right)\right]. \tag{5.10b}$$

In order to find the second variation w.r.t. bosonic fields, we employ a series expansion around the saddle point

$$\begin{aligned}\mathcal{S}_F^{(0)} + \delta\mathcal{S}_F\left[\delta\boldsymbol{\psi}\right] &= -\operatorname{Tr}\ln\left[-\mathrm{i}\omega_n + \underline{H}_{\boldsymbol{k}}^{\overline{\boldsymbol{\psi}}} + \underline{H}_{k_1,k_2}^{\delta\boldsymbol{\psi}}\right] = -\operatorname{Tr}\ln\left[\left(-\mathrm{i}\omega_n + \underline{H}_{\boldsymbol{k}}^{\overline{\boldsymbol{\psi}}}\right)\left(1 - \underline{G}_{k_1}^{\overline{\boldsymbol{\psi}}}\underline{H}_{k_1,k_2}^{\delta\boldsymbol{\psi}}\right)\right] \\ &= -\operatorname{Tr}\ln\left[-\mathrm{i}\omega_n + \underline{H}_{\boldsymbol{k}}^{\overline{\boldsymbol{\psi}}}\right] + \operatorname{Tr}\sum_{l=1}^{\infty}\frac{1}{l}\left(\underline{G}_{k_1}^{\overline{\boldsymbol{\psi}}}\underline{H}_{k_1,k_2}^{\delta\boldsymbol{\psi}}\right)^l .\end{aligned} \tag{5.11}$$

The variation of the Hamiltonian is given by

$$\underline{H}_{k_1,k_2}^{\delta\boldsymbol{\psi}} = \sum_q\sum_\mu \left.\frac{\partial\underline{H}_{k_1,k_2}^{\boldsymbol{\psi}}}{\partial\psi_{q,\mu}}\right|_{\overline{\boldsymbol{\psi}}}\delta\psi_{q,\mu} + \frac{1}{2}\sum_{q_1,q_2}\sum_{\mu\nu}\left.\frac{\partial^2\underline{H}_{k_1,k_2}^{\boldsymbol{\psi}}}{\partial\psi_{q_1,\mu}\partial\psi_{q_2,\nu}}\right|_{\overline{\boldsymbol{\psi}}}\delta\psi_{q_1,\mu}\delta\psi_{q_2,\nu} + \mathcal{O}\left(\delta\boldsymbol{\psi}^3\right) , \tag{5.12}$$

and

$$\underline{G}_k^{\overline{\boldsymbol{\psi}}} = \left(\mathrm{i}\omega_n - \underline{H}_{\boldsymbol{k}}^{\overline{\boldsymbol{\psi}}}\right)^{-1} \tag{5.13}$$

defines the PF Green's function at the MF saddle point $\overline{\boldsymbol{\psi}}$. Explicit expressions of SB-dependent MF hopping matrix $\underline{H}_{\boldsymbol{k}}^{\overline{\boldsymbol{\psi}}}$ for models discussed within this thesis are derived in Appendix B. The leading order variation of the action is found by collecting all second-order terms w.r.t. fluctuation fields $\delta\boldsymbol{\psi}$ in the series expansion given by Equation (5.11)[1]

$$\mathcal{S}_F^{(2)} = \frac{1}{2}\sum_{q_1,q_2}\sum_{\mu\nu}\delta\psi_{q_1,\mu}\delta\psi_{q_2,\nu}\operatorname{tr}\left(\sum_k \underline{G}_k^{\overline{\boldsymbol{\psi}}}\left.\frac{\partial^2\underline{H}_{k,k}^{\boldsymbol{\psi}}}{\partial\psi_{q_1,\mu}\partial\psi_{q_2,\nu}}\right|_{\overline{\boldsymbol{\psi}}} + \sum_{k_1k_2}\underline{G}_{k_1}^{\overline{\boldsymbol{\psi}}}\left.\frac{\partial\underline{H}_{k_1,k_2}^{\boldsymbol{\psi}}}{\partial\psi_{q_1,\mu}}\right|_{\overline{\boldsymbol{\psi}}}\underline{G}_{k_2}^{\overline{\boldsymbol{\psi}}}\left.\frac{\partial\underline{H}_{k_2,k_1}^{\boldsymbol{\psi}}}{\partial\psi_{q_2,\nu}}\right|_{\overline{\boldsymbol{\psi}}}\right) . \tag{5.14}$$

The details on how to evaluate the occurring derivatives depend on whether the underlying MF saddle point spontaneously breaks translation symmetry due to magnetic order. In Section 5.2.1, we provide a complete derivation for the simplest case, i.e., the PM. The calculation for spiral magnetic saddle points with ordering vector $\boldsymbol{Q}$ works in principle analogous but is quite elaborate and requires multiple suitable index shifts to adapt a compact form. It has been thoroughly derived in Reference [55] and we will summarize the results in Section 5.2.2 and Appendix C.

5.2.1 Paramagnetic ground states

A paramagnetic MF ground state is characterized by $\boldsymbol{p} = \boldsymbol{\beta} = \boldsymbol{Q} = 0$. In this limit, there are no external periodicity or sublattice indices, and the fluctuation matrix simplifies to

$$\mathcal{M}_{\mu,\nu}(q) = \frac{1}{2}\left.\frac{\partial^2\mathcal{S}}{\partial\psi_{\mu,-q}\partial\psi_{\nu,q}}\right|_{\overline{\boldsymbol{\psi}}} . \tag{5.15}$$

[1] Despite the PFs have formally been integrated out exactly, the highest appearing order in the context of Gaussian fluctuations is $\mathcal{O}\left(\boldsymbol{\phi}^4\right)$, which is why this calculation is also referred to as a one-loop calculation. This can be seen if the bosonic series expansion is applied before the PFs are integrated. The fluctuation matrix can then be derived through Wick's theorem [116]. Our approach, however, is more elegant and easier to generalize beyond the Hubbard model.

Bosonic part

Since the bosonic part only contains on-site and equal-time contributions, i.e., $\Delta \boldsymbol{r} = \Delta\tau = 0$, its derivatives can be conveniently calculated in the space-time domain. In order to do so, we define

$$\delta_{r,\tilde{r}} = \delta_{\boldsymbol{r}_i,\tilde{\boldsymbol{r}}_i}\delta(\tau - \tilde{\tau}) \ , \tag{5.16}$$

where $\delta_{\Delta \boldsymbol{r}_i,0}$ denotes the Kronecker delta and $\delta(\tau)$ the Dirac delta function and rewrite the bosonic action according to

$$\mathcal{S}_B = \sum_{\tilde{\boldsymbol{r}}_i,\Delta\tilde{\boldsymbol{r}}_i} \iint_0^\beta d\tilde{\tau}\, d\Delta\tilde{\tau}\, \mathcal{L}_B\left[\psi_{\tilde{r}}, \psi_{\tilde{r}+\Delta\tilde{r}}\right] \delta_{\Delta\tilde{r},0} \ . \tag{5.17}$$

The bosonic part of the fluctuation matrix is then found to be

$$\begin{aligned}\mathcal{M}^B_{\mu,\nu}(\Delta r) &= \frac{\sqrt{N\beta}}{2} \frac{\partial^2 \mathcal{S}_B}{\partial\psi_{\mu,r}\partial\psi_{\mu,r+\Delta r}}\bigg|_{\overline{\psi}} = \frac{\sqrt{N\beta}}{2} \sum_{\tilde{\boldsymbol{r}}_i,\Delta\tilde{\boldsymbol{r}}_i} \iint_0^\beta d\tilde{\tau}\, d\Delta\tilde{\tau}\, \frac{\partial^2 \mathcal{L}_B^{\overline{\psi}}}{\partial\psi_\mu\partial\psi_\nu} \delta_{\Delta\tilde{r},0}\left[\delta_{r,\tilde{r}}\,\delta_{\Delta r,\Delta\tilde{r}} + \delta_{\mu,\nu}\,\delta_{r+\Delta r,\tilde{r}}\,\delta_{r,\tilde{r}+\Delta\tilde{r}}\right] \\ &= \frac{\sqrt{N\beta}}{2} \frac{\partial^2 \mathcal{L}_B^{\overline{\psi}}}{\partial\psi_\mu\partial\psi_\nu}\delta(\Delta r) \ .\end{aligned} \tag{5.18a}$$

Since the matrix elements are delta-correlated in space-time, they become uniform in the momentum-Matsubara frequency domain

$$\mathcal{M}^B_{\mu,\nu}(q) = \frac{1}{\sqrt{N\beta}} \int_0^\beta d\Delta\tau \sum_{\Delta \boldsymbol{r}_i} \mathrm{e}^{\mathrm{i}\boldsymbol{q}\Delta\boldsymbol{r}_i}\mathrm{e}^{-\mathrm{i}\omega_n\Delta\tau}\left[\mathcal{M}(\Delta r)\right]_{\mu,\nu} = \frac{1}{2}\frac{\partial^2 \mathcal{L}_B^{\overline{\psi}}}{\partial\psi_\mu\partial\psi_\nu} \ , \tag{5.18b}$$

and are simply determined by the respective derivatives of the MF Lagrangian. However, we need to dedicate special notice to the remaining time derivative in the bosonic Lagrangian associated with the complex d-field:[1]

$$\mathcal{M}^B_{d_1,d_2}(\Delta r) = \frac{\sqrt{N\beta}}{2}\mathrm{i}\partial_{\Delta\tau}\delta_{\Delta \boldsymbol{r}_i}\delta(\Delta\tau) = \frac{\sqrt{N\beta}}{2}\mathrm{i}\delta_{\Delta \boldsymbol{r}_i,0}\,\delta'(\Delta\tau) \ , \tag{5.19a}$$

which yields

$$\mathcal{M}^B_{d_1,d_2}(q) = \frac{1}{\sqrt{N\beta}} \int_0^\beta d\Delta\tau \sum_{\Delta \boldsymbol{r}} \mathrm{e}^{\mathrm{i}\boldsymbol{q}\Delta\boldsymbol{r}}\mathrm{e}^{-\mathrm{i}\omega_n\Delta\tau}\frac{\sqrt{N\beta}}{2}\mathrm{i}\delta_{\Delta \boldsymbol{r}_i,0}\,\delta'(\tau) = \frac{1}{2}\omega_n \ . \tag{5.19b}$$

[1] $\delta'(\Delta\tau)$ denotes the distributional derivative of the Dirac delta function.

Consequently, the bosonic fluctuation matrix for PM saddle points in the basis of Equation (5.4a) is given by [53][1]

$$\underline{\mathcal{M}}^{B} = \frac{1}{2}\begin{pmatrix} 2U-4\overline{\beta}_0 & \omega_n & 0 & -4\overline{d}_1 & 0 & 0 & 0 & 0 & 0 & 0 \\ -\omega_n & 2U-4\overline{\beta}_0 & 0 & 0 & 0 & 0 & 0 & 0 & 0 & 0 \\ 0 & 0 & -2\overline{\beta}_0 & -2\overline{p}_0 & 0 & 0 & 0 & 0 & 0 & 0 \\ -4\overline{d}_1 & 0 & -2\overline{p}_0 & 0 & 0 & 0 & 0 & 0 & 0 & 0 \\ 0 & 0 & 0 & 0 & -2\overline{\beta}_0 & -2\overline{p}_0 & 0 & 0 & 0 & 0 \\ 0 & 0 & 0 & 0 & -2\overline{p}_0 & 0 & 0 & 0 & 0 & 0 \\ 0 & 0 & 0 & 0 & 0 & 0 & -2\overline{\beta}_0 & -2\overline{p}_0 & 0 & 0 \\ 0 & 0 & 0 & 0 & 0 & 0 & -2\overline{p}_0 & 0 & 0 & 0 \\ 0 & 0 & 0 & 0 & 0 & 0 & 0 & 0 & -2\overline{\beta}_0 & -2\overline{p}_0 \\ 0 & 0 & 0 & 0 & 0 & 0 & 0 & 0 & -2\overline{p}_0 & 0 \end{pmatrix}. \tag{5.20}$$

Pseudofermionic part

In order to calculate the PF part of the fluctuation matrix, we need to evaluate the derivatives of $\underline{H}^{\psi}_{k_1,k_2}$ determined by the functions

$$\underline{Z}_k = (\underline{\mathbb{1}}_{2O\times 2O}\sqrt{N\beta}\,\delta_{k,0}) \oplus \underline{z}_k\,, \tag{5.21a}$$

$$\underline{B}_k = \underline{0}_{2O\times 2O} \oplus \underline{\beta}_k\,. \tag{5.21b}$$

w.r.t. the fluctuation fields and evaluate them at the MF saddle point $\overline{\psi}$. As shown in detail in Appendix A.6 this can be done by exploiting that all fields are uniform at the MF saddle point in the space-time domain

$$\left.\frac{\partial \underline{Z}_{\mu,r}}{\partial \psi_{r,\tilde{\mu}}}\right|_{\overline{\psi}} = \left.\frac{\partial \underline{Z}}{\partial \psi_{\tilde{\mu}}}\right|_{\overline{\psi}}, \tag{5.22}$$

which results in

$$\underline{z}_k\big|_{\overline{\psi}} = \sqrt{N\beta}\,\delta_{k,0}\,\underline{z}\big|_{\overline{\psi}}\,, \quad \underline{z}^{\dagger}_k\big|_{\overline{\psi}} = \sqrt{N\beta}\,\delta_{k,0}\,\underline{z}\big|_{\overline{\psi}} \tag{5.23a}$$

$$\left.\frac{\partial \underline{z}_k}{\partial \psi_{q,\mu}}\right|_{\overline{\psi}} = \delta_{k,q}\left.\frac{\partial \underline{z}}{\partial \psi_{\mu}}\right|_{\overline{\psi}}, \quad \left.\frac{\partial \underline{z}^{\dagger}_k}{\partial \psi_{q,\mu}}\right|_{\overline{\psi}} = \delta_{k,-q}\left.\frac{\partial \underline{z}^{\dagger}}{\partial \psi_{\mu}}\right|_{\overline{\psi}} \tag{5.23b}$$

$$\left.\frac{\partial^2 \underline{z}_k}{\partial \psi_{q_1,\mu}\partial \psi_{q_2,\nu}}\right|_{\overline{\psi}} = \frac{1}{\sqrt{N\beta}}\delta_{k,q_1+q_2}\left.\frac{\partial^2 \underline{z}}{\partial \psi_{\mu}\partial \psi_{\nu}}\right|_{\overline{\psi}}, \quad \left.\frac{\partial^2 \underline{z}^{\dagger}_k}{\partial \psi_{q_1,\mu}\partial \psi_{q_2,\nu}}\right|_{\overline{\psi}} = \frac{1}{\sqrt{N\beta}}\delta_{k,-q_1-q_2}\left.\frac{\partial^2 \underline{z}^{\dagger}}{\partial \psi_{\mu}\partial \psi_{\nu}}\right|_{\overline{\psi}} \tag{5.23c}$$

$$\left.\frac{\partial \underline{\beta}_k}{\partial \psi_{\mu,q}}\right|_{\overline{\psi}} = \underline{\tau}^{\nu}\delta_{\psi_{\mu},\beta_{\nu}}\delta_{k,q}\,. \tag{5.23d}$$

The derivatives of $\underline{Z}_k$ and $\underline{B}_k$ can now be inferred with the definition in Equation (5.21a), i.e., first and second derivatives of matrix entries associated with non-interacting degrees of freedom vanish, whereas zeroth derivative terms are considered by the unity matrix as precisely defined in Equation (A.34). Since the LMs

[1] Following Reference [53], the same result can also be found if the FT is performed before taking the derivatives.

enter the Hamiltonian linear, only first derivatives are non-zero and their matrix structure follows from the definition of $\underline{\beta}$ in Equation (3.33f). For shortness of notation, we define

$$\underline{Z}_0 = \underline{Z}^\top\big|_{\overline{\psi}}\,, \tag{5.24a}$$

$$\underline{Z}_\mu = \frac{\partial \underline{Z}^\top}{\partial \psi_\mu}\bigg|_{\overline{\psi}}\,, \tag{5.24b}$$

$$\underline{Z}_{\mu\nu} = \frac{\partial^2 \underline{Z}^\top}{\partial \psi_\mu \partial \psi_\nu}\bigg|_{\overline{\psi}}\,, \tag{5.24c}$$

$$\underline{B}_\mu = \underline{0}_{2O\times 2O} \oplus (\underline{\tau}^\nu)^\top \delta_{\psi_\mu,\beta_\nu} \tag{5.24d}$$

and we call these functions slave-boson weights. Those uniform derivatives are most conveniently evaluated by in the Pauli-matrix expanded form of the $\underline{z}$-matrix

$$\underline{z} = \mathcal{Z}_+ \underline{\tau}^0 + \mathcal{Z}_- \sum_{\mu=1}^{3} \frac{\boldsymbol{p}}{p} \underline{\tau}^\mu\,, \tag{5.25a}$$

with

$$\mathcal{Z}_\pm = \frac{z_+ \pm z_-}{2}\,, \quad z_\pm = \frac{p_0(e+d) \pm p(e-d)}{\sqrt{2\left[1-d^2-(p_0\pm p)^2/2\right]\left[1-e^2-(p_0\mp p)^2/2\right]}}\bigg|_{e=\sqrt{1-d_1^2-d_2^2-p_0^2-\boldsymbol{p}^2}}\,, \tag{5.25b}$$

which is deduced in Appendix A.4. Notice that we need to replace the e-field utilizing the α constraint before taking the derivatives in the chosen basis. Combining all previous results, we may determine the derivatives of the Hamiltonian defined in Equation (5.9b)

$$\frac{\partial \underline{H}^\psi_{k_1,k_2}}{\partial \psi_{q,\mu}}\bigg|_{\overline{\psi}} = \frac{\delta_{q,k_1-k_2}}{\sqrt{N\beta}}\left[\underline{B}_\mu + \left(\underline{Z}^\dagger_\mu\right)\underline{\mathcal{H}}_{\boldsymbol{k}_2}\underline{Z}_0 + \underline{Z}^\dagger_0\underline{\mathcal{H}}_{\boldsymbol{k}_1}\underline{Z}_\mu\right]\,, \tag{5.26a}$$

$$\frac{\partial^2 \underline{H}^\psi_{k,k}}{\partial \psi_{q_1,\mu}\partial \psi_{q_2,\nu}}\bigg|_{\overline{\psi}} = \frac{1}{N\beta}\delta_{q_1,-q_2}\left[\underline{Z}^\dagger_{\mu\nu}\underline{\mathcal{H}}_{\boldsymbol{k}}\underline{Z}_0 + \underline{Z}^\dagger_0\underline{\mathcal{H}}_{\boldsymbol{k}}\underline{Z}_{\mu\nu} + \underline{Z}^\dagger_\mu\underline{\mathcal{H}}_{\boldsymbol{k}-\boldsymbol{q}_1}\underline{Z}_\nu + \underline{Z}^\dagger_\nu\underline{\mathcal{H}}_{\boldsymbol{k}+\boldsymbol{q}_1}\underline{Z}_\mu\right]\,, \tag{5.26b}$$

which is shown in detail in Appendix A.6. Applying these results to the action in Equation (5.14) and the definition of the fluctuation matrix given by Equation (5.15), we find

$$\begin{aligned}\mathcal{M}^F_{\mu,\nu}(q) = \frac{1}{2N\beta}\sum_k \mathrm{tr}\Big[&\underline{G}^{\overline{\psi}}_k\left[\underline{Z}^\dagger_{\mu\nu}\underline{\mathcal{H}}_{\boldsymbol{k}}\underline{Z}_0 + \underline{Z}_0\underline{\mathcal{H}}_{\boldsymbol{k}}\underline{Z}_{\mu\nu} + \underline{Z}^\dagger_\mu\underline{\mathcal{H}}_{\boldsymbol{k}+\boldsymbol{q}}\underline{Z}_\nu + \underline{Z}^\dagger_\nu\underline{\mathcal{H}}_{\boldsymbol{k}-\boldsymbol{q}}\underline{Z}_\mu\right]\\ &+\underline{G}^{\overline{\psi}}_k\left[\underline{Z}^\dagger_\mu\underline{\mathcal{H}}_{\boldsymbol{k}+\boldsymbol{q}}\underline{Z}_0 + \underline{Z}_0\underline{\mathcal{H}}_{\boldsymbol{k}}\underline{Z}_\mu + \underline{B}_\mu\right]\underline{G}^{\overline{\psi}}_{k+q}\left[\underline{Z}^\dagger_\nu\underline{\mathcal{H}}_{\boldsymbol{k}}\underline{Z}_0 + \underline{Z}_0\underline{\mathcal{H}}_{\boldsymbol{k}+\boldsymbol{q}}\underline{Z}_\nu + \underline{B}_\nu\right]\Big]\,.\end{aligned} \tag{5.27}$$

This equation can be interpreted as scattering processes of the bosonic fluctuation fields with the PF mean-field background as graphically illustrated by the Feynman diagrams in Figure 5.1.

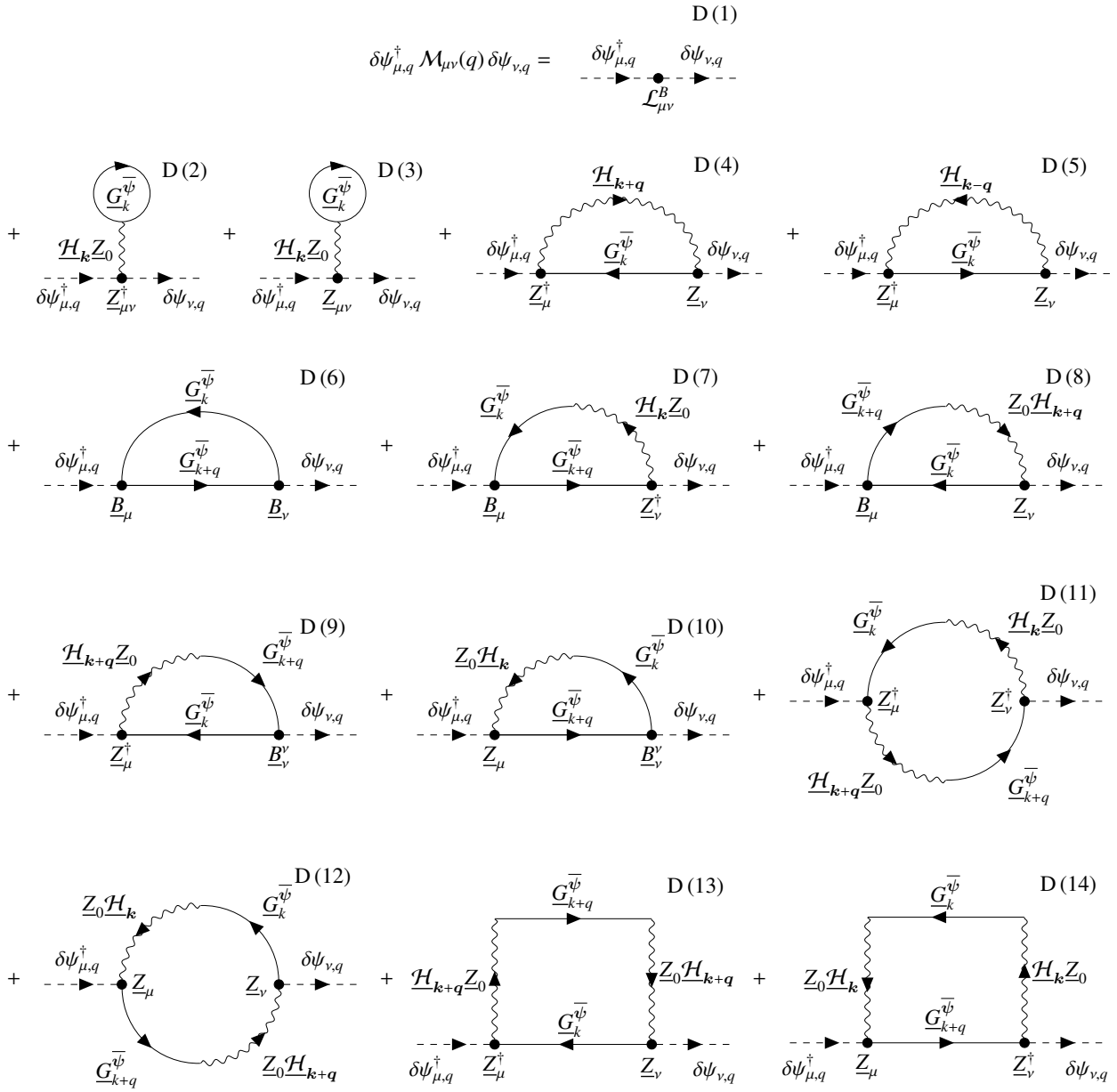

Figure 5.1: The fluctuation matrix can be interpreted as a result of scattering of bosonic fluctuation fields with the PF mean-field background. The corresponding scattering processes are illustrated through the Feynman diagrams D(1)-D(14), where k is the internal energy-momentum four-index, which needs to be integrated out and q represents the external bosonic index carried by the fluctuation matrix. The diagrams are sorted by the scattering order from zeroth (D(1): bosonic Lagrangian, no scattering at the MF background), to first (D(2)-D(5): processes including one interaction line and one MF Green's function) and second (D(6)-D(14): processes featuring two MF Green's functions). The rescaled bare Hamiltonian $\underline{\mathcal{H}}_{\boldsymbol{k}}\underline{Z}_0$ can be interpreted as a PF static but momentum-dependent interaction. The bosonic vertices denoted by black circles fulfill energy and momentum conservation. The diagrams D(1)-D(3) yield constants (except for $\mu, \nu \in \{d_1, d_2\}$). D(4)-D(5) are momentum-dependent but frequency-independent due to the static interaction lines. Finally, D(6)-D(14) yield dynamic and momentum-dependent contributions because the PF Green's function can also carry bosonic Matsubara frequencies.

The occurring Matsubara summations can be calculated analytically in a basis where the MF hopping matrix $\underline{H}_{\boldsymbol{k}}^{\overline{\psi}}$ and the MF Green's $\underline{G}_{\boldsymbol{k}}^{\overline{\psi}}$ function are diagonal

$$\underline{U}_{\boldsymbol{k}}\underline{H}_{\boldsymbol{k}}^{\overline{\psi}}\underline{U}_{\boldsymbol{k}}^{\dagger} = \varepsilon_{\boldsymbol{k}}^{s}\delta_{s,s'} \tag{5.28a}$$

$$\underline{U}_{\boldsymbol{k}}\underline{G}_{\boldsymbol{k}}^{\overline{\psi}}\underline{U}_{\boldsymbol{k}}^{\dagger} = \left(\mathrm{i}\omega_m - \varepsilon_{\boldsymbol{k}}^{s}\right)^{-1}\delta_{s,s'}\,, \tag{5.28b}$$

whereat s acts as multi-index, representing orbital and spin degrees of freedom, and the unitary matrices fulfill $\underline{U}_{\boldsymbol{k}}\underline{U}_{\boldsymbol{k}}^{\dagger} = \underline{\mathbb{1}}$. The Matsubara summations are determined by

$$\frac{1}{\beta}\sum_{\mathrm{i}\omega_m}\mathrm{tr}\,\underline{G}_{\boldsymbol{k}}^{\overline{\psi}}\underline{\mathcal{A}}_{\boldsymbol{k},\boldsymbol{q}} = \sum_{s,b,c}\left[\underline{U}_{\boldsymbol{k}}^{\dagger}\right]^{s,b}\frac{1}{\beta}\sum_{\mathrm{i}\omega_m}\left(\mathrm{i}\omega_m - \varepsilon_{\boldsymbol{k}}^{b}\right)^{-1}\left[\underline{U}_{\boldsymbol{k}}\right]^{b,c}\left[\underline{\mathcal{A}}_{\boldsymbol{k},\boldsymbol{q}}\right]^{c,s} = \sum_{s} n_{\mathrm{F}}\left(\varepsilon_{\boldsymbol{k}}^{s}\right)\left[\underline{U}_{\boldsymbol{k}}\underline{\mathcal{A}}_{\boldsymbol{k},\boldsymbol{q}}\underline{U}_{\boldsymbol{k}}^{\dagger}\right]^{s,s}\,, \tag{5.29a}$$

$$\begin{aligned}\frac{1}{\beta}\sum_{\mathrm{i}\omega_m}\mathrm{tr}\,\underline{G}_{\boldsymbol{k}}^{\overline{\psi}}\underline{\mathcal{B}}_{\boldsymbol{k},\boldsymbol{q}}\underline{G}_{\boldsymbol{k}+\boldsymbol{q}}^{\overline{\psi}}\underline{\mathcal{C}}_{\boldsymbol{k},\boldsymbol{q}} &= \sum_{\substack{s,b,c\\d,e,s'}}\left[U_{\boldsymbol{k}}^{\dagger}\right]^{s,b}\frac{1}{\beta}\sum_{\mathrm{i}\omega_m}\left(\mathrm{i}\omega_m - \varepsilon_{\boldsymbol{k}}^{b}\right)^{-1}U_{\boldsymbol{k}}^{b,c}\mathcal{B}_{\boldsymbol{k},\boldsymbol{q}}^{c,d}\left[U_{\boldsymbol{k}+\boldsymbol{q}}^{\dagger}\right]^{d,e}\left(\mathrm{i}\omega_m + \mathrm{i}\omega_n - \varepsilon_{\boldsymbol{k}+\boldsymbol{q}}^{e}\right)^{-1}U_{\boldsymbol{k}+\boldsymbol{q}}^{e,s'}\mathcal{C}_{\boldsymbol{k},\boldsymbol{q}}^{s',s}\\ &= \sum_{s,s'}\frac{n_{\mathrm{F}}\left(\varepsilon_{\boldsymbol{k}}^{s}\right) - n_{\mathrm{F}}\left(\varepsilon_{\boldsymbol{k}+\boldsymbol{q}}^{s'} + \mathrm{i}\omega_n\right)}{\mathrm{i}\omega_n + \varepsilon_{\boldsymbol{k}}^{s} - \varepsilon_{\boldsymbol{k}+\boldsymbol{q}}^{s'}}\left[\underline{U}_{\boldsymbol{k}}\underline{\mathcal{B}}_{\boldsymbol{k},\boldsymbol{q}}\underline{U}_{\boldsymbol{k}+\boldsymbol{q}}^{\dagger}\right]^{s,s'}\left[\underline{U}_{\boldsymbol{k}+\boldsymbol{q}}\underline{\mathcal{C}}_{\boldsymbol{k},\boldsymbol{q}}\underline{U}_{\boldsymbol{k}}^{\dagger}\right]^{s',s}\,,\end{aligned} \tag{5.29b}$$

where specifics are elaborated in Appendix A.5. Notice that we only sum over fermionic Matsubara frequencies $\omega_m = (2n+1)\pi/\beta$, while the bosonic Matsubara frequency $\omega_n = 2n\pi/\beta$ remains as external degree of freedom of the fluctuation fields. The Fermi-Dirac distribution is invariant under the addition of a bosonic Matsubara frequency[1] $n_{\mathrm{F}}\left(\varepsilon_{\boldsymbol{k}+\boldsymbol{q}}^{s'} + \mathrm{i}\omega_n\right) = n_{\mathrm{F}}\left(\varepsilon_{\boldsymbol{k}+\boldsymbol{q}}^{s'}\right)$ and by identifying the matrices $\mathcal{A}_{\boldsymbol{k},\boldsymbol{q}}, \mathcal{B}_{\boldsymbol{k},\boldsymbol{q}}, \mathcal{C}_{\boldsymbol{k},\boldsymbol{q}}$ with the respective matrices in Equation (5.27), we obtain the final form of the PF part of the fluctuation matrix [53, 54, 56, 99]

$$\begin{aligned}\mathcal{M}_{\mu,\nu}^{F}(q) = \frac{1}{2N}\sum_{\boldsymbol{k}}\Bigg(&\sum_{s} n_{\mathrm{F}}\left(\varepsilon_{\boldsymbol{k}}^{s}\right)\left[\underline{U}_{\boldsymbol{k}}\left(\underline{Z}_{\mu\nu}^{\dagger}\underline{\mathcal{H}}_{\boldsymbol{k}}\underline{Z}_0 + \underline{Z}_0\underline{\mathcal{H}}_{\boldsymbol{k}}\underline{Z}_{\mu\nu} + \underline{Z}_{\mu}^{\dagger}\underline{\mathcal{H}}_{\boldsymbol{k}+\boldsymbol{q}}\underline{Z}_{\nu} + \underline{Z}_{\nu}^{\dagger}\underline{\mathcal{H}}_{\boldsymbol{k}-\boldsymbol{q}}\underline{Z}_{\mu}\right)\underline{U}_{\boldsymbol{k}}^{\dagger}\right]^{s,s}\\ &+\sum_{s,s'} L_{\mathrm{F}}\left(\varepsilon_{\boldsymbol{k}}^{s}, \varepsilon_{\boldsymbol{k}+\boldsymbol{q}}^{s'}, \mathrm{i}\omega_n\right)\left[\underline{U}_{\boldsymbol{k}}\left(\underline{Z}_{\mu}^{\dagger}\underline{\mathcal{H}}_{\boldsymbol{k}+\boldsymbol{q}}\underline{Z}_0 + \underline{Z}_0\underline{\mathcal{H}}_{\boldsymbol{k}}\underline{Z}_{\mu} + \underline{B}_{\mu}\right)\underline{U}_{\boldsymbol{k}+\boldsymbol{q}}^{\dagger}\right]^{s,s'}\left[\underline{U}_{\boldsymbol{k}+\boldsymbol{q}}\left(\underline{Z}_{\nu}^{\dagger}\underline{\mathcal{H}}_{\boldsymbol{k}}\underline{Z}_0 + \underline{Z}_0\underline{\mathcal{H}}_{\boldsymbol{k}+\boldsymbol{q}}\underline{Z}_{\nu} + \underline{B}_{\nu}\right)\underline{U}_{\boldsymbol{k}}^{\dagger}\right]^{s',s}\Bigg)\end{aligned} \tag{5.30}$$

where

$$L_{\mathrm{F}}\left(\varepsilon_{\boldsymbol{k}}^{s}, \varepsilon_{\boldsymbol{k}+\boldsymbol{q}}^{s'}, \mathrm{i}\omega_n\right) = \frac{n_{\mathrm{F}}\left(\varepsilon_{\boldsymbol{k}}^{s}\right) - n_{\mathrm{F}}\left(\varepsilon_{\boldsymbol{k}+\boldsymbol{q}}^{s'}\right)}{\mathrm{i}\omega_n + \varepsilon_{\boldsymbol{k}}^{s} - \varepsilon_{\boldsymbol{k}+\boldsymbol{q}}^{s'}} \tag{5.31a}$$

is known as Lindhard function. The remaining momentum sum needs to be evaluated numerically and guidelines for an efficient implementation and analysis are provided in Appendix D. Moreover, we want to emphasize that the convergence of the Lindhard function is problematic in the static limit ($\mathrm{i}\omega_n = 0$) but can be recovered by implementing

$$\lim_{\varepsilon_{\boldsymbol{k}+\boldsymbol{q}}\to\varepsilon_{\boldsymbol{k}}} L_{\mathrm{F}}\left(\varepsilon_{\boldsymbol{k}}, \varepsilon_{\boldsymbol{k}+\boldsymbol{q}}, 0\right) = \frac{\partial n_{\mathrm{F}}\left(\varepsilon_{\boldsymbol{k}}\right)}{\partial\varepsilon_{\boldsymbol{k}}} = -\frac{\beta}{4\cosh^2\left(\beta\epsilon_{\boldsymbol{k}}/2\right)}\,. \tag{5.31b}$$

[1] This is because a condensate of a fermion and a boson is a fermionic quasiparticle.

An evaluation of real frequencies ω requires the analytic continuation [39] $\mathrm{i}\omega \to \omega + \mathrm{i}\eta$ with $\eta \to 0^+$ to all occurring Matsubara frequencies, i.e., $\mathcal{M}_B(\mathrm{i}\omega_n)$ and $\mathcal{M}_F(\mathrm{i}\omega_n)$. This so-called Wick rotation reverts the imaginary times applied to the time evolution operator in Equation (3.3d) which was used to derive the path integral back to real times. Consequently, ω is a continuous frequency suitable for describing dynamic correlations and excitation spectra. The infinitesimal η needs to be positive in order to represent the causal retarded function, whereas the respective advanced function is found for $\eta < 0$. This procedure is usually applied in the context of Matsubara Green's functions, which is also the case here since we identify $\mathcal{G}(\mathrm{i}\omega_n) = -\mathcal{M}^{-1}(\mathrm{i}\omega_n)$.

Symmetries of the fluctuation matrix

Since we employ a basis of fluctuation fields, which is real-valued in the space-time domain, the fluctuation matrix

$$\mathcal{M}_{\mu,\nu}(q) = \frac{1}{2}\frac{\partial^2 \mathcal{S}}{\partial\psi_{\mu,-q}\partial\psi_{\nu,q}}\bigg|_{\overline{\psi}} \tag{5.32}$$

satisfies $\mathcal{M}_{\mu,\nu}(q) = \mathcal{M}_{\nu,\mu}(-q)$ per definition. Moreover, for spin-rotation-invariant (SRI) models, it holds

$$\left[\underline{\mathcal{H}}\,,\,\underline{Z}_\mu^{(\dagger)}\right]_- = \left[\underline{G}^{\overline{\Psi}}\,,\,\underline{Z}_\mu^{(\dagger)}\right]_- = \left[\underline{G}^{\overline{\Psi}}\,,\,\underline{\mathcal{H}}_k\right]_- = \left[\underline{G}^{\overline{\Psi}}\,,\,\underline{B}_\mu\right]_- = 0 \tag{5.33}$$

in the PM limit. With Equation (5.27), we can then infer $\mathcal{M}_{\mu,\nu}(\underline{Z}^\dagger) = \mathcal{M}_{\nu,\mu}(\underline{Z})$, i.e., interchanging the indices is equivalent to conjugate transposing the $\underline{Z}$- matrix. Since $\underline{Z}$ can be written as a superposition of the hermitian Pauli matrices, we may determine $\underline{Z}^\dagger$ by complex conjugation of the prefactors $(\mathcal{Z}_+, \mathcal{Z}_-)$ where the imaginary unit i only occurs together with the d_2 field. As a consequence, the PM fluctuation matrix obeys the symmetry [53]

$$\begin{aligned} &\mathcal{M}_{\mu\nu}(q) = -\mathcal{M}_{\nu\mu}(q) = -\mathcal{M}_{\mu\nu}(-q) \qquad (\mu = d_2, \nu \neq d_2) \cup (\mu \neq d_2, \nu = d_2)\,, \\ &\mathcal{M}_{\mu\nu}(q) = \mathcal{M}_{\nu\mu}(q) = \mathcal{M}_{\mu\nu}(-q) \qquad \text{otherwise}\,, \end{aligned} \tag{5.34}$$

i.e., it is a symmetric matrix w.r.t. all fields except for d_2, where it is antisymmetric[1].

Moreover, the spin and charge sector are decoupled for SRIs models, i.e., the fluctuation matrix is block-diagonal w.r.t. charge fields $\psi_c = (d_1, d_2, p_0, \beta_0)$ and spin fields (p_1, β_1), (p_2, β_2), (p_3, β_3), i.e., charge and the spin fluctuations of every Cartesian direction are independent. This property is obvious for the bosonic fluctuation matrix given by Equation (5.20) and for the PF part, it can be verified by using [53]

$$\frac{\partial \underline{z}}{\partial\psi_c}\bigg|_{\overline{\psi}} \propto \underline{\mathbb{1}}_2\,,\quad \frac{\partial \underline{z}}{\partial p_\mu}\bigg|_{\overline{\psi}} \propto \underline{\tau}^\mu\,,\quad \frac{\partial^2 \underline{z}}{\partial p_\mu \partial\psi_c}\bigg|_{\overline{\psi}} \propto \underline{\tau}^\mu\,,\quad \frac{\partial^2 \underline{z}}{\partial p_\mu \partial p_\nu}\bigg|_{\overline{\psi}} = 0 \quad \text{for } \mu \neq \nu\,, \tag{5.35}$$

which leads to a vanishing trace in Equation (5.27) for all matrix elements that couple the spin and charge sector or different spin directions. As we will learn in Section 5.3.2, this greatly simplifies the calculation of susceptibilities[2].

[1] Despite the antisymmetry of the fluctuation matrix w.r.t. d_2, the second-order action is real-valued since all antisymmetric contributions vanish with the Matsubara summation $\mathcal{S}_A^{(2)} = \sum_{\mathrm{i}\omega_n} \delta\psi_{\mu,-q}\mathcal{M}_{\mu,d_2}(q), \delta d_{2,q} + \delta d_{2,-q}\mathcal{M}_{\mu,d_2}(q)\delta\psi_{\mu,q} = \sum_{\mathrm{i}\omega_n} \delta\psi_{\mu,-q}\mathcal{M}_{\mu,d_2}(q)\delta d_{2,q} + \delta d_{2,q}\mathcal{M}_{\mu,d_2}(-q)\delta\psi_{\mu,-q} = \sum_{\mathrm{i}\omega_n} \delta\psi_{\mu,-q}\mathcal{M}_{\mu,d_2}(q), \delta d_{2,q} - \delta d_{2,q}\mathcal{M}_{\mu,d_2}(q)\delta\psi_{\mu,-q} = 0$.

[2] The decoupling of spin and charge sector still holds for the TKI model discussed in Chapter 12, although it is not SRI, which can also be verified by the evaluation of the trace, despite being less apparent.

5.2.2 Magnetic ground states

The derivation of the magnetic fluctuation matrix, i.e., the second-order variation around a magnetic saddle point, works principally analogous to the PM case. There is, however, a subtlety that makes the calculation more complicated and numerical costly. Every type of magnetic order except for ferromagnetism (FM) has an underlying enlarged magnetic unit cell due to the non-uniform MF

$$\boldsymbol{p}_i = p \begin{pmatrix} \cos(\boldsymbol{Q}\boldsymbol{R}_i) \\ \sin(\boldsymbol{Q}\boldsymbol{R}_i) \\ 0 \end{pmatrix}, \quad \boldsymbol{\beta}_i = \beta \begin{pmatrix} \cos(\boldsymbol{Q}\boldsymbol{R}_i) \\ \sin(\boldsymbol{Q}\boldsymbol{R}_i) \\ 0 \end{pmatrix}. \tag{5.36}$$

We may nevertheless exploit the periodicity in the context of the magnetic unit cell by expanding every quantity that depends on bosonic fields $\boldsymbol{\psi}_i$ (i.e., $\underline{Z}$-matrices and the bosonic Lagrangian) and its derivatives in a Fourier series w.r.t. the MF ordering vector $\boldsymbol{Q}$

$$\underline{Z}_i\Big|_{\overline{\boldsymbol{\psi}}} = \sum_{a=-\infty}^{\infty} \underline{Z}_{0,a}\, \mathrm{e}^{-\mathrm{i}a\boldsymbol{Q}\boldsymbol{R}_i}, \quad \partial_\mu \underline{Z}_i\Big|_{\overline{\boldsymbol{\psi}}} = \sum_{a=-\infty}^{\infty} \underline{Z}_{\mu,a}\, \mathrm{e}^{-\mathrm{i}a\boldsymbol{Q}\boldsymbol{R}_i}, \quad \partial_{\mu\nu} \underline{Z}_i\Big|_{\overline{\boldsymbol{\psi}}} = \sum_{a=-\infty}^{\infty} \underline{Z}_{\mu\nu,a}\, \mathrm{e}^{-\mathrm{i}a\boldsymbol{Q}\boldsymbol{R}_i}. \tag{5.37}$$

As shown in Section A.6, the zeroth, first, and second variation in momentum space are then given by

$$\underline{Z}_k\Big|_{\overline{\boldsymbol{\psi}}} = \sqrt{N\beta} \sum_a \underline{Z}_{0,a}\, \delta_{(\boldsymbol{k}+a\boldsymbol{Q},\mathrm{i}\omega_n),0}, \tag{5.38a}$$

$$\delta\underline{Z}_k\Big|_{\overline{\boldsymbol{\psi}}} = \sum_a \sum_{\tilde{\mu}} \underline{Z}_{\tilde{\mu},a}\, \delta\psi_{\tilde{\mu},\boldsymbol{k}+a\boldsymbol{Q},\mathrm{i}\omega}, \tag{5.38b}$$

$$\delta^2\underline{Z}_k\Big|_{\overline{\boldsymbol{\psi}}} = \frac{1}{\sqrt{N\beta}} \sum_a \sum_{\tilde{\mu},\tilde{\nu}} \sum_{k_1} \underline{Z}_{\tilde{\mu}\tilde{\nu},a}\, \delta\psi_{\tilde{\mu},k_1} \delta\psi_{\tilde{\nu},(\boldsymbol{k}+a\boldsymbol{Q},\mathrm{i}\omega_n)-k_1}. \tag{5.38c}$$

While the dependence on Matsubara frequency $\mathrm{i}\omega_n$ is equivalent to the PM case, we notice that the magnetic MF background initiates additional correlations between fluctuation fields with a momentum difference of $a\boldsymbol{Q}$, which makes the enlarged basis defined in Equations (5.4) and (5.5) necessary. Fourier coefficients with label a and $a + P$ are equivalent and need to be summed up to account for the periodicity of our basis [55]

$$\underline{Z}_0^a = \sum_{n=-\infty}^{\infty} \underline{Z}_{0,Pn+a \bmod P}, \quad \underline{Z}_\mu^a = \sum_{n=-\infty}^{\infty} \underline{Z}_{\mu,Pn+a \bmod P}, \quad \underline{Z}_{\mu\nu}^a = \sum_{n=-\infty}^{\infty} \underline{Z}_{\mu\nu,Pn+a \bmod P}, \quad L_{\mu\nu}^a = \sum_{n=-\infty}^{\infty} L_{\mu\nu,Pn+a \bmod P}. \tag{5.39}$$

Bosonic part

We consider the bosonic part of the action with the Lagrangian $\mathcal{L}_B = \sum_{\boldsymbol{r}_i} L_i$ in momentum-space

$$\mathcal{S}_B = \int_0^\beta d\tau \sum_{\boldsymbol{r}_i} L_i(\tau) = \frac{1}{\sqrt{N\beta}} \int_0^\beta d\tau \sum_{\boldsymbol{r}_i} \sum_q \mathrm{e}^{-\mathrm{i}\boldsymbol{q}\boldsymbol{r}_i + \mathrm{i}\omega_n \tau} L_q = \sqrt{N\beta}\, L_0. \tag{5.40a}$$

Next, we apply Equation (5.38c) by identifying $L_{\mu\nu}$ with $\underline{Z}_{\mu\nu}$ and find [55]

$$\left[\mathcal{M}^B(q)\right]_{\mu,\nu}^{a,b} = \frac{1}{2} \frac{\delta^2 \sqrt{N\beta}\, L_0}{\delta\psi_{\mu,-\boldsymbol{q}-a\boldsymbol{Q},-\mathrm{i}\omega_n} \delta\psi_{\nu,\boldsymbol{q}+b\boldsymbol{Q},\mathrm{i}\omega_n}} = \frac{1}{2} \frac{\sum_n \sum_{\tilde{\mu},\tilde{\nu}} \sum_{k_1} L_{\tilde{\mu}\tilde{\nu}}^n \delta\psi_{\tilde{\mu},k_1} \delta\psi_{\tilde{\nu},(0+a\boldsymbol{Q},i\omega_n)-k_1}}{\delta\psi_{\mu,-\boldsymbol{q}-a\boldsymbol{Q},-\mathrm{i}\omega_n} \delta\psi_{\nu,\boldsymbol{q}+b\boldsymbol{Q},\mathrm{i}\omega_n}} = \frac{1}{2} L_{\mu\nu}^{b-a}. \tag{5.40b}$$

Notice that $L_{\mu\nu}^{b-a}$ represents the sum over all equivalent Fourier coefficients with the index $b-a$ of the second derivative of L_i evaluated at the MF saddle point as indicated by Equations (C.7) and (5.39). For the spin spiral of the underlying magnetic MF, all Fourier coefficients with $|b-a|>1$ vanish. The explicit matrices for AFM and FM are summarized in Appendix C.

Pseudofermionic part

For the PF part, we need to consider the Fourier coefficients of the $\underline{Z}$-matrix and its first and second derivatives and further the first derivative of the $\underline{B}$-matrix in analogy to the PM calculation. Since the $\boldsymbol{Q}$ dependence of the $\underline{Z}$-matrix is given by the term proportional to $\boldsymbol{p}/p$, all Fourier coefficients $\underline{Z}_{0,a}$ vanish for $|a|>1$. Taking the derivative w.r.t. a spin field p_μ yields two additional Fourier components, i.e., $\underline{Z}_{\mu,a}$ vanishes for $|a|>2$ and $\underline{Z}_{\mu\nu,a}$ for $|a|>3$. Since the LMs appear linear, only $\underline{B}_{\mu,a=0}$ is non zero, i.e., they do not induce coupling between different $\boldsymbol{Q}$-blocks. The PF Greens function $\underline{G}^{\overline{\psi}}$ at the saddle point has to be defined in the same basis of $\boldsymbol{Q}$-blocks as the fluctuation fields, i.e.,

$$\phi_q^a = \phi_{\boldsymbol{q}+a\boldsymbol{Q},\mathrm{i}\omega_n}\,, \tag{5.41}$$

with $a\in\{0,1,\ldots,P-1\}$, where $\boldsymbol{\phi}$ contains all spin and orbital degrees of freedom as defined in Equation (4.12)[1]. As a consequence, it is

$$\dim \underline{G}^{\overline{\psi}} = P\dim\underline{\mathcal{H}} = P\dim\underline{Z} \tag{5.42}$$

because the bare Hamiltonian $\underline{\mathcal{H}}$ is defined in the non-magnetic basis, which makes the evaluation of the trace and Matsubara sum in Equation (5.14) tricky. It has been shown in Reference [55] that the fluctuation matrix can still be expressed in a compact form through several complicated index shifts, and we will only present the result here

$$\begin{aligned}
[\mathcal{M}^F(q)]_{\mu,\nu}^{a,b} = \frac{1}{2}\sum_{\boldsymbol{k}\in\mathrm{BZ}_0}\sum_s n_\mathrm{F}\left(\varepsilon_{\boldsymbol{k}}^s\right)\Big[&\underline{U}_{\boldsymbol{k}}\Big(\left[\underline{Z}_{\mu\nu}^\dagger\right]^b\otimes\left[\underline{\mathcal{H}}_{\boldsymbol{k}+a\boldsymbol{Q}}\underline{Z}_0^a\right]+\left[\underline{Z}_0^\dagger\right]^b\otimes\left[\underline{\mathcal{H}}_{\boldsymbol{k}+b\boldsymbol{Q}}\underline{Z}_{\mu\nu}^a\right]\\
&+\left[\underline{Z}_\mu^\dagger\right]^b\otimes\left[\underline{\mathcal{H}}_{\boldsymbol{k}+\boldsymbol{q}+(a+b)\boldsymbol{Q}}\underline{Z}_\nu^a\right]+\left[\underline{Z}_\nu^\dagger\right]^b\otimes\left[\underline{\mathcal{H}}_{\boldsymbol{k}-\boldsymbol{q}}\underline{Z}_\mu^a\right]\Big)\underline{U}_{\boldsymbol{k}}^\dagger\Big]^{s,s}\\
+\frac{1}{2}\sum_{\boldsymbol{k}\in\mathrm{BZ}_Q}\sum_{s,s'}L_\mathrm{F}\left(\varepsilon_{\boldsymbol{k}}^s,\varepsilon_{\boldsymbol{k}+\boldsymbol{q}}^{s'},\mathrm{i}\omega_n\right)&\\
\times\Big[\sum_v\underline{U}_{\boldsymbol{k}}\Big(\left[\underline{Z}_\mu^\dagger\right]^v\otimes\left[\underline{\mathcal{H}}_{\boldsymbol{k}+\boldsymbol{q}+(v+a)\boldsymbol{Q}}\underline{Z}_0^{v+a}\right]+\left[\underline{Z}_0^\dagger\right]^v\otimes\left[\underline{\mathcal{H}}_{\boldsymbol{k}+v\boldsymbol{Q}}\underline{Z}_\mu^{v+a}\right]+\underline{\mathfrak{B}}_\mu^{v,v+a}\Big)\underline{U}_{\boldsymbol{k}+\boldsymbol{q}}^\dagger\Big]^{s,s'}&\\
\times\Big[\sum_u\underline{U}_{\boldsymbol{k}+\boldsymbol{q}}\Big(\left[\underline{Z}_\nu^\dagger\right]^{u+b}\otimes\left[\underline{\mathcal{H}}_{\boldsymbol{k}+u\boldsymbol{Q}}\underline{Z}_0^u\right]+\left[\underline{Z}_0^\dagger\right]^{u+b}\otimes(\underline{\mathcal{H}}_{\boldsymbol{k}+\boldsymbol{q}+(u+b)\boldsymbol{Q}}\underline{Z}_\nu^u+\underline{\mathfrak{B}}_\nu^{u+b,u}\Big)\underline{U}_{\boldsymbol{k}}^\dagger\Big]^{s',s}&\,.
\end{aligned}\tag{5.43}$$

We further elaborate on the definition of the Fourier coefficient vectors $\underline{Z}_0^a$ and the dyadic product ("$\otimes$") in Appendix C, where we also provide a list of all non-zero Fourier coefficients and show their explicit form in the case of AFM and FM. Guidelines for an efficient numerical implementation of the fluctuation matrix and related data analysis are discussed in Appendix D.

[1] Even though we can express the MF Greens function of SRI models in a reduced basis that does not introduce additional fields as discussed in Section 4.3, we need to apply the full enlarged basis for the fluctuation calculation, which can be constructed by symmetrization of the reduced basis. Fluctuations about incommensurate magnetic saddle points are thus not accessible.

In the PM limit ($\overline{p} \to 0, \overline{\beta} \to 0$), the magnetic fluctuation matrix becomes block diagonal w.r.t. to the external momenta indices, i.e., $\mathcal{M}^{a,b}_{\mu\nu}(q) \to \delta_{a,b}\mathcal{M}^{a,b}_{\mu\nu}(q)$ and a change of the index can be recast into a momentum translation $\mathcal{M}^{a+1,a+1}_{\mu\nu}(\boldsymbol{q}, \mathrm{i}\omega_n) = \mathcal{M}^{a,a}_{\mu\nu}(\boldsymbol{q} + \boldsymbol{Q}, \mathrm{i}\omega_n)$. Consequently, the full PM Brillouin zone can be recovered and the theory reduces to that PM case described by Section 5.2.1 [117].

5.3 Dynamic susceptibilities and mean-field stability

This section shows how to calculate dynamic susceptibilities utilizing the fluctuation matrix and how these expressions are related to measurable quantities and the stability of the MF saddle point. We first summarize basic knowledge of linear response theory based on Coleman's textbook [48] in Section 5.3.1. Afterward, explicit representations of dynamic susceptibilities within the SB formalism are derived in Section 5.3.2. Finally, we elaborate on the interpretation of these quantities in the context of phase transitions and collective modes in Section 5.3.3.

5.3.1 Linear response theory

Linear response theory in quantum mechanics addresses systems described by a Hamiltonian $\hat{H}_0$ that are subject to an external force or source field $f(t)$ or $f(\tau)$ which couples to a variable A, which is usually an operator or a field, i.e.,

$$\hat{H} - \hat{H}_0 = \hat{H}_c = -f(t)\hat{A}\,, \qquad \hat{H} - \hat{H}_0 = \hat{H}_c = -f(\tau)\hat{A}\,. \tag{5.44}$$

Since we calculate susceptibilities through the imaginary-time formalism and then recover the real-time quantities by analytic continuation $\mathrm{i}\omega_n = \omega + \mathrm{i}\eta$, we provide equations for both cases. The susceptibility χ is defined by the linear response of A to the external force [48]

$$\langle \delta A(t)\rangle = \int_{-\infty}^{\infty} \chi(t-t')f(t')dt'\,, \quad \langle \delta A(\omega)\rangle = \chi(\omega)f(\omega)\,, \tag{5.45a}$$

$$\langle \delta A(\tau)\rangle = \int_{0}^{\beta} \chi(\tau-\tau')f(\tau')d\tau'\,, \quad \langle \delta A(\mathrm{i}\omega_n)\rangle = \chi(\mathrm{i}\omega_n)f(\mathrm{i}\omega_n)\,, \tag{5.45b}$$

where $\langle \delta A\rangle = \langle A(t)\rangle - \langle A\rangle_0$ represents a deviation from the equilibrium. Utilizing the Heisenberg representation of operators, one finds [48]

$$\chi(t-t') = \mathrm{i}\left\langle \left[\hat{A}(t)\,,\, \hat{A}(t')\right]_- \right\rangle \Theta(t-t')\,, \tag{5.46a}$$

$$\chi(\tau-\tau') = \langle \mathcal{T}_\tau \delta A(\tau)\delta A(\tau')\rangle\,. \tag{5.46b}$$

We moreover define the correlation function

$$S(t-t') = \langle A(t)A(t')\rangle = \int_{-\infty}^{\infty} \frac{d\omega}{2\pi} \mathrm{e}^{-\mathrm{i}\omega(t-t')} S(\omega) \tag{5.47}$$

that can be interpreted as fluctuations of $\hat{A}$ and is also called structure factor. Depending on the method of measurement, either the susceptibility χ or the structure factor S are accessible, but both quantities are connected via the fluctuation-dissipation theorem [118]

$$S(\omega) = 2\hbar\left(1 + n_\zeta(\omega)\right) \operatorname{Im}\chi(\omega)\,, \tag{5.48}$$

Susceptibility	Coupling Hamiltonian	Static, uniform limit	Experimental accessibility
$\chi_s^{\alpha\beta}(\tau) = \left\langle \mathcal{T}_\tau \delta S^\alpha(\tau) \delta S^\beta(0) \right\rangle$	$H_c = \boldsymbol{S}\boldsymbol{B}_{\text{ext}}(\tau)$	$\chi_s^{\alpha\beta}(q=0) = \left.\frac{\partial \left\langle S^\alpha_{q=0} \right\rangle}{\partial B^\beta_{\text{ext},q=0}}\right\vert_{B_{\text{ext}}=0}$	Spin structure factor $S(\boldsymbol{q}, t)$ via INS
$\chi_c(\tau) = \langle \mathcal{T}_\tau \delta n(\tau) \delta n(0) \rangle$	$H_c = n\phi_{\text{ext}}(\tau)$	$\chi_c(q=0) = \left.\frac{\partial \langle n_{q=0} \rangle}{\partial \phi_{\text{ext},q=0}}\right\vert_{\phi_{\text{ext}}=0}$	Im $\chi_c(\boldsymbol{q}, \omega)$ via EELS [119] or RXS [120]
$\sigma^{\alpha\beta}(\tau) = \left\langle \mathcal{T}_\tau \delta j^\alpha(\tau) \delta j^\beta(0) \right\rangle$	$H_c = \boldsymbol{j}\boldsymbol{E}_{\text{ext}}(\tau)$	$\sigma^{\alpha\beta}(q=0) = \left.\frac{\partial \left\langle j^\alpha_{q=0} \right\rangle}{\partial E^\beta_{\text{ext},q=0}}\right\vert_{E_{\text{ext}}=0}$	Optical conductivity $\sigma(\omega)$ via reflection measurements

Table 5.1: Overview of susceptibilities, their respective coupling to external fields, and experimental accessibility. The spin susceptibility χ_s describes the magnetization response to an external magnetic field, and the static limit recovers the magnetic compressibility. The charge susceptibility χ_c captures the electron density response to an external potential, and the static limit yields the electronic compressibility. Finally, the conductivity σ represents the response of charge carriers to an external electric field and reduces to the inverse resistivity known from Ohm's law in the static limit.

where n_ζ is the Bose-Einstein distribution if A is bosonic and the Fermi-Dirac distribution if A is fermionic. Unlike its classical analog, where $2\hbar\left(1 + n_\zeta(\omega)\right) \to 2k_B T/\omega$, a quantum system features fluctuations even at zero temperature. These so-called quantum-fluctuations are also captured within the SB formalism and manifest, e.g., in non-vanishing structure factors at $U = T = 0$. Real and imaginary parts of susceptibilities are connected by the Kramers-Kronig relations

$$\chi(z) = \int \frac{d\omega}{\pi} \frac{1}{z - \omega} \operatorname{Im} \chi(\omega) \,, \tag{5.49}$$

which allows the interpret the dissipative part Im χ as a spectral function for excitations.

Table 5.1 lists the most common types of response functions, i.e., the spin susceptibility, charge susceptibility, and conductivity, and identifies the respective external coupling force f. Moreover, it provides the static limit with a spatially uniform source $f(q = 0)$, which is known as thermodynamic sum rule [121] and presents a brief overview of how the discussed quantities are experimentally accessible. Since we investigate systems with time translation invariance, we may w.l.o.g. choose $\tau' = 0$. Another important quantity that is not directly related to a response function, is the so-called lesser Green's function $G_<$, which is the correlation function of holes (i.e., $\hat{A} = \hat{c}_{\boldsymbol{k},\sigma}$). It can be measured by angle-resolved photoemission spectroscopy (ARPES), where X-rays are used to eject electrons from the material, and consequently, the measured intensity is proportional to the hole fluctuations [48]

$$I(\boldsymbol{k}, \omega) \propto \int d^4 r \left\langle \hat{f}^\dagger(r) \hat{f}(0) \right\rangle \mathrm{e}^{-\mathrm{i}(\boldsymbol{k}\boldsymbol{r} - \omega t)} = G_<(\boldsymbol{k}, \omega) = 2\pi n_{\mathrm{F}}(-\omega) A(\boldsymbol{k}, -\omega) \,, \tag{5.50}$$

where $A(\boldsymbol{k}, \omega) = \frac{1}{\pi} \operatorname{Im} G(\boldsymbol{k}, \omega)$ is the spectral function. This technique can be applied to measure BSs and FSs at the surface of a probe[1].

[1] References [122] and [123] applied a different SB representation to calculate fluctuation corrections to the electron Green's function, which directly relates to the spectral function and allows to access dynamic contributions of the self-energy. An adaptation to the presented formalism of magnetic fluctuations could be of interest in future studies. The fluctuating part of the PM electron Green's function in the space imaginary-time domain is given by $\delta G(\boldsymbol{r}, \tau) = -\left\langle \mathcal{T}_\tau \hat{f}(r, \tau) \hat{f}^\dagger(0, 0) \right\rangle = G^{\overline{\Psi}}(r, \tau) \left\langle \delta z(r, \tau) \delta z(0, 0) \right\rangle$. In the magnetic domain, the index structure of the MF Green's function and SB weights need to be considered.

5.3.2 Slave-boson representation of susceptibilities

To calculate response functions within the SB scheme, we evaluate the Fourier transformation of Equation (5.46b) in the momentum and Matsubara frequency domain, where susceptibilities adopt a convenient form due to translation symmetry. The occurring quantum mechanical expectation value can be calculated with the addition of source fields and the generalized Gaussian integral defined in Equation (3.1g), yielding [53, 55][1]

$$\begin{aligned}\left\langle \delta\psi^{-a}_{\mu,-q}\delta\psi^{b}_{\nu,q}\right\rangle &= \frac{1}{Z^{(2)}}\int \mathcal{D}\left[\boldsymbol{\delta\psi}^*,\boldsymbol{\delta\psi}\right]\delta\psi^{-a}_{\mu,-q}\,\delta\psi^{b}_{\nu,q}\,\exp\left(-\mathcal{S}^{(2)}[\boldsymbol{\delta\psi}^*,\boldsymbol{\delta\psi}]\right)\\ &= \lim_{\boldsymbol{J},\boldsymbol{J}^*\to 0}\frac{1}{Z^{(2)}}\int \mathcal{D}\left[\boldsymbol{\delta\psi}^*,\boldsymbol{\delta\psi}\right]\partial_{J^{a}_{\mu,q}}\partial_{J^{-b}_{\nu,-q}}\exp\left(-\sum_{\substack{\tilde{q},\tilde{\mu},\tilde{\nu}\\ \tilde{a},\tilde{b}}}\delta\psi^{-\tilde{a}}_{\tilde{\mu},-\tilde{q}}\mathcal{M}^{\tilde{a},\tilde{b}}_{\tilde{\mu},\tilde{\nu}}(\tilde{q})\delta\psi^{\tilde{b}}_{\tilde{\nu},\tilde{q}}+\sum_{\tilde{q},\tilde{\mu}}J^{-\tilde{a}}_{\tilde{\mu},-\tilde{q}}\delta\psi^{\tilde{a}}_{\tilde{\mu},\tilde{q}}+\delta\psi^{-\tilde{a}}_{\tilde{\mu},-\tilde{q}}J_{\tilde{\mu},\tilde{q}}\right)\\ &= \left[\mathcal{M}^{-1}(q)\right]^{a,b}_{\mu,\nu} = -\mathcal{G}^{a,b}_{\mu,\nu}(q)\,.\end{aligned} \tag{5.51a}$$

Susceptibilities are then determined by superpositions of matrix elements of the bosonic propagator[2]

$$\chi(q) = \sum_{\mu,\nu,a,b} C^{a,b}_{\mu,\nu}\left\langle \delta\psi^{-a}_{\mu,-q}\delta\psi^{b}_{\nu,q}\right\rangle = -\sum_{\mu,\nu,a,b} C^{a,b}_{\mu,\nu}\mathcal{G}^{a,b}_{\mu,\nu}(q)\,. \tag{5.51b}$$

Spin susceptibility

In order to calculate the spin susceptibility

$$\chi_s^{\alpha\beta}(q) = \left\langle \delta S^{\alpha}_{-q}\delta S^{\beta}_{q}\right\rangle\,, \tag{5.52a}$$

we need to express the fluctuations of the spin operator by means of the bosonic fluctuation field basis $\delta\boldsymbol{\psi}$ around the MF saddle point with magnetic ordering vector $\boldsymbol{Q}$, resulting in [55]

$$\delta S_q = \sqrt{\frac{1}{N\beta}}\int_0^{\beta} d\tau\sum_{\boldsymbol{r}} e^{i\boldsymbol{q}\boldsymbol{r}-i\omega_n\tau}\left(\overline{p}_0\delta\boldsymbol{\rho}_r+\overline{\boldsymbol{p}}_r\delta p_{0,r}\right) = \overline{p}_0\delta\boldsymbol{\rho}_q+\frac{1}{2}p\left(\boldsymbol{\lambda}\delta p_{0,\boldsymbol{q}+\boldsymbol{Q},i\omega_n}+\boldsymbol{\lambda}^*\delta p_{0,\boldsymbol{q}-\boldsymbol{Q},i\omega_n}\right)\,, \tag{5.52b}$$

where we applied the notations $\boldsymbol{\lambda} = (1,i,0)^{\top}$ and $\boldsymbol{\rho} = (p_1,-p_2,p_3)^{\top}$. With Equation (5.52b), one can infer the general form of the spin susceptibility for an arbitrary ordering vector $\boldsymbol{Q}$ and it is derived in Appendix C. Here, we want to focus on the most common magnetic orders, i.e., fluctuations around PM, FM and AFM mean-field saddle points. For these types of magnetic order models without SOC, the spin susceptibility matrix adopts diagonal form and splits into a longitudinal part $\chi_s^{l}(q) = \chi_s^{1,1}(q)$ parallel to the magnetic MF background and a transversal component perpendicular to it: $\chi_s^{t}(q) = \chi_s^{2,2}(q) = \chi_s^{3,3}(q)$. The full spin-rotation invariance (SRI) of the unordered state is thus reduced to SRI in the transversal plane of the symmetry-broken state. Explicit expressions of the spin susceptibility are listed in Table 5.2.

[1] Remember that the chosen basis satisfies $\left(\delta\psi^{a}_{\mu,q}\right)^* = \delta\psi^{-a}_{\mu,-q}$.

[2] Notice that translation invariant susceptibilities in the space-time domain are given by $\chi(\boldsymbol{r},\tau) = \frac{1}{\sqrt{N\beta}}\int_0^{\beta}d\tau'\sum_{\boldsymbol{R}}\sum_{\mu,\nu,a,b}C^{a,b}_{\mu,\nu}\left\langle \mathcal{T}_{\tau}\delta\psi_{\mu,\boldsymbol{R}}(\tau)\delta\psi_{\nu,\boldsymbol{R}+\boldsymbol{r}}(\tau+\tau')\right\rangle$.

Magnetic order of the mean-field background	**Dynamic susceptibilities**: Longitudinal and transversal spin $\left(\chi_s^l, \chi_s^t\right)$, bare (χ_0) and charge (χ_c) susceptibility
PM: $p = 0, \boldsymbol{Q} = 0$; Number of sites per unit cell: $P = 1$	$\chi_s^l(q) = \chi_s^t(q) = -\overline{p}_0^2 \mathcal{G}_{p_\alpha,p_\alpha} = \overline{p}_0^2 \dfrac{\mathcal{M}_{\beta_\alpha,\beta_\alpha}}{\mathcal{M}_{p_\alpha,p_\alpha}\mathcal{M}_{\beta_\alpha,\beta_\alpha} - \mathcal{M}_{p_\alpha,\beta_\alpha}\mathcal{M}_{\beta_\alpha,p_\alpha}}$ $\chi_0(q) = -2\mathcal{M}_{\beta_0,\beta_0} = -2\mathcal{M}_{\beta_\alpha,\beta_\alpha}$ $\chi_c(q) = -4\overline{d}_1^2 \mathcal{G}^{0,0}_{d_1,d_1} - \overline{p}_0^2 \mathcal{G}^{0,0}_{p_0,p_0} - 2\overline{d}_1\overline{p}_0 \left(\mathcal{G}^{0,0}_{d_1,p_0} + \mathcal{G}^{0,0}_{p_0,d_1}\right)$
FM: $p \neq 0, \boldsymbol{Q} = 0$; Number of sites per unit cell: $P = 1$	$\chi_s^l(q) = -\overline{p}_0^2 \mathcal{G}_{p_1,p_1} - \overline{p}\,\overline{p}_0 \left(\mathcal{G}_{p_1,p_0} + \mathcal{G}_{p_0,p_1}\right) - \overline{p}^2 \mathcal{G}_{p_0,p_0}$ $\chi_s^t(q) = -\overline{p}_0^2 \mathcal{G}_{p_2,p_2} = -\overline{p}_0^2 \mathcal{G}_{p_3,p_3}$ $\chi_0(q) = -2\mathcal{M}_{\beta_0,\beta_0}$ $\chi_c(q) = -4\overline{d}_1^2 \mathcal{G}_{d_1,d_1} - \overline{p}_0^2 \mathcal{G}_{p_0,p_0} - 2\overline{d}_1\overline{p}_0 \left(\mathcal{G}_{d_1,p_0} + \mathcal{G}_{p_0,d_1}\right)$ $-2\overline{d}_1\overline{p} \left(\mathcal{G}_{d_1,p_1} + \mathcal{G}_{p_1,d_1}\right) - \overline{p}_0\overline{p} \left(\mathcal{G}_{p_0,p_1} + \mathcal{G}_{p_1,p_0}\right) - \overline{p}^2 \mathcal{G}_{p_1,p_1}$
AFM: $p \neq 0$, $\boldsymbol{Q} \in \{(\pi,0,0),(\pi,\pi,0),(\pi,\pi,\pi)\}$ and symmetry/lower dimensional equivalents; Number of sites per unit cell $P = 2$	$\chi_s^l(q) = -\overline{p}_0^2 \mathcal{G}^{0,0}_{p_1,p_1} - \overline{p}\,\overline{p}_0 \left(\mathcal{G}^{0,1}_{p_1,p_0} + \mathcal{G}^{1,0}_{p_0,p_1}\right) - \overline{p}^2 \mathcal{G}^{1,1}_{p_0,p_0}$ $\chi_s^t(q) = -\overline{p}_0^2 \mathcal{G}^{0,0}_{p_2,p_2} = -\overline{p}_0^2 \mathcal{G}^{0,0}_{p_3,p_3}$ $\chi_0(q) = -2\mathcal{M}^{0,0}_{\beta_0,\beta_0}$ $\chi_c(q) = -4\overline{d}_1^2 \mathcal{G}^{0,0}_{d_1,d_1} - \overline{p}_0^2 \mathcal{G}^{0,0}_{p_0,p_0} - 2\overline{d}_1\overline{p}_0 \left(\mathcal{G}^{0,0}_{d_1,p_0} + \mathcal{G}^{0,0}_{p_0,d_1}\right)$ $-2\overline{d}_1\overline{p} \left(\mathcal{G}^{0,1}_{d_1,p_1} + \mathcal{G}^{1,0}_{p_1,d_1}\right) - \overline{p}_0\overline{p} \left(\mathcal{G}^{0,1}_{p_0,p_1} + \mathcal{G}^{1,0}_{p_1,p_0}\right) - \overline{p}^2 \mathcal{G}^{1,1}_{p_1,p_1}$

Table 5.2: This table sums up, how to calculate the spin, charge and bare susceptibility by means of the fluctuation field propagator $\mathcal{G}^{a,b}_{\mu,\nu}(q) = -\left[\mathcal{M}^{-1}(q)\right]^{a,b}_{\mu,\nu}$ for underlying PM, FM and AFM mean-field saddle points. The spin susceptibility splits into a longitudinal part χ_s^l parallel to the MF magnetization and a transversal component χ_s^t perpendicular to it.

Charge susceptibility

The charge susceptibility

$$\chi_c(q) = \left\langle \delta n_{-q} \delta n_q \right\rangle \,, \tag{5.53a}$$

can be obtained analogous, utilizing [55]

$$\delta n_q = 2\overline{d}_1 \delta d_{1,q} + \overline{p}_0 \delta p_{0,q} + \frac{\overline{p}}{2} \sum_{\alpha=1}^{3} \left(\lambda_\alpha^* \delta p_{\alpha,\boldsymbol{q}+\boldsymbol{Q},i\omega_n} + \lambda_\alpha \delta p_{\alpha,\boldsymbol{q}-\boldsymbol{Q},i\omega_n}\right) \,. \tag{5.53b}$$

The general form is derived in Appendix C, while the most common applications for PM, FM and AFM order are listed in Table 5.2. The charge susceptibility is directly related to the electronic compressibility $\kappa_T = n^2 \partial n / \partial \mu_0$, which can be noticed by identifying the external potential ϕ_{ext} in Table 5.1 with the chemical potential μ_0

$$\chi_c(q=0) = \frac{\partial \left\langle n_{q=0} \right\rangle}{\partial \mu_0} = n^2 \kappa_T \,. \tag{5.54}$$

We, moreover, want to discuss the bare susceptibility $\chi_0(q)$ which is sometimes also called polarizability and can be understood as charge susceptibility of the effectively free MF band structure with $\chi_c(q) = \chi_0(q)$ in the non-interacting limit $U = 0$ [124]. It can be evaluated with the PF representation of the charge density operator and the application of Wick's theorem

$$\begin{aligned}\chi_0(q) = \left\langle n_{-q} n_q \right\rangle_0 &= \frac{1}{Z^{(0)}} \int \mathcal{D}[f^*, f]\, f^*_{k_1+q} f_{k_1} f^*_{k_2-q} f_{k_2} \exp\left(\sum_k f^\dagger_k \left[\mathcal{P}_f \underline{G}^{\overline{\psi}}_k \right]^{-1} f_k - \mathcal{S}^{(0)}_B \right) \\ &= -\frac{1}{N\beta} \sum_k \mathrm{tr}\left(\mathcal{P}_f \underline{G}^{\overline{\psi}}_{k+q} \mathcal{P}_f \underline{G}^{\overline{\psi}}_k \right) ,\end{aligned} \tag{5.55a}$$

where $\mathcal{P}_f = \underline{0}_{2O\times 2O} \oplus \underline{\mathbb{1}}_2$ projects onto the interacting electrons. This result can be identified with diagram D(6) in Figure 5.1 and consequently we find

$$-\frac{1}{2}\chi_0(q) = \mathcal{M}_{\beta_0,\beta_0}(q) . \tag{5.55b}$$

In opposite to other susceptibilities, χ_0 is not directly impacted by the interaction, besides the renormalization of the MF band structure, and thus not well-suited to investigate FS instabilities in our case. However, it is an indicator of FS nesting and of major importance for other approximation techniques like, e.g., random phase approximation (RPA), where the corresponding diagram is summed up to infinite order.

Conductivity

The charge susceptibility and conductivity are not independent because the external potential and electric field are connected by $\boldsymbol{E}_{\mathrm{ext}} = -\boldsymbol{\nabla}\phi_{\mathrm{ext}}$ and the continuity equation, yielding [39]

$$\boldsymbol{j}(q) = \underline{\sigma}(q)\boldsymbol{E}_{\mathrm{ext}}(q) = -\mathrm{i}\underline{\sigma}(q)\boldsymbol{q}\phi_{\mathrm{ext}}(q) , \tag{5.56a}$$

$$0 = -\mathrm{i}\omega n_q + \mathrm{i}\boldsymbol{q}\boldsymbol{j}(q) . \tag{5.56b}$$

Combining these results and using $n_q = \chi_c(q)\phi_{\mathrm{ext}}(q)$, the dynamical conductivity for isotropic systems is given by

$$\sigma(\boldsymbol{q},\omega) = \frac{-\mathrm{i}\omega}{\boldsymbol{q}^2}\chi_c(\boldsymbol{q},\omega) . \tag{5.57a}$$

Since we obtain the charge susceptibility via analytic continuation $\omega_n \to \omega + \mathrm{i}\eta$, we have to add the convergence factor to all appearing frequencies. The optical conductivity is then found in the limit of vanishing momentum

$$\sigma(\omega + \mathrm{i}\eta) = \lim_{\boldsymbol{q}\to 0} \frac{-\mathrm{i}\omega + \eta}{\boldsymbol{q}^2}\chi_c(\boldsymbol{q}, \omega + \mathrm{i}\eta) . \tag{5.57b}$$

The convergence parameter η needs to remain finite for numerical evaluation, and it may be identified with the inverse scattering time $\tau_s = 1/\eta$ of a Drude conductivity [14, 53]

$$\sigma_D(\omega, \tau_s) = \frac{\sigma_0}{1+\omega^2\tau_s^2} + \mathrm{i}\frac{\sigma_0\omega\tau_s}{1+\omega^2\tau_s^2} , \tag{5.58}$$

and we find $\lim_{\eta\to 0}\sigma_0 = \infty$, if the model does not feature an explicit source of dissipation.

5.3.3 Collective modes and phase transitions

Within the analysis of dynamic susceptibilities, we can infer the existence of collective excitations and determine their dispersion relation. Such a collective mode is characterized by a coherent oscillation of a large number of electrons with the same wave-vector $\boldsymbol{q}$ and frequency ω in the absence of external fields [125]. They are therefore defined by poles of the susceptibility or equivalently

$$1/\chi(\boldsymbol{q},\omega) = 0 \quad \Rightarrow \quad \text{Dispersion relation } \omega(\boldsymbol{q}) \text{ of the collective mode .} \tag{5.59a}$$

Specifically, in the case of a diverging spin susceptibility $1/\chi_s(q) = 0$, the quasiparticles (QPs) represent spin density waves and are called magnons [126]. In analogy, the QPs of charge density waves come along with a diverging charge susceptibility $1/\chi_c(q) = 0$ and are called plasmons [125]. In practice, we need to perform the analytic continuation $\mathrm{i}\omega_n \to \omega + \mathrm{i}\eta$ with $\eta \to 0^+$ in order to evaluate susceptibilities at finite frequencies. Collective modes manifest in delta-peaks of $\mathrm{Im}\,\chi(\boldsymbol{q},\omega+\mathrm{i}\eta)$, which are broadened by the convergence parameter η that acts like a dissipative energy scale or an inverse lifetime in analogy to $\mathrm{Im}\,\Sigma$ in FL-theory. A collective excitation at zero frequency is the signature of a FS instability, i.e., a phase transition with spontaneous symmetry breaking

$$1/\chi(\boldsymbol{q},\omega=0) = 0 \quad \Rightarrow \quad \text{Phase transition .} \tag{5.59b}$$

Typical broken symmetries are spin-rotation-symmetry (magnons), translation-symmetry (enlargement of the unit cell due to charge or spin order), lattice symmetries (nematic order) or U(1) gauge-symmetry (superconductivity).

In the context the Gaussian fluctuations, we may think of susceptibilities as bosonic QP Green's functions $\mathcal{G}_{s/c} = \chi_{s/c}^{-1}$ that initiate a breakdown of the path integral for $\mathcal{G}_{s/c} \leq 0$. Apart from roots of $1/\chi_{s/c}(\omega=0)$ at phase transitions, we do indeed find negative domains if the external parameters are chosen such that the system is tuned further into the broken symmetry phase, which can be interpreted as condensation energy of the bound state. However, the MF approximation has already broken down at this point, and the respective analysis of susceptibilities is not accurate anymore. Reliable information about the nature of the symmetry broken phase should thus be acquired exactly at the critical point. This way, susceptibilities can also be applied to determine critical exponents and Landau interaction functions [53, 127].

5.4 Fluctuation corrections to the magnetization

We may also utilize the fluctuation formalism to improve the quality of the MF solution by calculating second-order corrections that yield from the bosonic theory of fluctuation fields with the action

$$\mathcal{S}^{(2)} = \sum_{\mathrm{i}\omega_n} \sum_{\boldsymbol{q}\in \mathrm{BZ}_Q} \sum_{\mu\nu} \sum_{ab} \delta\psi^{-a}_{\mu,-q} \left[\mathcal{G}^{-1}(q)\right]^{a,b}_{\mu,\nu} \delta\psi^{b}_{\nu,q} \,. \tag{5.60}$$

Despite being quadratic, the effective theory does for two reasons not represent free bosons, which comes along with subtleties that make the evaluation complicated and numerically costly. First of all Equation (5.60) contains anomalous contributions w.r.t. the complex d-field that keeps its phase in the radial gauge. As a consequence, the Lagrangian features terms proportional to dd and d^*d^* that do not enter in a free theory, but

can principally be integrated out analytically[1] [80]. Secondly, the fluctuation theory features a complicated time dependence that is not delta-correlated ($\Delta\tau_B \neq 0$) as opposed to a free theory. It is due to the fact that only the original fermions are delta-correlated in time, whereas the PF and SB fields have individual dynamics with $0 = \Delta\tau = \Delta\tau_F + \Delta\tau_B$. This can be seen by inverse FT of the dynamic Lindhard function, which can be determined analytically with the application of Reference [128]

$$\begin{aligned} -\left[\mathcal{G}^{-1}(\boldsymbol{q}, \Delta\tau_B)\right]^{a,b}_{\mu,\nu} = \mathcal{M}^{a,b}_{\mu,\nu}(\boldsymbol{q}, \Delta\tau_B) &\propto \frac{1}{\beta}\sum_{\mathrm{i}\omega_n} \mathrm{e}^{\mathrm{i}\omega_n \Delta\tau_B} \frac{1}{N}\sum_{\boldsymbol{k},s,s'} \left[f^{s}_{\boldsymbol{k},\boldsymbol{q}} + C^{s,s'}_{\boldsymbol{k},\boldsymbol{q}} L_{\mathrm{F}}\left(\varepsilon^{s}_{\boldsymbol{k}}, \varepsilon^{s'}_{\boldsymbol{k}+\boldsymbol{q}}, \mathrm{i}\omega_n\right)\right] \\ &= \frac{1}{N}\sum_{\boldsymbol{k},s,s'} \left[\delta(\Delta\tau_B) f^{s}_{\boldsymbol{k},\boldsymbol{q}} - C^{s,s'}_{\boldsymbol{k},\boldsymbol{q}} \exp\left(\Delta\tau_B\left(\varepsilon^{s'}_{\boldsymbol{k}+\boldsymbol{q}} - \varepsilon^{s}_{\boldsymbol{k}}\right) + \beta\varepsilon^{s}_{\boldsymbol{k}}\right) n_{\mathrm{F}}\left(\varepsilon^{s}_{\boldsymbol{k}}\right) n_{\mathrm{F}}\left(\varepsilon^{s'}_{\boldsymbol{k}+\boldsymbol{q}}\right)\right]. \end{aligned} \tag{5.61}$$

Unlike a free theory, an analytical evaluation of the occurring bosonic Matsubara summations is thus not possible.

The calculation of the bosonic partition function that yields corrections to the free energy is problematic because it involves non-convergent Matsubara summations and will not be further discussed in this thesis[2]. However, uniform expectation values of the fluctuation fields are easier to access because they do not explicitly require the integration of bosonic fields and can be interpreted as corrections to the respective MF variables. These are determined by the respective equal space-time Green's function

$$\left\langle \delta\psi_\mu \delta\psi_\nu \right\rangle = \left\langle \delta\psi^{a}_{\mu}(r)\delta\psi^{b}_{\nu}(r+\Delta r)\right\rangle\Big|_{\Delta r=0} = -\mathcal{G}^{a,b}_{\mu,\nu}(\Delta\boldsymbol{r}=0, \Delta\tau = 0^-) = -\frac{1}{N\beta}\sum_{\mathrm{i}\omega_n}\sum_{\boldsymbol{q}\in \mathrm{BZ}_{\boldsymbol{Q}}} \mathrm{e}^{\mathrm{i}\omega_n 0^-}\mathcal{G}^{a,b}_{\mu,\nu}(q) \tag{5.62}$$

that does not depend on r due to translation symmetry. The occurring Matsubara summation needs to be performed numerically and converges if $\mathcal{G}^{ab}_{\mu\nu}(\mathrm{i}\omega) = \mathcal{O}\left(\omega_n^{-(1+\epsilon)}\right)$ with $\epsilon > 0$. In the case of $\epsilon = 0$, numerical convergence can be recovered by a convergence factor 0^-, which originates from the discrete nature of the path integral and preserves causality. The matrix elements of interest decay quadratically for large frequencies, i.e., the infinite sum numerically converges by employing a suitable cutoff

$$\sum_{n=-\infty}^{\infty} \mathcal{G}^{a,b}_{\mu,\nu}(\mathrm{i}\omega) \to \sum_{n=-n_c}^{n_c} \mathcal{G}^{ab}_{\mu\nu}(\mathrm{i}\omega) \tag{5.63}$$

[1] These terms are "hidden" in the off-diagonal matrix elements $\mathcal{G}_{d_1 d_2}$, considering our basis $d = d_1 + \mathrm{i}d_2$. A free theory is defined by $\mathcal{L}^{(0)} = \sum_\alpha \xi^*_\alpha\left(-\mathrm{i}\omega_n + \varepsilon_\alpha\right)\xi_\alpha$.

[2] The calculation of $F^{(2)} = -T\ln Z^{(2)} = -T\ln\int \mathcal{D}\left[\boldsymbol{\delta\psi}^*, \boldsymbol{\delta\psi}\right]\exp\left(-\boldsymbol{\delta\psi}^*\underline{\mathcal{M}}\boldsymbol{\delta\psi}\right) = -T\frac{1}{N\beta}\sum_{\mathrm{i}\omega_n}\sum_{\boldsymbol{q}}\ln\det\underline{\mathcal{M}}(q)$ requires integration of all bosonic fields and has, as far as we know, not been established in the literature. We quickly sketch the obstacles which would need to be resolved to evaluate this type of energy correction. Firstly, all normalizations and Jacobi determinants that conveniently cancel for the analysis of correlation functions, including the impact of dynamic Lagrange multipliers within the radial Read-Newns gauge, need to be considered here. Secondly, the occurring Matsubara sum does not converge because $\underline{\mathcal{M}}$ contains eigenvalues of the order $\mathcal{O}(\omega_n)$, which yield from the bosonic part $\mathcal{S}^{(2)}_B$. These divergences are an artifact of the continuous-time description because only the formalism with discrete-time, where the limit of an infinite number of time slices is taken at the very end of a calculation, is formally correct, as we pointed out in Chapter 3. This problem also occurs for free particles and can be resolved through an adequate convergence factor [originating in the fact that two fields are always separated by a single time slice in the discrete description, see Equation (3.5b)] and complex integration [compare Equation (3.19b)]. This procedure, however, cannot be directly applied here because the eigenvalues of $\underline{\mathcal{M}}$ have no simple analytic form due to the occurring Lindhard function. A promising approach to resolve that problem is separating the divergent and convergent part of $\underline{\mathcal{M}}$ by means of the matrix identity $\underline{\mathcal{M}}_{\mathrm{div.}} + \underline{\mathcal{M}}_{\mathrm{conv.}} = \underline{\mathcal{M}}_{\mathrm{div.}}\left(\mathbb{1} + \underline{\mathcal{M}}^{-1}_{\mathrm{div}}\underline{\mathcal{M}}_{\mathrm{conv.}}\right)$ and treating the diverging part in an analytical manner, while remaining part decays fast enough for a successful numerical evaluation. Following Reference [80], the calculation could also be done in the Cartesian gauge with static Lagrange multipliers to avoid gauge problems in the path integral. In that case, however, the unphysical zero modes which have been discussed in Section 3.2.1 need to be projected out [86] before the evaluation of the determinant.

that should be chosen such that $\omega_{n_c} = 2\pi n_c/\beta \gtrsim W$, where W is the bandwidth of the MF band structure. Therefore, especially the evaluation at low temperatures becomes numerically costly.

Corrections to the MF magnetization ($m^{(0)} = \overline{p}_0\overline{p}$) are accordingly given by the equal space-time expectation value of the spin fluctuation $m^{(2)} = \langle \delta p_0 \delta p \rangle$, which is determined by the respective equal space-time Green's function matrix element. We explicitly consider the cases of FM, where the MF solution is spatially uniform, and AFM where we have to consider the non-vanishing Fourier coefficients of p_1 w.r.t. the MF ordering vector $\boldsymbol{Q}$[1]

$$m^{(2)}_{\mathrm{FM}} = -\frac{1}{N\beta} \sum_{\mathrm{i}\omega_n} \sum_{\boldsymbol{q}\in \mathrm{BZ}_0} \mathcal{G}_{p_0,p_1}(q) \,, \tag{5.64a}$$

$$m^{(2)}_{\mathrm{AFM}} = -\frac{1}{N\beta} \sum_{\mathrm{i}\omega_n} \frac{1}{2} \sum_{\boldsymbol{q}\in \mathrm{BZ}_0} \mathcal{G}^{0,1}_{p_0,p_1}(q) \,. \tag{5.64b}$$

To sum up, the expectation value of the net magnetization m up to second order is then given by

$$m = m^{(0)} + m^{(2)} + \mathcal{O}\left(\delta\psi^3\right) \,. \tag{5.65}$$

The presented evaluation of second-order corrections is numerically expensive because it involves two independent momentum summations (the PF sum to determine the fluctuation matrix and the bosonic sum) and one Matsubara summation (the PF Matsubara summation has been performed analytically).

[1] In the case of AFM order, we need to multiply by $\frac{1}{2}$ to account for the smaller magnetic BZ and we find the matrix elements $\mathcal{G}^{0,1}_{p_0,p_1}, \mathcal{G}^{1,0}_{p_0,p_1}, \mathcal{G}^{0,1}_{p_1,p_0}, \mathcal{G}^{1,0}_{p_1,p_0}$ to be equivalent within the summation. Moreover, we find $\mathcal{G}^{0,0}_{p_0,p_1}$ to vanish due to the sublattice structure of the AFM.

II

The 2D Hubbard model in the context of the high-T_c cuprates

In this part, we introduce the two-dimensional one-band Hubbard model as an archetypal approach to the many-body problem and argue why it serves as a minimal model for the high-T_c cuprates. We then provide a comprehensive analysis of the model by means of the SB technique, including the discussion of Mott physics, magnetic phases, collective modes, phase-separation, and compare our findings with results from other theoretical methods. Finally, we identify a parameter regime that features an intertwining of spin and charge order, where our results are in excellent agreement with recent experimental findings in the of electron-doped compounds like, e.g., $Nd_{2-x}Ce_xCuO_4$ (NCCO).

The content of this part has partially been published in References [53] and [55].

CHAPTER 6

The Hubbard model and the many-body problem

The Hubbard model, independently conceived in 1963 by Martin Gutzwiller [106], Junjiro Kanamori [129] and John Hubbard [35] is one of the legendary models in theoretical physics that captures the essence of various emergent phenomena despite being simple and descriptive [36]. Almost 60 years later, it has remained relevant in the current research and puzzles scientists up to this day. Initially, it was intended to explain itinerant ferromagnetism (FM) in transition metals like, e.g., iron or nickel, as an interaction effect, since the phenomenon could not be explained with the free electron gas [18], where particles are only indirectly correlated by the quantum mechanical Pauli exclusion principle [16]. However, as we will learn, FM only plays a minor role after all, whereas the corresponding phase diagram is dominated by antiferromagnetism (AFM) and superconductivity (SC).

The model is based on the tight-binding approximation, where electrons are assumed to be fairly localized around positively charged ions that form a periodic potential or lattice in terms of Wannier states [130]. Wave functions, associated with different lattice sites i, j hybridize as a result of the transfer integrals t_{ij} between the orbitals, which introduces a kinetic energy scale and allows the electrons to hop from site to site. The Hubbard Hamiltonian adds a potential energy scale to the picture, which relates lattice sites occupied by two electrons with different spin $(\uparrow,\downarrow)$ with the energy cost $U > 0$, as a consequence of the screened repulsive Coulomb interaction. We further involve the chemical potential μ_0 to control the total number of electrons in the grand canonical ensemble, which yields

$$H^{\text{Hub}} = -\sum_{<ij>,\sigma} t_{ij}\, \hat{f}^{\dagger}_{i,\sigma}\hat{f}_{j,\sigma} - \mu_0 \sum_{i,\sigma} \hat{f}^{\dagger}_{i,\sigma}\hat{f}_{i,\sigma} + U\sum_{i} \hat{f}^{\dagger}_{i,\uparrow}\hat{f}_{i,\uparrow}\hat{f}^{\dagger}_{i,\downarrow}\hat{f}_{i,\downarrow} \tag{6.1a}$$

$$= \sum_{\boldsymbol{k},\sigma} \xi_{\boldsymbol{k},\sigma}\hat{f}^{\dagger}_{\boldsymbol{k},\sigma}\hat{f}_{\boldsymbol{k},\sigma} + U\sum_{i} \hat{f}^{\dagger}_{i,\uparrow}\hat{f}_{i,\uparrow}\hat{f}^{\dagger}_{i,\downarrow}\hat{f}_{i,\downarrow}\,, \tag{6.1b}$$

in the second quantization notation (compare Chapter 2). By imposing periodic boundary conditions (PBC), the kinetic part of the Hamiltonian can be diagonalized by Fourier transformation (FT) in a basis of Bloch states [22], which allows for calculating the exact ground state in the non-interacting limit ($U = 0$). Within this thesis, we consider nearest neighbor (NN) hopping with an amplitude t and next-to-nearest neighbor (NNN) hopping t' on the square lattice, which leads to the dispersion relation

$$\xi_{\boldsymbol{k},\sigma} = -2t\left(\cos k_x + \cos k_y\right) - 4t'\cos(k_x)\cos(k_y) - \mu_0\,. \tag{6.1c}$$

We will w.l.o.g. define $t = 1$ in the following, i.e., we relate all energy scales to the NN hopping transfer integral. In the non-interacting limit, the dispersion $\xi_{\boldsymbol{k},\sigma}$ is equivalent to the spin degenerate eigenvalues $\varepsilon_{\boldsymbol{k}}$

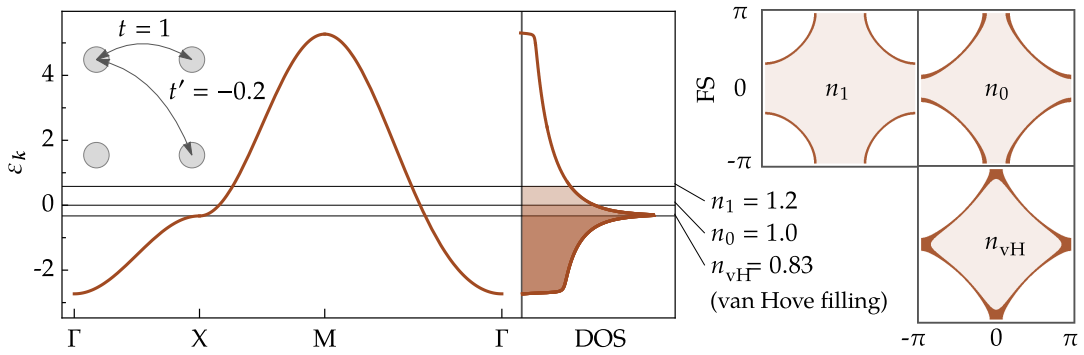

Figure 6.1: Band structure on the high symmetry path [$\Gamma = (0,0)^\top - \mathrm{X} = (0,\pi)^\top - \mathrm{M} = (\pi,\pi)^\top - \Gamma$] with according DOS (left side), and Fermi surfaces (FSs) representing three different electron fillings n (right side) for the Hubbard model in the non-interacting limit ($U = 0$) and $t' = -0.2$. The DOS logarithmically divergences at $n_{\mathrm{vH}} \approx 0.83$ (van Hove divergence). The hopping scheme is chosen such that the model approximately describes the physics of high-T_c cuprate materials (compare Chapter 7), where the van Hove singularity plays an important role, since a high DOS may catalyze FS instabilities once interactions are taken into consideration. Figure adapted from [57] with permission of the author.

of the Hamiltonian in the one-particle picture, where $\boldsymbol{k}$ is a good quantum number to describe the system. Figure 6.1 exemplarily shows the corresponding band structure (BS) and Fermi surfaces (FSs) for three different electron fillings n. We observe that there are states below and above the Fermi level as a consequence of the electron hopping, i.e., the total energy can be minimized by the delocalization of electrons for partially filled systems, which besides the prediction of energy gaps, is one of the key results of band theory in condensed matter physics. Figure 6.1 moreover shows the density of states (DOS), which is defined by $D(\omega) = dn/d\omega$ and can be interpreted as the number of states per energy interval $d\omega$. It is given by the trace over the spectral function[1] [39]

$$D(\omega) = \mathrm{Tr}_{\boldsymbol{k},\sigma} A(\omega, \boldsymbol{k}, \sigma) = \frac{2}{\pi} \lim_{\eta \to 0} \sum_{\boldsymbol{k}} \frac{\eta}{(\omega - \varepsilon_{\boldsymbol{k}})^2 + \eta^2} = 2 \sum_{\boldsymbol{k}} \delta(\omega - \varepsilon_{\boldsymbol{k}}) \,, \tag{6.2}$$

and employs a logarithmic divergence[2] at the saddle point of the BS. This so-called van Hove singularity is named after its discoverer, who first observed the divergence in 1953 in the context of phonons [131]. It is a special feature of two-dimensional (2D) tight-binding models and does not occur in 1D or 3D[3] [132]. The value of the critical filling n_{vH} depends on the details of the hopping scheme, but it always remains present.

Like in most branches of physics, the properties of a system are mainly determined by the interplay of kinetic and potential energy degrees of freedom, which are here represented by the transfer integrals t, t' and the Hubbard interaction U respectively. As we have learned before, the ground state energy can be decreased by the delocalization of the itinerant electrons. However, this behavior is inhibited by the Hubbard interaction, which effectively reduces their mobility and, to some extent, favors a localized picture. These competing processes promote various interesting phenomena, and the Hubbard model has become the archetypical model to study strong correlations among condensed matter theorists, featuring a plethora of FS instabilities despite its elegant simplicity. The interest in the model spiked twice in history due to breakthroughs in experimental physics. First, in 1986 with the discovery of high-temperature superconductivity (HTS) by

[1] The spectral function is defined by the imaginary part of the Green's function $A(\omega) = \mathrm{Im}\, G(\omega + \mathrm{i}\eta)$, where η is a positive infinitesimal, which is introduced by analytical continuation from Matsubara frequencies to real frequencies to preserve causality. Moreover, $\delta(\omega)$ represents the Dirac Delta function that yields from the limit $\eta \to 0$.
[2] The electron filling given by the energy integral over the DOS remains well defined due to the logarithmic nature of the divergence.
[3] In 1D or 3D there still is a critical point, where the DOS is not differentiable. It, however, does not diverge.

Bednorz and Müller [8] and the high-T_c cuprates (HTCCs) that are approximately described by the Hubbard model and its high-U limit, the t-J model [133], as we will further discuss in Chapter 7. Since then, researchers hope to get a deeper insight into the still not fully understood pairing mechanism of unconventional SC by studying the Hubbard model, and that journey continues up to this day. Secondly, since the 2000s, physicists were able to directly experimentally realize the Hubbard model by cold atom trapping [134, 135], which gave its popularity another boost.

The problem, however, is very hard to solve and an exact solution has only been obtained in 1D [136]. Its physical relevance catalyzed the development of analytical and numerical techniques to approximately solve the many-body problem. Prominent examples are dynamical mean-field theory (DMFT) [40], quantum Monte Carlo (QMC) [38], functional renormalization group (FRG) [42], density matrix embedding theory (DMET) [41] and of course mean-field (MF) plus fluctuation methods like the slave-boson (SB) theory described in Part I that we will apply in Chapters 8 and 9 to analyze the 2D Hubbard model. These techniques have revealed various FS instabilities and non-Fermi liquid (FL) behavior like metal-to-insulator or Mott transitions [50, 58, 122, 137], superconductivity [41, 138], different types of magnetic order [53, 105], stripes in the context of charge-order (CO) [55, 120, 139, 140] and the pseudogap (PG) [141] that cannot be explained without the impact of interactions.

The dimensionality of the model also plays an important role. Since electrons are more confined in 2D rather than 3D and feature the van Hove singularity at a critical filling, interactions effects that drive the previously mentioned phenomena are expected to be more dominant. Theoretically, such long-range order should not exist in two dimensions in the thermodynamic limit at finite temperatures due to the Mermin-Wagner-Hohenberg (MWH) theorem [142, 143]. Magnetism and superconductivity, however, have been experimentally observed in quasi-two-dimensional materials like the HTCCs, which can be explained by interlayer coupling or anisotropy due to spin-orbit coupling (SOC). Moreover, a recent discussion initiated by Bertrand Halperin questions the applicability of the MWH theorem in 2D systems due to finite size effects [144, 145]. Finally, it is important to note that the approximations that come along with the SB theory described in Part I do not respect the MWH-theorem, i.e., the method is suitable to investigate long-range order in 2D as experimental findings suggest.

As mentioned previously, a prominent example of such a quasi-two-dimensional system are the HTCCs, which became famous with the discovery of HTS. In Chapter 7, we will summarize crucial features of these materials and argue why they can approximately be described by the one-band Hubbard model. Afterward, we present a comprehensive study of the 2D Hubbard model in Chapter 8, where the results are also compared with other theoretical methods and contextualized with the HTCCs. Finally, Chapter 9 identifies a parameter domain featuring intertwined spin and charge order in excellent agreement with recent experimental findings in electron-doped HTCCs [120, 140].

CHAPTER 7

The high-T_c cuprates and superconductivity

On April 8th, 1911, the dutch physicist Heike Kamerlingh Onnes wrote into his lab notebook [146] "*Kwik nagenoeg nul. Herhaald met goud*" (*Mercury['s resistance] practically zero [at 3 K]. Repeated with gold*) and discovered superconductivity (SC), a quantum mechanical state where the electrical resistivity goes to zero below a critical temperature T_c, as a result of his effort to liquefy Helium [7, 147]. Over time, more and more elements and compounds were identified to feature SC with a rise in critical temperature T_c that saturated around 30 Kelvin as illustrated by green circles in Figure 7.1. It took 46 years until a theoretical description was established by John Bardeen, Leon Cooper, and John Robert Schrieffer in 1957, which is referred to as BCS-theory of conventional superconductivity and explains the phenomenon by the formation of Cooper pairs [28, 102]. The pairing is explained by an effective attractive potential between electrons induced by electron-phonon coupling, yielding the order parameter $\Delta_{ii} = \left\langle \hat{f}^\dagger_{i,\uparrow} \hat{f}^\dagger_{i,\downarrow} \right\rangle \neq 0$.

In 1986, Bednorz and Müller discovered that a totally different material type, namely the cuprate $Ba_2Cu_3LaO_7$ (LBCO) also featured superconductivity at a for that time surprisingly high critical temperature of about $35K$ and the field of high-temperature superconductors (HTSs) was founded [8]. Shortly after, it was observed that a substitution of the rare earth element could drastically increase the critical temperature up to $92K$ for $YBa_2Cu_3O_{7-x}$ (YBCO), which was a major breakthrough because it was the first superconductor that could be cooled with liquid nitrogen [148]. It was succeeded to push T_c for this material class of high-T_c cuprates (HTCCs) even higher as illustrated by blue diamonds in Figure 7.1, but it still remains far below room temperature, and there was no major improvement since the late 1990s. The pairing mechanism in HTSs differs from conventional superconductivity, is still not fully understood and its further deciphering and the search for room-temperature SCs is a major goal in contemporary condensed matter physics. It is, however, consensus that the pairing for this so-called unconventional superconductivity is due to electron-electron interactions (rather than an electron-phonon coupling), where an adequate order parameter is given by $\Delta_{ij,\sigma\sigma'} = \left\langle \hat{f}^\dagger_{i,\sigma} \hat{f}^\dagger_{j,\sigma'} \right\rangle \neq 0$ with $i \neq j$.

A popular theoretical approach to study unconventional SC is to calculate the $\boldsymbol{k}$-dependent pairing vertex $V^{\sigma_1\sigma_2}_{\sigma,\sigma'}(\boldsymbol{k},\boldsymbol{q})$ (e.g., by FRG) and solve the self-consistent MF gap equation [42]

$$\Delta_{\boldsymbol{q},\sigma\sigma'} = -\frac{1}{N} \sum_{\boldsymbol{k},\sigma_1\sigma_2} V^{\sigma_1\sigma_2}_{\sigma,\sigma'}(\boldsymbol{k},\boldsymbol{q}) \frac{\Delta_{\boldsymbol{k},\sigma_1\sigma_2}}{2\varepsilon_{\boldsymbol{k}}} \tanh\left(\frac{\varepsilon_{\boldsymbol{k}}}{2T}\right) . \tag{7.1}$$

Unlike conventional SC, which can analyzed by means of the spin- and charge-rotation invariant Kotliar–Ruckenstein (SCRIKR) slave-boson representation [68], a SB approach for unconventional SC has not been established. The reason is that the corresponding order parameter would require defining a non-local constraint that connects neighboring lattice sites, whereas the implemented constraints are local, i.e., on the

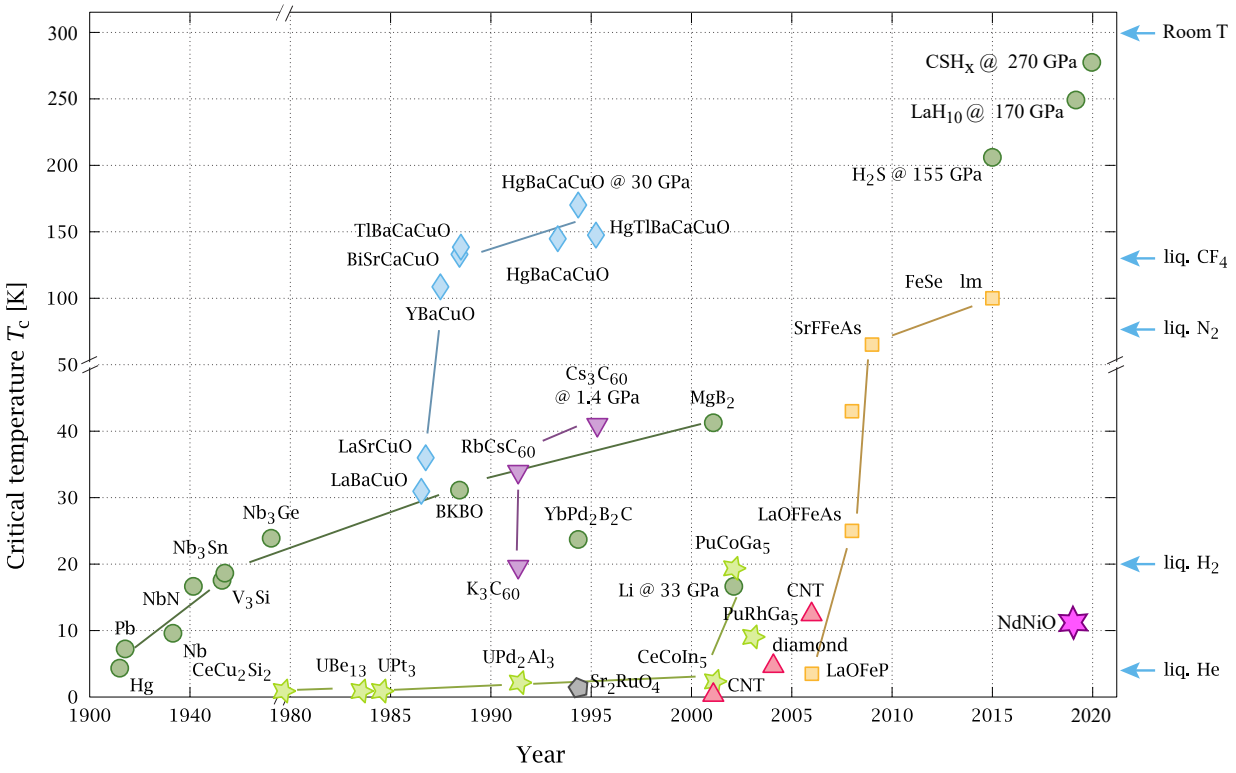

Figure 7.1: Historical overview of discovering superconducting elements and materials with their respective critical temperature T_c. High-T_c cuprate materials that are discussed within this thesis feature unconventional superconductivity and are shown in blue; conventional superconductors are represented by green circles and heavy-fermion-based superconductors by green stars. Figure reprinted from [149].

same lattice site [compare Equation (2.14)]. A SB method that combines both types of constraints consistently is yet to be found. We will, therefore, not explicitly discuss superconducting phases in this thesis and focus our discussion on the underdoped regime of the HTCCs, where SC is not present. We are, however, investigating a method to approximately calculate the frequency-dependent pairing vertex by means of the SB fluctuations in order to solve the dynamic analog of Equation (7.1) [57].

7.1 Effective one-band Hubbard model for high-T_c cuprates

A common denominator of all HTCC materials are copper-oxide planes (CuO_2), separated by interlayers that usually contain rare-earth elements that act as charge reservoirs as exemplarily shown in Figure 7.2(a). There is only weak coupling between different planes such that the main physics is believed to be described by quasi-2D systems, and the electron density in those planes can be manipulated by a process called doping, where the rare-earth elements are partially substituted [150].

The copper ions are in the oxidation state Cu^{2+} with the electron configuration $3d^9$, and associated orbitals are energetically split by the crystal field of the surrounding oxygen octahedron into a low energy triplet t_{2g}, containing orbitals that feature nodes at the oxygen ions (d_{xy}, d_{xz}, d_{yz}), and a higher energy e_g doublet with the $d_{x^2-y^2}$ and $d_{3z^2-r^2}$ orbitals. Furthermore, the degeneracy of the e_g doublet is lifted by the Jahn-Teller effect [151], i.e., the distortion from the perfect octahedron, which effectively removes the $d_{3z^2-r^2}$ orbital. These results imply a three-band model, featuring a half-filled $d_{x^2-y^2}$ orbital for the copper and doubly occupied

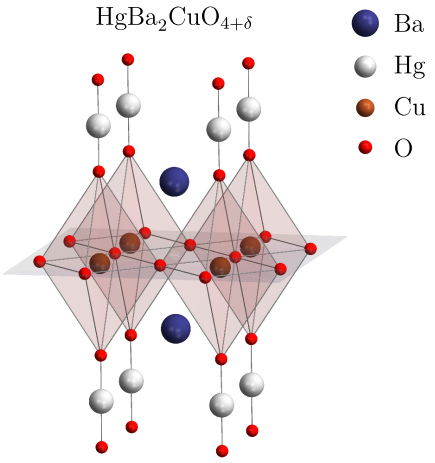

(a) Crystal structure of the cuprate material Hg1201 [157, 158]. Figure created with *crystallica* [159].

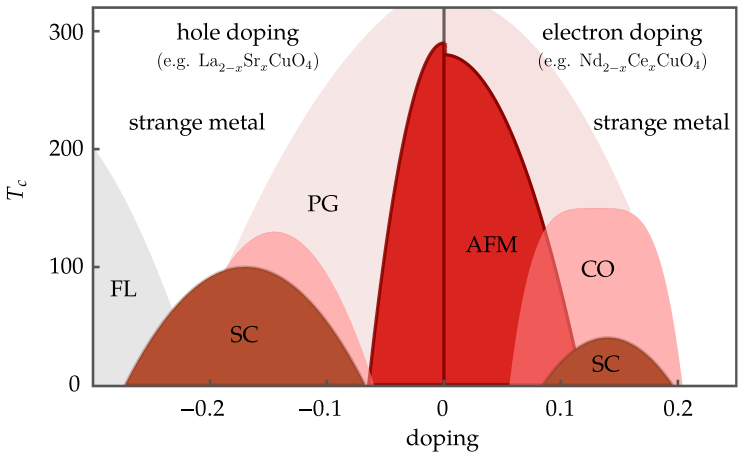

(b) Schematic universal phase diagram of the HTCCs as function of temperature T and doping δ based on results of the established literature [133, 140, 157, 160, 161]. The electron filling is given by $n = 1 + \delta$ and the regime for $|\delta| \lesssim 0.1$ is referred to as underdoped.

Figure 7.2: Basic crystal structure and schematic phase diagram of the high-T_c cuprates based on experimental and theoretical results. The doping δ manipulates the electron density in the two-dimensional CuO_2-plane and can be tuned by partially substituting rare earth elements in the crystal. The system is theoretically well approximated by the one-band 2D Hubbard model. Figure adapted from [57].

p-orbitals for the oxygen ions O^{2-}, to be an effective model [152, 153] with partially filled bands. Experimental findings, however, show a large charge gap at half-filling, i.e., a breakdown of the band theory [154], which can be explained by a Mott transition[1] as a strong correlation effect [156], which is actually covered by the single orbital Hubbard model.

Also, for doped HTCCs, experiments suggest that there is only one band at the Fermi-level [162]. Moreover, as pointed out by Hanke *et al.* [163] many theoretical studies featuring the one band model find the Fermiology, magnetic ordering and $d_{x^2-y^2}$ superconducting pairing in qualitative agreement with experimental observations [162, 164–167]. In that picture, only the copper $d_{x^2-y^2}$ orbital remains, which can be approximated by the one-band Hubbard model on a 2D simple cubic lattice. Due to these findings, the HTCCs are commonly believed to incorporate the physics "*of doping a Mott insulator*" [133]. Doped electrons occupy the $3d^{10}$ orbital, whereas holes are mainly absorbed by the oxygen orbitals, which raises the question of why those can be neglected in the case of hole doping. A possible explanation was given with the formation of a so-called Zhang-Rice (ZR) singlet between a spin residing in the half-filled copper orbital and a hole on the adjacent oxygen orbitals [168, 169]. The one band description can be recovered through a second-order perturbation calculation, where the oxygen orbitals are integrated out. The apparent particle-hole asymmetry can be recovered by a finite next-to-nearest neighbor (NNN) hopping t' as a phenomenological parameter, despite it is not in strict agreement with the ZR picture. Ab initio calculations suggest that $t' \approx -0.2$ is a reasonable choice to represent many HTCC materials [170]. We will therefore apply the one-band 2D Hubbard model given by Equation (6.1) as effective HTCC model and analyze it with the SB scheme. There is, however, an ongoing discussion on its validity and possible limitations in the scientific community.

[1] There is another school of thought that the HTCCs should be regarded as charge-transfer insulators, where the insulating properties arise from hopping between the $3d^{10}$ and $2p$ orbitals within the unit cell rather than hopping between different unit cells like in the case of Mott physics [155].

7.2 Generic phase diagram

The two most crucial experimental possibilities to manipulate HTCC compounds are to control the temperature T and the doping δ away from half-filling $n = 1 - \delta$ by substituting rare earth elements in the crystal. The phase diagram as a function of these parameters looks qualitatively very similar for many different HTCC materials and is summarized by the schematic universal phase diagram in Figure 7.2(b). As discussed earlier, the undoped ground state is insulating, which can be explained by a Mott transition with antiferromagnetic spin alignment. The antiferromagnetism (AFM) persists away from half-filling as conducting magnetic ground state and occupies a larger domain in the case of electron doping. Superconducting domes are present for both types of doping, but the highest critical temperature T_c is consistently found for hole doping, with its maximum around $n \approx n_{\mathrm{vH}}$ (optimally doped). Moreover, a so-called and not yet fully understood pseudogap (PG) regime is identified at the vicinity to half-filling, up to high temperatures. The PG is characterized by partial energy gaps at the Fermi surface (FS) resulting in Fermi arcs and is also associated with local minima of the density of states (DOS) that can be measured by means of the specific heat [171–173]. A significant part of the remaining phase diagram also shows non-Fermi liquid (FL) behavior, such as a linear resistivity as a function of temperature rather than a quadratic dependency, and is often called *strange metal*.

Recently, research on charge-order (CO) and stripe phases have risen in popularity. This type of order is primarily observed in the underdoped regime for electron doping, intertwines with the AFM ground state, and could also be relevant to gain a better understanding of PG physics [157]. Ultimately, people hope to get a deeper insight into the superconducting pairing mechanism by studying spin fluctuations and the nature of the other surrounding phases in order to demystify the fascinating phenomenon of HTS [174, 175].

The SB method is especially capable of describing intertwined spin and charge order, which is why we set the main focus on the underdoped regime and present results for the Hubbard model with explicit context to the HTCCs in Chapter 9.

CHAPTER 8

Slave-boson analysis of the 2D Hubbard model

In this chapter, we present a comprehensive analysis of the 2D Hubbard model defined in Equation (6.1) on the square lattice, by means of the slave-boson (SB) theory described in Part I. The discussion includes a Mott transition at half-filling (Section 8.1), magnetic mean-field (MF) phase diagrams (Section 8.2) as well as static correlations (Section 8.3) and collective modes (Section 8.4) in the spin and charge channel. Afterward, we investigate emerging inhomogeneous phases that arise from charge fluctuations about the AFM mean-field ground state (Section 8.5) and lead up to the discussion of intertwined spin and charge order in the context of electron doped high-T_c cuprates (HTCCs) in Chapter 9. We, moreover, compare our results with the findings of other theoretical methods to provide an estimation of the quality of the SB approximation. We do not explicitly discuss superconducting instabilities because the SB technique presented in Part I is not suitable to express non-local order parameters, which are required to describe unconventional superconductivity (SC). The content of this chapter is based on References [53] and [55], but also complemented with a variety of previously unpublished results. Data that has been published before in the references above is annotated in the caption of respective figures.

We will keep technical details short in order to achieve a smooth presentation and refer the reader to respective relevant sections in Part I to get a deeper insight into the underlying formalism. Just for a quick recap, the SB approach that we apply yields an exact representation of the original model, where the Hubbard interaction becomes quadratic in fermionic fields at the cost of a more complicated hopping scheme that mixes fermionic and bosonic degrees of freedom. The corresponding ground state can be determined approximately through a bosonic MF ansatz, where the remaining fermionic degrees of freedom are integrated out. Gaussian fluctuations of the bosonic fields around the MF saddle point are applied to analyze dynamic correlations and to investigate emerging Fermi surface (FS) instabilities of the renormalized band structure (BS) in order to judge the stability of the MF ground state.

8.1 Mott transition at half-filling

According to Fermi liquid (FL)-theory, it is expected that a half-filled band always features a conducting state because there are quasi-free electrons at the FS that can carry charge. There are, however, exceptions to that assumption. In 1949, Nevil Francis Mott proposed his idea of an insulating state for a half-filled band [137], which was theoretically supported by the analysis of the Hubbard model in 1964 [58] and explained the phenomenon by interaction effects. The problem can intuitively be understood as follows: We learned in Chapter 6 that free electrons in metals tend to delocalize in order to minimize their total energy. However, the Hubbard interaction applies an energy penalty if two electrons occupy the same lattice site, and for a half-filled system, this potential energy cost cannot entirely be avoided as long as the electrons remain to

be itinerant. Imagine a critical U_c, where the interaction energy cost is so high that delocalizing does not minimize the total energy anymore, but the electrons are rather frozen out and localized. The resulting state is insulating and called Mott insulator (MI), whereby the critical interaction U_c enables the Mott transition. The existence of such a state is supported experimentally. It is e.g., widely believed that the HTCC are MIs at zero doping [133].

Within our SB scheme, we have two accessible quantities to search for the signature of an emerging Mott state. Firstly, the kinetic energy in the system, and secondly, the opening of an energy gap. In order to investigate those, we minimize the MF free energy (FE) by solving the saddle point equations

$$\left.\frac{\partial F_{\text{eff}}^{(0)}}{\partial p_0}\right|_{(4.26)} = \left.\frac{\partial F_{\text{eff}}^{(0)}}{\partial \mu_{\text{eff}}}\right|_{(4.26)} = 0\,, \tag{8.1a}$$

$$\left.\frac{\partial F_{\text{eff}}^{(0)}}{\partial p}\right|_{(4.26)} = \left.\frac{\partial F_{\text{eff}}^{(0)}}{\partial p_0}\right|_{(4.26)} = \left.\frac{\partial F_{\text{eff}}^{(0)}}{\partial \beta}\right|_{(4.26)} = \left.\frac{\partial F_{\text{eff}}^{(0)}}{\partial \mu_{\text{eff}}}\right|_{(4.26)} = \left.\frac{\partial F_{\text{eff}}^{(0)}}{\partial \boldsymbol{Q}}\right|_{(4.26)} = 0\,, \tag{8.1b}$$

according to Section 4.4 at half-filling ($n = 1$). We distinguish between explicitly paramagnetic (PM) solutions, where we enforce $p = 0$ and solve the reduced saddle point equations given by Equation (8.1a)[1] and MF ground states that allow for magnetic order as determined by Equation (8.1b). The eigenvalues $\varepsilon_{\boldsymbol{k},\sigma}$ of the renormalized BS that enter the FE are derived in Appendix B.1 and yield

$$\varepsilon_{\boldsymbol{k},\pm} = \frac{1}{2}\left[\left(\mathcal{Z}_+^2 + \mathcal{Z}_-^2\right)\left(\xi_{\boldsymbol{k}} + \xi_{\boldsymbol{k}-\boldsymbol{Q}}\right) \pm \Delta_{\boldsymbol{k}}^{\boldsymbol{Q}}\right] - \mu_{\text{eff}}\,, \tag{8.2a}$$

with the magnetic gap function

$$\Delta_{\boldsymbol{k}}^{\boldsymbol{Q}} = \sqrt{\left[\left(\mathcal{Z}_+^2 - \mathcal{Z}_-^2\right)\left(\xi_{\boldsymbol{k}} - \xi_{\boldsymbol{k}-\boldsymbol{Q}}\right)\right]^2 + 4\left[\mathcal{Z}_+\mathcal{Z}_-\left(\xi_{\boldsymbol{k}} + \xi_{\boldsymbol{k}-\boldsymbol{Q}}\right) + \beta\right]^2}\,. \tag{8.2b}$$

In the PM limit, it is $\mathcal{Z}_- = \beta = 0$ and the spin-degenerate eigenvalues adapt the simplified form

$$\varepsilon_{\boldsymbol{k}} = z_0^2\xi_{\boldsymbol{k}} - \mu_{\text{eff}}\,. \tag{8.2c}$$

Moreover, we defined $\mu_{\text{eff}} = \mu_0 - \beta_0$, $\xi_{\boldsymbol{k}}$ represents the dispersion of the non-interacting system defined by Equation (6.1c), and the properties of the SB-weights $\mathcal{Z}_+$, $\mathcal{Z}_-$, z_0 and LMs β_0, β are summarized in Table 4.1.

The hopping amplitudes that dictate the kinetic energy scale are renormalized by $t_{ij} \to z_0^2 t_{ij}$ for PM and $t_{ij} \to \mathcal{Z}_+^2 t_{ij}$ for magnetic saddle points respectively[2] and the localized Mott state can be identified by a vanishing hopping amplitude. Equation (8.1a) can be solved analytically for $t' = T = 0$ [53] and yields $U_c = 128/\pi^2 \approx 12.97$ with $z_0|(U_c) = 0$ and $p_0(U_c) = 1$, i.e., every lattice site is exactly singly occupied, which describes the frozen insulating state that we illustrated earlier. The numeric solution of the magnetic saddle point equations yields an antiferromagnetic (AFM) ground state with $\mathcal{Z}_+ > 0$ as shown in Figure 8.1(a).

The opening of a Mott gap in the PM ground state can again be shown analytically with a discontinuity of the chemical potential [50, 53]

$$\Delta^{\text{Mott}} = \lim_{\delta\to 0}\left|\mu_0(n = 1+\delta) - \mu_0(n = 1-\delta)\right|\,. \tag{8.3}$$

[1] The magnetization is given by $m = pp_0$.

[2] The interaction-enabled rescaling of the kinetic energy is, however, not simply given by z_0^2, because the LM β_0 also affects it by increasing the effective chemical potential $\mu_{\text{eff}} = \mu_0 - \beta_0$.

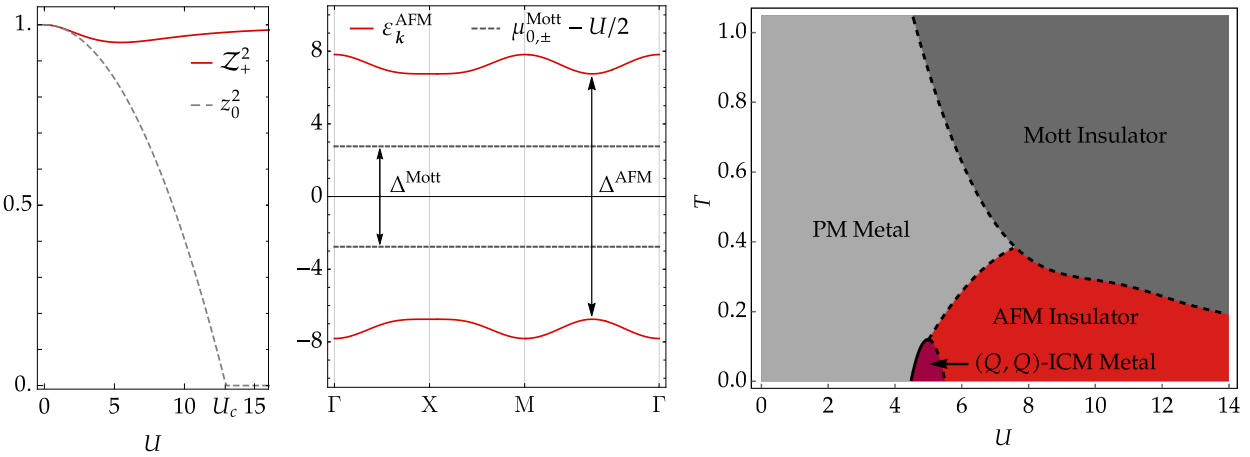

(a) Renormalized hopping amplitudes for $t' = 0$ at zero temperature and half-filling.

(b) Mott gap vs. AFM band gap on the high symmetry path of the BZ for $t' = 0$ at zero temperature, half-filling and $U = 15$.

(c) Interaction-temperature dependent phase diagram for $t' = 1/\sqrt{3}$ and half-filling. Dashed lines indicate first- and solid lines second-order phase transitions. Figure adapted from [53].

Figure 8.1: The Mott transition can be identified by a vanishing renormalized hopping amplitude z_0^2 and the opening of a gap in the chemical potential within the PM MF. Allowing magnetic ordering, we find an AFM band insulator with a larger gap to be energetically favored above the Mott state at zero temperature. At finite temperatures, we find a first order transition from the AFM to the Mott state and a critical point, where T_{Neel} is maximized. Figure 8.1(c) is in good qualitative agreement with a corresponding DMFT analysis [40].

It opens exactly at $U = U_c$ and we find $\Delta^{\mathrm{Mott}} \to U$ for $U \to \infty$, which is the signature of the upper Hubbard band that can also be seen as collective modes in the charge susceptibility (compare Section 8.4). The magnetic solution is also insulating, but the gap $\Delta^{\mathrm{AFM}} \approx |2\beta|$ is due to the finite magnetization[1] , which is the signature of a band insulator (BI) rather than a MI. The Mott signature is partially restored in the limit $U \to \infty$, where we find $\Delta^{\mathrm{AFM}} \to \Delta^{\mathrm{Mott}}$. The respective gaps are shown in Figure 8.1(b) for $U > U_c$. According to the MF analysis, the magnetic state is always energetically favored above the PM Mott state for $T = 0$ and $U < \infty$, which is supported by the size of the corresponding gaps. Finite temperatures, however, energetically improve the PM Mott insulator compared to the AFM band insulator and induce first-order phase transitions among those states as shown in Figure 8.1(c). We do not find a ground state that can clearly be identified to be an antiferromagnetic Mott insulator (AFMMI) as expected in the HTCCs, which is likely due to omissions of the MF theory. Recent studies suggest that doublon-holon binding has to be considered in order to describe such a state, which has been achieved with a different SB representation at half-filling [122, 176].

To complete the discussion, we want to take a closer look at the average double occupancy, ground-state energy, and magnetization, which are displayed in Figure 8.2 as a function of the interaction. Conveniently, we may compare our results at half-filling with statistically exact methods like auxiliary-field quantum Monte Carlo (AFQMC) and approximative cluster calculations like density matrix embedding theory (DMET) that often struggle with doping due to the sign problem or finite-size effects. The double occupancy d^2 and the ground state energy E are slightly overestimated by the SB mean-field solution due to missing contributions of dynamic fluctuations that usually lower the total energy. Nevertheless, the biggest deviation is found in the MF magnetization ($m = pp_0$), which tends towards the fully magnetized state ($m \to 1/2$) for $U \to \infty$, and exceeds the exact Heisenberg value $m_{\mathrm{He}} \approx 0.31$ [41, 179] that should be approached by far.

[1] β is the LM that enforces the equivalence of the PF and bosonic representation of the spin operator.

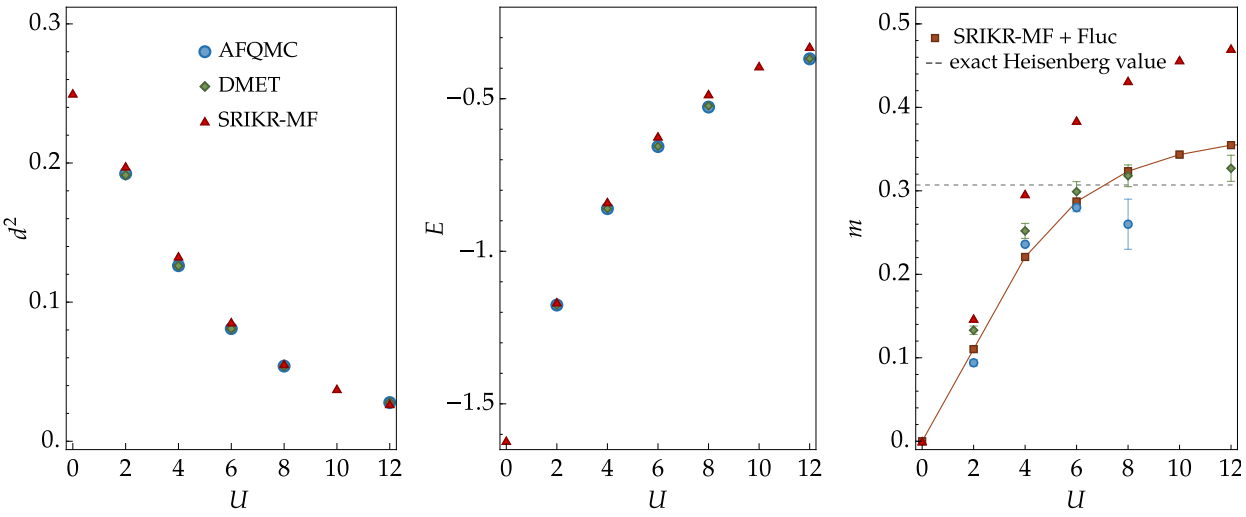

(a) Average double occupancy per lattice site.

(b) Ground state energy per lattice site.

(c) Staggered magnetization, SRIKR-MF with fluctuation corrections.

Figure 8.2: Double occupancy, ground state energy and magnetization for the Hubbard model at half-filling, $t' = 0$ and low temperature for different theoretical methods in comparison. The SB mean-field magnetization (red triangles) overestimates the expected value that is given by the exact Heisenberg value for high interactions. With the addition of fluctuation corrections (solid line), the results can be massively improved and become comparable to non-MF methods. DMET data from [41, 177], AFQMC data from [177, 178], exact Heisenberg value from [179].

We may, however, calculate second corrections to the magnetization through Gaussian fluctuations around the magnetic MF saddle point and the corresponding bosonic fluctuation field Green's function

$$\mathcal{G}^{a,b}_{\mu,\nu}(q) = -\left\langle \delta\psi^{-a}_{\mu,-q}\delta\psi^{b}_{\nu,q}\right\rangle = -\left[\underline{\mathcal{M}}^{-1}(q)\right]^{a,b}_{\mu,\nu}\,, \tag{8.4a}$$

that we derived by means of the fluctuation matrix

$$\mathcal{M}^{a,b}_{\mu,\nu} = \frac{1}{2}\frac{\partial^2\mathcal{S}}{\partial\psi^{-a}_{\mu,-q}\partial\psi^{b}_{\nu,q}}\bigg|_{\overline{\psi}} \tag{8.4b}$$

as a quadratic expansion of the action $\mathcal{S}$ in Section 5.2. The basis contains all SB fields and LM-fields

$$\delta\boldsymbol{\psi}^{a}_{q} = \left(\delta d_{1,q+a\boldsymbol{Q}}\,,\delta d_{2,q+a\boldsymbol{Q}}\,,\delta p_{0,q+a\boldsymbol{Q}}\,,\delta\beta_{0,q+a\boldsymbol{Q}}\,,\delta p_{1,q+a\boldsymbol{Q}}\,,\delta\beta_{1,q+a\boldsymbol{Q}}\,,\delta p_{2,q+a\boldsymbol{Q}}\,,\delta\beta_{2,q+a\boldsymbol{Q}}\,,\delta p_{3,q+a\boldsymbol{Q}}\,,\delta\beta_{3,q+a\boldsymbol{Q}}\right)^{\top}\,, \tag{8.4c}$$

and describes the second-order deviation $\delta\boldsymbol{\psi}^{a}_{q} = \boldsymbol{\psi}^{a}_{q} - \overline{\boldsymbol{\psi}}$ from the static MF saddle point with magnetic ordering vector $\boldsymbol{Q}$. Moreover, the four-index $q = (\boldsymbol{q}, \mathrm{i}\omega_n)$ represents the momentum and bosonic Matsubara frequency. Following the discussion in Section 5.4, corrections to the magnetization are given by the translation-invariant equal space-time expectation value of the magnetic fluctuations $\langle\delta p\delta p_0\rangle$, that can be obtained by numerically evaluating the Matsubara-frequency and momentum summation back to the real space-time basis. The result is shown by squares in Figure 8.2(c) and demonstrates a massive improvement over the MF magnetization and comes even closer to the AFQMC results compared to DMET at intermediate interactions U. We conclude that the SB mean-field representation seems to have a bias towards magnetism and to overrate the magnetization, which can significantly be improved by considering fluctuation contributions. While the SB results seem unfavorable to the other methods at half-filling, the formalism comes along with the advantage that it can

easily be applied for doping, zero temperature, large unit cells, and inhomogeneous phases, where many other methods tend to struggle.

8.2 Magnetic mean-field phase diagram

Like the Mott transition, itinerant magnetism is also determined by the competition of kinetic and potential degrees of freedom. At sufficiently low interactions, the ground state usually remains paramagnetic and can be described by FL-theory, i.e., an effectively non-interacting state with renormalized parameters. For the PM slave-boson band structure, the respective renormalization of the hopping amplitude $t_{ij} \to z_0 t_{ij}$ also implicates a reduction of the bandwidth (BW) $W \to z_0^2 W$ along with the effective mass $m_{\text{eff}} = z_0^{-2}$, and the on-site energy is increased by $-\mu_0 \to -\mu_0 + \beta_0$. At a critical interaction, the spins become macroscopically correlated and align with a finite magnetization as long-range order that spontaneously breaks the continuous SU(2) spin-rotation-symmetry and except for the case of ferromagnetism (FM) also translation-symmetry. A very common type of magnetic order at intermediate interactions U is antiferromagnetism (AFM). It can be interpreted as the most itinerant type of magnetism, i.e., it offers a good tradeoff between kinetic and potential energy in the system. Spins on neighboring lattice sites align anti-parallel, which reduces the number of doubly occupied sites in order to save potential energy, but still allows a direct hopping between nearest neighbors (NNs) without conflicting with the Pauli exclusion principle in order to minimize kinetic energy through delocalization. Ferromagnetism (FM), the most well-known type of magnetic order, on the other hand, does not allow direct hopping between occupied NNs and is, therefore, a localized rather frozen state that is often found at higher U and remains to be conducting through doped holes or electrons[1]. It was, in fact, proven analytically by Yosuke Nagaoka in 1966 that a single, hole doped to the half-filled Hubbard model, invokes FM at infinite interaction [180] and the mechanism was recently experimentally observed in a quantum dot plaquette [181]. Another complementing approach to explain magnetic instabilities is FS nesting, i.e., the property that a large density of electrons at the Fermi-level is connected by the same wave vector $\boldsymbol{q}$, which catalyzes a collective mode with the respective ordering vector in the presence of interactions. However, this explanation is less intuitive because there is no direct illustration in real space.

The interaction-filling dependent magnetic phase diagrams shown in Figure 8.3 follow from solving the saddle point equation given by Equation (8.1b) and clearly reflect the intuitive physics discussed above. They moreover feature spiral magnetic states in the x-y plane according to the MF ansatz

$$\boldsymbol{p} = p \begin{pmatrix} \cos(\boldsymbol{Q}\boldsymbol{R}_i) \\ \sin(\boldsymbol{Q}\boldsymbol{R}_i) \\ 0 \end{pmatrix}, \tag{8.5}$$

introduced in Section 4.1, where $\boldsymbol{Q}$ is the magnetic ordering vector and $\boldsymbol{R}_i$ represents the position on the lattice. The ordering vector that minimizes the FE is visualized by the color code, where FM is recovered for $\boldsymbol{Q} = (0,0)^\top$ (blue squares), and AFM for $\boldsymbol{Q} = (\pi,\pi)^\top$ (red squares). The magnetic unit cells can become very large for the spiral phases and tend to infinity or, in other words, fill the whole crystal if $\boldsymbol{Q}$ is not given by a

[1] In models with additional hybridizing orbitals, FM is usually more common because the conduction can also happen in another orbital, while the strongly interacting orbital can be frozen out without a large energy penalty.

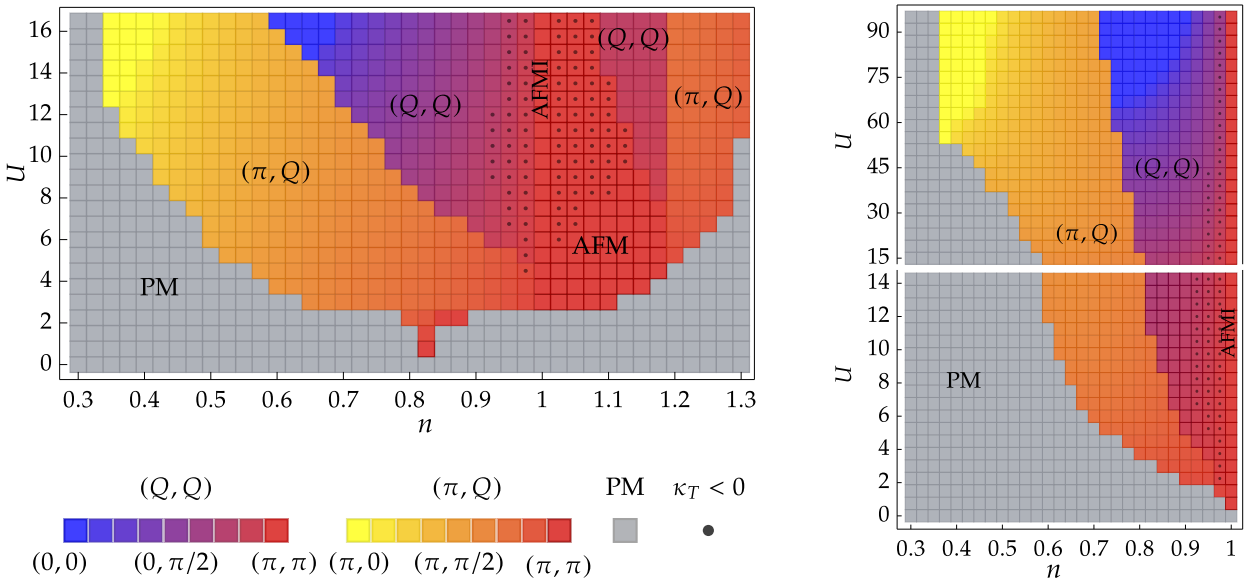

(a) Magnetic MF phase diagram for $t' = -0.2$ and $T = 0$.

(b) Magnetic MF phase diagram, $t' = T = 0$.

Figure 8.3: Magnetic phase diagrams as function of the electron filling n and interaction U. The ordering vector $\boldsymbol{Q}$ evolves continuously within the spiral magnetic phases, as indicated by the color scheme. An abrupt color change indicates a first-order phase transition that comes along with a discontinuity of the magnetization m, whereas smooth color gradients indicate second-order phase transitions. Domains featuring negative electronic compressibility κ_T indicate an unstable ground state and are annotated with black dots. Figures adapted from [53].

rational number times π. That type of order is called incommensurate magnet (ICM), where the momentum $\boldsymbol{k}$ is usually not a good quantum number anymore[1].

Figure 8.3(a) features a finite next-to-nearest neighbor (NNN) hopping $t' = -0.2$ that breaks particle-hole symmetry (PHS)[2]. At the van Hove singularity $n = n_{\mathrm{vH}} \approx 0.83$, AFM order already formates at very low interaction due the diverging DOS and associated nesting effects. Figure 8.3(b) does not feature NNN hopping, which recovers PHS (i.e., $n \to 2 - n$) and the van Hove singularity is situated at half-filling. As previously discussed in Section 8.1, the half-filled state is an AFM insulator that becomes conducting for arbitrarily small doping like the rest of the phase diagram. In that context, it is remarkable that the SB mean-field approximation respects Nagaoka FM where a single doped hole recovers a finite conductivity, since the FM phase tends towards half-filling for high U according to in Figure 8.3(b). Overall, the FM is the only magnetic state we find to feature a vanishing double occupation $d^2 = 0$ and fully maximized magnetization $m = pp_0 = n/2$. A supplementing discussion of the phase diagram that shows band structures and Fermi surfaces is included in Reference [53]. Figure 8.4 displays the temperature-dependent phase diagram with fixed interactions. For small U, the magnetic phase boundary centers around the van Hove singularity and the Neel temperature, which defines the phase boundary to the PM, increases for higher interactions as expected. Moreover, it is notable that the AFM occupies a larger part of the parameter space at higher temperatures, which could be explained by a less prominent role of nesting effects due to temperature-induced blurring of the FS.

[1] In models without spin-orbit coupling (SOC) like the Hubbard model, we can still use $\boldsymbol{k}$ as a quantum number within the basis discussed in Section 4.3.

[2] Results for the opposite sign of the NNN hopping are not independent and can be recovered by the particle hole transformation $\hat{f}_{i,\sigma} \to (-1)^i \hat{f}^\dagger_{i,\sigma}$, $t' \to -t'$, $n \to 2 - n$ for bipartite lattices [182].

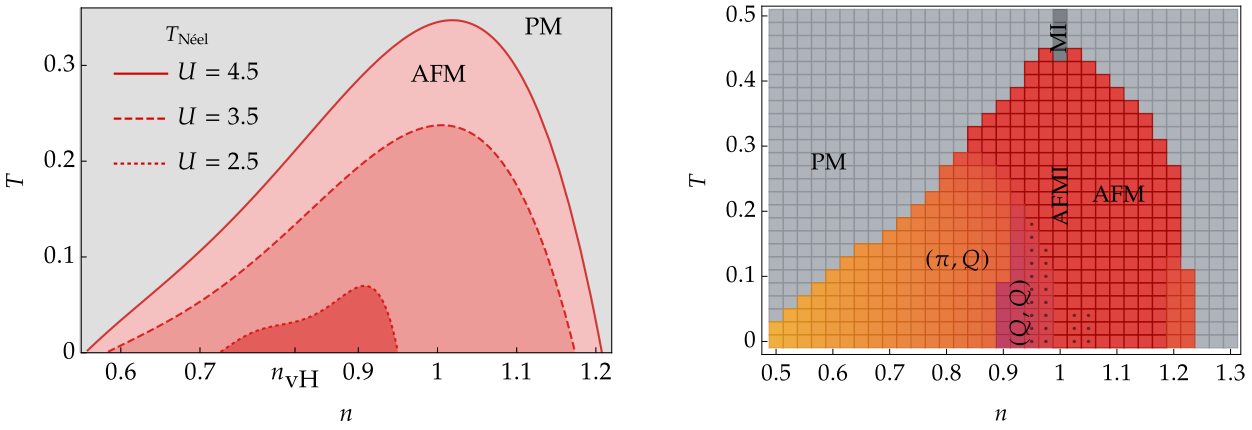

(a) $T_{\text{Néel}}$ for $t' = -0.2$ and different interactions.

(b) Magnetic phase diagram for $t' = -0.2$ and $U = 6.5$.

Figure 8.4: Magnetic phase diagrams dependent on the electron filling n and temperature T at fixed interactions. Increasing temperatures favor the AFM over other magnetic orders and decrease the tendency towards negative compressibilities. Figures adapted from [53].

A common feature of the phase diagrams are domains of negative electronic compressibility

$$\kappa_T = \frac{1}{n^2} \frac{\partial n}{\partial \mu_0} \tag{8.6}$$

in the vicinity of half-filling above a certain interaction strength, which are indicated by black dots in Figures 8.3 and 8.4, and have also been observed in previous studies [71, 105, 182]. At the sign change, κ_T diverges, i.e., an infinitesimal increase of the chemical potential implies the addition of an infinite amount of electrons, which is clearly unphysical and the signature of an instability of the magnetic MF ground state. We will further elaborate on the nature of the thereby emerging inhomogeneous phases in Section 8.5 and Chapter 9. The strong tendency towards AFM in the vicinity of half-filling qualitatively fits the physics of HTCCs. Since the presented method is blind for superconductivity and likely to be biased towards magnetism as discussed previously, we expect there to be a superconducting dome hidden below the spiral phases that may be catalyzed by magnetic correlations as other theoretical methods and experimental evidence suggests [41, 183–185].

8.3 Correlations and criticality

We can acquire momentum and frequency-resolved information about correlations beyond the MF ground state by utilizing the Gaussian fluctuations derived in Chapter 5. The most prominent application is executing a stability analysis of the saddle point by means of the static spin and charge susceptibility, i.e., the linear response functions to an external magnetic field or electric potential, respectively. Due to the SB constraints, these functions have purely bosonic representations, which are equivalent to the corresponding fermionic form of the original model (compare Table 2.1)

$$\chi_s^{\alpha\beta}(q) = \left\langle \delta S_{-q}^{\alpha} \delta S_q^{\beta} \right\rangle , \tag{8.7a}$$

$$\chi_c(q) = \left\langle \delta n_{-q} \delta n_q \right\rangle . \tag{8.7b}$$

These functions are given by superpositions of matrix elements of the fluctuation field Green's function $\mathcal{G}$ that we defined in Equation (8.4), i.e.,

$$\chi(q) = \sum_{\mu,\nu,a,b} C^{a,b}_{\mu,\nu} \left\langle \delta\psi^{-a}_{\mu,-q} \delta\psi^{b}_{\nu,q} \right\rangle = - \sum_{\mu,\nu,a,b} C^{a,b}_{\mu,\nu} \mathcal{G}^{a,b}_{\mu,\nu}(q) \,. \tag{8.7c}$$

The explicit expressions for fluctuations about magnetic and non-magnetic saddle points are summarized in Table 5.2. As elaborated further in Section 5.3.3, a FS instability is signaled by a diverging static susceptibility in the respective channel that comes along with a breakdown of the path integral formalism about the MF ground state. If the interaction is increased beyond the onset of the instability, we find an enlarged negative regime of the susceptibility, which can be interpreted as condensation energy of the emerging bound state. A quantitative assessment of the fluctuations in this regime, however, is limited because of the breakdown of the MF.

In the following, we first discuss susceptibilities about PM saddle points that we express using Landau parameters in Section 8.3.1. We, moreover, show the corresponding structure factors that are measurable quantities. In Section 8.3.2, we determine critical exponents of the divergences and also include susceptibilities about AFM ground states. Finally, we take a look at the dynamical conductivity, i.e., the linear response function to an external electric field, in Section 8.3.3.

8.3.1 Landau factors

We rewrite the static spin susceptibility, which adapts a scalar form due to the spin-rotation-symmetry of the PM mean-field background, in terms of the auxiliary function F_a [53, 127]

$$\chi_s(\boldsymbol{q}, \omega = 0) = \frac{\chi_0(\boldsymbol{q}, \omega = 0)}{1 + F_a(\boldsymbol{q})} \,, \tag{8.8a}$$

which is a generalization of the Landau factor known from FL-theory [48] to finite wave-vectors. The function $\chi_0(q)$ defines the bare susceptibility that can be interpreted as the response function of the non-interacting quasiparticle (QP) system, but it carries an indirect dependence of U due to the renormalization of the PM mean-field band structure (compare Section 5.3.2). A Landau factor of $F_a(q) = -1$ coincides with a diverging susceptibility and therefore signals a magnetic instability with the respective ordering vector $\boldsymbol{Q} = \boldsymbol{q}$, which is demonstrated in Figure 8.5(a) for an exemplary set of parameters. As discussed in Reference [53], this method can be applied to determine the whole PM phase boundary, and we find it to be perfectly consistent with the MF phase diagrams discussed in Section 8.2 for second-order phase boundaries, i.e., a divergence in $\chi_s(\omega = 0, \boldsymbol{q} = \boldsymbol{Q})$ coincides with the formation of a finite magnetization m with the magnetic MF ordering vector $\boldsymbol{Q}$. First-order phase transitions that come along with a discontinuity in m, however, are not directly visible to the fluctuation formalism because associated PM mean-field saddle-points feature a local minimum with a meta-stable ground state in that case.

Leading order frequency contributions can be considered with the Landau damping function $\Gamma(\boldsymbol{q}, \omega)$ and the parametrization

$$\chi_s(\boldsymbol{q}, \omega) = \frac{\chi_0(\boldsymbol{q}, \omega = 0)}{1 + F_a(\boldsymbol{q}) - \mathrm{i}\omega/\Gamma(\boldsymbol{q}, \omega)} \,. \tag{8.8b}$$

As exemplarily illustrated in Figure 8.5(b), we find $\Gamma(\boldsymbol{q}, 0) \propto |\boldsymbol{q}|$ for small $|\boldsymbol{q}|$, which hints towards a linear magnon dispersion relation that will be further discussed in Section 8.4. Moreover, we determine the Landau damping to be very high for momenta that are larger than the diameter of the FS.

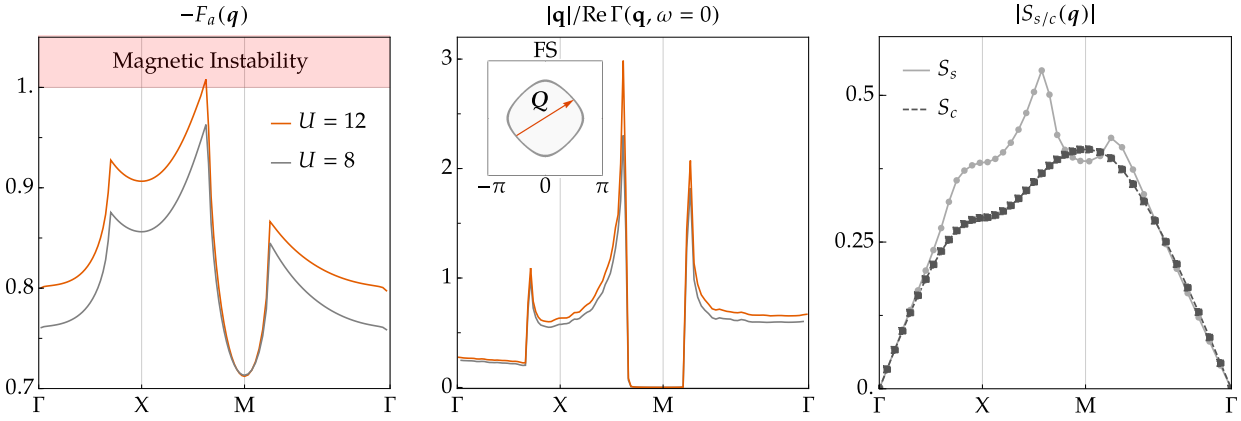

(a) Landau factor for $n = 0.6$, $t' = 0$ at zero temperature. A magnetic instability is implicated for $-F_a(q) \geq 1$.

(b) Rescaled inverse Landau damping for $n = 0.6$, $t' = 0$ at zero temperature.

(c) Spin and charge structure factor for $n = 0.6$, $t' = 0$ and $U = 8$ in the low temperature limit and Lorentzian broadening $\eta = 0.01$.

Figure 8.5: We present Landau factors for two different interactions, where the lower one supports a stable PM and the higher one indicates a magnetic phase transition towards an ICM with ordering vector $\boldsymbol{Q} \approx (\pi, 0.625\pi)^\top$. The determined critical interaction U_c and resulting ordering vector are in perfect agreement with the magnetic MF phase diagram displayed in Figure 8.3(b). The emerging order can be understood as a nesting effect, where $\boldsymbol{Q}$ connects large densities on the FS as shown in the inset of Figure 8.5(b). As expected, the Landau damping Γ becomes very high for momenta larger than the diameter of the FS. The magnetic instability is also visible in the spin structure factor, whereas the charge structure factor does not employ a sharp peak and is maximized around the M point. Figures adapted from [53].

Finally, Figure 8.5(c) shows the spin and charge structure factors [53]

$$S_{s,c}(\boldsymbol{q}) = -\int_0^\infty \frac{d\omega}{\pi} \,\mathrm{Im}\,\chi_{c,s}(\boldsymbol{q}, \omega + \mathrm{i}\eta)\,, \tag{8.9}$$

which are measurable quantities as explained in Section 5.3.1. While the charge structure factor $S_c(\boldsymbol{q})$ remains unobtrusive, the spin structure factor $S_c(\boldsymbol{q})$ also captures the enhancement around $\boldsymbol{q} = \boldsymbol{Q}$ that is found in the spin susceptibility. In general, we do not detect any charge instabilities within the PM domain, except for high temperatures in the vicinity of half-filling due to the Mott transition.

8.3.2 Critical exponents

We can describe the scaling law at the magnetic instability by expanding the spin susceptibility around the divergence with respective critical exponents α, β

$$\chi_s^{\mathrm{PM}}(\boldsymbol{Q}, \omega = 0) \propto |n - n_c|^{-\alpha}\,, \tag{8.10a}$$
$$\chi_s^{\mathrm{PM}}(\boldsymbol{Q}, \omega = 0) \propto (T - T_c)^{-\gamma}\,. \tag{8.10b}$$

As exemplarily shown in Figure 8.6(a), we can numerically evaluate them by fitting, and find $\alpha = 1/2$ for the ICM instability with $\boldsymbol{Q} = (\pi, Q)$ and $\alpha = 1$ for the AFM. The temperature scaling law was determined to be $\gamma = 1$ for both cases [53] like the Curie-Weiß law of FMs[1].

[1]Notice that $\chi_s^{\mathrm{PM}}(\boldsymbol{q} = 0, \omega = 0)$ does not diverge at AFM transitions, i.e., our results do not contradict the usual scaling laws regarding the Néel temperature [19].

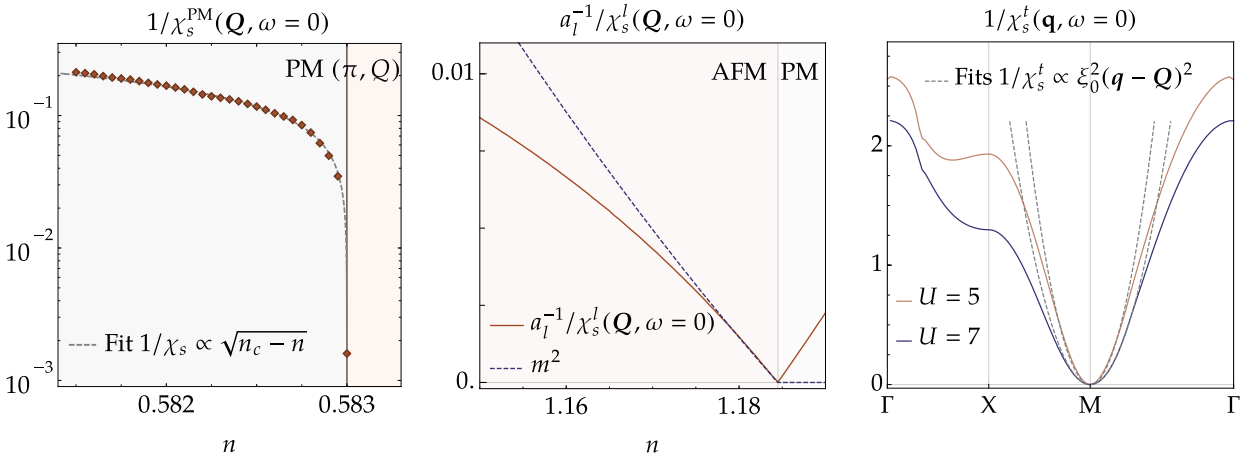

(a) Inverse spin susceptibility about the PM ground state for $t' = 0$ and $U = 12$ in the zero temperature limit.

(b) Inverse longitudinal spin susceptibility about an AFM ground state and magnetization for $t' = -0.2$, $U = 4.5$ and $T = 0.1$.

(c) Inverse transversal spin susceptibility about an AFM ground state for $t' = -0.2$, $n = 1.05$ and $T = 0.005$.

Figure 8.6: We demonstrate scaling laws of the spin susceptibility around the critical point of the magnetic phase transition as function of the electron filling n and momentum $\boldsymbol{q}$. Within the AFM domain that features a finite MF magnetization m, the spin susceptibility splits into a longitudinal and transversal component that become equivalent to the PM spin susceptibility as the magnetization vanishes. Figures adapted from References [53] and [55].

We moreover analyze the critical behavior of the susceptibility within the AFM ground state. With a finite MF magnetization, the spin susceptibility splits into a longitudinal component χ_s^l parallel to the polarization of the MF spins and a transversal part χ_s^t in the perpendicular plane, i.e., the full spin rotation symmetry in the PM is reduced to rotation symmetry in that plane. We demonstrate in Figures 8.6(b) and 8.6(c) that the scaling laws

$$\chi_s^l(\boldsymbol{q},\omega=0) = \frac{D(0)}{r + \xi_0^2(\boldsymbol{q}-\boldsymbol{Q})^2}\,, \tag{8.11a}$$

$$\chi_s^t(\boldsymbol{q},\omega=0) = \frac{D(0)}{\xi_0^2(\boldsymbol{q}-\boldsymbol{Q})^2}\,, \tag{8.11b}$$

which are also identified within random phase approximation (RPA) [127, 186] are fulfilled for $\boldsymbol{q} \approx \boldsymbol{Q}$ [55]. The parameter ξ_0 is the microscopic spin correlation length, and $D(0)$ is approximately given by the DOS at the Fermi level. The divergence of the longitudinal spin susceptibility disappears with a finite magnetization due to the coefficient r, which we find to be proportional to the magnetization squared $r = a_l m^2$ as expected [127]. The transversal component remains gapless and features a sharp divergence at $\boldsymbol{q} = \boldsymbol{Q}$ in the whole AFM domain. This remaining singularity is the Goldstone mode of the broken SU(2) symmetry and will be further discussed in the context of spin waves in Section 8.4. Whereas this magnon mode is part of a stable AFM, we also observe a breakdown of the magnetic MF ground state signaled by divergences in χ_s^l and χ_c at high U in the vicinity of half-filling. The resulting emerging order is inhomogeneous and will be further discussed in Section 8.5 and Chapter 9.

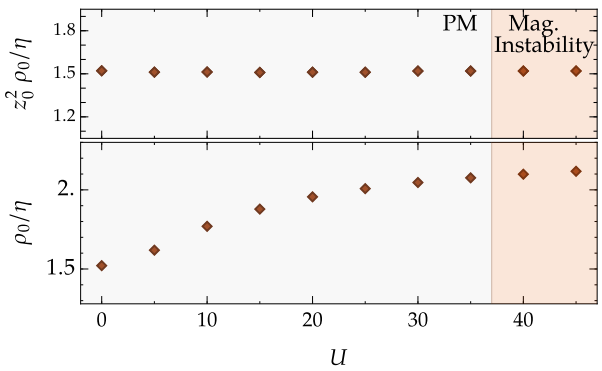

(a) Rescaled zero-temperature resistivity as function of U for $n = 0.5$.

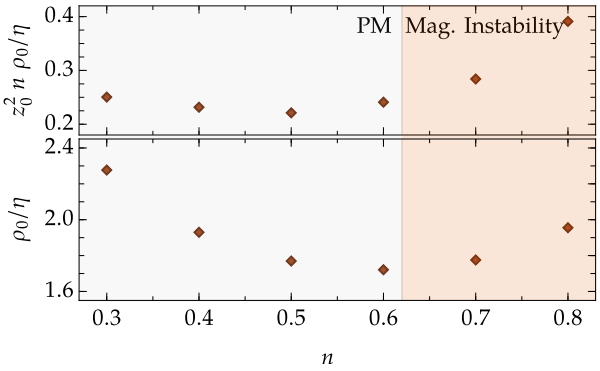

(b) Rescaled zero-temperature resistivity as function of n for $U = 10$.

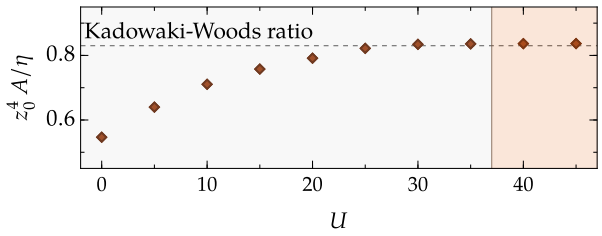

(c) Rescaled temperature-coefficient of the resistivity as function of U for $n = 0.5$.

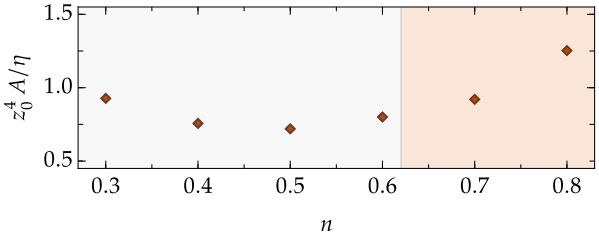

(d) Rescaled temperature-coefficient of the resistivity as function of n for $U = 10$.

Figure 8.7: We present the coefficients of the dc-resistivity $\rho(T) = \rho_0 + AT^2$ as function of filling and interaction for $t' = 0$ and $\eta = 0.1$. For the Hubbard model, the SB weight z_0 is related to the effective mass by $m_{\text{eff}} = z_0^{-2}$, and we find the Kadowaki-Woods ratio $A/m_{\text{eff}}^2 = \text{const.}$ to be fulfilled for large interactions U. The orange-colored part of the plots features a divergence in χ_s, i.e., the PM ground state that we assume for the calculation of the conductivity is to be understood as hypothetical. Figure adapted from [53].

8.3.3 Conductivity

The dynamical conductivity is the linear response function to an external electric field $\boldsymbol{j}(q) = \underline{\sigma}(q)\boldsymbol{E}_{\text{ext}}(q)$. It is not an independent susceptibility, but rather coupled to $\chi_c(q)$, i.e., the response function to an external electric potential ϕ_{ext}, by the relation $\boldsymbol{E}_{\text{ext}} = -\boldsymbol{\nabla}\phi_{\text{ext}}$. As shown in Section 5.3.2 their connection is given by

$$\sigma(\omega + \mathrm{i}\eta) = \lim_{\boldsymbol{q}\to 0} \frac{-\mathrm{i}\omega + \eta}{\boldsymbol{q}^2} \chi_c(\boldsymbol{q}, \omega + \mathrm{i}\eta) \,, \tag{8.12a}$$

where η is the broadening due to analytic continuation from Matsubara to real frequencies, and it needs to remain finite for the numerical evaluation. In Reference [53], we established the dynamical conductivity for PM ground states of the Hubbard model at low temperatures to fit a Drude model [14]

$$\sigma_D(\omega, \tau_s) = \frac{\sigma_0}{1 + \omega^2\tau_s^2} + \mathrm{i}\frac{\sigma_0\omega\tau_s}{1 + \omega^2\tau_s^2} \,, \tag{8.12b}$$

where the broadening is identified with the inverse scattering time $\eta = 1/\tau_s$. In agreement with the Drude model, we determine $\sigma_0 \to \infty$ for $\eta \to 0$, because our MF ground state does not feature a momentum dissipation mechanism like phonons or umklapp scattering. We find the temperature-dependence of the dc-resistivity [53]

$$\rho(T) = \frac{1}{\sigma_0(T)} = \rho_0 + AT^2 \,, \tag{8.12c}$$

which is the expected result for a Fermi liquid (FL), where the scattering rate of electrons is proportional to T^2. The dependence of the coefficients as a function of interaction and doping is shown in Figure 8.7. Notably, we observe $\rho_0 z_0^2$ to be almost independent of U, i.e., the dc-resistivity scales with the effective mass $\rho_0 \propto m_{\text{eff}}$, which is given by $m_{\text{eff}} = z_0^{-2}$ for the 2D Hubbard model. Moreover, the expression $n\rho_0/m_{\text{eff}}$ that is density-independent in the Drude model features a weak dependence on the electron filling n.

In 1968, it was observed by Michael Rice that there is a close scaling relation between the resistivity coefficient A and the coefficient γ in the electronic contribution to the specific heat of metals $C(T) = \gamma T$ [187]. It was generalized to heavy-fermion metals and is now known as Kadowaki-Woods ratio [188]

$$\frac{A}{\gamma^2} = \text{const.} \tag{8.12d}$$

and A can vary over eight orders of magnitude for different materials [48]. Since, it is $\gamma \propto D(0) \propto m_{\text{eff}} = z_0^{-2}$, Figure 8.7(c) demonstrates that the ratio is be fulfilled at high interactions. For future studies, it could be of interest to calculate the dc-resistivity for small dopings near the Mott transition at high temperatures to investigate if there is a switch towards a linear temperature dependence $\rho(T) = \rho_0 + BT$, which is observed in the *strange metal* phase of the HTCCs.

8.4 Excitation spectra and collective modes

In agreement with the interpretation of Pines and Bohm in 1953 [189], we find the excitation spectra of susceptibilities to be composed of a particle-hole continuum as a consequence of incoherent quasiparticle (QP) excitations (in our case initiated by the MF ground state) supplemented by sharp peaks that indicate collective excitations generated by fluctuations of the ground state (in our case Gaussian fluctuations about the saddle point). As we discussed in Section 5.3.3, such a collective mode is characterized by a coherent oscillation of a large number of electrons with the same wave-vector $\boldsymbol{q}$ and frequency ω in the absence of external fields [125]. The dispersion relation $\omega(\boldsymbol{q})$ is thus determined by poles of the respective susceptibility

$$1/\chi_{s,c}(\boldsymbol{q}, \omega) \to 0 \quad \Rightarrow \quad \text{Dispersion relation } \omega(\boldsymbol{q}) \text{ of the collective mode ,} \tag{8.13}$$

that we calculate according to Equation (8.7). Corresponding modes are identified with spin-density-waves (SDWs) for χ_s (also called magnons) and charge-density-waves (CDWs) for χ_c (also called plasmons) and turn into gapless Goldstone modes if the collective excitation occurs at zero frequency $\omega = 0$, which yields a phase transition as discussed in Section 8.3. In order to calculate susceptibilities at finite frequencies, we need to perform the analytical continuation $\mathrm{i}\omega_n \to \omega + \mathrm{i}\eta$, where the convergence parameter η plays the role of an inverse lifetime of the bosonic QP excitation that manifests in the imaginary part of the susceptibility in analogy to the spectral function for electrons. From a theoretical standpoint, the dynamics of the d-field are essential to describe collective modes because all other SB fields are static in the radial gauge. In the following, we will investigate the excitation spectra $\operatorname{Im}\chi(\boldsymbol{q}, \omega)$, where collective modes appear as bright lines, for PM and AFM ground states.

8.4.1 Paramagnetic ground states

Figure 8.8 shows the frequency-dependent spectrum of the charge susceptibility χ_c and bare susceptibility χ_0 on the high symmetry path of the BZ for $n = 0.6$ and different interactions. χ_0 can be thought of as

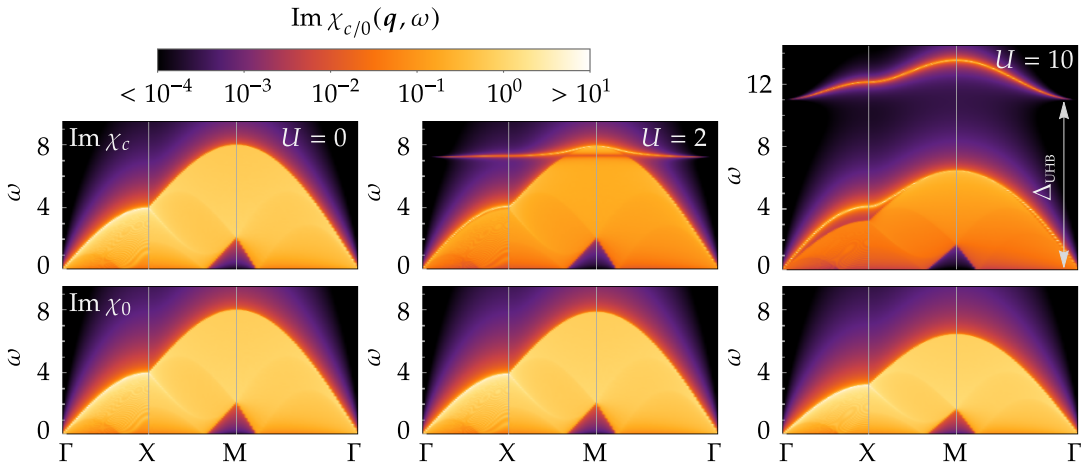

Figure 8.8: Imaginary part of the charge susceptibility (upper panel) and bare susceptibility (lower panel) for three different interactions at $n = 0.6$, $t' = 0$, $\eta = 0.005$ and zero temperature. Both quantities are equivalent in the limit of vanishing interactions and show a spectrum of continuous particle-hole excitations. At finite U, the charge susceptibility develops two collective modes that manifest as sharp, bright lines in the spectrum. The first one is called upper Hubbard band (UHB) and is situated at $\omega \approx U$ for high interactions U. The second one is of zero-sound type and manifests at the high-frequency edge of the particle-hole continuum. Figure adapted from [53, 57].

the susceptibility of the non-interacting system (equally for spin and charge) and does in opposite to χ_c not contain fluctuation effects of the SB fields. Expectedly, we find $\chi_c = \chi_0$ at $U = 0$ in agreement with the respective limit in RPA [53, 190]. Both quantities show a continuous particle-hole excitation spectrum, whose bandwidth (BW) is found to be $W = 8z_0^2$ and coincides with the BW of the underlying MF band structure according to Equation (8.2c) as expected[1]. For $U = 0$, the non-interacting limit $z_0 = 1$ is recovered, and the SB-weight z_0 decreases along with the BW for higher interactions (we find $z_0 \approx 0.9$ for $U = 10$). There is a gap around the M-point, because the diameter of the FS is smaller than the respective connecting momentum overlaps.

Fore finite interactions, we see a transfer of spectral weight into two emerging collective modes in the charge susceptibility that manifest as sharp peaks with a dispersion relation $\omega(\boldsymbol{q})$. Firstly, the upper Hubbard band (UHB) that is separated from the particle-hole continuum by a gap Δ_{UHB} that increases with interaction and approaches $\Delta_{\mathrm{UHB}} \approx U$ for large interactions [53, 190]. The gap can be understood in the limit of zero hopping ($t = 0$), where only two energy levels exist at $\omega = 0$, and $\omega = U$ and these flat bands are distorted by the delocalization of the electrons for finite t. We find the gap to grow with doping and the UHB mode to vanish at half-filling, and, notably, the feature is not captured by RPA calculations [190]. The second collective mode occurs at the upper edge of the particle-hole continuum and is called zero-sound mode because it features a linear dispersion relation for small momenta. Both collective modes vanish for $\boldsymbol{q} \to 0$ and at $\omega = 0$, i.e., there is no indication for a gapless charge instability.

[1]The bare susceptibility features an implicit dependence on U because of the renormalization of the MF band structure that represents an effectively non-interacting theory of fermionic QPs. The BW of χ_0, therefore, becomes interaction-dependent, even though it does not carry any information about Gaussian fluctuations.

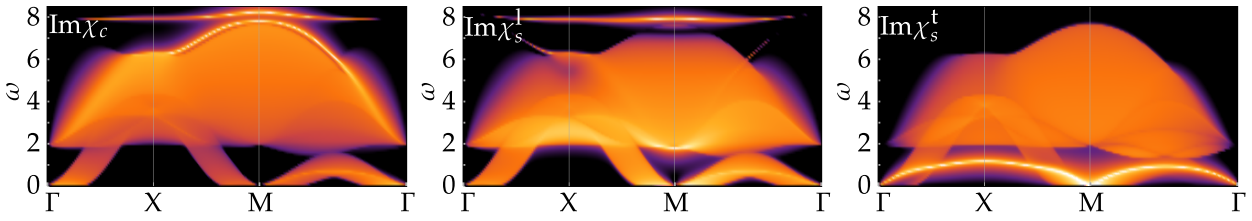

(a) Charge susceptibility with UHB and zero sound mode around the M-point.

(b) Longitudinal spin susceptibility with UHB and gapped magnon mode around the M-point.

(c) Transversal spin susceptibility with gapless mode around the M-point, affirming the AFM MF ground state.

Figure 8.9: We present the spectrum of the charge susceptibility and longitudinal & transversal spin susceptibility about a stable AFM ground state with $n = 1.05, U = 5, t' = -0.2, T = 0.005$ and $\eta = 0.01$. The particle-hole continuum features a gap, which is due to the band gap of the AFM band structure $\Delta^{\text{AFM}} \approx 2$, however, it only appears partially due to the finite doping. The color scheme is analogous to Figure 8.8. Figure adapted from [55].

8.4.2 Antiferromagnetic ground states

Now, we investigate the excitation spectrum for a stable AFM ground state[1] with small electron doping $n = 1.05$, $U = 5$ for the long-range hopping model $t' = -0.2$. As discussed earlier, the spin susceptibility is decomposed into a longitudinal part χ_s^l parallel to the MF magnetization and a transversal component χ_s^t perpendicular to it. As opposed to PM fluctuations, the spin and charge sector are coupled for the AFM ground state, which makes the analysis particularly interesting, and the respective spectra are shown in Figure 8.9.

First of all, we notice that all susceptibilities feature a partial energy gap in the particle-hole continuum that is due to the band gap of the AFM band structure $\Delta^{\text{AFM}} \approx 2$. For $\omega < \Delta^{\text{AFM}}$, only excitations in the conduction band contribute, whereas $\omega > \Delta^{\text{AFM}}$ also allows scattering processes in the valence band. At high frequencies, we identify the UHB in χ_c and χ_s^l, which was also visible in the charge susceptibility of PM ground states. The zero sound mode is recovered as well in χ_c, but the spectral weight is more concentrated around the M-point. The transversal spin susceptibility features a gapless SDW mode around the M-point, which of course coincides with the MF ordering vector of the AFM $\boldsymbol{Q} = (\pi, \pi)^\top$ and affirms the magnetic ground state. We determine the magnon dispersion relation by fitting and find the expected scaling [81, 127]

$$\omega^2 = c_t^2(\boldsymbol{q} - \boldsymbol{Q})^2 + \mathrm{i}\frac{\omega}{\tau_t} \tag{8.14a}$$

around the Goldstone-mode with spin-wave velocity $c_t \approx 1.32$ and QP lifetime $\tau_t \approx 100$ [55].

The longitudinal spin susceptibility χ_s^l also features a collective magnon mode around the M-point, but it becomes gapped at the magnetic phase transition, where the spin-rotation invariance (SRI) is broken due to the finite MF magnetization. The continuous opening of the gap Δ_{SDW} due to a second-order phase transition with increasing interaction U is demonstrated in Figure 8.10. By parameter fitting, we recover the dispersion relation [127]

$$\omega^2 = \Delta_{\text{SDW}}^2 + c_l^2(\boldsymbol{q} - \boldsymbol{Q})^2 + \mathrm{i}\frac{\omega}{\tau_l}\,. \tag{8.14b}$$

8.5 Phase separation and inhomogeneity

To conclude this chapter, we will investigate the origin of negative compressibilities $\kappa_T \propto \partial n/\partial \mu_0$ that we identified in parts of the magnetic phase diagrams discussed in Section 8.2. In a non-interacting system,

[1] i.e., it features a positive compressibility $\kappa_T > 0$ and no divergences in the static charge and longitudinal spin susceptibility.

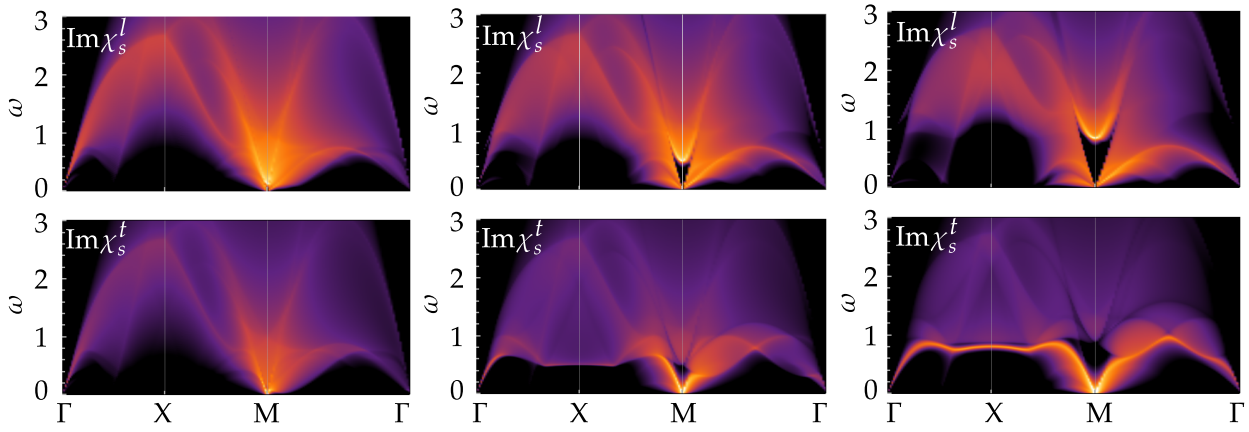

(a) U=3.25. **(b)** U=4.25. **(c)** U=5.25.

Figure 8.10: Longitudinal (χ_s^l) and transversal (χ_s^t) spin susceptibility about a stable AFM mean-field ground state for $n = 1.16, t' = -0.2, T = 0.005$ and $\eta = 0.01$ for different interactions U. At the magnetic phase transition and smaller interactions $U \lesssim 3.25$ it is $\chi_s^l = \chi_s^t$. For higher U, i.e., deeper in the magnetic phase, χ_s^l opens a gap, while χ_s^t remains to feature a gapless spin-density-wave (SDW) around the MF ordering vector $\boldsymbol{Q} = (\pi, \pi)^\top$. The color scheme is analogous to Figure 8.8. Figure adapted from [55].

statistical physics dictates that κ_T is always positive, i.e., a rise of the chemical potential increases the total electron filling, and it is guaranteed the function $n(\mu_0)$ is unique and invertible. This property allows for a Legendre transformation between the free energy (FE) $F^{(0)}(n, T)$ with base variable n and the grand potential (GP) $\Omega^{(0)}(\mu_0, T)$ that depends on the chemical potential μ_0

$$F^{(0)}(T, n) = \Omega^{(0)}(T, \mu_0) - \mu_0 \left(\frac{\partial \Omega^{(0)}}{\partial \mu_0} \right)_T = \Omega^{(0)}(T, \mu_0) + \mu_0 n \ , \tag{8.15}$$

for an equivalent description of the MF ground state for both thermodynamic potentials. Due to the interaction-induced renormalization of the band structure, however, it becomes possible that $\mu_0(n)$ is not a monotonous function, coinciding with discontinuities or divergent and negative domains of $\kappa_T(n)$, as illustrated in Figure 8.11 for $t' = -0.2$ and $U = 7$ by the red dotted line. This property results in a breakdown of the uniform statistical physics description, and the saddle points of both potentials are not equivalent. It is also directly tied to a FS instability in the charge channel since the compressibility is proportional to the static, uniform charge susceptibility

$$\kappa_T = \frac{1}{n^2} \frac{\partial n}{\partial \mu_0} \propto \chi_c(\boldsymbol{q} = 0, \omega = 0) \propto \left\langle (n - \langle n \rangle)^2 \right\rangle \ , \tag{8.16}$$

and also to the variance of the filling elaborated on in Section 4.6 from a theoretical perspective. This instability can be circumvented by phase separation (PS), i.e., an inhomogeneous spatial mixture of two different phases whose boundary effects are neglected within our MF description [55]. Classical examples for the same phenomenon are e.g., an emulsion of vinegar and oil, i.e., two liquids that do not mix, or the coexistence of the liquid and gas phase that can be described with the Van der Waals equation [191].

Specifically, in our case, the GP features a first-order phase transition with two different energy degenerate ground states $\Omega_1^{(0)}(T, \mu_0^c) = \Omega_2^{(0)}(T, \mu_0^c)$ at a critical chemical potential μ_0^c that yields two distinct fillings

$$n_{1/2} = -\left. \frac{\partial \Omega_{1/2}^{(0)}}{\partial \mu_0} \right|_{\mu_0^c} \ , \tag{8.17a}$$

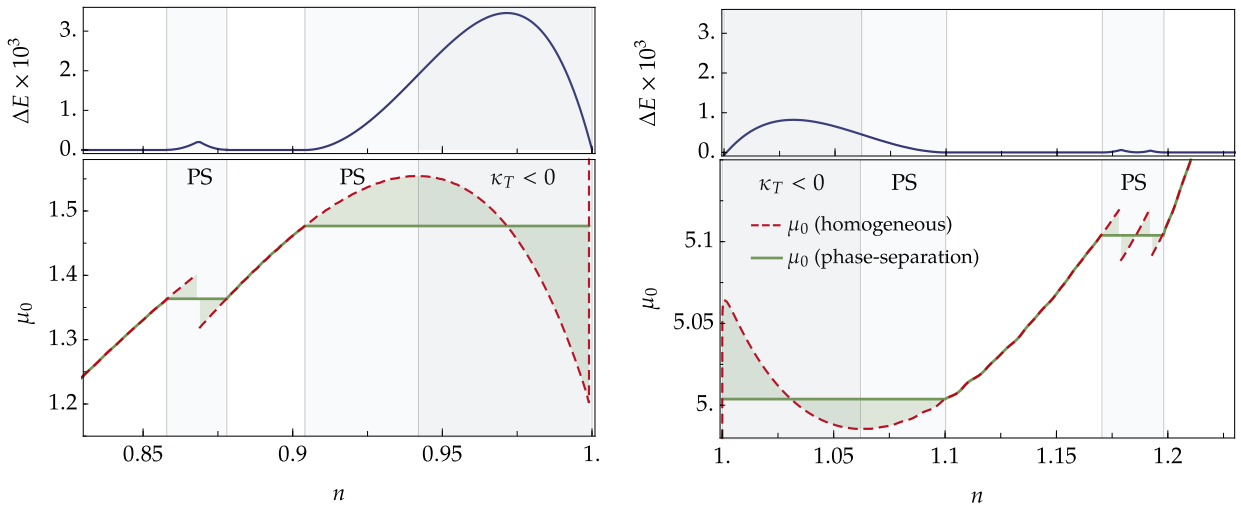

(a) The PS at lower filling is among the magnetic phases with ordering vectors $(\pi, Q)^\top + (Q, Q)^\top$ and $(\pi, Q)^\top +$ AFM for higher filling.

(b) The PS at lower filling is among the magnetic phases AFM + AFM and AFM + $(Q, Q)^\top$ & $(Q, Q)^\top + (\pi, Q)^\top$ for higher filling.

Figure 8.11: The lower panel shows the chemical potential μ_0 as a function of the filling as it is determined by the homogeneous ground state of the FE (red dashed line) for $U = 7$, $t' = -0.2$ and $T = 0.005$. It employs discontinuities and local extrema, which results in divergences and negative regimes of the electronic compressibility $\kappa_T \propto \partial n / \partial \mu_0$. The therefore implied FS instability can be circumvented by phase separation (PS) of two different, energy-degenerate ground states of the GP and a constant chemical potential within the phase separated ground state (green line). The upper panel shows the energy difference $\Delta E = F - \Omega$ between the homogeneous and inhomogeneous ground state and confirms that the phase-separated state minimizes the energy, which was also proven analytically in Section 4.6.

resulting in a discontinuity of n, with $n_1 < n_2$ w.l.o.g. There is no uniform ground state of the GP for fillings in between. Those can, however, be recovered by PS of the two degenerate states

$$\Omega_{\text{PS}}^{(0)} = x\Omega_1^{(0)} + (1-x)\Omega_2^{(0)} \quad \Longrightarrow \quad n = xn_1 + (1-x)n_2 \,, \tag{8.17b}$$

at the constant chemical potential $\mu_0 = \mu_0^c$, and $x \in [0, 1]$ represents the proportion of the phase volume of $\Omega_1^{(0)}$ in the crystal. The respective chemical potential as a function of the filling is shown in green in Figure 8.11, and it differs from the chemical potential of the uniform ground state of the FE only in the phase-separated domains. The critical fillings $n_{1/2}$ can equivalently be determined without explicit knowledge of the GP by a Maxwell construction, where the green areas below and above μ_0^c have to be equal in size [compare Equation (4.39)]. We have proven in Section 4.6 that the phase-separated ground state indeed minimizes the energy in comparison to the uniform saddle point of the FE and the respective condensation energy is displayed in the upper panel of Figure 8.11. Since an explicit FS instability is only present for $\kappa_T^{-1} \leq 0$ (annotated by dark gray areas) according to Equation (8.16), the uniform ground state can be considered to be meta-stable in the remaining part of the phase-separated domain (annotated by light gray areas).

The resulting low-temperature phase diagram that considers PS is shown in Figure 8.12(a) for $t' = -0.2$ and electron-doping. The PS in the vicinity of half-filling is due to domains with negative compressibility of the homogeneous state and will be further discussed in the following. On the other side, the PS occurring for $n > 1.15$ is due to a discontinuity of $\mu_0(n)$. It is less relevant because the condensation energy is much smaller (compare Figure 8.11), the explicit FS instability only happens at a single point of the homogeneous ground state, and the large doping is of minor interest for the high-T_c cuprates (HTCCs). The $\text{AFM}_1 + \text{AFM}_2$ state in the

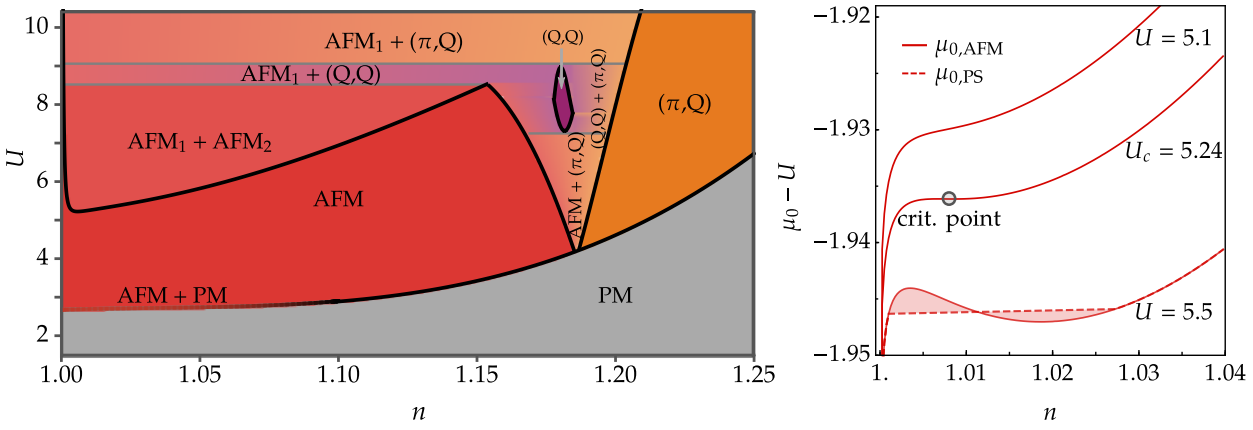

(a) The phase transition from PM to AFM is of first-order, with a large jump in magnetization around $n = 1$ that decreases for higher filling and becomes a second-order transition at $n \approx 1.15$.

(b) The compressibility κ_T diverges at the critical point ($n_c = 1.008, U_c = 5.24$) and other points with $\partial\mu_0/\partial n = 0$, which signals the onset of PS.

Figure 8.12: Electron-doped magnetic phase diagram for $t' = -0.2$ and $T = 0.005$, where domains of negative compressibility featured in Figure 8.3(a) are circumvented by phase separation (PS) of two individually stable, homogeneous phases. This approach, however, neglects the impact of phase boundaries that are expected to increase the true ground state energy. Figure adapted from [55].

underdoped regime is of special interest because that part of the HTCC phase diagram is known to feature AFM ordering, and nanoscale phase separation has actually been observed by ARPES measurements for $n < 1.125$ [162] and various other types of charge inhomogeneities have also been reported [120, 140, 192, 193]. The critical interaction that marks the onset of that type of PS is found to be $U_c \approx 5.24$ and coincides with a saddle point of $\mu_0(n_c)$ and a divergence of κ_T as illustrated in Figure 8.12(b). For higher U, the saddle point splits into two extrema with $\kappa_T < 0$ in between, and the singularity disappears for $U < U_c$. Figure 8.13(a) shows the static charge susceptibility at the critical filling n_c for two different interactions, and we identify a divergence at the Γ-point in agreement with Equation (8.16) as expected[1]. The fluctuation results are, therefore, fully consistent with the MF analysis in the context of PS. We moreover find the two mixing phases $\text{AFM}_{1/2}$ to be individually stable, i.e., they do not feature divergences in the static charge or longitudinal spin susceptibility. The MF properties of the two different AFM ground states allow for a better understanding of the ordering mechanism. AFM_1, for all interactions, represents a half-filled state ($n_1 = 1$) with a very high magnetization, where $\mu_{0,1}$ is situated at the lower edge of the conduction band. Thereby, doped electrons are fully absorbed in AFM_2, with $n_2 > 1$ and a much lower magnetization. In conclusion, doped electrons hinder the "ideal" characteristics of the AFM, where neighbored sites are occupied by exactly one electron with opposite spin, which is reflected by the decrease in magnetization for larger doping. Thus it is energetically favorable to partly recover the "ideal" half-filled AFM in specific domains of the real-space crystal in the sense of PS at high interactions in comparison to the homogeneous state, where doped electrons are distributed evenly.

Similar results w.r.t. PS have been reported in previous SB studies, which also show the hole-doped phase diagram in agreement with our conclusion but lack the $\text{AFM}_1 + \text{AFM}_2$ phase for electron-doping [53, 71, 105, 111, 182]. For hole-doping, we find PS of the magnetic phases[2] $(\text{Q,Q})^\top + \text{AFM}_1$. A proper fluctuation

[1] In general, such a divergence of $\chi_c(\boldsymbol{q} = 0, \omega = 0)$ could also be explained by a Pomeranchuk instability and emerging nematic order [194]. We therefore investigated lattice symmetry breaking order parameters ϵ like $\xi(\boldsymbol{k}) \to \xi(\boldsymbol{k}) + \epsilon(\cos k_x - \cos k_y)$ and found $\lim_{\epsilon\to 0} \partial F(\epsilon)/\partial\epsilon = 0$, i.e., we could not find a propensity for this type of order on MF level.

[2] For the hole-doped part, the chemical potential of the AFM_1 phase is of course situated at the upper edge of the valence band, but it also features half-filling and similarly large magnetization like the electron-doped part.

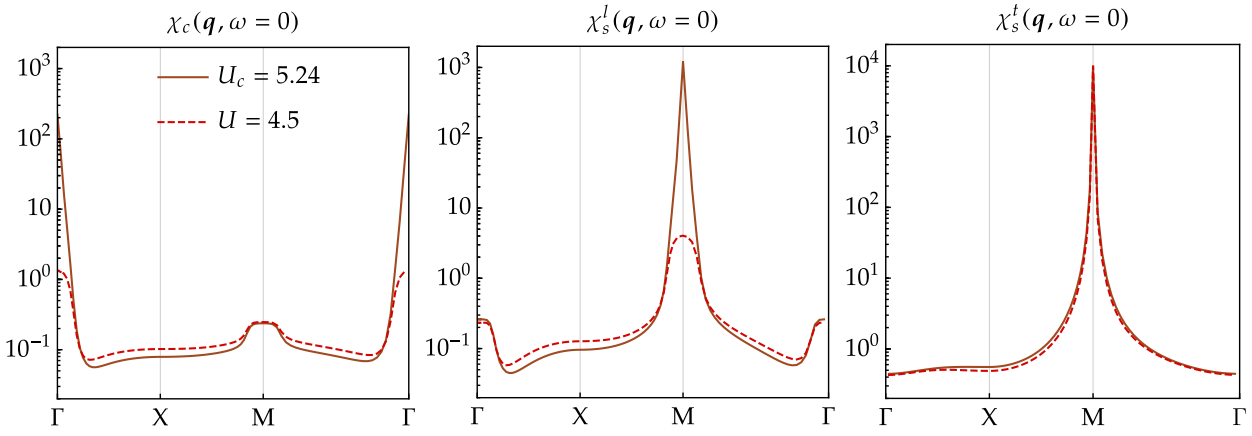

(a) Charge susceptibility. **(b)** Longitudinal spin susceptibility. **(c)** Transversal spin susceptibility.

Figure 8.13: Static susceptibilities on the high symmetry path of the BZ for $n_c = 1.008, t' = -0.2, T = 0.005$ and two different interactions. The charge susceptibility diverges at the Γ point for $U \geq U_c$, which implicates the onset of PS in agreement with the MF results. The longitudinal spin susceptibility also diverges for $U \geq U_c$ around the M-point due to the coupling of the spin and charge sector. The transversal spin susceptibility employs a pole at the M-point for both interactions, which affirms the underlying AFM ground state. Figure adapted from [55].

analysis for these phases, however, cannot be provided because the homogeneous ground state of the FE is an incommensurate magnet that cannot properly be tracked with the existing formalism. The onset of PS has also been observed by different theoretical methods like DMFT+QMC in the PM domain of the Hubbard model, which predicts a coexistence of insulating and metallic phases connected by a first-order transition in the context of a diverging compressibility that could explain the volume collapse in Cerium [195]. Moreover, other studies report a reentrant behavior of the PS w.r.t. temperature, i.e., its disappearance at $T = 0$ and very high temperatures, and support the particle-hole asymmetry that we also find [196–198]. For the SB formalism, PS also vanishes for high temperatures, but remains present in the limit $T \to 0$. The biggest omission of the described MF phase separation is that boundary effects between the mixing phases are neglected, which motivates a quantitative comparison with other methods and a more refined approach to investigate domain walls. We already provided such a benchmark at half-filling in Figure 8.2. Although there is fewer data available for finite doping due to limitations of many theoretical methods, there are suitable results from a DMET [41] and SB cluster study [139] that we investigate in the following.

Figure 8.14(a) compares the SB ground state free energy (FE) with the corresponding FE from DMET on a cluster with 16 lattice sites at $U = 6$. Similar to the half-filled case discussed in Figure 8.2, the DMET energy is smaller because it considers fluctuations effects that are neglected for the MF approach and lower the ground state energy. Moreover, DMET also includes superconducting order that is expected for $n \lesssim 0.85$ and not captured by the SB method, which questions the validity of a direct comparison. On the other hand, we find the ordering vector of the occurring $(\pi, Q)^\top$ MF phases to fit surprisingly well to the spin profile of the DMET benchmark data, if the periodicity implied by Q approximately fits the applied 2×8 cluster size. We also observe a strong correlation between inhomogeneous order in DMET and a negative compressibility within the SB formalism [53]. The ordering vectors within the $(Q, Q)^\top$ phase, however, does match the DMET spin order. Coincidently, there are enhanced inconsistencies between 2×8 and 4×4 clusters [41], which is a sign of finite size problems due to large magnetic unit cells that are predicted by the SB theory.

Figure 8.14(b) shows the ground state FE of a slave-boson MF cluster study that combines AFM order with charge stripes and domain walls, featuring up to 32 lattice sites per unit cell at $U = 12$ [139]. Remarkably, it

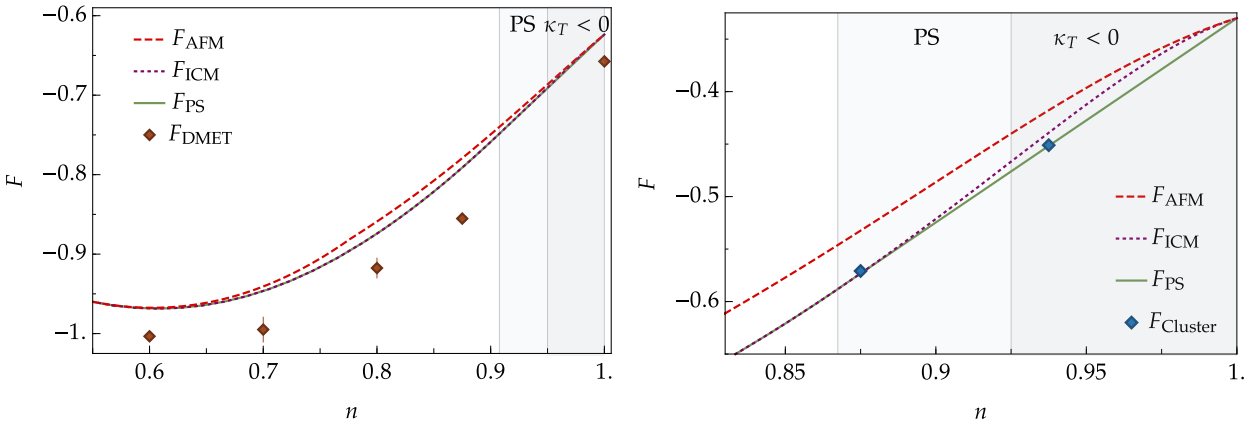

(a) Comparison of the FE for different MF saddle points and a DMET study for $t' = -0.2$ and $U = 6$ in the zero-temperature limit.

(b) Comparison of the FE for different MF saddle points for $t' = -0.2$ and $U = 12$ in the zero-temperature limit.

Figure 8.14: Quantitative comparison of the homogeneous and inhomogeneous SB mean-field ground state energy with other theoretical methods for hole-doping. Figure 8.14(a) shows DMET data from Reference [41] for a system with 16 lattice sites. The corresponding ground state energy is 3 to 8% lower than the SB results because it also considers superconducting order and fluctuation contributions. It may, however, be limited w.r.t. inhomogeneous order due to the associated small number of lattice sites. Figure 8.14(b) shows benchmark data from a SB mean-field cluster study [139] with up to 32 lattice sites per unit cell that features combined spin and charge-order with almost the same FE as our phase-separated ground state.

almost exactly matches the FE of the phase-separated ground state at the two available fillings. This could indicate that the true unit cell is larger 32 sites and that PS is indeed a strong tool to approximate the ground state. We will further investigate emerging charge-order (CO) and domain walls via fluctuations on the metastable, homogeneous MF saddle point in Chapter 9 and directly compare the results with experimental findings in the HTCCs.

CHAPTER 9

Intertwined spin and charge order in the electron-doped high-T_c cuprates

In Chapters 6 and 7, we learned that the Hubbard model – with its competing kinetic and potential energy scales – is archetypical to study itinerant, correlation induced, ordering phenomena and that it acts as a minimal model to describe the high-T_c cuprates (HTCCs) and their plethora of different phases. Subsequently, we presented a comprehensive slave-boson analysis of the 2D Hubbard model, with a focus on magnetic phases and phase separation (PS) in Chapter 8. This chapter will complement our investigation by discussing charge-density-waves (CDWs) that emerge on top of the antiferromagnetic ground state. Such phases of intertwined spin and charge order have been observed in the HTCCs [120, 140, 161, 192, 193], and we will show that our results are in remarkable agreement with recent experimental findings [120]. There is a high interest in demystifying this type of order because it is on the one side believed to be competing with superconductivity (SC) or on the other side may also synergize as superconducting pairing glue [174, 175, 183–185]. Moreover, we will present a temperature-dependent phase diagram that includes charge-order (CO), and we will elaborate on two further experimental observables, the magnetization, and specific heat.

9.1 Competing types of charge-order

In Section 8.5, we identified a domain of PS for small electron doping $\delta \lesssim 0.15$, where an undoped AFM (AFM_1, $n_1 = 1$) state mixes inhomogeneously with another AFM state (AFM_2, $n_2 = 1 + \delta$) that carries the additional doped electrons with a lower magnetization. The instability of the homogeneous ground state w.r.t. PS is signaled by a diverging compressibility $1/\kappa_T = 0$ or equivalently a pole of the static charge susceptibility at the Γ-point: $1/\chi_c(0,0) = 0$. However, for slightly smaller interactions, there is a metastable domain of the homogeneous AFM with finite κ_T, despite the phase-separated state being lower in energy. We analyzed static susceptibilities based on those meta-stable saddle points of the free energy (FE) at finite momenta to investigate further FS instabilities beyond the MF phase separation that unfortunately neglects boundary effects. We, indeed, find divergences of $\chi_c(\boldsymbol{Q}^c, \omega = 0)$ on the Γ-X high symmetry line (HSL)[1]. These imply an intertwining of spin and charge order, whose spatial periodicity is determined by the charge ordering vector $\boldsymbol{Q}^c$. Corresponding behavior has been measured in the HTCCs via resonant X-ray scattering (RXS) [120, 140, 161, 193], and it has been an open question if the phenomenon can be attributed to FS-nesting effects [120]. We even find two distinct peaks that can be identified as bright features in Figure 9.1(a), which exemplarily

[1]The longitudinal static spin susceptibility diverges coincidingly with the static charge susceptibility and a momentum shift $\chi_c(\boldsymbol{Q}, 0) \leftrightarrow \chi_s^l(\boldsymbol{Q} + \text{M}, 0)$ due to the spin-charge coupling in the AFM mean-field ground state. As discussed previously, the static transversal spin susceptibility features a sharp divergence at the M-point, incorporating the Goldstone mode of the symmetry broken AFM.

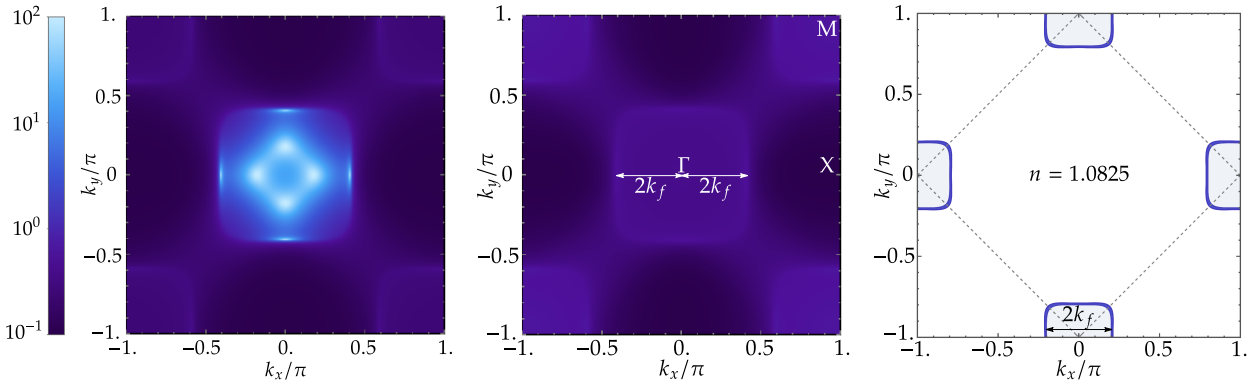

(a) Charge susceptibility $\chi_c(\boldsymbol{q}, \omega = 0)$. **(b)** Bare susceptibility $\chi_0(\boldsymbol{q}, \omega = 0)$. **(c)** AFM Fermi surface.

Figure 9.1: Static charge & bare susceptibility in the BZ, and Fermi surface (FS) of the underlying AFM ground state for $n = 1.0825, U = 6.6, t' = -0.15$ and $T = 0.005$ in the extended zone scheme. The bare susceptibility employs a flat maximum as the consequence of a FS nesting effect with $|\boldsymbol{q}| \approx 2k_f$. The charge susceptibility on the other hand is significantly enhanced in the vicinity of the Γ-point and features two sharp peaks in particular that indicate charge instabilities. The first occurs at $\boldsymbol{Q}_1^c \approx (0, 2k_f)$ and can be attributed to the nesting. The second is broader with a smaller ordering vector $\boldsymbol{Q}_2^c \approx (0, 0.17\pi)$ and cannot be understood as a FS effect.

shows the charge susceptibility in the Brillouin zone (BZ) within the extended zone scheme for $\delta = 0.0825$[1]. Moreover, Figure 9.1(b) illustrates the static bare susceptibility $\chi_0(\boldsymbol{q})$ that can be considered as the response function of the effectively non-interacting MF quasiparticle band structure. It does, in general, not feature divergences but is suitable to quantify FS nesting. The corresponding FS is displayed in Figure 9.1(c) and employs a large momentum overlap for $|\Delta\boldsymbol{q}| = 2k_f$ due to its almost square-like shape that we find to be in good agreement with previous studies including experimental ARPES data [120, 140]. The resulting finite, nesting induced, peak can be seen in $\chi_0(2k_f)$ as well as $\chi_s^t(\boldsymbol{Q}_1^c)$, and $\chi_s^l(\boldsymbol{Q}_1^c)$ and leads to a very sharp divergence of χ_c at $\boldsymbol{Q}_1^c \approx (2k_f, 0)^\top$. On the other hand, the second pole of $\chi_c(\boldsymbol{Q}_2^c)$ is broader, happens at lower momentum[2] $Q_2^c < Q_1^c$ and cannot be explained by nesting since the bare or spin susceptibility does not have a similar feature.

The resulting charge-ordering vectors $\boldsymbol{Q}_{1,2}^c$ at the respective critical interaction U_c with $\chi_c^{-1}(\boldsymbol{Q}_{1,2}^c) = 0$ as a function of the electron filling n are illustrated in Figure 9.2(a). A dashed line visualizes the leading ordering vector at the corresponding filling, and we detect a discontinuous jump from Q_2^c to Q_1^c at $n \approx 1.1$. These findings suggest that CO in the HTCCs is determined by multiple competing effects, which has also recently been hypothesized for the hole-doped regime, due to the detection of non-monotonous behavior of $\boldsymbol{Q}^c$ [193]. The interaction-dependent phase diagram that accounts for the results of the previously discussed susceptibility analysis, as well as phase separation, and homogeneous AFM ground states, is given by Figure 9.2(b). We cannot provide a precise distinction between PS and CDW phases for $U > U_c$ as indicated by the dotted line because our formalism does not allow investigating the emerging, symmetry broken state beyond the nature of the leading instability.

According to Luttinger's theorem, the area enclosed by the FS is proportional to the doping, which implies $2k_f \propto \sqrt{2\delta}$ in our case with the assumption of a square-shaped FS. As illustrated in Figure 9.2(a), Q_1^c closely follows that curve, which further supports the claim of a nesting effect, and it shows remarkable quantitative agreement with RXS measurements of the CO wavevector in $Nd_{2-x}Ce_xCuO_4$ (NCCO) [120]. With decreasing doping, the respective peak loses spectral weight, as itinerant degrees of freedom become less dominant

[1] Due to C_{4v} symmetry, on eights of the BZ is sufficient to describe the system, i.e., only two of the eight bright peaks are independent.
[2] We define $\boldsymbol{Q}_{1,2}^c = (Q_{1,2}^c, 0)^\top$.

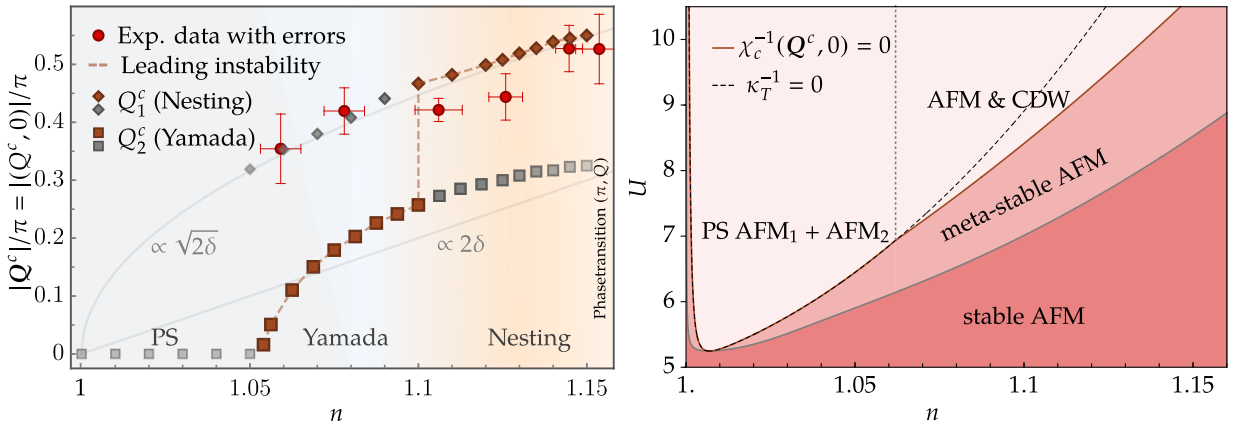

(a) Ordering vector of the CDW that emerges about the AFM mean-field ground state at $U = U_c$. We find two distinct peaks with a transition of the leading instability at $n \approx 1.1$. Experimental RXS data of $\boldsymbol{Q}^c$ from [120]. Figure adapted from [200].

(b) The homogeneous, meta-stable AFM is a local minimum of the FE that does not feature explicit FS instabilities, despite the global minimum being the phase-separated state. $\chi_c^{-1}(\boldsymbol{Q}^c, 0) = 0$ defines U_c applied in Figure 9.2(a). Figure adapted from [55].

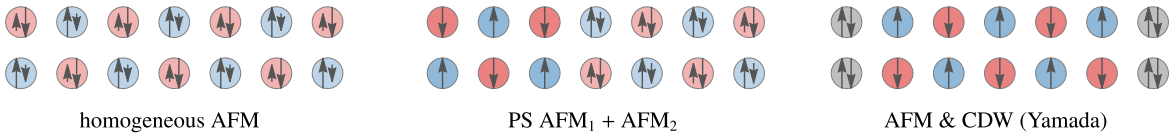

(c) Schematic illustration of three different types of doped AFMs in real space. Figure adapted from [57].

Figure 9.2: Charge instabilities emerging on the AFM ground state for $t' = -0.2$ and $T = 0.005$ as a function of the electron-doping and interaction. According to ab initio data, the NN transfer integral can be estimated by $t \approx -0.46eV$ [170, 201], i.e., the applied temperature translates to roughly 25 Kelvin. The onset of PS is signaled by a diverging electronic compressibility κ_T, coinciding with poles of the static charge susceptibility at zero momentum. CDWs that are found for $n \gtrsim 1.05$, whose ordering vectors $\boldsymbol{Q}_{1,2}^c$ are shown in Figure 9.2(a), yield from divergences of the charge susceptibility at finite momentum at a lower interaction.

closer to half-filling, and it disappears entirely at $\delta \lesssim 0.05$, where the FS becomes circular. The behavior of the second peak features $Q_2^c/\pi \approx 2\delta$ for intermediate dopings [55], reminiscent of the so-called Yamada relation known from the hole-doped HTCCs [199]. Q_2^c approaches zero at $\delta \approx 0.055$ in a square-root-like functional behavior, which we interpret as the transition from a CDW to PS. Fulfillment of the Yamada relation implies a periodic length of the emerging charge-ordered unit cell, which is inversely proportional to the doping $Q_2^c/\pi = 2\delta \Leftrightarrow P = 1/\delta$. Thereby, the doped charges can be distributed by the formation of vertical, doubly occupied domain walls at the edge of the unit cell, while recovering the undoped AFM in between as illustrated in Figure 9.2(c) [55, 200].

To sum up, we identify three different types of COs that emerge within the doped AFM ground state at sufficiently high interaction. According to our results, these ordering mechanisms are driven by partially restoring the "*ideal*", half-filled AFM in the real-space lattice by clustering the doped charges. The half-filled Hubbard model is reduced to an AFM Heisenberg model in the limit of infinite interactions, where the itinerant degrees of freedom are frozen out and the potential energy can be minimized by the formation of the antiferromagnetism. If the interaction is sufficiently low ($U \lesssim 5.25$), this localized picture is not yet accurate and the doped electrons distribute uniformly to form a stable AFM with a reduced MF magnetization (compare Figure 9.2(c), left). Above the critical interaction we observe that small doping ($\delta \lesssim 0.05$) leads to PS, where the half-filled AFM is retained in the major part of the lattice in order to minimize potential energy,

and the doped charges are randomly distributed to form islands of a weaker magnetized AFM (compare Figure 9.2(c), middle). For slightly larger doping ($0.05 \lesssim \delta \lesssim 0.1$), this behavior is succeeded by the formation of a periodic CDW, whose ordering vector approximately satisfies the Yamada relation, which we interpret as the emergence of doubly occupied domain walls in order to once more partially recover the half-filled AFM (Figure 9.2(c), right). As the kinetic energy of the electrons becomes more important with larger doping, there is a transition towards the nesting-enabled CO, which we interpret as an itinerant CDW, where the previously described localized picture is not accurate anymore. These results pose the question, of why there is yet no hard experimental evidence for the Yamada-type CO on the electron-doped side. Possible explanations could be shortcomings of our theoretical description, crystal defects that hinder the formation of the domain walls, or an interplay with the pseudogap (PG) phase. Especially the relevance of CO for PG physics should be further investigated because the domain walls, as well as the partially restored half-filled AFM, could hinder electron transport or reduce the DOS at the Fermi level. Moreover, we find PS and the Yamada-type CO associated with this behavior to persist up to much higher temperatures than the nesting-enabled CO [200], which is further reminiscent of the PG appearance.

Finally, we provide a rough approximation of the estimated difference in ground state energies of the uniform AFM compared to the Yamada-type intertwined AFM and CDW at high interactions in the localized picture. Thereby, we consider the spin-exchange of a $t-J$ model that describes the Hubbard model in the strong-coupling limit in the vicinity of half-filling [81]. Furthermore, we neglect the kinetic part ($t \to 0$) and apply the SB mean-field approach, assuming AFM order:

$$H^{\text{loc.}} = |J| \sum_{<ij>} \left(\hat{\mathbf{S}}_i \hat{\mathbf{S}}_j - \frac{1}{4} \hat{n}_i \hat{n}_j \right) \to - |J| \sum_{<ij>} \left(p_i^2 p_{0,i}^2 + \frac{1}{4} n_i n_j \right) . \tag{9.1a}$$

Moreover, we presume there to be no empty sites ($e = 0$), and the MF spin $S = pp_0$ to be maximized in the homogeneous AFM, which implies $p_0 = p$ and yields $pp_0 = (1 - n/2)$ under consideration of the SB constraints given by Equations (4.26a) and (4.26b). Under these conditions, we find

$$H^{\text{loc.}}_{\text{hom.}} \to - |J| \, N \left[2 + 2(n-1)^2 \right] , \tag{9.1b}$$

where N is the number of lattice sites. In order to compute the MF energy of the domain wall structure illustrated on the right side of Figure 9.2(c), we need to calculate the energy of the unit cell[1] and multiply it with the number of unit cells, i.e., $N\delta/2 = N(n-1)/2$, according to the Yamada relation. The result is given by

$$H^{\text{loc.}}_{\text{CDW}} \to - |J| \, N \, (1 + n) , \tag{9.1c}$$

and thus the energy is minimized for the vertical stripe phase in the underdoped regime ($H^{\text{loc.}}_{\text{CDW}} < H^{\text{loc.}}_{\text{hom.}}$), which is also supported by a SB mean-field cluster study for hole doping [139]. Unlike our MF description of phase separation, this emerging CDW takes boundary effects into account and is more sophisticated in that sense. It, however, becomes less efficient for small dopings because of the respective large unit cells, which could explain why the stripe order disappears for $n \lesssim 0.055$. After all, the presented SB method is viable for the types of order associated with the underdoped HTCCs because it does not suffer from finite-size effects, unlike other approaches like, e.g., QMC or DMET, and our results are supported by experimental evidence.

[1] This can conveniently be done by considering the energy of the half-filled AFM, which is given by $-2\,|J|\,N$ and taking the energy differences into account that appear due to the doubly occupied domain walls.

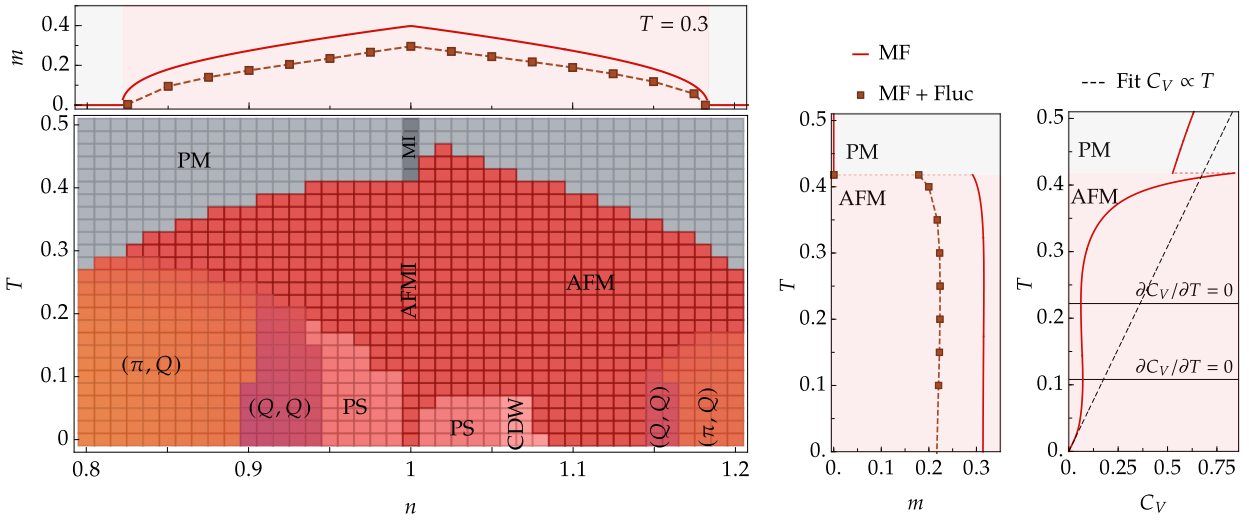

(a) The phase transition from the PM to the AFM is of first order, with a maximized gap around half-filling due to the Mott parent state.

(b) Magnetization for $n = 1.07$.

(c) Specific heat for $n = 1.07$.

Figure 9.3: Temperature-dependent SB analysis for $U = 6.5$ and $t' = -0.15$. Except for superconducting phases, which are excluded in our SB analysis, the phase diagram in Figure 9.3(a) qualitatively resembles the generic HTCC phase diagram shown in Figure 7.2(b). However, magnetism seems to occupy a larger domain than expected, which may be due to a bias of the SB method, and we find the MF magnetization to be significantly reduced by fluctuations, as shown in the upper panel of Figure 9.3(a) and Figure 9.3(b). In addition, the specific heat employs anomalous behavior with a local maximum at low temperatures near emerging PS and CDW phases but recovers the linear dependence $C_V \propto T$ in the limit $T \to 0$.

9.2 Temperature-dependent phase diagram

To conclude, we examine the temperature-dependence of crucial, experimentally accessible quantities for an exemplary set of parameters, i.e., $U = 6.5$ and $t' = -0.15$. Figure 9.3(a) shows the temperature- and doping-dependent phase diagram under consideration of the aforementioned charge-inhomogeneous phases. Excluding superconductivity, it qualitatively resembles the generic HTCC phase diagram in Section 7.2, since we identify domes of charge-order in the underdoped regime and a stronger propensity towards AFM order for electron-doping. As discussed earlier, the type of CDWs that we predict is affirmed by experiments in the HTCCs [120, 140, 161, 192, 193], and also nanoscale PS has been reported [133, 162]. However, apart from the fact that we cannot directly track superconductivity with the SB method, we observe the general trend that the phase volume of magnetic domains is overestimated. This may be due to a bias of the chosen MF, and thereby we find the magnetization to be significantly reduced by fluctuation corrections, as shown in the upper panel of Figure 9.3(a) and Figure 9.3(b). Furthermore, ab initio calculations suggest that the effective interaction decreases with doping [201], which could further reduce the propensity towards magnetism away from half-filling.

Finally, we calculate the specific heat according to Section 4.6.3 and observe anomalous, plateau-like behavior with a local maximum at low temperatures ($T \approx 0.108$) that appears coincidingly with the emergence

of charge-inhomogeneous phases (i.e., CDWs and PS), as shown in Figure 9.3(c)[1]. Similar properties of the specific heat have been reported in the pseudogap (PG) phase, which is associated with a partial reduction of the electronic DOS [171, 172, 202]. Moreover, theoretical studies suggest that charge-ordered phases can open such partial gaps at the Fermi energy [139], and their relevance to understanding PG physics is debated in the current literature. We find the charge-ordered domain to extend towards higher temperatures if the interaction is increased and note that the presented U is rather on the lower end of the expected range of the one-band HTCC model. Some estimations yield that it could be as high 12 [139, 170] and possibly doping-dependent [140]. The enhancement of C_V at the magnetic transition can be explained by magnon contributions to the specific heat [203], and the usual behavior $C_V = \gamma T$ is recovered at sufficiently low temperatures. For future studies, it could be interesting to study the temperature-dependence of the conductivity in analogy to Section 8.3.3, but in proximity to half-filling and at higher temperatures, in order to investigate if there is a transition towards a strange-metal phase.

[1]It is noteworthy that the local maximum only appears, if the implicit temperature dependence of the SB mean-field variables is considered ($\partial p/\partial T \neq 0$, etc.). If that dependence is neglected, C_V resembles a free electron gas at low temperatures.

III

Magnetism and topology in Kondo materials

In this part, we discuss interaction-dependent properties of Kondo materials by means of the slave-boson method. First, we elaborate on the underlying Kondo effect, emphasize its relevance in the current literature and introduce commonly applied microscopic models to describe the problem. We then investigate Kondo metals in the context of heavy fermions, magnetic order, and an effective RKKY-interaction based on the doped periodic Anderson model (PAM). Finally, we consider Kondo insulators based on a generalized periodic Anderson model with additional spin-orbit coupling and classify emerging magnetic and non-magnetic phases in the regard topology through corresponding $\mathbb{Z}_2$ invariants.
The content of this part has partially been published in Reference [54] or is in preparation for publication [56].

CHAPTER 10

Local moments and the Kondo effect

After the discovery of superconductivity in 1911, the scientific community was once more surprised by a temperature-dependent resistivity measurement in Kamerlingh Onnes Laboratory at Leiden University in 1934, when the three dutch physicists W.J. de Haas, J.H. de Boer, and G.J. van den Berg found a puzzling *resistance minimum* in gold wires at low temperatures [29]. According to *Matthiessen's rule* [204], the resistivity was believed to be decomposed into a temperature-independent contribution due to crystal defects complemented by an electron-phonon (lattice vibrations) scattering term, whose impact increased with temperature with a determined proportionality $\rho_{\text{el-ph}} \propto T^5$ according to Felix Bloch's theoretical approach in 1930 [205]. At that time, the electrical resistance was, therefore, expected to decrease monotonously by lowering the temperature and, except for superconductors, approach a constant value. The unusual behavior could also not be explained by electron-electron scattering, which was established by Lev Landau and Isaak J. Pomerantschuk in 1936 to feature a quadratic temperature dependence [206] and can be understood in the context of Fermi liquid (FL) theory [23, 48] as previously discussed in Section 8.3.3.

The puzzle remained unsolved for more than 30 years. However, experimental observations in Bell Laboratories in the early 60s acquired significant hints towards the underlying mechanism that liked the resistivity minimum to small concentrations of magnetic impurities, e.g., iron in niobium, that did not always yield a net magnetic moment in the respective compound [207, 208]. This technical achievement to carefully tune magnetic impurities in the parts per million range attracted theorists to investigate the topic in the following years. In 1961, Philip W. Anderson formulated an important second quantized model that describes emerging magnetic moments in metals due to interactions between localized electrons, referred to as the Anderson impurity model (AIM) [62]. Jun Kondo finally explained the resistance minimum in 1964 through a perturbation calculation of an s-d spin-exchange model, established by Tadao Kasuya in 1956, which is today known as the Kondo model (KM) [209]. His result was a logarithmic contribution to the resistivity at low temperatures as a consequence of a many-body effect, yielding in temperature dependence [210][1]

$$\rho(T) = \underbrace{\rho_0}_{\text{crystal defects}} + \underbrace{AT^2}_{\text{el-el scattering}} + \underbrace{BT^5}_{\text{el-ph scattering}} + \underbrace{C \ln(W/T)}_{\text{Kondo effect for } T \gtrsim T_K} \tag{10.1}$$

in total. We will introduce the AIM and KM along with their periodic generalizations, the Kondo lattice model (KLM), and the periodic Anderson model (PAM) in Section 10.3. These two models are connected via the Schrieffer–Wolff (SW) transformation in the limit of strong correlations and constitute the basis of our theoretical investigation of Kondo materials in Chapters 11 and 12.

[1] Dependent on the specific material, additional phononic contributions $\propto T^3$ arise [22], and the high-temperature regime is dominated by $\rho \propto T$ as classical limit, where the phonon energy is also $\propto T$ due to the equipartition theorem.

A serious omission of Kondo's result was that the logarithmic term led to a divergence of the resistivity in the limit $T \to 0$, which clearly indicated a breakdown of the perturbation calculation at some point. The search for an appropriate description in the zero-temperature limit, i.e., the *Kondo problem*, once more attracted theorists to study the field more deeply in the 60s and 70s. An extension of the perturbative approach proved to be insufficient but moved the singularity to a finite temperature, which is called *Kondo temperature* T_K [63], and defines the only characteristic energy scale of the problem [12]. In 1970, Philip W. Anderson suggested an intuitive explanation of the Kondo effect by means of a perturbative renormalization group method, known as *Poor man's scaling* [211], which was, however, still not applicable for $T \ll T_K$. His approach found an effective coupling of local moments and conduction electrons that increases with lowering the temperature and effectively screens the net magnetic moment. Shortly after, the Kondo problem was finally solved in 1974 employing a non-perturbative technique, i.e., the *numerical renormalization group*, that Kenneth G. Wilson developed himself and refined Anderson's result [212][1]: While local moments are asymptotically free for $T \gg T_K$, the conduction electrons start to screen the magnetic impurity for $T \gtrsim T_K$ by forming a many-body Kondo singlet, whose binding energy is given by the Kondo temperature. In the limit $T \to 0$, the local interactions become so strong that the magnetic moment is fully screened, and a Fermi liquid with finite resistivity is recovered [12].

Although the original Kondo problem for a single impurity was now well understood, it was acknowledged in the late 70s that the same phenomenon could also occur in dense Kondo lattices with large numbers of periodically distributed local moments. That insight launched an entirely new material class, the *heavy fermion* metals that we will further discuss in Section 10.1. Insulating heavy fermion materials are nowadays referred to as Kondo insulators (KIs) and will be introduced in Section 10.2. For both material types, many open questions remain, and we will apply the slave-boson (SB) formalism in Chapters 11 and 12 to address some of these problems.

After all, the popularity of Kondo physics has again spiked in recent years, since the related interplay between localized and itinerant degrees of freedom in the presence of strong correlations determines the unconventional behavior of different quantum materials beyond the original idea of local magnetic moments and may even provide practical applications [12, 214]. To be specific, the Kondo effect may also occur in artificial structures like quantum dots or also in the absence of spin, if another quantum number, e.g., orbital degrees of freedom, gives rise to energy-degenerate states and such an orbital Kondo effect has been observed in RuO_2 in 2020 [215]. Moreover, the phenomenon involves quantum entanglement, and a recent theoretical study suggests that it becomes long-ranged at the Kondo-destruction near a quantum critical point [216]. Finally, some heavy-fermion materials employ triplet-superconductivity and are possible hosts of Majorana fermions. Those observations pave the way for possible quantum logic gate devices and quantum computing within the scope of Kondo physics [12].

10.1 Heavy fermions

In 1975, K. Andres, J. E. Graebner, and H.R. Ott measured an unexpectedly high specific heat coefficient γ in the intermetallic compound $CeAl_3$, which was about 1600 times larger than in copper [217]. It is given by the proportionality factor of the electronic specific heat at low temperatures and can directly be associated with

[1]The innovative renormalization group concept was later generalized and broadly applied to different many-body problems, e.g., high-temperature-superconductivity [213] and has been established as a powerful numeric tool. For his contributions, Wilson was awarded the Nobel prize in 1982.

the (renormalized) density of states (DOS) $D^*(0)$ at the Fermi-level [48]

$$C_V = \gamma T \,, \qquad \gamma = \frac{\pi^2 k_B^2}{3} D^*(0) \,. \tag{10.2a}$$

The therefore implied enhancement of the DOS can also be identified with an increased effective mass m^* of the FL quasiparticles (QPs) that we define by a quadratic expansion of the band dispersion around the Fermi surface (FS) in order to relate it to a free electron model with mass $m = m_e$[1]

$$\varepsilon_k = \frac{k^2}{2m^*} + \mathcal{O}\left(k^3\right) \,, \qquad \frac{m^*}{m} = \frac{D^*(0)}{D(0)} \,. \tag{10.2b}$$

For $CeAl_3$, the effective mass yields about 1000 bare electron masses ($m^*/m \approx 1000$), and with the discovery of other compounds, e.g., UBe_{13} and $CeCu_6$ [218] that show similar behavior, the material class of *heavy electrons* or *heavy fermions* was founded. Partially filled f-orbitals were identified to be a common denominator of these compounds, and it was established that a lattice version of the Kondo effect, i.e., a periodic arrangement of localized, strongly interacting electrons immersed in a sea conduction electrons, was responsible for the unusual behavior [219]. The high effective masses were then explained by Kondo resonances of the local moments at the Fermi-level for an overall paramagnetic (PM) state due to screening by the conduction electrons [12].

Many heavy fermion materials, however, also employ magnetic ordering, especially antiferromagnetism (AFM) [220, 221] and in some cases also ferromagnetism (FM) [222], with an oftentimes weak net magnetization that can be as small as $m \lesssim 10^{-2}\mu_B$. The magnetic instabilities compete with the Kondo effect, and to quote Piers Coleman: heavy fermions are therefore considered to be "*on the edge of magnetism*" [218]. The ordering process is, on the one hand, driven by itinerant magnetism due to the enlarged DOS at the Fermi-level, and on the other hand, by local moment formation as a consequence of a spin-exchange coupling induced by hybridization with the sea of conduction electrons, known as Ruderman–Kittel–Kasuya–Yosida (RKKY) interaction [12]. In opposite to magnetic phases, the Kondo effect emerges continuously by lowering the temperature, and there is no thermal phase transition. At zero temperature, however, many experiments indicate that it can be destructed instantaneously at a so-called quantum critical point (QCP), which can, e.g., be seen in a discontinuous jump of the Hall-coefficient as a function of a suitable control parameter [12]. The corresponding *Kondo-destruction* is triggered by quantum fluctuations rather than thermal fluctuations and can manifest in metal-to-metal, metal-to-Mott insulator, or magnetic transitions.

A qualitative classification of chemical elements that feature strong correlations and employ a propensity to form local moments and heavy fermion compounds was given in 1983 by J. L. Smith and E. A. Kmetko with their "*nearly periodic table of transition elements*" [223] that is shown in Figure 10.1. The degree of localization is governed by two trends: Orbitals with a higher principal quantum number contain more radial nodes and tend to be more delocalized. Moreover, moving along a row in the periodic table or from d to f orbitals increases the nuclear charge that pulls the electrons closer towards the nucleus. As a result, the shells can be ordered by

$$5d < 4d < 3d < 5f < 4f \tag{10.3}$$

from low to high localization. The itinerant, strongly correlated systems in the lower-left corner of the phase diagram tend to be conventional superconductors at low temperatures, whereas materials on the upper right employ a strong propensity towards local moments. The elements on the crossover are particularly

[1] In a free electron gas, it is $D(0) \propto m$ [19].

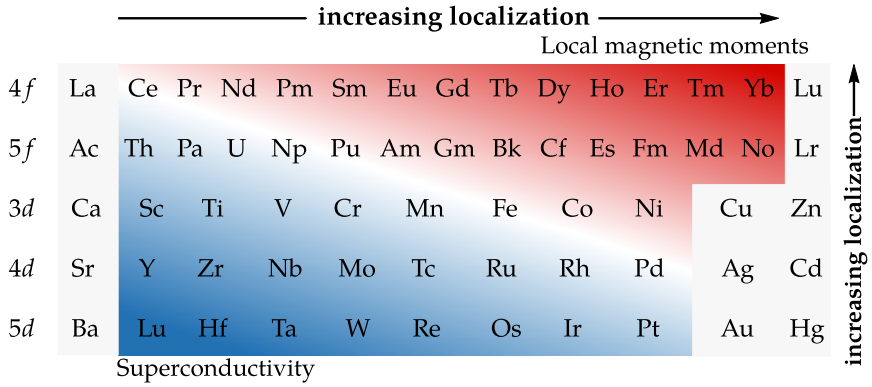

(a) Elements with a gray background featuring empty (left side) or full (right side) d and f shells are not directly relevant for the localized interaction picture and are only included for completeness.

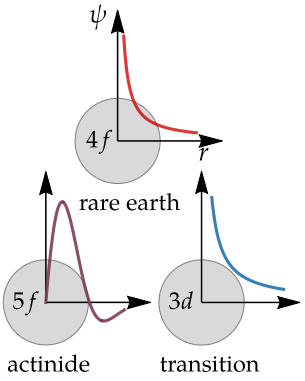

(b) Schematic wave function ψ for differently localized orbitals.

Figure 10.1: Kmetko-Smith diagram [223], which describes the trend of strongly correlated transition metals with partially filled orbitals towards localization. The arrangement does not fully recover the order of the periodic table of elements because the electron configuration is unexpected in some cases due to interaction effects. Elements on the upper right corner tend to be magnetic Mott insulators, whereas the lower-left corner is dominated by itinerant non-magnetic behavior that favors superconductivity. Materials on the crossover indicated by the white line are particularly interesting because their physical properties are very susceptible to perturbations or external forces. Figure adapted from [48, 57].

interesting due to the competing processes and also especially susceptible to perturbations. In that regard, e.g., the lattice structure, corrosion resistance, and magnetic properties of iron can be dramatically changed by adding chromium and nickel to obtain stainless steel [223]. Moreover, the cerium and uranium-based heavy fermion compounds and the iron-based superconductors are associated with that crossover.

As a matter of fact, Frank Steglich *et al.* discovered by studying $CeCuSi_2$ in 1979 that heavy fermion materials themselves could also be superconducting [224], and many more heavy-fermion superconductors (SCs) have been reported ever since. An earlier observation of superconductivity in UBe_{13} in 1973 was dismissed as an artifact, because conventional superconductivity order was believed to be impossible in dense magnetic systems [225]. An especially interesting heavy-fermion SC is $YbRh_2Si_2$, because it features strange metal behavior with liner resistivity as a function of temperature followed by a superconducting transition at lower temperatures [226]. This similarity to the high-T_c cuprate raises the question of whether the Cooper-pairing mechanism of both material classes has a common origin.

10.2 Kondo insulators

Kondo insulators are basically heavy-fermion semiconductors, where the chemical potential lies in a narrow energy gap that opens at low temperatures due to the hybridization of localized and conduction electrons as a result of the Kondo effect. From a quasiparticle perspective, KIs can be considered to be highly renormalized band insulators [218]. The first material to be classified as KI is Samarium hexaboride (SmB_6), after it had already been discovered in the late 60s that the material is a local moment metal at room temperature that continuously transforms into a PM semiconductor with a tiny gap of approximately 10meV at low temperatures [227]. Another feature of KIs are *mixed-valence states*, i.e., a fractional occupation of the f-orbitals where,

e.g., samarium is present in both Sm^{2+} and Sm^{3+} ions [228]. Until now, many other KIs with similar behavior have been found.

In 2010, Maxim O. Dzero, Kai Sun, Victor M. Galitski, and Piers Coleman suggested that KIs could be topological, and proposed the term topological Kondo insulator (TKI) [32]. Theoretical studies on SmB_6 suggest the existence of three topologically protected Dirac cones at the surface [54, 99, 229, 230] that could explain the existence of a resistivity plateau that had been measured below 3K and seemed to be unaffected by the sample quality [231]. We will introduce a minimal model for TKIs in Section 10.3.4 and elaborate on interaction-induced magnetic and topological properties by means of the SB method in Chapter 12.

10.3 Microscopic models

In Sections 10.3.1 and 10.3.2, we will define the aforementioned impurity models, namely the Kondo model (KM) and Anderson impurity model (AIM) and their periodic counterparts, i.e., the Kondo lattice model (KLM) and periodic Anderson model (PAM). The two models are related by the Schrieffer–Wolff (SW) transformation in the limit of high correlations, as will be discussed in Section 10.3.3. Finally, we introduce a minimal model for TKIs that is based on the PAM with additional spin-orbit coupling (SOC) in Section 10.3.4. In Chapters 11 and 12, we will apply the SB formalism to the introduced periodic models in order to investigate interaction effects in heavy-fermion metals and topological Kondo insulators.

10.3.1 Kondo model

The KM was the first model to effectively describe the physics of the Kondo effect and couples a sea of conduction electrons created by $\hat{c}^\dagger_{\boldsymbol{k},\sigma}$ in the tight-binding approximation to a single magnetic impurity with spin operator $\hat{\mathbf{S}}$ via a spin-exchange coupling J defined by the Hamiltonian [48, 209][1]

$$H^{\mathrm{KM}} = H_0 + H_J = \sum_{\boldsymbol{k},\sigma} \hat{c}^\dagger_{\boldsymbol{k},\sigma} \xi_{\boldsymbol{k}} \hat{c}_{\boldsymbol{k},\sigma} + \sum_{\boldsymbol{k}\boldsymbol{k}'} \sum_{\sigma\sigma'} J\, \hat{c}^\dagger_{\boldsymbol{k},\sigma} \boldsymbol{\tau}_{\sigma,\sigma'} \hat{c}_{\boldsymbol{k}',\sigma'} \hat{\mathbf{S}} \,. \tag{10.4}$$

A convenient method to calculate the resistivity minimum and extract the Kondo temperature T_K, is to apply Abrikosov's pseudo-fermion (sometimes also called *slave-fermion*) representation [45], for the local spin $\hat{\mathbf{S}} = \frac{1}{2} \hat{f}^\dagger_\sigma \boldsymbol{\tau}_{\sigma,\sigma'} \hat{f}_{\sigma'}$. It is only exact if the occupation of the auxiliary fermionic operators $\hat{f}^\dagger_\sigma$ is constrained to one $n_f = 1$, which can be implemented in full analogy to the slave-boson theory by a projector with a complex Lagrange multiplier field (compare Section 2.2.2). A consecutive second-order perturbation calculation of the scattering amplitude $\mathcal{T}$ in the resulting fermionic model yields the well known logarithmic contribution to the resistivity [48, 57]

$$\rho(T) \propto |\mathcal{T}|^2 \propto (1 + 4JD(0) \ln W/T) \,, \tag{10.5a}$$

where W is the half-width of the conduction band. The breakdown of the perturbative calculation can be defined by the temperature, where second-order contributions become larger than the first-order term, which determines the Kondo scale

$$1 = 4JD(0) \ln W/T_K \quad \Leftrightarrow \quad T_K = W \mathrm{e}^{-\frac{1}{4D(0)J}} \,. \tag{10.5b}$$

[1] The spin operator of the conduction electrons at lattice site i is defined by $\hat{\mathbf{s}}_i = \frac{1}{2} \sum_{\sigma,\sigma'} \hat{c}^\dagger_{i,\sigma} \boldsymbol{\tau}_{\sigma,\sigma'} \hat{c}_{i,\sigma'}$, which is equivalent to the respective expression in momentum space in Equation (10.4) for $i = 0$, and $\boldsymbol{\tau}$ represents the vector of Pauli-matrices. The coupling constant J may in general be momentum dependent ($J_{\boldsymbol{k},\boldsymbol{k}'}$). For the purpose of this thesis, we restrict ourselves to constant couplings, which is sufficient for most applications.

The KLM with momentum-independent coupling constant follows from a periodic arrangement of the impurity $\hat{\mathbf{S}}\hat{\mathbf{s}} \to \sum_i \hat{\mathbf{S}}_i \hat{\mathbf{s}}_i$ [219, 232][1]

$$H^{\mathrm{KLM}} = H_0 + H_J = \sum_{\boldsymbol{k},\sigma} \hat{c}^\dagger_{\boldsymbol{k},\sigma} \xi_{\boldsymbol{k}} \hat{c}_{\boldsymbol{k},\sigma} + \sum_{\boldsymbol{k}\boldsymbol{k}'} \sum_{\sigma\sigma'} J\, \hat{c}^\dagger_{\boldsymbol{k},\sigma} \boldsymbol{\tau}_{\sigma,\sigma'} \hat{c}_{\boldsymbol{k}',\sigma'} \hat{\mathbf{S}}_{\boldsymbol{k}'-\boldsymbol{k}} \,. \tag{10.6}$$

10.3.2 Anderson model

The AIM, introduced by Philip W. Anderson in 1961 [62] with the aim to describe local moment formation, combines two essential ideas. Firstly, the localizing impact of the Coulomb repulsion, represented by a Hubbard interaction in the f-electrons, which hinders the electron movement and can induce a metal-to-insulator transition (Mott transition) in the high coupling regime (compare Section 8.1). Secondly, the formation of virtual-bound state resonances, which Anderson interprets as a tunneling process between the localized f-electrons ($\hat{f}^\dagger_\sigma$) and the conduction sea ($\hat{c}^\dagger_\sigma$) with an amplitude of V that acts as hybridization. The corresponding Hamiltonian with a singly impurity at $i = 0$ and f-electron on-site potential ϵ_f is given by [48][1]

$$H^{\mathrm{AIM}} = \overbrace{\sum_{\boldsymbol{k},\sigma} \hat{c}^\dagger_{\boldsymbol{k},\sigma} \xi_{\boldsymbol{k}} \hat{c}_{\boldsymbol{k},\sigma} + \sum_{\boldsymbol{k},\sigma} \left(V \hat{c}^\dagger_{\boldsymbol{k},\sigma} \hat{f}_\sigma + V^* \hat{f}^\dagger_\sigma \hat{c}_{\boldsymbol{k},\sigma} \right) + \underbrace{\epsilon_f \sum_\sigma \hat{f}^\dagger_\sigma \hat{f}_\sigma + U \hat{f}^\dagger_\uparrow \hat{f}_\uparrow \hat{f}^\dagger_\downarrow \hat{f}_\downarrow}_{\text{atomic part}}}^{\text{resonant part}} \,. \tag{10.7}$$

The PAM follows from a periodic arrangement of the impurities, i.e., the terms of Equation (10.7) associated with the interacting f-electrons are extended to the whole lattice [63][1]

$$H^{\mathrm{PAM}} = H_d + H_{\mathrm{hyb}} + H_f \,, \tag{10.8a}$$

with

$$H_d = -t \sum_{\langle i,j \rangle,\sigma} \hat{c}^\dagger_{i,\sigma} \hat{c}_{j,\sigma} - \mu_0 \sum_{i,\sigma} \hat{c}^\dagger_{i,\sigma} \hat{c}_{i,\sigma} = \sum_{\boldsymbol{k},\sigma} \hat{c}^\dagger_{\boldsymbol{k},\sigma} \xi_{\boldsymbol{k}} \hat{c}_{\boldsymbol{k},\sigma} \,, \tag{10.8b}$$

$$H_{\mathrm{hyb}} = V \sum_{i,\sigma} \left(\hat{c}^\dagger_{i,\sigma} \hat{f}_{i,\sigma} + \hat{f}^\dagger_{i,\sigma} \hat{c}_{i,\sigma} \right) = V \sum_{\boldsymbol{k},\sigma} \left(\hat{c}^\dagger_{\boldsymbol{k},\sigma} \hat{f}_{\boldsymbol{k},\sigma} + \hat{f}^\dagger_{\boldsymbol{k},\sigma} \hat{c}_{\boldsymbol{k},\sigma} \right) \,, \tag{10.8c}$$

$$H_f = U \sum_i \hat{f}^\dagger_{i,\uparrow} \hat{f}_{i,\uparrow} \hat{f}^\dagger_{i,\downarrow} \hat{f}_{i,\downarrow} + (\epsilon_f - \mu_0) \sum_{i,\sigma} \hat{f}^\dagger_{i,\sigma} \hat{f}_{i,\sigma} = U \sum_i \hat{f}^\dagger_{i,\uparrow} \hat{f}_{i,\uparrow} \hat{f}^\dagger_{i,\downarrow} \hat{f}_{i,\downarrow} + (\epsilon_f - \mu_0) \sum_{\boldsymbol{k},\sigma} \hat{f}^\dagger_{\boldsymbol{k},\sigma} \hat{f}_{\boldsymbol{k},\sigma} \,. \tag{10.8d}$$

Moreover, we include the chemical potential μ_0 that couples to the total electron density to control the filling $n = n_c + n_f$. In the non-interacting limit, the natural basis is in momentum space, and the energy bands can be calculated analytically as shown in Appendix B.2. The hybridization leads to the opening of an energy gap with an insulating ground state at half-filling, which is demonstrated in Figure 10.2(a). Due to the lack of direct hopping between different f-orbitals, the energy bands are narrow, which makes the PAM a suitable minimal model to study heavy fermion systems. In Chapter 11, we will apply the SB representation introduced in Part I to the PAM in order to account for the Hubbard term and study the interaction-dependent phase diagram.

[1] In general, the hybridization V may be momentum-dependent ($V_{\boldsymbol{k}}$) in analogy to the coupling constant J in the KM, but for the purpose of this thesis, we only consider a momentum-independent hybridization in the PAM.

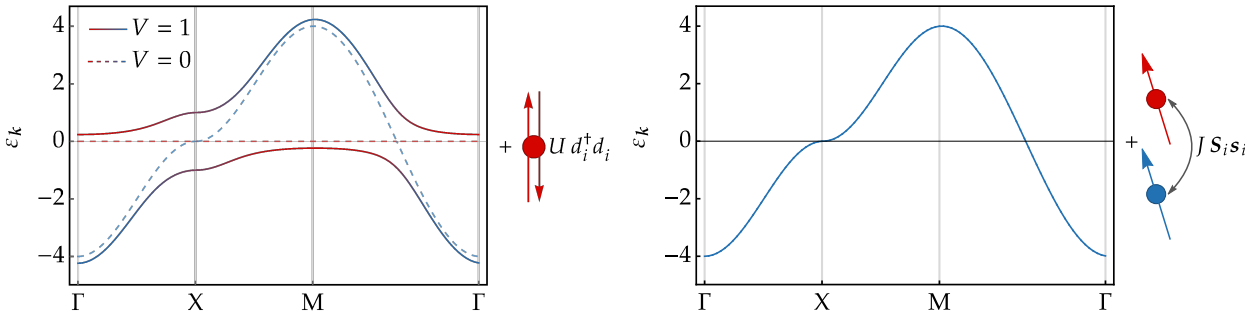

(a) Band structure of the PAM for $\mu_0 = \epsilon_f = U = 0$. Finite hybridizations V open a gap such that the ground state is insulating at half-filling. The weights of the interacting f-orbital and conduction orbital are visualized by red and blue color, respectively.

(b) Band structure of the conduction band in the KLM. It is equivalent to respective BS of the PAM for vanishing hybridization [blue dashed line in Figure 10.2(a)].

Figure 10.2: In the PAM, local moments are represented by an f-orbital with a Hubbard-type interaction U and zero hopping amplitude that hybridizes with the conduction orbital. On the other hand, the KLM considers a spin-exchange interaction J between the local moment $\boldsymbol{S}$ and the spin $\boldsymbol{s}$ of the conduction electrons. Both models are connected by the SW transformation and become equivalent for strong correlations in the extended Kondo limit.

10.3.3 Schrieffer-Wolff transformation

The AIM and KM are related by a canonical transformation that was first described by Schrieffer and Wolff in 1966 [233]. It projects out empty and double occupations of the magnetic impurity and only allows virtual excitations of those within the lowest order perturbation theory [63]. Both models become equivalent in the so-called *Kondo limit*, which identifies the KM as a low energy description of the AIM in the strong coupling regime. Later, it was shown that a similar relation holds between their periodic counterparts, where the KLM is expected to represent an effective model of the PAM in the *Kondo regime*, where the Kondo coupling constant is approximately given by $J \approx V^2 \left(\frac{1}{\epsilon_f + U} + \frac{1}{-\epsilon_f}\right)$ [48, 232]. The mapping from PAM to KLM becomes exact in the extended Kondo limit (EKL), which is defined by [234]

$$\epsilon_f = -\frac{U}{2}\,, \quad \frac{V^2}{U} = \text{const.}\,, \quad U \to \infty\,, \quad V \to \infty\,, \quad \Rightarrow n_f = 1\,. \tag{10.9a}$$

A consequence of the limit is that the f-orbital is half-filled ($n_f = 1$), which ultimately initiates the spin-exchange term as a kind of a reverse of Abrikosov's previously discussed pseudo-fermion representation. The coupling constant in the EKL is positive [232, 234]

$$J = \frac{4V^2}{U}\,, \tag{10.9b}$$

which favors AFM ordering in agreement with experimental observations in Kondo materials. Summing up, the SW transformation projects the interacting f-electrons to local moments by means of the hybridization V, while the conduction band recovers its non-hybridized form as illustrated in Figure 10.2.

10.3.4 Minimal model for topological Kondo insulators

A minimal model for TKIs can be built based on the PAM with the addition of a small hopping amplitude t_{ij}^f between the localized f-electrons. Moreover, a crucial ingredient for topological phases is that the

hybridization is an odd function of $\boldsymbol{k}$, which implies that it needs to be non-on-site [32]. This is because the localized electrons in KIs are usually derived from atomic f-orbitals, which are odd under parity, while the hybridizing conduction d-orbitals are even under parity. A minimal model with those ingredients that preserves time-reversal symmetry (TRS) and inversion symmetry (IS) is given by [54, 99, 230]

$$H^{\mathrm{TKI}} = H_d + H_{\mathrm{hyb}} + H_f + H_{\mathrm{int}} \,, \tag{10.10a}$$

with

$$H_d = -\sum_{\langle ij\rangle}\sum_{\sigma} t^d_{ij}\hat{c}^\dagger_{d,i,\sigma}\hat{c}_{d,j,\sigma} - \mu_0\sum_{i,\sigma}\hat{c}^\dagger_{i,\sigma}\hat{c}_{i,\sigma} \,, \tag{10.10b}$$

$$H_{\mathrm{hyb}} = \sum_{\alpha}\sum_{\langle i<j\rangle_\alpha}\sum_{\sigma\sigma'} \mathrm{i}V\left(\hat{f}^\dagger_{i,\sigma}\tau^\alpha_{\sigma\sigma'}\hat{c}_{j,\sigma'} - \hat{f}^\dagger_{j,\sigma}\tau^\alpha_{\sigma\sigma'}\hat{c}_{i,\sigma'} + \mathrm{h.c.}\right) \,, \tag{10.10c}$$

$$H_f = -\sum_{<ij>,\sigma} t^f_{ij}\,\hat{f}^\dagger_{i,\sigma}\hat{f}_{j,\sigma} + \sum_{i,\sigma}\hat{f}^\dagger_{i,\sigma}\left(\epsilon_f - \mu_0\right)\hat{f}_{i,\sigma} \,, \tag{10.10d}$$

$$H_{\mathrm{int}} = U\sum_i \hat{f}^\dagger_{i,\uparrow}\hat{f}_{i,\uparrow}\hat{f}^\dagger_{i,\downarrow}\hat{f}_{i,\downarrow} \,, \tag{10.10e}$$

and features band inversions at time-reversal-invariant momenta (TRIM) that initiate topological transitions. The model employs spin-orbit coupling (SOC) in the hybridization term given by Equation (10.10c) and $\langle i < j\rangle_\alpha$ indicates NN bonds with $i < j$ in α-direction and $\tau^\alpha_{\sigma\sigma'}$ represents the α-th Pauli matrix acting on spin space. Such a SOC, which features TRS and IS is called centrosymmetric. In Chapter 12, we will apply the SB representation discussed in Part I to the TKI model to account for the Hubbard term and study interaction-enabled magnetic and topological transitions.

CHAPTER 11

Emerging Kondo regime in the periodic Anderson model

In this chapter, we will investigate the 2D periodic Anderson model (PAM), introduced in Section 10.3.2, by means of the slave-boson (SB) method that we derived in Part I. Firstly, in Section 11.1, we identify an emerging Kondo regime in the parameter space of the PAM that features an AFM mean-field (MF) ground state with huge effective masses that, however, turns out to be unstable w.r.t. Gaussian fluctuations. Section 11.2 adds another conduction band to the model and discusses a domain that is dominated by the effective RKKY-interaction inducing magnetic frustration due to destructive interference of the two conduction band pockets. The results are partially included in Reference [56], which is in preparation for publication.

11.1 Heavy fermions and magnetism

The Kondo problem and theoretical understanding of heavy fermions have driven the development of auxiliary particle (slave-boson) methods, pioneered by Barnes in 1976 [46, 235] for the Anderson impurity model (AIM) and the PAM by Coleman in 1984 [47] in the limit of infinite interactions. KR slave-bosons, which are the foundation for the SB representation applied in this thesis, provided a description for finite interactions U in 1986 [49]. An advantage of this formalism is that it treats local and non-local physics on the same footing and allows for both: correlation-induced mass enhancement and the formation of magnetic order. Early works, however, suggested that the Kondo energy scale (T_K) was not recovered [236], whereas later applications of the KR-SB method at least compared well to QMC calculations at half-filling and found the occurrence of magnetic order in qualitative agreement with experiments [74]. Other theoretical methods like, e.g., DMFT tend to struggle with the coinciding importance of localized and itinerant degrees of freedom, and reliable results have been difficult to obtain despite the problem being around for multiple decades. One of the remaining fundamental questions is the exact origin of the large quasiparticle (QP) mass.

In the following, we will revisit the problem and fully exploit the capacities of the SB formalism presented in Part I, including a magnetic MF analysis for arbitrary doping and the evaluation of Gaussian fluctuations about (para-) magnetic saddle points. In order to target the Kondo regime and seek for heavy fermions in the PAM defined in Equation (10.8), we aim to tune the free parameters such that the Kondo lattice model (KLM) represents an effective low energy description. As previously discussed in Section 10.3.3, both models are connected by the SW transformation that projects out double occupations of the interacting f-orbital. We, therefore, restrict our analysis to half-filled f-orbitals $n_f = 1$ in accordance with the extended Kondo limit (EKL). This constraint can be enforced by coupling the f-electrons to a particle reservoir, where the on-site energy ϵ_f acts as effective chemical potential. We moreover fix the hopping and hybridization amplitude

$t = V = 1$, such that the interaction U and total filling n, which is controlled by the chemical potential μ_0, remain as free parameters.

In order to map out the magnetic phase diagram, we numerically solve the SB saddle point equations [56]

$$\left.\frac{\partial F_{\text{eff}}^{(0)}}{\partial p}\right|_{(4.29)} = \left.\frac{\partial F_{\text{eff}}^{(0)}}{\partial p_0}\right|_{(4.29)} = \left.\frac{\partial F_{\text{eff}}^{(0)}}{\partial \beta}\right|_{(4.29)} = \left.\frac{\partial F_{\text{eff}}^{(0)}}{\partial \epsilon_{\text{eff}}}\right|_{(4.29)} = \left.\frac{\partial F_{\text{eff}}^{(0)}}{\partial \mu_0}\right|_{(4.29)} = \left.\frac{\partial F_{\text{eff}}^{(0)}}{\partial \boldsymbol{Q}}\right|_{(4.29)} = 0 \tag{11.1}$$

to minimize the MF free energy (FE). Details on calculating the FE and implementing the additional constraint of half-filled f-orbitals are provided in Section 4.4.3. The corresponding renormalized QP hopping matrix is derived in Appendix B.2, and its eigenvalues that enter the FE are given by the roots of a fourth-order polynomial that is defined in Equation (B.21). The resulting zero-temperature phase diagram in the vicinity of half-filling ($n = 2$) is shown in Figure 11.1(a). The MF ground states are metallic and employ a second-order FM instability at $U_c \approx 1$ except for half-filling, where the ground state is insulating due to the hybridization gap with an AFM transition at $U_c \approx 2$. In analogy to our analysis in the Hubbard model, the PM phase boundary can equivalently be determined by means of a diverging static spin susceptibility $1/\chi_s^{\text{PM}}(\boldsymbol{q} = \boldsymbol{Q}, \omega = 0)$ about the PM ground state, i.e., we find PM fluctuations to be in perfect agreement with results from the magnetic MF. Explicit expressions for the susceptibilities are summarized in Table 5.2 and given by superpositions of the fluctuation field propagator $\mathcal{G}_{\mu,\nu}^{a,b}(\boldsymbol{q}, \mathrm{i}\omega)$ that we derived in Section 5.2. For half-filled f-orbitals, the PM spin susceptibility adapts an RPA-like simple form [56]

$$\chi_s^{\text{PM}}(\boldsymbol{q}, \omega = 0) \propto \frac{\chi_0(\boldsymbol{q})}{1 + \chi_0(\boldsymbol{q}) \mathcal{M}_{p_1,p_1} / \left(2p_0^2\right)} \,. \tag{11.2a}$$

The matrix element $\mathcal{M}_{p_1,p_1}$ does not depend on $\boldsymbol{q}$ or ω and the bare susceptibility at zero momentum $\chi_0(\boldsymbol{q} = 0, \omega = 0) = D^*(0)$ is given by the renormalized DOS at the Fermi-level. FM instabilities can thus be determined by the equation

$$1 = -D^*(0) \mathcal{M}_{p_1,p_1} / 2p_0^2 \,, \tag{11.2b}$$

similar to the Stoner criterion in the Hubbard model. Those emerge as a direct consequence of the high DOS at the Fermi-level, that naturally arises in the PAM, and thus hinder the formation of heavy fermions within a PM ground state. The AFM domain in the vicinity to half-filling at intermediate interactions $2 \lesssim U \lesssim 3.5$ cannot be explained by such a nesting effect. It is rather to be identified with an emerging Kondo regime, where the PAM is effectively represented by the KLM with a positive Kondo coupling constant $J \approx 4V^2/U$ that drives AFM order, which is also observed in many heavy-fermion materials [218]. This hypothesis is also supported by the fact that we detect the scaling $U_c^{\text{AFM}} \propto V^2$ for high U, which coincides with the EKL, whereas the critical interaction towards the FM does not follow such a simple scaling relation.

We now want to investigate the effective masses of the (magnetic) MF band structures (BSs) that are related to the DOS by

$$m^* = \pi D^*(0) \tag{11.3a}$$

in two spatial dimensions and are visualized as a function of interaction and filling in Figure 11.1(a) as a 3D plot. At $U = 0$, the effective mass is already relatively large ($m^* \approx 10$) due to the construction of the PAM. With finite interactions, the PM band structure is renormalized by $V \to z_0 V$, with $z_0 \leq 0$ and $\epsilon_f \to \epsilon_f + \beta_0$ with $\beta_0 \geq 0$, i.e., the effective hybridization (f-electron on-site energy) is decreased (increased) by interaction

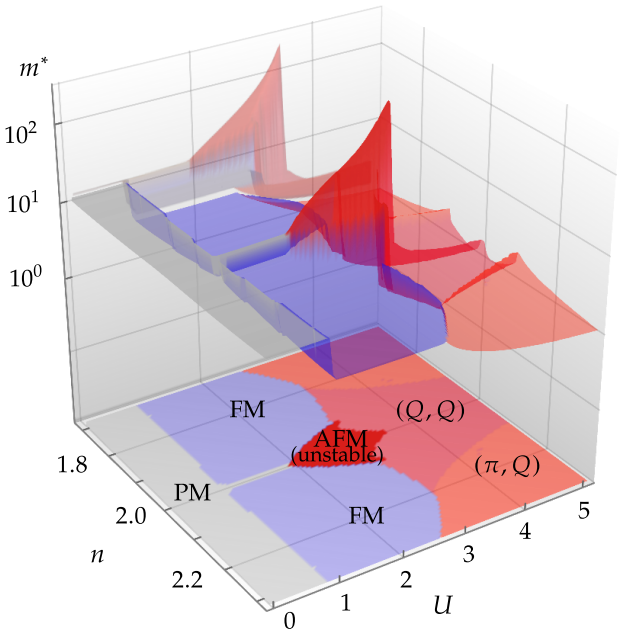

(a) Magnetic phase diagram of the PAM at $T = 0$ around half-filling, with effective mass m^* in the top panel. Figure adapted from [56].

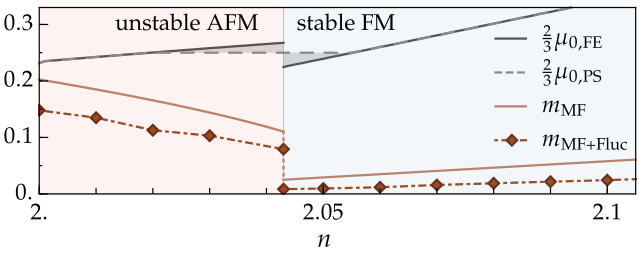

(b) MF magnetization m with fluctuation corrections and chemical potential as a function of the filling n for $U = 2.4$ at $T = 0.005$.

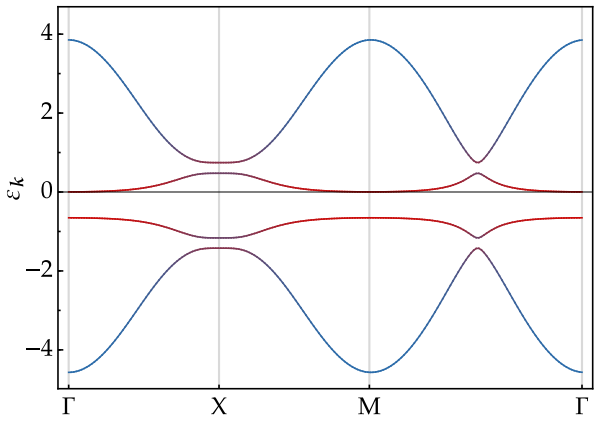

(c) Band structure of the unstable AFM ground state for $n = 2.01$ and $U = 2.4$. Red (blue) color indicates the orbital weight of the f-orbital (conduction orbital).

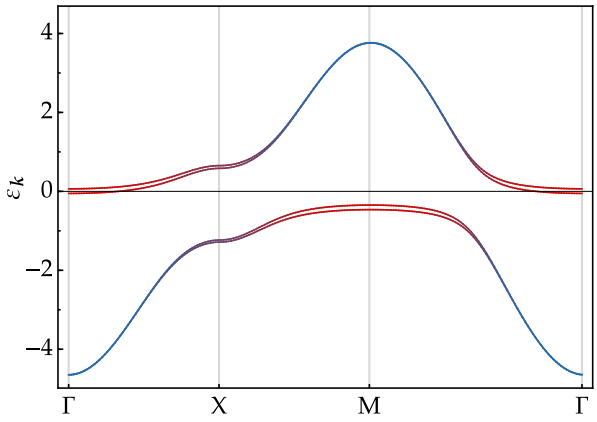

(d) Band structure of the stable FM ground state for $n = 2.08$ and $U = 2.4$. Red (blue) color indicates the orbital weight of the f-orbital (conduction orbital).

Figure 11.1: The magnetic phase diagram of the PAM is dominated by FM and AFM order in the low to intermediate coupling regime. The FM instability arises due to a modified Stoner criterion as a consequence of large densities of the PM Fermi surface, yielding a stable MF ground state with a small magnetic gap that significantly reduces the DOS at the Fermi-level. The AFM mean-field ground state competes with the FM and globally minimizes the free energy close to half-filling and comes along with a drastic interaction-induced enhancement of the effective mass ($m^*_{\mathrm{max}} \approx 250$) in opposition to the FM state. It, however, appears to be unstable w.r.t. Gaussian fluctuations. Both ground states feature phase separation for parts of the phase diagram due to the respective first-order transition. The FM employs a very low magnetization that is even further decreased by fluctuation corrections and almost approaches zero at the phase transition.

effects, and we find the DOS to follow the scaling relation [237][1]

$$D^*(0) = \left(1 + \frac{z_0^2 V^2}{(\mu_0 - \epsilon_f - \beta_0)^2}\right) D\left(\frac{z_0^2 V^2}{\mu_0 - \epsilon_f - \beta_0}\right), \tag{11.3b}$$

[1]Notice that $D^*(0)$ represents the renormalized paramagnetic DOS at Fermi-level and $D(\omega)$ describes the DOS of the bare non-hybridized conduction band.

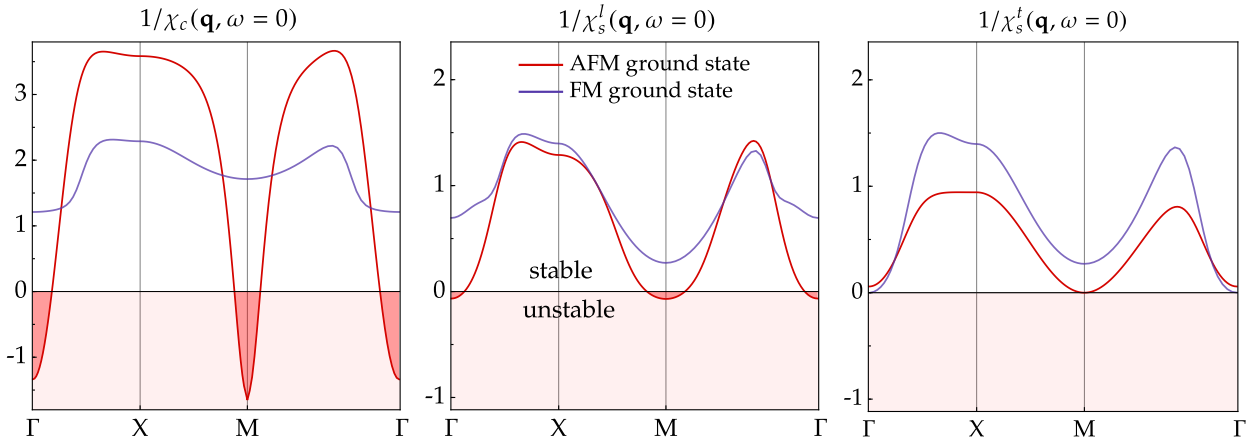

(a) Inverse charge susceptibility. **(b)** Inverse longitudinal spin susceptibility. **(c)** Inverse transversal spin susceptibility.

Figure 11.2: Inverse static susceptibilities around an AFM mean-field ground state for $n = 2.01, U = 2.4$, and FM mean-field ground state for $n = 2.03, U = 1.5$, and $T = 0.005$. Fermi surface instabilities are indicated by an enlarged negative domain, i.e., the AFM is unstable, whereas the FM appears to be stable. Gapless spin waves, which arise due to the finite MF magnetization, can be seen in χ_s^t and manifest around $\boldsymbol{q} = (\pi, \pi)^\top$ for the AFM and $\boldsymbol{q} = (0, 0)^\top$ for the FM as expected. Figure adapted from [56].

in good approximation. It moderately grows with interaction, but a significant increase of m^* cannot be found in the PM domain because of the formation of magnetic states, which was also concluded in other theoretical studies [238]. FM ordering even drastically reduces m^* to the level of a free-electron mass ($m^* \approx 1$) by opening a small magnetic gap around the Γ-point, which is exemplarily displayed in Figure 11.1(d). The AFM domain on the other side employs a massive increase of the effective mass as a function of interaction from $m^* \approx 1$ to $m^* \approx 250$ that is finally negated by a first-order transition towards $(Q, Q)^\top$ incommensurate order at $U \approx 3.5$, which recovers $m^* \lesssim 3$. An exemplary BS of the corresponding AFM mean-field ground state is shown in Figure 11.1(c) in the extended zone scheme. The back-folding pushes additional DOS to the Fermi-level and results in tiny pockets around the Γ and M-point.

A fluctuation analysis of the magnetic saddle points by means of the static charge and spin susceptibilities that are exemplarily presented in Figure 11.2, however, reveals that the AFM ground state is unstable due to divergences of χ_c and χ_s^l around the Γ and M-point. Although the general signature of Kondo physics is contained in our previous analysis, we, therefore, conclude that KR slave-bosons are not capable of sufficiently describing the problem because we cannot write down a stable MF ground state that globally minimizes the FE in that domain. The FM, on the other side, is stable w.r.t. Gaussian fluctuations. It only features a sharp divergence of the transversal spin susceptibility $\chi_s^t(\boldsymbol{q} = 0)$ at the Γ-point, which is expected due to the gapless spin waves associated with the finite MF magnetization.

Finally, we want to take a look at the doping-dependent properties of the MF ground states. Firstly, there is phase separation (PS) between the AFM and FM due to a discontinuity of the chemical potential $\mu_0(n)$ at the first-order transition, which can be seen for $U = 2.4$, and $n_c \approx 2.043$ in Figure 11.1(b). The constant chemical potential of the PS ground state is indicated by the dashed line[1]. We do, however, not find domains of negative electronic compressibility like for the Hubbard model discussed in Section 8.5. The apparent competition

[1]Theoretically, there could also be irregularities in the context of ϵ_f, which acts as effective chemical potential of the f-orbital to constrain $n_f = 1$. In order to have an equivalent description of the free energys $F(n_f)$ and $F(\epsilon_f)$, we require the compressibility of the f-electrons $\kappa_T^f = -\partial n_f / \partial \epsilon_f$ be a monotonous function, which is satisfied for our findings.

between the two magnetic phases can also be seen in the transversal spin susceptibility in Figure 11.2(c), where $\chi^t_{s,\mathrm{AFM}}$ is also enhanced around $\boldsymbol{q} = (0,0)^\top$, and $\chi^t_{s,\mathrm{FM}}$ employs a maximum around $\boldsymbol{q} = (\pi,\pi)^\top$. After all, the instability of the AFM phase cannot be explained by the phenomenon because it also occurs outside of the PS domain.

Secondly, we investigate the mean-field magnetization $m^{(0)} = m_{\mathrm{MF}}$, which is also plotted in Figure 11.1(b). We find the FM to be very weakly magnetized, with a minimum of $m_{\mathrm{MF}} \approx 0.025$ at the transition to the AFM (the fully magnetized state is normalized to $m = \frac{1}{2}$). Such a weak FM has also been reported in other theoretical studies [238] and small magnetic moments have been observed in many heavy-fermion materials, e.g., $CeAl_3$, UPt_3 and YbRhSb [220–222]. The AFM has an overall much higher magnetization. We also computed second order fluctuation corrections to the magnetization $m^{(2)}$ according to Section 5.4. Interestingly, the resulting fluctuation-corrected net magnetization $m^{(0)} + m^{(2)} = m_{\mathrm{MF+Fluc}}$ is even lower, as illustrated by the diamond-shaped data points in Figure 11.1(b), and goes down to a minimal value of $m_{\mathrm{MF+Fluc}} \approx 0.008$ at n_c. The strength of the respective order is also reflected in the critical temperature that marks the destruction of the magnetic state, i.e., the Néel temperature for the AFM with $T_{\mathrm{Neel}} \lesssim 0.12$, and Curie temperature for the FM with $T_{\mathrm{Curie}} \lesssim 0.04$ for $U = 2.4$. The transitions are of second-order, and the whole demagnetization takes place in a very small temperature interval of $\Delta T \approx 0.01$. These energy scales indicate that the magnetic order might be easily destroyed by disorder, which is present in many heavy fermion materials and could possibly extend the Kondo regime. Related questions are of particular interest because FM heavy-fermion materials have also been reported to feature unconventional superconductivity, and the fundamental mechanisms of these compounds are not fully understood [222].

11.2 Generalized model with two conduction bands

We generalize the PAM by adding a second conduction orbital that hybridizes with the f-electrons with the same on-site amplitude V. We do not allow hybridizations between the conduction bands but define on-site energies $\epsilon_{d_{1,2}}$, which result in an energy splitting $\Delta\epsilon_d = \epsilon_{d_2} - \epsilon_{d_1}$ that is crucial for the Fermiology of the model [56], and we will analyze its impact on the magnetic properties in this section. The corresponding Hamiltonian is given by [56]

$$H^{\mathrm{PAM}}_{2\,\mathrm{cond.}} = \tilde{H}_d + \tilde{H}_{\mathrm{hyb}} + H_f \,, \tag{11.4a}$$

with

$$\tilde{H}_d = \sum_{d=1}^{2}\left(-t\sum_{\langle i,j\rangle,\sigma}\hat{c}^\dagger_{i,\sigma,d}\hat{c}_{j,\sigma,d} + \sum_{i,\sigma}(\epsilon_d - \mu_0)\,\hat{c}^\dagger_{i,\sigma,d}\hat{c}_{i,\sigma,d}\right) = \sum_{\boldsymbol{k}}\hat{\boldsymbol{c}}^\dagger_{\boldsymbol{k}}\underline{\mathcal{H}}^d_{\boldsymbol{k}}\hat{\boldsymbol{c}}_{\boldsymbol{k}} \,, \tag{11.4b}$$

$$\tilde{H}_{\mathrm{hyb}} = V\sum_{d=1}^{2}\sum_{i,\sigma}\left(\hat{c}^\dagger_{i,\sigma,d}\hat{f}_{i,\sigma} + \hat{f}^\dagger_{i,\sigma}\hat{c}_{i,\sigma,d}\right) \,, \tag{11.4c}$$

$$H_f = U\sum_i \hat{f}^\dagger_{i,\uparrow}\hat{f}_{i,\uparrow}\hat{f}^\dagger_{i,\downarrow}\hat{f}_{i,\downarrow} + (\epsilon_f - \mu_0)\sum_{i,\sigma}\hat{f}^\dagger_{i,\sigma}\hat{f}_{i,\sigma} \,, \tag{11.4d}$$

where $\hat{\boldsymbol{c}}^\dagger_{\boldsymbol{k}} = \left(\hat{c}^\dagger_{\boldsymbol{k},\uparrow,d_1},\ \hat{c}^\dagger_{\boldsymbol{k},\downarrow,d_1},\ \hat{c}^\dagger_{\boldsymbol{k},\uparrow,d_2},\ \hat{c}^\dagger_{\boldsymbol{k},\downarrow,d_2}\right)$ is the spinor of conduction electrons in momentum space. The SW projection introduced in Section 10.3.3 may be generalized to $H^{\mathrm{PAM}}_{2\,\mathrm{cond.}}$ and maps its low energy physics in the limit of strong correlations onto a two-conduction-band KLM. The coupling constant in the EKL is given

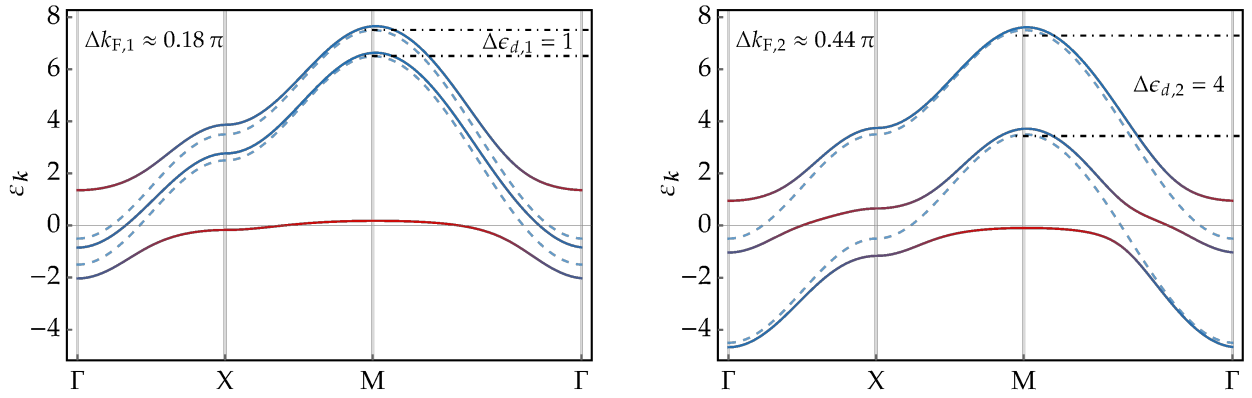

(a) $U = 0.8$, $\epsilon_{d_1} = -1$, and $n_f = V = 1$, $\mu_0 = -3.5$, $\epsilon_{d_2} = 0$.

(b) $U = 3.8$, $\epsilon_{d_1} = -4$ and $n_f = V = 1$, $\mu_0 = -3.5$, $\epsilon_{d_2} = 0$.

Figure 11.3: Solid lines represent the band structure (BS) of the interaction-renormalized two-conduction-band PAM [Equation (11.4a)] in the PM regime. Red coloring indicates spectral weight of the interacting f-orbital, which is half-filled. Dashed lines show the BS of the bare conduction Hamiltonian [Equation (11.4b)] that enters the KLM [Equation (11.5)]. The two sub-figures demonstrate the profound impact of the energy splitting $\Delta\epsilon_d$ of the conduction bands to the Fermiology of the problem, where Δk_{F} represents the Fermi-vector difference of the conduction band pockets.

by $J = 4V^2/U$, i.e., we may approximate it to be independent of ϵ_d, resulting in the Hamiltonian [56]

$$H^{\mathrm{KLM}}_{2\,\mathrm{cond.}} = \sum_{k,k'} \hat{c}^\dagger_k \underline{J} \hat{c}_{k'} \cdot \hat{\mathbf{S}}_{k'-k} + \tilde{H}_d \,, \tag{11.5a}$$

with the matrix representation of the coupling constant

$$\underline{J} = \frac{4V^2}{U} \underline{\mathbb{1}}_2 \otimes \underline{\tau} \,, \tag{11.5b}$$

where the unity matrix $\underline{\mathbb{1}}_2$ acts in orbital-space and $\underline{\tau}$ is the vector of Pauli matrices acting on spin-space. The BS of the interaction-renormalized two-conduction-band PAM in comparison to the bare conduction Hamiltonian $\tilde{H}_d$ is illustrated for two different energy splittings $\Delta\epsilon_d$ in Figure 11.3.

11.2.1 The RKKY-interaction

An effective long-range correlation of localized spins that is believed to have a profound impact on the magnetic properties of heavy-fermion materials is the so-called Ruderman–Kittel–Kasuya–Yosida (RKKY) interaction. It was initially formulated in 1954 to describe the indirect magnetic exchange coupling of nuclear magnetic moments mediated by conduction electrons in order to explain unexpectedly broad spin resonance lines in metallic silver [239]. The theory was then generalized by Tado Kasuya and Kei Yosida to spins of localized f-electrons that are indirectly coupled through a sea of conduction electrons, which initiated its high relevance to Kondo physics [209, 240].

Following References [56], [57], and [99], we may derive the RKKY interaction based on the two-conduction-band KLM defined in Equation (11.5) within a path integral scheme by integrating out the conduction electrons and expanding the resulting action up to second-order in $\hat{\mathbf{S}}$. The technical details are in analogy to the

calculation of SB Gaussian fluctuations in Section 5.2, yielding the partition function

$$\begin{aligned} Z &= \int \mathcal{D}[\boldsymbol{S}] \exp\left(\mathrm{Tr}\ln\left[-\underline{G}_k^{-1}\delta_{k,k'} + \underline{\boldsymbol{J}}\boldsymbol{S}_{k'-k}\right]\right) \\ &= \int \mathcal{D}[\boldsymbol{S}] \exp\left(\mathrm{Tr}\ln\left[-\underline{G}_k^{-1}\delta_{k,k'}\right] - \frac{1}{2}\mathrm{Tr}\left[\underline{G}_k\underline{\boldsymbol{J}}\boldsymbol{S}_{k'-k}\right]^2 + \mathcal{O}\left(\boldsymbol{S}^3\right)\right) \\ &\approx \int \mathcal{D}[\boldsymbol{S}] \exp\left(\mathrm{Tr}\ln\left[-\underline{G}_k^{-1}\delta_{k,k'}\right]\right) \exp\left(-\frac{1}{2}\mathrm{Tr}\, S^\alpha_{-\boldsymbol{q}} S^\beta_{\boldsymbol{q}} \underline{G}_{\boldsymbol{k},\mathrm{i}\omega_n} \underline{J}^\alpha \underline{G}_{\boldsymbol{k}+\boldsymbol{q},\mathrm{i}\omega_n} \underline{J}^\beta\right), \end{aligned} \tag{11.6}$$

where $G_{\boldsymbol{k},\mathrm{i}\omega_n} = \left(\mathrm{i}\omega_n - \underline{\mathcal{H}}^d_{\boldsymbol{k}}\right)^{-1}$ denotes the Green's function of the conduction Hamiltonian an the linear order of $\hat{\boldsymbol{S}}$ is zero due to the vanishing trace over Pauli the matrices. From Equation (11.6) we may extract the effective RKKY-Hamiltonian of localized spins $\hat{\boldsymbol{S}}$

$$H^{\mathrm{RKKY}} = \sum_{\alpha,\beta}\sum_{\boldsymbol{q}} \hat{S}^\alpha_{-\boldsymbol{q}} J^{\mathrm{RKKY}}_{\alpha,\beta,\boldsymbol{q}} \hat{S}^\beta_{\boldsymbol{q}}\,, \tag{11.7a}$$

and evaluate the occurring Matsubara summation in analogy to Equation (5.29a) to determine the coupling constant

$$J^{\mathrm{RKKY}}_{\alpha,\beta,\boldsymbol{q}} = \frac{1}{2}\sum_{\boldsymbol{k}}\sum_{\mathrm{i}\omega_n} \mathrm{tr}\, \underline{G}_{\boldsymbol{k},\mathrm{i}\omega_n} \underline{J}^\alpha \underline{G}_{\boldsymbol{k}+\boldsymbol{q},\mathrm{i}\omega_n} \underline{J}^\beta = \frac{1}{2}\left(\frac{4V^2}{U}\right)^2 \sum_{\boldsymbol{k},s,s'} \frac{n_{\mathrm{F}}\left(\varepsilon^d_{\boldsymbol{k},s}\right) - n_{\mathrm{F}}\left(\varepsilon^d_{\boldsymbol{k}+\boldsymbol{q},s'}\right)}{\varepsilon^d_{\boldsymbol{k},s} - \varepsilon^d_{\boldsymbol{k}+\boldsymbol{q},s'}} \delta_{\alpha,\beta} = -\frac{1}{2}\left(\frac{4V^2}{U}\right)^2 \chi^d_0(\boldsymbol{q})\delta_{\alpha,\beta}. \tag{11.7b}$$

The effective momentum-dependent coupling constant is thus proportional to the bare susceptibility $\chi^d_0(\boldsymbol{q})$ of the conduction Hamiltonian $\tilde{H}_d$, whose eigenvalues are labeled by $\varepsilon^d_{\boldsymbol{k},s}$ [48, 241]. The spatial dependence of J^{RKKY} is obtained by inverse Fourier transformation

$$J^{\mathrm{RKKY}}_{\boldsymbol{r}} = \frac{1}{\sqrt{N}}\sum_{\boldsymbol{q}} e^{\mathrm{i}\boldsymbol{q}\boldsymbol{r}} J^{\mathrm{RKKY}}_{\boldsymbol{q}}\,. \tag{11.7c}$$

For the one-conduction band PAM, it can be obtained analytically under the assumptions of a free electron gas, which is valid for small, circular FSs with Fermi vector k_{F} in the lattice model, yielding [241]

$$J^{\mathrm{RKKY}}_r \propto \begin{cases} \frac{1}{r^3}\left(\cos(2k_{\mathrm{F}}r) - \frac{\sin(2k_{\mathrm{F}}r)}{2k_{\mathrm{F}}r}\right) & \text{for 1 conduction band PAM in 3D} \\ J_0(k_{\mathrm{F}}r)Y_0(k_{\mathrm{F}}r) + J_1(k_{\mathrm{F}}r)Y_1(k_{\mathrm{F}}r) & \text{for 1 conduction band PAM in 2D}\,, \end{cases} \tag{11.7d}$$

where J_n and Y_n are Bessel functions of first and second kind, respectively. The RKKY-interaction is thus very sensitive to the Fermiology of the conduction Hamiltonian and oscillates within an enveloping function $\propto 1/r^3$ in 3D and $\propto 1/r^2$ in 2D with a periodicity that is approximately given by πk_{F}. For two conduction bands, J^{RKKY}_r is decomposed into two terms that can each be approximated by Equation (11.7d) with Fermi-vectors of the respective pocket plus an additional inter-band contribution. These properties give rise to the existence of interference effects, which may have a significant impact on the magnetic order in the two-conduction band PAM.

In order to shape the intuition about the RKKY-interaction and the requirements to the parameter regime of the PAM where it becomes dominant, we want to point out analogies to the Hubbard model. It has been known since the late 60s that the strong-coupling regime of the Hubbard model can be represented by the so-called t-J model, which essentially features a non-interacting orbital in addition to an AFM spin-exchange

coupling [242, 243]. A very similar relation is given between the PAM and KLM by the SW transformation. The main difference of those models is that the t-J model couples spins of the same orbital, whereas the KLM correlates spins of two different orbitals. If the Hubbard model is half-filled, the t-J model reduces to a short-range AFM Heisenberg model due to the Mott transition [244]. The KLM, on the other hand, can be mapped to the RKKY-Hamiltonian by integrating out the conduction electrons. It can be interpreted as a long-range Heisenberg model, whose magnetic ground state precisely depends on the explicit form of J_r^{RKKY}. In summary, itinerant models with a Hubbard-type interaction reduce to non-itinerant spin-exchange models in certain limits:

$$\begin{array}{ccccc} \text{Hubbard model} & \xrightarrow[\text{coupling}]{\text{strong}} & t\text{-}J\text{- model} & \xrightarrow[\text{Mott-limit}]{\text{half-filling}} & \text{AFM Heisenberg Hamiltonian} \\ \text{Periodic Anderson model} & \xrightarrow[\text{coupling}]{\text{strong}} & \text{Kondo lattice model} & \xrightarrow[\text{d-electrons}]{\text{integrate}} & \text{RKKY-Hamiltonian .} \end{array} \tag{11.8}$$

11.2.2 RKKY-induced magnetic frustration

We aim to find a parameter regime in the two-conduction-band PAM defined in Equation (11.4) that is dominated by the previously derived RKKY-interaction with a long-range coupling of the localized moments. Thus, we once more constrain the f-orbital to be half-filled $n_f = 1$ in accordance with the EKL and fix $V = t = 1$. We are primarily interested in investigating how the difference of conduction band Fermi vectors $\Delta k_{\mathrm{F}} = k_{\mathrm{F},2} - k_{\mathrm{F},1}$, which determines the interference of J_r^{RKKY}, affects the magnetic ordering. It can be directly tuned by the energy splitting of the conduction orbitals $\Delta\epsilon_d = \epsilon_{d_2} - \epsilon_{d_1}$. In order to fix one of the pockets as a reference point, we choose $\mu_0 = -3.5, \epsilon_{d_2} = 0$ and keep ϵ_{d_1} and U as free parameters.

To map out the magnetic phase diagram by means of the SB method [56], we once solved the saddle point equations given by Equation (11.1), where the eigenvalues that enter the FE are determined by numerically diagonalizing the renormalized hopping matrix of the two-conduction-band PAM, i.e., Equation (B.23). The result is presented by Figure 11.4(a), and we indeed find the critical interaction U_c that marks the onset of magnetic order to be highly dependent on Δk_{F}, with a sharp maximum at $\Delta k_{\mathrm{F}} \approx 0.44\pi$[1]. The respective conduction-band Fermi surfaces along with another exemplary set with smaller $\Delta k_{\mathrm{F}} \approx 0.18\pi$ and an associated lower critical interaction are shown in Figure 11.4(b). Moreover, Figure 11.3 displays the matching band structures. In order to investigate whether frustration effects mediated by the RKKY-interaction could explain the peak, we numerically evaluated the spatial dependence of J_r^{RKKY} by means of Equation (11.7c), and the result for the two previously chosen Δk_{F} is summarized in Figure 11.4(c). For small pockets, we find J_r^{RKKY} to be relatively short-ranged with a positive NN coupling, similar like one would expect for the one-conduction-band PAM. Increasing the diameter of the second pocket, however, initiates frustration effects that manifest as a long-ranged RKKY profile with multiple coupling constants that are in the same order of magnitude in addition to an overall decreased interaction scale that can especially be seen by comparing the NN coupling of the two chosen Δk_{F}.

In the following, we provide two more arguments, why the domain around the maximum of U_c at $\Delta k_{\mathrm{F}} \approx 0.44\pi$ can be associated with an RKKY-dominated parameter regime of the two-conduction-band PAM. Firstly, we expect double occupied sites to be mainly projected out in that limit. The applied constraint $n_f = 1$ that is enforced by tuning the on-site energy ϵ_f, however, only tunes the total filling, while the distribution to

[1] In order to achieve the plotted differences in Δk_{F}, we tuned ϵ_{d_1} from 0 to −7.5. The PM phase boundary is determined by second-order magnetic transitions and can be equivalently found by divergences of the static spin susceptibility $1/\chi_s^{\mathrm{PM}}(\boldsymbol{q} = \boldsymbol{Q}, \omega = 0) = 0$.

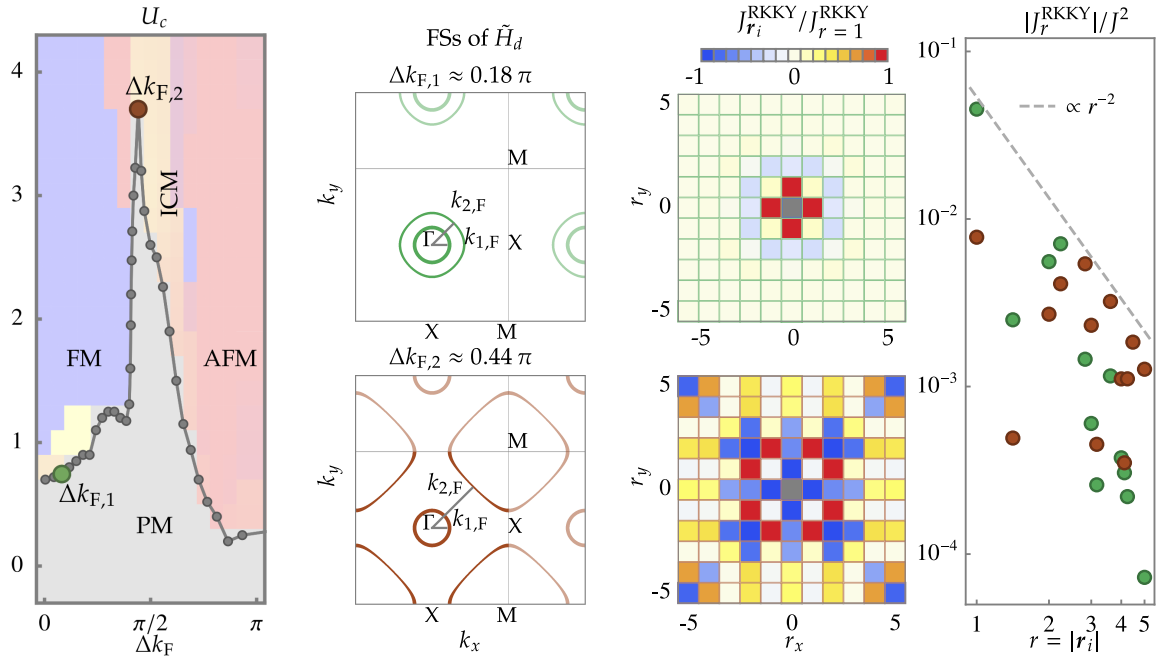

(a) SB magnetic MF phase diagram. **(b)** Conduction Hamiltonian FSs that define Δk_F. **(c)** Normalized, spatially dependent RKKY-interaction for the two different Δk_F in Figure 11.4(b).

Figure 11.4: The SB mean-field phase diagram of the two-conduction-band PAM features a sharp peak of the critical interaction U_c that marks the onset of magnetism as a function of the difference of Fermi surface (FS) diameters Δk_F of the bare (non-hybridized) conduction bands. Corresponding FSs are exemplarily shown and can be understood as Schrieffer–Wolff projection of the PAM. The difference Δk_F also significantly determines the functional behavior of the RKKY-interaction that we find to be parametrically frustrated and overall decreased in strength around the maximum of U_c, which allows the identification of an RKKY-dominated regime of the PAM. Figure adapted from [56, 57].

empty, doubly, and singly occupied sites is determined by the PM saddle point equations with $n_f = 2d^2 + p_0^2$. We find the maximum of single occupation to be aligned with the highest value of U_c ($p_0^2 \approx 0.71$ at $\Delta k_{F,2}$), which supports the applicability of the SW projection as an approximation in that domain. Secondly, the frustration also manifests in the slave-boson MF free energy $F_{\boldsymbol{Q}}^{(0)}$ via multiple (up to six) local minima at different magnetic ordering vectors $\boldsymbol{Q}$ and the formation of incommensurate magnetism (ICM) around $\Delta k_{F,2}$. In opposition, it becomes much more smooth for in the domains of small U_c, where magnetic instabilities are predominantly of the FM and AFM type. Remarkably, a Luttinger-Tisza analysis [245] of the RKKY-coupling around $\Delta k_{F,2}$ even yields qualitatively matching ICM phases, which also supports the applicability of H^{RKKY} as low energy description of the PAM around that point.

To sum up, we have shown that tuning the size of two different conduction electron pockets can initiate a sharp maximum of the critical interaction U_c as a consequence of frustration in the effective RKKY-interaction. Although we cannot directly write down a Kondo ground state within the SB scheme, we expect the interplay between the RKKY-interaction and Kondo physics to become relevant [246]. Moreover, the maximum in U_c coincides with a minimum of the Néel temperature $T_{\text{Néel}}$ and the frustration effect could be a starting point to understand why $T_{\text{Néel}}$ can differ significantly in various heavy-fermion compounds [218, 247]. Finally, a PM high-interaction regime is also of interest in the context of heavy-fermion superconductivity.

CHAPTER 12

Topology and magnetism in Kondo insulators

Three-dimensional (3D) topological insulators (TIs) describe materials that are insulating in the interior due to a finite energy gap between the valence and conduction band of the bulk Hamiltonian but can transport electrons on their boundaries because of robust, topologically protected surface states (TSSs). The concept of topological Kondo insulators (TKIs) was introduced by Maxim O. Dzero *et al.* in 2010 [32] and combines the properties of Kondo insulators (KIs) with the occurrence of topologically non-trivial phases. He pointed out that KIs provide the key ingredients that are required for topological order: Despite being strongly correlated systems, their renormalized ground state can oftentimes be considered to be adiabatically connected to non-interacting limit, and their multi-orbital band structure (BS) is insulating at low temperatures due to an emerging hybridization gap mediated by the Kondo effect. Moreover, KIs feature intrinsically strong spin-orbit coupling (SOC) that promotes topological phases if it arises in the form of a *centrosymmetric* hybridization that preserves inversion- and time-reversal symmetry (TRS). This specific form can be achieved in Hamiltonians, where the hybridizing f- and conduction orbitals have opposite parity.

A couple of actual materials have been proposed to be TKIs, with the most promising candidate being samarium hexaboride (SmB_6), where multiple theoretical studies predict TSSs in the form of three gapless surface cones [57, 229, 230, 248, 249]. There is, however, some controversy about the nature of the true ground state of the material. On the one hand, experimental evidence from transport, scanning tunneling, quantum oscillation, and ARPES measurements confirms the existence of gapless surface states [250–254], and SARPES data indicates that these are spin-polarized [255], which implies a topological scenario. On the other hand, also arguments for a topologically trivial ground state [256, 257] or even a bulk-metallic transition under high pressure [258] have been reported. In addition, specifics of the magnetic properties are still under debate. Multiple studies suggest a paramagnetic (PM) ground state with intrinsic spin fluctuations [259, 260], but also A-type ($\boldsymbol{Q} = [\pi, \pi, 0]^\top$) [261, 262] and Néel type ($\boldsymbol{Q} = [\pi, \pi, \pi]^\top$) antiferromagnetism (AFM) under high pressure [258, 263] and surface ferromagnetism (FM) [254] have been observed.

This chapter will discuss magnetic and topological phases in KIs based on the two-band TKI model that we introduced in Section 10.3.4 as a generalization of the periodic Anderson model (PAM) with additional f-electron hopping and centrosymmetric SOC. First of all, in Section 12.1, we summarize basic knowledge on topology in condensed matter physics (CMP) that will be necessary to classify the topological phases that arise within the TKI model. In Section 12.2, we will account for the Hubbard interaction of the f-electrons through the slave-boson (SB) mean-field approach and elaborate on why the centrosymmetric SOC is an essential ingredient for non-trivial topology. Based on Reference [54], we map out the interaction-dependent phase diagram shown in Figure 12.3 and contextualize our findings with the material SmB_6. We identify multiple topologically distinct magnetic and non-magnetic phases and provide a stability analysis that reveals their robustness w.r.t. Gaussian fluctuations. Resulting from the interplay of topology and magnetism, we find an

antiferromagnetic topological insulator (ATI) at high interactions and discuss the respective TSSs that emerge in the form of one-dimensional chiral hinge modes in Section 12.3.

12.1 Basics on topology in condensed matter physics

Topology is a branch in mathematics that addresses the properties of geometrical objects that are conserved (i.e., topologically invariant) under continuous transformations such as twisting and bending without closing or opening up holes. Its origin goes back to Euler's ideas, which arguably provided the first practical application with the solution of the well-known *Seven Bridges of Königsberg problem* in 1736 [264]. Poincaré's *Analysis Situs* achieved a further ground-breaking success that broadly established the field in 1895. The relevance of the concept in CMP was, however, not realized until the 1980s and the discovery of the quantum Hall effect (QHE) by Klaus von Klitzing in Würzburg [31]. The phenomenon can be theoretically described by means of the so-called Chern Number, a topological invariant [265–267]. In the following, we will summarize the basic concepts of topology in CMP based on Reference [99].

12.1.1 Topological phases

After the introduction of Lev Landau's famous article "*On the theory of phase transitions*" in 1937 [25], it had been believed that different phases could be distinguished through their symmetries and the definition of a *local order parameter*. Such transitions towards an ordered phase are usually fueled by interaction effects and arise suddenly below a certain critical temperature by spontaneously breaking symmetries of the initial system. A prominent example that we have extensively discussed within this thesis are magnetic phases, where the magnetization m serves as local order parameter ($m = pp_0$ within the SB scheme) and breaks spin-rotation invariance (SRI) as well as TRS and depending on the specific problem possibly also translation- and lattice-symmetries. This point of view had to be adjusted with the discovery of topological phases that cannot be quantified by a local order parameter but rather depend on the global properties of the ground state. Those can be classified with so-called topological invariants that are characterized by discrete sets of integers and will be further discussed in Section 12.1.2. Corresponding phase transitions also appear in non-interacting systems and without symmetry-breaking.

Within that scope, two phases are – in reminiscence of the geometric origin of the field – *topologically equivalent* if they are connected by an *adiabatic* change of parameters of the underlying Hamiltonian. Such a change has to uphold a one-to-one correspondence between associated states [39], which holds for band insulators (BIs) due to their finite energy gap[1]. If the allowed adiabatic transformations are additionally restricted to uphold certain underlying symmetries of the system, otherwise equivalent phases can be distinguished by different topological classes, yielding symmetry-protected topological (SPT) phases [268]. A ground state that is equivalent to an atomic limit, where all electrons are exponentially localized in position space and infinitely separated, is not topological and referred to as trivial BI [269]. We can summarize topological order in CMP as follows [99]: Topological phases are characterized by a discrete set of integers called topological invariants that can only change if the bulk energy gap closes or if the protecting symmetry of the SPT phase is broken.

[1] There are also topological quantum states that are not BIs, e.g., Weyl semimetals or topological superconductors that will, however, not be further discussed within this thesis.

Surface states and the bulk boundary correspondence

A central property of TIs are gapless surface states that are exponentially located at the boundaries of the system[1]. While the bulk of a TI is insulating, the energy gap is therefore closed on the surface, which makes it conducting on the exterior. In CMP, on usually employs periodic boundary conditions (PBC) because the resulting translation symmetry enables the momentum $\boldsymbol{k}$ in the Brillouin zone (BZ) as a good quantum number that greatly simplifies the problem. This assumption, however, only allows the investigation of the bulk, which is arguably the reason why topological order in CMP has been overlooked for so long, and Wolfgang Pauli once allegedly said: "*God made the bulk; the surface was invented by the devil*".

By means of topological invariants that are defined within the bulk, we can, nevertheless, infer the existence of topologically protected surface states (TSSs), which are robust w.r.t. local perturbations and the geometry of the probe, without explicitly breaking the PBCs. This remarkable feature can be explained intuitively [99]: The vacuum as an atomic limit is topologically trivial, while a non-trivial topological invariant of a TI within the bulk can only change if the energy gap closes or if the protecting symmetry of the SPT phase is broken. Therefore, if two states with different topological invariants meet at a spatial interface that respects the protecting symmetry, the energy gap has to close, which creates the TSS. This profound relationship between the global properties of the bulk and the TSS is known as *bulk-boundary-correspondence* [270, 271]. A general, rigorous mathematical proof of the concept is difficult but has been achieved for specific models [272]. Since 2007, the existence of such topological states in quantum matter has experimentally been verified in multiple materials [273–275].

Higher-order topology

In 3D systems, the concept of the bulk-boundary-correspondence can be generalized to higher-order topological insulators (HOTIs) [276, 277]. Under certain conditions, the surface states of the 3D TI gap out, but gapless one-dimensional states at the hinges or zero-dimensional states at the corners of the system remain. First experimental evidence of a HOTI has recently been found in elementary Bismuth [278].

12.1.2 Topological invariants

An intuitive mathematical understanding of topological invariants can be given as follows: A function of continuous parameters is mapped to a discrete integer quantity (the topological invariant) that jumps discontinuously at topological phase transitions and remains unchanged for parameter changes within the same phase. In CMP, it often involves an integral of a band structure quantity within the BZ. However, the concept is not limited to quantum mechanical systems, and topological order can, e.g., also be realized by a periodic arrangement of mechanical springs or electrical circuits [279].

For the topological classification of the TKI model discussed in this thesis, we will apply the $\mathbb{Z}_2$ invariants for the 3D topological insulator given by Equation (12.7). For completeness, we will nevertheless provide a short overview of the most important topological invariants with historical context based on Reference [99]. Those quantities were initially derived for non-interacting systems. Therefore, the SB formalism is quite convenient to investigate topological order in the context of strong correlations because the interaction-renormalized MF band structure behaves like an effectively non-interacting quasiparticle Hamiltonian.

[1] Topology can arise in arbitrary spatial dimensions, by "*surface*" we generally address boundaries of the respective dimension, i.e., actual surfaces in 3D, edges in 2D or endpoints in 1D.

The Chern number

In 1980, Klaus von Klitzing made a surprising discovery while performing experiments with a silicon metal-oxide-semiconductor field-effect transistor at low temperatures with a strong perpendicular magnetic field. He observed that the Hall resistivity developed plateaus at integer multiples of e^2/h, where e is the elementary charge and h the Planck constant, while the classical solution according to the Maxwell equations suggested a linear increase as a function of the magnetic field. Although the plateaus had been theoretically predicted a few years earlier [280], the apparent robustness w.r.t. sample geometry and local perturbations was puzzling. An elegant explanation of the exact quantization was then given by Robert B. Laughlin in 1981 by means of gauge invariance [281], and a first connection to topology was made shortly afterward with the introduction of the Thouless–Kohmoto–Nightingale–den Nijs (TKNN) invariant [282]. This integer-valued quantity could only change if the bulk gap closes and coincides with the number of chiral edge states associated with the QHE and thereby explained the quantization of the Hall conductivity

$$\sigma_{xy} = -\frac{e^2}{h} C \,. \tag{12.1}$$

It was later understood that the TKNN invariant was equivalent to the Chern number C, which was known from the branch of topology in mathematics [265–267]. It is the first topological invariant discussed in CMP and explains the robustness of the QHE as a topological effect.

The Chern number can intuitively be introduced by analogy with the so-called Euler characteristic, a geometric quantity. According to the Gauss-Bonnet theorem of differential geometry, it is given by the integral over the so-called Gaussian curvature $F_G(x)$ on a boundary-less 2D compact Riemann surface M [99, 283]

$$2 - 2g = \frac{1}{2\pi} \int_M d^2x \, F_G(\boldsymbol{x}) \,. \tag{12.2}$$

The integer-valued number g is a topological invariant called *genus* and can be interpreted as the number of holes of an object that does not change by smooth bending or twisting. Based on that property, there is a well-known joke around mathematicians that "*a topologist is a person who can't tell the difference between a donut and a coffee cup*" [284]. In CMP, the Euler characteristic is replaced by the Chern number [283]

$$C = \frac{1}{2\pi} \int_{\mathrm{BZ}} d^2k \, \mathcal{F}(\boldsymbol{k}) \,, \tag{12.3a}$$

the Rieman manifold by the BZ and the analogue of the Gaussian curvature is the so-called *Berry curvature* [285]

$$\mathcal{F}(\boldsymbol{k}) = \sum_{a=1}^{n} \mathcal{F}_a(\boldsymbol{k}) \,, \tag{12.3b}$$

with

$$\mathcal{F}_a(\boldsymbol{k}) = \frac{\partial \mathcal{A}_{a,2}(\boldsymbol{k})}{\partial k_1} - \frac{\partial \mathcal{A}_{a,1}(\boldsymbol{k})}{\partial k_2} \,. \tag{12.3c}$$

The sum has to be performed over all occupied energy bands a and the function $\mathcal{A}$ is called *Berry connection*, with

$$\mathcal{A}_{a,j}(\boldsymbol{k}) = \mathrm{i} \left\langle \boldsymbol{u}_a(\boldsymbol{k}) \middle| \partial_{k_j} \middle| \boldsymbol{u}_a(\boldsymbol{k}) \right\rangle \,, \tag{12.3d}$$

where $|\boldsymbol{u}_a(\boldsymbol{k})\rangle$ denote the Bloch-eigenstates of the Hamiltonian. Aligning with the concept of topology, it is only well defined if there is a finite energy gap between occupied and unoccupied bands.

Periodic table of topological invariants

According to Alex Atland's and Martin R. Zirnbauer's work in 1997, non-interacting electron systems can be categorized by means of the properties of the respective Hamiltonian w.r.t. time-reversal symmetry (TRS) represented by the operator $\hat{\mathcal{T}}$, particle-hole symmetry (PHS) $\hat{\mathcal{P}}$ and Chiral symmetry $\hat{\mathcal{C}} = \hat{\mathcal{T}}\hat{\mathcal{P}}$ [286]. The time-reversal (TR) and particle-hole operators are anti-unitary, i.e., $\hat{\mathcal{T}}^2 = \pm 1, \hat{\mathcal{P}}^2 = \pm 1$ and by accounting for all possible combinations of those values or the absence of respective symmetries, there are ten different Altland–Zirnbauer (AZ) symmetry classes [287]. In addition, the number of spatial dimensions plays an important role of whether topological order is feasible or not. In 2008, all AZ classes with non-trivial topology were identified in 3D, and the concept was generalized to arbitrary dimensions shortly after [288, 289]. It turned out that the pattern repeats with a periodicity of $D \rightarrow D + 8$, which leads to the *Periodic table of topological invariants*. The corresponding topological invariants are either $\mathbb{Z}$-valued (e.g., the Chern number that does feature an underlying symmetry) or $\mathbb{Z}_2$-valued (i.e., the only possible values are 0 and 1).

An important model for a Chern insulator that significantly pushed the field of topology in CMP was proposed by Dunkin Haldane in 1988 on the 2D honeycomb lattice [290]. It did not require an external magnetic field like the QHE, but TRS was intrinsically broken by a complex hopping between the sublattices. In 2005, Charles L. Kane and Eugene J. Mele developed a model that restored TRS by effectively stacking two copies of the Haldane model, one for spin up and one for spin down, with opposite Chern numbers [291]. It features the quantum spin Hall effect (QSHE) that employs gapless, counter-propagating edge modes with opposite spin (*helical* edge states) that are protected by the so-called spin Chern number as topological invariant. One year later, Andrei B. Bernevig, Taylor L. Hughes, and Shou-Cheng Zhang introduced their prominent model for the QSHE in the presence of strong SOC in mercury telluride quantum wells [292] that was supported by the first experimental observation of the QSHE by Molenkams group in Würzburg in 2007 [273]. While the QSHE requires spin conservation, Charles L. Kane and Eugene J. Mele showed around the same time that there was another topological invariant if spin conservation was broken, e.g., by a Rashba-type SOC [291]. To be specific, it is a $\mathbb{Z}_2$ invariant, where the value 0 yields trivial and 1 non-trivial topology and coincides with the AII AZ-symmetry class in the presence of TRS with $\hat{\mathcal{T}}^2 = -1$[1] and can also be generalized to 3D. Finally, we will conclude our summary on topology in CMP with the discussion of those TRS protected $\mathbb{Z}_2$ invariants that we will later apply to topologically classify the TKI model.

$\mathbb{Z}_2$ invariant for the 2D topological insulator

The protecting symmetry of the $\mathbb{Z}_2$ invariant in TIs is time-reversal symmetry (TRS) and the respective transformation reverses the arrow of time $\hat{\mathcal{T}} : t \rightarrow -t$. The fulfillment of the canonic commutator $[\hat{x}\ ,\ \hat{p}]_- = \mathrm{i}\hbar$ dictates that it is anti-unitary, i.e., it can be represented by a unitary matrix $\underline{U}$ times the operator of complex conjugation $\mathcal{K}$

$$\hat{\mathcal{T}} = \underline{U}\mathcal{K}\ . \tag{12.4a}$$

[1] $\hat{\mathcal{T}}^2 = -1$ holds for fermionic spin-$\frac{1}{2}$ systems.

For a spin-$\frac{1}{2}$ system, it fulfills [293]

$$\hat{\mathcal{T}}^2 = -1 \quad \Leftrightarrow \quad \hat{\mathcal{T}}^\dagger = \hat{\mathcal{T}} = -\hat{\mathcal{T}}^{-1} \,, \tag{12.4b}$$

and flips the spin σ as well as the momentum $\boldsymbol{k}$ of the corresponding fermionic creation operator

$$\hat{\mathcal{T}}\hat{c}^\dagger_{k,\uparrow}\hat{\mathcal{T}}^{-1} = -\hat{c}^\dagger_{-k,\downarrow} \,. \tag{12.4c}$$

A concrete operator-representation is therefore given by

$$\hat{\mathcal{T}} = -\mathrm{i}\underline{\tau}^y\mathcal{K} \,, \tag{12.4d}$$

where $\underline{\tau}^y$ is the second Pauli-matrix in spin space, and $\hat{\mathcal{T}}$ acts diagonal in orbital space. It can be shown that the Bloch matrix $\underline{\mathcal{H}}_{\boldsymbol{k}}$ of a TR-symmetric Bloch Hamiltonian $H = \sum_{\boldsymbol{k}} \hat{\boldsymbol{c}}^\dagger_{\boldsymbol{k}}\underline{\mathcal{H}}_{\boldsymbol{k}}\hat{\boldsymbol{c}}_{\boldsymbol{k}}$ with $\left[H \,,\, \hat{\mathcal{T}}\right]_- = 0$ transforms like[1] [293]

$$\hat{\mathcal{T}}\underline{\mathcal{H}}_{\boldsymbol{k}}\hat{\mathcal{T}}^{-1} = \underline{\mathcal{H}}_{-\boldsymbol{k}} \,. \tag{12.5a}$$

Also, TRS implies a relationship between the Bloch wave-function $|\boldsymbol{u}_a(\boldsymbol{k})\rangle$ that satisfies $\underline{\mathcal{H}}_{\boldsymbol{k}}\,|\boldsymbol{u}_a(\boldsymbol{k})\rangle = \varepsilon^a_{\boldsymbol{k}}\,|\boldsymbol{u}_a(\boldsymbol{k})\rangle$ and its time-reversed counterpart, which is an eigenstate of $\underline{\mathcal{H}}_{-\boldsymbol{k}}$ with the same eigenvalue

$$\underline{\mathcal{H}}_{-\boldsymbol{k}}\hat{\mathcal{T}}\,|\boldsymbol{u}_a(\boldsymbol{k})\rangle = \hat{\mathcal{T}}\underline{\mathcal{H}}_{\boldsymbol{k}}\hat{\mathcal{T}}^{-1}\hat{\mathcal{T}}\,|\boldsymbol{u}_a(\boldsymbol{k})\rangle = \hat{\mathcal{T}}\varepsilon^a_{\boldsymbol{k}}\,|\boldsymbol{u}_a(\boldsymbol{k})\rangle = \varepsilon^a_{\boldsymbol{k}}\hat{\mathcal{T}}\,|\boldsymbol{u}_a(\boldsymbol{k})\rangle \,. \tag{12.5b}$$

Moreover, these states are orthogonal according to Kramers theorem [294]

$$\left\langle \boldsymbol{u}_a(\boldsymbol{k}) \middle| \hat{\mathcal{T}} \middle| \boldsymbol{u}_a(\boldsymbol{k}) \right\rangle = 0 \,. \tag{12.5c}$$

As a consequence, the energy bands are two-fold degenerate at time-reversal-invariant momenta (TRIM) Γ_i that satisfy $\Gamma_i = -\Gamma_i + G$, where G is a reciprocal lattice vector. In 2D, there are four TRIM

$$\Gamma_i \in \left\{(0,0)^\top \,, (0,\pi)^\top \,, (\pi,0)^\top \,, (\pi,\pi)^\top\right\} \,, \tag{12.6a}$$

and the respective degenerate states are called Kramers pairs.

According to the pioneering work in 2005, the $\mathbb{Z}_2$ invariant ν of the 2D topological insulator can be calculated the evaluation of the Pfaffian of the matrix $\left\langle \boldsymbol{u}_a(\boldsymbol{k}) \middle| \hat{\mathcal{T}} \middle| \boldsymbol{u}_b(-\boldsymbol{k}) \right\rangle$ at the TRIM, where the band indices a, b label occupied Kramers pairs [291, 295]. In 2007, Liang Fu and C. L. Kane were able to show that the formula was simplified in the presence of additional inversion symmetry $\hat{\mathcal{I}} : \boldsymbol{r} \to -\boldsymbol{r}$, where ν is determined by the inversion eigenvalues of the Bloch states at the TRIM [274]

$$(-1)^\nu = \prod_{i=1}^{4}\prod_a \xi_{i,a} \,. \tag{12.6b}$$

Inversion symmetry guarantees the parity

$$\xi_{i,a} = \left\langle \boldsymbol{u}_a(\Gamma_i) \middle| \hat{\mathcal{I}} \middle| \boldsymbol{u}_a(-\Gamma_i) \right\rangle = \pm 1 \tag{12.6c}$$

[1] The Bloch matrix may contain spin and orbital degrees of freedom that are contained in the spinor $\hat{\boldsymbol{c}}^\dagger_{\boldsymbol{k}}$ and will be labeled by the multi-index a in the following.

to be well defined at the TRIM and a labels all occupied Kramers pairs. The TSSs for a non-trivial $\mathbb{Z}_2$ invariant $\nu = 1$ are helical edge states in analogy to the QSHE, with time-reversal being the protecting symmetry [99].

$\mathbb{Z}_2$ invariants for the 3D topological insulator

The same concept can be generalized to 3D systems with TRS [296, 297], which yields four $\mathbb{Z}_2$ invariants $(\nu_0, \nu_1, \nu_2, \nu_3)$ for a total of $2^4 = 16$ topologically distinct states. First of all there are three $\mathbb{Z}_2$ invariants (ν_1, ν_2, ν_3) that classify so-called weak topological insulators (WTIs). These correspond to a stacking of 2D TI layers, which requires translation invariance. WTIs are thus susceptible to disorder. With additional inversion symmetry, the invariants can be calculated by [99]

$$(-1)^{\nu_i} = \prod_{j,k_i=\pi} \prod_{a} \xi_{j,a} \,, \tag{12.7a}$$

where the parities $\xi_{i,a}$ defined in Equation (12.6c) have to be evaluated at the TRIM in 3D

$$\Gamma_i \in \left\{(0,0,0)^\top, (0,0,\pi)^\top, (0,\pi,0)^\top, (\pi,0,0)^\top, (0,\pi,\pi)^\top, (\pi,0,\pi)^\top, (\pi,\pi,0)^\top, (\pi,\pi,\pi)^\top\right\} \tag{12.7b}$$

that satisfy $k_i = \pi$ and the index a again labels all occupied Kramers pairs. The strong index ν_0 does not require any additional symmetry besides TRS and can be thought of as a true 3D invariant. In the presence of inversion symmetry, it is given by[1]

$$(-1)^{\nu_0} = \prod_{i=1}^{8} \prod_{a} \xi_{i,a} \,, \tag{12.7c}$$

and the respective topological phase is referred to as strong topological insulator (STI). Non-trivial indices $\nu_i = 1$ implicate TSSs on boundaries of the 3D crystal. These manifest as gapless Dirac cones on the surface Brillouin zone (SBZ) and are spin-polarized. This effect is called *spin-momentum-locking* as a unique feature of 3D TIs [99, 271]. The STI features an odd number of surface cones, whereas the WTI employs an even number. According to the *fermion-doubling-theorem* theorem proved by Holger B. Nielsen and Masao Ninomiya in 1981, chiral Dirac cones in 2D systems always come in pairs [298, 299]. This theorem still holds, but in 3D, they may appear on opposite boundaries, i.e., they can be spatially separated [271]. The previously discussed symmetry-protected gapless surface cones occur at high symmetry points (HSPs) of the SBZ if an odd number of band inversions of the respective bulk HSPs is projected onto them [99, 274].

Topological crystalline insulators

For completeness, we want to mention that there are additional topological invariants, which are protected by point group symmetries of the lattice (e.g., mirror or rotation symmetry), and constitute the class of topological crystalline insulators (TCIs) [300]. A systematic approach to classify topological phases in all possible BSs of weakly correlated materials was proposed by Bernevig's group with the topological quantum chemistry [269]. The key insight is to define a topologically non-trivial phase by the property that it "*cannot be continued to any atomic limit without either closing a gap or breaking a symmetry*" [269] and analyzing all 230 crystal symmetry groups in that regard. The approach was recently generalized to the 1651 magnetic space groups [301].

[1] Without inversion, symmetry the STI and WTI phases are still well defined, but the calculation of the respective invariants is more complicated [293].

12.2 Topological Kondo insulator phase diagram

In order to map out the interaction-dependent phase diagram of the minimal TKI model and study its magnetic and topological properties, we apply the slave-boson representation introduced in Part I to Equation (10.10) and employ a static, uniform MF approximation for the bosonic fields [57]. We start off with a PM ansatz ($p = \beta = 0$), which results in the 4×4 quasiparticle (QP) hopping matrix

$$\underline{H}_{\boldsymbol{k}}^{\mathrm{PM}} = \begin{pmatrix} \left(\xi_{\boldsymbol{k}}^{d} - \mu_0\right) \underline{\tau}^0 & z_0 \boldsymbol{V}_{\boldsymbol{k}} \underline{\boldsymbol{\tau}} \\ z_0 \boldsymbol{V}_{\boldsymbol{k}} \underline{\boldsymbol{\tau}} & \left(z_0^2 \xi_{\boldsymbol{k}}^{f} + \epsilon_f + \beta_0 - \mu_0\right) \underline{\tau}^0 \end{pmatrix} \tag{12.8a}$$

that is derived in Appendix B.3 with the according basis

$$\hat{\boldsymbol{\phi}}_{\boldsymbol{k}} = \left(\hat{c}_{\boldsymbol{k},\uparrow}, \quad \hat{c}_{\boldsymbol{k},\downarrow}, \quad \hat{f}_{\boldsymbol{k},\uparrow}, \quad \hat{f}_{\boldsymbol{k},\downarrow}\right)^{\mathsf{T}} . \tag{12.8b}$$

Conduction electrons with spin σ and momentum $\boldsymbol{k}$ are represented by $\hat{c}_{\boldsymbol{k},\sigma}$ and $\hat{f}_{\boldsymbol{k},\sigma}$ describes pseudofermions (PFs) that are associated with the interacting f-electrons within the SB representation. The dispersions $\xi_{\boldsymbol{k}}^{d,f}$ of the conduction and f-electrons depend on the specific hopping scheme but are even functions of $\boldsymbol{k}$. Due to the spin-dependent nearest neighbor (NN) hybridization V of the TKI model in real space, it features a momentum dependent SOC

$$\boldsymbol{V}_{\boldsymbol{k}} \underline{\boldsymbol{\tau}} = -2V \left(\sin k_x \underline{\tau}^x + \sin k_y \underline{\tau}^y + \sin k_z \underline{\tau}^z\right) , \tag{12.8c}$$

where $\underline{\tau}^\alpha$ denotes the α-th Pauli matrix and $\underline{\tau}^0$ the unity matrix in spin space. In analogy to the PAM that we analyzed by means of the SB method in Chapter 11, the hopping amplitudes of the interacting electrons are renormalized by $t_f \to z_0^2 t_f$, $V \to z_0 V$ with $z_0 \leq 1$ and the effective on-site potential of the f-electrons is increased by $\epsilon_f \to \epsilon_f + \beta_0$ with $\beta_0 \geq 0$. The specific values are determined by the solution of the saddle point equations that depend on the Hubbard interaction U and recover $z_0 \to 1, \beta_0 \to 0$ in the non-interacting limit $U \to 0$.

As previously discussed, the conduction electrons are even under parity, whereas the f-electrons are odd, i.e., the respective operators transform under inversion $\hat{\mathcal{I}}$ according to

$$\hat{\mathcal{I}} \hat{c}_{\boldsymbol{k},\sigma}^{(\dagger)} \hat{\mathcal{I}}^{-1} = \hat{c}_{-\boldsymbol{k},\sigma}^{(\dagger)} , \tag{12.9a}$$

$$\hat{\mathcal{I}} \hat{f}_{\boldsymbol{k},\sigma}^{(\dagger)} \hat{\mathcal{I}}^{-1} = -\hat{f}_{-\boldsymbol{k},\sigma}^{(\dagger)} . \tag{12.9b}$$

As we elaborated on in Section 12.1.2, the TR-transformation $\hat{\mathcal{T}}$ yields[1]

$$\hat{\mathcal{T}} \hat{c}_{\boldsymbol{k},\sigma}^{(\dagger)} \hat{\mathcal{T}}^{-1} = \mathrm{sgn}(\sigma) \hat{c}_{-\boldsymbol{k},-\sigma}^{(\dagger)} , \tag{12.9c}$$

$$\hat{\mathcal{T}} \hat{f}_{\boldsymbol{k},\sigma}^{(\dagger)} \hat{\mathcal{T}}^{-1} = \mathrm{sgn}(\sigma) \hat{f}_{-\boldsymbol{k},-\sigma}^{(\dagger)} . \tag{12.9d}$$

After all, inversion acts diagonal in spin space and TR diagonal on orbital space, which allows for the following matrix representations of the operators:

$$\hat{\mathcal{I}} = \begin{pmatrix} \underline{\tau}^0 & 0 \\ 0 & -\underline{\tau}^0 \end{pmatrix}, \tag{12.9e}$$

$$\hat{\mathcal{T}} = \begin{pmatrix} -\mathrm{i}\tau^y & 0 \\ 0 & -\mathrm{i}\tau^y \end{pmatrix} \mathcal{K}. \tag{12.9f}$$

Finally, since the diagonal elements of $\underline{H}_{\boldsymbol{k}}^{\mathrm{PM}}$ w.r.t. orbital space are even functions of $\boldsymbol{k}$ and the off-diagonal hybridization is odd $V_{\boldsymbol{k}} = -V_{-\boldsymbol{k}}$, we can directly verify that the Hamiltonian fulfills inversion and time-reversal symmetry, i.e.,

$$\hat{\mathcal{I}}\, \underline{H}_{\boldsymbol{k}}^{\mathrm{PM}}\, \hat{\mathcal{I}}^{-1} = \underline{H}_{-\boldsymbol{k}}^{\mathrm{PM}}, \tag{12.9g}$$

$$\hat{\mathcal{T}}\, \underline{H}_{\boldsymbol{k}}^{\mathrm{PM}}\, \hat{\mathcal{T}}^{-1} = \underline{H}_{-\boldsymbol{k}}^{\mathrm{PM}}, \tag{12.9h}$$

which is due to the centrosymmetric form of the SOC. The coinciding presence of both of these symmetries allows for classifying the topological phases of the Hamiltonian through the $\mathbb{Z}_2$ invariant of the 3D topological insulator by means of Equation (12.7). Moreover, the hopping matrix remains invariant under the application of both symmetry transformations $\hat{\mathcal{T}}\,\hat{\mathcal{I}}\,\underline{H}_{\boldsymbol{k}}^{\mathrm{PM}}\,\hat{\mathcal{I}}^{-1}\,\hat{\mathcal{T}}^{-1} = \underline{H}_{\boldsymbol{k}}^{\mathrm{PM}}$, which implicates that the energy spectrum is doubly degenerate with the eigenvalues

$$\varepsilon_{\boldsymbol{k},\pm}^{\mathrm{PM}} = \frac{1}{2}\left(\xi_{\boldsymbol{k}}^{d} + z_0^2\xi_{\boldsymbol{k}}^{f} + \epsilon_f + \beta_0 - 2\mu_0\right) \pm \sqrt{\frac{1}{4}\left(\xi_{\boldsymbol{k}}^{d} - z_0^2\xi_{\boldsymbol{k}}^{f} - \epsilon_f - \beta_0\right)^2 + (2Vz_0)^2\left(\sin^2 k_x + \sin^2 k_y + \sin^2 k_z\right)}. \tag{12.10}$$

This property can be thought of as Kramer's pair at each momentum $\boldsymbol{k}$ that reduces to a degeneracy at the TRIM if inversion symmetry is broken. It becomes apparent that the gap of the corresponding BS can close at the TRIM, which enables the possibility of topological phase transitions. The hybridization gap of the PAM, whose PM eigenvalues are given by Equation (B.22), on the other hand, can never close for $V \neq 0$, which explains why it is not topological.

12.2.1 Model parameters for SmB_6

The previously derived minimal model can be considered to describe the physics of TKIs in general. However, in the following, we want to specifically address the most promising candidate of being a TKI, i.e., samarium hexaboride (SmB_6). Its 3D crystal structure, which is sketched in Figure 12.1(a), is of the caesium-chloride type, where a cube of samarium atoms encloses a boron octahedron with a lattice constant of $a_{SmB_6} \approx 4.13$Å. It shows the KI typical metal to semiconductor transition at around 50K with the opening of a small bulk gap $\Delta_B \approx 20$meV. Moreover, it is a mixed-valence compound, where the samarium ion is simultaneously present in the Sm^{2+} and Sm^{3+} state, with an average valence of $Sm^{2.56+}$ [227, 228, 255]. The crystal field of the boron octahedron splits its $5d$ orbitals into a t_{2g} triplet and an e_g doublet, where only the e_g orbitals, which are even under parity, remain in the low energy description. The situation of the $4f$-orbitals is more complicated, but DFT calculations predict a split into three $4f_{5/2}$ and four $4f_{7/2}$ orbitals that are odd under inversion [56, 228]. A

[1] Notice that we have shown in Section 2.1.2 that the PFs within the SB representation behave analogous to the original fermions under TR.

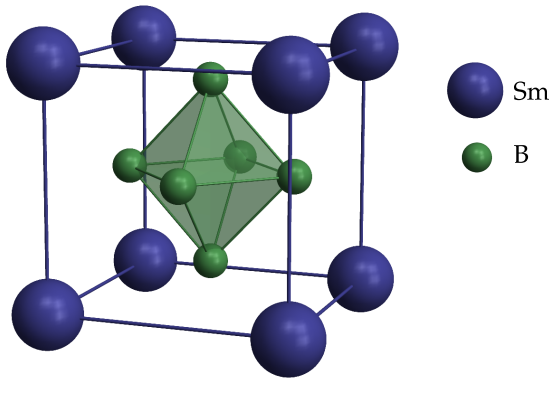

(a) Crystal structure of SmB_6. Figure adapted from [99].

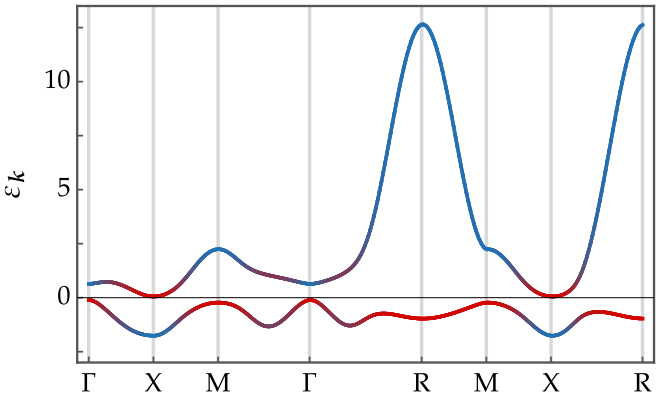

(b) Renormalized band structure for $U = 11.25$, $\epsilon_f = -12$, zero temperature and half-filling ($n = 2$).

Figure 12.1: Paramagnetic, interaction-renormalized band structure of the minimal TKI model according to Equation (12.10). While the model is expected to contain essential physics of TKIs in general, we aim to specifically describe samarium hexaboride, whose crystal structure is shown in Figure 12.1(a). Following Reference [99], we, therefore, chose the hopping amplitudes $t_d = 1, t'_d = -0.4, t_f = -0.1, t'_f = 0.04$, and $V = 0.5$. In Figure 12.1(b), red coloring indicates spectral weight of the interacting f-electrons and blue coloring of the conduction electrons. Consequently, there is a band inversion at the X point that identifies the ground state of being a STI according to Equation (12.7c). The MF solution for the given parameters yields $z_0 = 0.84, \beta_0 = 9.96, \mu_0 = -1.84$.

comprehensive description of SmB_6 would, therefore, require to consider five orbitals [99], but our minimal two-band model captures the essential physics of even conduction orbitals hybridizing with odd, localized f-orbitals.

Based on Reference [99], we choose the hopping amplitudes of the TKI model to recover the physics of SmB_6 as realistically as possible. Multiple *ab initio* calculations expect a band inversion at the X-point [248, 302, 303], which can be realized by introducing a finite NNN hopping in our model. Besides, an insulating ground state is only possible if the d- and f-orbital hoppings (t_d and t_f) have opposite signs and if the ratio between NN and NNN hoppings is approximately equal for both orbitals. Also, we expect $t_d \gg t_f$ in a Kondo material. In compliance with these constraints, we fix [99]

$$t_d = 1\,, \quad t'_d = -0.4\,, \quad t_f = -0.1\,, \quad t'_f = 0.04\,, \quad V = 0.5 \tag{12.11}$$

for the rest of our discussion, and analyze the insulating state at half-filling ($n = 2$) with ϵ_f and U as free parameters. The respective dispersions $\xi_{\boldsymbol{k}}^{d,f}$ are given by Equation (B.30). The interaction-renormalized paramagnetic MF ground state is determined by the solution of the saddle point equations[1]

$$\frac{\partial F^{(0)}}{\partial e} = \frac{\partial F^{(0)}}{\partial d} = \frac{\partial F^{(0)}}{\partial \beta_0} = \frac{\partial F^{(0)}}{\partial \mu_0} = 0 \tag{12.12}$$

that were derived in Section 4.4, and the eigenvalues that enter the free energy $F^{(0)}$ are given by Equation (12.10). The mixed-valence of SmB_6 is only considered on average with the MF occupation of the f-orbital $n_f = 2d^2 + p_0^2 + p^2$, which is determined by the saddle point and strongly depends on the on-site potential ϵ_f and its renormalization β_0. The band structure of the ground state is exemplarily shown in Figure 12.1(b) for $\epsilon_f = -12$ and $U = 11.25$. As expected, it features a small energy gap and a band inversion, i.e., f-orbital

[1]Notice that we explicitly set $p = \beta = 0$ for PM solutions, which also removes the magnetic ordering vector $\boldsymbol{Q}$ from the equations. Furthermore, we can eliminate an arbitrary SB field due to the constraints and choose p_0 w.l.o.g.

character in the d-band, at the X-point. Because of the opposite parity of d- and f-orbitals, we can effectively determine the $\mathbb{Z}_2$ invariants given by Equation (12.7) by counting the number of band inversions at the TRIM, where an odd number yields non-trivial topology. Accordingly, the presented band structure represents a STI phase with $(\nu_0, \nu_x, \nu_y, \nu_z) = (1, 1, 1, 1)$, which is expected to feature topologically protected surface states at the $\bar{\Gamma}$- and $\bar{\mathrm{X}}$-point of the surface Brillouin zone (SBZ). The existence of such gapless Dirac cones at all theoretically predicted surfaces has been numerically confirmed in Reference [99]. Coinciding surface sates have been experimentally observed in SmB_6 [255], which indicates that the STI(X) phase of our model is the most promising regime of describing the actual material. The implied surface conductivity could explain the long-lasting mystery of a for KIs unusual resistivity plateau in SmB_6 at low temperatures [227, 231, 304]. A full analysis of the topological phases in the PM domain is given in Reference [99], and those are also included in our final phase diagram in Figure 12.3 that we will further discuss in the following. The trivial band insulator is generally recovered if the energy splitting $\epsilon_f + \beta_0$ between the conduction and f-orbital becomes so large enough that one of the orbitals is almost fully occupied ($n_f \approx 0$ or $n_f \approx 2$).

12.2.2 Antiferromagnetic instability

Due to the spin-orbit coupling in the TKI model, we cannot write down a general SB hopping matrix for arbitrary magnetic ordering vectors $\boldsymbol{Q}$ like in case of Hubbard model or PAM. Instead, we have to explicitly increase the dimension of the matrix in accordance with the size of the respective magnetic unit cell as we explained in Section 4.3. We, therefore, determine the leading ordering vector through divergences of the static spin susceptibility around a PM saddle point [54]. The explicit expressions for the susceptibilities are summarized in Table 5.2 and they are given by superpositions of matrix elements of the fluctuation field propagator $\mathcal{G}^{ab}_{\mu\nu}$ that we derived in Chapter 5. Charge and spin susceptibilities about the ground state that matches the band structure in Figure 12.1(b) are plotted in Figure 12.2 with a gray dashed line. The presented PM ground state is stable because none of the susceptibilities features a divergence, and we find χ_s to be a scalar quantity despite the SOC of the model. The spin susceptibility, however, is significantly enhanced around the R-point [$\boldsymbol{q} = (\pi, \pi, \pi)^\top$], which identifies Néel antiferromagnetism (AFM) to be the leading type of magnetic order with a divergence of $\chi_s(\boldsymbol{q} = \mathrm{R})$ at slightly higher interaction.

To describe the implied AFM mean-field ground states, we need to calculate the slave-boson quasiparticle hopping matrix $\underline{H}^{\mathrm{AFM}}_{\boldsymbol{k}}$ with magnetic ordering vector $\boldsymbol{Q} = (\pi, \pi, \pi)^\top$. Since there are two atoms in the respective magnetic unit cell, it is given by an 8×8 matrix, which is derived in Appendix B.3.1 with the final result being Equation (B.28). Now, we can map out the magnetic phase diagram by solving the AFM saddle point equations

$$\frac{\partial F^{(0)}}{\partial e} = \frac{\partial F^{(0)}}{\partial d} = \frac{\partial F^{(0)}}{\partial \beta_0} = \frac{\partial F^{(0)}}{\partial \mu_0} = \frac{\partial F^{(0)}}{\partial p} = \frac{\partial F^{(0)}}{\partial \beta} = 0\,. \tag{12.13}$$

The energy bands that enter the corresponding free energy are given by the eigenvalues of $\underline{H}^{\mathrm{AFM}}_{\boldsymbol{k}}$, denoted by $\varepsilon^{\mathrm{AFM}}_{\boldsymbol{k}}$, and need to be determined numerically. Notice that despite the SOC of the model, $\varepsilon^{\mathrm{AFM}}_{\boldsymbol{k}}$ does not depend on the orientation of the MF spin, which is proven in Appendix B.4. The resulting magnetic and topological phase diagram as a function of the free parameters ϵ_f and U is shown in Figure 12.3. As expected, the AFM domain is centered around the ideal case of a half-filled f-orbital ($n_f = 1$), and there is no magnetic order for $U \ll |\epsilon_f|$ and $\epsilon_f \gtrsim 0$, because it is fully occupied ($n_f = 2$) or empty ($n_f = 0$) in these limits. The transition from the PM to AFM is of second order and yields an antiferromagnetic insulator (AFMI) that turns into a metallic state at high interactions because a warping of the band structure pushes d-electrons towards the Fermi surface. Exemplary band structures of the AFM ground state are included in Reference [305].

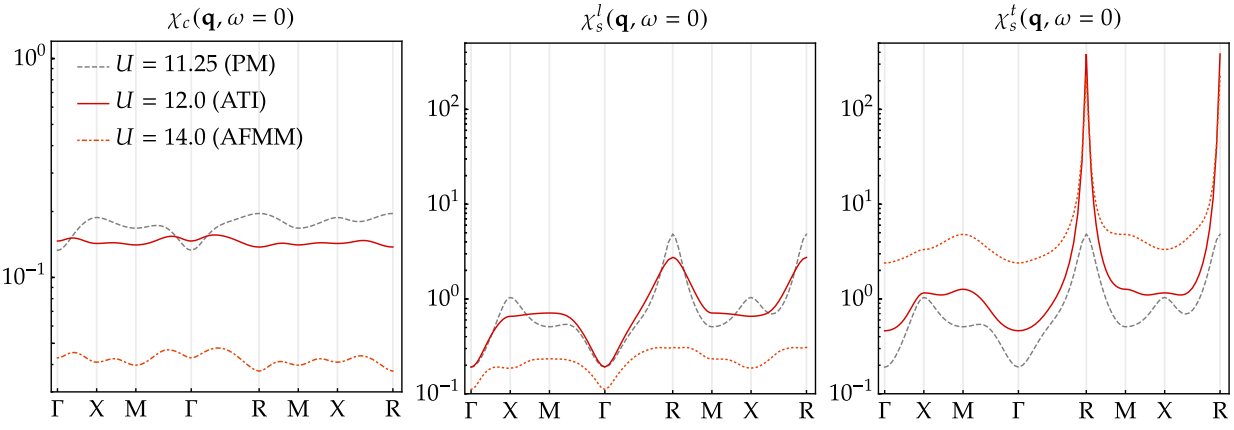

(a) Charge susceptibility. **(b)** Longitudinal spin susceptibility. **(c)** Transversal spin susceptibility.

Figure 12.2: Static susceptibilities for $\epsilon_f = -12, T = 0.005$ and different interactions. The lowest shown interaction ($U = 11.25$) describes a stable PM, which can be identified because χ_s^l and χ_s^t are degenerate and finite. However, the spin susceptibility features a sharp peak at $\boldsymbol{Q} = \mathrm{R} = (\pi, \pi, \pi)^\top$, which points towards an emerging Néel AFM instability at higher interactions. A corresponding solution of the AFM mean-field equations yields a magnetic saddle point for $U \geq 11.6$. Fluctuations about the respective AFM ground states feature gapless spin-waves that manifest in sharp divergences of the transversal spin susceptibility $\chi_s^t(\boldsymbol{q} = \boldsymbol{Q})$ (polarized perpendicular the MF magnetization) as expected. Since χ_s^l and χ_c stay finite within the AFM domain, these phases are stable w.r.t. Gaussian fluctuations.

From the previously discussed fluctuation analysis of PM ground states, we could, strictly speaking, only infer the leading magnetic ordering vector in the vicinity of the PM phase boundary. However, the stability of the AFM ground state could not be guaranteed deeper into the phase. Therefore, we also calculated fluctuations around magnetic saddle points and evaluated the corresponding susceptibilities, which are exemplarily displayed in Figure 12.2 for an insulating and metallic AFM at $\epsilon_f = -12$. In analogy to the PAM, the spin susceptibility splits into a longitudinal part χ_s^l parallel to the MF magnetization and a transversal part χ_s^t perpendicular to it. χ_s^t features a sharp divergence at $\boldsymbol{q} = \boldsymbol{Q}$, which is no indication for a FS instability but rather the expected signature of gapless spin-waves associated with the Néel AFM. χ_s^l does not employ any divergences and is even suppressed for higher interactions, which confirms $\boldsymbol{Q} = (\pi, \pi, \pi)^\top$ as the correct magnetic ordering vector. Moreover, the charge susceptibility χ_c stays finite and is overall small. We find similar results for other pairs of (ϵ_f, U) and thus conclude that the whole magnetic domain is stable w.r.t. Gaussian fluctuations.

12.2.3 $\mathbb{Z}_2$ invariant for the antiferromagnetic topological insulator

Finally, we want to topologically classify the occurring AFMI phase. The previously discussed $\mathbb{Z}_2$ invariants, however, are not applicable because the anti-parallel ordering of neighbored spins breaks TRS. Nevertheless, based on the pioneering work by Roger *et al.* in 2010 [306], there is another $\mathbb{Z}_2$ invariant for the antiferromagnetic topological insulator (ATI), which can be understood as analog to the STI. In contrast, WTIs cannot be recovered due to the broken translation symmetry. In the following, we will again apply a Fu-Kane-type of classification for the ATI in the presence of inversion symmetry, which was established by Fang *et al.* in 2013 [307].

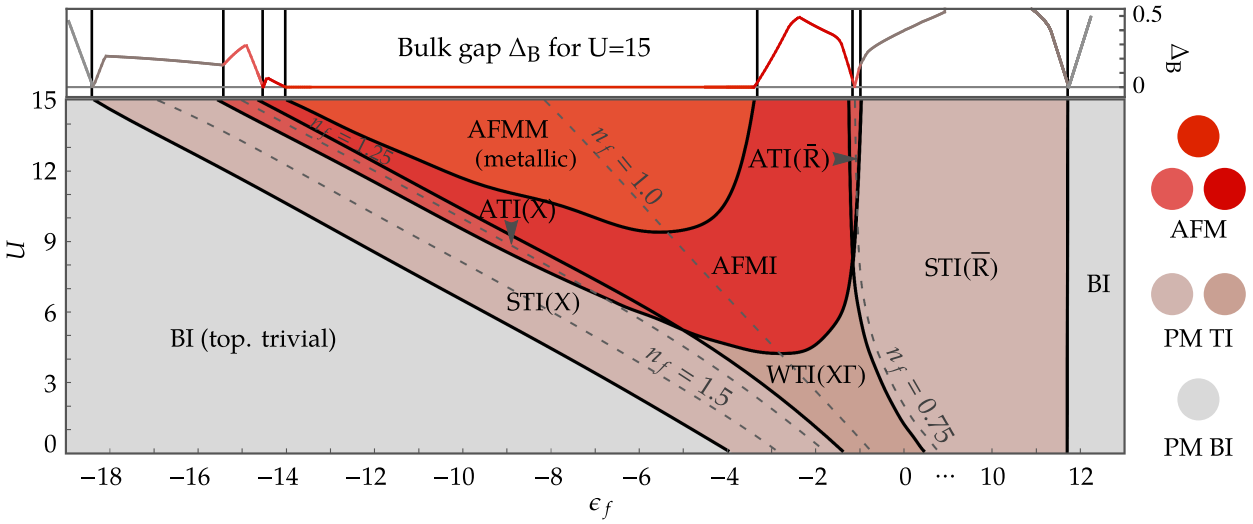

Figure 12.3: Magnetic and topological phase diagram for the TKI model dependent on the Hubbard interaction U and on-site potential ϵ_f of the f-electrons at zero temperature. Following Reference [99], the hopping amplitudes are chosen such that the STI(X) phase matches experimental findings in SmB_6, i.e., $t_d = 1, t'_d = -0.4, t_f = -0.1, t'_f = 0.04, V = 0.5$. Levels of equal f-orbital occupation (n_f) are indicated by gray dashed lines. Besides the trivial BI, we find two topological phases, i.e., the WTI and STI in the paramagnetic regime. The red-colored domain marks a Néel AFM [$\boldsymbol{Q} = (\pi, \pi, \pi)^\top$] ground state that has been shown to be stable w.r.t. Gaussian fluctuations and centers around $n_f = 1$. An antiferromagnetic topological insulator (ATI) emerges as a back-folded version of the STI at the magnetic phase boundary. Moreover. we identify a topologically-trivial antiferromagnetic insulator (AFMI) and antiferromagnetic metal (AFMM).The bulk gap of the ground state at $U = 15$ is illustrated in the top panel. It closes at every topological transition except for the magnetic phase boundary, where, however, the breaking of time-reversal symmetry allows for the determined change in topology. Figure adapted from [54].

Since $\hat{\mathcal{T}}$ effectively flips the spin, we can recover a symmetry transformation, which leaves magnetic Hamiltonian invariant, by combining time-reversal with a translation by one lattice site in α-direction $\hat{T}_{r_\alpha}$:

$$\hat{\mathcal{T}}' = \hat{\mathcal{T}}\hat{T}_{r_\alpha} = \hat{\mathcal{T}}\,\mathrm{e}^{-\mathrm{i}k_\alpha r_\alpha}\,, \quad \left[H^{\mathrm{TKI}}\,,\,\hat{\mathcal{T}}'\right]_- = \left[\hat{T}_{r_\alpha}\,,\,\hat{\mathcal{T}}'\right]_- = 0\,. \tag{12.14}$$

Because $\hat{\mathcal{T}}'$ commutes with the Hamiltonian and $\underline{H}^{\mathrm{AFM}}_{\boldsymbol{k}}$ preserves inversion symmetry, the energy bands $\varepsilon^{\mathrm{AFM}}_{\boldsymbol{k}}$ are doubly degenerate at every momentum $\boldsymbol{k}$ in analogy to the Kramers pairs in the PM phase. Therefore $\hat{\mathcal{T}}'$ serves as a suitable replacement for $\hat{\mathcal{T}}$ in the context of a topology protecting symmetry. Due to the AFM order, $\boldsymbol{Q} = (\pi, \pi, \pi)^\top$ becomes a reciprocal lattice vector, with the associated magnetic BZ being halved in size compared to the paramagnetic BZ. Accordingly, the R-point is folded onto the Γ-point, and the M-point becomes equivalent to the X-point. As a consequence, the $k_i = \pi$ plane is folded onto the $k_i = 0$ plane, which removes the WTI as potential topological phase. Therefore, a single $\mathbb{Z}_2$ invariant for the ATI remains, which is given by [56, 57, 307]

$$(-1)^{\nu_{\mathrm{AFM}}} = \prod_{i=1}^{4}\prod_{a}\xi_{i,a}\,, \tag{12.15a}$$

where a labels the two associated degenerate pairs of occupied bands, and

$$\xi_{i,a} = \left\langle \boldsymbol{u}_a(\Gamma_i)\,\middle|\,\hat{\mathcal{I}}\,\middle|\,\boldsymbol{u}_a(-\Gamma_i)\right\rangle = \pm 1 \tag{12.15b}$$

Phase	Bulk gap	Magnetic order	$\mathbb{Z}_2$ invariants $(\nu_0;\nu_x,\nu_y,\nu_z;\nu_{\text{AFM}})$	Band inversions	TSSs on suitable surfaces
BI	Yes	No	$(0;0,0,0;-)$	-	No
WTI(ΓX)	Yes	No	$(0;1,1,1;-)$	Γ, X	2D surface states
STI($\bar{\text{R}}$)	Yes	No	$(1;1,1,1;-)$	Γ, X, M	2D surface states
STI(X)	Yes	No	$(1;1,1,1;-)$	X	2D surface states
ATI(X)	Yes	Yes	$(-;-,-,-;1)$	X	2D surface states & 1D hinge states
ATI($\bar{\text{R}}$)	Yes	Yes	$(-;-,-,-;1)$	Γ, X^2	2D surface states & 1D hinge states
AFMI	Yes	Yes	$(-;-,-,-;0)$	Γ, X	No
AFMM	No	Yes	$(-;-,-,-;-)$	-	No

Table 12.1: Overview over topological and magnetic phases in the TKI model based on References [54, 57, 99]. The two phases that are associated with SmB_6 are printed in bold. Quantities that are not well defined are denoted by "$-$". The $\mathbb{Z}_2$ invariants are calculated via Equations (12.7) and (12.15a), and the underlying (para-) magnetic band structures yield from solutions of the saddle point Equations (12.12) and (12.13). Topological gapless surface cones occur at HSPs of the SBZ if an odd number of band inversions of the respective bulk HSPs is projected onto them.

defines the inversion eigenvalues of the respective Bloch eigenstates at the four remaining time-reversal-times-translation invariant points

$$\Gamma_i \in \left\{(0,0,0)^\top, (0,0,\pi)^\top, (0,\pi,0)^\top, (\pi,0,0)^\top\right\} . \tag{12.15c}$$

In order to evaluate Equation (12.15a), the AFM hopping matrix needs to adapt a Bloch form that satisfies $\underline{H}^{\text{AFM}}_{\boldsymbol{k}} = \underline{H}^{\text{AFM}}_{\boldsymbol{k}+\boldsymbol{Q}}$. A respective gauge along with a suitable matrix representation of the inversion operator $\hat{\mathcal{I}}$ is derived in Appendix B.3.1.

Within our numerical analysis, we do indeed find an ATI phase with non-trivial index ($\nu_{\text{AFM}} = 1$) that appears as folded version of the STI at the magnetic phase boundary. We also identify a trivial AFMI phase ($\nu_{\text{AFM}} = 0$) that can be interpreted as folded version of the WTI [57]. Similar results have also been found in a previous slave-boson study at infinite interaction ($U \to \infty$) [308]. We have now classified all occurring topological and magnetic phases that are summarized in Table 12.1 and built up the phase diagram shown in Figure 12.3. In Section 12.1.1, we argued that a topological phase transition could only occur due to a non-adiabatic deformation of the band structure, e.g., through closing the bulk gap or if the protecting symmetry of the SPT phase is broken. The top panel of Figure 12.3 demonstrates exemplarily for $U = 15$ that a bulk gap closing happens between all topologically distinct phases except for the transition from the STI to ATI phase. The onset of magnetic order, however, breaks TRS as protecting symmetry of the STI, which enables the topological phase transition, although there is a finite bulk gap. Also, the emerging AFM is not connected to the PM state by adiabatic continuity[1], since the spin gap closes $[1/\chi^l_s(\boldsymbol{q} = \boldsymbol{Q}) = 0]$ at the magnetic transition.

It is remarkable how much of the experimental findings in SmB_6 are captured in our simple model. As pointed out earlier, the TSSs in the STI(X) phase match the experimentally measured surface cones in the material [255]. Moreover, SmB_6 is known to develop long-range magnetic order under pressure that ultimately leads to a metallic phase [258, 263, 309]. Since increasing pressure usually initiates a higher effective interaction by confining the localized electrons, this transition can be identified in Figure 12.3 for

[1] i.e., it cannot be described with a perturbative renormalization of parameters within Fermi liquid theory [39].

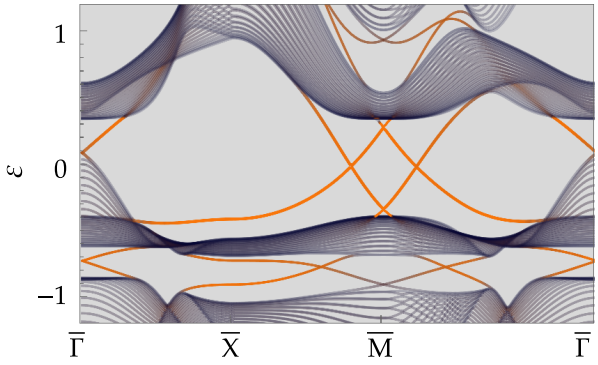

(a) Gapless surface states for the $(1,0,0)$-surface termination that preserves $\hat{\mathcal{T}}'$.

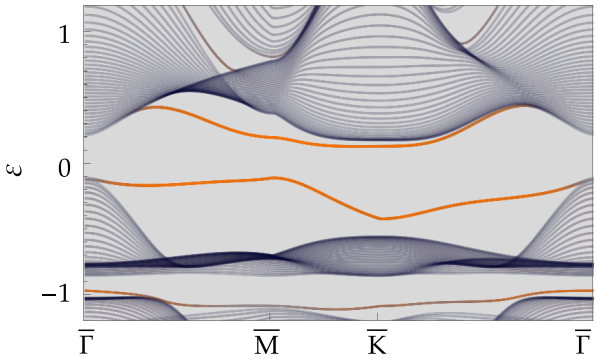

(b) Gapped surface states for the $(1,1,1)$-surface termination that breaks $\hat{\mathcal{T}}'$.

Figure 12.4: Energy spectrum of the TKI model on the high-symmetry-lines of the surface Brillouin zone (SBZ) for $U = 15, \epsilon_f = -15$ with broken PBCs in one direction to investigate the impact of the thereby created surfaces. Accordingly, we used 40 unit cells in our numeric open boundary calculation. Localization on the surface is denoted by orange coloring. Figure reprinted from Reference [56] with permission of the author.

a constant $\epsilon_f \lesssim -6$ in the STI(X) phase by increasing the interaction U. Moreover, Nakajima *et al.* reported surface-ferromagnetism with gapless one-dimensional edge states in SmB_6, which points towards a possible ATI phase [254]. Furthermore, long-range magnetic order at ambient pressure was recently observed in magnetically alloyed $Sm_{1-x}Eu_xB_6$, which also features robust surface states and appears as a promising candidate for the experimental realization of an ATI [310].

12.3 Topologically protected surface states

Finally, we want to investigate the topologically protected surface states (TSSs) in the ATI. A comprehensive study of the TSSs in the PM domain has already been provided in Reference [99].

12.3.1 Two-dimensional surface states

First of all, we consider 2D surface states by breaking the periodic boundary conditions (PBC) in a specific direction to create two surfaces, i.e., we are left with two momentum quantum numbers that define the surface Brillouin zone (SBZ). The respective energy spectrum is given by the eigenvalues of a large hopping matrix, whose dimension grows linearly with the distance of the surfaces. We solved the problem numerically employing a *Mathematica* script with 40 magnetic unit cells. The result for two different surface terminations of the ATI is shown in Figure 12.4. The spectrum features many densely packed modes because a large number of bulk states are projected onto the SBZ. The point of interest, however, is the appearance of gapless surface states that cannot be found in the bulk spectrum under the application of PBCs.

The surface termination with normal vector $(1,0,0)^\top$ chosen in Figure 12.4(a) respects the $\hat{\mathcal{T}}'$-symmetry and features the expected TSS at the $\overline{\Gamma}$-point of the SBZ and also a gapless mode around the $\overline{\mathrm{M}}$-point [57]. On the other hand, the $(1,1,1)$-surface termination displayed in Figure 12.4(b) breaks the $\hat{\mathcal{T}}'$-symmetry, and the respective spectrum remains gapped. Interestingly, we also find gapless modes in the AFMI phase. These are, however, not protected by the AFM $\mathbb{Z}_2$ invariant and also feature a trivial mirror Chern number [57] but appear to be quite robust in our numeric calculation. Therefore, they could just appear accidentally or be protected

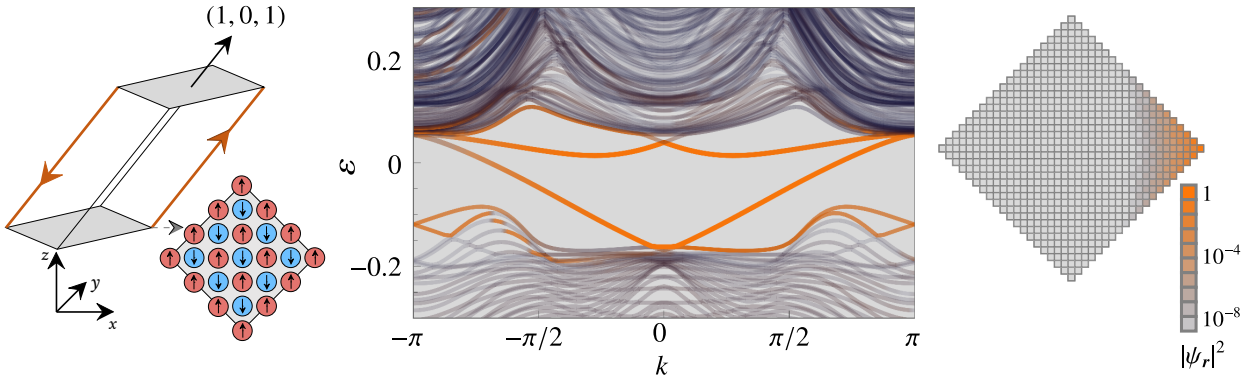

(a) Nanowire geometry along the (1,0,1) direction. Blue and red represent opposite spins.

(b) Energy spectrum of open the boundary calculation that features a 1D chiral gapless hinge mode, while the 2D surface states are gapped.

(c) Exponentially localized eigenstate at the hinge for $k = \pi/2$.

Figure 12.5: Open boundary calculation for a 1D nanowire geometry, whose lateral surfaces break $\hat{\mathcal{T}}'$. PBCs are kept in $(1, 0, 1)$-direction, which yields the quantum number k. The color code of the energy eigenstates shows that the gapless mode is exponentially localized at the hinges of the wire. A magnetic unit cell contains two lattice sites, and we used $20 \times 20 + 19 \times 19$ sites for the numeric open boundary calculation. Figure adapted from [54, 57].

by another, yet unknown, topological invariant. We moreover observe that the position of the surface cones weakly depends on the orientation of the MF spins that did not play a role for the bulk spectrum.

12.3.2 One-dimensional hinge states

The ATI phase can additionally be classified as an axion insulator (AXI) that is characterized by a finite magnetoelectric polarization and was initially studied in the field of electrodynamics [311]. On surface terminations that break $\hat{\mathcal{T}}'$ and preserve $\hat{\mathcal{I}}$, AXIs feature gapless chiral hinge modes that are also the signature of a higher-order topological insulator (HOTI) [56, 57, 271, 312]. A suitable geometry can be achieved by stacking squares in the (1,0,1) direction, as illustrated in Figure 12.5(a). The lateral surfaces of the according nanowire employ a parallel spin alignment and correspond to (1,1,1) surfaces that break $\hat{\mathcal{T}}'$. The respective energy spectrum is determined by an open boundary calculation, where PBCs are kept in the (1,0,1)-direction, i.e., a single scalar momentum k remains a good quantum number. Figure 12.5 demonstrates that the gapless chiral mode is present and exponentially localized at the hinges of the nanowire. Experimental evidence for such an AXI has recently been observed in $MnBi_2Te_4$ and Bi_2Se_3 thin films [313, 314], and also the previously mentioned detection of 1D edge states in the context of surface FM in SmB_6 points towards a possible HOTI phase [254].

After all, the TKI model serves as a neat example to demonstrate the bulk-boundary-correspondence in topological systems and provides a rich collection of topologically distinct phases that also considers the interplay between topology and magnetism. According to the theoretical predictions that show remarkable qualitative agreement to experimental findings, pressurized SmB_6 might actually be an ATI.

Chapter 13

Conclusions and outlook

The goal of this thesis was to study emergent phenomena like e.g., magnetism or charge inhomogeneities in strongly correlated electron systems by utilizing Kotliar–Ruckenstein slave-bosons [49]. Part I provided a pedagogical review of the slave-boson method that built up to generalizations of the established theory, which proved to be essential to obtain novel results in the context of the high-T_c cuprates and Kondo systems that we discussed in Parts II and III. In the following, we summarize the main achievements of each part and finally provide an outlook that addresses further ideas and open questions in condensed matter physics.

Methodological development

Within this thesis, we were concerned with electrons on a lattice being subject to a quartic Hubbard interaction that cannot be treated exactly by analytical measures. The spin-rotation invariant Kotliar–Ruckenstein (SRIKR) slave-boson (SB) representation reviewed in Chapter 2 recasts such models into an effective quadratic theory for the fermions with the complication of additional bosonic degrees of freedom. To exactly recover the physical subspace, additional constraints are required that we implemented within the field-theoretical description of Chapter 3. As discussed in Chapter 4, a mean-field (MF) approximation of the bosons reduces the problem to renormalized, effectively non-interacting fermions, whose ground state is determined by a solution of the saddle point equations. Besides magnetic order, these allow for phase separation (PS), i.e., an inhomogeneous mixture of different phases, which comes along with subtleties for the analytic and numeric treatment, as we thoroughly discussed. Finally, in Chapter 5, we extended the established formalism of Gaussian fluctuations around paramagnetic (PM) saddle points to allow additional non-interacting orbitals and also encompass magnetic saddle points [55]. Moreover, we proposed a reduced fluctuation basis while reproducing previous results and thoroughly elaborated on the gauge problem, which is a subtlety of the fluctuation calculation. The essence of the fluctuation calculation is to integrate out the fermions and expand fluctuation fields up to leading order for an overall quadratic bosonic theory that can again be addressed by analytical measures to assess the MF stability. For magnetic saddle points, we also newly proposed a method to determine second-order corrections to the MF magnetization.

In order to quantify the quality of approximations that come along with the SB treatment of the electronic Hubbard interaction, we provided various consistency checks and compared our results to other theoretical methods: First of all, we found that second-order magnetic instabilities can equally be determined by a divergence of the spin susceptibility around a paramagnetic ground state or the onset of a finite magnetization within a magnetic MF ansatz. This consensus affirms the consistency between MF and fluctuation calculations that are technically quite different and makes possible remaining errors in the analytics or numerical implementation highly unlikely. We observe similar conformance in the charge channel in the context of

phase separation (PS) that we find between different magnetic phases in certain domains. While the onset of PS can be studied from a mere MF perspective through an analysis of the chemical potential, it is expected to be accompanied by a divergence of the charge susceptibility at the Γ-point that we consistently identify within the magnetic fluctuation results. Secondly, we showed that an evaluation of dynamic SB susceptibilities qualitatively recovers well-known physical properties like, e.g., a Drude-like dynamical conductivity within a PM Fermi liquid (FL) phase (see Figure 8.7), and a linear spin-wave dispersion for the antiferromagnet (see Figure 8.10). Finally, the well-studied 2D Hubbard model provides a broad pool of data from different theoretical methods [177] that we applied to benchmark our results from SB theory. A comparison of the staggered magnetization with statistically exact quantum Monte Carlo (QMC) simulations at half-filling reveals an overestimation of the respective slave-boson MF data, especially at high interactions. With addition of the newly implemented fluctuation corrections, however, our results closely approach the QMC data and even compare favorable to density matrix embedding theory (DMET) at low to intermediate interactions (see Figure 8.2). Furthermore, we were able to qualitatively reproduce a phase diagram from dynamical mean-field theory (DMFT) in the context of Mott physics (see Figure 8.1), and our phase-separated ground state energy matches the outcome of a previous MF cluster study for finite doping (see Figure 8.14).

After all, we, therefore, acknowledge the SB technique as a proper tool to investigate models with Hubbard-type interactions, which is applicable for arbitrary doping and interaction and in the thermodynamic limit. Its, arguably, most unique virtues are the analysis of ordered phases with large unit cells (e.g., incommensurate magnetic or charge order) and Kondo systems where localized and itinerant degrees of freedom are equally important. These characteristics were discussed broadly within this thesis and are particularly challenging for many other theoretical methods.

Application to the high-T_c cuprates

Chapter 6 introduced the Hubbard model as an archetypal problem to study emergent phenomena in the context of the many-body problem and provided a suitable literature overview. One of the main reasons why it is still popular after more than 50 years is its applicability to the high-T_c cuprates (HTCCs) as minimal 2D model. For these materials, many open questions, especially regarding the pairing mechanism of unconventional superconductivity and the corresponding role of magnetic, charge-inhomogeneous, and strange metal phases, remain, as we elaborated in Chapter 7. Therefore, Chapter 8 provided an extensive SB analysis of the 2D Hubbard model, where we discussed Mott physics, magnetic phases, critical exponents, and collective modes apart from the aforementioned consistency checks. We also highlighted the emergence of incommensurate magnetic order and phase separation between different magnetic phases in the underdoped regime. In Chapter 9, we discussed this type of order more deeply in the electron-doped regime with context to actual materials and experimental data. The evaluation of magnetic fluctuations around AFM mean-field ground states revealed emerging charge-order (CO) that we find based on the bare Hubbard model without additional assumptions in agreement with experimental evidence [120, 161, 193]. Interestingly, we identify two distinct, competing charge ordering vectors [$\boldsymbol{Q}_{1/2}^{\mathrm{CO}} = (Q_{1/2}, 0)^\top$] and the respective dominant type of order varies with doping and temperature (see Figure 9.2). The larger ordering vector Q_1 appears for higher doping ($\delta \lesssim 0.15$), can be explained by a Fermi surface (FS) nesting effect and matches experimental data of the material $Nd_{2-x}Ce_xCuO_4$ (NCCO) [120] even quantitatively. The second peak at $Q_2 < Q_1$ cannot be attributed to FS nesting and rather resembles the Yamada relationship [199], implying the formation of periodic, doubly occupied domain walls to distribute the doped electrons ($\delta \lesssim 0.1$). It shows a transition towards phase separation ($\boldsymbol{Q} = 0$) at very small doping ($\delta \lesssim 0.05$). We interpret these three drivers of charge-inhomogeneities

as mechanisms to partially restore the localized, half-filled AFM in the real-space lattice by clustering doped charges. While recent experimental data provides indications for the existence of competing effects in regard of CO for hole doping [193], hard evidence for a Yamada-type instability with electron doping is still lacking. Finally, we find the charge-inhomogeneous phases to be accompanied by a local maximum in the specific heat as a function of temperature, which could be of interest for further experimental investigations, especially in the context of pseudogap physics (see Figure 9.3).

Application to Kondo systems

Chapter 10 initiated the discussion of Kondo systems with a general review of the Kondo effect and the introduction of associated material classes, i.e., heavy fermion metals and Kondo insulators, within the historical context. We, moreover, elaborated on the most successful microscopic models to describe the phenomenon, i.e., the periodic Anderson model (PAM) and Kondo lattice model (KLM), and on how they are connected by the Schrieffer–Wolff (SW) transformation in the strong-coupling limit.

In Chapter 11, we then studied magnetism and heavy fermions in Kondo metals based on the PAM and accounted for the associated Hubbard interaction through the SB formalism. We conclude that we do not find heavy fermions in the paramagnetic regime because an interaction-enabled increase of the density of states (DOS) yields ferromagnetic order as the consequence of an adapted Stoner criterion. The respective MF magnetization, however, is very low and almost drops to zero under consideration of fluctuation corrections such that a non-magnetic heavy-fermion state might be recovered with the impact of disorder in actual materials. Furthermore, we identify an AFM domain associated with parameters of an expected Kondo regime at low doping that features huge effective masses but proves to be unstable w.r.t. Gaussian fluctuations. In that part of the phase diagram, we cannot determine a stable ground state within the SB scheme, which points towards a possible Kondo state whose complexity may be beyond the capabilities of mean-field theory. Furthermore, we elaborated on the role of the RKKY interaction, an effective spin-exchange coupling mediated by the conduction electrons, for the two-conduction-band PAM. In that context, we reported magnetic frustration due to destructive interference of two conduction band pockets with different diameters that might impact the Néel temperatures of actual materials or could be a host to different types of order.

Finally in Chapter 12, we investigated Kondo insulators (KIs) with respective topological and magnetic properties based on a 3D PAM with additional centrosymmetric spin-orbit coupling (SOC). We thereby complemented the analysis of the model in the paramagnetic regime [99] by considering the possibility for magnetic FS instabilities and identifying an AFM domain at intermediate to high interaction that proves to be stable w.r.t. Gaussian fluctuations. With the evaluation of appropriate $\mathbb{Z}_2$ invariants, we topologically classify an antiferromagnetic topological insulator (ATI) featuring one-dimensional chiral hinge modes, and other non-trivial phases, which are summarized in Figure 12.3. While our approach in general concerns possible phases in the material class of topological Kondo insulators (TKIs), our hopping amplitudes are tuned such that we specifically address the material SmB_6, which is widely believed to be the first TKI. In that regard, we predict the ground state of being a strong topological insulator (STI) with a f-electron filling of $n_f \approx 1.3$ that accounts for the mixed-valence of the compound on average, and features topologically protected surface states (TSSs) that are supported by experimental evidence in SmB_6 [255]. According to our calculations, an increase of the interaction strength leads to a transition towards the ATI phase that ultimately turns into a metallic state. Correspondingly, long-range AFM order and a metallic state have been observed in pressurized [258] and alloyed [310] SmB_6 and there is experimental evidence pointing towards an ATI phase [254]. While

the exact nature of the ground state of SmB_6 is still under debate, our results support the hope to discover exciting physical properties associated with the material.

Outlook

One of the most extensive research areas in condensed matter physics remains to be unconventional superconductivity. While we discussed phases that arise in its close proximity, we did not explicitly address the superconducting ground because the applied slave-boson representation is not suitable to describe corresponding non-local order parameters. For future investigations in the context of superconductivity, we, therefore, propose the idea to construct an effective vertex by utilizing the SB Gaussian fluctuations [57] and to solve the superconducting gap equation accordingly through conventional fermionic mean-field theory. This approach allows to study the full frequency dependence of the superconducting order parameter and is not limited to high-T_c cuprates (HTCCs) but could also be applied to the PAM in order to study heavy-fermion superconductivity.

Another open question is the detailed understanding of strange metals [48] that employ a linear temperature-dependence of the conductivity rather than a quadratic one expected for Fermi liquids. This characteristic is well known from the HTCCs but also appears in other superconducting compounds, e.g., twisted bilayer graphene [315], infinite-layer nickelates [316], heavy-fermion superconductors, and Kondo systems near quantum critical points. Strange metal behavior is thus a common denominator of different material classes employing unconventional superconductivity, and its understanding could be a key to deciphering the underlying pairing mechanism [226]. Within this thesis, we developed the framework to obtain the temperature coefficient of the conductivity through the SB charge susceptibility and demonstrated corresponding results in a Fermi liquid environment. For future studies, this technique could be applied to parameter regimes with expected strange metal behavior in order to investigate the phenomenon in the context of the HTCCs and Kondo materials based on non-magnetic and magnetic ground states.

Finally, we want to bring to mind a generalization of the KR slave-bosons [51] that allows for multiple interacting orbitals and has lately been further developed to consider fluctuations in order to study s-wave superconducting pairing [52]. This formalism could be applied to high-parametric strongly correlated systems in the future and, e.g., be of particular interest in the context of magic-angle twisted bilayer graphene, which has recently been associated with heavy fermion physics [317].

After all, we elaborated on various emergent phenomena within condensed matter physics. Some of them are now well understood, while others remain puzzling. With the rise of topology and especially the observation of higher-order topological insulators (HOTIs) [277], new phases have been added to the list. As history has taught, emergence often comes with a surprise, so who knows what kind of exotic quantum states are still waiting to be discovered?

IV

Appendices

Appendix A

Details on the slave-boson formalism

A.1 Proof of slave-boson related commutation relations

In the following, we adopt Einsteins sum convention, where summation over every index that appears at least twice in a summand is implied. We moreover will apply the identities

$$\epsilon_{ijk}\epsilon_{ilm} = \delta_{jl}\delta_{km} - \delta_{jm}\delta_{kl}\,, \tag{A.1a}$$

$$\underline{\tau}^i\underline{\tau}^j = \delta_{ij}\underline{\mathbb{1}}_2 + \mathrm{i}\epsilon_{ijk}\underline{\tau}^k\,, \tag{A.1b}$$

where ϵ_{ijk} represents the Levi-Civita symbol and $\underline{\tau}^i$ the i-th Pauli matrix.

Commutators of constraint operators with the Hamiltonian

As stated in Section 2.2, the Hamiltonian commutes with all five constraint operators $\mathcal{A}$, $\mathcal{B}_0$ and $\mathcal{B}_i$ defined in Equation (2.18). To be specific, the constraint operators even commute with the fermionic creation operator

$$\left[\hat{f}^\dagger_\sigma\,,\,\hat{\mathcal{A}}\right]_- = 0\,,\quad \left[\hat{f}^\dagger_\sigma\,,\,\hat{\mathcal{B}}_0\right]_- = 0\,,\quad \left[\hat{f}^\dagger_\sigma\,,\,\hat{\boldsymbol{\mathcal{B}}}\right]_- = 0\,, \tag{A.2a}$$

whose SB representation is given by

$$\hat{f}^\dagger_\sigma = \sum_{\sigma'}\hat{z}^\dagger_{\sigma\sigma'}\hat{f}^\dagger_{\sigma'} = \sum_{\sigma'}\left(\hat{p}^\dagger_{\sigma\sigma'}\hat{e} + \hat{d}^\dagger\hat{\tilde{p}}_{\sigma\sigma'}\right)\hat{f}^\dagger_{\sigma'}\,. \tag{A.2b}$$

Since the constraint operators are hermitian ($\mathcal{A} = \mathcal{A}^\dagger\,, \mathcal{B}_0 = \mathcal{B}_0^\dagger\,, \hat{\mathcal{B}}_\mu = \hat{\mathcal{B}}_\mu^\dagger$) they also commute with the fermionic annihilation operator and thus with the Hamiltonian. We exemplarily prove the most difficult commutator in the context of

$$\hat{\mathcal{B}}_\mu = \sum_{\sigma\sigma'}\tau^\mu_{\sigma\sigma'}\hat{f}^\dagger_{\sigma'}\hat{f}_\sigma - \left(\hat{p}^\dagger_0\hat{p}_\mu + \hat{p}^\dagger_\mu\hat{p}_0 - \mathrm{i}\epsilon_{\mu ij}\hat{p}^\dagger_i\times\hat{p}_j\right)\,,\quad \mu\in\{1,2,3\}\,, \tag{A.2c}$$

while the remaining others can be calculated in the same manner. We start with the bosonic part of the constraint operator, and after application of the canonic commutation relations, we find

$$\begin{aligned}\left[\hat{p}^\dagger_\mu\hat{p}_0 + \hat{p}^\dagger_0\hat{p}_\mu - \mathrm{i}\epsilon_{\mu il}\hat{p}^\dagger_i\hat{p}_l\,,\,\hat{z}^\dagger_{\sigma\sigma'}\hat{f}^\dagger_{\sigma'}\right]_- &= \left[\hat{p}^\dagger_\mu\hat{p}_0 + \hat{p}^\dagger_0\hat{p}_\mu - \mathrm{i}\epsilon_{\mu il}\hat{p}^\dagger_i\hat{p}_l\,,\,\left(\frac{1}{2}\hat{e}\hat{p}^\dagger_{\mu'}\tau^{\mu'}_{\sigma\sigma'} + \frac{1}{2}\hat{d}^\dagger\left(\hat{p}_0\tau^0_{\sigma\sigma'} - \hat{p}_{\mu'}\tau^{\mu'}_{\sigma\sigma'}\right)\right)\hat{f}^\dagger_{\sigma'}\right]_- \\ &= \frac{1}{2}\hat{e}\left(\hat{p}^\dagger_\mu\tau^0_{\sigma\sigma'} + \hat{p}^\dagger_0\tau^\mu_{\sigma\sigma'} - \mathrm{i}\epsilon_{\mu il}\hat{p}^\dagger_i\tau^l_{\sigma\sigma'}\right)\hat{f}^\dagger_{\sigma'} + \frac{1}{2}\hat{d}^\dagger\left(\hat{p}_0\tau^\mu_{\sigma\sigma'} - \hat{p}_\mu\tau^0_{\sigma\sigma'} + \mathrm{i}\epsilon_{\mu il}\hat{p}_l\tau^i_{\sigma\sigma'}\right)\hat{f}^\dagger_{\sigma'}\,.\end{aligned} \tag{A.2d}$$

The PF part yields

$$\left[\tau^{\mu}_{\sigma_2\sigma'}\hat{f}^{\dagger}_{\sigma'}\hat{f}_{\sigma_2}\,,\,\hat{z}^{\dagger}_{\sigma\sigma_1}\hat{f}^{\dagger}_{\sigma_1}\right]_{-} = \hat{z}^{\dagger}_{\sigma\sigma_1}\tau^{\mu}_{\sigma_1\sigma'}\hat{f}^{\dagger}_{\sigma'} = \left(\frac{1}{2}\hat{e}\sum_{i=0}^{3}\hat{p}^{\dagger}_{i}\tau^{i}_{\sigma\sigma_1}\tau^{\mu}_{\sigma_1\sigma'} + \frac{1}{2}\hat{d}^{\dagger}\left(\hat{p}_0\delta_{\sigma\sigma_1}\tau^{\mu}_{\sigma_1\sigma'} - \sum_{i=1}^{3}\hat{p}_i\tau^{i}_{\sigma\sigma_1}\tau^{\mu}_{\sigma_1\sigma'}\right)\right)\hat{f}^{\dagger}_{\sigma'}\,, \tag{A.2e}$$

and after multiplying out the Pauli matrices, we find that the commutators of Equations (A.2d) and (A.2e) yield the same result and thus confirm

$$\left[\hat{\mathcal{B}}_i\,,\,\hat{z}^{\dagger}_{\sigma\sigma_1}\hat{f}^{\dagger}_{\sigma_1}\right]_{-} = 0\,. \tag{A.2f}$$

Proof of the spin algebra in slave-boson representation

In the following, we show that the spin operator within the SB representation defined in Equation (A.5a) fulfills the SU(2) spin algebra.

$$\begin{aligned}
\left[\hat{S}^i\,,\,\hat{S}^l\right]_{-} &= \frac{1}{4}\left[\hat{p}^{\dagger}_0\hat{\rho}_i + \hat{\rho}^{\dagger}_i\hat{p}_0 - \mathrm{i}\epsilon_{ijk}\hat{\rho}^{\dagger}_j\hat{\rho}_k, \hat{p}^{\dagger}_0\hat{\rho}_l + \hat{\rho}^{\dagger}_l\hat{p}_0 - \mathrm{i}\epsilon_{lmn}\hat{\rho}^{\dagger}_m\hat{\rho}_n\right] \\
&= \frac{1}{4}\Big(\hat{p}^{\dagger}_0\hat{p}_0\delta_{il} - \hat{\rho}^{\dagger}_l\hat{\rho}_i - \mathrm{i}\epsilon_{lmn}\hat{p}^{\dagger}_0\hat{\rho}_n\delta_{im} + \hat{\rho}^{\dagger}_i\hat{\rho}_l - \hat{p}^{\dagger}_0\hat{\rho}_0\delta_{il} + \mathrm{i}\epsilon_{lmn}\hat{p}_0\hat{\rho}^{\dagger}_m\delta_{in} \\
&\quad + \mathrm{i}\epsilon_{ijk}\hat{\rho}_k\hat{p}^{\dagger}_0\delta_{jl} - \mathrm{i}\epsilon_{ijk}\hat{\rho}^{\dagger}_j\hat{p}_0\delta_{kl} - \epsilon_{ijk}\epsilon_{lmn}\hat{\rho}^{\dagger}_j\hat{\rho}_n\delta_{km} + \epsilon_{ijk}\epsilon_{lmn}\hat{\rho}^{\dagger}_m\hat{\rho}_k\delta_{nj}\Big) \\
&= \frac{1}{4}\left(\hat{\rho}^{\dagger}_l\hat{\rho}_i - \mathrm{i}\epsilon_{lik}\hat{p}^{\dagger}_0\hat{\rho}_k + \hat{\rho}^{\dagger}_i\hat{\rho}_l + \mathrm{i}\epsilon_{lki}\hat{p}_0\hat{\rho}^{\dagger}_k + \mathrm{i}\epsilon_{ilk}\hat{\rho}_k\hat{p}^{\dagger}_0 - \mathrm{i}\epsilon_{ikl}\hat{\rho}^{\dagger}_k\hat{p}_0 - \epsilon_{ijk}\epsilon_{nlk}\hat{\rho}^{\dagger}_j\hat{\rho}_n + \epsilon_{kij}\epsilon_{lmj}\hat{\rho}^{\dagger}_m\hat{\rho}_k\right) \\
&= \frac{1}{4}\left(\hat{\rho}^{\dagger}_i\hat{\rho}_l - \hat{\rho}^{\dagger}_l\hat{\rho}_i + 2\mathrm{i}\epsilon_{ilk}\hat{p}^{\dagger}_0\hat{\rho}_k + 2\mathrm{i}\epsilon_{ilk}\hat{\rho}^{\dagger}_k\hat{p}_0 - \hat{\rho}^{\dagger}_l\hat{\rho}_i + \delta_{il}\hat{\rho}^{\dagger}_k\hat{\rho}_k + \hat{\rho}^{\dagger}_i\hat{\rho}_l - \delta_{il}\hat{\rho}^{\dagger}_k\hat{\rho}_k\right) \\
&= \frac{\mathrm{i}}{2}\left(\epsilon_{ilk}(\hat{p}^{\dagger}_0\hat{\rho}_k + \hat{\rho}^{\dagger}_k\hat{\rho}_0) + \mathrm{i}(\hat{\rho}^{\dagger}_l\hat{\rho}_i - \hat{\rho}^{\dagger}_i\hat{\rho}_l)\right) = \mathrm{i}\epsilon_{ilk}\hat{S}^k\,.
\end{aligned} \tag{A.3}$$

Commutators between constraint operators

As stated in Section 2.2, the constraint operators $\mathcal{A}$, $\mathcal{B}_0$ and $\mathcal{B}_i$ defined in Equation (2.18) commutate among themselves in the constrained subspace. We exemplarily calculate the most difficult commutator

$$\boldsymbol{\mathcal{B}} = \hat{p}^{\dagger}_0\hat{\boldsymbol{p}} + \hat{\boldsymbol{p}}^{\dagger}\hat{p}_0 - \mathrm{i}\hat{\boldsymbol{p}}^{\dagger}\times\hat{\boldsymbol{p}} - \sum_{\sigma\sigma'}\underline{\boldsymbol{\tau}}_{\sigma\sigma'}\hat{f}^{\dagger}_{\sigma'}\hat{f}_{\sigma} \stackrel{!}{=} 0\,, \tag{A.4a}$$

while the others can be derived analogously. Since fermions and bosons commute among each other, we are left to calculate the commutators of the bosonic and fermionic parts, respectively. The fermionic part is most conveniently evaluated by commutating two fermions from the very left to the very right of the quartic expression. The commutator is then given by the extra terms which yield from the fermionic anticommutation relation $\left[\hat{f}^{\dagger}_{\sigma}\,,\,\hat{f}_{\sigma'}\right]_{+} = \delta_{\sigma\sigma'}$:

$$\left[\tau^{i}_{\sigma_1\sigma_2}\hat{f}^{\dagger}_{\sigma_2}\hat{f}_{\sigma_1}, \tau^{j}_{\sigma_3\sigma_4}\hat{f}^{\dagger}_{\sigma_4}\hat{f}_{\sigma_3}\right] = \tau^{j}_{\sigma_3\sigma_1}\tau^{i}_{\sigma_1\sigma_2}\hat{f}^{\dagger}_{\sigma_2}\hat{f}_{\sigma_3} - \tau^{i}_{\sigma_1\sigma_2}\tau^{j}_{\sigma_2\sigma_4}\hat{f}^{\dagger}_{\sigma_4}\hat{f}_{\sigma_1} = -2\mathrm{i}\epsilon_{ijk}\tau^{k}_{\sigma_1\sigma_2}\hat{f}^{\dagger}_{\sigma_2}\hat{f}_{\sigma_1}. \tag{A.4b}$$

The bosonic commutator is evaluated in full analogy to Equation (A.3) since the sign of p_2 does not change the result of the calculation. Both parts independently fulfill the spin algebra if rescaled by a factor of $\frac{1}{2}$, yielding

$$\left[\mathcal{B}^i/2\,,\,\mathcal{B}^j/2\right]_{-} = \mathrm{i}\epsilon_{ijk}\mathcal{B}^k/2\,, \tag{A.4c}$$

and consequently the commutator vanishes on the constrained subspace.

A.2 Proof of slave-boson operator representations

The general strategy to find representations of the original fermionic operators within the SB scheme is to apply Equation (2.10a) and exploit the constraint given by Equation (2.14b) to simplify respective terms to ideally find a purely bosonic or purely pseudofermionic expression in the end. Due to Equation (2.14a), two annihilation operators on the very right side annihilate any state on the constrained subspace, and thus those terms vanish. Consequently, the best strategy to simplify terms is to commutate all bosonic annihilation operators to the right side until only quadratic terms remain.

Spin density operator

The spin density operator is given by

$$\begin{aligned}\hat{\mathbf{S}} &= \frac{1}{2}\sum_{\sigma\sigma'}\hat{f}^\dagger_\sigma \boldsymbol{\tau}_{\sigma\sigma'}\hat{f}_{\sigma'} = \frac{1}{2}\sum_{\sigma\sigma'\sigma_1\sigma_2}\hat{z}^\dagger_{\sigma\sigma_1}\hat{f}^\dagger_{\sigma_1}\boldsymbol{\tau}_{\sigma\sigma'}\hat{z}_{\sigma_2\sigma'}\hat{f}_{\sigma_2} = \left(\hat{p}^\dagger_{\sigma\sigma_1}\hat{p}_{\sigma_2\sigma'} + \frac{1}{2}\hat{d}^\dagger\hat{d}\,\delta_{\sigma_1\sigma_2}\delta_{\sigma\sigma'}\right)\frac{1}{2}\boldsymbol{\tau}_{\sigma\sigma'}\hat{f}^\dagger_{\sigma_1}\hat{f}_{\sigma_2} \\ &= \sum_{\sigma\sigma'\sigma_1}\hat{p}^\dagger_{\sigma\sigma_1}\boldsymbol{\tau}_{\sigma\sigma'}\hat{p}_{\sigma_1\sigma'} = \operatorname{tr}\underline{\hat{p}}\,\underline{\boldsymbol{\tau}}^\top\underline{\hat{p}}^\dagger = \frac{1}{2}\left(\hat{p}^\dagger_0\hat{\boldsymbol{\rho}} + \hat{\boldsymbol{\rho}}^\dagger\hat{p}_0 - \mathrm{i}\hat{\boldsymbol{\rho}}^\dagger\times\hat{\boldsymbol{\rho}}\right)\,,\end{aligned} \tag{A.5a}$$

with

$$\hat{\boldsymbol{\rho}} = \left(\hat{p}_1, -\hat{p}_2, \hat{p}_3\right)^\top\,. \tag{A.5b}$$

The mixed representation shown in Table 2.1 can be derived by applying Equation (2.14b) to the first term in Equation (A.5a).

Charge density operator

The charge density operator is defined by

$$\begin{aligned}\hat{n} &= \sum_\sigma \hat{f}^\dagger_\sigma\hat{f}_\sigma = \sum_{\sigma\sigma_1\sigma_2}\hat{z}^\dagger_{\sigma\sigma_1}\hat{f}^\dagger_{\sigma_1}\hat{z}_{\sigma_2\sigma}\hat{f}_{\sigma_2} = \left(\hat{p}^\dagger_{\sigma\sigma_1}\hat{p}_{\sigma_2\sigma} + \hat{d}^\dagger\hat{d}\,\delta_{\sigma_1\sigma_2}\right)\hat{f}^\dagger_{\sigma_1}\hat{f}_{\sigma_2} \\ &= 4\hat{p}^\dagger_{\sigma\sigma_1}\hat{p}_{\sigma_1\sigma} + \hat{d}^\dagger\hat{d}\left(\sum_{\mu=0}^{3}\hat{p}^\dagger_\mu\hat{p}_\mu + 2\hat{d}^\dagger\hat{d}\right) = \sum_{\mu=0}^{3}\hat{p}^\dagger_\mu\hat{p}_\mu + 2\hat{d}^\dagger\hat{d}\,.\end{aligned} \tag{A.6a}$$

By direct comparison with Equation (2.14c), we identify that a solely PF representation that is equivalent on the constrained subspace is given by

$$\hat{n} = \sum_\sigma \hat{f}^\dagger_\sigma\hat{f}_\sigma\,. \tag{A.6b}$$

Operator of double occupancy

The operator of double occupancy is defined by

$$\hat{D} = \hat{f}^\dagger_\sigma\hat{f}_\sigma\hat{f}^\dagger_{-\sigma}\hat{f}_{-\sigma}\,, \tag{A.7a}$$

which can be recast to squaring the charge density operator in the different representations given by Equations (A.6a) and (A.6b)

$$\hat{n}^2 = \hat{n} + \hat{f}_\sigma^\dagger \hat{f}_\sigma \hat{f}_{-\sigma}^\dagger \hat{f}_{-\sigma} = \hat{n} + \hat{f}_\sigma^\dagger \hat{f}_\sigma \hat{f}_{-\sigma}^\dagger \hat{f}_{-\sigma} = \hat{n} + \hat{d}^\dagger \hat{d} \ . \tag{A.7b}$$

By comparison of terms, we find the bosonic representation

$$\hat{D} = \hat{d}^\dagger \hat{d} \ , \tag{A.7c}$$

and its PF counterpart

$$\hat{D} = \hat{f}_\sigma^\dagger \hat{f}_\sigma \hat{f}_{-\sigma}^\dagger \hat{f}_{-\sigma} \ . \tag{A.7d}$$

A.3 Gauge fixing

Based on References [50] and [53], we explicitly show in the following that the phases of the e, p_0 and $\boldsymbol{p}$ fields can be removed in the radial gauge by a $\mathrm{SU}(2) \otimes \mathrm{U}(1) \otimes \mathrm{U}(1)$ gauge transformation. The ghost phases appear because of the five constraints as conserved quantities and need to be removed or projected out in order to have a well-defined functional integral. At the end of the calculation, the spurious phase information will be absorbed in the Lagrange multipliers, promoting them to time-dependent fields. We start with the SB Lagrangian given by Equation (3.25) and rewrite it via the $\underline{p}$-matrices[1]

$$\mathcal{L} = \sum_{i \neq j} H^{(0)} \left[\left(z^\dagger\right)_{i,\sigma\sigma'} f^*_{i,\sigma'} \ , \ f_{j,\sigma_1} z_{j,\sigma_2\sigma_1} \right] - \mu_0 \sum_i \sum_\sigma f^*_{i,\sigma} f_{i,\sigma} \tag{A.8a}$$

$$+ \sum_i \left[\alpha_i \left(e_i^* e_i + 2 \sum_{\sigma_1\sigma} \left(p_i^\dagger\right)_{\sigma_1\sigma} p_{i,\sigma\sigma_1} + d_i^* d_i - 1 \right) - \sum_{\mu=0}^{3} \beta_{\mu,i} \sum_{\sigma\sigma'} \left(2 \sum_{\sigma_1} \left(p_i^\dagger\right)_{\sigma_1\sigma'} \tau^\mu_{\sigma'\sigma} p_{i,\sigma\sigma_1} + d^* \tau^\mu_{\sigma'\sigma} \delta_{\sigma\sigma'} d - f^*_\sigma \tau^\mu_{\sigma'\sigma} f_{\sigma'} \right) \right] \tag{A.8b}$$

$$+ \sum_i \left[d_i^* (\partial_\tau + U) d_i + e_i^* \partial_\tau e_i + 2 \sum_{\sigma_1\sigma} \left(p_i^\dagger\right)_{\sigma_1\sigma} \partial_\tau p_{i,\sigma\sigma_1} + \sum_\sigma f^*_\sigma \partial_\tau f_\sigma \right] . \tag{A.8c}$$

Now, we rewrite all fields on each lattice site in the radial gauge by means of their absolute value and phase

$$e = \mathrm{e}^{\mathrm{i}\theta} |e| \ , \quad e^* = \mathrm{e}^{-\mathrm{i}\theta} |e| \ , \quad d = \mathrm{e}^{\mathrm{i}\Phi} |d| \ , \quad d^* = \mathrm{e}^{-\mathrm{i}\Phi} |d| \ , \tag{A.9a}$$

$$p_{\sigma\sigma'} = \sum_{\sigma_1} \mathrm{e}^{\mathrm{i}\chi_0} U_{\sigma\sigma_1} q_{\sigma_1\sigma'} \ , \quad \left(p^\dagger\right)_{\sigma\sigma'} = \sum_{\sigma_1} \mathrm{e}^{-\mathrm{i}\chi_0} q_{\sigma\sigma_1} \left(U^\dagger\right)_{\sigma_1\sigma'} \ , \tag{A.9b}$$

and define

$$q_{\sigma\sigma'} = \frac{1}{2} \sum_{\mu=0}^{3} q_\mu \tau^\mu_{\sigma\sigma'} \ , \tag{A.9c}$$

$$U_{\sigma\sigma'} = \exp\left(\mathrm{i} \sum_{\alpha=1}^{3} \chi_\alpha \tau^\alpha_{\sigma\sigma'} \right) = \delta_{\sigma\sigma'} \cos\chi + \mathrm{i} \sum_{\alpha=1}^{3} \frac{\sin\chi}{\chi} \chi_\alpha \tau^\alpha_{\sigma\sigma'} \ , \tag{A.9d}$$

[1] The non-interacting degrees of freedom remain invariant and are summarized in the function $H^{(0)}$, which only depends on the creation and annihilation operators in SB representation.

with $q_\mu \in \mathbb{R}$. Moreover, we need to find the consistent transformation of the time reversed $\underline{\tilde{p}}$-matrix[1]

$$\begin{aligned}\tilde{p}_{\sigma\sigma'} &= \operatorname{sgn}(\sigma)\operatorname{sgn}(\sigma')p_{-\sigma'-\sigma} = \operatorname{sgn}(\sigma')\operatorname{sgn}(\sigma'')\exp\left(\mathrm{i}\sum_{\mu=0}^{3}\chi_\mu\tau^\mu_{-\sigma'-\sigma''}\right)\operatorname{sgn}(\sigma'')\operatorname{sgn}(\sigma)q_{-\sigma''-\sigma} \\ &= e^{\mathrm{i}\chi_0}\tilde{q}_{\sigma\sigma''}\left(\delta_{\sigma''\sigma'}\cos\chi - \mathrm{i}\sum_{\alpha=1}^{3}\frac{\sin\chi}{\chi}\chi_\alpha\tau^\alpha_{\sigma''\sigma'}\right) = \mathrm{e}^{\mathrm{i}\chi_0}\tilde{q}_{\sigma\sigma''}\left(U^\dagger\right)_{\sigma''\sigma'}\,, \\ \left(\tilde{p}^\dagger\right)_{\sigma\sigma'} &= \mathrm{e}^{-\mathrm{i}\chi_0}U_{\sigma\sigma''}\tilde{q}_{\sigma''\sigma'}.\end{aligned} \tag{A.9e}$$

We simultaneously apply the following SU(2) ⊗ U(1) ⊗ U(1) gauge transformation, where the phases match their counterparts in the radial expressions given by Equation (A.9)

$$f_\sigma \to \mathrm{e}^{-\mathrm{i}\chi_0}f_{\sigma'}\left(U^\dagger\right)_{\sigma'\sigma}\,, \tag{A.10a}$$

$$d \to \mathrm{e}^{\mathrm{i}(\theta+2\chi_0)}d\,, \tag{A.10b}$$

$$p_{\sigma\sigma'} \to \mathrm{e}^{\mathrm{i}\theta}p_{\sigma\sigma'}\,, \tag{A.10c}$$

$$\tilde{p}_{\sigma\sigma'} \to \mathrm{e}^{\mathrm{i}\theta}\tilde{p}_{\sigma\sigma'}\,. \tag{A.10d}$$

In the following, we show term by term that the Lagrangian remains invariant except for removing five phases that are absorbed into Lagrange multipliers, promoting them to time-dependent fields.

Pseudo-fermionic terms

$$\begin{aligned}\sum_{\sigma\sigma'}f^*_\sigma\delta_{\sigma\sigma'}f_{\sigma'} &\to \sum_{\sigma\sigma'}\mathrm{e}^{\mathrm{i}\chi_0}U_{\sigma\sigma_1}f^*_{\sigma_1}\delta_{\sigma\sigma'}\mathrm{e}^{-\mathrm{i}\chi_0}f_{\sigma_2}U^\dagger_{\sigma_2\sigma'} = \sum_{\sigma,\sigma'}f^*_\sigma\delta_{\sigma\sigma'}f_{\sigma'}\,, \\ \left(z^\dagger\right)_{\sigma\sigma'}f^*_{\sigma'} &\to q_{\sigma\sigma'}|e|f^*_{\sigma'} + d^*\tilde{q}_{\sigma\sigma'}f^*_{\sigma'}, \\ f_{\sigma'}z_{\sigma'\sigma} &\to f_{\sigma'}|e|q_{\sigma'\sigma} + f_{\sigma'}\tilde{q}_{\sigma'\sigma}d\,.\end{aligned} \tag{A.11}$$

Lagrange-multiplier terms

$$\alpha\left(e^*e + 2\sum_{\sigma_1\sigma}p^\dagger_{\sigma_1\sigma}p_{\sigma\sigma_1} + d^*d - 1\right) \to \alpha\left(|e^2| + 2\sum_{\sigma_1\sigma}q_{\sigma_1\sigma}q_{\sigma\sigma_1} + d^*d - 1\right). \tag{A.12}$$

Rather than directly considering the second term in Equation (A.8b), we look at the transformation properties of the second constraint given by Equation (2.14b) in matrix representation

$$\sum_{\sigma_2\sigma_3}U_{\sigma\sigma_2}f^*_{\sigma_2}f_{\sigma_3}\left(U^\dagger\right)_{\sigma_3\sigma'} = 2\sum_{\sigma_1\sigma_2\sigma_3}q_{\sigma_1\sigma_2}\left(U^\dagger\right)_{\sigma_2\sigma'}U_{\sigma\sigma_3}q_{\sigma_3\sigma_1} + \delta_{\sigma\sigma'}d^*d\,. \tag{A.13}$$

In order to obtain four scalar equations, we expand by means of Pauli matrices in the unitary rotated basis. Applying $\sum_{\sigma\sigma'}U_{\sigma'\sigma_4}\tau^\mu_{\sigma_4\sigma_5}(U)^\dagger_{\sigma_5\sigma}$ with $\mu \in \{0,1,2,3\}$ on both sides of Equation (A.13) yields the transformation

[1] Within the calculation, we apply the identity $\operatorname{sgn}(\sigma')\operatorname{sgn}(\sigma)\tau^\alpha_{-\sigma-\sigma'} = -\tau^\alpha_{\sigma\sigma'}$.

properties of the second constraint enforced by new static Lagrange multipliers β_μ

$$\begin{aligned} &-\sum_{\mu=0}^{3}\beta_\mu\sum_{\sigma\sigma'}\left(2\sum_{\sigma_1}\left(p^\dagger\right)_{\sigma_1\sigma'}\tau^\mu_{\sigma'\sigma}p_{\sigma\sigma_1}+d^*\tau^\mu_{\sigma'\sigma}\delta_{\sigma\sigma'}d-f^*_\sigma\tau^\mu_{\sigma'\sigma}f_{\sigma'}\right)\\ \to&\sum_{\sigma\sigma'}f^*_\sigma\left(\beta_0\delta_{\sigma\sigma'}+\sum_{\mu=1}^{3}\beta_\mu\tau^\mu_{\sigma'\sigma}\right)f_{\sigma'}-\beta_0\left(\sum_{\mu=0}^{3}q_\mu^2+2d^*d\right)-\sum_{\mu=1}^{3}\beta_\mu 2q_\mu q_0. \end{aligned} \tag{A.14}$$

Again, the p-fields lose their phase information, which vanishes the cross product $\boldsymbol{p}^*\times\boldsymbol{p}$, while the rest remains invariant.

Time-derivative terms

Finally, we investigate the time derivative terms given by Equation (A.8c). Notice that total derivatives like $2|e|\partial_\tau|e| = \partial_\tau|e|^2$ vanish due to the periodic boundary conditions of the path integral

$$\begin{aligned} &d^*(\partial_\tau+U)d+e^*\partial_\tau e+2\sum_{\sigma_1\sigma}\left(p^\dagger\right)_{\sigma_1\sigma}\partial_\tau p_{\sigma\sigma_1}+\sum_\sigma f^*_\sigma\partial_\tau f_\sigma\\ \to&(\mathrm{i}\dot\theta+2\mathrm{i}\dot\chi_0+U)d^*d+\mathrm{i}\dot\theta|e^2|+\sum_{\sigma\sigma_1\sigma_2\sigma_3}\left[-2\mathrm{i}(\dot\chi+\dot\theta)q_{\sigma_1\sigma}q_{\sigma\sigma_1}+\dot U_{\sigma_3\sigma_1}\left(U^\dagger\right)_{\sigma_1\sigma_2}q_{\sigma_2\sigma}q_{\sigma\sigma_3}\right]\\ &+\sum_{\sigma\sigma_1\sigma_2}\left[f^*_\sigma\partial_\tau f_\sigma-\mathrm{i}\dot\chi_0 f^*_\sigma f_\sigma+f^*_{\sigma_1}(\dot U^\dagger)_{\sigma_2\sigma}U_{\sigma\sigma_1}f_{\sigma_2}\right]. \end{aligned} \tag{A.15}$$

With $n_\alpha=\chi_\alpha/\chi$, the time derivatives of the unitary matrix are found to be[1]

$$\sum_{\sigma\sigma_1\sigma_2\sigma_3}\dot U_{\sigma_3\sigma_1}\left(U^\dagger\right)_{\sigma_1\sigma_2}q_{\sigma_2\sigma}q_{\sigma\sigma_3}=\mathrm{i}q_0\sum_{\alpha=1}^{3}q_\alpha\left(n_\alpha\dot\chi+\dot n_\alpha\sin\chi\cos\chi-\sum_{ij}\epsilon_{\alpha ij}\dot n_i n_j\sin^2\chi\right), \tag{A.16a}$$

$$\sum_\sigma\left(\dot U^\dagger\right)_{\sigma_2\sigma}U_{\sigma\sigma_1}=-\mathrm{i}\sum_{\alpha=1}^{3}\left(n_\alpha\dot\chi+\dot n_\alpha\sin\chi\cos\chi-\sum_{ij}\epsilon_{\alpha ij}\dot n_i n_j\sin^2\chi\right)\tau^\alpha_{\sigma_2\sigma_1}. \tag{A.16b}$$

Using all previous results, terms containing the phase factors χ_0, $\boldsymbol{\chi}$ and θ can be absorbed into the Lagrange multipliers by

$$\left(\alpha+\mathrm{i}\dot\theta\right)\to\alpha\,, \tag{A.17a}$$

$$(\beta_0+\mathrm{i}\dot\chi_0)\to\beta_0\,, \tag{A.17b}$$

$$\left(\boldsymbol{\beta}-\mathrm{i}\left(\boldsymbol{n}\dot\chi+\dot{\boldsymbol{n}}\sin\chi\cos\chi-\dot{\boldsymbol{n}}\times\boldsymbol{n}\sin^2\chi\right)\right)\to\boldsymbol{\beta}\,. \tag{A.17c}$$

A.4 Pauli matrix expansion of the z-matrix

Any hermitian 2×2 matrix can be expressed in the basis of Pauli matrices $\underline{\boldsymbol{\tau}}$ and the identity matrix $\underline{\tau}^0$

$$\underline{\mathcal{A}}=a_0\underline{\tau}^0+\boldsymbol{a}\cdot\underline{\boldsymbol{\tau}}\,, \tag{A.18a}$$

[1] Notice that $\partial_\tau\mathbb{1}=\partial_\tau(U_{\sigma_3\sigma_1}U^\dagger_{\sigma_1\sigma_2})=0 \;\Leftrightarrow\; \dot U_{\sigma_3\sigma_1}U^\dagger_{\sigma_1\sigma_2}=-U_{\sigma_3\sigma_1}\dot U^\dagger_{\sigma_1\sigma_2}$ and $0=\partial_\tau(n_\alpha n_\alpha)\;\Leftrightarrow\sum_\alpha n_\alpha\,\dot n_\alpha=0$.

and it can be diagonalized by a unitary transformation

$$\underline{U}_{\hat{a}}^{\dagger}\underline{\mathcal{A}}\,\underline{U}_{\hat{a}} = a_0\underline{\tau}^0 + a\underline{\tau}^3 \,, \tag{A.18b}$$

such that $\underline{U}_{\hat{a}}^{\dagger}$ only depends on $\hat{\boldsymbol{a}} = \boldsymbol{a}/a$ with $a = |\boldsymbol{a}|$. Consequently it holds

$$\underline{U}_{\hat{a}}^{\dagger}\left(a_0\underline{\tau}^0 \pm \boldsymbol{a}\cdot\underline{\boldsymbol{\tau}}\right)\underline{U}_{\hat{a}} = a_0\underline{\tau}^0 \pm a\underline{U}_{\hat{a}}^{\dagger}\left(\hat{\boldsymbol{a}}\cdot\underline{\boldsymbol{\tau}}\right)\underline{U}_{\hat{a}} \,. \tag{A.18c}$$

These properties will be applied to rewrite the $\underline{z}$-matrix, which reproduces the correct non-interacting limit defined in Equation (A.19), in the basis of Pauli matrices in order to eliminate non-diagonal matrices in the denominator. We consider $\underline{z}$ w.r.t. the field theory basis of coherent states in the radial gauge, i.e., operators are replaced by fields, and only the d-field remains as a complex variable, while e, p_0, and $\boldsymbol{p}$ are real-valued. We moreover replace the M-factor defined in Equation (4.7) by $\sqrt{2}$ utilizing the α-constraint[1]. With these assumptions, it is

$$\underline{z} = \left(e\,\underline{L}\,\sqrt{2}\underline{R}\,\underline{p} + \underline{\tilde{p}}^{\dagger}\,\underline{L}\,\sqrt{2}\,\underline{R}d\right) \,, \tag{A.19a}$$

with

$$\underline{L} = \left((1-d^*d)\underline{\tau}_0 - 2\,\underline{p}^{\dagger}\underline{p}\right)^{-1/2} \,, \tag{A.19b}$$

$$\underline{R} = \left(\left(1-e^2\right)\underline{\tau}_0 - 2\,\underline{\tilde{p}}^{\dagger}\underline{\tilde{p}}\right)^{-1/2} \,. \tag{A.19c}$$

We can rewrite the products

$$\begin{aligned} 4\,\underline{p}^{\dagger}\underline{p} &= \sum_{\mu,\mu'}\left(p_0\underline{\tau}^0 + p_\mu\underline{\tau}^\mu\right)\left(p_0\underline{\tau}^0 + p_{\mu'}\underline{\tau}^{\mu'}\right) = p_0^2\underline{\tau}^0 + 2p_0(\boldsymbol{p}\cdot\underline{\boldsymbol{\tau}}) + \boldsymbol{p}^2\underline{\tau}^0 \,, \\ 4\,\underline{\tilde{p}}^{\dagger}\underline{\tilde{p}} &= \sum_{\mu,\mu'}\left(p_0\underline{\tau}^0 + p_\mu\underline{\tau}^\mu\right)\left(p_0\underline{\tau}^0 + p_{\mu'}\underline{\tau}^{\mu'}\right) = p_0^2\underline{\tau}^0 - 2p_0(\boldsymbol{p}\cdot\underline{\boldsymbol{\tau}}) + \boldsymbol{p}^2\underline{\tau}^0 \,, \end{aligned} \tag{A.20}$$

and realize that $\left[\underline{R}\,,\,\underline{p}\right]_- = \left[\underline{L}\,,\,\underline{\tilde{p}}^{\dagger}\right]_- = 0$. We may thus express the $\underline{z}$-matrix as [99]

$$\underline{z} = \left[\left(1-d^*d-\tfrac{p_0^2+\boldsymbol{p}^2}{2}\right)\underline{\tau}^0 - p_0(\boldsymbol{p}\cdot\underline{\boldsymbol{\tau}})\right]^{-\frac{1}{2}}\frac{1}{\sqrt{2}}\left[(e+d)p_0\underline{\tau}^0 + (e-d)(\boldsymbol{p}\cdot\underline{\boldsymbol{\tau}})\right]\left[\left(1-e^2-\tfrac{p_0^2+\boldsymbol{p}^2}{2}\right)\underline{\tau}^0 + p_0(\boldsymbol{p}\cdot\boldsymbol{\sigma})\right]^{-\frac{1}{2}} \,. \tag{A.21}$$

With Equation (A.18c), we realize that all three matrices can be diagonalized by the same unitary transformation[2] $\underline{U}_{\hat{p}}$. Consequently, we may insert $\underline{\mathbb{1}}_2 = \underline{U}_{\hat{p}}^{\dagger}\underline{U}_{\hat{p}}$ between them and diagonalize each matrix independently by means of Equation (A.18b) and the eigenvalues of $\underline{z}$ are thus given by the product of respective diagonal entries

$$\underline{U}_{\hat{p}}\underline{z}\,\underline{U}_{\hat{p}}^{\dagger} = \begin{pmatrix} z_+ & 0 \\ 0 & z_- \end{pmatrix} = \frac{z_+ + z_-}{2}\underline{\tau}^0 + \frac{z_+ - z_-}{2}\underline{\tau}^3 = \mathcal{Z}_+\underline{\tau}^0 + \mathcal{Z}_-\underline{\tau}^3 \,, \tag{A.22}$$

[1] On MF level, this constraint is exactly fulfilled, and the replacement is justified. As we argue in Section 5.1, we also do not consider fluctuations of M because those would have an unphysical origin and need to be inhibited.

[2] The inverse square root terms can be expanded in a power series and one may insert $\underline{\mathbb{1}}_2 = \underline{U}_{\hat{p}}^{\dagger}\underline{U}_{\hat{p}}$ between each appearing power to diagonalize all occurring matrices separately and express the diagonalized infinite series again as an inverse square root.

Summand function $g(\mathrm{i}\omega_n)$	**Matsubara summation** $S_\zeta = \frac{1}{\beta}\sum_{n=-\infty}^{+\infty} g(\mathrm{i}\omega_n)$
$\dfrac{1}{\mathrm{i}\omega_n - \varepsilon}$	$-\zeta n_\zeta(\varepsilon)$
$\dfrac{1}{(\mathrm{i}\omega_n - \varepsilon_1)(\mathrm{i}\omega_n - \varepsilon_2)}$	$-\zeta \dfrac{n_\zeta(\varepsilon_1) - n_\zeta(\varepsilon_2)}{\varepsilon_1 - \varepsilon_2}$
$\zeta \ln(-\mathrm{i}\omega_n + \varepsilon)$	$\zeta \ln\left(1 - \zeta \mathrm{e}^{-\varepsilon/T}\right)$
$\dfrac{\varepsilon_3}{(\mathrm{i}\omega_n - \varepsilon_1)(\mathrm{i}\omega_n - \varepsilon_2) - \varepsilon_3^2}$	$\zeta \dfrac{n_\zeta[(\varepsilon_1 + \varepsilon_2 - \Delta)/2] - n_\zeta[(\varepsilon_1 + \varepsilon_2 + \Delta)/2]}{\Delta}\varepsilon_3$
$\dfrac{\mathrm{i}\omega_n - \varepsilon_1}{(\mathrm{i}\omega_n - \varepsilon_1)(\mathrm{i}\omega_n - \varepsilon_2) - \varepsilon_3^2}$	$-\zeta \dfrac{(\varepsilon_1 - \varepsilon_2 + \Delta) n_\zeta[(\varepsilon_1 + \varepsilon_2 - \Delta)/2] + (\varepsilon_2 - \varepsilon_1 + \Delta) n_\zeta[(\varepsilon_1 + \varepsilon_2 + \Delta)/2]}{2\Delta}$

Table A.1: List of Matsubara summations applied within in this thesis and evaluated by means of Reference [128]. We define $\Delta = \sqrt{(\varepsilon_1 - \varepsilon_2)^2 + 4\varepsilon_3^2}$. Moreover, n_ζ denotes the statistical distribution and ω_n the Matsubara frequency defined by Equations (A.25) and (A.26).

with

$$z_\pm = \frac{p_0(e+d) \pm p(e-d)}{\sqrt{2\left[1 - d^2 - (p_0 \pm p)^2/2\right]\left[1 - e^2 - (p_0 \mp p)^2/2\right]}} \,. \tag{A.23}$$

We may now rotate back to the original basis by means of Equations (A.18b) and (A.18c) and find

$$\underline{z} = \underline{U}_{\hat{p}}^\dagger \left(\mathcal{Z}_+ \underline{\tau}^0 + \frac{\mathcal{Z}_-}{p} p \underline{\tau}^3\right) \underline{U}_{\hat{p}} = \mathcal{Z}_+ \underline{\tau}^0 + \mathcal{Z}_- \frac{\boldsymbol{p}}{p} \underline{\boldsymbol{\tau}} \,. \tag{A.24}$$

A.5 Matsubara summations

In the context of the imaginary-time path integral formalism, we often need to evaluate summations over discrete frequencies that respect the periodic (anti-periodic) boundary conditions of the bosonic (fermionic) time evolution operator. These so-called Matsubara frequencies are given by

$$\omega_n = \frac{2n\pi}{\beta} \qquad n \in \mathbb{Z}_0 \quad \text{for bosons} \,, \tag{A.25a}$$

$$\omega_n = \frac{(2n+1)\pi}{\beta} \qquad n \in \mathbb{Z}_0 \quad \text{for fermions} \,, \tag{A.25b}$$

with the inverse temperature β. In the limit of infinitesimal time slices, i.e., continuous imaginary time where the path integral becomes exact, summations must be performed from minus infinity to infinity. Corresponding infinite series can be evaluated analytically by mapping to a complex contour integral utilizing a weight function with simple poles situated at the Matsubara frequencies. Suitable functions are the Bose-Einstein distribution for bosons and the Fermi-Dirac distribution for fermions

$$n_1(z) = n_\mathrm{B}(z) = \frac{1}{\mathrm{e}^{\beta z} - 1} \,, \tag{A.26a}$$

$$n_{-1}(z) = n_\mathrm{F}(z) = \frac{1}{\mathrm{e}^{\beta z} + 1} \,, \tag{A.26b}$$

with

$$\text{Res}\left[n_\zeta(\mathrm{i}\omega_n)\right] = \zeta\frac{1}{\beta}\,, \tag{A.27}$$

and ζ denotes the statistical sign, being $\zeta = 1$ for bosons and $\zeta = -1$ for fermions. Consequently, it is [39]

$$S_\zeta = \frac{1}{\beta}\sum_{n=-\infty}^{+\infty} g(\mathrm{i}\omega_n) = \zeta\oint dz\, g(z)n_\zeta(z)\,, \tag{A.28}$$

and the complex contour integral can by evaluated by means of the residue theorem. If the summand is of the order $g(\mathrm{i}\omega_n) = \mathcal{O}\left(1/\mathrm{i}\omega_n\right)$ or higher, the sum does not converge and it needs to be evaluated with the addition of a convergence factor $g(z) \to g(z)\mathrm{e}^{-\eta z}$ with $\eta \to 0^+$. The necessity of this factor originates in the fact that only the discrete formulation of the path integral, where "equal-time" terms actually differ by a single time slice $\eta = \beta/M$ [compare Equation (3.5b)] is formally correct. The limit to continuous time is well defined if taken at the very end of a calculation. However, the Matsubara representation takes this limit before the evaluation of the sum, which needs to be compensated by the convergence factor. Table A.1 summarizes results for Matsubara summations, which are applied within this thesis. They have been evaluated utilizing the *Mathematica* script of Yi-Zhuang You from the university of San Diego, which is publicly available on Github [128].

A.6 Differentials of fluctuation-fields

In order to compute Gaussian fluctuations, we are required to calculate derivatives of the bosonic $\underline{Z}_k$ factors in momentum space w.r.t. individual fluctuation fields $\delta\psi_{\mu,q}$ and evaluate them at the MF saddle point $\overline{\psi}$ as discussed in Section 5.2. In the following, we present the occurring calculations in detail. We aim to calculate the derivatives $\left.\frac{\partial \underline{H}^{\psi}_{k_1,k_2}}{\partial\psi_{q,\mu}}\right|_{\overline{\psi}}$ and $\left.\frac{\partial^2 \underline{H}^{\psi}_{k,k}}{\partial\psi_{q_1,\mu}\partial\psi_{q_2,\nu}}\right|_{\overline{\psi}}$ of the SB-dependent Hamiltonian

$$\underline{H}^{\psi}_{k_1,k_2} = \delta_{k_1,k_2}\left(\underline{\epsilon} - \mu_0\right) + \frac{1}{\sqrt{N\beta}}\left(\underline{B}\right)^{\top}_{k_1-k_2} + \frac{1}{N\beta}\sum_k \left(\underline{Z}^{\dagger}\right)^{\top}_{k-k_1}\underline{\mathcal{H}}_k\left(\underline{Z}\right)^{\top}_{k-k_2}\,, \tag{A.29}$$

with

$$\underline{Z}_k = \left(\underline{\mathbb{1}}_{2O\times 2O}\sqrt{N\beta}\,\delta_{k,0}\right)\oplus\underline{z}_k\,, \tag{A.30a}$$

$$\underline{B}_k = \underline{0}_{2O\times 2O}\oplus\underline{\beta}_k\,. \tag{A.30b}$$

Spatially uniform mean-field saddle point

We start with the analysis of a spatially uniform MF saddle point that satisfies

$$\left.\frac{\partial \underline{Z}_{\mu,r}}{\partial\psi_{r,\tilde{\mu}}}\right|_{\overline{\psi}} = \left.\frac{\partial \underline{Z}_{\mu}}{\partial\psi_{\tilde{\mu}}}\right|_{\overline{\psi}}\,, \tag{A.31}$$

which holds for PM or FM order. The zeroth, first and second order differentials around the MF saddle point are found to be

$$\begin{aligned}
\underline{z}_k &= \frac{1}{\sqrt{N\beta}} \sum_{\boldsymbol{r}_i} \int_0^\beta d\tau\, \mathrm{e}^{-\mathrm{i}\boldsymbol{k}\boldsymbol{r}_i + \mathrm{i}\omega_n\tau} \underline{z}_r \Big|_{\overline{\psi}} = \underline{z}\Big|_{\overline{\psi}} \frac{1}{\sqrt{N\beta}} \sum_{\boldsymbol{r}_i} \int_0^\beta d\tau\, \mathrm{e}^{-\mathrm{i}\boldsymbol{k}\boldsymbol{r}_i + \mathrm{i}\omega_n\tau} = \sqrt{N\beta}\, \delta_{k,0}\, \underline{z}\Big|_{\overline{\psi}} \,, \\
\delta\underline{z}_k &= \frac{1}{\sqrt{N\beta}} \sum_{\boldsymbol{r}_i} \sum_{\tilde{\mu}} \int_0^\beta d\tau\, \mathrm{e}^{-\mathrm{i}\boldsymbol{k}\boldsymbol{r}_i + \mathrm{i}\omega_n\tau} \frac{\partial \underline{z}_r}{\partial \psi_{r,\tilde{\mu}}}\Big|_{\overline{\psi}} \delta\psi_{r,\tilde{\mu}} = \sum_{\tilde{\mu}} \frac{\partial \underline{z}}{\partial \psi_{\tilde{\mu}}}\Big|_{\overline{\psi}} \delta\psi_{k,\tilde{\mu}} \,, \\
\delta^2\underline{z}_k &= \frac{1}{\sqrt{N\beta}} \sum_{\boldsymbol{r}_i} \sum_{\tilde{\mu},\tilde{\nu}} \int_0^\beta d\tau\, \mathrm{e}^{-\mathrm{i}\boldsymbol{k}\boldsymbol{r}_i + \mathrm{i}\omega_n\tau} \frac{\partial^2 \underline{z}_r}{\partial \psi_{\tilde{\mu},r} \partial \psi_{\tilde{\nu},r}}\Big|_{\overline{\psi}} \delta\psi_{\tilde{\mu},r} \delta\psi_{\tilde{\nu},r} \,, \\
&= \frac{1}{\sqrt{N\beta}^3} \sum_{\tilde{\mu},\tilde{\nu}} \frac{\partial^2 \underline{z}}{\partial \psi_{\tilde{\mu}} \partial \psi_{\tilde{\nu}}}\Big|_{\overline{\psi}} \sum_{k_1,k_2} \sum_{\boldsymbol{r}_i} \int_0^\beta d\tau \mathrm{e}^{\mathrm{i}\boldsymbol{r}_i(\boldsymbol{k}_1+\boldsymbol{k}_2-\boldsymbol{k})} \mathrm{e}^{\mathrm{i}\tau(\omega_n-\omega_{n_1}-\omega_{n_2})} \delta\psi_{\tilde{\mu},k_1} \delta\psi_{\tilde{\nu},k_2} \\
&= \frac{1}{\sqrt{N\beta}} \sum_{\tilde{\mu},\tilde{\nu}} \frac{\partial^2 \underline{z}}{\partial \psi_{\tilde{\mu}} \partial \psi_{\tilde{\nu}}}\Big|_{\overline{\psi}} \sum_{k_1} \delta\psi_{k_1,\tilde{\mu}} \delta\psi_{k-k_1,\tilde{\nu}} \,.
\end{aligned} \tag{A.32}$$

Consequently, derivatives w.r.t. SB fields are given by

$$\frac{\partial \underline{z}_k}{\partial \psi_{q,\mu}}\Big|_{\overline{\psi}} = \delta_{k,q} \frac{\partial \underline{z}}{\partial \psi_\mu}\Big|_{\overline{\psi}} \,, \qquad \frac{\partial \underline{z}_k^\dagger}{\partial \psi_{q,\mu}}\Big|_{\overline{\psi}} = \delta_{k,-q} \frac{\partial \underline{z}^\dagger}{\partial \psi_\mu}\Big|_{\overline{\psi}} \,, \tag{A.33a}$$

$$\frac{\partial^2 \underline{z}_k}{\partial \psi_{q_1,\mu} \partial \psi_{q_2,\nu}}\Big|_{\overline{\psi}} = \frac{1}{\sqrt{N\beta}} \delta_{k,q_1+q_2} \frac{\partial^2 \underline{z}}{\partial \psi_\mu \partial \psi_\nu}\Big|_{\overline{\psi}} \,, \qquad \frac{\partial^2 \underline{z}_k^\dagger}{\partial \psi_{q_1,\mu} \partial \psi_{q_2,\nu}}\Big|_{\overline{\psi}} = \frac{1}{\sqrt{N\beta}} \delta_{k,-q_1-q_2} \frac{\partial^2 \underline{z}^\dagger}{\partial \psi_\mu \partial \psi_\nu}\Big|_{\overline{\psi}} \,. \tag{A.33b}$$

Derivatives or the $\underline{Z}_k$-factors with additional non-interacting orbitals can be inferred with the definition in Equation (A.30a) by adding a direct sum of unity or zero matrices

$$\underline{Z}_k\Big|_{\overline{\psi}} = \sqrt{N\beta}\, \delta_{k,0} \left(\underline{\mathbb{1}}_{2O\times 2O} \oplus \underline{z}\Big|_{\overline{\psi}} \right) \,, \tag{A.34a}$$

$$\frac{\partial \underline{Z}_k^{(\dagger)}}{\partial \psi_{q,\mu}}\Big|_{\overline{\psi}} = \underline{0}_{2O\times 2O} \oplus \frac{\partial \underline{z}_k^{(\dagger)}}{\partial \psi_{q,\mu}}\Big|_{\overline{\psi}} \,, \tag{A.34b}$$

$$\frac{\partial^2 \underline{Z}_k^{(\dagger)}}{\partial \psi_{q_1,\mu} \partial \psi_{q_2,\nu}}\Big|_{\overline{\psi}} = \underline{0}_{2O\times 2O} \oplus \frac{\partial^2 \underline{z}_k^{(\dagger)}}{\partial \psi_{q_1,\mu} \partial \psi_{q_2,\nu}}\Big|_{\overline{\psi}} \,. \tag{A.34c}$$

The remaining MF derivatives of the $\underline{z}$-matrix can conveniently be evaluated in the Pauli matrix expanded form given by Equation (A.24). Notice that in the basis chosen for the fluctuations, we need to replace the e-field by means of the α-constraint $1 = e^2 + d_1^2 + d_2^2 + p_0^2 + \boldsymbol{p}^2$ before taking derivatives. The derivatives of the LM-fields are particularly easy because they enter the Lagrangian only linearly. Hence, it is

$$\frac{\partial \underline{B}_k}{\partial \psi_{\mu,q}}\Big|_{\overline{\psi}} = \underline{0}_{2O\times 2O} \oplus \sum_{\tilde{\mu},\nu} \frac{\partial \beta_\nu \underline{\tau}^\nu}{\partial \psi_{\tilde{\mu}}} \frac{\partial \delta\psi_{k,\tilde{\mu}}}{\partial \psi_{\mu,q}} = \underline{0}_{2O\times 2O} \oplus \underline{\tau}^\nu \delta_{\psi_\mu,\beta_\nu} \delta_{k,q} \,. \tag{A.35}$$

For shortness of notation, we define

$$\underline{Z}_0 = \underline{Z}^\top\Big|_{\overline{\psi}} \,, \tag{A.36a}$$

$$\underline{Z}_{\mu} = \left.\frac{\partial \underline{Z}^{\top}}{\partial \psi_{\mu}}\right|_{\overline{\psi}}, \tag{A.36b}$$

$$\underline{Z}_{\mu\nu} = \left.\frac{\partial^2 \underline{Z}^{\top}}{\partial \psi_{\mu}\partial \psi_{\nu}}\right|_{\overline{\psi}}, \tag{A.36c}$$

$$\underline{B}_{\mu} = \underline{0}_{2O\times 2O} \oplus (\underline{\tau}^{\nu})^{\top}\, \delta_{\psi_{\mu},\beta_{\nu}}, \tag{A.36d}$$

and find

$$\begin{aligned}
\left.\frac{\partial \underline{H}^{\psi}_{k_1,k_2}}{\partial \psi_{q,\mu}}\right|_{\overline{\psi}} &= \frac{1}{\sqrt{N\beta}}\underline{B}_{\mu}\delta_{q,k_1-k_2} + \frac{1}{N\beta}\sum_{k}\left[\delta_{k-k_1,-q}\underline{Z}^{\dagger}_{\mu}\underline{\mathcal{H}}_{k}\,\underline{Z}_0\delta_{k-k_2,0}\sqrt{N\beta} + \sqrt{N\beta}\delta_{k-k_1,0}\underline{Z}^{\dagger}_0\underline{\mathcal{H}}_{k}\,\underline{Z}_{\mu}\delta_{k-k_2,q}\right] \\
&= \frac{\delta_{q,k_1-k_2}}{\sqrt{N\beta}}\left[\underline{B}_{\mu} + \left(\underline{Z}^{\dagger}_{\mu}\right)\underline{\mathcal{H}}_{k_2}\,\underline{Z}_0 + \underline{Z}^{\dagger}_0\underline{\mathcal{H}}_{k_1}\,\underline{Z}_{\mu}\right], \\
\left.\frac{\partial^2 \underline{H}^{\psi}_{k,k}}{\partial \psi_{q_1,\mu}\partial \psi_{q_2,\nu}}\right|_{\overline{\psi}} &= \frac{1}{N\beta}\sum_{\tilde{k}}\Big[\delta_{\tilde{k}-k,-q_1-q_2}\underline{Z}^{\dagger}_{\mu\nu}\underline{\mathcal{H}}_{\tilde{k}}\,\underline{Z}_0\delta_{\tilde{k}-k,0} + \delta_{\tilde{k}-k,0}\underline{Z}^{\dagger}_0\underline{\mathcal{H}}_{\tilde{k}}\,\underline{Z}_{\mu\nu}\delta_{\tilde{k}-k,q_1+q_2} \\
&\qquad + \delta_{\tilde{k}-k,-q_1}\underline{Z}^{\dagger}_{\mu}\underline{\mathcal{H}}_{\tilde{k}}\,\underline{Z}_{\nu}\delta_{\tilde{k}-k,q_2} + \delta_{\tilde{k}-k,-q_2}\underline{Z}^{\dagger}_{\nu}\underline{\mathcal{H}}_{\tilde{k}}\,\underline{Z}_{\mu}\delta_{\tilde{k}-k,q_1}\Big] \\
&= \frac{1}{N\beta}\delta_{q_1,-q_2}\left[\underline{Z}^{\dagger}_{\mu\nu}\underline{\mathcal{H}}_{k}\,\underline{Z}_0 + \underline{Z}^{\dagger}_0\underline{\mathcal{H}}_{k}\,\underline{Z}_{\mu\nu} + \underline{Z}^{\dagger}_{\mu}\underline{\mathcal{H}}_{k-q_1}\,\underline{Z}_{\nu} + \underline{Z}^{\dagger}_{\nu}\underline{\mathcal{H}}_{k+q_1}\,\underline{Z}_{\mu}\right].
\end{aligned} \tag{A.37}$$

Spatially periodic mean-field saddle point

In order to calculate fluctuations around a MF saddle point with an enlarged magnetic unit cell, we need to expand every non-uniform quantity $\Xi_{\boldsymbol{r}}$ (i.e., the $\underline{Z}$-matrices and the bosonic Lagrangian) and respective derivatives at the saddle point as a Fourier series of the MF ordering vector $\boldsymbol{Q}$

$$\Xi_{\boldsymbol{r}_i}\Big|_{\overline{\psi}} = \sum_{a=-\infty}^{\infty}\overline{\Xi}_a\, \mathrm{e}^{-\mathrm{i}a\boldsymbol{Q}\boldsymbol{r}_i}, \tag{A.38a}$$

$$\partial_{\mu}\Xi_{\boldsymbol{r}_i}\Big|_{\overline{\psi}} = \sum_{a=-\infty}^{\infty}\Xi_{a,\mu}\, \mathrm{e}^{-\mathrm{i}a\boldsymbol{Q}\boldsymbol{r}_i}, \tag{A.38b}$$

$$\partial_{\mu\nu}\Xi_{\boldsymbol{r}_i}\Big|_{\overline{\psi}} = \sum_{a=-\infty}^{\infty}\Xi_{a,\mu\nu}\, \mathrm{e}^{-\mathrm{i}a\boldsymbol{Q}\boldsymbol{r}_i}, \tag{A.38c}$$

and we reemploy the notation where the index μ represents taking the derivative w.r.t. ψ_{μ}

$$\overline{\Xi} = \Xi\Big|_{\overline{\psi}}, \quad \Xi_{\mu} = \left.\frac{\partial \Xi}{\partial \psi_{\mu}}\right|_{\overline{\psi}}, \quad \Xi_{\mu\nu} = \left.\frac{\partial^2 \Xi}{\partial \psi_{\mu}\partial \psi_{\nu}}\right|_{\overline{\psi}}. \tag{A.39}$$

We now can repeat the calculation presented in Equation (A.32). Since the MF ansatz is still static, the frequency dependence is unchanged, but the Fourier series results in an additional sum over Kronecker deltas with a momentum kick of $\boldsymbol{Q}$

$$\Xi_k\big|_{\overline{\psi}} = \sqrt{N\beta}\sum_a \overline{\Xi}_a\, \delta_{\mathrm{i}\omega_n,\boldsymbol{k}+a\boldsymbol{Q},0} \tag{A.40a}$$

$$\delta\Xi_k\big|_{\overline{\psi}} = \sum_a \sum_{\tilde{\mu}} \Xi_{a,\tilde{\mu}}\, \delta\psi_{\mathrm{i}\omega_n,\boldsymbol{k}+a\boldsymbol{Q},\tilde{\mu}} \tag{A.40b}$$

$$\delta^2\Xi_k\big|_{\overline{\psi}} = \frac{1}{\sqrt{N\beta}}\sum_a \sum_{\tilde{\mu},\tilde{\nu}} \sum_{k_1} \Xi_{a,\mu\nu}\delta\psi_{k_1,\tilde{\mu}}\delta\psi_{(\mathrm{i}\omega,\boldsymbol{k}+a\boldsymbol{Q})-k_1,\tilde{\nu}}\,. \tag{A.40c}$$

The fluctuation basis has thus to be enlarged to include correlations between fields with a momentum difference of $a\boldsymbol{Q}$. For commensurate $\boldsymbol{Q}$, this basis stays finite.

Appendix B

Derivation of mean-field matrices

In the following, we explicitly derive the SB mean-field (MF) hopping matrices for the three different models, i.e., the Hubbard model, periodic Anderson model (PAM), and topological Kondo insulator (TKI) model, discussed in this thesis based on References [53] and [54]. We moreover provide the respective eigenvalues that define the magnetic MF band structure if analytically accessible and discuss the impact of rotating the MF magnetization axis.

According to Section 4.3, the MF action

$$\mathcal{S}^{(0)} = \mathcal{S}_B^{(0)} + \mathcal{S}_F^{(0)} \tag{B.1a}$$

decouples into a purely bosonic part that does not depend on details of the models

$$\mathcal{S}_B^{(0)} = N\beta \left[Ud^2 + \alpha(e^2 + d^2 + p_0^2 + p^2 - 1) - \beta_0(2d^2 + p_0^2 + p^2) - 2\beta p_0 p \right] , \tag{B.1b}$$

and a PF part whose particular basis of spinors and explicit form yields from specifics of the hopping scheme but can generally be expressed by

$$\mathcal{S}_F^{(0)} = \sum_k \left(\phi_k^Q\right)^\dagger \left[-\mathrm{i}\omega_n + \underline{H}_{\boldsymbol{k}}^{\psi,Q}\right] \phi_k^Q = -\sum_k \left(\phi_k^Q\right)^\dagger \left[\underline{G}_k^\psi\right]^{-1} \phi_k^Q , \tag{B.1c}$$

with the MF Green's function

$$\underline{G}_k^\psi = \left(\mathrm{i}\omega_n - \underline{H}_{\boldsymbol{k}}^{\psi,Q}\right)^{-1} . \tag{B.1d}$$

The SB-dependent hopping matrix $\underline{H}_{\boldsymbol{k}}^{\psi,Q}$ is to be determined by application of the spiral magnetic MF

$$\boldsymbol{p}_i(\tau) \to p \begin{pmatrix} \cos(\boldsymbol{Q}\boldsymbol{R}_i) \\ \sin(\boldsymbol{Q}\boldsymbol{R}_i) \\ 0 \end{pmatrix} , \quad \boldsymbol{\beta}_i(\tau) \to \beta \begin{pmatrix} \cos(\boldsymbol{Q}\boldsymbol{R}_i) \\ \sin(\boldsymbol{Q}\boldsymbol{R}_i) \\ 0 \end{pmatrix} , \tag{B.2a}$$

$$p_{0,i}(\tau) \to p_0 , \tag{B.2b}$$

$$e_i(\tau) \to e , \tag{B.2c}$$

$$d_i(\tau) \to d , \tag{B.2d}$$

$$\alpha_i(\tau) \to \alpha , \tag{B.2e}$$

$$\beta_{0,i}(\tau) \to \beta_0 , \tag{B.2f}$$

defined in Section 4.1 for the bosonic degrees of freedom and consecutive Fourier transformation of the pseudofermions (PFs) in Equation (3.30a). The Lagrange multiplier (LM) part of $\underline{H}_k^{\psi,Q}$ does not depend on the specifics of the model and is given by[1]

$$\begin{aligned} H_\beta &= \sum_i \boldsymbol{f}_i^\dagger \begin{pmatrix} \beta_0 & \beta\, \mathrm{e}^{\mathrm{i}\boldsymbol{Q}\boldsymbol{R}_i} \\ \beta\, \mathrm{e}^{-\mathrm{i}\boldsymbol{Q}\boldsymbol{R}_i} & \beta_0 \end{pmatrix} \boldsymbol{f}_i = \frac{1}{N} \sum_{\boldsymbol{k},\boldsymbol{k}'} \sum_i \mathrm{e}^{-\mathrm{i}\boldsymbol{k}\boldsymbol{R}_i} \mathrm{e}^{\mathrm{i}\boldsymbol{k}'\boldsymbol{R}_i} \boldsymbol{f}_{\boldsymbol{k}}^\dagger \begin{pmatrix} \beta_0 & \beta\, \mathrm{e}^{\mathrm{i}\boldsymbol{Q}\boldsymbol{R}_i} \\ \beta\, \mathrm{e}^{-\mathrm{i}\boldsymbol{Q}\boldsymbol{R}_i} & \beta_0 \end{pmatrix} \boldsymbol{f}_{\boldsymbol{k}'} \\ &= \sum_{\boldsymbol{k},\boldsymbol{k}'} \boldsymbol{f}_{\boldsymbol{k}}^\dagger \begin{pmatrix} \beta_0\, \delta_{\boldsymbol{k},\boldsymbol{k}'} & \beta\, \delta_{\boldsymbol{k}',\boldsymbol{k}-\boldsymbol{Q}} \\ \beta\, \delta_{\boldsymbol{k}',\boldsymbol{k}+\boldsymbol{Q}} & \beta_0\, \delta_{\boldsymbol{k},\boldsymbol{k}'} \end{pmatrix} \boldsymbol{f}_{\boldsymbol{k}'} = \sum_{\boldsymbol{k}} \left(\boldsymbol{f}_{\boldsymbol{k}}^{\boldsymbol{Q}}\right)^\dagger \begin{pmatrix} \beta_0 & \beta \\ \beta & \beta_0 \end{pmatrix} \boldsymbol{f}_{\boldsymbol{k}}^{\boldsymbol{Q}}\,, \end{aligned} \tag{B.3}$$

with

$$\boldsymbol{f}_{\boldsymbol{k}} = \begin{pmatrix} f_{\boldsymbol{k},\uparrow} \\ f_{\boldsymbol{k},\downarrow} \end{pmatrix}, \tag{B.4a}$$

$$\boldsymbol{f}_{\boldsymbol{k}}^{\boldsymbol{Q}} = \begin{pmatrix} f_{\boldsymbol{k},\uparrow} \\ f_{\boldsymbol{k}-\boldsymbol{Q},\downarrow} \end{pmatrix}, \tag{B.4b}$$

and we define the periodicity index a that is associated with a momentum shift w.r.t. the magnetic ordering vector $\boldsymbol{Q}$

$$f_{\boldsymbol{k},\sigma}^a = \left[\boldsymbol{f}_{\boldsymbol{k}+a\boldsymbol{Q}}\right]_\sigma\,. \tag{B.4c}$$

B.1 Hubbard model

The Hamiltonian of the one-band Hubbard model in SB representation within the field theoretical description is given by

$$H^{\mathrm{Hub}} = H_t + H_{\mathrm{loc.}} + H_{\mathrm{int.}} = -\sum_{<ij>} \sum_{\sigma\sigma_1\sigma'} t_{ij}^f\, f_{i,\sigma}^* z_{i,\sigma_1\sigma}^\dagger z_{j,\sigma'\sigma_1} f_{j,\sigma'} - \mu_0 \sum_{i,\sigma} f_{i,\sigma}^* f_{i,\sigma} + U \sum_i d_i^* d_i\,. \tag{B.5}$$

B.1.1 Slave-boson-dependent quasiparticle matrix

In order to calculate the SB dependent MF hopping matrix $\underline{H}^{\psi,Q}$, we need to Fourier-transform the PF part of the Hamiltonian after applying the MF ansatz to the $\underline{z}$-matrices according to Equation (4.8a) [53]. We

[1] In the last calculation step, we exploit that the sum is invariant under index shifts: $\sum_k f_{k-Q,\sigma}^* f_{k-Q,\sigma'} = \sum_k f_{k,\sigma}^* f_{k\sigma'}$.

moreover define $\boldsymbol{R}_i - \boldsymbol{R}_j = \boldsymbol{R}_{ij}$ and utilize the basis $\boldsymbol{f}_i^\dagger = \left(f_{i,\uparrow}^*,\ f_{i,\downarrow}^*\right)$:

$$\begin{aligned}
H_{tf} &= \sum_{<ij>} t_{ij}^f \boldsymbol{f}_i^\dagger \begin{pmatrix} \mathcal{Z}_+ & \mathcal{Z}_- \mathrm{e}^{\mathrm{i}\boldsymbol{Q}\boldsymbol{R}_i} \\ \mathcal{Z}_- \mathrm{e}^{-\mathrm{i}\boldsymbol{Q}\boldsymbol{R}_i} & \mathcal{Z}_+ \end{pmatrix} \begin{pmatrix} \mathcal{Z}_+ & \mathcal{Z}_- \mathrm{e}^{\mathrm{i}\boldsymbol{Q}\boldsymbol{R}_j} \\ \mathcal{Z}_- \mathrm{e}^{-\mathrm{i}\boldsymbol{Q}\boldsymbol{R}_j} & \mathcal{Z}_+ \end{pmatrix} \boldsymbol{f}_j \\
&= \sum_{<ij>} t_{ij}^f \boldsymbol{f}_i^\dagger \begin{pmatrix} \mathcal{Z}_+^2 + \mathcal{Z}_-^2 \mathrm{e}^{\mathrm{i}\boldsymbol{Q}(\boldsymbol{R}_i - \boldsymbol{R}_j)} & \mathcal{Z}_+\mathcal{Z}_- \left(\mathrm{e}^{\mathrm{i}\boldsymbol{Q}\boldsymbol{R}_i} + \mathrm{e}^{\mathrm{i}\boldsymbol{Q}\boldsymbol{R}_j}\right) \\ \mathcal{Z}_+\mathcal{Z}_- \left(\mathrm{e}^{-\mathrm{i}\boldsymbol{Q}\boldsymbol{R}_i} + \mathrm{e}^{-\mathrm{i}\boldsymbol{Q}\boldsymbol{R}_j}\right) & \mathcal{Z}_+^2 + \mathcal{Z}_-^2 \mathrm{e}^{-\mathrm{i}\boldsymbol{Q}(\boldsymbol{R}_i - \boldsymbol{R}_j)} \end{pmatrix} \boldsymbol{f}_j \\
&= \frac{1}{N} \sum_{\boldsymbol{k}\boldsymbol{k}'} \sum_{<ij>} t_{ij}^f \mathrm{e}^{-\mathrm{i}\boldsymbol{k}\boldsymbol{R}_i} \mathrm{e}^{\mathrm{i}\boldsymbol{k}'(\boldsymbol{R}_i - \boldsymbol{R}_{ij})} \boldsymbol{f}_{\boldsymbol{k}}^\dagger \begin{pmatrix} \mathcal{Z}_+^2 + \mathcal{Z}_-^2 \mathrm{e}^{\mathrm{i}\boldsymbol{Q}\boldsymbol{R}_{ij}} & \mathcal{Z}_+\mathcal{Z}_- \mathrm{e}^{\mathrm{i}\boldsymbol{Q}\boldsymbol{R}_i} \left(1 + \mathrm{e}^{-\mathrm{i}\boldsymbol{Q}\boldsymbol{R}_{ij}}\right) \\ \mathcal{Z}_+\mathcal{Z}_- \mathrm{e}^{-\mathrm{i}\boldsymbol{Q}\boldsymbol{R}_i} \left(1 + \mathrm{e}^{\mathrm{i}\boldsymbol{Q}\boldsymbol{R}_{ij}}\right) & \mathcal{Z}_+^2 + \mathcal{Z}_-^2 \mathrm{e}^{-\mathrm{i}\boldsymbol{Q}\boldsymbol{R}_{ij}} \end{pmatrix} \boldsymbol{f}_{\boldsymbol{k}'} \\
&= \sum_{\boldsymbol{k}\boldsymbol{k}'} \sum_{\boldsymbol{R}_{ij}} t_{ij}^f \mathrm{e}^{-i\boldsymbol{k}'\boldsymbol{R}_{ij}} \boldsymbol{f}_{\boldsymbol{k}}^\dagger \begin{pmatrix} \delta_{\boldsymbol{k}',\boldsymbol{k}} \left(\mathcal{Z}_+^2 + \mathcal{Z}_-^2 \mathrm{e}^{\mathrm{i}\boldsymbol{Q}\boldsymbol{R}_{ij}}\right) & \delta_{\boldsymbol{k}',\boldsymbol{k}-\boldsymbol{Q}}\, \mathcal{Z}_+\mathcal{Z}_- \left(1 + \mathrm{e}^{-\mathrm{i}\boldsymbol{Q}\boldsymbol{R}_{ij}}\right) \\ \delta_{\boldsymbol{k},\boldsymbol{k}'-\boldsymbol{Q}}\, \mathcal{Z}_+\mathcal{Z}_- \left(1 + \mathrm{e}^{\mathrm{i}\boldsymbol{Q}\boldsymbol{R}_{ij}}\right) & \delta_{\boldsymbol{k},\boldsymbol{k}'} \left(\mathcal{Z}_+^2 + \mathcal{Z}_-^2 \mathrm{e}^{-\mathrm{i}\boldsymbol{Q}\boldsymbol{R}_{ij}}\right) \end{pmatrix} \boldsymbol{f}_{\boldsymbol{k}'} \,.
\end{aligned} \tag{B.6a}$$

We define the dispersion

$$\xi_{\boldsymbol{k}} = \sum_{\boldsymbol{R}_{ij}} t_{ij}^f \mathrm{e}^{-\mathrm{i}\boldsymbol{k}\boldsymbol{R}_{ij}} \,, \tag{B.6b}$$

and with appropriate index shifts in momentum $\boldsymbol{k} \to \boldsymbol{k} + \boldsymbol{Q}$, we may express H_t in the basis $\boldsymbol{f}_{\boldsymbol{k}}^{\boldsymbol{Q}}$ defined in Equation (B.4b)

$$H_{tf} = \sum_{\boldsymbol{k}} \left(\boldsymbol{f}_{\boldsymbol{k}}^{\boldsymbol{Q}}\right)^\dagger \begin{pmatrix} \mathcal{Z}_+^2 \xi_{\boldsymbol{k}} + \mathcal{Z}_-^2 \xi_{\boldsymbol{k}-\boldsymbol{Q}} & \mathcal{Z}_+\mathcal{Z}_- \left(\xi_{\boldsymbol{k}-\boldsymbol{Q}} + \xi_{\boldsymbol{k}}\right) \\ \mathcal{Z}_+\mathcal{Z}_- \left(\xi_{\boldsymbol{k}-\boldsymbol{Q}} + \xi_{\boldsymbol{k}}\right) & \mathcal{Z}_+^2 \xi_{\boldsymbol{k}-\boldsymbol{Q}} + \mathcal{Z}_-^2 \xi_{\boldsymbol{k}} \end{pmatrix} \boldsymbol{f}_{\boldsymbol{k}}^{\boldsymbol{Q}} \,. \tag{B.6c}$$

With the inclusion of the diagonal chemical potential term and the LM part given by Equation (B.3), we finally find the SB-dependent MF hopping matrix

$$\underline{H}_{\boldsymbol{k},\mathrm{Hub}}^{\psi,\boldsymbol{Q}} = \begin{pmatrix} \mathcal{Z}_+^2 \xi_{\boldsymbol{k}} + \mathcal{Z}_-^2 \xi_{\boldsymbol{k}-\boldsymbol{Q}} + \beta_0 - \mu_0 & \mathcal{Z}_+\mathcal{Z}_- \left(\xi_{\boldsymbol{k}-\boldsymbol{Q}} + \xi_{\boldsymbol{k}}\right) + \beta \\ \mathcal{Z}_+\mathcal{Z}_- \left(\xi_{\boldsymbol{k}-\boldsymbol{Q}} + \xi_{\boldsymbol{k}}\right) + \beta & \mathcal{Z}_+^2 \xi_{\boldsymbol{k}-\boldsymbol{Q}} + \mathcal{Z}_-^2 \xi_{\boldsymbol{k}} + \beta_0 - \mu_0 \end{pmatrix} . \tag{B.7}$$

In a two-dimensional (2D) hopping scheme with nearest neighbor (NN) hopping t and next-to-nearest neighbor (NNN) hopping t' on the square lattice, it is

$$\xi_{\boldsymbol{k}} = -2t \left(\cos k_x + \cos k_y\right) - 4t' \cos k_x \cos k_y \,. \tag{B.8}$$

The eigenvalues of $\underline{H}_{\boldsymbol{k},\mathrm{Hub}}^{\psi,\boldsymbol{Q}}$ are given by

$$\mathcal{E}_{\boldsymbol{k},\mathrm{Hub}}^{\pm} = \frac{1}{2} \left[\left(\mathcal{Z}_+^2 + \mathcal{Z}_-^2\right) \left(\xi_{\boldsymbol{k}} + \xi_{\boldsymbol{k}-\boldsymbol{Q}}\right) \pm \Delta_{\boldsymbol{k}}^{\boldsymbol{Q}}\right] + \beta_0 - \mu_0 \,, \tag{B.9}$$

with the magnetic gap function

$$\Delta_{\boldsymbol{k}}^{\boldsymbol{Q}} = \sqrt{\left[\left(\mathcal{Z}_+^2 - \mathcal{Z}_-^2\right) \left(\xi_{\boldsymbol{k}} - \xi_{\boldsymbol{k}-\boldsymbol{Q}}\right)\right]^2 + 4 \left[\mathcal{Z}_+\mathcal{Z}_- \left(\xi_{\boldsymbol{k}} + \xi_{\boldsymbol{k}-\boldsymbol{Q}}\right) + \beta\right]^2} \,. \tag{B.10}$$

In the PM limit, it is $\mathcal{Z}_- = \beta = 0$ and the spin-degenerate eigenvalues adapt the simplified form

$$\mathcal{E}_{\boldsymbol{k},\mathrm{Hub}}^{\mathrm{PM}} = z_0^2 \xi_{\boldsymbol{k}} + \beta_0 - \mu_0 \,. \tag{B.11}$$

B.1.2 Constrained expectation values

In Sections 4.1 and 4.4.1, we argued that the MF constraints match the quantum mechanical expectation values of the SB and PF representations of the spin and charge density. In the following, we support that claim with an explicit calculation for the Hubbard model utilizing the respective equal space-time Green's function

$$\left\langle f_\sigma^\dagger f_{\sigma'} \right\rangle = G^{\overline{\psi}}_{\sigma\sigma'}(\Delta r = 0^-) = \frac{1}{N\beta} \sum_k G^{\overline{\psi}}_{k,\sigma\sigma'} \,. \tag{B.12}$$

Based on the operator representations summarized in Table 2.1, the afore mentioned expectation values in Fourier-space are given by

$$\left\langle \hat{n}_{F,q} \right\rangle = \frac{1}{N\beta} \int_0^\beta d\tau \sum_{r_i} \mathrm{e}^{\mathrm{i}\boldsymbol{q}\boldsymbol{r}_i + \mathrm{i}\omega_n \tau} \left\langle \hat{n}_{F,r_i} \right\rangle = \frac{1}{N\beta} \sum_k \left\langle \hat{f}_k^\dagger \hat{f}_{k-q} \right\rangle \,, \tag{B.13a}$$

$$\left\langle \hat{\mathbf{S}}_{F,q} \right\rangle = \frac{1}{N\beta} \int_0^\beta d\tau \sum_{r_i} \mathrm{e}^{\mathrm{i}\boldsymbol{q}\boldsymbol{r}_i + \mathrm{i}\omega_n \tau} \left\langle \hat{\mathbf{S}}_{F,r_i} \right\rangle = \frac{1}{N\beta} \frac{1}{2} \sum_k \left\langle \hat{f}_k^\dagger \, \underline{\boldsymbol{\tau}} \, \hat{f}_{k-q} \right\rangle \,, \tag{B.13b}$$

$$\left\langle \hat{n}_{B,q} \right\rangle = \frac{1}{N\beta} \int_0^\beta d\tau \sum_{r_i} \mathrm{e}^{\mathrm{i}\boldsymbol{q}\boldsymbol{r}_i + \mathrm{i}\omega_n \tau} \left\langle \hat{n}_{B,r_i} \right\rangle = \left(p_0^2 + p^2 + 2d^2 \right) \delta_{q,0} \,, \tag{B.13c}$$

$$\left\langle \hat{\mathbf{S}}_{B,q} \right\rangle = \frac{1}{N\beta} \int_0^\beta d\tau \sum_{r_i} \mathrm{e}^{\mathrm{i}\boldsymbol{q}\boldsymbol{r}_i + \mathrm{i}\omega_n \tau} \left\langle \hat{\mathbf{S}}_{B,r_i} \right\rangle = p p_0 \begin{pmatrix} \frac{1}{2}\left(\delta_{\boldsymbol{q},\boldsymbol{Q}} + \delta_{\boldsymbol{q},-\boldsymbol{Q}} \right) \\ \frac{1}{2\mathrm{i}}\left(\delta_{\boldsymbol{q},\boldsymbol{Q}} - \delta_{\boldsymbol{q},-\boldsymbol{Q}} \right) \\ 0 \end{pmatrix} \delta_{\mathrm{i}\omega_n,0} \,. \tag{B.13d}$$

Utilizing Equation (B.7), the MF Green's matrix for the Hubbard model in the basis $\boldsymbol{f}_k^Q$ is found to be

$$\underline{G}_k^\psi = \frac{1}{D_{k,Q}} \begin{pmatrix} \mathrm{i}\omega_n + \mu_0 + \beta_0 - \mathcal{Z}_-^2 \xi_k - \mathcal{Z}_+^2 \xi_{k-Q} & \beta + \mathcal{Z}_+ \mathcal{Z}_- \left(\xi_k + \xi_{k-Q} \right) \\ \beta + \mathcal{Z}_+ \mathcal{Z}_- \left(\xi_k + \xi_{k-Q} \right) & \mathrm{i}\omega_n + \mu_0 + \beta_0 - \mathcal{Z}_+^2 \xi_k - \mathcal{Z}_-^2 \xi_{k-Q} \end{pmatrix} \,, \tag{B.14a}$$

where

$$D_{k,Q} = \left(\mathrm{i}\omega_n + \mu_0 + \beta_0 - \mathcal{Z}_-^2 \xi_k - \mathcal{Z}_+^2 \xi_{k-Q} \right) \left(\mathrm{i}\omega_n + \mu_0 + \beta_0 - \mathcal{Z}_+^2 \xi_k - \mathcal{Z}_-^2 \xi_{k-Q} \right) \left(\beta + \mathcal{Z}_+ \mathcal{Z}_- \left(\xi_k + \xi_{k-Q} \right) \right)^2 \,. \tag{B.14b}$$

To evaluate PF expectation values within the MF approximation, we need to identify the momentum $\boldsymbol{q}$ with the MF spinor that only allows correlations with an overlap of $\boldsymbol{q} \in \{0, \boldsymbol{Q}\}$. Within the applied basis given by Equation (B.4b), we therefore find[1]

$$\left\langle \hat{n}_{F,q} \right\rangle = \frac{1}{N\beta} \sum_k \left(G^{\overline{\psi}}_{k,\uparrow\uparrow} + G^{\overline{\psi}}_{k,\downarrow\downarrow} \right) \delta_{q,0} \,, \tag{B.15a}$$

$$\left\langle \hat{\mathbf{S}}_{F,q} \right\rangle = \frac{1}{N\beta} \sum_k \begin{pmatrix} \frac{1}{2}\left(G^{\overline{\psi}}_{k,\uparrow\downarrow} \delta_{\boldsymbol{q},\boldsymbol{Q}} + G^{\overline{\psi}}_{k,\downarrow\uparrow} \delta_{\boldsymbol{q},-\boldsymbol{Q}} \right) \\ \frac{1}{2\mathrm{i}}\left(G^{\overline{\psi}}_{k,\uparrow\downarrow} \delta_{\boldsymbol{q},\boldsymbol{Q}} - G^{\overline{\psi}}_{k,\downarrow\uparrow} \delta_{\boldsymbol{q},-\boldsymbol{Q}} \right) \\ \left(G^{\overline{\psi}}_{k,\uparrow\uparrow} - G^{\overline{\psi}}_{k,\downarrow\downarrow} \right) \delta_{\boldsymbol{q},0} \end{pmatrix} \delta_{\mathrm{i}\omega,0} \,. \tag{B.15b}$$

[1] The Fourier components of $\left\langle \hat{f}_{k,\downarrow}^\dagger \hat{f}_{k-q,\uparrow} \right\rangle$, which do not explicitly show in the basis can be inferred by shifting $\boldsymbol{k} \to \boldsymbol{k} + \boldsymbol{Q}$ and using $\sum_k \hat{f}_k^\dagger \hat{f}_k = \sum_k \hat{f}_{k+Q}^\dagger \hat{f}_{k+Q}$.

The occurring Matsubara summations can be carried out analytically (for details see Appendix A.5) and the remaining momentum-sum needs to be evaluated numerically at the saddle point, yielding

$$\frac{1}{N\beta}\sum_{\mathrm{i}\omega_n}\sum_{\boldsymbol{k}\in\mathrm{BZ}_0}\left(G^{\overline{\psi}}_{k,\uparrow\uparrow}+G^{\overline{\psi}}_{k,\downarrow\downarrow}\right)=\frac{1}{N}\sum_{\boldsymbol{k}}\left[n_{\mathrm{F}}\left(\varepsilon^{+}_{\boldsymbol{k}}\right)+n_{\mathrm{F}}\left(\varepsilon^{-}_{\boldsymbol{k}}\right)\right]=2d^2+p_0^2+p^2\,, \tag{B.16a}$$

$$\frac{1}{N\beta}\sum_{k}\left(G^{\overline{\psi}}_{k,\uparrow\uparrow}-G^{\overline{\psi}}_{k,\downarrow\downarrow}\right)=\frac{1}{N}\sum_{\boldsymbol{k}}\left(\mathcal{Z}_+^2-\mathcal{Z}_-^2\right)\left(\xi_{\boldsymbol{k}}-\xi_{\boldsymbol{k}-\boldsymbol{Q}}\right)\frac{n_{\mathrm{F}}\left(\varepsilon^{+}_{\boldsymbol{k}}\right)-n_{\mathrm{F}}\left(\varepsilon^{-}_{\boldsymbol{k}}\right)}{\Delta^{Q}_{\boldsymbol{k}}}=0\,, \tag{B.16b}$$

$$\frac{1}{N\beta}\sum_{k}G^{\overline{\psi}}_{k,\uparrow\downarrow}=\frac{1}{N\beta}\sum_{k}G^{\overline{\psi}}_{k,\downarrow\uparrow}=\frac{1}{N}\sum_{\boldsymbol{k}}\left(\beta+\mathcal{Z}_+\mathcal{Z}_-\left(\xi_{\boldsymbol{k}}+\xi_{\boldsymbol{k}-\boldsymbol{Q}}\right)\right)\frac{n_{\mathrm{F}}\left(\varepsilon^{+}_{\boldsymbol{k}}\right)-n_{\mathrm{F}}\left(\varepsilon^{-}_{\boldsymbol{k}}\right)}{\Delta^{Q}_{\boldsymbol{k}}}=pp_0\,. \tag{B.16c}$$

The quantities $\varepsilon^{\pm}_{\boldsymbol{k}}$ and $\Delta^{Q}_{\boldsymbol{k}}$ have been defined in Equations (B.9) and (B.10) and $n_{\mathrm{F}}(\omega)$ denotes the Fermi-Dirac distribution. Combining the results of Equations (B.13), (B.15), and (B.16), we realize that all Fourier components of the PF and SB expectation values of the charge and spin operator match at the saddle point and thus the MF constraints are fulfilled exactly.

B.2 Periodic Anderson model

Based on Reference [56] by Klett, Riegler *et al.*, we discuss two types of PAMs in this thesis. These do not employ hopping amplitudes within the interacting orbital but feature on-site hybridizations between non-interacting conduction electrons and interacting f-electrons expressed by the Hamiltonian[1]

$$H^{\mathrm{PAM}}=\sum_{d=1,2}H_d+H_{\mathrm{hyb}}+H_f\,, \tag{B.17a}$$

with

$$H_d=-t\sum_{\langle i,j\rangle,\sigma}c^{*}_{d,i,\sigma}c_{d,j,\sigma}+(\epsilon_d-\mu_0)\sum_{i,\sigma}c^{*}_{d,i,\sigma}c_{d,i,\sigma}\,, \tag{B.17b}$$

$$H_{\mathrm{hyb}}=V\sum_{d,i,\sigma,\sigma'}\left(c^{*}_{d,i,\sigma}z_{i,\sigma'\sigma}f_{i,\sigma'}+f^{*}_{i,\sigma}z^{\dagger}_{i,\sigma'\sigma}c_{d,i,\sigma'}\right)\,, \tag{B.17c}$$

$$H_f=U\sum_i d^{*}_i d_i+(\epsilon_f-\mu_0)\sum_{i,\sigma}f^{*}_{i,\sigma}f_{i,\sigma}\,, \tag{B.17d}$$

within the field theoretical description in SB representation. In analogy to Section B.1, we apply the basis $\boldsymbol{f}^{\dagger}_i=\left(f^{*}_{i,\uparrow}\,,\ f^{*}_{i,\downarrow}\right)$ and $\boldsymbol{c}^{\dagger}_i=\left(c^{*}_{i,\uparrow}\,,\ c^{*}_{i,\downarrow}\right)$ and calculate H_{hyb} for one d-orbital

$$\begin{aligned}H_{\mathrm{hyb}}&=V\sum_i\boldsymbol{c}^{\dagger}_i\begin{pmatrix}\mathcal{Z}_+ & \mathcal{Z}_-\,\mathrm{e}^{\mathrm{i}\boldsymbol{Q}\boldsymbol{R}_i}\\ \mathcal{Z}_-\,\mathrm{e}^{-\mathrm{i}\boldsymbol{Q}\boldsymbol{R}_i} & \mathcal{Z}_+\end{pmatrix}\boldsymbol{f}_i+\mathrm{h.c.}=\frac{1}{N}\sum_{\boldsymbol{k}\boldsymbol{k}'}V\sum_i\boldsymbol{c}^{\dagger}_{\boldsymbol{k}}\mathrm{e}^{-\mathrm{i}\boldsymbol{k}\boldsymbol{R}_i}\mathrm{e}^{\mathrm{i}\boldsymbol{k}'\boldsymbol{R}_i}\begin{pmatrix}\mathcal{Z}_+ & \mathcal{Z}_-\,\mathrm{e}^{\mathrm{i}\boldsymbol{Q}\boldsymbol{R}_i}\\ \mathcal{Z}_-\,\mathrm{e}^{-\mathrm{i}\boldsymbol{Q}\boldsymbol{R}_i} & \mathcal{Z}_+\end{pmatrix}\boldsymbol{f}_{\boldsymbol{k}'}+\mathrm{h.c.}\\ &=\sum_{\boldsymbol{k}\boldsymbol{k}'}\boldsymbol{c}^{\dagger}_{\boldsymbol{k}}\begin{pmatrix}\delta_{\boldsymbol{k},\boldsymbol{k}'}V\mathcal{Z}_+ & \delta_{\boldsymbol{k},\boldsymbol{k}'-\boldsymbol{Q}}V\mathcal{Z}_-\\ \delta_{\boldsymbol{k},\boldsymbol{k}'-\boldsymbol{Q}}V\mathcal{Z}_- & \delta_{\boldsymbol{k},\boldsymbol{k}'}V\mathcal{Z}_+\end{pmatrix}\boldsymbol{f}_{\boldsymbol{k}'}+\mathrm{h.c.}\,.\end{aligned} \tag{B.18a}$$

[1] This Hamiltonian could easily be extended to allow f-electron hopping in full analogy to the SB-dependent hopping matrix of the Hubbard model or non-local spin diagonal hybridization.

With appropriate index shifts in momentum $\boldsymbol{k} \to \boldsymbol{k} + \boldsymbol{Q}$, we find

$$H_{\text{Hyb}} = \sum_{\boldsymbol{k}} \left(\phi_{\boldsymbol{k}}^{\boldsymbol{Q}}\right)^{\dagger} \begin{pmatrix} 0 & 0 & V\mathcal{Z}_+ & V\mathcal{Z}_- \\ 0 & 0 & V\mathcal{Z}_- & V\mathcal{Z}_+ \\ V\mathcal{Z}_+ & V\mathcal{Z}_- & 0 & 0 \\ V\mathcal{Z}_- & V\mathcal{Z}_+ & 0 & 0 \end{pmatrix} \phi_{\boldsymbol{k}}^{\boldsymbol{Q}} \,, \tag{B.18b}$$

within the basis

$$\phi_{\boldsymbol{k}}^{\boldsymbol{Q}} = \begin{pmatrix} c_{\uparrow,\boldsymbol{k}} \\ c_{\downarrow,\boldsymbol{k}-\boldsymbol{Q}} \\ f_{\uparrow,\boldsymbol{k}} \\ f_{\downarrow,\boldsymbol{k}-\boldsymbol{Q}} \end{pmatrix} . \tag{B.18c}$$

The remaining terms are calculated in full analogy to Section B.1.

B.2.1 One-conduction-band model

For the PAM with one d-orbital, we chose w.l.o.g. $\epsilon_1 = 0$. The hopping terms of the c-electrons have to be expressed in the $\boldsymbol{Q}$-shifted basis as well, yielding

$$\underline{H}_{\boldsymbol{k},\text{PAM}}^{\psi,\boldsymbol{Q}} = \begin{pmatrix} \xi_{\boldsymbol{k}} - \mu_0 & 0 & V\mathcal{Z}_+ & V\mathcal{Z}_- \\ 0 & \xi_{\boldsymbol{k}-\boldsymbol{Q}} - \mu_0 & V\mathcal{Z}_- & V\mathcal{Z}_+ \\ V\mathcal{Z}_+ & V\mathcal{Z}_- & \epsilon_f + \beta_0 - \mu_0 & \beta \\ V\mathcal{Z}_- & V\mathcal{Z}_+ & \beta & \epsilon_f + \beta_0 - \mu_0 \end{pmatrix} , \tag{B.19}$$

with

$$\xi_{\boldsymbol{k}} = -2t(\cos k_x + \cos k_y) \,. \tag{B.20}$$

The eigenvalues $\mathcal{E}_{\boldsymbol{k},\text{PAM}}^{o,s}$ are given by the roots of the quartic equation

$$a\,(\mathcal{E} + \mu_0)^4 + b\,(\mathcal{E} + \mu_0)^3 + c\,(\mathcal{E} + \mu_0)^2 + d\,(\mathcal{E} + \mu_0) + e = 0 \,, \tag{B.21}$$

with

$$\begin{aligned} a &= 1 \,, \\ b &= -2\tilde{\beta}_0 - \left(\xi_{\boldsymbol{k}} + \xi_{\boldsymbol{k}-\boldsymbol{Q}}\right) \,, \\ c &= \tilde{\beta} + \xi_{\boldsymbol{k}}\xi_{\boldsymbol{k}-\boldsymbol{Q}} + 2\tilde{\beta}_0\left(\xi_{\boldsymbol{k}} + \xi_{\boldsymbol{k}-\boldsymbol{Q}}\right) - V^2\mathcal{Z}_p \,, \\ d &= -\tilde{\beta}(\xi_{\boldsymbol{k}} + \xi_{\boldsymbol{k}-\boldsymbol{Q}}) - 2\tilde{\beta}_0\xi_{\boldsymbol{k}}\xi_{\boldsymbol{k}-\boldsymbol{Q}} + V^2\left(\frac{1}{2}\mathcal{Z}_p(\xi_{\boldsymbol{k}} + \xi_{\boldsymbol{k}-\boldsymbol{Q}}) + \mathcal{Z}_\beta\right) \,, \\ e &= \tilde{\beta}\xi_{\boldsymbol{k}}\xi_{\boldsymbol{k}-\boldsymbol{Q}} - \frac{V^2}{2}\mathcal{Z}_\beta(\xi_{\boldsymbol{k}} + \xi_{\boldsymbol{k}-\boldsymbol{Q}}) + V^4\left(\mathcal{Z}_-^2 - \mathcal{Z}_+^2\right)^2 \,, \end{aligned}$$

and

$$\begin{aligned}\tilde{\beta}_0 &= \beta_0 + \epsilon_f \,, \\ \mathcal{Z}_p &= 2\left(\mathcal{Z}_+^2 + \mathcal{Z}_-^2\right) \,, \\ \tilde{\beta} &= \tilde{\beta}_0^2 - \beta^2 \,, \\ \mathcal{Z}_\beta &= 2\tilde{\beta}_0\left(\mathcal{Z}_+^2 + \mathcal{Z}_-^2\right) - 4\beta\mathcal{Z}_+\mathcal{Z}_- \,.\end{aligned}$$

They can be calculated analytically utilizing Ferrari's method [318, 319]. The explicit analytic form is not very descriptive but comes with a considerable performance boost in the numerical evaluation compared to numerical diagonalization algorithms. In the PM limit, the eigenvalues adapt the simple form

$$\varepsilon^{\mathrm{PM},\pm}_{\boldsymbol{k},\mathrm{PAM}} = \frac{1}{2}\left(\xi_{\boldsymbol{k}} + \epsilon_f + \beta_0 - 2\mu_0\right) \pm \sqrt{\frac{1}{4}\left(\xi_{\boldsymbol{k}} - \epsilon_f - \beta_0\right)^2 + (Vz_0)^2} \,. \tag{B.22}$$

B.2.2 Two-conduction-band model

The hopping matrix of the three orbital model is determined analogously, yielding

$$\underline{H}^{\psi,Q}_{\boldsymbol{k},\mathrm{PAM}'} = \begin{pmatrix} \xi_{\boldsymbol{k}} + \epsilon_1 - \mu_0 & 0 & 0 & 0 & V\mathcal{Z}_+ & V\mathcal{Z}_- \\ 0 & \xi_{\boldsymbol{k}-\boldsymbol{Q}} + \epsilon_1 - \mu_0 & 0 & 0 & V\mathcal{Z}_- & V\mathcal{Z}_+ \\ 0 & 0 & \xi_{\boldsymbol{k}} + \epsilon_2 - \mu_0 & 0 & V\mathcal{Z}+ & V\mathcal{Z}_- \\ 0 & 0 & 0 & \xi_{\boldsymbol{k}-\boldsymbol{Q}} + \epsilon_2 - \mu_0 & V\mathcal{Z}_- & V\mathcal{Z}_+ \\ V\mathcal{Z}_+ & V\mathcal{Z}_- & V\mathcal{Z}_+ & V\mathcal{Z}_- & \epsilon_f + \beta_0 - \mu_0 & \beta \\ V\mathcal{Z}_- & V\mathcal{Z}_+ & V\mathcal{Z}_- & V\mathcal{Z}_+ & \beta & \epsilon_f + \beta_0 - \mu_0 \end{pmatrix} , \tag{B.23}$$

with the extended basis $\boldsymbol{\phi}^Q_{\boldsymbol{k}} = \left(c_{1,\uparrow,\boldsymbol{k}},\, c_{1,\downarrow,\boldsymbol{k}-\boldsymbol{Q}},\, c_{2,\uparrow,\boldsymbol{k}},\, c_{2,\downarrow,\boldsymbol{k}-\boldsymbol{Q}},\, f_{\uparrow,\boldsymbol{k}},\, f_{\downarrow,\boldsymbol{k}-\boldsymbol{Q}}\right)^\top$. There is no general analytic form for the eigenvalues, i.e., they need to be evaluated numerically.

B.3 Topological Kondo insulator model

Based on Reference [54] by Klett, Ok, Riegler *et al.*, the 3D Hamiltonian of the TKI model on the simple cubic lattice in within the effective SB field theory is given by

$$H^{\mathrm{TKI}} = H_d + H_{\mathrm{hyb}} + H_f + H_{\mathrm{int}} \,, \tag{B.24a}$$

with

$$H_d = -\sum_{\langle ij\rangle}\sum_{\sigma} t^d_{ij} c^*_{d,i,\sigma} c_{d,j,\sigma} - \mu_0 \sum_{i,\sigma} c^*_{i,\sigma} c_{i,\sigma} \,, \tag{B.24b}$$

$$H_{\mathrm{hyb}} = H^{fc}_{\mathrm{hyb}} + H^{cf}_{\mathrm{hyb}} = \sum_{\alpha}\sum_{\langle i<j\rangle_\alpha}\sum_{\sigma\sigma'\sigma_1} \mathrm{i}V\left(f^*_{i,\sigma} z^\dagger_{i,\sigma_1\sigma} \tau^\alpha_{\sigma_1\sigma'} c_{j,\sigma'} - f^*_{j,\sigma} z^\dagger_{j,\sigma_1\sigma} \tau^\alpha_{\sigma_1\sigma'} c_{i,\sigma'} + \mathrm{h.c.}\right) \,, \tag{B.24c}$$

$$H_f = -\sum_{<ij>}\sum_{\sigma\sigma_1\sigma'} t^f_{ij}\, f^*_{i,\sigma} z^\dagger_{i,\sigma_1\sigma} z_{j,\sigma'\sigma_1} f_{j,\sigma'} + \sum_{i,\sigma} f^*_{i,\sigma}\left(\epsilon_f - \mu_0\right) f_{i,\sigma} \,, \tag{B.24d}$$

$$H_{\text{int}} = U \sum_i d_i^* d_i \,, \tag{B.24e}$$

where τ^α denotes the αth Pauli-matrix in spin space. In the following, we derive the SB-dependent MF hopping matrix for the TKI model based on References [54] and [305]. Because of the spin-orbit coupling (SOC) in the context of hybridization terms, the matrix cannot be represented in a minimal basis independent of $\boldsymbol{Q}$ like the previously discussed spin-diagonal models. The basis has rather to be explicitly enlarged by the factor P, such that $P\boldsymbol{Q}$ is a reciprocal lattice vector $\boldsymbol{G}$ with $\boldsymbol{k} + \boldsymbol{G} = \boldsymbol{k}$ as we discussed in Section 4.3.

B.3.1 Antiferromagnetic order

We choose the ordering vector to describe AFM or stripe order with $P = 2$, i.e.,

$$\boldsymbol{Q} \in \left\{ (\pi, \pi, \pi)^\top, (\pi, \pi, 0)^\top, (\pi, 0, 0)^\top \right\} \,, \tag{B.25}$$

consequently $\underline{H}^{\psi,\boldsymbol{Q}}_{\boldsymbol{k},\text{TKI}}$ represents a 8×8 matrix. In analogy to Section B.1, we apply the basis $\boldsymbol{f}_i^\dagger = \left(f_{i,\uparrow}^*, f_{i,\downarrow}^*\right)$ and $\boldsymbol{c}_i^\dagger = \left(c_{i,\uparrow}^*, c_{i,\downarrow}^*\right)$ and further define $\hat{\boldsymbol{R}}_\alpha$ to be the unit vector in α-direction, with $\alpha \in \{x, y, z\}$ to calculate[1]

$$\begin{aligned} H^{fc}_{\text{hyb}} &= \mathrm{i}\frac{V}{N/2} \sum_{\boldsymbol{k},\boldsymbol{k}'} \sum_{i,\alpha} \boldsymbol{f}_{\boldsymbol{k}}^\dagger \mathrm{e}^{-\mathrm{i}\boldsymbol{k}\boldsymbol{R}_i} \left(\mathrm{e}^{\mathrm{i}\boldsymbol{k}'\hat{\boldsymbol{R}}_\alpha} - e^{-\mathrm{i}\boldsymbol{k}'\hat{\boldsymbol{R}}_\alpha} \right) \begin{pmatrix} \mathcal{Z}_+ & \mathcal{Z}_- \mathrm{e}^{\mathrm{i}\boldsymbol{Q}\boldsymbol{R}_i} \\ \mathcal{Z}_- \mathrm{e}^{-\mathrm{i}\boldsymbol{Q}\boldsymbol{R}_i} & \mathcal{Z}_+ \end{pmatrix} \tau^\alpha \mathrm{e}^{\mathrm{i}\boldsymbol{k}'\boldsymbol{R}_i} \boldsymbol{c}_{\boldsymbol{k}'} \\ &= \mathrm{i}V \sum_{\boldsymbol{k},\boldsymbol{k}'} \sum_\alpha \boldsymbol{f}_{\boldsymbol{k}}^\dagger \begin{pmatrix} \mathcal{Z}_+ \, \delta_{\boldsymbol{k}',\boldsymbol{k}} \, 2\mathrm{i} \sin\left(\boldsymbol{k}\hat{\boldsymbol{R}}_\alpha\right) & \mathcal{Z}_- \, \delta_{\boldsymbol{k}',\boldsymbol{k}-\boldsymbol{Q}} \, 2\mathrm{i} \sin\left((\boldsymbol{k}-\boldsymbol{Q})\hat{\boldsymbol{R}}_\alpha\right) \\ \mathcal{Z}_- \, \delta_{\boldsymbol{k}',\boldsymbol{k}+\boldsymbol{Q}} \, 2\mathrm{i} \sin\left((\boldsymbol{k}+\boldsymbol{Q})\hat{\boldsymbol{R}}_\alpha\right) & \mathcal{Z}_+ \, \delta_{\boldsymbol{k}',\boldsymbol{k}} \, 2\mathrm{i} \sin\left(\boldsymbol{k}\hat{\boldsymbol{R}}_\alpha\right) \end{pmatrix} \tau^\alpha \boldsymbol{c}_{\boldsymbol{k}'} \,. \end{aligned}$$

Since we adopt a basis, where $2\boldsymbol{Q}$ is a reciprocal lattice vector, it is $\boldsymbol{k} + \boldsymbol{Q} = \boldsymbol{k} - \boldsymbol{Q}$, and thus we may write

$$H^{fc}_{\text{hyb}} = \mathrm{i}V \sum_{\boldsymbol{k},\boldsymbol{k}'} \sum_\alpha \boldsymbol{f}_{\boldsymbol{k}}^\dagger \left[\mathcal{Z}_+ \, \delta_{\boldsymbol{k}',\boldsymbol{k}} \, 2\mathrm{i} \sin\left(\boldsymbol{k}\hat{\boldsymbol{R}}_\alpha\right) \underline{\tau}^0 + \mathcal{Z}_- \, \delta_{\boldsymbol{k}',\boldsymbol{k}+\boldsymbol{Q}} \, 2\mathrm{i} \sin\left((\boldsymbol{k}+\boldsymbol{Q})\hat{\boldsymbol{R}}_\alpha\right) \underline{\tau}^x \right] \tau^\alpha \boldsymbol{c}_{\boldsymbol{k}'} \,.$$

After appropriate index shifts, we may express the hybridization terms by

$$H^{fc}_{\text{hyb}} = \sum_{\boldsymbol{k}} \left(\boldsymbol{f}^{\boldsymbol{Q}}_{\boldsymbol{k}}\right)^\dagger \underline{H}^{fc}_{\text{hyb}} \boldsymbol{c}^{\boldsymbol{Q}}_{\boldsymbol{k}} \,, \tag{B.26a}$$

with

$$\underline{H}^{fc}_{\text{hyb}} = -V \begin{pmatrix} \mathcal{Z}_+ s_{z,\boldsymbol{k}} & \mathcal{Z}_+ (s_{x,\boldsymbol{k}} - \mathrm{i}s_{y,\boldsymbol{k}}) & \mathcal{Z}_- (s_{x,\boldsymbol{k}+\boldsymbol{Q}} + \mathrm{i}s_{y,\boldsymbol{k}+\boldsymbol{Q}}) & -\mathcal{Z}_- s_{z,\boldsymbol{k}+\boldsymbol{Q}} \\ \mathcal{Z}_+ (s_{x,\boldsymbol{k}} + \mathrm{i}s_{y,\boldsymbol{k}}) & -\mathcal{Z}_+ s_{z,\boldsymbol{k}} & \mathcal{Z}_- s_{z,\boldsymbol{k}+\boldsymbol{Q}} & \mathcal{Z}_- (s_{x,\boldsymbol{k}+\boldsymbol{Q}} - \mathrm{i}s_{y,\boldsymbol{k}+\boldsymbol{Q}}) \\ \mathcal{Z}_- (s_{x,\boldsymbol{k}} + \mathrm{i}s_{y,\boldsymbol{k}}) & -\mathcal{Z}_- s_{z,\boldsymbol{k}} & \mathcal{Z}_+ s_{z,\boldsymbol{k}+\boldsymbol{Q}} & \mathcal{Z}_+ (s_{x,\boldsymbol{k}+\boldsymbol{Q}} - \mathrm{i}s_{y,\boldsymbol{k}+\boldsymbol{Q}}) \\ \mathcal{Z}_- s_{z,\boldsymbol{k}} & \mathcal{Z}_- (s_{x,\boldsymbol{k}} - \mathrm{i}s_{y,\boldsymbol{k}}) & \mathcal{Z}_+ (s_{x,\boldsymbol{k}+\boldsymbol{Q}} + \mathrm{i}s_{y,\boldsymbol{k}+\boldsymbol{Q}}) & -\mathcal{Z}_+ s_{z,\boldsymbol{k}+\boldsymbol{Q}} \end{pmatrix} \,, \tag{B.26b}$$

$$\boldsymbol{f}^{\boldsymbol{Q}}_{\boldsymbol{k}} = \left(f_{\boldsymbol{k},\uparrow}, f_{\boldsymbol{k},\downarrow}, f_{\boldsymbol{k}+\boldsymbol{Q},\uparrow}, f_{\boldsymbol{k}+\boldsymbol{Q},\downarrow}\right)^\top \,, \tag{B.26c}$$

$$\boldsymbol{c}^{\boldsymbol{Q}}_{\boldsymbol{k}} = \left(c_{\boldsymbol{k},\uparrow}, c_{\boldsymbol{k},\downarrow}, c_{\boldsymbol{k}+\boldsymbol{Q},\uparrow}, c_{\boldsymbol{k}+\boldsymbol{Q},\downarrow}\right)^\top \,, \tag{B.26d}$$

$$s_{\alpha,\boldsymbol{k}} = 2\sin\left(k_\alpha\right) \,. \tag{B.26e}$$

[1] Since we explicitly double the number of bands in the magnetic basis, there are only $N/2$ different momenta, with N being the number of lattice sites, which is considered in the normalization of the Fourier transformation.

The remaining terms H_d and H_f are calculated in full analogy to Sections B.1 and B.2. However, the respective matrices have to be symmetrized to the extended basis $H_{\boldsymbol{k}} \to H_{\boldsymbol{k}} + H_{\boldsymbol{k}+\boldsymbol{Q}}$, yielding

$$\underline{H}^{\boldsymbol{Q}}_{d,\boldsymbol{k}} = \begin{pmatrix} \xi^d_{\boldsymbol{k}} - \mu_0 & 0 & 0 & 0 \\ 0 & \xi^d_{\boldsymbol{k}} - \mu_0 & 0 & 0 \\ 0 & 0 & \xi^d_{\boldsymbol{k}+\boldsymbol{Q}} - \mu_0 & 0 \\ 0 & 0 & 0 & \xi^d_{\boldsymbol{k}+\boldsymbol{Q}} - \mu_0 \end{pmatrix},$$

$$\underline{H}^{\boldsymbol{Q}}_{f,\boldsymbol{k}} = \begin{pmatrix} \mathcal{Z}_+^2 \xi^f_{\boldsymbol{k}} + \mathcal{Z}_-^2 \xi^f_{\boldsymbol{k}+\boldsymbol{Q}} + \epsilon_f - \mu_0 & 0 & 0 & \mathcal{Z}_+\mathcal{Z}_- \left(\xi^f_{\boldsymbol{k}+\boldsymbol{Q}} + \xi^f_{\boldsymbol{k}}\right) \\ 0 & \mathcal{Z}_+^2 \xi^f_{\boldsymbol{k}} + \mathcal{Z}_-^2 \xi^f_{\boldsymbol{k}+\boldsymbol{Q}} + \epsilon_f - \mu_0 & \mathcal{Z}_+\mathcal{Z}_- \left(\xi^f_{\boldsymbol{k}+\boldsymbol{Q}} + \xi^f_{\boldsymbol{k}}\right) & 0 \\ 0 & \mathcal{Z}_+\mathcal{Z}_- \left(\xi^f_{\boldsymbol{k}} + \xi^f_{\boldsymbol{k}+\boldsymbol{Q}}\right) & \mathcal{Z}_+^2 \xi^f_{\boldsymbol{k}+\boldsymbol{Q}} + \mathcal{Z}_-^2 \xi^f_{\boldsymbol{k}} + \epsilon_f - \mu_0 & 0 \\ \mathcal{Z}_+\mathcal{Z}_- \left(\xi^f_{\boldsymbol{k}} + \xi^f_{\boldsymbol{k}+\boldsymbol{Q}}\right) & 0 & 0 & \mathcal{Z}_+^2 \xi^f_{\boldsymbol{k}+\boldsymbol{Q}} + \mathcal{Z}_-^2 \xi^f_{\boldsymbol{k}} + \epsilon_f - \mu_0 \end{pmatrix},$$

$$\underline{H}_{\beta} = \begin{pmatrix} \beta_0 & 0 & 0 & \beta \\ 0 & \beta_0 & \beta & 0 \\ 0 & \beta & \beta_0 & 0 \\ \beta & 0 & 0 & \beta_0 \end{pmatrix}. \tag{B.27}$$

With these definitions, the final result is given by[1]

$$\underline{H}^{\psi,\boldsymbol{Q}}_{\boldsymbol{k},\mathrm{TKI}} = \begin{pmatrix} \underline{H}^{\boldsymbol{Q}}_{d,\boldsymbol{k}} & \underline{H}^{fc}_{\mathrm{hyb}} \\ \left(\underline{H}^{fc}_{\mathrm{hyb}}\right)^{\dagger} & \underline{H}^{\boldsymbol{Q}}_{f,\boldsymbol{k}} + \underline{H}_{\beta} \end{pmatrix}, \tag{B.28}$$

within the basis

$$\phi^{\boldsymbol{Q}}_{\boldsymbol{k}} = \left(c_{\boldsymbol{k},\uparrow}, \quad c_{\boldsymbol{k},\downarrow}, \quad c_{\boldsymbol{k}+\boldsymbol{Q},\uparrow}, \quad c_{\boldsymbol{k}+\boldsymbol{Q},\downarrow}, \quad f_{\boldsymbol{k},\uparrow}, \quad f_{\boldsymbol{k},\downarrow}, \quad f_{\boldsymbol{k}+\boldsymbol{Q},\uparrow}, \quad f_{\boldsymbol{k}+\boldsymbol{Q},\downarrow}\right)^{\top}. \tag{B.29}$$

In Chapter 12, we consider NN and NNN hopping for the d- and f-electrons with the dispersions

$$\xi^d_{\boldsymbol{k}} = -2t_d \left(\cos k_x + \cos k_y + \cos k_z\right) - 4t'_d \left(\cos k_x \cos k_y + \cos k_x \cos k_z + \cos k_y \cos k_z\right), \tag{B.30a}$$

$$\xi^f_{\boldsymbol{k}} = -2t_f \left(\cos k_x + \cos k_y + \cos k_z\right) - 4t'_f \left(\cos k_x \cos k_y + \cos k_x \cos k_z + \cos k_y \cos k_z\right). \tag{B.30b}$$

The eigenvalues of $\underline{H}^{\psi,\boldsymbol{Q}}_{\mathrm{TKI}}$ are doubly degenerate due to Kramer's pairs [294] and are determined numerically. To avoid over-counting in the free energy (FE), the occurring $\boldsymbol{k}$-summation must be performed over the magnetic Brillouin zone $\mathrm{BZ}_{\boldsymbol{Q}}$, which is halved in size compared to the paramagnetic BZ of the original basis

$$\sum_{\boldsymbol{k}\in\mathrm{BZ}_{\boldsymbol{Q}}} = \frac{1}{2} \sum_{\boldsymbol{k}\in\mathrm{BZ}_0}. \tag{B.31}$$

As shown in Reference [305], the MF analysis can, in principle, be adapted to investigate arbitrary commensurate ordering vectors. The dimension of $\underline{H}^{\psi,\boldsymbol{Q}}_{\boldsymbol{k},\mathrm{TKI}}$, however, grows with the number of atoms in the unit magnetic unit cell P and consequently, a numerical analysis becomes costly.

[1] This 8×8 description correctly contains the ferromagnetic ($\boldsymbol{Q} = 0$) and paramagnetic limit. However, these cases can be expressed within a more convenient 4×4 matrix.

Bloch form

Equation (B.28) does not represent a Bloch matrix, i.e., $\underline{H}^{\psi,Q}_{\boldsymbol{k},\mathrm{TKI}} \neq \underline{H}^{\psi,Q}_{\boldsymbol{k}+Q,\mathrm{TKI}}$. A Bloch form, which satisfies $\underline{\tilde{H}}^{\psi,Q}_{\boldsymbol{k},\mathrm{TKI}} = \underline{\tilde{H}}^{\psi,Q}_{\boldsymbol{k}+Q,\mathrm{TKI}}$ can be found by means of a unitary transformation

$$\underline{\tilde{H}}^{\psi,Q}_{\boldsymbol{k},\mathrm{TKI}} = \underline{U}^{\dagger}_{B,\boldsymbol{k}} \underline{H}^{\psi,Q}_{\boldsymbol{k},\mathrm{TKI}} \underline{U}_{B,\boldsymbol{k}} \,. \tag{B.32}$$

A suitable basis transformation is given by [305]

$$\begin{aligned}
c^{\dagger}_{1,\boldsymbol{k}} &= \frac{1}{\sqrt{2}} e^{\mathrm{i}k_x} c^{\dagger}_{\boldsymbol{k}} + \frac{1}{\sqrt{2}} c^{\dagger}_{\boldsymbol{k}+Q} \,, \\
c^{\dagger}_{2,\boldsymbol{k}} &= -\frac{1}{\sqrt{2}} e^{\mathrm{i}k_x} c^{\dagger}_{\boldsymbol{k}} + \frac{1}{\sqrt{2}} c^{\dagger}_{\boldsymbol{k}+Q} \,, \\
f^{\dagger}_{1,\boldsymbol{k}} &= \frac{1}{\sqrt{2}} e^{\mathrm{i}k_x} f^{\dagger}_{\boldsymbol{k}} + \frac{1}{\sqrt{2}} f^{\dagger}_{\boldsymbol{k}+Q} \,, \\
f^{\dagger}_{2,\boldsymbol{k}} &= -\frac{1}{\sqrt{2}} e^{\mathrm{i}k_x} f^{\dagger}_{\boldsymbol{k}} + \frac{1}{\sqrt{2}} f^{\dagger}_{\boldsymbol{k}+Q} \,,
\end{aligned} \tag{B.33}$$

with

$$\left(\tilde{\phi}^{Q}_{\boldsymbol{k}}\right)^{\dagger} = \underline{U}^{\dagger}_{B,\boldsymbol{k}} \left(\phi^{Q}_{\boldsymbol{k}}\right)^{\dagger} \,, \tag{B.34}$$

where $\left(\tilde{\phi}^{Q}_{\boldsymbol{k}}\right)^{\dagger}$ represents the basis on the left side of Equation (B.33). This unitary transformation does, of course, not impact the eigenvalues. Eigenvectors, however, are subject to change. This subtlety is important to calculate topological invariants through eigenvalues of the inversion operator, which are only well defined for Bloch matrices (compare Section 12.2.3). The inversion operator $\hat{\mathcal{I}}$ in the Bloch basis is given by

$$\hat{\mathcal{I}} = U^{\dagger}_{B,-\boldsymbol{k}} \begin{pmatrix}
1 & 0 & 0 & 0 & 0 & 0 & 0 & 0 \\
0 & 1 & 0 & 0 & 0 & 0 & 0 & 0 \\
0 & 0 & 1 & 0 & 0 & 0 & 0 & 0 \\
0 & 0 & 0 & 1 & 0 & 0 & 0 & 0 \\
0 & 0 & 0 & 0 & -1 & 0 & 0 & 0 \\
0 & 0 & 0 & 0 & 0 & -1 & 0 & 0 \\
0 & 0 & 0 & 0 & 0 & 0 & -1 & 0 \\
0 & 0 & 0 & 0 & 0 & 0 & 0 & -1
\end{pmatrix} U_{B,\boldsymbol{k}} \,. \tag{B.35}$$

The inversion eigenvalues of the n-th Kramer's pair at time-reversal-invariant momentum (TRIM) Γ_j can be obtained by evaluating

$$\xi[n,\Gamma_j] = \langle \pm\sigma, n, -\boldsymbol{k} | \, \mathcal{I} \, | \pm\sigma, n, \boldsymbol{k} \rangle \,, \tag{B.36}$$

where $|\pm\sigma, n, \boldsymbol{k}\rangle$ represents the two eigenvectors for the n-th Kramer's pair of the hopping matrix defined in Equation (B.32), with wave vector $\boldsymbol{k}$ and pseudo spin σ.

B.3.2 Ferromagnetic order

For ferromagnetic (FM) order, i.e., $\boldsymbol{Q} = 0$, the SB-dependent hopping matrix reduces to

$$\underline{H}^{\psi,0}_{\boldsymbol{k},\mathrm{TKI}} = \begin{pmatrix} \underline{H}^{0}_{d,\boldsymbol{k}} & \underline{H}^{\psi,0}_{\mathrm{hyb},\boldsymbol{k}} \\ \left(\underline{H}^{\psi,0}_{\mathrm{hyb},\boldsymbol{k}}\right)^{\dagger} & \underline{H}^{\psi,0}_{f,\boldsymbol{k}} + \underline{H}_{\beta} \end{pmatrix} \tag{B.37a}$$

within the four-dimensional basis

$$\boldsymbol{\phi}_{\boldsymbol{k}} = \left(c_{\boldsymbol{k},\uparrow}, \quad c_{\boldsymbol{k},\downarrow}, \quad f_{\boldsymbol{k},\uparrow}, \quad f_{\boldsymbol{k},\downarrow}\right)^{\top}, \tag{B.37b}$$

and

$$\underline{H}^{0}_{d,\boldsymbol{k}} = \begin{pmatrix} \xi^{d}_{\boldsymbol{k}} - \mu_0 & 0 \\ 0 & \xi^{d}_{\boldsymbol{k}} - \mu_0 \end{pmatrix}, \tag{B.37c}$$

$$\underline{H}^{\psi,0}_{\mathrm{hyb},\boldsymbol{k}} = V \sum_{\alpha} \left(\mathcal{Z}_{+}\underline{\tau}^{\alpha} s_{\alpha,\boldsymbol{k}} + \mathcal{Z}_{-}\underline{\tau}^{\alpha}\underline{\tau}^{1} s_{\alpha,\boldsymbol{k}}\right), \tag{B.37d}$$

$$\underline{H}^{\psi,0}_{f,\boldsymbol{k}} = \begin{pmatrix} \mathcal{Z}_{+}^{2}\xi^{f}_{\boldsymbol{k}} + \mathcal{Z}_{-}^{2}\xi^{f}_{\boldsymbol{k}} - \mu_0 + \epsilon_f & 2\mathcal{Z}_{+}\mathcal{Z}_{-}\xi^{f}_{\boldsymbol{k}} \\ 2\mathcal{Z}_{+}\mathcal{Z}_{-}\xi^{f}_{\boldsymbol{k}} & \mathcal{Z}_{+}^{2}\xi^{f}_{\boldsymbol{k}} + \mathcal{Z}_{-}^{2}\xi^{f}_{\boldsymbol{k}} - \mu_0 + \epsilon_f \end{pmatrix}, \tag{B.37e}$$

$$\underline{H}_{\beta} = \begin{pmatrix} \beta_0 & \beta \\ \beta & \beta_0 \end{pmatrix}. \tag{B.37f}$$

The matrix employs a Bloch form and the respective inversion operator $\mathcal{I}$ is given by

$$\hat{\mathcal{I}} = \begin{pmatrix} 1 & 0 & 0 & 0 \\ 0 & 1 & 0 & 0 \\ 0 & 0 & -1 & 0 \\ 0 & 0 & 0 & -1 \end{pmatrix}. \tag{B.38}$$

In the PM limit, i.e., $p \to, \beta \to 0$, the SB weights reduce to $\mathcal{Z}_{+} \to z_0$ and $\mathcal{Z}_{-} \to 0$ (compare Table 4.1). In this case the two-fold degenerate eigenvalues of $\underline{H}^{\psi,0}_{\boldsymbol{k},\mathrm{TKI}}$ adapt the simple form

$$\varepsilon^{\mathrm{PM},\pm}_{\boldsymbol{k},\mathrm{TKI}} = \frac{1}{2}\left(\xi^{d}_{\boldsymbol{k}} + z_0^2\xi^{f}_{\boldsymbol{k}} + \epsilon_f + \beta_0 - 2\mu_0\right) \pm \sqrt{\frac{1}{4}\left(\xi^{d}_{\boldsymbol{k}} - z_0^2\xi^{f}_{\boldsymbol{k}} - \epsilon_f - \beta_0\right)^2 + (2Vz_0)^2\left(\sin^2 k_x + \sin^2 k_y + \sin^2 k_z\right)}. \tag{B.39}$$

B.4 Mean-field spin rotation

In Section 4.1, we chose the bosonic MF spin to form a spiral in the x-y plane. In the following, we will discuss the impact on the MF hopping matrices $\underline{H}^{\psi,\mathcal{Q}}$, if that polarization plane is rotated. A spin rotation by θ around the axis $\hat{\boldsymbol{n}}$ of a second quantized Hamiltonian may be achieved by rotating the spinor $\boldsymbol{f}^{\dagger} = \left(\hat{f}^{\dagger}_{\uparrow}, \hat{f}^{\dagger}_{\downarrow}\right)$

by means of the unitary spin rotation operator [70]

$$\underline{U}_{\hat{\boldsymbol{n}},\theta} = \mathrm{e}^{-\mathrm{i}\theta\hat{\boldsymbol{n}}\underline{\boldsymbol{\tau}}/2}\,, \tag{B.40a}$$

via

$$\hat{f}^\dagger_{\mathrm{rot}} = \underline{U}^\dagger_{\hat{\boldsymbol{n}},\theta}\hat{f}^\dagger = \underline{U}^\dagger_{\hat{\boldsymbol{n}},\theta}\left(\hat{\underline{z}}^\dagger\right)^\top \underline{U}_{\hat{\boldsymbol{n}},\theta}\underline{U}^\dagger_{\hat{\boldsymbol{n}},\theta}\hat{f}^\dagger\,. \tag{B.40b}$$

In order to rotate the MF spin, we only rotate the bosonic part of the SB spinor, and we need to apply the same transformation to the Lagrange multiplier $\boldsymbol{\beta}$, i.e.,

$$\begin{aligned}
\begin{pmatrix} \mathcal{Z}_+ & \mathcal{Z}_-\,\mathrm{e}^{\mathrm{i}QR} \\ \mathcal{Z}_-\,\mathrm{e}^{-\mathrm{i}QR} & \mathcal{Z}_+ \end{pmatrix} &\rightarrow U^\dagger_{\hat{\boldsymbol{n}},\theta}\begin{pmatrix} \mathcal{Z}_+ & \mathcal{Z}_-\,\mathrm{e}^{\mathrm{i}QR} \\ \mathcal{Z}_-\,\mathrm{e}^{-\mathrm{i}QR} & \mathcal{Z}_+ \end{pmatrix} U_{\hat{\boldsymbol{n}},\theta}\,, \\
\begin{pmatrix} 0 & \beta\,\mathrm{e}^{\mathrm{i}QR} \\ \beta e^{-\mathrm{i}QR} & 0 \end{pmatrix} &\rightarrow U^\dagger_{\hat{\boldsymbol{n}},\theta}\begin{pmatrix} 0 & \beta\mathrm{e}^{\mathrm{i}QR} \\ \beta e^{-\mathrm{i}QR} & 0 \end{pmatrix} U_{\hat{\boldsymbol{n}},\theta}\,.
\end{aligned} \tag{B.41}$$

For spin-rotation invariant models, this results in an overall unitary transformation of the hopping matrix $\underline{H}^{\psi,Q}$, whose eigenvalues remain invariant. Moreover, since the bosonic Lagrangian is diagonal in spin space, the FE is invariant as well, and all rotations are equivalent on MF level. For Hamiltonians, which break spin-rotation symmetry, the MF can be extended to include the parameters θ and $\hat{\boldsymbol{n}}$ through Equation (B.41). In the case of $\underline{H}^{\psi,Q}_{\mathrm{TKI},\boldsymbol{k}}$, the sub-matrices transform as

$$\begin{aligned}
\underline{H}^{fc}_{\mathrm{hyb}} &\rightarrow -V\sum_\alpha \begin{pmatrix} \mathcal{Z}_+ s_{\alpha,\boldsymbol{k}}\tau^\alpha & \mathcal{Z}_- s_{\alpha,\boldsymbol{k}+\boldsymbol{Q}} U^\dagger_{\hat{\boldsymbol{n}},\theta}\,\tau^1\,U_{\hat{\boldsymbol{n}},\theta}\tau^\alpha \\ \mathcal{Z}_- s_{\alpha,\boldsymbol{k}} U^\dagger_{\hat{\boldsymbol{n}},\theta}\,\tau^1\,U_{\hat{\boldsymbol{n}},\theta}\tau^\alpha & \mathcal{Z}_+ s_{\alpha,\boldsymbol{k}+\boldsymbol{Q}}\tau^\alpha \end{pmatrix}, \\
\underline{H}^{\psi,Q}_{f,\boldsymbol{k}} &\rightarrow \begin{pmatrix} \left(\mathcal{Z}_+^2\xi^f_{\boldsymbol{k}} + \mathcal{Z}_-^2\xi^f_{\boldsymbol{k}+\boldsymbol{Q}} + \beta_0 - \mu\right)\tau^0 & \left(\mathcal{Z}_+\mathcal{Z}_-\left(\xi^f_{\boldsymbol{k}+\boldsymbol{Q}} + \xi^f_{\boldsymbol{k}}\right) + \beta\right) U^\dagger_{\hat{\boldsymbol{n}},\theta}\,\tau^1\,U_{\hat{\boldsymbol{n}},\theta} \\ \left(\mathcal{Z}_+\mathcal{Z}_-\left(\xi^f_{\boldsymbol{k}} + \xi^f_{\boldsymbol{k}+\boldsymbol{Q}}\right) + \beta\right) U^\dagger_{\hat{\boldsymbol{n}},\theta}\,\tau^1\,U_{\hat{\boldsymbol{n}},\theta} & \left(\mathcal{Z}_+^2\xi^f_{\boldsymbol{k}+\boldsymbol{Q}} + \mathcal{Z}_-^2\xi^f_{\boldsymbol{k}} + \beta_0 - \mu\right)\tau^0 \end{pmatrix}.
\end{aligned} \tag{B.42}$$

It becomes apparent that rotating the magnetization plane of the MF ansatz is equivalent to rotating the direction of the spin-orbit coupling (SOC). It can be shown, e.g., using *Mathematica*, that the eigenvalues of $\underline{H}^{\psi,Q}_{\boldsymbol{k},\mathrm{TKI}}$ remain invariant under this transformation, and thus the polarization of the MF spin does not impact the saddle point solution. This is due to the time-reversal (TR) and inversion symmetry of H^{TKI}, where a rotation of the SOC occurs on a degenerate subspace of the Hamiltonian

$$U_{\hat{\boldsymbol{n}},\theta}\,|\sigma,n,\boldsymbol{k}\rangle = U_{1,\hat{\boldsymbol{n}},\theta}\,|\sigma,n,\boldsymbol{k}\rangle + U_{2,\hat{\boldsymbol{n}},\theta}\,|-\sigma,n,\boldsymbol{k}\rangle \quad \text{with} \quad \underline{H}^{\psi,Q}_{\boldsymbol{k},\mathrm{TKI}}\,|\pm\sigma,n,\boldsymbol{k}\rangle = \mathcal{E}^\nu_{\boldsymbol{k}}\,|\pm\sigma,n,\boldsymbol{k}\rangle\,, \tag{B.43}$$

where $|\pm\sigma,n,\boldsymbol{k}\rangle$ represents the two eigenvectors for the n'th Kramer's pair with the degenerate eigenvalues $\mathcal{E}^\nu_{\boldsymbol{k}}$, wave vector $\boldsymbol{k}$ and pseudo spin σ.

Appendix C

Details on magnetic fluctuations

Based on Reference [55], we further elaborate on the result for the PF part of the magnetic fluctuation matrix introduced in Section 5.2.2

$$
\begin{aligned}
[\mathcal{M}^F(q)]^{a,b}_{\mu,\nu} = \frac{1}{2}\sum_{\boldsymbol{k}\in \mathrm{BZ}_0}\sum_{s} n_{\mathrm{F}}\left(\varepsilon^s_{\boldsymbol{k}}\right) \Big[\underline{U}_{\boldsymbol{k}} \Big(\left[\underline{Z}^\dagger_{\mu\nu}\right]^b \otimes \left[\underline{\mathcal{H}}_{\boldsymbol{k}+a\boldsymbol{Q}}\underline{Z}^a_0\right] + \left[\underline{Z}^\dagger_0\right]^b \otimes \left[\underline{\mathcal{H}}_{\boldsymbol{k}+b\boldsymbol{Q}}\underline{Z}^a_{\mu\nu}\right] \\
+ \left[\underline{Z}^\dagger_\mu\right]^b \otimes \left[\underline{\mathcal{H}}_{\boldsymbol{k}+\boldsymbol{q}+(a+b)\boldsymbol{Q}}\underline{Z}^a_\nu\right] + \left[\underline{Z}^\dagger_\nu\right]^b \otimes \left[\underline{\mathcal{H}}_{\boldsymbol{k}-\boldsymbol{q}}\underline{Z}^a_\mu\right] \Big)\underline{U}^\dagger_{\boldsymbol{k}} \Big]^{s,s} \\
+ \frac{1}{2}\sum_{\boldsymbol{k}\in \mathrm{BZ}_Q}\sum_{s,s'} L_{\mathrm{F}}\left(\varepsilon^s_{\boldsymbol{k}}, \varepsilon^{s'}_{\boldsymbol{k}+\boldsymbol{q}}, \mathrm{i}\omega_n\right) \\
\times \Big[\sum_v \underline{U}_{\boldsymbol{k}} \left(\left[\underline{Z}^\dagger_\mu\right]^v \otimes \left[\underline{\mathcal{H}}_{\boldsymbol{k}+\boldsymbol{q}+(v+a)\boldsymbol{Q}}\underline{Z}^{v+a}_0\right] + \left[\underline{Z}^\dagger_0\right]^v \otimes \left[\underline{\mathcal{H}}_{\boldsymbol{k}+v\boldsymbol{Q}}\underline{Z}^{v+a}_\mu\right] + \underline{\mathfrak{B}}^{v,v+a}_\mu \right) \underline{U}^\dagger_{\boldsymbol{k}+\boldsymbol{q}} \Big]^{s,s'} \\
\times \Big[\sum_u \underline{U}_{\boldsymbol{k}+\boldsymbol{q}} \left(\left[\underline{Z}^\dagger_\nu\right]^{u+b} \otimes \left[\underline{\mathcal{H}}_{\boldsymbol{k}+u\boldsymbol{Q}}\underline{Z}^u_0\right] + \left[\underline{Z}^\dagger_0\right]^{u+b} \otimes \left(\underline{\mathcal{H}}_{\boldsymbol{k}+\boldsymbol{q}+(u+b)\boldsymbol{Q}}\underline{Z}^u_\nu + \underline{\mathfrak{B}}^{u+b,u}_\nu \right) \underline{U}^\dagger_{\boldsymbol{k}} \Big]^{s',s} .
\end{aligned}
\tag{C.1}
$$

Thereby, we provide definitions of the momentum-shifted Fourier coefficient matrices $\underline{Z}^a$, and we list the explicit expressions for all non-vanishing coefficients. Moreover, we elaborate on the special cases of AFM and FM order, and exemplarily demonstrate the construction of $[\mathcal{M}^F(q)]^{a,b}_{\mu,\nu}$ to illustrate the applied index-shifts.

In analogy to the PM case, all fermionic Matsubara summations have been evaluated analytically to derive Equation (C.1). In order to do so, the pseudofermion MF Green's function and consequently $\varepsilon^s_{\boldsymbol{k}}$ and $\underline{U}_{\boldsymbol{k}}$ must be written in the fermionic basis

$$
\phi^a_k = \phi_{\boldsymbol{k}+a\boldsymbol{Q},\mathrm{i}\omega_n} , \tag{C.2}
$$

with $a \in \{0, 1, \ldots, P-1\}$, and $\phi^a_k = \phi^{a+P}_k$ that has been defined in Equation (4.12). The second momentum sum needs to be performed over the magnetic, back-folded BZ, which relates to the paramagnetic BZ by $P\sum_{\boldsymbol{k}\in \mathrm{BZ}_Q} = \sum_{\boldsymbol{k}\in \mathrm{BZ}_0}$. Although MF Hamiltonians for SRI models can be expressed in the reduced basis defined in Equation (4.15) that exploits a block-diagonality between spin and momentum shifts, we need to apply the

full, symmetrized Bloch basis here. The corresponding MF Green's matrix is of the form

$$\underline{G}^{\overline{\psi}}_{\boldsymbol{k}} = \begin{pmatrix} \underline{G}^{\overline{\psi}}_{\boldsymbol{k},\boldsymbol{k}} & \underline{G}^{\overline{\psi}}_{\boldsymbol{k},\boldsymbol{k}+\boldsymbol{Q}} & \cdots & \underline{G}^{\overline{\psi}}_{\boldsymbol{k},\boldsymbol{k}+(P-1)\boldsymbol{Q}} \\ \underline{G}^{\overline{\psi}}_{\boldsymbol{k}+\boldsymbol{Q},\boldsymbol{k}} & \underline{G}^{\overline{\psi}}_{\boldsymbol{k}+\boldsymbol{Q},\boldsymbol{k}+\boldsymbol{Q}} & & \\ \vdots & & \ddots & \\ \underline{G}^{\overline{\psi}}_{\boldsymbol{k}+(P-1)\boldsymbol{Q},\boldsymbol{k}} & & & \underline{G}^{\overline{\psi}}_{\boldsymbol{k}(P-1)\boldsymbol{Q},\boldsymbol{k}+(P-1)\boldsymbol{Q}} \end{pmatrix}, \tag{C.3}$$

i.e., momentum degrees of freedom are relabeled to band degrees of freedom by means of magnetic back folding. As a consequence it is

$$\dim \underline{G}^{\overline{\psi}}_{\boldsymbol{k}} = P \dim \underline{\mathcal{H}}_{\boldsymbol{k}} = P \dim \underline{Z}^{a} \,, \tag{C.4}$$

because the bare Hamiltonian $\underline{\mathcal{H}}_{\boldsymbol{k}}$ is defined in the non-magnetic basis. The Fourier coefficient matrix $\underline{Z}^{a}$ as been introduced in Equation (5.39)[1]. The complicated index structure in Equation (C.1) achieves that the bare Hamiltonian is back-folded to the magnetic basis of the Green's function under consideration of the external indices a, b. In order to do so, we define a vector of the Fourier coefficient matrices

$$\underline{\boldsymbol{Z}} = \left(\underline{Z}^{0}, \underline{Z}^{1}, \dots, \underline{Z}^{P-1}\right)^{\top} \,, \tag{C.5a}$$

and introduce an external index that cyclically rotates the order of the vector components

$$\underline{\boldsymbol{Z}}^{a} = \left(\underline{Z}^{(-a) \bmod P}, \underline{Z}^{(-a+1) \bmod P}, \dots, \underline{Z}^{(-a+P-1) \bmod P}\right)^{\top} \,, \tag{C.5b}$$

while the dimension $\dim \underline{\boldsymbol{Z}}^{a} = P \dim \underline{Z}$ is unchanged. The dyadic product of these vectors is constructed by

$$\underline{\boldsymbol{Z}}^{a} \otimes \underline{\mathcal{H}}_{\boldsymbol{k}} \underline{\boldsymbol{Z}}^{b} = \begin{pmatrix} \underline{Z}^{(-a) \bmod P} \underline{\mathcal{H}}_{\boldsymbol{k}} \underline{Z}^{(-b) \bmod P} & \cdots & \underline{Z}^{(-a) \bmod P} \underline{\mathcal{H}}_{\boldsymbol{k}} \underline{Z}^{(-b+P-1) \bmod P} \\ \vdots & \ddots & \vdots \\ \underline{Z}^{(-a+P-1) \bmod P} \underline{\mathcal{H}}_{\boldsymbol{k}} \underline{Z}^{(-b) \bmod P} & \cdots & \underline{Z}^{(-a+P-1) \bmod P} \underline{\mathcal{H}}_{\boldsymbol{k}} \underline{Z}^{(-b+P-1) \bmod P} \end{pmatrix}. \tag{C.5c}$$

We also employ the basis-adapted LM matrix

$$\underline{\mathfrak{B}}^{a,b}_{\mu} = \begin{pmatrix} \underline{B}^{(-a) \bmod P, (-b) \bmod P}_{\mu} & \cdots & \underline{B}^{(-a) \bmod P, (-b+P-1) \bmod P}_{\mu} \\ \vdots & \ddots & \vdots \\ \underline{B}^{(-a+P-1) \bmod P, (-b) \bmod P}_{\mu} & \cdots & \underline{B}^{(-a+P-1) \bmod P, (-b+P-1) \bmod P}_{\mu} \end{pmatrix}, \tag{C.6a}$$

where

$$\underline{B}^{a,b}_{\mu} = \begin{cases} \underline{B}_{\mu} & \text{if } a = b = 0 \,, \\ 0 & \text{otherwise} \end{cases} \tag{C.6b}$$

and $\underline{B}_{\mu}$ has been defined in Equation (5.24).

[1] We have droped the subindex that denotes the order of the derivative w.r.t. the bosonic fields ψ_{μ}, ψ_{ν} for simplicity. It is implied that $\underline{Z}^{a}$ represents $\underline{Z}^{a}_{0}$, $\underline{Z}^{a}_{\mu}$, and $\underline{Z}^{a}_{\mu\nu}$ in full analogy.

Fourier coefficient matrices

Following Reference [55], we subsequently provide the Fourier coefficients of the $\underline{z}$-matrix and its derivatives within the expansion

$$\underline{z}_i\Big|_{\overline{\psi}} = \sum_{a=-\infty}^{\infty} \underline{z}_{0,a}\, \mathrm{e}^{-\mathrm{i}a\boldsymbol{Q}\boldsymbol{R}_i}\,, \quad \partial_\mu \underline{z}_i\Big|_{\overline{\psi}} = \sum_{a=-\infty}^{\infty} \underline{z}_{\mu,a}\, \mathrm{e}^{-\mathrm{i}a\boldsymbol{Q}\boldsymbol{R}_i}\,, \quad \partial_{\mu\nu} \underline{z}_i\Big|_{\overline{\psi}} = \sum_{a=-\infty}^{\infty} \underline{z}_{\mu\nu,a}\, \mathrm{e}^{-\mathrm{i}a\boldsymbol{Q}\boldsymbol{R}_i}\,. \tag{C.7}$$

These determine the Fourier coefficients of the $\underline{Z}$-matrix[1]

$$\underline{Z} = \underline{\mathbb{1}}_{2O\times 2O} \oplus \underline{z}\,, \tag{C.8}$$

introduced in Section 5.2.2. It has been shown in Equation (A.24) that the $\underline{z}$-matrix can conveniently be expressed by

$$\underline{z} = \left[\mathcal{Z}_+ \underline{\tau}^0 + \mathcal{Z}_- \sum_{\mu=1}^{3} \frac{p_\mu}{p} \underline{\tau}^\mu\right]_{e=\sqrt{1-d_1^2-d_2^2-p_0^2-\boldsymbol{p}^2}}\,. \tag{C.9}$$

Remember that we have to replace the e field by means of the α-constraint in our fluctuation basis before taking derivatives, which is implied in the following. All quantities are to be evaluated at the saddle point of the magnetic MF ansatz defined in Equation (4.2), where the $\boldsymbol{p}$-field carries the spatial dependence

$$\boldsymbol{p}_i = p \begin{pmatrix} \cos(\boldsymbol{Q}\boldsymbol{R}_i) \\ \sin(\boldsymbol{Q}\boldsymbol{R}_i) \\ 0 \end{pmatrix}, \tag{C.10}$$

Zeroth derivative

$$\underline{z}_{0,0} = \mathcal{Z}_+\big|_{\overline{\psi}} \underline{\tau}^0\,, \tag{C.11a}$$

$$\underline{z}_{0,\pm 1} = \frac{1}{2}\mathcal{Z}_-\big|_{\overline{\psi}} \left(\underline{\tau}^1 \pm \mathrm{i}\left[\underline{\tau}^2\right]^\top\right). \tag{C.11b}$$

Notice that only the zeroth Fourier coefficient is unity for the non interacting orbitals $\underline{Z}_{0,0} = \underline{\mathbb{1}}_{2O\times 2O} \oplus \underline{z}_{0,0}$, while all other Fourier coefficients are zero in that regard $\underline{Z}_{0,a\neq 0} = \underline{\mathbb{0}}_{2O\times 2O} \oplus \underline{z}_{0,a\neq 0}$.

First derivatives

Due to the magnetic MF ansatz, taking the derivative w.r.t. a spin field $\psi^s \in \{p_1, p_2, p_3\}$ yields two extra non-vanishing Fourier coefficients, while derivatives w.r.t. a charge field $\psi^c \in \{p_0, d_1, d_2\}$ do not impact the spatial dependence:

$$\underline{z}_{\mu,0} = \frac{\partial \mathcal{Z}_+}{\partial \psi^c_\mu}\bigg|_{\overline{\psi}} \underline{\tau}^0\,, \tag{C.12a}$$

$$\underline{z}_{\mu,\pm 1} = \frac{1}{2}\frac{\partial \mathcal{Z}_-}{\partial \psi^c_\mu}\bigg|_{\overline{\psi}} \left(\underline{\tau}^1 \pm \mathrm{i}\left[\underline{\tau}^2\right]^\top\right). \tag{C.12b}$$

[1] The number of non-interacting orbitals is denoted by O.

We further have to distinguish between in-plane spin fields (p_1, p_2) and the perpendicular spin field with $\overline{p}_3 = 0$. In the following, we adapt the notation $p_1^{\pm} = \frac{1}{2}\overline{p}$ and $p_2^{\pm} = \pm\frac{1}{2\mathrm{i}}\overline{p}$ and find for the derivatives w.r.t. in-plane spin fields $\mu \in \{p_1, p_2\}$

$$\underline{z}_{\mu,0} = \left(\frac{\partial \mathcal{Z}_-}{\partial p} + \frac{\mathcal{Z}_-}{p}\right)\Big|_{\overline{\psi}} \frac{[\underline{\tau}^{\mu}]^{\top}}{2} \,, \tag{C.12c}$$

$$\underline{z}_{\mu,\pm 1} = \frac{\partial \mathcal{Z}_+}{\partial p}\Big|_{\overline{\psi}} \frac{p_{\mu}^{\mp}}{\overline{p}} \underline{\tau}^0 \,, \tag{C.12d}$$

$$\underline{z}_{\mu,\pm 2} = \left(\frac{\partial \mathcal{Z}_-}{\partial p} - \frac{\mathcal{Z}_-}{p}\right)\Big|_{\overline{\psi}} \sum_{\nu=1}^{3} \frac{p_{\mu}^{\mp} p_{\nu}^{\mp}}{\overline{p}^2} [\underline{\tau}^{\nu}]^{\top} \,, \tag{C.12e}$$

and

$$\underline{z}_{p_3,0} = \frac{\mathcal{Z}_-}{p}\Big|_{\overline{\psi}} \underline{\tau}^3 \,. \tag{C.12f}$$

For first and second derivatives, the non-interacting unity part is of course zero $\underline{Z}_{\mu,a} = \underline{\mathbb{0}}_{2O\times 2O} \oplus \underline{z}_{\mu,a}$.

Second derivatives

Derivatives w.r.t. two charge fields ψ^c are given by

$$\underline{z}_{\mu\nu,0} = \frac{\partial^2 \mathcal{Z}_+}{\partial \psi_{\mu}^c \partial \psi_{\nu}^c}\Big|_{\overline{\psi}} \underline{\tau}_0 \,, \tag{C.13a}$$

$$\underline{z}_{\mu\nu,\pm 1} = \frac{1}{2}\frac{\partial^2 \mathcal{Z}_-}{\partial \psi_{\mu}^c \partial \psi_{\nu}^c}\Big|_{\overline{\psi}} \left(\underline{\tau}^1 \pm \mathrm{i}\left[\underline{\tau}^2\right]^{\top}\right) \,. \tag{C.13b}$$

Mixed derivatives w.r.t. a charge field ψ_{ν}^c and an in-plane spin field $\mu \in \{p_1, p_2\}$ are given by

$$\underline{z}_{\mu\nu,0} = \left(\frac{\partial^2 \mathcal{Z}_-}{\partial p \partial \psi_{\nu}^c} + \frac{\partial \mathcal{Z}_-}{p \partial \psi_{\nu}^c}\right)\Big|_{\overline{\psi}} \frac{[\underline{\tau}^{\mu}]^{\top}}{2} \,, \tag{C.13c}$$

$$\underline{z}_{\mu\nu,\pm 1} = \frac{\partial^2 \mathcal{Z}_+}{\partial p \partial \psi_{\nu}^c}\Big|_{\overline{\psi}} \frac{p_{\mu}^{\mp}}{\overline{p}} \underline{\tau}^0 \,, \tag{C.13d}$$

$$\underline{z}_{\mu\nu}^{\pm 2} = \left(\frac{\partial^2 \mathcal{Z}_-}{\partial p \partial \psi_{\nu}^c} - \frac{\partial \mathcal{Z}_-}{p \partial \psi_{\nu}^c}\right)\Big|_{\overline{\psi}} \sum_{\alpha=1}^{3} \frac{p_{\mu}^{\mp} p_{\alpha}^{\mp}}{\overline{p}^2} [\underline{\tau}^{\alpha}]^{\top} \,, \tag{C.13e}$$

and mixed derivatives featuring p_3 yield

$$\underline{z}_{\mu p_3,0} = \frac{\partial \mathcal{Z}_-}{p \partial \psi_{\mu}^c}\Big|_{\overline{\psi}} \underline{\tau}_3 \,. \tag{C.13f}$$

Finally, second derivatives w.r.t. two in-plane spin fields $\mu, \nu \in \{p_1, p_2\}$ are found to be

$$\underline{z}_{\mu\nu,0} = \left(\frac{\partial^2 \mathcal{Z}_+}{\partial p^2} + \frac{\partial \mathcal{Z}_+}{p \partial p}\right)\Big|_{\overline{\psi}} \frac{\delta_{\mu\nu}\underline{\tau}_0}{2} \,, \tag{C.13g}$$

$$\underline{z}_{\mu\nu,\pm1} = \left(p\frac{\partial^2\mathcal{Z}_-}{\partial p^2} - 3\frac{\partial\mathcal{Z}_-}{\partial p} + 3\frac{\mathcal{Z}_-}{p}\right)\Big|_{\overline{\psi}} \sum_{\alpha=1}^{3}\left(p_\mu^\mp p_\nu^\mp p_\alpha^\pm + \frac{\delta_{\mu\nu}\overline{p}^2}{2}p_\alpha^\mp\right)\frac{[\underline{\tau}^\alpha]^\top}{\overline{p}^4} \tag{C.13h}$$

$$+ \frac{1}{p^2}\left(\frac{\partial\mathcal{Z}_-}{\partial p} - \frac{\mathcal{Z}_-}{p}\right)\Big|_{\overline{\psi}}\left(p_\mu^\mp [\underline{\tau}^\nu]^\top + p_\nu^\mp [\underline{\tau}^\mu]^\top + \delta_{\mu\nu}\sum_{\alpha=1}^{3} p_\alpha^\mp [\underline{\tau}^\alpha]^\top\right), \tag{C.13i}$$

$$\underline{z}_{\mu\nu,\pm2} = \left(\frac{\partial^2\mathcal{Z}_+}{\partial p^2} - \frac{\partial\mathcal{Z}_+}{p\partial p}\right)\Big|_{\overline{\psi}} \frac{p_\mu^\mp p_\nu^\mp}{p^2}\underline{\tau}^0, \tag{C.13j}$$

$$\underline{z}_{\mu\nu,\pm3} = \left(p\frac{\partial^2\mathcal{Z}_-}{\partial p^2} - 3\frac{\partial\mathcal{Z}_-}{\partial p} + 3\frac{\mathcal{Z}_-}{p}\right)\Big|_{\overline{\psi}} \frac{p_\mu^\mp p_\nu^\mp}{\overline{p}^4}\sum_{\alpha=1}^{3} p_\alpha^\mp [\underline{\tau}^\alpha]^\top. \tag{C.13k}$$

and derivatives w.r.t. one arbitrary spin field $\mu \in \psi_\mu^s$ and $\nu = p_3$ yield

$$\underline{z}_{\mu p_3,0} = \delta_{\mu 3}\frac{\partial\mathcal{Z}_+}{p\partial p}\underline{\tau}^0, \tag{C.13l}$$

$$\underline{z}_{\mu p_3,\pm1} = \frac{1}{\overline{p}^2}\left(\frac{\partial\mathcal{Z}_-}{\partial p} - \frac{\mathcal{Z}_-}{p}\right)\left(\left(1-\delta_{\mu p_3}\right)p_\mu^\mp\underline{\tau}^3 + \delta_{\mu p_3}\sum_{\alpha=1}^{3} p_\alpha^\mp [\underline{\tau}^\alpha]^\top\right). \tag{C.13m}$$

Susceptibilities

As discussed in Section 5.3.2, dynamic susceptibilities around the MF saddle point are given by superpositions of matrix elements of the fluctuation field Green's function $\underline{\mathcal{G}} = -\underline{\mathcal{M}}^{-1}$. The spin susceptibility around a MF saddle point with arbitrary ordering vector $\boldsymbol{Q}$ can be inferred with Equation (5.52b) and is given by [55]

$$\chi_s^{\alpha\beta}(q) = \left\langle \delta S_{-q}^\alpha \delta S_q^\beta \right\rangle = (-1)^{\alpha+\beta-1}\Big[\overline{p}_0^2\,\mathcal{G}_{p_\alpha,p_\beta}^{0,0}(q) + \tfrac{1}{2}\overline{p}\,\overline{p}_0\Big(\lambda_\beta^*\,\mathcal{G}_{p_\alpha,p_0}^{0,1}(q) + \lambda_\beta\,\mathcal{G}_{p_\alpha,p_0}^{0,P-1}(q) + \lambda_\alpha^*\,\mathcal{G}_{p_0,p_\beta}^{P-1,0}(q) + \lambda_\alpha\mathcal{G}_{p_0,p_\beta}^{1,0}(q)\Big)$$
$$+ \frac{1}{4}\overline{p}^2\Big(\lambda_\alpha^*\lambda_\beta^*\,\mathcal{G}_{p_0,p_0}^{P-1,1}(q) + \lambda_\alpha^*\lambda_\beta\,\mathcal{G}_{p_0,p_0}^{P-1,P-1}(q) + \lambda_\alpha\lambda_\beta^*\mathcal{G}_{p_0,p_0}^{1,1}(q) + \lambda_\alpha\lambda_\beta\mathcal{G}_{p_0,p_0}^{1,P-1}(q)\Big)\Big], \tag{C.14a}$$

with $\alpha,\beta \in \{1,2,3\}$ and $\boldsymbol{\lambda} = (1,\mathrm{i},0)^\top$. The general charge susceptibility can be found analogously with Equation (5.53b) [55]

$$\begin{aligned}\chi_c(q) = \left\langle n_{-q} n_q \right\rangle = &-4\overline{d}_1^2\mathcal{G}_{d_1,d_1}^{0,0} - \overline{p}_0^2\mathcal{G}_{p_0,p_0}^{0,0} - 2\overline{d}_1\overline{p}_0\left(\mathcal{G}_{d_1,p_0}^{0,0} + \mathcal{G}_{p_0,d_1}^{0,0}\right)\\ &- \overline{d}_1\overline{p}\sum_{\alpha=1}^{3}\left(\lambda_\alpha^*\mathcal{G}_{d_1,p_\alpha}^{0,1} + \lambda_\alpha\mathcal{G}_{d_1,p_\alpha}^{0,P-1} + \lambda_\alpha^*\mathcal{G}_{p_\alpha,d_1}^{P-1,0} + \lambda_\alpha\mathcal{G}_{p_\alpha,d_1}^{1,0}\right)\\ &- \frac{\overline{p}_0\overline{p}}{2}\sum_{\alpha=1}^{3}\left(\lambda_\alpha^*\mathcal{G}_{p_0,p_\alpha}^{0,1} + \lambda_\alpha\mathcal{G}_{p_0,p_\alpha}^{0,P-1} + \lambda_\alpha^*\mathcal{G}_{p_\alpha,p_0}^{P-1,0} + \lambda_\alpha\mathcal{G}_{p_\alpha,p_0}^{1,0}\right)\\ &- \frac{\overline{p}^2}{4}\sum_{\alpha,\beta=1}^{3}\left(\lambda_\alpha^*\lambda_\beta^*\mathcal{G}_{p_\alpha,p_\beta}^{P-1,1} + \lambda_\alpha^*\lambda_\beta\mathcal{G}_{p_\alpha,p_\beta}^{P-1,P-1} + \lambda_\alpha\lambda_\beta^*\mathcal{G}_{p_\alpha,p_\beta}^{1,1} + \lambda_\alpha\lambda_\beta\mathcal{G}_{p_\alpha,p_\beta}^{1,P-1}\right).\end{aligned} \tag{C.14b}$$

C.1 Antiferromagnetic mean-field ground states

AFM saddle points are defined by the periodicity $P = 2$, i.e., $\boldsymbol{Q} \in \{(\pi,0,0)^\top, (\pi,\pi,0)^\top, (\pi,\pi,\pi)^\top\}$ in addition to its lower-dimensional and symmetry equivalents. Consequently it is $a,b \in \{0,1\}$ and we need to sum up all equivalent Fourier coefficients, i.e., odd and even ones respectively in accordance with Equation (5.39).

Bosonic part

The bosonic part of the fluctuation matrix is found with Equation (5.40b), yielding

$$\left[\underline{\mathcal{M}}^B\right]^{0,0}_{\mathrm{AFM}} = \left[\underline{\mathcal{M}}^B\right]^{1,1}_{\mathrm{AFM}} = \frac{1}{2}\begin{pmatrix} 2U-4\overline{\beta}_0 & \omega_n & 0 & -4\overline{d}_1 & 0 & 0 & 0 & 0 & 0 & 0 \\ -\omega_n & 2U-4\overline{\beta}_0 & 0 & 0 & 0 & 0 & 0 & 0 & 0 & 0 \\ 0 & 0 & -2\overline{\beta}_0 & -2\overline{p}_0 & 0 & 0 & 0 & 0 & 0 & 0 \\ -4\overline{d}_1 & 0 & -2\overline{p}_0 & 0 & 0 & 0 & 0 & 0 & 0 & 0 \\ 0 & 0 & 0 & 0 & -2\overline{\beta}_0 & -2\overline{p}_0 & 0 & 0 & 0 & 0 \\ 0 & 0 & 0 & 0 & -2\overline{p}_0 & 0 & 0 & 0 & 0 & 0 \\ 0 & 0 & 0 & 0 & 0 & 0 & -2\overline{\beta}_0 & -2\overline{p}_0 & 0 & 0 \\ 0 & 0 & 0 & 0 & 0 & 0 & -2\overline{p}_0 & 0 & 0 & 0 \\ 0 & 0 & 0 & 0 & 0 & 0 & 0 & 0 & -2\overline{\beta}_0 & -2\overline{p}_0 \\ 0 & 0 & 0 & 0 & 0 & 0 & 0 & 0 & -2\overline{p}_0 & 0 \end{pmatrix}, \tag{C.15a}$$

$$\left[\underline{\mathcal{M}}^B\right]^{0,1}_{\mathrm{AFM}} = \left[\underline{\mathcal{M}}^B\right]^{1,0}_{\mathrm{AFM}} = L_{\mu\nu,-1} + L_{\mu\nu,1} = \frac{1}{2}\begin{pmatrix} 0 & 0 & 0 & 0 & 0 & 0 & 0 & 0 & 0 & 0 \\ 0 & 0 & 0 & 0 & 0 & 0 & 0 & 0 & 0 & 0 \\ 0 & 0 & 0 & 0 & -\overline{\beta} & -\overline{p} & 0 & 0 & 0 & 0 \\ 0 & 0 & 0 & 0 & -\overline{p} & 0 & 0 & 0 & 0 & 0 \\ 0 & 0 & -\overline{\beta} & -\overline{p} & 0 & 0 & 0 & 0 & 0 & 0 \\ 0 & 0 & -\overline{p} & 0 & 0 & 0 & 0 & 0 & 0 & 0 \\ 0 & 0 & 0 & 0 & 0 & 0 & 0 & 0 & 0 & 0 \\ 0 & 0 & 0 & 0 & 0 & 0 & 0 & 0 & 0 & 0 \\ 0 & 0 & 0 & 0 & 0 & 0 & 0 & 0 & 0 & 0 \\ 0 & 0 & 0 & 0 & 0 & 0 & 0 & 0 & 0 & 0 \end{pmatrix}. \tag{C.15b}$$

Since $p_2 = p\sin(\boldsymbol{Q}\boldsymbol{R}_i) = 0$, the magnetization is polarized towards the x-direction and matrix elements that couple to p_2 and β_2 vanish with the Fourier coefficient sum. As a consequence, the longitudinal spin fields (p_1, β_1) couple to the charge fields, while the transversal spin fields (p_2, β_2) and (p_3, β_3) remain decoupled and block diagonal.

Pseudofermionic part

Summing up all equivalent Fourier coefficients yields

$$\underline{z}^1_0 = \underline{z}_{0,-1} + \underline{z}_{0,1}\,, \tag{C.16a}$$

$$\underline{z}^0_\mu = \underline{z}_{\mu,-2} + \underline{z}_{\mu,0} + \underline{z}_{\mu,2}\,, \tag{C.16b}$$

$$\underline{z}^1_{\mu} = \underline{z}_{\mu,-1} + \underline{z}_{\mu,1} \,, \tag{C.16c}$$

$$\underline{z}^0_{\mu\nu} = \underline{z}_{\mu\nu,-2} + \underline{z}_{\mu\nu,0} + \underline{z}_{\mu\nu,2} \,, \tag{C.16d}$$

$$\underline{z}^1_{\mu\nu} = \underline{z}_{\mu\nu,-3} + \underline{z}_{\mu\nu,-1} + \underline{z}_{\mu\nu,1} + \underline{z}_{\mu\nu,3} \,. \tag{C.16e}$$

Based on Reference [55], we provide a list of all coefficient matrices. In the following, the indices μ, ν represent charge fields $\psi^c \in \{p_0, d_1, d_2\}$ while the spin fields p_1, p_2, p_3 are denoted explicitly.
Zeroth derivatives:

$$\underline{z}^0_0 = \mathcal{Z}_+\Big|_{\underline{\psi}} \underline{\tau}^0 \,, \quad \underline{z}^1_0 = \mathcal{Z}_-\Big|_{\underline{\psi}} \underline{\tau}^1 \,. \tag{C.17a}$$

First derivatives:

$$\begin{gathered} \underline{z}^0_{\mu} = \frac{\partial \mathcal{Z}_+}{\partial \psi^c_\mu}\Big|_{\underline{\psi}} \underline{\tau}^0 \,, \quad \underline{z}^0_{p_1} = \frac{\partial \mathcal{Z}_-}{\partial p}\Big|_{\underline{\psi}} \underline{\tau}^1 \,, \quad \underline{z}^0_{p_2} = \frac{\mathcal{Z}_-}{p}\Big|_{\underline{\psi}} \left[\underline{\tau}^2\right]^\top \,, \quad \underline{z}^0_{p_3} = \frac{\mathcal{Z}_-}{p}\Big|_{\underline{\psi}} \underline{\tau}^3 \,, \\ \underline{z}^1_{\mu} = \frac{\partial \mathcal{Z}_-}{\partial \psi^c_\mu}\Big|_{\underline{\psi}} \underline{\tau}^1 \,, \quad \underline{z}^1_{p_1} = \frac{\partial \mathcal{Z}_+}{\partial p}\Big|_{\underline{\psi}} \underline{\tau}^0 \,, \quad \underline{z}^1_{p_2} = \underline{z}^1_{p_3} = 0 \,. \end{gathered} \tag{C.17b}$$

Second derivatives:

$$\begin{gathered} \underline{z}^0_{\mu\nu} = \frac{\partial^2 \mathcal{Z}_+}{\partial \psi^c_\mu \partial \psi^c_\nu}\Big|_{\underline{\psi}} \underline{\tau}^0 \,, \quad \underline{z}^0_{\mu p_1} = \frac{\partial^2 \mathcal{Z}_-}{\partial p \partial \psi^c_\mu}\Big|_{\underline{\psi}} \underline{\tau}^1 \,, \quad \underline{z}^0_{\mu p_2} = \frac{\partial \mathcal{Z}_-}{p \partial \psi^c_\mu}\Big|_{\underline{\psi}} \left[\underline{\tau}^2\right]^\top \,, \quad \underline{z}^0_{\mu p_3} = \frac{\partial \mathcal{Z}_-}{p \partial \psi^c_\mu}\Big|_{\underline{\psi}} \underline{\tau}^3 \,, \\ \underline{z}^0_{p_1 p_1} = \frac{\partial^2 \mathcal{Z}_+}{\partial p^2}\Big|_{\underline{\psi}} \underline{\tau}^0 \,, \quad \underline{z}^0_{p_2 p_2} = \underline{z}^0_{p_3 p_3} = \frac{\partial \mathcal{Z}_+}{p \partial p}\Big|_{\underline{\psi}} \underline{\tau}^0 \,, \quad \underline{z}^0_{p_1 p_2} = \underline{z}^0_{p_1 p_3} = \underline{z}^0_{p_2 p_3} = 0 \,, \\ \underline{z}^1_{\mu\nu} = \frac{\partial^2 \mathcal{Z}_-}{\partial \psi^c_\mu \partial \psi^c_\nu}\Big|_{\underline{\psi}} \underline{\tau}^1 \,, \quad \underline{z}^1_{\mu p_1} = \frac{\partial^2 \mathcal{Z}_+}{\partial p \partial \psi^c_\mu}\Big|_{\underline{\psi}} \underline{\tau}^0 \,, \quad \underline{z}^1_{\mu p_2} = \underline{z}^1_{\mu p_3} = 0 \,, \\ \underline{z}^1_{p_1 p_1} = \frac{\partial^2 \mathcal{Z}_-}{\partial p^2}\Big|_{\underline{\psi}} \underline{\tau}^1 \,, \quad \underline{z}^1_{p_2 p_2} = \underline{z}^1_{p_3 p_3} = \left(\frac{\partial \mathcal{Z}_-}{p \partial p} - \frac{\mathcal{Z}_-}{p^2}\right)\Big|_{\underline{\psi}} \underline{\tau}^1 \,, \\ \underline{z}^1_{p_1 p_2} = \left(\frac{\partial \mathcal{Z}_-}{p \partial p} - \frac{\mathcal{Z}_-}{p^2}\right)\Big|_{\underline{\psi}} \left[\underline{\tau}^2\right]^\top \,, \quad \underline{z}^1_{p_1 p_3} = \left(\frac{\partial \mathcal{Z}_-}{p \partial p} - \frac{\mathcal{Z}_-}{p^2}\right)\Big|_{\underline{\psi}} \underline{\tau}^3 \,, \quad \underline{z}^1_{p_2 p_3} = 0 \,. \end{gathered} \tag{C.17c}$$

Finally, we illustrate the matrix construction featuring the dyadic product with a simple example

$$\left[\underline{\boldsymbol{Z}}^\dagger_{\mu\nu}\right]^b \otimes \left[\underline{\mathcal{H}}_{k+aQ} \underline{\boldsymbol{Z}}^a_0\right]\Big|_{b=0,a=0} = \begin{pmatrix} \left[\underline{Z}^0_{\mu\nu}\right]^\dagger \underline{\mathcal{H}}_k \underline{Z}^0_0 & \left[\underline{Z}^0_{\mu\nu}\right]^\dagger \underline{\mathcal{H}}_{k+Q} \underline{Z}^1_0 \\ \left[\underline{Z}^1_{\mu\nu}\right]^\dagger \underline{\mathcal{H}}_k \underline{Z}^0_0 & \left[\underline{Z}^1_{\mu\nu}\right]^\dagger \underline{\mathcal{H}}_{k+Q} \underline{Z}^1_0 \end{pmatrix} , \tag{C.18a}$$

$$\left[\underline{\boldsymbol{Z}}^\dagger_{\mu\nu}\right]^b \otimes \left[\underline{\mathcal{H}}_{k+aQ} \underline{\boldsymbol{Z}}^a_0\right]\Big|_{b=0,a=1} = \begin{pmatrix} \left[\underline{Z}^0_{\mu\nu}\right]^\dagger \underline{\mathcal{H}}_{k+Q} \underline{Z}^1_0 & \left[\underline{Z}^0_{\mu\nu}\right]^\dagger \underline{\mathcal{H}}_k \underline{Z}^0_0 \\ \left[\underline{Z}^1_{\mu\nu}\right]^\dagger \underline{\mathcal{H}}_{k+Q} \underline{Z}^1_0 & \left[\underline{Z}^1_{\mu\nu}\right]^\dagger \underline{\mathcal{H}}_k \underline{Z}^0_0 \end{pmatrix} , \tag{C.18b}$$

$$\left[\underline{\boldsymbol{Z}}^\dagger_{\mu\nu}\right]^b \otimes \left[\underline{\mathcal{H}}_{k+aQ} \underline{\boldsymbol{Z}}^a_0\right]\Big|_{b=1,a=0} = \begin{pmatrix} \left[\underline{Z}^1_{\mu\nu}\right]^\dagger \underline{\mathcal{H}}_k \underline{Z}^0_0 & \left[\underline{Z}^1_{\mu\nu}\right]^\dagger \underline{\mathcal{H}}_{k+Q} \underline{Z}^1_0 \\ \left[\underline{Z}^0_{\mu\nu}\right]^\dagger \underline{\mathcal{H}}_k \underline{Z}^0_0 & \left[\underline{Z}^0_{\mu\nu}\right]^\dagger \underline{\mathcal{H}}_{k+Q} \underline{Z}^1_0 \end{pmatrix} , \tag{C.18c}$$

$$\left[\underline{\boldsymbol{Z}}^\dagger_{\mu\nu}\right]^b \otimes \left[\underline{\mathcal{H}}_{k+aQ} \underline{\boldsymbol{Z}}^a_0\right]\Big|_{b=1,a=1} = \begin{pmatrix} \left[\underline{Z}^1_{\mu\nu}\right]^\dagger \underline{\mathcal{H}}_{k+Q} \underline{Z}^1_1 & \left[\underline{Z}^1_{\mu\nu}\right]^\dagger \underline{\mathcal{H}}_k \underline{Z}^0_0 \\ \left[\underline{Z}^0_{\mu\nu}\right]^\dagger \underline{\mathcal{H}}_{k+Q} \underline{Z}^1_0 & \left[\underline{Z}^0_{\mu\nu}\right]^\dagger \underline{\mathcal{H}}_k \underline{Z}^0_0 \end{pmatrix} . \tag{C.18d}$$

C.2 Ferromagnetic mean-field ground states

For a FM saddle point, it is $\boldsymbol{Q} = 0$, $P = 1$ and thus $a = b = 0$, i.e., the basis is spatially uniform like in the PM case. Consequently, all Fourier coefficients are equal and need to be summed up. In order to do so, we may use the results of the previous section

$$\underline{\mathcal{M}}^B_{\mathrm{FM}} = \left[\underline{\mathcal{M}}^B\right]^{0,0}_{\mathrm{AFM}} + \left[\underline{\mathcal{M}}^B\right]^{0,1}_{\mathrm{AFM}} , \tag{C.19a}$$

$$\underline{z}_0\Big|_{\mathrm{FM}} = \underline{z}^0_0\Big|_{\mathrm{AFM}} + \underline{z}^1_0\Big|_{\mathrm{AFM}} , \tag{C.19b}$$

$$\underline{z}_\mu\Big|_{\mathrm{FM}} = \underline{z}^0_\mu\Big|_{\mathrm{AFM}} + \underline{z}^1_\mu\Big|_{\mathrm{AFM}} , \tag{C.19c}$$

$$\underline{z}_{\mu\nu}\Big|_{\mathrm{FM}} = \underline{z}^0_{\mu\nu}\Big|_{\mathrm{AFM}} + \underline{z}^1_{\mu\nu}\Big|_{\mathrm{AFM}} . \tag{C.19d}$$

In the limit $p \to 0$ and $\beta \to 0$, the theory reduces to fluctuations around a PM saddle point as derived in Section 5.2.1.

Appendix D

On the numerical implementation and performance

A significant amount of my Ph.D. time was spent to numerically implement SB mean-field and fluctuation equations, to optimize the performance, and to analyze the respective results. The following therefore shares insights gained during that time on how to effectively fulfill these numerical tasks.

In that regard, we want to acknowledge Markus Legner, who provided a working C++ code to evaluate PM mean-field saddle point equations and PM fluctuations. In close collaboration with Michael Klett and Jannis Seufert, we further developed the numerics in C++ to encompass magnetic MFs, respective fluctuations, and implemented the novel applications presented within this thesis. We want to also acknowledge Florian Goth, who was a major help in regard of performance optimization. Publishing a unified, fully documented code in collaboration with all developers is considered as a future project.

D.1 Minimization algorithm

A (magnetic) SB mean-field solution is determined by the saddle points of the grand potential (GP) [Equation (4.21)] or free energy (FE) [Equations (4.27) and (4.28)], where the respective potential needs to be minimized w.r.t. the SB parameters and maximized w.r.t. the Lagrange multipliers (LMs). The ground state is given by the respective global minimum, which makes the extremization a non-trivial problem because a general analytical solution cannot be obtained and numerical algorithms are susceptible to converge towards local rather than global minima.

To determine saddle point solutions, we applied the simplex algorithm provided by the GNU Scientific Library within `gsl_multimin.h` [320]. Thereby, we performed a full maximization (i.e., minimization of the potential times a minus sign) w.r.t. the Lagrange multipliers (i.e., β, β_0, and μ_0/μ_{eff} in case of the FE) between every minimization step, which effectively yields a minimization on the constrained subspace. As shown in Section 4.4.1, the potentials are concave functions of the LMs, i.e., the maximization is unique and converges quickly. The minimization algorithm may, however, become stuck in a local minimum rather than the global one. For the PM saddle point equations (i.e., β and p are explicitly set to zero and do not participate in the minimization), this is a minor issue because there is usually only a single minimum according to our numerical experience with the models presented within this thesis[1]. For the magnetic saddle point equations it is, however, a different story and local minima as a function of the order parameter p and ordering vector $\boldsymbol{Q}$ are common for finite doping.

The following algorithm has proven quite successful to find the global minimum for models without spin-orbit coupling (SOC), where $\boldsymbol{Q}$ can be tuned as a continuous parameter:

[1] The only parameter regime where we identified two distinct minima of the FE within the PM description is in proximity to the Mott limit ($n \approx 1$) of the PM Hubbard model at high temperatures, with minima for $d = 0$ and $d \neq 0$ respectively.

1. Sample the ordering vector $\boldsymbol{Q}$ on the high symmetry lines (HSLs) with N_{HSL} equally distributed points, such that $\boldsymbol{Q} \to Q$ becomes a scalar quantity on these lines[1].
2. Perform a minimization at each sample point for constant Q with two different sets of starting parameters (e, p_0, p, d), one of which featuring a small magnetic order parameter ($p \approx 0.1$) and the second featuring a large one ($p \approx 0.5$)[2].
3. Choose the global minimum of the FE (or equivalently GP) from all previously calculated saddle points and perform a minimization, where Q is added to the simplex algorithm as a continuous variable on the respective HSL[3].
4. Compare the resulting saddle point energy with the ground state energy of an explicit PM calculation (i.e., without dependence on $\boldsymbol{Q}$,p, β) and pick the lower one as the global minimum[4].

For many applications, however, sampling only the high symmetry points (HSPs) or excluding certain HSLs may be sufficient and should be considered to save calculation time. The above algorithm is especially recommended in the situation of multiple competing magnetic phases. In that context it is helpful to gain an intuition by plotting the FE as function of $\boldsymbol{Q}$ and p (while minimizing w.r.t. all other parameters).

D.2 Performance optimization

To boost the performance of the code, we need to identify the computational bottleneck, which is usually a momentum sum in condensed matter physics. In our case the calculation of the pseudofermion (PF) part of the FE [or equally GP, i.e., Equations (4.24) and (4.20)] for the MF and the PF part of the fluctuation matrix [i.e., Equations (5.30) and (5.43)] for the Gaussian fluctuations. The bottlenecks are, therefore, the respective integrands, which need to be evaluated on a discrete mesh of N^d momenta in the Brillouin zone (BZ), with d being the spatial dimension. In order to save calculation time, consider the following remarks.

Analytical vs. numerical diagonalization

If possible, implement analytic solutions for eigenvalues of the MF-renormalized Hamiltonian. These can, e.g., be obtained for magnetic saddle points of the Hubbard model and PAM, as shown in Appendix B, which comes along with a significant speed boost compared to the application of numerical diagonalization algorithms.

Momentum grid

Avoid unnecessary function calls in the integrands by storing data in advance that is called multiple times during a calculation (*time–memory trade-off*). In concrete terms, we save relevant data on a grid of N discrete integers $n_i \in [0, 1, ...N-1]$ per dimension d that represent the possible momenta $k_i = 2\pi n_i/N$ in the BZ of a simple cubic lattice. The corresponding momentum sum is to be performed over the respective N^d momenta.

[1] The HSLs for a simple cubic lattice are $\Gamma - X - M - \Gamma$ in 2D and $\Gamma - X - M - \Gamma - R - M - X - R$ in 3D.
[2] To be even safer to find the global minimum, this could be repeated multiple times with random starting parameters. However, the suggested procedure is mostly sufficient according to our numerical experience. In proximity to expected Mott physics, it is recommended to also implement two sets of starting parameters, with $d = 0$ and $d > 0$.
[3] This process refines the solution due to the continuous Q, which is relevant for incommensurate magnetism and the calculation of the compressibility [Equation (4.42)] by means of the finite difference method.
[4] This is important to track first-order transitions from the PM to a non-magnetic ground state. Also, the PM minimization converges quickly and serves as a benchmark/consistency check of the magnetic solution in the limit $p \to 0$.

Application for the MF: Renormalized MF eigenvalues that enter the integrand depend on the dispersion $\xi_{\boldsymbol{k}}$ of the free system, which contains trigonometric functions that are numerically costly. Therefore $\xi_{\boldsymbol{k}}, \xi_{\boldsymbol{k}+\boldsymbol{Q}}$, and related quantities should be stored on the momentum grid to avoid such function calls during the minimization procedure in order to significantly reduce the calculation time[1]. Moreover, the dependence on MF parameters can be reduced to the variables $\mathcal{Z}_+, \mathcal{Z}_-, \beta_0, \beta, \mu_0$ (compare Table 4.1). Suitable functions of these parameters can also be prestored, but need to be updated every time before evaluating of the sum.

Application for the fluctuations: Storing data in advance can drastically reduce computation time if it is desired to determine the fluctuation matrix $\mathcal{M}_{\mu,\nu}(\boldsymbol{q}, \omega)$ at multiple momenta or frequencies at the same saddle point. Thereby, we save the eigensystem $(\varepsilon_{\boldsymbol{k}}, \underline{U}_{\boldsymbol{k}})$ and corresponding values of the Fermi-Dirac distribution $n_{\mathrm{F}}(\varepsilon_{\boldsymbol{k}})$ of the MF Hamiltonian, as well as the bare Hamiltonian $\mathcal{H}_{\boldsymbol{k}}$ on the momentum-grid. This same grid can now be applied to calculate the fluctuation matrix at multiple different momenta if $\boldsymbol{q}$ is chosen such that $\boldsymbol{k}+\boldsymbol{q}$ is also a grid point. This procedure enormously saves calculation time in regard of the weight matrices $\mathcal{W}^{s,s'}$ that enter Equations (5.30) and (5.43). If $\mathcal{M}_{\mu,\nu}$ is calculated at constant momentum for different frequencies ω, the weight matrices as a whole can be stored to further optimize.

Lattice symmetries and reduced momentum integration

It is well known, that lattice symmetries can be utilized to effectively express momentum sums through only a fraction of the BZ, while the rest can be recovered via symmetry transformations from the respective irreducible wedge. This can, e.g., be exploited in the momentum sum of the MF free energy in order to save calculation time. With four-fold rotation and mirror symmetry (C_{4v} symmetry), coinciding with the models discussed within this thesis, the irreducible portion of the BZ is 1/8 in 2D and 1/48 in 3D and applicable to magnetic ordering vectors $\boldsymbol{Q}$ that do not break the C_{4v} symmetry (i.e., PM, FM, and AFM). Thereby, HSPs, HSLs, and other remaining points are scaled by weight factors (i.e., the number of symmetry-equivalent points) that are listed in the following and need to be considered as proportionality factors during the momentum sum[2]:

Two dimensions: Weight 1: HSPs (Γ, M); Weight 2: HSP (X); Weight 4: HSLs (Γ-X, X-M, M-Γ, excluding the HSPs); Weight 8: Remaining triangle with $k_x \in (0,\pi) \wedge k_y < k_x$, excluding the HSLs.

Three dimensions: Weight 1: HSPs (Γ, R); Weight 3: HSPs (X, M); Weight 6: HSLs (Γ-X, M-R); Weight 8: HSL (Γ-R); Weight 12: HSLs (Γ-M, X-M, X-R); Weight 24 for the four triangular surfaces cornered by the HSLs: $k_x \in (0,\pi) \wedge k_y < k_x \wedge k_z = 0$, $k_x \in (0,\pi) \wedge k_y < k_x \wedge k_z = k_y$, $k_x \in (0,\pi) \wedge k_y = k_x \wedge k_z < k_x$, $k_x = \pi \wedge k_y \in (0,\pi) \wedge k_z < k_y$; Weight 48 for the enclosed volume of the triangular pyramid, i.e., $k_x \in (0,\pi) \wedge k_y < k_x \wedge k_z < k_y$.

Parallelization

The code can conveniently be parallelized, e.g., by using OpenMP. It is usually most efficient to parallelize the evaluation of different input parameters, but also parallelizing the momentum sum can be effective if the integration grid is not too small.

[1] If Q is included as a continuous parameter of the simplex minimization algorithm, we have to either calculate ξ_{k+Q} without the grid (not recommended) or employ a very large grid of ξ_k to extract ξ_k and ξ_{k+Q} accurately for every $\boldsymbol{Q}$ and respective discretized momenta of the summation.

[2] Be aware of the correct integral normalization, i.e., $(2N)^d$, if there are N discretized momenta between Γ and X and d spatial dimensions.

D.3 Pitfalls to avoid

Last but not least, consider the following remarks to avoid pitfalls during the numerical implementation or data analysis:

- **Benchmark results with certain known limits in order to eliminate implementation errors:** For the MF minimization, e.g., the analytical solution for the half-filled Hubbard model [53], or the PM and non-interacting limit (Table 4.1). Moreover, the PM limit of the magnetic fluctuation matrix has been established in Section 5.2.2. Also, consider the consistency checks discussed in Chapter 13.
- **Make sure that results from the parallelized code are recovered without parallelization in order to eliminate possible errors from race conditions.**
- **Choose efficient basis of MFs and consistent starting values for the simplex minimization algorithm:** Apply the substitutions suggested in Section 4.4.3 to reduce the number of minimization parameters for the FE. This is especially required for the Hubbard model to guarantee convergence. For a correct evaluation of fluctuations, one has to resubstitute according to Equations (4.27c) and (4.30c) at the respective saddle point. Moreover, the starting values of the SBs need to satisfy all MF constraints and these quantities are required to remain positive semidefinite during the minimization process[1].
- **Be aware of local minima:** The simplex minimization may get stuck in local minima, especially for competing magnetic phases or near the Mott transition. Consider the algorithm presented in Section D.1 to seek the global minimum.
- **Perform a consistent back-folding in the context of the momentum grid:** I.e., make sure that terms like ε_{k+q} back-folded to the BZ by exploiting $\boldsymbol{k} + 2\pi n \to \boldsymbol{k}$.
- **Be aware of the convergence parameter η that yields from analytical continuation ($\mathrm{i}\omega_n \to \omega + \mathrm{i}\eta$):** Static susceptibilities can be calculated most efficiently for $\omega = \eta = 0$, and finite but arbitrarily small temperature T. In that case, however, the zero momentum limit of the occurring Lindhard function needs to be implemented according to Equation (5.31b). Finite ω requires $\eta > 0$ for convergent numerics. Remember that η does not only enter the Lindhard function but also the bosonic part of the fluctuation matrix [Equation (5.20)], and it must be consistently chosen in Equation (5.57b) for the evaluation of the conductivity.
- **Monitor the convergence of the momentum summations:** The sufficient number of integration points N^d strongly depends on the specific application. MF integrals usually converge faster than fluctuation quantities[2]. Fluctuations around gapped ground states converge much quicker than metallic states that employ a FS. In that context, an enhanced DOS at the Fermi-level requires a higher number of integration points, which makes fluctuation calculations in the context of heavy fermions in the PAM particularly challenging. Finally, finite (ω, η) usually leads to a slower convergence of the associated Lindhard function, and η should typically be much smaller than all other energy scales. Decreasing η, however, requires increasing N in order to uphold convergence, where $N \propto 1/\eta$ can act as a rule of thumb.

[1] This can, e.g., be achieved by adding a large energy penalty to the FE if this additional constraint is violated.

[2] Reasonable MF convergence for the Hubbard model and PAM can already be achieved for $N^2 \gtrsim 100^2$ and $N^3 \gtrsim 20^3$ for the AFM TKI model with exploiting the previously discussed irreducible 3D wedge, although a higher resolution is recommended to refine the results. For fluctuations, we typically applied $N^2 \gtrsim 512^2$, $N^3 \gtrsim 64^3$, dependent on the specific parameter regime.

Bibliography

[1] M. L. Cohen, "*Essay: Fifty Years of Condensed Matter Physics*", Phys. Rev. Lett. **101**, 250001 (2008).

[2] P. J. Mulvey and S. Nicholson, "*Trends in Physics PhDs*", Reports on enrollment and degrees (2014).

[3] J. D. Martin, "*When condensed-matter physics became king*", Physics Today **72**, 30 (2019).

[4] J. D. Martin, "*What's in a Name Change?: Solid State Physics, Condensed Matter Physics, and Materials Science*", Phys. Perspect. **17**, 3 (2015).

[5] Massachusetts Institute of Technology, *Physicists find a novel way to switch antiferromagnetism on and off*, 2021, URL: `https://www.sciencedaily.com/releases/2021/05/210506125748.htm` (visited on 01/31/2022).

[6] T. Jungwirth, X. Marti, P. Wadley, and J. Wunderlich, "*Antiferromagnetic spintronics*", Nature nanotechnology **11**, 231 (2016).

[7] H. Onnes, "*The Resistance of Pure Mercury at Helium Temperatures*", Commun. Phys. Lab. Univ. Leiden **12**, 1 (1911).

[8] J. G. Bednorz and K. A. Müller, "*Possible high T_c superconductivity in the Ba-La-Cu-O system*", Z. Phys. B **64**, 189 (1986).

[9] H. Nordwig, *Supraleiter-Kabel: Die Stromleitung der Zukunft?*, 2021, URL: `https://www.swr.de/wissen/supraleiter-stromkabel-100.html` (visited on 01/31/2022).

[10] L. Sharpe, *Superconducting maglev train unveiled in China*, 2021, URL: `https://eandt.theiet.org/content/articles/2021/01/superconducting-maglev-train-unveiled-in-china/` (visited on 01/31/2022).

[11] C. Nayak, S. H. Simon, A. Stern, M. Freedman, and S. Das Sarma, "*Non-Abelian anyons and topological quantum computation*", Reviews of Modern Physics **80**, 1083 (2008).

[12] S. Kirchner and S. Bühler-Paschen, "*Kondo-Mania*", Physik in unserer Zeit **53**, 142 (2022).

[13] H. Davy and J. Davy, *The collected works of Sir Humphry Davy*, (Smith, Elder & Co., 1839)

[14] P. Drude, "*Zur Elektronentheorie der Metalle*", Annalen der Physik **306**, 566 (1900).

[15] E. Schrödinger, "*An undulatory theory of the mechanics of atoms and molecules*", Physical Review **28**, 1049 (1926).

[16] W. Pauli, "*Über den Zusammenhang des Abschlusses der Elektronen-gruppen im Atom mit der Komplexstruktur der Spektren*", Z. Physik **31**, 765 (1925).

[17] E. Fermi, "*Zur Quantelung des idealen einatomigen Gases*", Zeitschrift für Physik **36**, 902 (1926).

[18] A. Sommerfeld, "*Zur Elektronentheorie der Metalle auf Grund der Fermischen Statistik*", Zeitschrift für Physik **47**, 1 (1928).

[19] C. Kittel, *Introduction to solid state physics (8th ed.)* (John Wiley & Sons, 2004)

[20] W. Friedrich, P. Knipping, and M. Laue, "*Interferenzerscheinungen bei Röntgenstrahlen*", Annalen der Physik **346**, 971 (1913).

[21] W. H. Bragg and W. L. Bragg, "*The reflection of X-rays by crystals*", Proceedings of the Royal Society of London. Series A: Mathematical, Physical and Engineering Sciences **88**, 428 (1913).

[22] F. Bloch, "*Über die Quantenmechanik der Elektronen in Kristallgittern*", Zeitschrift für Physik **52**, 555 (1929).

[23] L. D. Landau, "*The theory of a Fermi liquid*", Sov. Phys. JETP **3**, 920 (1957).

[24] P. W. Anderson, "*More Is Different. Broken symmetry and the nature of the hierarchical structure of science.*", Science **177**, 4047 (1972).

[25] L. D. Landau, "*On the theory of phase transitions*", Zh. Eksp. Teor. Fiz. **7**, 19 (1937).

[26] E. Ising, "*Beitrag zur Theorie des Ferromagnetismus*", Zeitschrift für Physik **31**, 253 (1925).

[27] M. L. Néel, "*Propriétés magnétiques des ferrites ; ferrimagnétisme et antiferromagnétisme*", Annales de Physique **12**, 137 (1948).

[28] J. Bardeen, L. N. Cooper, and J. R. Schrieffer, "*Theory of Superconductivity*", Phys. Rev. **108**, 1175 (1957).

[29] W. J. D. Haas, J. D. Boer, and G. V. D. Berg, "*The electrical resistance of gold, copper and lead at low temperatures*", Physica **34**, 1115 (1934).

[30] J. Kondo, "*Resistance Minimum in Dilute Magnetic Alloys*", Progress of Theoretical Physics **32**, 37 (1964).

[31] K. V. Klitzing, G. Dorda, and M. Pepper, "*New Method for High-Accuracy Determination of the Fine-Structure Constant Based on Quantized Hall Resistance*", Phys. Rev. Lett. **45** (1980).

[32] M. Dzero, K. Sun, V. Galitski, and P. Coleman, "*Topological Kondo Insulators*", Phys. Rev. Lett. **104**, 105408 (2010).

[33] W. Kohn and L. J. Sham, "*Self-consistent equations including exchange and correlation effects*", Physical Review **140**, A1133 (1965).

[34] R. O. Jones, "*Density functional theory: Its origins, rise to prominence, and future*", Rev. Mod. Phys. **87**, 897 (2015).

[35] J. Hubbard, "*Electron correlations in narrow energy bands*", Proc. R. Soc. London, Ser. A **276**, 238 (1963).

[36] Editorial, "*The Hubbard model at half a century*", Nature Physics **9**, 523 (2013).

[37] A. Weiße and H. Fehske, "*Exact Diagonalization Techniques*", *Computational Many-Particle Physics. Lecture Notes in Physics*, vol. 739, (Springer, Berlin, Heidelberg, 2008) pp. 529–544.

[38] C. N. Varney *et al.*, "*Quantum Monte Carlo study of the two-dimensional fermion Hubbard model*", Phys. Rev. B **80** (2009).

[39] H. Bruus and K. Flensberg, *Many-body quantum theory in condensed matter physics*, (2002)

[40] A. Georges, G. Kotliar, W. Krauth, and M. J. Rozenberg, "*Dynamical mean-field theory of strongly correlated fermion systems and the limit of infinite dimensions*", Rev. Mod. Phys. **68**, 13 (1996).

[41] B.-X. Zheng and K.-L. C. Garnet, "*Ground-state phase diagram of the square lattice Hubbard model from density matrix embedding theory*", Phys. Rev. B **93**, 35126 (2016).

[42] C. Platt, W. Hanke, and R. Thomale, "*Functional Renormalization Group for multi-orbital Fermi Surface Instabilities*", Advances in Physics **62**, 453 (2013).

[43] T. Holstein and H. Primakoff, "*Field Dependence of the Intrinsic Domain Magnetization of a Ferromagnet*", Phys. Rev. **58**, 1098 (1940).

[44] J. Schwinger, *On angular momentum*, tech. rep., 1952.

[45] A. A. Abrikosov, "*Electron scattering on magnetic impurities in metals and anomalous resistivity effects*", Physics Physique Fizika **2**, 5 (1965).

[46] S. E. Barnes, "*New method for the Anderson model*", J. Phys. F: Metal Phys **6**, 1375 (1976).

[47] P. Coleman, "*New approach to the mixed-valence problem*", Phys. Rev. B **29**, 3035 (1984).

[48] P. Coleman, *Introduction to Many-Body Physics*, (Cambridge University Press, 2015)

[49] G. Kotliar and A. E. Ruckenstein, "*New functional integral approach to strongly correlated fermi systems: The gutzwiller approximation as a saddle point*", Physical Review Letters **57**, 1362 (1986).

[50] R. Frésard and P. Wölfle, "*Unified Slave Boson Representation of Spin and Charge Degrees of Freedom for Strongly Correlated Fermi Systems*", International Journal of Modern Physics B **6**, 685 (1992).

[51] F. Lechermann, A. Georges, G. Kotliar, and O. Parcollet, "*Rotationally invariant slave-boson formalism and momentum dependence of the quasiparticle weight*", Phys. Rev. B **76**, 1 (2007).

[52] T. H. Lee, N. Lanatà, M. Kim, and G. Kotliar, "*Efficient Slave-Boson Approach for Multiorbital Two-Particle Response Functions and Superconductivity*", Physical Review X **11**, 041040 (2021).

[53] D. Riegler, M. Klett, T. Neupert, R. Thomale, and P. Wölfle, "*Slave-boson analysis of the two-dimensional Hubbard model*", Phys. Rev. B **101**, 235137 (2020).

[54] M. Klett *et al.*, "*Topology and magnetism in the Kondo insulator phase diagram*", Phys. Rev. B(R) **101**, 161112 (2020).

[55] J. Seufert, D. Riegler, M. Klett, R. Thomale, and P. Wölfle, "*Breakdown of charge homogeneity in the two-dimensional Hubbard model: Slave-boson study of magnetic order*", Phys. Rev. B **103**, 165117 (2021).

[56] M. Klett, D. Riegler, R. Thomale, and P. Wölfle, "*Emerging Kondo regime in the periodic Anderson model*", in preparation (2022).

[57] M. Klett, "*Auxiliary particle approach for strongly correlated electrons. How interactions shape order*", PhD thesis, University of Würzburg, 2021.

[58] J. Hubbard, "*Electron correlations in narrow energy bands III. An improved solution.*", Proc. R. Soc. London, Ser. A **281**, 401 (1964).

[59] P. Wölfle and T. Li, "*Spin fluctuation contribution to the specific heat of strongly correlated fermions*", Z. Phys. B-Condensed Matter **78**, 45 (1990).

[60] T. Li, Y. S. Sun, and P. Wölfle, "*Dynamic response functions of Hubbard model in Gutzwiller approximation*", Zeitschrift für Physik B Condensed Matter **82**, 369 (1991).

[61] W. Zimmermann, R. Frésard, and P. Wölfle, "*Spin and charge structure factor of the two-dimensional Hubbard model*", Phys. Rev. B **56**, 10097 (1997).

[62] P. Anderson, "*Localized Magnetic States in Metals*", Phys. Rev. **124**, 41 (1961).

[63] A. Hewson, *The Kondo Problem to Heavy Fermions*, (Cambridge University Press, 1993)

[64] P. Dirac, "*The Quantum Theory of the Emission and Absorption of Radiation*", Proc. Roy. Soc. [A] **114**, 243 (1927).

[65] P. Jordan and E. Wigner, "*Über das Paulische Äquivalenzverbot*", Zeitschrift für Physik **47**, 631 (1928).

[66] T. Li, P. Wölfle, and P. J. Hirschfeld, "*Spin rotation invariant slave boson approach to the Hubbard model*", Phys. Rev. B **40**, 6817 (1989).

[67] B. R. Bulka, "*On Antiferromagnetism, Charge Density Wave, and Superconductivity in the Extended Hubbard Model Studied by Means of the Slave-Boson Method*", Physica Status Solidi (B) **180**, 401 (1993).

[68] B. R. Bulka and S. Robaszkiewicz, "*Superconducting properties of the attractive Hubbard model: A slave-boson study*", Physical Review B **54**, 13138 (1996).

[69] S. Weinberg, *Lectures on Quantum Mechanics*, (Cambridge University Press, 2013)

[70] F. Schwabl, *Quantenmechanik, eine Einführung*, 7th ed., (Springer-Verlag Berlin Heidelberg, 1988)

[71] R. Frésard and P. Wölfle, "*Spiral magnetic states in the large-U Hubbard model: a slave boson approach*", J. Phys.: Condens. Matter **4**, 3625 (1992).

[72] T. C. Li and W. Rasul, "*Gutzwiller dynamic susceptibility: Consequences for the transport properties of transition metals*", Phys. Rev. B **39**, 4630 (1989).

[73] R. Frésard and P. Wölfle, "*Unified Slave Boson Representation ERRATA*", International Journal of Modern Physics B **06** (1992).

[74] B. Möller and P. Wölfle, "*Magnetic order in the periodic Anderson model*", Physical Review B **48**, 10320 (1993).

[75] W. Ziegler, P. Dieterich, A. Muramatsu, and W. Hanke, "*Slave-boson study in the SU(2)-invariant representation: Coupled layers in the one-band Hubbard model*", Phys. Rev. B **53**, 1231 (1996).

[76] R. Frésard, J. Kroha, and P. Wölfle, "*The Pseudoparticle Approach to Strongly Correlated Electron Systems*", *Strongly Correlated Systems*, (Springer, Berlin, Heidelberg, 2012) pp. 65–101.

[77] E. Noether, "*Invariante Variationsprobleme*", Nachr. d. König. Gesellsch. d. Wiss. zu Göttingen, Math-phys. Klasse **1**, 235 (1918).

[78] J. Ward, "*An identity in Quantum Electrodynamics*", Phys. Rev. **78**, 182 (1950).

[79] Y. Takahashi, "*On the Generalized Ward Identity*", Nuovo Cim. **6**, 371 (1957).

[80] P. Dietrich, "*Slave-Boson-Formulierung des Hubbard-Modells und Berechnung von Fluktuationskorrekturen*", PhD thesis, University of Würzburg, 1994.

[81] A. Auerbach, *Interacting electrons and quantum magnetism*, (Springer-Verlag New York, 1994)

[82] P. A. M. Dirac, "*The Lagrangian in Quantum Mechanics*", Physikalische Zeitschrift der Sowjetunion **3**, 64 (1933).

[83] R. P. Feynman, "*Space-time approach to non-relativistic quantum mechanics*", Rev. Mod. Phys. **20**, 367 (1948).

[84] J. Schwinger, "*The Theory of Quantized Fields. IV*", Phys. Rev. **92**, 1283 (1953).

[85] D. Sherrington, "*A new method of expansion in the quantum many-body problem. III. The density field*", Proceedings of the Physical Society **91** (1967).

[86] J. W. Negle and H. Orland, *Quantum Many-Particle Systems*, (Perseus Books, 1988)

[87] R. J. Glauber, "*Coherent and Incoherent States of the Radiation Field*", Phys. Rev. **131** (1963).

[88] F. Berezin, *The Method of Second Quantization*, (Academic Press, 1966)

[89] T. E. Matsubara, "*A New Approach to Quantum-Statistical Mechanics*", Progress of Theoretical Physics **14**, 351 (1955).

[90] A. A. Abrikosov, L. P. Gor' Kov, and I. E. Dzyaloshinskii, "*On the application of quantum field theory methods to problems of quantum statistics at finite temperatures*", J. Exptl. Theoret. Phys. (U.S.S.R.) **36**, 900 (1959).

[91] L. D. Faddeev and V. N. Popov, "*Feynman diagrams for the Yang-Mills field*", Physics Letters B **25**, 29 (1967).

[92] J. Rasul and T. Li, "*One-loop corrections to the Gutzwiller approach to strongly interacting fermions, with application to liquid He*", J.Phys.C **21**, 5119 (1988).

[93] J. W. Rasul, T. Li, and H. Beck, "^{3}He *as an almost-localized Fermi liquid: Strong-coupling calculation of the superfluid transition temperature*", Phys. Rev. B **39**, 4191 (1989).

[94] M. Lavagna, "*Functional-integral approach to strongly correlated Fermi systems: Quantum fluctuations beyond the Gutzwiller approximation*", Phys. Rev. B **41**, 142 (1990).

[95] T. Li, "*Dynamical charge response function of the Hubbard model in the slave-boson approach*", Phys. Rev. B **46**, 9301 (1992).

[96] T. Jolicoeur and J. C. Le Guillou, "*Fluctuations beyond the Gutzwiller approximation in the slave-boson approach*", Phys. Rev. B(R) **44**, 43 (1991).

[97] N. Read and D. M. Newns, "*A new functional integral formalism for the degenerate Anderson model*", J. Phys. C: Solid State Phys. **16**, 1055 (1983).

[98] N. Read and D. M. Newns, "*On the solution of the Coqblin-Schrieffer Hamiltonian by the large-N expansion technique*", J. Phys. C: Solid State Phys. **16**, 3273 (1983).

[99] M. Legner, "*Topological Kondo insulators*", PhD thesis, ETH Zürich, 2016.

[100] R. Frésard and T. Kopp, "*Slave bosons in radial gauge: the correct functional integral representation and inclusion of non-local interactions*", Nuclear Physics B **594**, 769 (2001).

[101] R. Frésard and T. Kopp, "*Exact results with the Kotliar-Ruckenstein slave-boson representation*", Annalen der Physik **524**, 175 (2012).

[102] J. Bardeen, L. N. Cooper, and J. R. Schrieffer, "*Microscopic Theory of Superconductivity*", Phys. Rev. **106**, 162 (1957).

[103] E. Arrigoni and G. C. Strinati, "*Doping-induced incommensurate antiferromagnetism in a Mott-Hubbard insulator*", Phys. Rev. B **8**, 7455 (1991).

[104] R. Frésard, M. Dzierzawa, and P. Wölfle, "*Slave-Boson Approach to Spiral Magnetic Order in the Hubbard Model*", Europhys. Lett. **15**, 325 (1991).

[105] P. A. Igoshev, M. A. Timirgazin, A. K. Arzhnikov, and V. Y. Irkhin, "*Effect of electron correlations on the formation of spiral magnetic states in the two-dimensional t- t' Hubbard model*", Jetp Lett. **98**, 150 (2013).

[106] M. C. Gutzwiller, "*Effect of Correlation on the Ferromagnetism of Transition Metals*", Phys. Rev. Lett. **10**, 159 (1963).

[107] M. C. Gutzwiller, "*Correlation of Electrons in a Narrow s Band*", Phys. Rev. **137**, 1726 (1965).

[108] W. Brinkmann and T. Rice, "*Application of Gutzwiller's Variational Method to the Metal-Insulator Transition*", Phys. Rev. B **2**, 4302 (1970).

[109] D. Vollhardt, "*Normal* ^{3}He*: an almost localized Fermi liquid*", Rev. Mod. Phys. **56**, 99 (1984).

[110] G. Baym and C. Pethick, *Landau Fermi-Liquid Theory: Concepts and Applications*, (John Wiley & Sons, 1991)

[111] P. A. Igoshev, M. A. Timirgazin, A. A. Katanin, A. K. Arzhnikov, and V. Y. Irkhin, "*Incommensurate magnetic order and phase separation in the two-dimensional Hubbard model with nearest-and next-nearest-neighbor hopping*", Phys. Rev. B **81** (2010).

[112] K. Huang, *Statistical Mechanics*, (John Wiley & Sons, 1963)

[113] W. Nolting, *Grundkurs Theoretische Physik 4/2 Thermodynamik*, (Springer Berlin Heidelberg, 2016)

[114] V. H. Dao and R. Frésard, "*Collective modes in the paramagnetic phase of the Hubbard model*", Phys. Rev. B **95**, 165127 (2017).

[115] J. Goldstone, A. Salam, and S. Weinberg, "*Broken Symmetries*", Phys. Rev. **127**, 965 (1962).

[116] G. C. Wick, "*The Evaluation of the Collision Matrix*", Phys. Rev. **80**, 268 (1950).

[117] J. Seufert, "*Fluctuations around magnetic ground states from the slave-boson saddle point approximation in Hubbard-type models*", PhD thesis, 2020.

[118] R. Kubo, "*The fluctuation-dissipation theorem*", Reports on Progress in Physics **29**, 255 (1966).

[119] S. Vig *et al.*, "*Measurement of the dynamic charge response of materials using low-energy, momentum-resolved electron energy-loss spectroscopy (M-EELS)*", SciPost Phys. **3**, 1 (2017).

[120] E. H. d. S. Neto *et al.*, "*Doping-dependent charge order correlations in electron-doped cuprates*", Science Advances **2** (2016).

[121] E. Pavarini, "*Linear Response Functions*", *DMFT at 25: Infinite Dimensions Modeling and Simulation Vol. 4.* (Verlag des Forschungszentrum Jülich, Germany, 2014) chap. 6.

[122] S. Zhou, Y. Wang, and Z. Wang, "*Doublon-holon binding, Mott transition, and fractionalized antiferromagnet in the Hubbard model*", Phys. Rev. B **89**, 195119 (2014).

[123] S. Zhou, L. Liang, and Z. Wang, "*Dynamical slave-boson mean-field study of the Mott transition in the Hubbard model in the large-z limit*", Phys. Rev. B **101**, 35106 (2020).

[124] R. Frésard, *The Slave-Boson Technique*, Jülich, 2015.

[125] R. v. Baltz, "*Plasmons and Surface Plasmons in Bulk Metals, Metallic Clusters, and Metallic Heterostructures*", *Spectroscopy and Dynamics of Collective Excitations in Solids*, ed. by B. Di Bartolo and S. Kyrkos, (Springer US, 1997) pp. 303–338.

[126] M. C. T. D. Müller, "*Spin-wave excitations and electron-magnon scattering in elementary ferromagnets from ab initio many-body perturbation theory*", PhD thesis, 2017.

[127] T. Moriya, *Spin Fluctuations in Itinerant Electron Magnetism*, Springer Series in Solid-State Sciences, (Springer Berlin Heidelberg, 1985)

[128] Y.-Z. You, *MatsubaraSum*, 2017, URL: `https://github.com/EverettYou/MatsubaraSum` (visited on 06/12/2021).

[129] J. Kanamori, "*Electron Correlation and Ferromagnetism of Transition Metals*", Progress of Theoretical Physics **30** (1963).

[130] A. Altland and B. Simons, "*Interaction effects in the tight-binding system*", *Condensed Matter Field Theory*, (Cambridge University Press, 2006)

[131] L. Van Hove, "*The Occurrence of Singularities in the Elastic Frequency Distribution of a Crystal*", Phys. Rev **86**, 1189 (1952).

[132] G. Bassani and G. Parravicini, "*Interband transitions and optical properties*", *Electronic States and Optical Transitions in Solids*, (1975) chap. 5, pp. 149–176.

[133] P. A. Lee, N. Nagaosa, and X.-G. Wen, "*Doping a Mott insulator: Physics of high-temperature superconductivity*", Rev. Mod. Phys. **78**, 17 (2006).

[134] M. Greiner, O. Mandel, T. Esslinger, T. Hänsch, and I. Bloch, "*Quantum phase transition from a superfluid to a Mott insulator in a gas of ultracold atoms*", Nature **415**, 39 (2002).

[135] R. Jördens, N. Strohmaier, K. Günter, H. Moritz, and T. Esslinger, "*A Mott insulator of fermionic atoms in an optical lattice*", Nature **455**, 204 (2008).

[136] E. H. Lieb and F. Y. Wu, "*Absence of Mott transition in an exact solution of the short-range, one-band model in one dimension*", Phys. Rev. Lett. **20**, 1445 (1968).

[137] N. F. Mott, "*The Basis of the Electron Theory of Metals, with Special Reference to the Transition Metals*", Proceedings of the Physical Society. Section A **62**, 416 (1949).

[138] C. J. Halboth and W. Metzner, "*Renormalization-group analysis of the two-dimensional Hubbard model*", Phys. Rev. B **61** (2000).

[139] M. Raczkowski, R. Frésard, and A. M. Oleś, "*Slave-boson approach to the metallic stripe phases with large unit cells*", Phys. Rev. B **73** (2006).

[140] M. Kang *et al.*, "*Evolution of charge order topology across a magnetic phase transition in cuprate superconductors*", Nature Physics **15**, 335 (2019).

[141] W. Wu *et al.*, "*Pseudogap and Fermi-Surface Topology in the Two-Dimensional Hubbard Model*", Phys. Rev. X **8** (2018).

[142] N. D. Mermin and H. Wagner, "*Absence of Ferromagnetism or Antiferromagnetism in One- or Two-Dimensional Isotropic Heisenberg Models*", Phys. Rev. Lett. **17**, 1133 (1966).

[143] P. C. Hohenberg, "*Existence of Long-Range Order in One and Two Dimensions*", Physical Review **158**, 383 (1967).

[144] B. I. Halperin, "*On the Hohenberg–Mermin–Wagner Theorem and Its Limitations*", Journal of Statistical Physics **175**, 521 (2018).

[145] G. Palle and D. K. Sunko, "*Physical limitations of the Hohenberg–Mermin–Wagner theorem*", Journal of Physics A: Mathematical and Theoretical **54**, 315001 (2021).

[146] D. Van Delft and P. Kes, "*The discovery of superconductivity*", Physics Today **63**, 38 (2010).

[147] K. Onnes, "*Further experiments with liquid helium. C. On the change of electric resistance of pure metals at very low temperatures etc. IV. The resistance of pure mercury at helium temperatures*", Proceedings of the Royal Netherlands Academy of Arts and Sciences **13**, 1274 (1911).

[148] M. K. Wu *et al.*, "*Superconductivity at 93 K in a new mixed-phase Y-Ba-Cu-O compound system at ambient pressure*", Phys. Rev. Lett. **58**, 908 (1987).

[149] P. Ray, *Timeline of Superconductivity*, 2020, URL: `https://upload.wikimedia.org/wikipedia/commons/b/bb/Timeline_of_Superconductivity_from_1900_to_2015.svg` (visited on 11/01/2021).

[150] M. Maple, "*High-temperature superconductivity in layered cuprates: Overview*", *Handbook on the Physics and Chemistry of Rare Earths. Volume 30.* (Elsevier, 2000) chap. 187, pp. 1–30.

[151] R. Englman, *The Jahn-Teller effect in molecules and crystals*, (London, New York, Wiley-Interscience, 1972)

[152] V. J. Emery, "*Theory of High-T_c Superconductivity in Oxides*", Phys. Rev. Lett. **58**, 2794 (1987).

[153] G. Dopf, A. Muramatsu, and W. Hanke, "*Consistent description of high-T_c superconductors with the three-band Hubbard model*", Physical Review Letters **68**, 353 (1992).

[154] P. Cai *et al.*, "*Visualizing the evolution from the Mott insulator to a charge-ordered insulator in lightly doped cuprates*", Nature Physics **12**, 1047 (2016).

[155] M. L. Kiesel, "*Unconventional Superconductivity in Cuprates, Cobaltates and Graphene: What is Universal and what is Material-Dependent in strongly versus weakly Correlated Materials ?*", PhD thesis, University of Würzburg, 2012.

[156] P. W. Anderson, "*The resonating valence bond state in La_2CuO_4 and superconductivity*", Science **235**, 1196 (1987).

[157] W. Tabis *et al.*, "*Charge order and its connection with fermi-liquid charge transport in a pristine high-T_c cuprate*", Nat Commun **5** (2014).

[158] W. Tabis *et al.*, "*Supplementary Information: Charge order and its connection with fermi-liquid charge transport in a pristine high-T_c cuprate*", Nat Commun **5**, 1 (2014).

[159] B. Eifert and C. Heiliger, *Crystallica*, 2016, URL: `https://library.wolfram.com/infocenter/MathSource/9372/`.

[160] N. Barisic *et al.*, "*Universal sheet resistance and revised phase diagram of the cuprate high-temperature superconductors*", Proceedings of the National Academy of Sciences of the United States of America **110**, 12235 (2013).

[161] R. Arpaia and G. Ghiringhelli, "*Charge Order at High Temperature in Cuprate Superconductors*", J. Phys. Soc. Jpn. **90**, 111005 (2021).

[162] A. Damascelli, Z. Hussain, and Z. X. Shen, "*Angle-resolved photoemission studies of the cuprate superconductors*", Rev. Mod. Phys. **75**, 473 (2003).

[163] W. Hanke, M. L. Kiesel, M. Aichhorn, S. Brehm, and E. Arrigoni, "*The 3-band Hubbard-model versus the 1-band model for the high-T_c cuprates: Pairing dynamics, superconductivity and the ground-state phase diagram*", Eur. Phys. J. Spec. Top. **188**, 15 (2010).

[164] M. Imada, T. Fujimori, and Y. Tokura, "*Metal-insulator transitions*", Rev. Mod. Phys. **70**, 1039 (1998).

[165] R. Preuss, W. Hanke, C. Gröber, and H. G. Evertz, "*Pseudogaps and Their Interplay with Magnetic Excitations in the Doped 2D Hubbard Model*", Phys. Rev. Lett. **79**, 1122 (1997).

[166] D. Sénéchal, P. L. Lavertu, M. A. Marois, and A. M. Tremblay, "*Competition between Antiferromagnetism and Superconductivity in High-T_c Cuprates*", Phys. Rev. Lett. **94**, 2 (2005).

[167] T. A. Maier, M. Jarrell, T. C. Schulthess, P. R. Kent, and J. B. White, "*Systematic study of d-wave superconductivity in the 2D repulsive Hubbard model*", Phys. Rev. Lett. **95**, 1 (2005).

[168] F. C. Zhang and T. M. Rice, "*Effective Hamiltonian for the superconducting Cu oxides*", Phys. Rev. B **37**, 3759 (1988).

[169] I. J. Hamad, L. O. Manuel, and A. A. Aligia, "*Generalized One-Band Model Based on Zhang-Rice Singlets for Tetragonal CuO*", Phys. Rev. Lett. **120**, 177001 (2018).

[170] M. Hirayama, Y. Yamaji, T. Misawa, and M. Imada, "*Ab initio effective Hamiltonians for cuprate superconductors*", Phys. Rev. B **98**, 134501 (2018).

[171] N. Momono, T. Matsuzaki, T. Nagata, M. Oda, and M. Ido, "*Pseudogap Behavior in the Electronic Specific Heat of $La_{2-x}Sr_xCuO_4$*", Journal of Low Temperature Physics **117**, 353 (1999).

[172] P. Curty and H. Beck, "*Thermodynamics and Phase Diagram of High Temperature Superconductors*", Phys. Rev. Lett. **91** (2003).

[173] A. Kanigel *et al.*, "*Evolution of the pseudogap from Fermi arcs to the nodal liquid*", Nature Physics **2**, 447 (2006).

[174] S. Dal Conte *et al.*, "*Disentangling the electronic and phononic glue in a high-T_c superconductor*", Science **335**, 1600 (2012).

[175] D. J. Scalapino, "*A common thread: The pairing interaction for unconventional superconductors*", Rev. Mod. Phys. **84**, 1383 (2012).

[176] P. Prelovšek, J. Kokalj, Z. Lenarčič, and R. H. Mckenzie, "*Holon-doublon binding as the mechanism for the Mott transition*", Phys. Rev. B **92**, 235155 (2015).

[177] J. P. F. Leblanc *et al.*, "*Solutions of the Two-Dimensional Hubbard Model: Benchmarks and Results from a Wide Range of Numerical Algorithms*", Phys. Rev. X **5** (2015).

[178] M. Qin, H. Shi, and S. Zhang, "*Benchmark study of the two-dimensional Hubbard model with auxiliary-field quantum Monte Carlo method*", Phys. Rev. B **94**, 85103 (2016).

[179] A. W. Sandvik, "*Finite-size scaling of the ground-state parameters of the two-dimensional Heisenberg model*", Phys. Rev. B **65**, 11678 (1997).

[180] Y. Nagaoka, "*Ferromagnetism in a narrow, almost half-filled s band*", Phys. Rev. **147**, 392 (1966).

[181] J. P. Dehollain *et al.*, "*Nagaoka ferromagnetism observed in a quantum dot plaquette*", Nature **579**, 528 (2020).

[182] P. A. Igoshev, M. A. Timirgazin, V. F. Gilmutdinov, A. K. Arzhnikov, and V. Y. Irkhin, "*Spiral magnetism in the single-band Hubbard model: The Hartree-Fock and slave-boson approaches*", J. Phys.: Condens. Matter **27**, 446001 (2015).

[183] J. M. Tranquada, B. J. Sternlieb, J. D. Axe, Y. Nakamura, and S. Uchida, "*Evidence for stripe correlations of spins and holes in copper oxide superconductors*", Nature **375**, 561 (1995).

[184] J. M. Tranquada *et al.*, "*Coexistence of, and Competition between, Superconductivity and Charge-Stripe Order in* $La_{1.6-x}Nd_{0.4}Sr_xCuO_4$", Phys. Rev. Lett. **78**, 338 (1997).

[185] S. A. Kivelson, G. Aeppli, and V. J. Emery, "*Thermodynamics of the interplay between magnetism and high-temperature superconductivity*", Proceedings of the National Academy of Sciences **98**, 11903 (2001).

[186] A. V. Chubukov and D. M. Frenkel, "*Renormalized perturbation theory of magnetic instabilities in the two-dimensional Hubbard model at small doping*", Phys. Rev. B **46**, 11884 (1992).

[187] M. J. Rice, "*Electron-electron scattering in transition metals*", Phys. Rev. Lett. **20**, 1439 (1968).

[188] K. Kadowaki and S. B. Woods, "*Universal relationship of the resistivity and specific heat in heavy-Fermion compounds*", Solid State Communications **58**, 507 (1986).

[189] D. Bohm and D. Pines, "*A Collective Description of Electron Interactions: III. Coulomb Interactions in a Degenerate Electron Gas*", Physical Review **92**, 609 (1953).

[190] V. H. Dao and R. Frésard, "*Collective modes in the paramagnetic phase of the Hubbard model*", Phys. Rev. B **95**, 165127 (2017).

[191] J. D. Van der Waals, *The equation of state for gases and liquids*, 1910.

[192] J. Lorenzana and G. Seibold, "*Dynamic properties of inhomogeneous states in cuprates (Review Article)*", Low. Temp. Phys. **32**, 320 (2006).

[193] S. Lee *et al.*, "*Generic character of charge and spin density waves in superconducting cuprates*", Proceedings of the National Academy of Sciences **119**, e2119429119 (2022).

[194] I. Pomeranchuk, "*Stability of a Fermi liquid*", Sov. Phys. JETP **8** (1959).

[195] G. Kotliar, S. Murthy, and M. J. Rozenberg, "*Compressibility Divergence and the Finite Temperature Mott Transition*", Phys. Rev. Lett. **4** (2002).

[196] E. Koch and R. Zeyher, "*Renormalization of the electron-phonon coupling in the one-band Hubbard model*", Phys. Rev. B **70**, 94510 (2004).

[197] M. Eckstein, M. Kollar, M. Potthoff, and D. Vollhardt, "*Phase separation in the particle-hole asymmetric Hubbard model*", Phys. Rev. B **75** (2007).

[198] M. Bejas, A. Greco, and H. Yamase, "*Strong particle-hole asymmetry of charge instabilities in doped Mott insulators*", New Journal of Physics **16**, 123002 (2014).

[199] K. Yamada *et al.*, "*Doping dependence of the spatially modulated dynamical spin correlations and the superconducting-transition temperature in* $La_{2-x}Sr_xCuO_4$", Phys. Rev. B **57**, 6165 (1998).

[200] M. Klett, J. Seufert, D. Riegler, P. Wölfle, and R. Thomale, "*Competing charge-orders in the electron-doped cuprates*", in preparation (2022).

[201] T. Das, R. S. Markiewicz, and A. Bansil, "*Intermediate Coupling Model of the Cuprates*", Advances in Physics **63**, 1 (2014).

[202] E. J. Calegari, S. G. Magalhaes, C. M. Chaves, and A. Troper, "*Pseudogap and the specific heat of high* T_c *superconductors*", Solid State Communications **158**, 20 (2013).

[203] S. J. Joshua, "*Magnon contribution to the specific heat and the validity of power laws in antiferromagnetic crystals*", Physica A: Statistical Mechanics and its Applications **261**, 135 (1998).

[204] A. Matthiessen, "*Report of the British Association for the Advancement of Science*", Rep. Br. Assoc. **32**, 144 (1862).

[205] F. Bloch, "*Zum elektrischen Widerstandsgesetz bei tiefen Temperaturen*", Zeitschrift für Physik **59**, 208 (1930).

[206] L. D. Landau and I. Pomeranchuk, "*Properties of metals at very low temperature*", Phys. Z. Sowjet **10**, 649 (1936).

[207] A. M. Clogston *et al.*, "*Local magnetic moment associated with an iron atom dissolved in various transition metal alloys*", Physical Review **125**, 541 (1962).

[208] M. Sarachik, E. Corenzwit, and L. Longinotti, "*Resistivity of Mo-Nb and Mo-Re Alloys Containing 1% Fe*", Phys. Rev **135**, 1041 (1964).

[209] T. Kasuya, "*A Theory of Metallic Ferro- and Antiferromagnetism on Zener's Model*", Progress of Theoretical Physics **16**, 45 (1956).

[210] J. Bass, W. P. Pratt, and P. A. Schroeder, "*The temperature-dependent electrical resistivities of the alkali metals*", Rev. Mod. Phys. **62**, 645 (1990).

[211] P. W. Anderson, "*A poor man's derivation of scaling laws for the Kondo problem*", Journal of Physics C: Solid State Physics **3**, 2436 (1970).

[212] K. G. Wilson, "*The renormalization group: Critical phenomena and the Kondo problem*", Rev. Mod. Phys. **47**, 773 (1975).

[213] C. Platt, W. Hanke, and R. Thomale, "*Functional renormalization group for multi-orbital Fermi surface instabilities*", Advances in Physics **62**, 453 (2013).

[214] L. Kouwenhoven and L. Glazman, "*Revival of the Kondo effect*", Physics World **14**, 33 (2001).

[215] S. S. Yeh *et al.*, "*Oxygen vacancy-driven orbital multichannel Kondo effect in Dirac nodal line metals* IrO_2 *and* RuO_2", Nat Commun **11**, 1 (2020).

[216] C. Wagner, T. Chowdhury, J. H. Pixley, and K. Ingersent, "*Long-Range Entanglement near a Kondo-Destruction Quantum Critical Point*", Phys. Rev. Lett. **121**, 147602 (2018).

[217] K. Andres, J. E. Graebner, and H. R. Ott, "$4f$*-Virtual-Bound-State Formation in* $CeAl_3$ *at Low Temperatures*", Phys. Rev. Lett. **35**, 1779 (1975).

[218] P. Coleman, *Heavy Fermions: Electrons at the Edge of Magnetism*, (John Wiley & Sons, Ltd, 2007)

[219] S. Doniach, "*The Kondo lattice and weak antiferromagnetism*", Physica B **91**, 231 (1977).

[220] S. Barth *et al.*, "*Onset of Magnetic Correlations in Ce*Al_3 *below 2 K*", Phys. Rev. Lett. **59**, 2991 (1987).

[221] G. Aeppli *et al.*, "*Magnetic order and fluctuations in superconducting* UPt_3", Phys. Rev. Lett. **60**, 615 (1988).

[222] Y. Muro *et al.*, "*Heavy-fermion weak-ferromagnet YbRhSb*", Phys. Rev. B **69**, 020401 (2004).

[223] J. L. Smith and E. A. Kmetko, "*Magnetism or bonding: A nearly periodic table of transition elements*", Journal of The Less-Common Metals **90**, 83 (1983).

[224] F. Steglich *et al.*, "*Superconductivity in the Presence of Strong Pauli Paramagnetism:* $CeCu_2Si_2$", Phys. Rev. Lett. **43**, 1892 (1979).

[225] E. Bucher, J. P. Maita, G. W. Hull, R. C. Fulton, and A. S. Cooper, "*Electronic properties of beryllides of the rare earth and some actinides*", Phys. Rev. B **11** (1975).

[226] D. H. Nguyen *et al.*, "*Superconductivity in an extreme strange metal*", Nat Commun **12**, 4341 (2021).

[227] A. Menth and E. Buehler, "*Magnetic and Semiconducting Properties of Sm*B_6", Phys. Rev. Lett. **22** (1969).

[228] J. C. Nickerson *et al.*, "*Physical Properties of* SmB_6", Phys. Rev. B **3** (1971).

[229] T. Takimoto, "SmB_6 *A Promising Candidate for a Topological Insulator*", J. Phys. Soc. Jpn. **80** (2011).

[230] M. Legner, A. Rüegg, and M. Sigrist, "*Topological invariants, surface states, and interaction-driven phase transitions in correlated Kondo insulators with cubic symmetry*", Phys. Rev. B **89**, 085110 (2014).

[231] M. Dzero, J. Xia, V. Galitski, and P. Coleman, "*Topological Kondo Insulators*", Annual Review of CondeTnsed Matter Physics **7**, 249 (2016).

[232] M. Lavagna and C. Pépin, "*The Kondo Lattice Model*", Acta Physica Polonica B **29**, 3753 (1998).

[233] J. R. Schrieffer and P. A. Wolff, "*Relation between the Anderson and Kondo Hamiltonians*", Phys. Rev. **149**, 491 (1966).

[234] P. Sinjukow and W. Nolting, "*Exact mapping of periodic Anderson model to Kondo lattice model*", Phys. Rev. B **65**, 212303 (2002).

[235] S. E. Barnes, "*New method for the Anderson model: 11. The* $U = 0$ *limit*", J. Phys. F : Metal Phys **7** (1977).

[236] T. M. Rice and K. Ueda, "*Gutzwiller method for heavy electrons*", Phys **34**, 6420 (1986).

[237] S. Burdin, V. Zlatić, and V. Zlatić, "*Multiple temperature scales of the periodic Anderson model: Slave boson approach*", Phys. Rev. B **79**, 1 (2009).

[238] K. Kubo, "*Ferromagnetism and Fermi surface transition in the periodic Anderson model: Second-order phase transition without symmetry breaking*", Phys. Rev. B **87**, 1 (2013).

[239] M. A. Ruderman and C. Kittel, "*Indirect Exchange Coupling of Nuclear Magnetic Moments by Conduction Electrons*", Phys. Rev. **96**, 99 (1954).

[240] K. Yosida, "*Magnetic Properties of Cu-Mn Alloys*", Phys. Rev **106**, 893 (1957).

[241] D. N. Aristov, "*Indirect RKKY interaction in any dimensionality*", Phys. Rev. B **55** (1997).

[242] H. Eskes and R. Eder, "*Hubbard model versus t-J model: The one-particle spectrum*", Phys. Rev. B **54**, 54 (1996).

[243] A. B. Harris and R. V. Lange, "*Single-Particle Excitations in Narrow Energy Bands*", Phys. Rev. **157** (1967).

[244] H.-P. Eckle, "*Models of Strongly Interacting Quantum Matter*", *Models of Quantum Matter: A First Course on Integrability and the Bethe Ansatz*, (Oxford University Press, 2019)

[245] J. M. Luttinger and L. Tisza, "*Theory of Dipole Interaction in Crystals*", Phys. Rev. **70** (1946).

[246] H. Prüser *et al.*, "*Interplay between the Kondo effect and the Ruderman–Kittel–Kasuya–Yosida interaction*", Nat Commun **5**, 1 (2014).

[247] H. V. Löhneysen, A. Rosch, M. Vojta, and P. Wölfle, "*Fermi-liquid instabilities at magnetic quantum phase transitions*", Rev. Mod. Phys. **79** (2007).

[248] F. Lu, J. Zhao, H. Weng, Z. Fang, and X. Dai, "*Correlated topological insulators with mixed valence*", Phys. Rev. Lett. **110**, 096401 (2013).

[249] M. Dzero and V. Galitski, "*A new exotic state in an old material: a tale of* SmB_6", Journal of Experimental and Theoretical Physics **117**, 499 (2013).

[250] D. J. Kim, J. Xia, and Z. Fisk, "*Topological surface state in the Kondo insulator samarium hexaboride*", Nature Materials **13**, 466 (2014).

[251] X. Zhang *et al.*, "*Hybridization, inter-ion correlation, and surface states in the Kondo insulator* SmB_6", Phys. Rev. X **3**, 011011 (2013).

[252] G. Li *et al.*, "*Two-dimensional Fermi surfaces in Kondo insulator* SmB_6", Science **346**, 1208 (2014).

[253] C. E. Matt *et al.*, "*Consistency between ARPES and STM measurements on* SmB_6", Phys. Rev. B **101**, 085142 (2020).

[254] Y. Nakajima, P. Syers, X. Wang, R. Wang, and J. Paglione, "*One-dimensional edge state transport in a topological Kondo insulator*", Nature Physics **12**, 213 (2015).

[255] N. Xu *et al.*, "*Direct observation of the spin texture in* SmB_6 *as evidence of the topological Kondo insulator*", Nat Commun **5**, 1 (2014).

[256] Z. H. Zhu *et al.*, "*Polarity-driven surface metallicity in* SmB_6", Phys. Rev. Lett. **111**, 216402 (2013).

[257] P. Hlawenka *et al.*, "*Samarium hexaboride is a trivial surface conductor*", Nature Communications **9** (2018).

[258] A. Barla *et al.*, "*High-pressure ground state of* SmB_6*: Electronic conduction and long range magnetic order*", Phys. Rev. Lett. **94**, 166401 (2005).

[259] P. K. Biswas *et al.*, "*Low-temperature magnetic fluctuations in the Kondo insulator* SmB_6", Phys. Rev. B(R) **89**, 161107 (2014).

[260] S. Gheidi *et al.*, "*Intrinsic Low-Temperature Magnetism in* SmB_6", Phys. Rev. Lett. **123** (2019).

[261] K. W. Chang and P. J. Chen, "*Anomalous* Z_2 *antiferromagnetic topological phase in pressurized* SmB_6", Phys. Rev. B **97**, 195145 (2018).

[262] W. T. Fuhrman *et al.*, "*Interaction Driven Subgap Spin Exciton in the Kondo Insulator* SmB_6", Phys. Rev. Lett. **114** (2015).

[263] Y. Zhou *et al.*, "*Quantum phase transition and destruction of Kondo effect in pressurized* SmB_6", Science Bulletin **62**, 1439 (2017).

[264] R. Shields, "*Cultural Topology: The Seven Bridges of Königsburg, 1736*", Theory, Culture & Society **29**, 43 (2012).

[265] S.-s. Chern, "*Characteristic Classes of Hermitian Manifolds*", The Annals of Mathematics **47**, 85 (1946).

[266] S.-S. Chern and J. Simons, "*Characteristic Forms and Geometric Invariants*", The Annals of Mathematics **99**, 48 (1974).

[267] M. Kohmoto, "*Topological invariant and the quantization of the Hall conductance*", Annals of Physics **160**, 343 (1985).

[268] Z. C. Gu and X. G. Wen, "*Tensor-entanglement-filtering renormalization approach and symmetry-protected topological order*", Phys. Rev. B **80**, 155131 (2009).

[269] B. Bradlyn *et al.*, "*Topological quantum chemistry*", Nature **547**, 298 (2017).

[270] B. I. Halperin, "*Quantized Hall conductance, current-carrying edge states, and the existence of extended states in a two-dimensional disordered potential*", Phys. Rev. B **25**, 2185 (1982).

[271] M. Z. Hasan and C. L. Kane, "*Colloquium: Topological insulators*", Rev. Mod. Phys. **82**, 3045 (2010).

[272] B. H. Chen and D. W. Chiou, "*An elementary rigorous proof of bulk-boundary correspondence in the generalized Su-Schrieffer-Heeger model*", Physics Letters A **384**, 126168 (2020).

[273] M. König *et al.*, "*Quantum spin hall insulator state in HgTe quantum wells*", Science **318**, 766 (2007).

[274] L. Fu and C. L. Kane, "*Topological insulators with inversion symmetry*", Phys. Rev. B **76**, 045302 (2007).

[275] M. Z. Hasan and J. E. Moore, "*Three-Dimensional Topological Insulators*", Annu. Rev. Condens. Matter Phys. **2**, 55 (2011).

[276] W. A. Benalcazar, B. A. Bernevig, and T. L. Hughes, "*Quantized electric multipole insulators*", Science **357**, 61 (2017).

[277] F. Schindler *et al.*, "*Higher-order topological insulators*", Science Advances **4** (2018).

[278] F. Schindler *et al.*, "*Higher-order topology in bismuth*", Nature Physics **14**, 918 (2018).

[279] C. H. Lee *et al.*, "*Topolectrical Circuits*", Commun Phys **1**, 1 (2018).

[280] T. Ando, Y. Matsumoto, and Y. Uemura, "*Theory of Hall Effect in a Two-Dimensional Electron System*", J. Phys. Soc. Jpn. **39** (1975).

[281] R. B. Laughlin, "*Quantized Hall conductivity in two dimensions*", Phys. Rev. B **23**, 5632 (1981).

[282] D. J. Thouless, M. Kohmoto, M. P. Nightingale, and M. den Nijs, "*Quantized Hall Conductance in a Two-Dimensional Periodic Potential*", Phys. Rev. Lett. **49**, 405 (1982).

[283] T. Neupert, "*Electron fractionalization in two-dimensional quantum systems : Majorana fermions and fractional topological insulators*", PhD thesis, 2013.

[284] C. Chamon, M. Goerbig, R. Moessner, and L. Cugliandolo, *Topological Aspects of Condensed Matter Physics: Lecture Notes of the Les Houches Summer School.* (2014)

[285] M. Berry, "*Quantal phase factors accompanying adiabatic changes*", Proc. R. Soc. Lond. A **392**, 45 (1984).

[286] A. Altland and M. R. Zirnbauer, "*Nonstandard symmetry classes in mesoscopic normal-superconducting hybrid structures*", Phys. Rev. B **55**, 1142 (1997).

[287] S. Ryu, A. P. Schnyder, A. Furusaki, and A. W. Ludwig, "*Topological insulators and superconductors: tenfold way and dimensional hierarchy*", New J. Phys. **12**, 065010 (2010).

[288] A. P. Schnyder, S. Ryu, A. Furusaki, and A. W. Ludwig, "*Classification of topological insulators and superconductors in three spatial dimensions*", Phys. Rev. B **78**, 195125 (2008).

[289] A. Kitaev, "*Periodic table for topological insulators and superconductors*", AIP Conference Proceedings **1134**, 22 (2009).

[290] F. D. Haldane, "*Model for a Quantum Hall Effect without Landau Levels: Condensed-Matter Realization of the "Parity Anomaly"*", Phys. Rev. Lett. **61**, 2015 (1988).

[291] C. L. Kane and E. J. Mele, "Z_2 *topological order and the quantum spin hall effect*", Phys. Rev. Lett. **95**, 146802 (2005).

[292] B. A. Bernevig, T. L. Hughes, and S. C. Zhang, "*Quantum spin hall effect and topological phase transition in HgTe quantum wells*", Science **314**, 1757 (2006).

[293] B. A. Bernevig, *Topological Insulators and Topological Superconductors*, (Princeton University Press, 2013)

[294] H. A. Kramers, "*Théorie générale de la rotation paramagnétique dans les cristaux*", Proceedings of the Royal Netherlands Academy of Arts and Sciences **33**, 959 (1930).

[295] L. Fu and C. L. Kane, "*Time reversal polarization and a* Z_2 *adiabatic spin pump*", Phys. Rev. B **74**, 195312 (2006).

[296] L. Fu, C. L. Kane, and E. J. Mele, "*Topological insulators in three dimensions*", Phys. Rev. Lett. **98**, 106803 (2007).

[297] J. E. Moore and L. Balents, "*Topological invariants of time-reversal-invariant band structures*", Phys. Rev. B **75**, 121306 (2007).

[298] H. B. Nielsen and M. Ninomiya, "*Absence of neutrinos on a lattice: (I). Proof by homotopy theory*", Nuclear Physics B **185**, 20 (1981).

[299] H. B. Nielsen and M. Ninomiya, "*The Adler-Bell-Jackiw anomaly and Weyl fermions in a crystal*", Physics Letters **130B**, 389 (1983).

[300] L. Fu, "*Topological crystalline insulators*", Phys. Rev. Lett. **106**, 106802 (2011).

[301] L. Elcoro *et al.*, "*Magnetic topological quantum chemistry*", Nat Commun **12**, 1 (2021).

[302] V. N. Antonov, B. N. Harmon, and A. N. Yaresko, "*Electronic structure of mixed-valence semiconductors in the* LSDA + U *approximation. II.* SmB_6 *and* YbB_{12}", Phys. Rev. B **66**, 165209 (2002).

[303] R. Yu, H. Weng, X. Hu, Z. Fang, and X. Dai, "*Model Hamiltonian for topological Kondo insulator Sm*B_6", New Journal of Physics **17**, 023012 (2015).

[304] W. A. Phelan *et al.*, "*Correlation between Bulk Thermodynamic Measurements and the Low-Temperature-Resistance Plateau in* SmB_6", Phys. Rev. X **4** (2014).

[305] M. Klett *et al.*, "*Supplemental material: Topology and magnetism in the Kondo insulator phase diagram*", Phys. Rev. B **101**, 1 (2020).

[306] R. S. Mong, A. M. Essin, and J. E. Moore, "*Antiferromagnetic topological insulators*", Phys. Rev. B **81**, 245209 (2010).

[307] C. Fang, M. J. Gilbert, and B. A. Bernevig, "*Topological insulators with commensurate antiferromagnetism*", Phys. Rev. B **88**, 085406 (2013).

[308] H. Li, Y. Zhong, Y. Liu, H. G. Luo, and H. F. Song, "Z_2 *classification for a novel antiferromagnetic topological insulating phase in three-dimensional topological Kondo insulator*", Journal of Physics: Condensed Matter **30**, 435601 (2018).

[309] N. P. Butch *et al.*, "*Pressure-Resistant Intermediate Valence in the Kondo Insulator* SmB_6", Phys. Rev. Lett. **116**, 156401 (2016).

[310] L. Miao *et al.*, "*Robust Surface States and Coherence Phenomena in Magnetically Alloyed* SmB_6", Phys. Rev. Lett. **126** (2021).

[311] F. Wilczek, "*Two Applications of Axion Electrodynamics*", Phys. Rev. Lett. **58**, 1799 (1987).

[312] N. Varnava and D. Vanderbilt, "*Surfaces of axion insulators*", Phys. Rev. B **98**, 245117 (2018).

[313] M. M. Otrokov *et al.*, "*Prediction and observation of an antiferromagnetic topological insulator*", Nature **576**, 416 (2019).

[314] S. Y. Xu *et al.*, "*Hedgehog spin texture and Berry's phase tuning in a magnetic topological insulator*", Nature Physics **8**, 616 (2012).

[315] Y. Cao *et al.*, "*Strange Metal in Magic-Angle Graphene with near Planckian Dissipation*", Phys. Rev. Lett. **124**, 076801 (2020).

[316] D. Li *et al.*, "*Superconductivity in an infinite-layer nickelate*", Nature **572**, 624 (2019).

[317] Z.-D. Song and B. A. Bernevig, "*MATBG as Topological Heavy Fermion: I. Exact Mapping and Correlated Insulators*", arXiv preprint (2021), arXiv: 2111.05865.

[318] G. Cardano, *Artis Magnae, Sive de Regulis Algebraicis Liber Unus*, (1545)

[319] M. Abramowitz and I. A. Stegun, *Handbook of Mathematical Functions: With Formulas, Graphs, and Mathematical Tables*, (United States Department of Commerce, 1964)

[320] GSL Team, *Multidimensional Minimization*, 2022, URL: https://www.gnu.org/software/gsl/doc/html/multimin.html (visited on 05/01/2022).

List of publications

1. **D. Riegler**, M. Klett, T. Neupert, R. Thomale, and P. Wölfle, "*Slave-boson analysis of the two-dimensional Hubbard model*", Phys. Rev. B **101**, 235137 (2020).

2. M. Klett*, S. Ok*, **D. Riegler***, P. Wölfle, R. Thomale, and T. Neupert, "*Topology and magnetism in the Kondo insulator phase diagram*", Phys. Rev. B **101**, 161112(R) (2020).

3. J. Seufert*, **D. Riegler***, M. Klett*, R. Thomale, and P. Wölfle, "*Breakdown of charge homogeneity in the 2D Hubbard model - slave-boson study of magnetic order*", Phys. Rev. B **103**, 165117 (2021).

4. M. Klett*, T. Schwemmer*, S. Wolf, X. Wu, **D. Riegler**, A. Dittmaier, D. Di Sante, G. Li, W. Hanke, S. Rachel and R. Thomale, *From high T_c to low T_c: Multiorbital effects in transition metal oxides* Phys. Rev. B, **104**, L100502 (2021).

5. M. Klett*, **D. Riegler***, P. Wölfle, and R. Thomale, "*Emerging Kondo regime in the periodic Anderson model*", (in preparation).

6. M. Klett*, J. Seufert*, **D. Riegler***, P. Wölfle, and R. Thomale, "*Competing types of charge-order in the electron-doped high-T_c cuprates*", (in preparation).

*These authors contributed equally to the work.

List of figures

List of tables

List of acronyms

1D	one-dimensional
2D	two-dimensional
3D	three-dimensional
ABC	anti-periodic boundary conditions
AFM	antiferromagnetism / antiferromagnet / antiferromagnetic
AFMI	antiferromagnetic insulator
AFMM	antiferromagnetic metal
AFMMI	antiferromagnetic Mott insulator
AFQMC	auxiliary-field quantum Monte Carlo
AIM	Anderson impurity model
ARPES	angle-resolved photoemission spectroscopy
ATI	antiferromagnetic topological insulator
AXI	axion insulator
AZ	Altland–Zirnbauer
BCS	Bardeen–Cooper–Schrieffer
BI	band insulator
BS	band structure
BW	bandwidth
BZ	Brillouin zone
CDW	charge-density-wave
CMP	condensed matter physics
CO	charge-order / charge-ordered
DFT	density functional theory
DMET	density matrix embedding theory
DMFT	dynamical mean-field theory
DOS	density of states
ED	exact diagonalization
EELS	electron-energy-loss-spectroscopy
EKL	extended Kondo limit

FE free energy
FL Fermi liquid
FM ferromagnetism / ferromagnet / ferromagnetic
FRG functional renormalization group
FS Fermi surface
FT Fourier transformation

GP grand potential

HOTI higher-order topological insulator
HSL high symmetry line
HSP high symmetry point
HTCC high-T_c cuprate
HTS high-temperature superconductor / high-temperature superconductivity

ICM incommensurate magnet / incommensurate magnetism / incommensurate magnetic
INS inelastic neutron scattering
IS inversion symmetry / inversion symmetric

KI Kondo insulator
KLM Kondo lattice model
KM Kondo model
KR Kotliar–Ruckenstein

LBCO Lanthanum barium copper oxide ($Ba_2Cu_3LaO_7$)
LM Lagrange multiplier

MF mean-field
MI Mott insulator
MWH Mermin-Wagner-Hohenberg

NCCO Neodymium cerium copper oxide ($Nd_{2-x}Ce_xCuO_4$)
NN nearest neighbor
NNN next-to-nearest neighbor

PAM periodic Anderson model
PBC periodic boundary conditions
PF pseudofermion / pseudofermionic
PG pseudogap
PHS particle-hole symmetry
PM paramagnetism / paramagnet / paramagnetic
PS phase separation / phase separated

QCP quantum critical point
QHE quantum Hall effect
QM quantum mechanics / quantum mechanical
QMC quantum Monte Carlo

QP quasiparticle
QSHE quantum spin Hall effect

RKKY Ruderman–Kittel–Kasuya–Yosida
RPA random phase approximation
RXS resonant X-ray scattering

SARPES spin- and angle-resolved photoemission spectroscopy
SB slave-boson
SBZ surface Brillouin zone
SC superconductivity
SCRIKR spin- and charge-rotation invariant Kotliar–Ruckenstein
SDW spin-density-wave
SOC spin-orbit coupling
SPT symmetry-protected topological
SRI spin-rotation invariance / spin-rotation invariant
SRIKR spin-rotation invariant Kotliar–Ruckenstein
STI strong topological insulator
SW Schrieffer–Wolff

TCI topological crystalline insulator
TI topological insulator
TRIM time-reversal-invariant momentum
TKI topological Kondo insulator
TKNN Thouless–Kohmoto–Nightingale–den Nijs
TR time-reversal
TRS time-reversal symmetry / time-reversal symmetric
TSS topologically protected surface state

UHB upper Hubbard band

WTI weak topological insulator

YBCO Yttrium barium copper oxide ($YBa_2Cu_3O_{7-x}$)

ZR Zhang-Rice

Acknowledgments

This thesis would not have been possible without the support of numerous colleagues and friends during my Ph.D. time. First and foremost, I would like to thank my advisor Ronny Thomale for giving me the opportunity to work in his group and sharing his extensive physical knowledge and out-of-the-box thinking that broadened my horizon in physics. Thereby, I often co-worked as a "*cooper pair*" – as Ronny would say with his unique style of humor – together with my close collaborator and good friend Michael Klett. After working through countless exercise sheets during my Bachelor's degree, Michael was also a moral and professional support during my Ph.D. and a vital contributor to all our projects and the development of the slave-boson method.

Moreover, I want to express my gratitude to my co-advisor, Titus Neupert, who was always a reliable partner and whose insights in topological Kondo insulators and especially higher-order topology were of major importance to establish the presented results. I also want to thank his former students Markus Legner, who introduced me to Kondo insulators and the auxiliary particle approach, and Seulgi Ok for numerous discussions about topological phases.

I am also sincerely grateful to Prof. Peter Wölfle for sharing his exhaustive knowledge about slave-bosons and Kondo physics, which helped to integrate my results within a broader physical context. Another slave-boson expert is Jannis Seufert, whom Michael and I introduced to the method during his Master's thesis. While I was predominantly occupied with evaluating the magnetic mean-field saddle point equations, he was in leading responsibility for the numerical implementation of the magnetic fluctuation matrix, with all its complicated index shifts. After many hours of benchmarking with the existing, independent code for paramagnetic fluctuations, we were finally able to make it work. He thus significantly contributed to many of the results, which I am very grateful for. Finally, I want to thank Florian Goth in that context, who, with his magic in performance optimization, was a great help in making the numerics fast and efficient.

I also want to thank Tobias Müller – who was my office mate together with Michael, making the three of us known as *Tobis Büro* – for endless discussions about physics beyond the mean-field tunnel vision and life in general. Moreover, I gratefully acknowledge all other members of the TP1, especially thinking of our trip to the APS March Meeting 2019 in Boston, where we shared an Airbnb and enjoyed our stay as a group.

Finally, I want to thank Melanie, Michael, Jannis, Korbinian, Elisabeth, Anne, Daniel, and Hans for reading parts of my thesis, and all my friends who cheered for me through the ups and downs during my Ph.D. Last but not least, I want to thank my parents and my sister for their constant love and support.